



## City Research Online

### City, University of London Institutional Repository

---

**Citation:** Zhang, S.H. (1982). The finite element analysis of thin-walled box spine-beam bridges. (Unpublished Doctoral thesis, City University London)

This is the accepted version of the paper.

This version of the publication may differ from the final published version.

---

**Permanent repository link:** <https://openaccess.city.ac.uk/id/eprint/7723/>

**Link to published version:**

**Copyright:** City Research Online aims to make research outputs of City, University of London available to a wider audience. Copyright and Moral Rights remain with the author(s) and/or copyright holders. URLs from City Research Online may be freely distributed and linked to.

**Reuse:** Copies of full items can be used for personal research or study, educational, or not-for-profit purposes without prior permission or charge. Provided that the authors, title and full bibliographic details are credited, a hyperlink and/or URL is given for the original metadata page and the content is not changed in any way.

THE FINITE ELEMENT ANALYSIS OF THIN-WALLED

BOX SPINE-BEAM BRIDGES

A thesis submitted for the degree of Doctor of Philosophy  
in the Department of Civil Engineering  
at The City University

by

S. H. Zhang

February, 1982

To my parents  
and  
to my beloved country

*ABSTRACT*

This thesis considers the theoretical and experimental analysis of thin-walled box spine-beam bridges. Existing methods available for the analysis of spine-beam bridges have been reviewed, with special attention being paid to thin-walled box beam theories. A new approach combining the finite element technique and the thin-walled beam theory, which is appropriate for design purposes, has been proposed. This approach is specially suitable for medium and long spans. It is intended to be a realistic and versatile method to be used during the preliminary analysis and design stage, when a full three-dimensional analysis is likely to be impractical.

Special features related to the bending analysis of thin-walled members and the warping torsion theory of open and closed section members are summarized in the thesis. In addition, supplementary formulae for the calculation of the stress distributions and the thin-walled section properties are derived. The distortional effect on single-spined box beams subjected to torsion has been extended to a general form based on the principles of ordinary folded plate theory.

A family of special one-dimensional sub-parametric elements has been developed. In addition to the usual truss and beam elements the family includes a general thin-walled box beam element which may be curved in space and may have a variable cross-section. Additional degrees of freedom have been included to account for the warping and distortion effects which occur in box beams. An inclined cable element with catenary action is included, and an approximate nonlinear process for the analysis of cable-stayed bridges has been correlated with tests on an actual bridge structure. A finite element-grillage approach for the analysis of multibox structures with deformable sections has also been developed. The complete family of elements has been incorporated into a computer program called CUBAS.

A supplementary program called PFRAN for calculating the distortional properties and the influence values of the equivalent Vierendeel frame has also been implemented.

The accuracy of the results obtained is demonstrated by comparison with results obtained by other published methods. A series of model box beams were tested to further substantiate the theoretical results. The model dimensions were chosen to highlight both warping and cross-sectional distortion effects. The degree of correlation obtained shows that the theoretical developments proposed in this thesis may be applied successfully to the analysis of box spine-beam bridges.

*ACKNOWLEDGEMENTS*

The research described herein was undertaken in the Civil Engineering Department of The City University. During the course of the research the author received kind help, valuable advice and helpful suggestions from many persons. In particular the author wishes to express his gratitude to the following:

To Professor P.O. Wolf as Head of Department, and to Professor J.E. Gibson as Head of the Structural Division, for the helpful way in which they accommodated the project and for their kind concern throughout the duration of the project.

To Dr. L.F. Boswell, who supervised this work, for all his constant encouragement, thoughtful arrangements and valuable advice throughout the project, without which the work would not have been fulfilled effectively.

To Dr. M.R. Barnes, who provided helpful and constant supervision during the course of the study, and gave many important suggestions after reading the thesis.

The author is extremely grateful to Dr. S. Gill, Dr. K.S. Viridi, Mr. D.A. Chamberlain, Mr. A.R. Mohamed and Mr. S.S. Wong for their valuable advice on many aspects of this project, and for their generous help in many ways. Dr. S. Gill devoted a great effort to help to improve the presentation of the thesis.

The author is also very grateful to Dr. L.P.R. Lyons for his help and advice regarding the LUSAS finite element program.

The assistance and effort provided by the technical staff of the Structures Laboratories is greatly appreciated by the author.

Thanks are due to Janet Prange who typed the manuscript.

A special word of thanks is given to my family and friends for their love, support and encouragement.

Last, but not least, the author would like to express his deep gratitude to Professor G.H. Lie for his help and concern, and to the Chinese Government for their financial support.

## NOTATION

Only the main symbols in the text are listed here. All other symbols are defined as they first appear.

$A$	cross-sectional area
$A_{sx}, A_{sy}$	effective shear cross-sectional areas in the x-direction and the y-direction respectively
$b$	total breadth of the top flange of the whole cross-section
$\mathbf{b}$	body force vector
$b_t, b_b$	top and bottom breadths between mid-lines of the side webs respectively
$b_{t,i}, b_{b,i}$	top and bottom breadths between mid-lines of webs of the $i^{\text{th}}$ cell respectively
$b_c$	breadth of cantilever slab
$b_{e,i}$	effective breadth between mid-lines of webs
$\bar{\mathbf{B}}$	strain matrix
$B_I$	torsional warping bimoment
$B_{II}$	distortional warping bimoment
$B_{ext}$	concentrated applied bimoment
$b_I$	distributed applied torsional warping bimoment
$b_{II}$	distributed applied distortional warping bimoment
$D$	transverse flexural rigidity of an individual plate
$D_t, D_b, D_h$	transverse flexural rigidities of the top and bottom slabs and the side webs respectively
$\bar{\mathbf{D}}$	generalized elasticity matrix
$\{\mathbf{D}_q\}$	displacement vector due to the open section shear flow $q_b$

$D_{q,i} = -\oint_i \frac{q_{b,i}}{t} ds$	$i^{\text{th}}$ term in the displacement vector $\{D_q\}$
$E$	Young's modulus of elasticity
$E_1 = E/1-\nu^2$	conversion modulus of elasticity
$E_{eq}$	equivalent modulus of elasticity of the inclined cable
$e_x, e_y$	eccentricities of the applied load relating to the shear centre in the x-direction and the y-direction respectively
$\bar{e}_y$	vertical ordinate of the twisting centre with reference to the mid-line of the top flange
$F$	structure nodal force vector
$F^e$	element nodal force vector
$\bar{F}$	applied force vector
$F_{s,x}, F_{s,y}$	shear-deformation factors in the x-direction and the y-direction respectively
$[f]$	flexibility influence coefficient matrix
$f_{ik} = -\int_{i,k} \frac{ds}{t}$	flexibility coefficient ——— integral along the common wall between cell i and cell k
$f_{ii} = \oint_i \frac{ds}{t}$	flexibility coefficient — contour integral along the circumference of cell i
$G$	shear modulus of elasticity
$G^e$	element geometrical function vector
$h$	depth between mid-lines of top and bottom slabs
$h_c$	length of the web
$I_{xx}, I_{yy}$	moments of inertia of entire cross-section about the centroidal x and y axes respectively
$\hat{i}, \hat{j}, \hat{k}$	unit vectors in the global X, Y and Z directions respectively
$J$	Jacobian factor
$J_1, J_2, J_3$	Jacobian factors at the 1st, 2nd and 3rd nodes of the element respectively

$J_V$	St. Venant torsional moment of inertia
$J_B$	Bredt torsional moment of inertia
$J_T$	total torsional moment of inertia
$J_C$	central second moment of area
$J_I$	torsional warping moment of inertia
$J_{II}$	distortional warping moment of inertia
$J_d$	distortional second moment of area
$K, K_0$	structure stiffness matrix
$K^e$	element stiffness matrix
$K_T$	tangent stiffness matrix
$k_d = E_1 J_d$	distortional frame stiffness of the box-section per unit length
$L$	horizontal length of the inclined cable or the length of span
$l$	length of element
$M$	shape functions for mapping the element geometry
$M_d$	distortional moment
$m_d$	distributed distortional moment
$m_{db}$	transverse distortional bending moment per unit length
$\bar{m}_{db}$	influence value of the transverse distortional bending moment per unit length
$m_{dH}$	distortional moment per unit length due to the horizontal eccentric loading
$m_{dR}$	additional distortional moment per unit length due to the initial in-plan curvature

$m_{dv}$	distortional moment per unit length due to the vertical eccentric loading
$m_{lb}$	longitudinal bending moment per unit width of the plate due to Poisson's ratio effect
$m_s$	transverse bending moment
$M_{T,v}$	St. Venant torsional moment component
$M_{T,B}$	Bredt torsional moment component
$M_{T,p}$	primary torsional moment referred to the St. Venant shear stresses and/or the Bredt shear stresses
$M_{T,I}$	secondary or flexural torsional moment resulting from the warping shear stresses
$M_T$	total torsional moment
$M_x, M_y$	internal bending moments about the centroidal x and y axes respectively
$M_{x,ext}$	concentrated applied moment about the X axis
$M_{y,ext}$	concentrated applied moment about the Y axis
$M_{z,ext}$	concentrated applied moment about the Z axis
$m_{x,ext}, m_{y,ext}$	distributed applied bending moments about the x and y axes respectively
$m_{z,ext}$	distributed applied twisting moment
$m_{zH}$	distributed applied twisting moment due to the horizontal eccentric loading
$m_{zV}$	distributed applied twisting moment due to the vertical eccentric loading
$\bar{N}$	shape functions for defining the displacement field
$N_z$	internal axial force

$P$	concentrated applied force vector
$P_x, P_y, P_z$	concentrated applied force components in the X, Y and Z directions respectively
$P_x, P_y, P_z$	distributed applied force components in the x, y and z directions respectively
$q$	shear flow
$q^e$	distributed force vector for an element
$q_b$	open section shear flow
$q_0$	statically indeterminate shear flow in longitudinal bending
$q_s$	total shear flow in longitudinal bending
$q_B$	Bredt's shear flow
$\bar{q}_B$	Bredt's unit shear flow function
$q_I^o$	redundant torsional warping shear flow for a closed section
$\bar{q}_I^o$	unit shear flow function in warping torsion for a closed section
$q_T$	torsional warping shear flow
$q_T$	total shear flow in warping torsion
$q_{II}^o$	redundant distortional warping shear flow
$\bar{q}_{II}^o$	unit shear flow function in distortion
$q_{II}$	distortional warping shear flow
$q_{db}$	transverse distortional shear force per unit length
$\bar{q}_{db}$	influence value of the transverse distortional shear force per unit length
$Q_x, Q_y$	internal shear forces in the x and y directions respectively
$\bar{q}_x = -S_y$	open section shear flow due to unit shear force ( $\frac{Q_x}{I_{yy}} = 1$ )

$\bar{q}_y = -S_x$	open section shear flow due to unit shear force ( $\frac{Q_y}{I_{xx}} = 1$ )
R	radius of curvature
R	residual force vector
$R_t$	perpendicular distance from the centre of twist to the tangent to the mid-line of wall at the point considered
S	curvilinear coordinate along mid-line of wall
$S_I$	sectorial statical moment of area for an open section
$\hat{S}_I$	sectorial statical moment of area for a closed section
$\{\bar{S}_I\}$	displacement vector of the flexibility equations for determining the redundant torsional warping shear flow
$\bar{S}_{I,i} = \oint_i \hat{S}_I \frac{ds}{t}$	$i^{\text{th}}$ term in the displacement vector $\{\bar{S}_I\}$
$S_{II}$	distortional statical moment of area
$\hat{S}_{II}$	reduced distortional statical moment of area
$\{\bar{S}_{II}\}$	displacement vector of the flexibility equations for determining the redundant distortional warping shear flow
$\bar{S}_{II,i} = \oint_i S_{II} \frac{ds}{t}$	$i^{\text{th}}$ term in the displacement vector $\{\bar{S}_{II}\}$
$S_x, S_y$	first moments of area about the centroidal x and y axes respectively
$\hat{S}_{\omega x}, \hat{S}_{\omega y}$	sectorial products of inertia about the centroidal x and y axes respectively
T	tensile force of the inclined cable along the chord
t	thickness of wall
$t_c$	thickness of cantilever slab
$t_t$	thickness of top slab
$t_b$	thickness of bottom slab

$t_h$	thickness of web
$t_p$	thickness of diaphragm
$\mathbf{u}$	vector of displacements at any point within a section
$\bar{\mathbf{u}}$	generalized displacement field in the local coordinate system
$u, v, w$	translations of the centroid along the x, y and z directions respectively
$U, V, W$	translations of the centroid along the X, Y and Z directions respectively
$u_t, v_n, w_z$	displacement components of a point on the mid-line of wall, in the generalized coordinate system (z, S)
$u_x, v_y, w_z$	displacement components of a point in the local Cartesian coordinate system
$u_1, v_1$	displacements of the top-left corner associated with the Vierendeel frame analysis, in the x and y directions respectively
$u_2, v_2$	displacements of the top-right corner associated with the Vierendeel frame analysis, in the x and y directions respectively
$\bar{u}_t, \bar{v}_t$	displacements of the top corner of the box-section associated with distortion, in the x and y directions respectively
$\bar{u}_b, \bar{v}_b$	displacements of the bottom corner of the box-section associated with distortion, in the x and y directions respectively
$v_h$	displacement tangential to the side web

$w_g$	weight per unit length of the inclined cable
$\hat{x}, \hat{y}, \hat{z}$	unit vectors in the local x, y and z directions respectively
$y_G$	vertical ordinate of the centroid with reference to the mid-line of the top flange
$y_S$	vertical ordinate of the shear centre with reference to the mid-line of the top flange
$\alpha$	stiffening factor for the effective breadth ratio
$\alpha_i, \lambda_i, \psi_i$	cross-sectional ratios associated with distortion
$\alpha_d$	ratio ( $b_b/b_t$ )
$\beta$	ratio ( $-\omega_{II,n+3} / \omega_{II,1}$ )
$\gamma_{x\bar{z}}, \gamma_{y\bar{z}}, \gamma_{\bar{z}s}$	shear strain
$\gamma_d$	distortional angle
$\bar{\gamma}_d$	influence distortional angle
$\delta$	vector of global nodal displacements
$\bar{\delta}$	vector of global displacements and derivatives at any point on the element axis
$\bar{\delta}^e$	vector of global nodal displacements and derivatives for an element
$\bar{\epsilon}$	generalized strain vector
$\epsilon_{\bar{z}}$	normal component of strain in the z direction
$\epsilon_s$	transverse normal strain component
$\zeta$	natural coordinate in the eta direction
$\zeta_d$	distortional distribution factor
$\eta_1, \eta_2$	parameters for frame stiffness or transverse corner moments respectively
$\theta_x, \theta_y$	rotations about the centroidal x and y axes respectively

$\theta_z$	total angle of twist
$\theta_{z,p}$	primary angle of twist
$\theta_{z,s}$	secondary angle of twist
$\varpi$	rate of twisting angle
$\lambda$	transformation matrix
$\mu_d$	initial curvature multiplication factor
$\mu_t$	torsional warping shear parameter
$\nu$	Poisson's ratio
$\xi_d$	torsional stiffness reduction factor
$\Pi$	external potential energy
$\rho$	weight density of the material
$\rho_z, \rho_s$	strain gauge readings in the longitudinal and transverse directions respectively
$\bar{\sigma}$	generalized stress vector
$\sigma_{db}$	transverse distortional bending stress
$\bar{\sigma}_{db}$	influence value of the transverse distortional bending stress
$\sigma_I$	torsional warping stress
$\sigma_{II}$	distortional warping stress
$\sigma_{z,b}$	longitudinal bending stress
$\sigma_z$	normal stress component in the z direction
$\sigma_s$	normal stress component in the transverse direction
$\sigma_R$	radial component of the longitudinal bending stress
$\tau_s$	shear stress in longitudinal bending
$\tau_v$	St. Venant shear stress
$\tau_B$	Bredt's shear stress

$\tau_I$	torsional warping shear stress
$\tau_T$	total shear stress in warping torsion
$\tau_{II}$	distortional warping shear stress
$\phi$	angle of the top flange with respect to the inclined side web
$\phi_{\bar{z}}$	rotation of the web
$\phi_x, \phi_y, \phi_z$	rotations about the global X, Y and Z axes respectively
$\psi_d$	rate of distortion
$\psi_{\bar{z},t}, \psi_{\bar{z},b}$	rotations of the top and bottom flanges respectively
$\psi_e$	effective breadth ratio
$\omega_I$	unit torsional warping function or the normalized sectorial coordinate for an open section
$\hat{\omega}_I$	unit torsional warping function or the normalized reduced sectorial coordinate for a closed section
$\omega_{II}$	unit distortional warping function
$\{\Omega\}$	displacement vector of the flexibility equations for determining the Bredt's shear flow function
$\Omega_i$	twice the enclosed area of the $i^{\text{th}}$ cell

## CONTENTS

	Page
Abstract	III
Acknowledgements	V
Notation	VII
Chapter 1	1
Introduction and Review of Available Analytical Methods	
1.1	1
General remarks and presentation of the thesis	
1.2	5
Types of structural action	
1.3	7
Review of analytical methods for thin-walled box spine-beam bridges	
1.3.1	7
Analysis of box beams as thin-walled beams	
1.3.2	11
Analysis of box beams as folded plate structures	
1.3.3	13
Analysis of box beams using the finite element method	
1.3.4	18
Some other methods of box beam analysis	
1.4	21
Coordinate systems and sign conventions	
1.5	22
Basic assumptions and fundamental equations of elasticity	
Chapter 2	36
Bending and Torsion of Thin-Walled Members	
2.1	36
Introduction	
2.2	37
Direct and shear stress distribution due to bending	
2.3	46
Effects of shear lag	
2.4	49
Pure torsion of open and closed section members	
2.5	54
Deformation of cross-sections	
2.6	57
State of stress system of warping torsion	
2.7	62
Shear centre and twisting centre	
2.8	67
Basic differential equation for warping torsion	
2.9	69
Calculation of sectional properties in bending and warping torsion	
Chapter 3	87
The Effect of Cross-Sectional Deformation on Single-Spined Box Beams Subjected to Torsion	
3.1	87
Introduction	
3.2	89
Distortional component of eccentric loading	

	Page	
3.3	Deformation of single-spined box beam	94
3.4	Distribution of normal and shear stresses over the cross-section	97
3.5	Resistance of cross-section to distortion	112
3.6	Calculation of transverse bending stresses and the properties of diaphragms	118
3.7	Single-spined box beams curved in plan	123
3.8	Basic differential equation for distortion	126
3.9	Interaction between bending, torsion and distortion	128
Chapter 4	A One Dimensional Finite Element Family	151
4.1	Introduction	151
4.2	Geometric definition	153
4.2.1	Geometric definition of a thin-walled box beam element	153
4.2.2	Definition of the local orthogonal coordinate system	154
4.3	Displacement field and degrees of freedom	158
4.3.1	Displacement field due to axial loading and bending	158
4.3.2	Displacement field due to warping torsion and distortion	159
4.3.3	Degrees of freedom	161
4.4	Strain components and stress resultants	162
4.4.1	Strains and stress resultants due to axial loading and bending	162
4.4.2	Strains and stress resultants due to warping torsion	166
4.4.3	Strains and stress resultants due to distortion	170
4.4.4	Generalized stress-strain relation	171
4.5	Transformation of nodal displacements	172
4.6	Sub-parametric formulation	176
4.6.1	Shape functions for mapping the element geometry	176
4.6.2	Shape functions for defining the displacement field	179
4.6.3	Displacement field	181
4.6.4	Strains	183
4.7	Element stiffness matrix and equivalent nodal forces	187

	Page	
4.8	Boundary conditions	190
4.9	Internal forces at the ends of the individual elements	193
Chapter 5	Numerical Examples and Applications	198
5.1	Introduction	198
5.2	Numerical examples	198
5.2.1	A deep cantilever beam	198
5.2.2	L-type cantilever frame	199
5.2.3	A semi-circular beam	199
5.2.4	Dome structure	200
5.3	Application to the analysis of single-spined box beams	200
5.3.1	A simply-supported box beam subjected to an eccentric live point load	200
5.3.2	A fixed-end box beam subjected to an eccentric live point load	201
5.3.3	Simply-supported box beam example given by Vlasov	201
5.3.4	Simply-supported box beam example given by Křistek	202
5.3.5	Sawko and Cope's simply-supported box girder model	202
5.3.6	Tapered box girder models given by Křistek	203
5.3.7	A double-cell box beam under twisting loads	205
5.3.8	A two-span 3-cell box-bridge given by Scordelis and Davis	205
5.3.9	A simply-supported single-box girder bridge curved in plan	206
5.4	Box beam diaphragms	207
5.5	Conclusion	209
Chapter 6	A Finite Element-Grillage Approach to the Analysis of Multibox Bridge Structures	237
6.1	General	237
6.2	Grillage idealization of multi-spined box beams	239
6.3	Determination of grillage element properties	242
6.4	An iterative process for assessing distortional effects	245
6.5	Numerical example of a composite twin-box beam	248
6.6	Analysis of articulated cellular bridge decks	249

	Page	
Chapter 7	Static Analysis of Cable-Stayed Bridges	272
7.1	Introductory remarks	272
7.2	Geometric configuration of cable-stayed bridges	274
7.2.1	Span arrangements	274
7.2.2	Stay geometry	275
7.2.3	Superstructure types	276
7.2.4	Tower types	276
7.3	Brief review of some of the existing analytical methods	277
7.4	Behaviour of catenary-stayed cables	278
7.5	Stiffness method of analysis with approximate nonlinear considerations	282
7.6	Numerical example and analysis of Santai cable-stayed bridge	289
Chapter 8	Experimental Investigation	320
8.1	Objectives of the experimental investigation	320
8.2	Description of the model structures	321
8.2.1	Dimensions and fabrication of the model	321
8.2.2	Material property	323
8.2.3	Instrumentation	324
8.2.4	Loading system and testing procedure	326
8.3	Experimental and theoretical results	327
8.3.1	Calculation of the experimental results	327
8.3.2	Theoretical solutions	332
8.3.3	Comparison of the theoretical and experimental results for the models	333
8.4	Summary and conclusions of the results obtained from the experimental work	338
Chapter 9	Conclusions and Recommendations for Future Work	393
References		399
Appendix I	Computer Program - CUBAS	415
I.1	General introduction	415
I.2	Scope and general procedure	416
I.3	Data input to CUBAS	418
I.4	Error diagnostics	439
I.5	Data input examples	443
I.5.1	A simply-supported single-box girder bridge curved in plan	443
I.5.2	Simply-supported twin-box beam model	444

	Page
Appendix II Data Input to Computer Program PFRAN	447
Appendix III Sectional Property Fomulae for a Trapezoidal Single-Cell Box-Section.	452

## CHAPTER 1

## INTRODUCTION AND REVIEW OF AVAILABLE ANALYTICAL METHODS

1.1 General remarks and presentation of the thesis

Many different deck arrangements are possible in bridge construction and a logical classification system can be proposed as shown in Fig. 1.1 (67). Box spine-beams have been used in single or multiple cells together with arrangements whereby several box beams are combined to form a complete bridge deck.

The essential difference between spine-beam bridges and other bridge superstructures is due mainly to differences in plan geometry. In practice, spine-beam bridges may be defined as structural members whose breadth and depth are small in relation to their length and which are, therefore, subjected mainly to longitudinal bending, transverse shear and torsion. They are generally stiff members whose cross-section consists of a hollow box beam having one or more cells, with or without cantilevers. Transverse diaphragms are normally provided only over the supports. The transition between the true spine type and the cellular slab is not always well defined, although Swann (136) specified that for spine-beams in general the total number of cells in the spine should be less than five. Typical cross-sections of bridges of this type which have been built in practice are shown in Fig. 1.2.

The spines provide the main source of strength in single-spined or multi-spined superstructures. The hollow box section of the spine contributes considerably to the torsional stiffness of the bridge and distributes the transverse (lateral) load. Thus, the box section leads to a significantly favourable pattern of flexural and shear stresses, when considered in

conjunction with its high longitudinal bending strength. This therefore results in saving of materials, and reduced depth of construction. The slender proportions and simple form of this type of bridge provide a pleasant appearance and in addition, this bridge type is easy to erect and maintain. These advantages explain the popular use of spine-beams in a variety of modern steel and prestressed concrete bridge structures. Box spine-beams are particularly advantageous to bridges having medium or long spans and to bridges which are curved in plan.

Structural design of spine-beam bridges presents many difficulties because of the complex nature of the interaction of individual elements. A large amount of research effort has been devoted to spine-beam analysis, and a considerable amount of literature has been published on the very wide range of analytical methods available. The existing methods can be classified into three general categories which are called the thin-walled beam theory, the folded plate method and the finite element method. Maisel and Roll (82, 83) have made an extensive literature survey and have reviewed almost all the methods developed hitherto. Many of these methods are complex, somewhat academic and have limitations in the structural forms they can idealize.

A three-dimensional finite element analysis can, of course, offer the most comprehensive treatment. It can readily take into account a variety of structural geometries, supports and loading conditions, and has made possible the accurate assessment of structural effects. However, such an analysis involves very extensive computations which lead to expensive computing costs and in some cases to voluminous computing output.

At the preliminary analysis and design stage it is likely to be impractical to conduct a full three-dimensional analysis, since the bridge geometries and loading conditions, etc., could be modified for instance.

It is, therefore, desirable at this stage to use a realistic but simplified method of analysis which is both accurate and economic. Such a method should indicate those areas which require a more accurate analysis.

As a result of the work presented in this thesis a finite beam approach, with idealization only in the spanwise direction, developed on the basis of thin-walled beam theory seems to fulfil the requirements discussed above.

The objectives of the present project may be summarized as follows:

1) To develop a general beam theory for the global analysis of box spine-beams. The scope of the development is limited to spine-beam bridges with at least one vertical axis of symmetry. The beam may have a variable cross-section and can be straight or curved in plan. Diaphragms can be specified at any node. The structure is treated in three-dimensional space and longitudinal warping effects as well as transverse distortion are taken into account. The effect of shear lag is included by adopting an "effective breadth" concept.

2) To establish a family of special one-dimensional sub-parametric elements and to present this analytical treatment in a form suitable for computer analysis. This objective comprises the writing and testing of a computer code. The purpose is to provide a program that can handle a wide variety of bridge structures such as straight or curved box spine-beams, multibox girders, articulated bridge decks and cable-stayed bridges. The associated program has been called CUBAS (City University Bridge Analysis System).

3) To carry out a comprehensive experimental investigation on different types of box beams, which can assess the appropriateness of the formulation and the accuracy of the results. An understanding of the structural action can also be obtained which would assist the development

of the theory.

Generally, it is hoped to provide designers with a practical analysis to be used for the initial design process when a complete stress analysis is unnecessary. The solution is sufficiently accurate for design purposes.

An attempt has been made to present this thesis in a form compatible with the objectives of the project. In this chapter the peculiar structural action of spine-beam construction is briefly described and existing analytical methods leading to the present study, are reviewed. Basic considerations and assumptions are established for further investigation.

In Chapter 2 a brief description of some special features related to the bending analysis of thin-walled members is presented. Moreover, an analytical process based on the warping torsion theory is summarized and supplementary formulae are developed. Following an ordinary folded plate approach, the effect of cross-sectional deformation on single-spined box beams subjected to torsion is investigated in Chapter 3. The method is extended to curved beams and the interaction between bending, torsion and distortion is discussed.

Based on the elastic theory described in Chapters 1 to 3, a complete derivation of the one-dimensional finite element family is given in Chapter 4. This provides the theoretical basis for the computer program described in Appendix I.

The verification and applications of the present study are given in Chapters 5 to 8. In Chapter 5, results from a few selected examples are given, and in Chapter 8 an extensive series of model tests is described. Chapter 6 further describes a finite element-grillage approach which extends the method to the analysis of multi-box systems. Applications to short span bridge structures such as the cellular

articulated bridge deck and to long span bridges such as the cable-stayed bridge are presented in Chapters 6 and 7 respectively. In order to assess accuracy, some of the examples and all of the tested models are calculated by full three-dimensional finite element analysis using the LUSAS computer program (79, 80).

Finally, in Chapter 9 the conclusions to which the present study leads and proposals for future studies are given. In addition, to establish the usefulness of the program CUBAS, its structure is briefly described in Appendix I, and the format of the input data as well as a description of the input parameters are included. Data input to a supplemental program PFRAN for calculating the distortional sectional properties and sectional property formulae for a trapezoidal single-cell box-section are presented in Appendices II and III respectively.

## 1.2 Types of structural action

In developing a simplified design method, it is necessary to know that it does in fact give an adequate representation of the required structural behaviour. Thus, it is worth indicating the range of types of structural action possible before deriving the corresponding formulations. In addition to assessing the load effects inherent in simple beam theory, the following structural characteristics are shown to be peculiar to spine-beam construction and may require special consideration under certain circumstances:

- 1) Distortion or deformation of the cross-section due to torsional loading arises from transverse bending of the walls of the box beam, causing a change of shape of the section. Resistance to distortion is provided either by transverse diaphragms or by increasing the bending strength of the walls of the box beam (see Fig. 1.3a).

2) Warping of the cross-section corresponds to out-of-plane or axial displacements of points on the cross-section, causing plane sections not to remain plane (see Fig. 1.3b). The longitudinal displacements caused by torsion and distortion are termed torsional warping and distortional warping respectively.

3) Shear lag is another form of warping resulting from shear deformation in the planes of the flanges, and leads to a decrease away from the webs, in the longitudinal bending stresses calculated by simple bending theory.

4) Poisson's ratio effects are significant when transverse bending stresses due to distortion of the cross-section can be of the same order as the longitudinal stresses associated with longitudinal bending, torsional and distortional warping. In such cases, the Poisson's ratio effect in transverse bending can generate longitudinal bending stresses in individual component plates of the box section which are by no means negligible.

5) Local effects in the slabs are induced by external loading applied between the webs or on the side cantilever.

6) Transverse membrane stresses, which are constant through the wall thickness, arise from differential shear stresses on cross-sections.

It is evident that a complex analysis will result if all the types of structural action in a box beam are considered. An approximate analytical approach requires the structural actions to be simplified to an acceptable degree of accuracy. Accordingly, the shear lag phenomenon can be considered by adopting an 'effective breadth' concept, and the Poisson's ratio effect is simulated by an empirical consideration based on experimental investigations (83).

In accordance with the principles of the ordinary theory of elasticity, the stresses arising from local bending may be calculated by a one-way frame solution with consideration of the respective effective lengths (see Fig. 1.4), independently of the global box beam analysis. Alternatively the influence surfaces for plates (47, 46, 101) may be used. Sawko and Mills (120) have proposed an analytical procedure for the design of cantilever slabs of spine-beam bridges in which the slabs are considered in isolation. Numerical examples indicate how small the transverse membrane stresses are. These stresses are constant through the wall thickness, and are not considered in the present treatment nor are they in the previous approaches given by other investigators (59, 42, 134, 135).

### 1.3 Review of analytical methods for thin-walled box spine-beam bridges

The analysis of box spine-beams has been a focus of attention for many investigators in recent years, and various theories and analytical methods have been developed. In this section a review of only the most relevant approaches for the static analysis of box spine-beam bridges will be described.

#### 1.3.1 Analysis of box beams as thin-walled beams

In this method the actual thin-walled space structure is regarded as a single beam. The first systematic study of the theory of thin-walled beams was carried out by Vlasov (146). In order to explain warping, Vlasov divided a torsional moment into 'pure' and 'flexural' components (152) which correspond to the St. Venant shear stresses and torsional warping shear stresses respectively. Vlasov introduced a new type of force termed a 'bimoment' and defined additional functions of the properties of a section,

calling them the sectorial coordinate and the torsional warping moment of inertia.

The analysis of such beams was later reformulated and generalized by Benscoter (10), Kollbrunner, Basler and Hajden (56, 57, 58, 59), and Heilig (42) for multicell boxes with arbitrary cross-sectional shapes. Dabrowski (22) has extended the theory to curved girders with thin-walled cross-sections. He presented an extensive collection of tables, together with influence lines and diagrams of internal forces for curved, single-span, two-span and three-span beams of constant section, arranged according to stiffness parameters and angles of curvature. The straight beam was treated as a limiting case and the tables are of use in the preliminary analysis of curved bridges of steel, composite or reinforced concrete construction.

In order to avoid the mathematical difficulties arising from solving the differential equation, an analytical method for predicting the torsional behaviour of thin-walled continuous members subject to torsion was presented by Khan and Tottenham (54). The method is based on a direct distribution of bimoments in a manner analogous to that of the well-known moment distribution method. The analysis is essentially a hand method which produces values of redundant bimoments in a continuous structure.

Vlasov (146) drew the analogy between the differential equation describing the response of a box beam to the distortional component of the loading and that of a beam on an elastic foundation (BEF). Subsequently, Wright et al (150) and Billington (11) evolved the BEF method for trapezoidal single cell boxes. This method considers both the distortional stiffness of the box walls and that of intermediate diaphragms or cross bracing. The deformation of the cross-section of a box beam is analogous to the deflection of a beam on an elastic foundation. Diaphragms in the

box beam, which prevent distortion but not warping, correspond to simple unyielding supports for the beam and an end support condition, where warping is prevented, is analogous to a built-in end support for the beam. A diaphragm, which provides elastic restraint to distortion, is analogous to an elastically yielding point support for a beam on an elastic foundation. Non-dimensional curves are presented which provide the maximum distortional stresses for boxes with regularly spaced interior diaphragms subjected to concentrated loading at mid-panel or uniformly distribution loading. The BEF method is also available for the analysis of box beams curved in plan resulting from the work of Billington (11).

Wright (151) proposed a simple distribution method for both multicell and multibox sections such that the distortional loading is found for each cell which is then treated independently using the BEF method for single cell boxes. This procedure has been shown to lead to very conservative results in some cases. Billington (11) has further proposed a grillage-BEF which forms the basis of a simplified method for the analysis of multibox systems. The method is compared with finite element analyses for a range of practical bridge structures.

Steinle (134, 135) derived the differential equation governing the distortional behaviour of a rectangular single cell section box beam, including the effect of shear deformation. The distortional stress resultants are represented by the distortional moment and the distortional bimoment. Thus, the expressions for the distortional stresses are analogous to those of warping torsion theory. Dabrowski (21) investigated the influence of shear deformation on the warping torsion of box beams with deformable cross-sections. In his comprehensive treatment (22), derivation of the differential equation for a trapezoidal single cell section box beam curved in plan, subjected to distortional loading, and neglecting the effect of shear deformation, was given. The equation includes additional

terms representing distortional forces caused by longitudinal bending moments.

More recently Kristek (62, 63) has provided an accurate elastic solution based on a set of differential equations. The analysis of a box girder with a deformable cross-section is carried out in two steps. The first step includes the girder with an absolutely rigid cross-section in its own plane, and the second step covers the distortional effect of the cross-section. The girder may have a variable cross-section (such as variable height and thickness of webs), and the various parts of the structure may be made of materials having different properties. The static system may also be fairly complex (continuous beams, frameworks etc.).

Abdel-Samad et al (1) and recently Maisel (84) have extended the generalized coordinate method developed by Vlasov (146) to account for torsional, distortional and shear lag effects in straight, thin-walled, box beams of uniform section. The position of an arbitrary point in the middle plane of the walls is determined by a local rectangular system of coordinates in which the z-axis and the beam axis are co-linear, the n-axis is normal to the middle plane of the plate, and coordinate, S, describes the distance on the middle plane from an initial generator. According to the thin-walled beam theory developed by Vlasov (146), the displacement components of a point on the middle plane may be written as a finite sum of products as follows

$$u(z, S) = \sum_{i=1}^m U_i(z) \phi_i(S) \quad (1.1)$$

In this decomposition the functions  $\phi_i$  are the longitudinal generalized coordinates, which are known and chosen in advance for each type of cross-section, and the functions  $U_i$  are unknown functions, which have to be solved. The solution procedure presented for the generalized coordinate method permits consideration of single cell or multicell sections with

side cantilevers and arbitrary end and interior boundary conditions.

During the investigation of the analysis of truss bridges, Lie (70, 71) has proposed a new approach as an extension of the theory of thin-walled beams. A set of fourth order differential equations has been established for the rectangular single cell section prismatic beam with a vertical axis of symmetry, considering the interaction between bending, torsion and distortion. In general, the solution indicates no centre of twist for a cross-section with a deformable contour. The only exception is the doubly-symmetric cross-section. The method has been extended by Lie to a trapezoidal single cell section beam, in an unpublished communication.

### 1.3.2 Analysis of box beams as folded plate structures

A box beam may be regarded as a special type of folded plate system in that it is composed of an assembly of flat plate strips forming a closed section. Methods of analysis originally developed for folded plates may thus be adapted for the analysis of box beams. In recent years much research has been devoted to the analysis of folded plates and two main methods have been established, these being the "Elasticity Method" and the "Ordinary Method".

Of these two methods, the Elasticity Method, which was conceived by Goldberg and Leve (36) for simply-supported prismatic shells, is the more accurate and it has been applied to box beam analysis as a direct stiffness approach by Scordelis (124, 125). More recently the method has also been extended by Meyer and Scordelis (87, 88) to the analysis of bridges curved in plan.

In this method, termed the "Folded Plate Method" by Scordelis, the bending of each plate element normal to its plane is analysed by plate

flexure theory, and its in-plane bending is analysed by plane stress theory. The external loads must be represented by Fourier Series. Although the theory is exact, it is limited in that it can only be applied to box beams with constant cross-sections and simply-supported ends. A combination of the displacement (stiffness) method and a force (flexibility) method has been extended by Scordelis to deal with the intermediate diaphragms and to deal with girders spanning over intermediate supports, provided that the extreme ends of such girders still remain simply-supported. In certain cases difficulty can be experienced with concentrated loading conditions because of the poor convergence of the harmonic series used in the analysis.

The Ordinary Method is an approximate technique which can be applied in cases where the length/width ratio of the component plates exceeds 3. Scordelis (126) has, in fact, successfully adapted the Ordinary Method, which he termed the "Finite Segmental Method", to the analysis of single span girders and continuous box girders. This method can be applied to structures with arbitrary boundary conditions at the two ends, yet it is restricted to the analysis of box girders containing uniform rectangular plates under loads applied at the ridges only.

Johnson and Lee (52) developed the Ordinary Method for application to the analysis of folded plates containing tapered elements, provided that the taper is not excessive. Subsequently, the Nodal Section Method, referring also to the Ordinary Method, was developed by Rockey and Evans (109, 110) for the analysis of straight box girder bridges. It is assumed in the Nodal Section Method that the bending action of each plate perpendicular to its plane can be represented by considering a transverse one-way slab strip, and the in-plane longitudinal bending action of an individual plate is similar to that of a beam spanning between the end diaphragms. The structure is then idealized by taking a number of arbitrarily spaced nodal sections in the transverse direction, elastically

supported by a system of interconnected plate beams which span longitudinally between the supporting diaphragms. The Nodal Section Method can be used for various support conditions, and can be applied to the analysis of girders in which the geometry of the cross-section varies along the span. Recently, Al-Rifaie and Evans (2, 3) have further extended the method to enable it to deal with the analysis of single-cell, simply-supported, curved girders.

### 1.3.3 Analysis of box beams using the finite element method

It is evident that the finite element method is the most powerful and versatile tool for structural analysis, in which complex geometries and difficult boundary conditions occur. Recent progress permits a full three-dimensional analysis of a spine-beam bridge to be carried out. Plate elements, flat shell or even semiloof shell elements are available for use in the idealization of box structures.

According to the configuration of box spine-beam bridges, triangular, rectangular or quadrilateral elements are usually used. The simplest elements suitable for the analysis are triangular elements (85), although a fine mesh division is necessary to obtain accurate results. The use of rectangular finite elements has been discussed by Rockey and Evans (108) and Zienkiewicz (154), and yields results of greater accuracy than those obtained from the triangular elements. Both of these two types have at each of the nodal points, two in-plane degrees of freedom  $u$ ,  $v$  and three out-of-plane degrees of freedom,  $w$ ,  $\theta_x$ ,  $\theta_y$  but not the in plane rotation  $\theta_z$ .

To achieve accurate results with economy it is advantageous to be able to represent the beam action of the wall in the formulation. The introduction of an additional in-plane rotation as a nodal variable has thus been investigated by several authors. MacLeod (81) developed a rectangular plane stress element with the two translations  $u$ ,  $v$ , while the

nodal rotation is taken alternatively as  $\frac{\partial v}{\partial x}$  and  $-\frac{\partial u}{\partial y}$  around the element. This element was used to analyse shear walls with openings. Lim et al (75) developed a quadrilateral element with the nodal rotation  $\theta_z$  taken as  $\frac{\partial v}{\partial x}$ . Sisodiya et al (129, 130) also developed an in-plane element with nodal variables  $u$ ,  $v$  and  $\frac{\partial v}{\partial x}$ . Two element geometries were formulated, a parallelogram and a quadrilateral. Moffat and Lim (94), and Fam and Turkstra (33) have recently developed elements with  $u$ ,  $v$  and  $\frac{\partial v}{\partial x}$  and  $\epsilon_x$  as nodal variables. These elements possess an accurate beam response and can approximate the web beam action with a relatively coarse mesh.

Scordelis (129, 125) used a rectangular in-plane element having  $u$ ,  $v$  and  $\theta_z$  as the degrees of freedom at each node, where  $\theta_z = \frac{1}{2} \left( \frac{\partial v}{\partial x} - \frac{\partial u}{\partial y} \right)$ , and a rectangular plate bending element with  $w$ ,  $\theta_x$  and  $\theta_y$  as the degrees of freedom at each node. Sawko and Cope (118) used in-plane elements alone to analyse multicell rectilinear box girder bridges. This method does not account for out-of-plane, or bending, rotations at the nodes. However, it can give fast solutions for bridges with narrow cells.

Lyons (80) has recently developed the ISOFLEX family of thin plate flexure elements with a translation  $w$  and two rotations  $\theta_x = -\frac{\partial v}{\partial z}$  and  $\theta_y = \frac{\partial u}{\partial z}$  as the "bending" nodal variables, and a family of extensional elements which includes nodal variables of  $u$ ,  $v$  and  $\theta_z = \frac{\partial v}{\partial x}$ . The combination of these two types of elements has formed the extensional-flexural elements or the so-called flat thin shell box elements (the ISOBOX elements, Ref. 79 and Fig. 1.5). Variable thickness can be accommodated, and since the elements are formulated in local element axes, directional material properties can be defined relative to the element orientation. The elements are particularly suitable for the analysis of shell boxes. Only a few high aspect elements are required along the length of a structure and a single

element over the depth of a web provides accurate results even in the vicinity of a support or a wheel load.

Irons (49) has developed a doubly curved shell element known as a semiloof shell element, but for cellular structures the additional computational expense associated with the double curvature would be unwarranted since in general, cellular structures are an assemblage of flat or almost flat plates.

In order to develop more accurate elements and reduce the computing time for the analysis of straight and curved box girder bridges, Jirousek et al (50) have presented a special macro-element for practical applications. The macro-elements may be viewed as transverse slices of the bridge. Each macro-element is formed using two types of special purpose elements: a modified Ahmad's thick shell element and an assembly element. After the assembly of the elements of the substructure has been completed, all internal degrees of freedom are eliminated by the standard process of static condensation. Thus only the degrees of freedom associated with nodes appearing in the two transverse planes delimiting the slices are retained for subsequent resolution in which each substructure is already viewed as a single large element. The effect of prestressing is properly taken into account in the form of appropriate local loads considered at the element level.

Although the conventional beam element has been extensively developed with straight or curved shapes in three-dimensions (100, 51, 92, 95), it is still characterized by an inability to represent distinctive features with special reference to the analysis of box beams. Research effort has been devoted by several investigators to extend the availability of one-dimensional finite elements.

Krahula (60) and Krajeinovic (61) derived the stiffness matrix for

a straight prismatic thin-walled element having an open section. In addition to the two-component displacements  $\xi$ ,  $\eta$  in the direction of the principal axes  $x$  and  $y$ , and the angular displacements  $\xi'$ ,  $\eta'$  and  $\phi$  about the  $x$ ,  $y$  and  $z$  directions respectively, the rate of the twisting angle  $\phi'$  was chosen so as to form another nodal variable corresponding to the torsional warping. Similar elements with seven degrees of freedom at each node,  $\{u, v, w, \theta_x, \theta_y, \theta_z, \nu\}$  where  $\nu = \frac{\partial \theta_z}{\partial z}$ , were proposed by Chai Hong Yoo (14) to facilitate the stability analysis of thin-walled assemblages. The generalized forces and displacements are shown in Fig. 1.5 and 1.6 referring to Refs. (61) and (14) respectively, in which the normal force  $P_z$  and the bending moments  $M_x$  and  $M_y$  are referred to as the centre of gravity, while the torque  $M_z(T)$  and the transverse forces  $Q_x$  and  $Q_y$  ( $V_x$  and  $V_y$ ) are referred to the shear centre. The force corresponding to the additional degree of freedom is the bimoment.

The shape functions for torsional behaviour, originally given by Krahula and adopted by Krajeinovic and Chai Hong Yoo, were derived from the exact solutions of the homogeneous equations. The shape functions are in the form of hyperbolic functions:

$$N_{\phi 6} = \frac{1}{D} [(1 - \text{chkl})\text{chkz} + \text{shklshkz} - \text{kzshkl} + (1 - \text{chkl} + \text{klshkl})]$$

$$N_{\phi 7} = \frac{1}{kD} [(kl\text{chkl} - \text{shkl})\text{chkz} + (\text{chkl} - 1 - \text{klshkl})\text{shkz} + \text{kz}(\text{chkl} - 1) + (\text{shkl} - \text{klchkl})]$$

$$N_{\phi 13} = \frac{1}{D} [(\text{chkl} - 1)\text{chkz} - \text{shklshkz} + \text{kzshkl} + (1 - \text{chkl})]$$

$$N_{\phi 14} = \frac{1}{kD} [(\text{shkl} - \text{kl})\text{chkz} + (1 - \text{chkl})\text{shkz} + \text{k}(\text{chkl} - 1)\text{z} + (\text{kl} - \text{shkl})]$$

$$\text{where } D = [\text{klshkl} + \text{z}(1 - \text{chkl})] \quad (1.2)$$

$$\text{and } k = \sqrt{(\text{GK}_T / \text{EI}_\omega)}$$

Barsoum and Gallagher (8) used cubic polynomials in evaluating the thin-walled beam stiffness matrix, whilst Ettouney and Kirby (27) used quadratic expansions accounting for the restraining of warping.

Bažant and Nimeiri (9) and Zyl (156) have contributed a skew-ended beam element for box beams curved or straight in space taking transverse distortion and longitudinal warping into consideration. In conformity with the method of separation of variables developed by Vlasov (146), the box element used in this study has sixteen degrees of freedom. These consist of the usual six degrees of freedom at each end, plus two new degrees of freedom at each end. These latter two are the transverse distortion mode and the longitudinal warping mode. The forces associated with these two displacements are the longitudinal bimoments (59, 42) and the transverse bimoments (62). The basic distribution of unknown displacement within the finite element are approximated by linear and quadratic forms. The cross-section can consist of a single cell with sloping webs and cantilevers and may be variable in depth and width along the span. Shear lag effects are neglected in the analysis.

Mikkolo and Paavola (90) have presented a somewhat similar approach for the analysis of a rectangular single-cell box girder with side cantilevers. Interpolated or shape functions are represented by cubic polynomials in each element as is commonly done in the finite element solution of beam problems. It is observed that the known displacement functions describing the deformation modes of the cross-section must be chosen in advance for each type of cross-section. Thus, difficulties exist in extending the method for more complicated or more general types of cross-section.

Lie (71) has presented a single cell straight beam element to investigate the bending-torsional vibration, and the stability and stress

of truss bridges. The bending-torsional displacements in the cross-sectional plane are expressed in terms of the lateral and vertical translations  $u(z)$  and  $v(z)$  of the "centre of the rigidities of shear" of the box section and the rotations  $\phi(z)$  and  $\psi(z)$  of the vertical and horizontal sides of the cross-section about the x and y axes respectively as shown in Fig. 1.8. In addition the continuity of the first derivatives of these displacements must also be maintained. As a result the degrees of freedom at each node are  $\{u, u', v, v', \phi, \phi', \psi, \psi'\}$ . All the displacement functions of the element are taken in the form of cubic parabolas.

#### 1.3.4 Some other methods of box beam analysis

Apart from the foregoing methods suitable for the analysis of box beams, there exist other approaches which will be described briefly here.

##### 1.3.4.1 Finite strip method

The finite strip method was developed by Cheung (16) as a hybrid of the finite element procedure, and was extended to the analysis of curved box beams. The method was also used by Scordelis and Meyer (87, 88) for the analysis of both curved folded plate structures and curved box beams. Loo and Cusens (77, 78) used a fifth order displacement interpolation function to formulate a refined finite strip solution.

The finite strip analysis is based on the principle of dividing the structure into a series of strips simply supported at their ends by diaphragms. These diaphragms are considered to be infinitely rigid in their own plane but perfectly flexible normal to their own plane. The finite strips are assembled transversely by using finite element techniques, yet the displacement components are in the form of Fourier series

longitudinally, and the external loads are also resolved into the same Fourier series for the corresponding displacement components.

The finite strip method has gained acceptance and is currently being used in practical design for the reduction of computational costs. However, due to the use of orthogonal functions the method is restricted to the analysis of simply supported box beam bridges.

#### 1.3.4.2 Space frame and grillage analyses for box beams

Many standard programs are already available for space frame and grillage analyses. The box beam can be idealized as a space frame using beam elements in three dimensions (Fig. 1.9). This method, as in the finite element method, needs a considerable amount of computer time and a multitude of input data. It does not, however, require the development of new programs nor detailed knowledge concerning the peculiarities of the behaviour of box beams, and can be used in the cases of variable cross-sections and arbitrary groundplans.

Some authors have also presented a grillage approach as an approximate process for the analysis of box beams. Lightfoot and Sawko (72, 73, 113) were among the first to utilize computers in the analysis of grillages related to structures such as slabs, beams and floors. Goldstein et al (37) and Sawko and Willcock (114) developed grillage analyses for bridge decks having varying sectional properties. The grillage approach was also successfully employed for the analysis of composite box girder bridges by Sawko and Mosley (121). Sawko (115) has also presented work on grillages consisting of members curved in plan and interconnected by transverse diaphragms. West (148) has presented recommendations for the grillage analysis of slab and pseudo-slab bridge decks.

Hambly and Pennells (41) have used grillage idealization to analyse cellular bridge decks such as multi-cell boxes with vertical and sloping webs and voided slabs. Detailed guidelines about the grillage mesh and the evaluation of stiffness parameters, which lead to a satisfactory representation of the structural behaviour of box beams, were given by the authors. Some guidance was also given on the interpretation of results for design calculations. Evans and Shanmugam (30) proposed a somewhat similar grillage approach for the analysis of cellular structures.

One of the merits of the grillage approach is that the structural behaviour of grids is more readily understood by bridge engineers and many accessible computer programs are available. It is, however, a coarse approximation of the true structure, and does not exactly express the peculiarities of the behaviour of spine-beams.

#### 1.3.4.3 Twisting analysis by the displacement method given by Richmond

Richmond (103) developed a method, termed the equivalent beam method by Maisel (83), which represents an approximate solution. This is suitable for rapid design with reference to distortional effects. A displacement solution for rectangular boxes with concentrated diaphragms was also proposed. The box beam was thought of as a series of bays between the diaphragms. The equilibrium conditions for an elementary section of box surrounding a diaphragm were formulated in terms of the displacements at the adjacent diaphragms, leading to a set of simultaneous equations when applied to each diaphragm.

Dalton and Richmond (23) extended the displacement method to include trapezoidal cross-sections, and the method was limited to boxes of constant depth and width, with a vertical axis of symmetry. Richmond

(104) also derived the more general differential equation for trapezoidal boxes with continuous diaphragms subjected to both torsional and distortional components of loading. He described its solution for simplified boundary conditions and loading. Furthermore, Richmond (105) introduced the matrix difference solution as a general numerical method for a box beam with discrete diaphragms.

As a result of the above literature survey, it can be seen that an analytical approach, which combines the finite element technique and the thin-walled beam theory, is appropriate for the design of box spine-beam bridges especially for medium and long spans. Incomplete attempts in this direction by previous researchers are developed and extended in this thesis to a relevant form, which results in low computing costs and ease of usage, whilst retaining an acceptable degree of accuracy and versatility.

#### 1.4 Coordinate systems and sign conventions

In this section an attempt is made to specify the coordinate systems and the main sign conventions. In order to perform reliable calculations it is necessary to derive the formulae throughout the thesis in a form consistent with accepted axes and sign conventions. For emphasis some of the specifications listed here will be repeated at appropriate positions in the following chapters.

All the structures considered are located in a Cartesian orthogonal coordinate system XYZ, which is termed the general coordinate system. For the analysis of bridge structures it is convenient to assume that the Y axis is normal to the horizontal and is taken as positive downwards. The loads and deflections due to gravity are then both positive quantities.

Two local coordinate systems are adopted in the formulation: the right-handed orthogonal system of coordinates xyz (Fig. 1.10), and the

curvilinear system  $S$  directed around the box cross-section (Fig. 1.11).

It is obvious that the stress resultants follow the same sign rules. The positive directions of the internal stress resultants acting on a positive cross-sectional face and of the applied loading are shown in Fig. 1.14. The shear forces  $Q_x$  and  $Q_y$  and the axial force  $N_z$  are positive when in the positive directions of the  $x$ ,  $y$  and  $z$  axes respectively. The bending moments  $M_x$  and  $M_y$  and the torsional moment  $M_T$  are positive when their right-hand corkscrew vectors are in the positive directions of the  $x$ ,  $y$  and  $z$  axes respectively. However, the distortional moment  $M_D$  is positive when in the negative sense of the twisting angle of  $\theta_z$ . In this thesis, the convention of Fig. 1.15 will be used to represent a positive bimoment. It will be noted in Fig. 1.14 that the positive directions of the externally applied loads acting on the beam elements shown, are the same as those of the resistive stress-resultants acting on the positive face of the cross-section shown.

### 1.5 Basic assumptions and fundamental equations of elasticity

The usual assumptions associated with linear elastic small displacement theory have been adopted, which can be generally stated as being that the structural material is homogeneous, isotropic and linearly elastic, and that the actual deformations are small compared with the structural dimensions.

Since this thesis is concerned mainly with the analysis of thin-walled box spine-beams, the definition of a thin-walled beam can be referred to the criteria given by Vlasov (146), Dabrowski (22), Kollbrunner and Basler (56), which have been summarized by Maisel (83). Note that the criteria are sometimes not strictly satisfied in practical bridge structures, but thin-walled theory has nevertheless been used for them. Additional

assumptions, which are mainly related to thin-walled structural behaviour, have been considered in this approach, and are as follows:

(i) The dimensions of the cross-sections are significantly less than the span lengths and less than the radii of curvature in the case of curved members. The length/width ratio of the component plate should normally exceed 3(29, 22).

(ii) The thicknesses of the walls are small compared with the dimensions of the cross-section.

(iii) Diaphragms are considered to be infinitely or finitely stiff in their own plane, but perfectly flexible in the direction normal to the plane.

(iv) Plane sections remain plane during pure bending deformation, but not necessarily normal to the beam axis, thus allowing for shear deformation.

(v) For warping torsion analysis, cross-sections are assumed to remain undeformed in their own plane, but may rotate about the flexural axis (locus of the shear centres) and be subject to longitudinal warping.

(vi) The in-plane longitudinal bending action of an individual component plate is analysed using elementary beam theory, and the shear deformation caused by distortion is neglected.

(vii) Transverse membrane strains and longitudinal bending strains of an individual plate are assumed to be zero. The bending action of the individual plate normal to its plane is represented by the flexural behaviour of an equivalent transverse frame.

Assumption (i) is an essential condition for the applicability of structural analysis by beam-type members and for the following assumptions.

A differential element of side  $ds \times dz$  and thickness  $t$  cut from the wall is shown in Fig. 1.16. In accordance with assumption (ii) concerning the small thickness of the wall, the direct and shear stresses normal to the plate surface, and the resistive torsional moments of the plate may be neglected. The stress system on the differential element is, therefore, specified by plane stresses  $\sigma_z$ ,  $\sigma_s$  and  $\tau_{zs}$ , and out-of-plane bending moments  $m_{db}$  and  $m_{lb}$ .

The equilibrium of the element in the  $z$  and  $S$  directions respectively may be expressed, neglecting body forces, as follows:

$$\frac{\partial q}{\partial s} + t \frac{\partial \sigma_z}{\partial z} = 0 \quad (1.3)$$

and

$$\frac{\partial q}{\partial z} + t \frac{\partial \sigma_s}{\partial s} = 0 \quad (1.4)$$

The displacement of a point on the wall can be represented by three components: two in-plane components  $u_t$  and  $v_n$ , and an axial component  $w_z$ . The three displacement components  $u_t$ ,  $v_n$  and  $w_z$  compose a right-handed orthogonal system which is shown in Fig. 1.17.

The strain components are expressed in terms of the displacements by the following equations

$$\epsilon_z = \frac{\partial w_z}{\partial z} \quad (1.5)$$

$$\epsilon_s = \frac{\partial u_t}{\partial s} + \frac{v_n}{R_n} \quad (1.6)$$

and 
$$\gamma_{zs} = \gamma_{sz} = \frac{\partial w_z}{\partial s} + \frac{\partial u_t}{\partial z} \quad (1.7)$$

where  $\epsilon_z$  and  $\epsilon_s$  are direct strains along the  $z$  axis and are tangential to

the mid-line of the wall respectively.  $\gamma_{zs}$  is the shear strain, and  $\frac{1}{R_n}$  is the curvature of the wall. It is obvious that for a straight wall the curvature equals zero.

Hooke's law is expressed by the following equation,

$$\begin{Bmatrix} \sigma_z \\ \sigma_s \\ \tau_{zs} \end{Bmatrix} = \frac{E}{1-\nu^2} \begin{bmatrix} 1 & \nu & 0 \\ \nu & 1 & 0 \\ 0 & 0 & \frac{1-\nu}{2} \end{bmatrix} \begin{Bmatrix} \epsilon_z \\ \epsilon_s \\ \gamma_{zs} \end{Bmatrix} \quad (1.8)$$

where  $E$  is Young's modulus of elasticity and  $\nu$  is Poisson's ratio.

The position of the x-y-z origin is taken to coincide with the centroid of the cross-section. The z axis is orientated along the longitudinal direction of the beam, and the x and y axes coincide with the principal axes of the cross-section, in which the y axis is fixed as the vertical axis of symmetry. The curvilinear coordinate  $S$  is taken as positive in the anticlockwise direction, as shown in Fig. 1.11, which also indicates the position of the origin for  $S$ .

For the sake of consistency we further specify the sign of the face of a cross-section. A positive cross-sectional face is one whose external normal points in the positive direction of the z axis. A negative cross-sectional face is one whose external normal points in the negative direction of the z axis. All the calculations in this thesis are referred to the positive faces of the cross-sections.

Displacement components of a point on the cross-section in the directions of the x, y and z axes are taken as positive when they lie in the positive directions of these axes. They are denoted by  $u_x$ ,  $v_y$  and  $w_z$  respectively, as shown in Fig. 1.12. Rotations  $\theta_x$  and  $\theta_y$  and the twisting

angle  $\theta_z$  are also shown, and are positive when the corresponding right-hand corkscrew vectors are in the positive directions of the x, y and z axes respectively. The positive directions of distortional displacements are given by Fig. 1.13 under torsional loading.

Resistive stresses caused by applied external loading exist in the structural members. For a positive cross-sectional face, a normal stress component is to be regarded as positive if it acts in the positive direction of an axis; otherwise it is negative. For a negative cross-sectional face, a stress component acting in the negative direction of an axis is positive. Shear stresses acting on a cross-section and in the positive direction of the curvilinear coordinate are positive, otherwise they are negative. As an exception, the shear stresses acting upwards in the interior walls separating neighbouring cells are negative, and are positive when acting downwards. The global transverse bending stresses due to distortion are associated with deformed shapes of cross-section as shown in Fig. 1.13. In this thesis, such stresses will be plotted in diagrams, where ordinates are drawn on the tension face, thus obviating the need for signs in these diagrams.

According to assumption (vii) and ignoring the effect of transverse membrane stresses due to their insignificance, we can obtain the relation between stresses and strains, which will be used throughout this thesis,

$$\sigma_z = E_1 \epsilon_z \quad (1.9)$$

$$\tau_{zs} = G \gamma_{zs}$$

where

$$E_1 = E / (1 - \nu^2) \quad (1.10)$$

is called the conversion modulus of elasticity, and

$$G = \frac{E}{2(1+\nu)}$$

is the shear modulus.

Assumption (vii) also implies that the longitudinal bending moment of the plate per unit width can be approximated by multiplying the corresponding transverse bending moment per unit length by Poisson's ratio,

$$m_{lb} = \nu m_{db} \quad (1.12)$$

A compatibility condition often used in this approach, which indicates the continuity of axial displacements, is expressed by the following equation,

$$\oint_i \frac{\partial w_i}{\partial s} ds = 0 \quad (1.13)$$

where, the subscript  $i$  indicates that the line integration is carried around the  $i^{\text{th}}$  cell. The equation must be satisfied for each cell of the box section.

Finally, it should be pointed out that all measurements in this thesis are based on SI (International System) units, i.e., the units for length are metres or millimetres, and for force are newtons or kilonewtons. All the values adopted from other references, which were in other unit systems, will remain in their previous form. However, converted values (to SI units) will be listed as well.

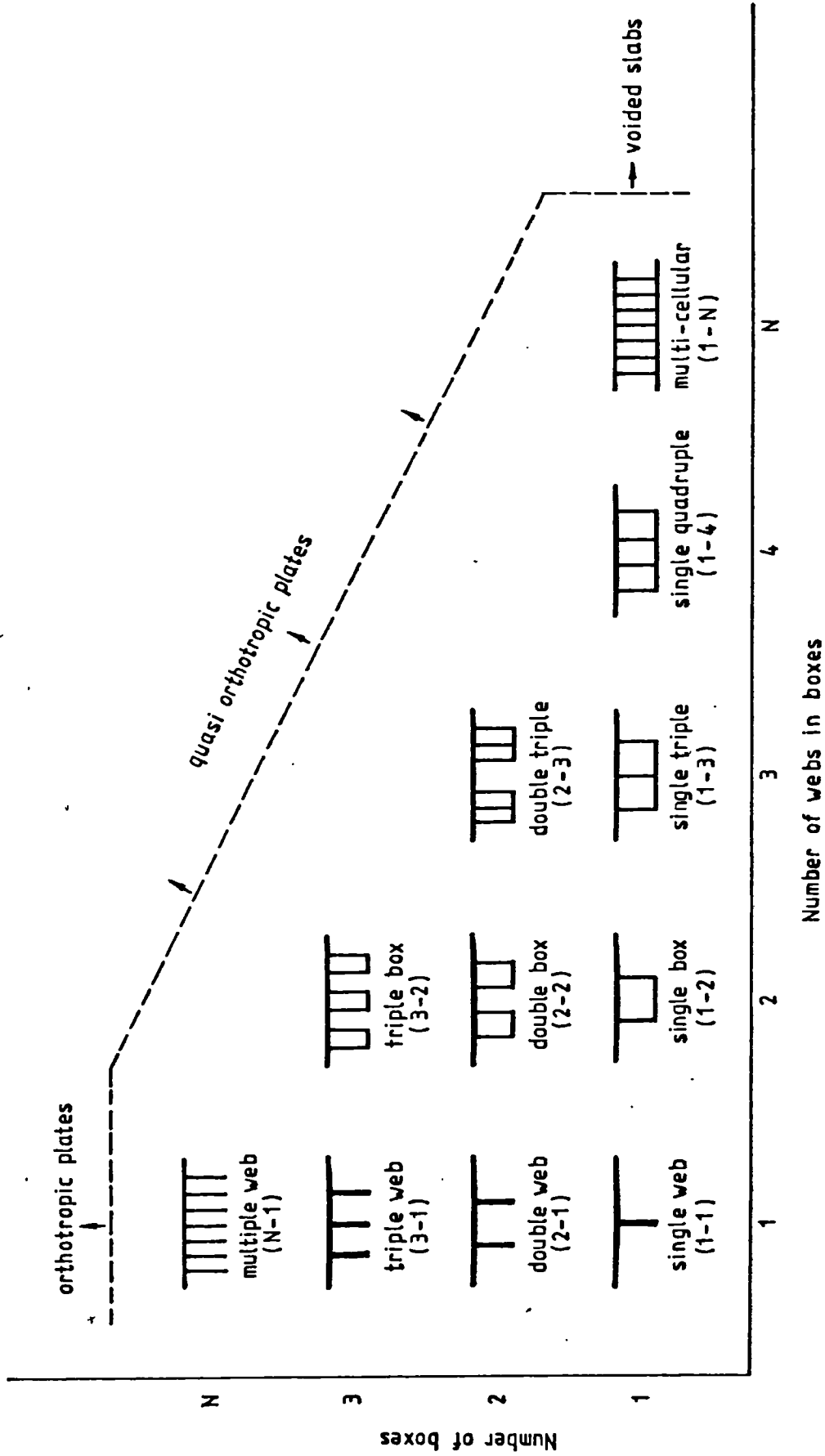


Fig. 1.1 Classification system of bridge decks

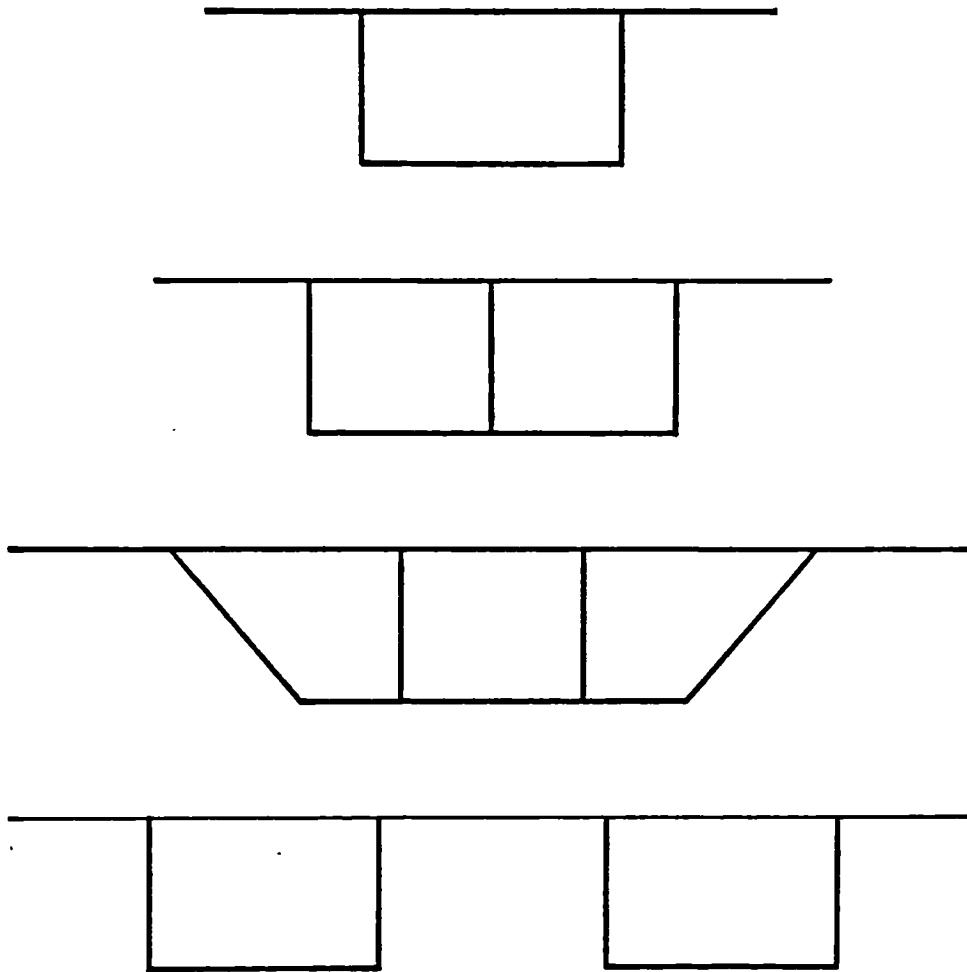
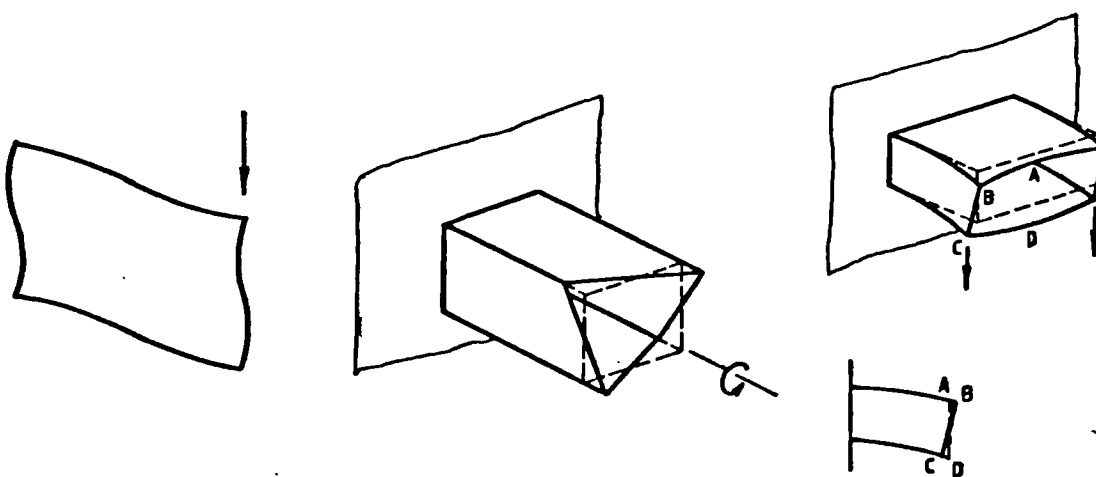


Fig. 1.2 Typical cross-sections for spine-beam bridges



a) Distortion or deformation of cross-section

(b) Warping of cross-section

(c) Shear lag in bending

Fig. 1.3 Types of structural action which may require special consideration in box beam bridges

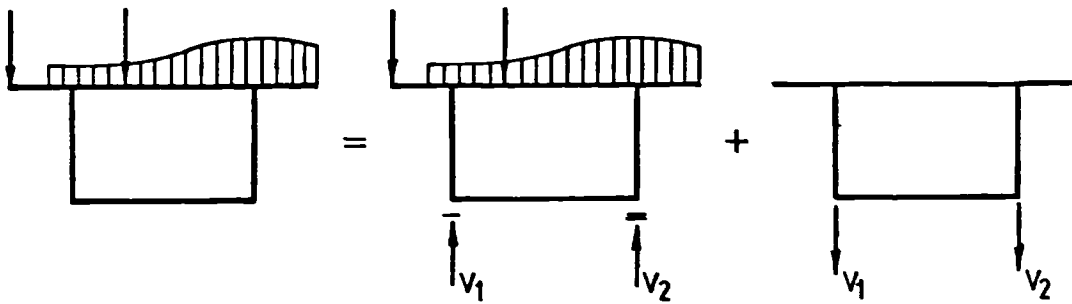


Fig. 1.4 Independent frame solution of the cross-section

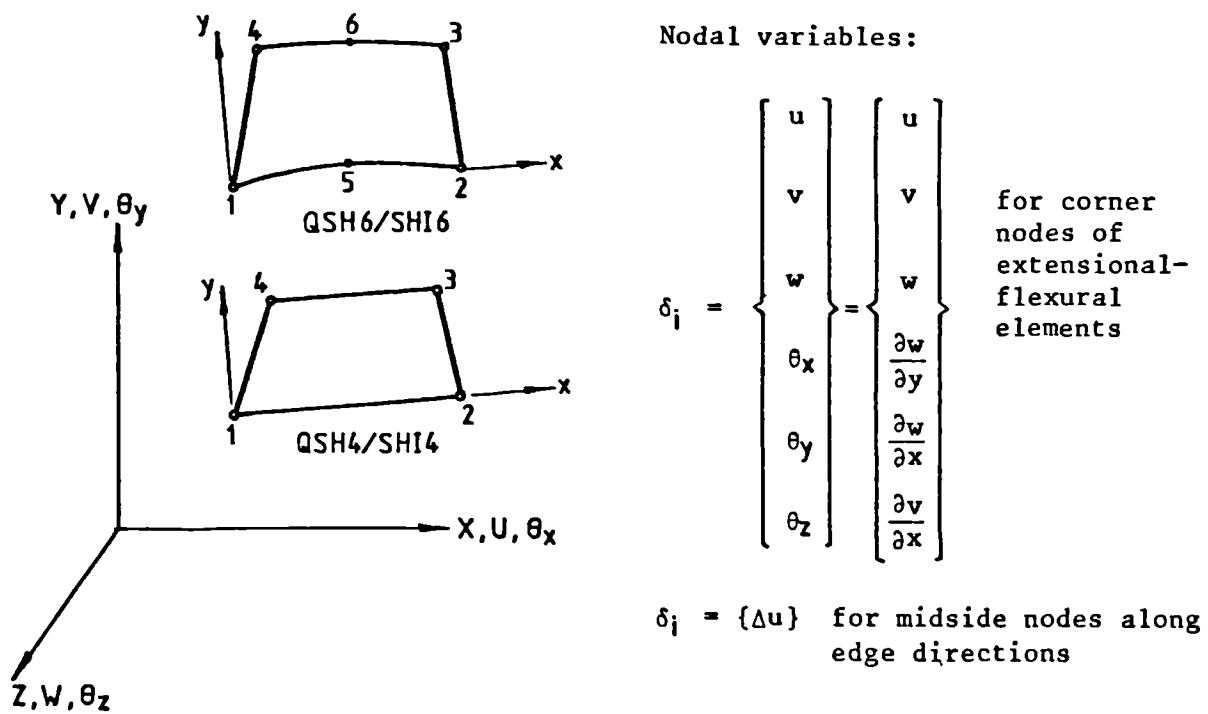


Fig. 1.5 Flat thin shell box elements in three-dimensions

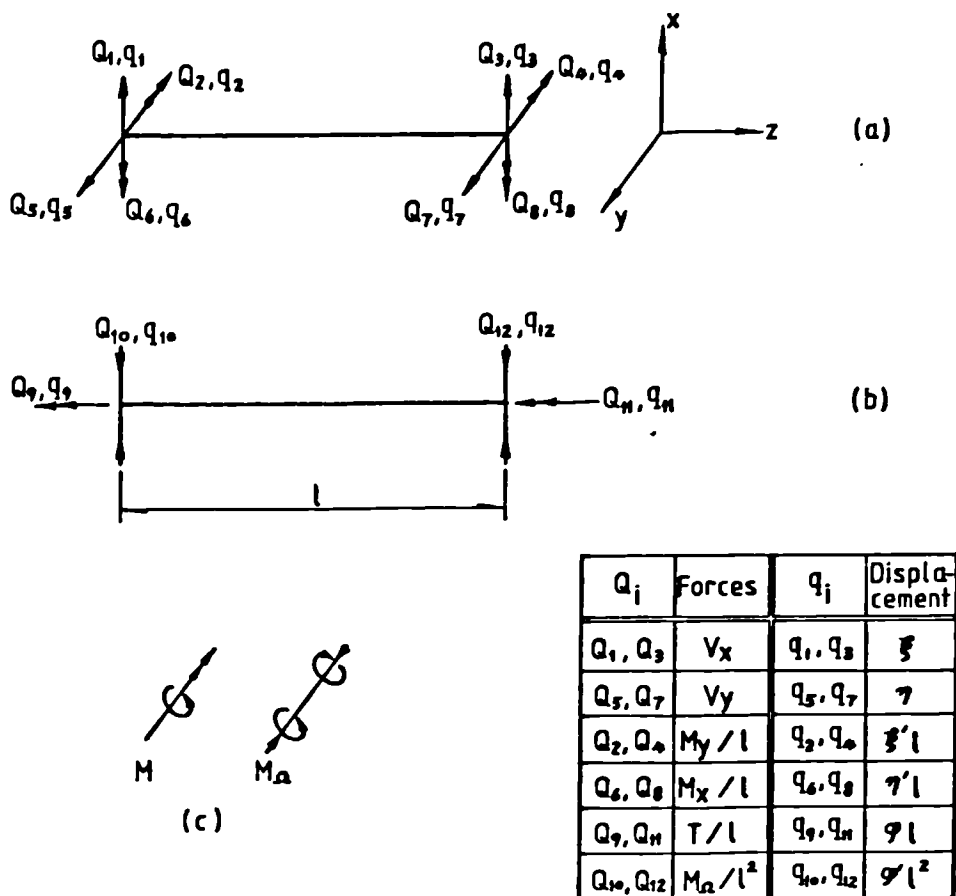


Fig. 1.6 Generalized forces and displacements. (a) transverse forces and bending moments; (b) torsion moments and bimoments; (c) moment and bimoment.

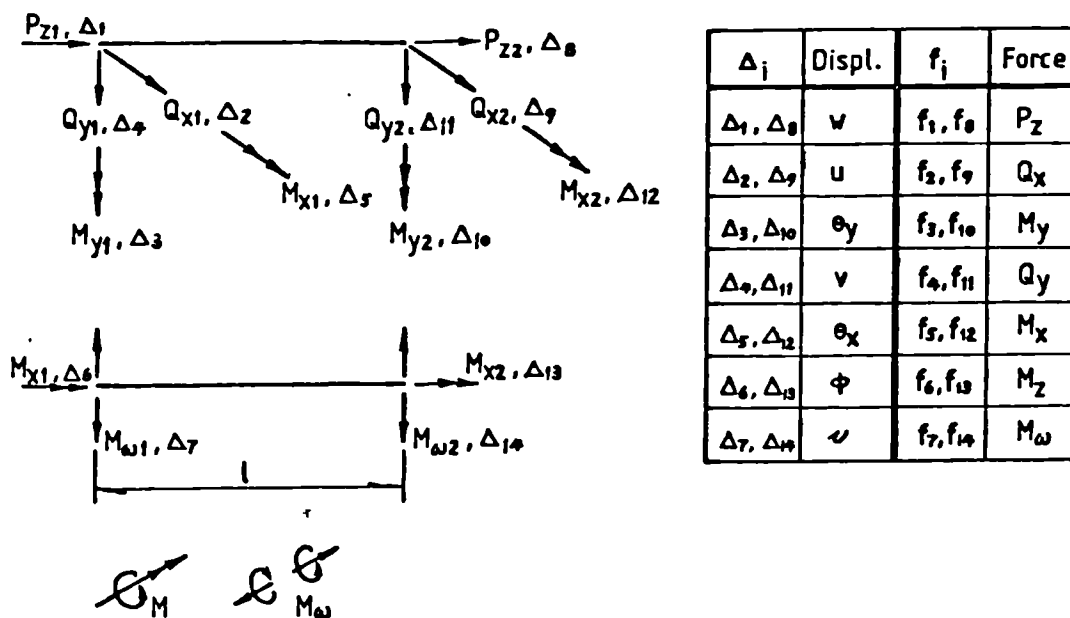


Fig. 1.7 Generalized forces and displacements

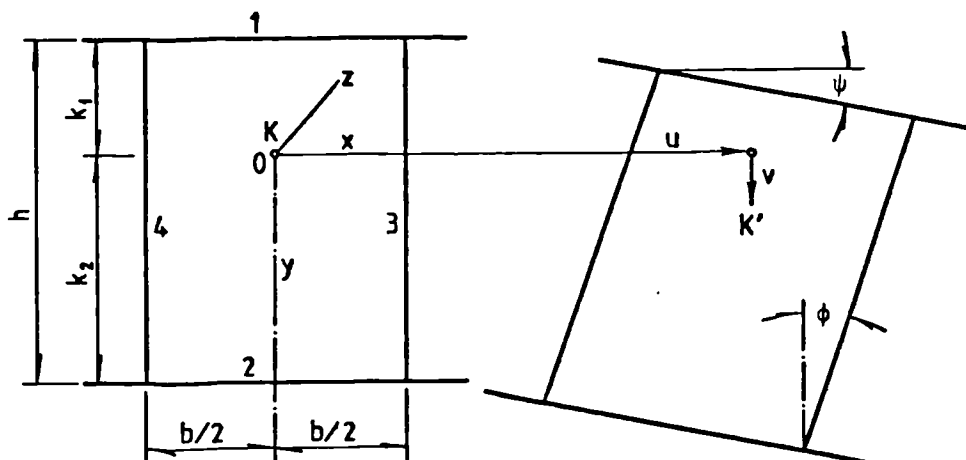


Fig. 1.8 Displacements in the box section plane

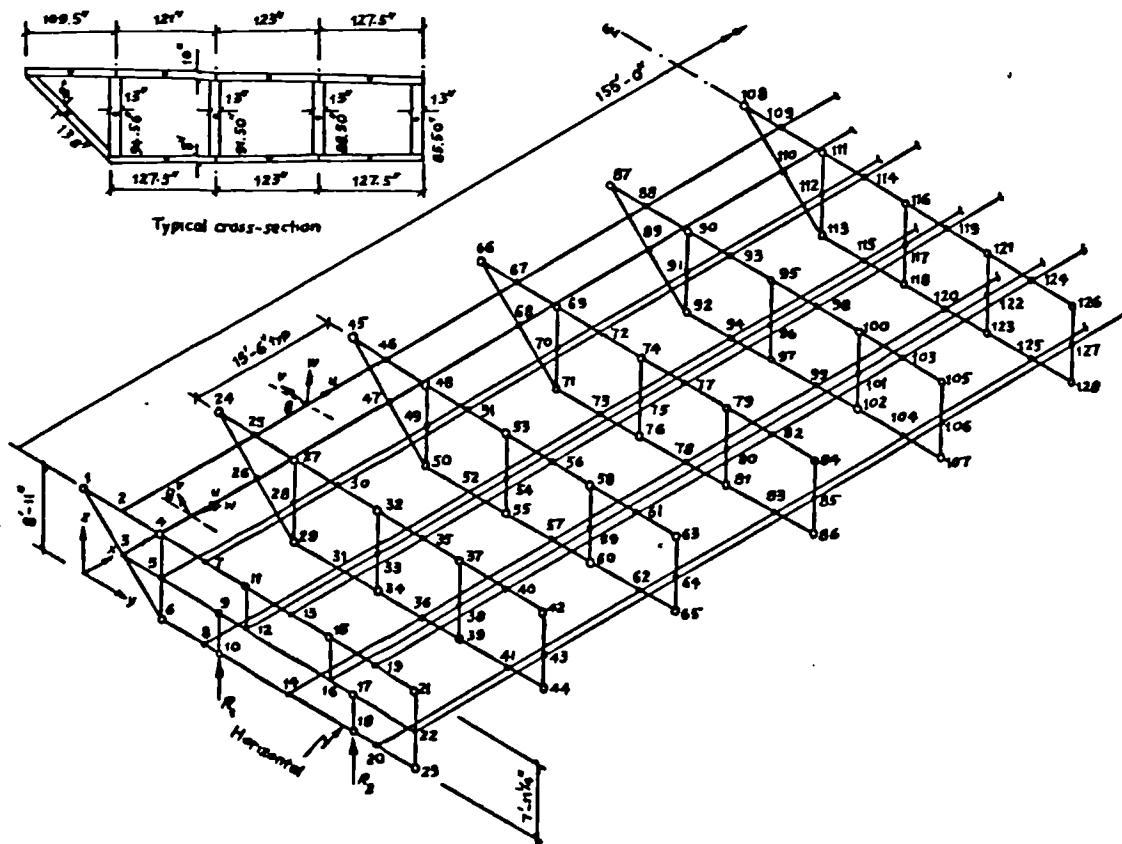


Fig. 1.9 Half-span of Jesmond Dene Bridge showing space frame idealization

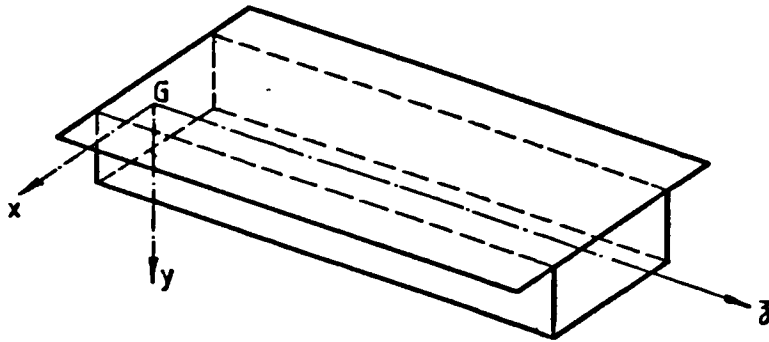


Fig. 1.10 Coordinate axes  $x$ ,  $y$  and  $z$

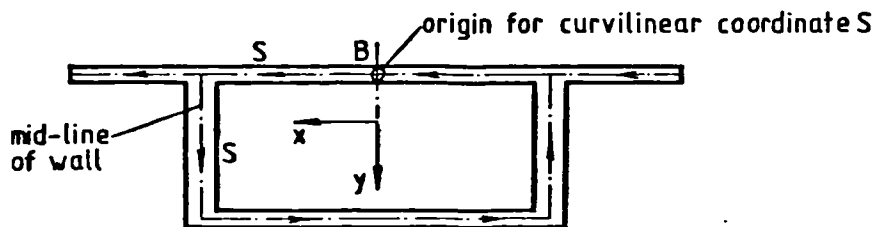


Fig. 1.11 Curvilinear coordinate  $S$ , showing origin and positive directions

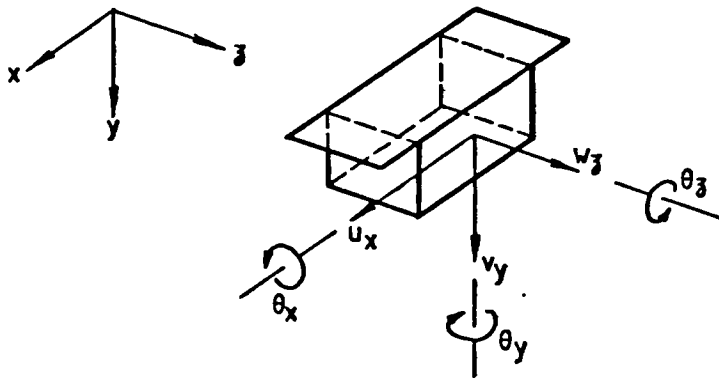


Fig. 1.12 Positive directions of displacement, rotation and twist

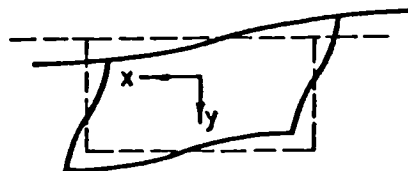


Fig. 1.13 Positive directions of distortional displacement for twisting loading on the cross-section

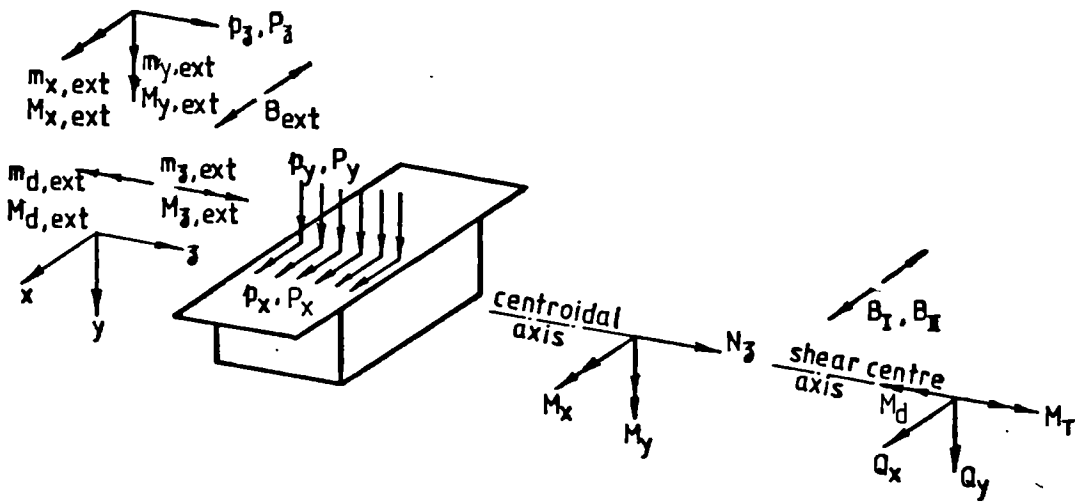
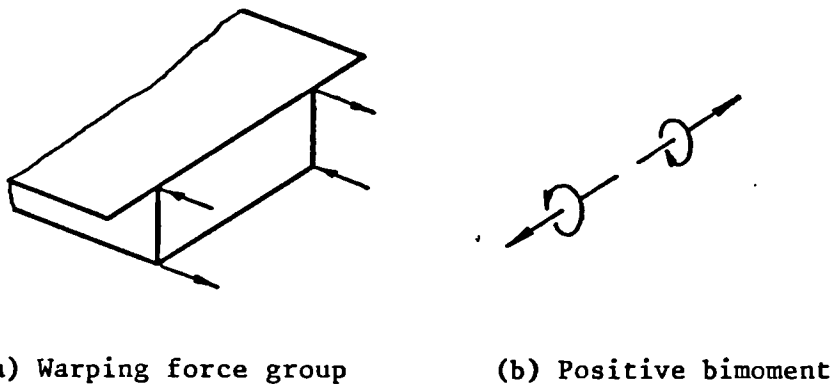


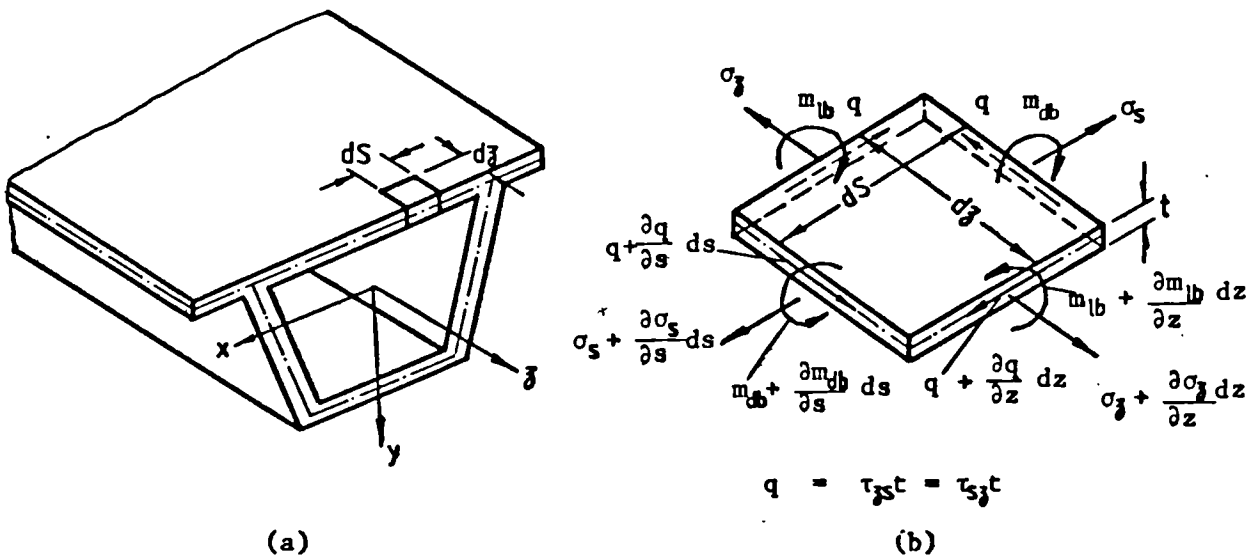
Fig. 1.14 Positive directions of internal stress-resultants and external loading



(a) Warping force group

(b) Positive bimoment

Fig. 1.15 Warping force group and bimoment



(a)

(b)

Fig. 1.16 Stress system on a differential element

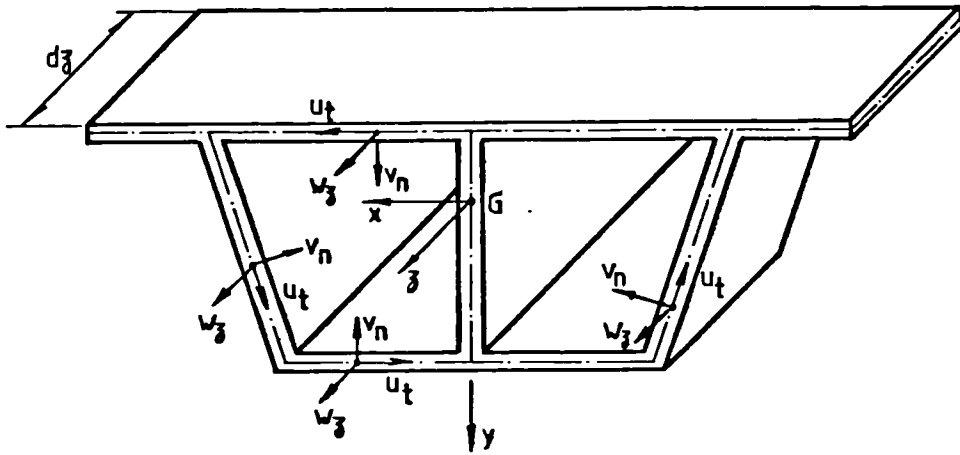


Fig. 1.17 Elementary frame showing displacement components

## CHAPTER 2

## BENDING AND TORSION OF THIN-WALLED MEMBERS

2.1 Introduction

The bending analysis of thin-walled members presents no more conceptual difficulties than those encountered in the investigation of the bending of solid-section beams. However, the distribution and the method of evaluation of the stress components, for example the evaluation of the shear stresses and of the position of the shear centre of the section, are different in the two analyses in some essential features. Moreover, in thin-walled members, the in-plane shear deformation of the flange plates may have a considerable influence on the distribution of longitudinal stresses within the flanges. This phenomenon, often termed shear lag, results in the deflections and the longitudinal stresses at the web-flange intersections of the section being greater than those given by the elementary theory of bending. For the sake of convenience, it is preferable in this chapter to present a brief description of some special features related to the bending analysis of thin-walled members.

In addition to bending action, bridge substructures are usually subjected to torsional loads arising from the eccentricity of loading and/or the in plan curvature of the bridge deck. The basic assumption in the development of the torsional theory of thin-walled sections is that of plane deformation being analogous to the pure bending case. It states that the cross-section as a whole may rotate, but that the form of the cross-sectional projection is not changed from its original shape. This assumption is valid only when the beam has a sufficient transverse stiffening system along its length.

The torsional shear deformation gives rise, in general, to non-planar longitudinal displacements which we call warping of the cross-section. In

pure torsion, only shear stresses exist and the longitudinal warping displacements are constant along the member, i.e., the rate of twist along the length of the member remains constant. In fact, axial restraints to warping always exist due to the variation of the section stiffness, and due to some support conditions or even non-uniformity of applied twisting moments along the span. As a result, additional direct stresses and associated shear stresses arise in the sections. This is called the axial constraint or warping stress system. In this sense this torsional phenomenon is termed specifically 'warping torsion' to be distinguished from 'pure torsion'.

The warping torsion theory of open and closed section members proposed and developed by Vlasov (146), Benscoter (10), Heileg (42), Kollbrunner and Hajden (57,58,59), Dabrowski (22) and Kristek (62) makes possible the solution of the warping torsion problem within acceptable accuracy. Accordingly, another main objective of this chapter is to summarize these analytical processes and to develop supplementary formulae whereby shear flows and warping forces in open and closed section bridge girders with a vertical axis of symmetry can be incorporated in the further development of the stiffness analysis presented in this thesis.

## 2.2 Direct and shear stress distribution due to bending

The derived procedure relating to the formulae for the evaluation of the normal bending stresses will not be stated here, and only the final expressions will be listed, since they are all well known. It is supposed that the origin of the x and y axes coincide with the centroid G of the cross-section. The neutral axis passes through the centroid of the cross-section and is inclined at some angle  $\alpha$  to the x axis where  $\alpha$  is considered to be positive in a clockwise sense. The normal stress at any point in the cross-section is expressed as,

$$\sigma_{z,b} = \left( \frac{-M_y I_{xx} - M_x I_{xy}}{I_{xx} I_{yy} - I_{xy}^2} \right) x + \left( \frac{M_x I_{yy} + M_y I_{xy}}{I_{xx} I_{yy} - I_{xy}^2} \right) y \quad (2.1)$$

where  $M_x$  and  $M_y$  are the internal bending moments about x and y axes respectively. The definition of the sectional properties in the above expression is given by

$$\begin{aligned} I_{xx} &= \int_A y^2 dA, \\ I_{yy} &= \int_A x^2 dA, \\ I_{xy} &= \int_A xy dA, \end{aligned} \quad (2.2)$$

which are the moments of inertia about the x and y axes and the product of inertia respectively.

Eq. 2.1 is usually written in the more convenient form:

$$\sigma_{\bar{x},b} = \frac{\bar{M}_x}{I_{xx}} y - \frac{\bar{M}_y}{I_{yy}} x \quad (2.3)$$

where

$$\bar{M}_x = \frac{M_x + M_y I_{xy}/I_{yy}}{1 - I_{xy}^2/I_{xx}I_{yy}} \quad \text{and} \quad \bar{M}_y = \frac{M_y + M_x I_{xy}/I_{xx}}{1 - I_{xy}^2/I_{xx}I_{yy}} \quad (2.4)$$

Since the y axis is fixed as an axis of symmetry in the present approach, then  $I_{xy}$  is zero and  $G_{xy}$  are principal axes. Eqs. 2.4 then reduces to

$$\bar{M}_x = M_x \quad \text{and} \quad \bar{M}_y = M_y, \quad (2.5)$$

and Eq. 2.3 becomes

$$\sigma_{\bar{x},b} = \frac{M_x}{I_{xx}} y - \frac{M_y}{I_{yy}} x \quad (2.6)$$

The shear flow and direct stresses acting on an element of the wall are related by Eq. 1.3, i.e.,

$$\frac{\partial q_s}{\partial s} + t \frac{\partial \sigma_{\bar{x},b}}{\partial z} = 0 \quad (2.7)$$

Differentiating Eq. 2.6 once, we have

$$\frac{\partial \sigma_{\bar{x},b}}{\partial z} = \frac{\partial M_x}{\partial z} \frac{y}{I_{xx}} - \frac{\partial M_y}{\partial z} \frac{x}{I_{yy}} \quad (2.8)$$

From the equilibrium condition  $\frac{\partial M_x}{\partial z} = Q_y$  and  $\frac{\partial M_y}{\partial z} = -Q_x$  we can write

$$\frac{\partial \sigma_{x,b}}{\partial z} = Q_y \frac{y}{I_{xx}} + Q_x \frac{x}{I_{yy}} \quad (2.9)$$

Substitution of Eq. 2.9 into Eq. 2.7 gives

$$\frac{\partial q_s}{\partial s} = - \frac{Q_y}{I_{xx}} \cdot t \cdot y - \frac{Q_x}{I_{yy}} \cdot t \cdot x \quad , \quad (2.10a)$$

or

$$\frac{\partial q_s}{\partial s} = - \bar{Q}_x \cdot t \cdot x - \bar{Q}_y \cdot t \cdot y \quad , \quad (2.10b)$$

where

$$\bar{Q}_x = \frac{Q_x}{I_{yy}} \quad , \quad \bar{Q}_y = \frac{Q_y}{I_{xx}} \quad . \quad (2.11)$$

For an open cross-section we may choose to make the open edge, where the shear stress must be zero, coincide with the origin of curvilinear coordinates  $S$ . Integrating Eq. 2.10(b) with respect to  $S$  from the origin for  $S$  to any point round the cross-section, we obtain,

$$q_s = - \bar{Q}_x \int_0^S t x ds - \bar{Q}_y \int_0^S t y ds = - \bar{Q}_x S_y - \bar{Q}_y S_x \quad (2.12)$$

$$\text{where } S_x = \int_0^S t y ds, \text{ and } S_y = \int_0^S t x ds, \quad (2.13)$$

are the first moments of area of the partial cross-section with respect to the  $x$  and  $y$  axes respectively.

In contradistinction to the case of the open section the mathematical difficulty in integration is attributable to the fact that the constants of integration are unknown. Compatibility conditions of deformation must then be introduced, since the problem is statically indeterminate.

For a single-spined box beam with  $n$  cells, there are  $n$  unknown constant shear flows, i.e., the degree of static indeterminacy is increased

by 1 with the addition of each closed cell. To resolve this difficulty, the section is imagined as cut open at  $n$  reference points, one in each cell, in order to convert the multi-cell beam into a single shear loaded open section beam. While the basic or open section shear flow  $q_b$  in the resulting open section can be determined by the use of Eq. 2.12, contiguous points on either side of the imaginary opening at the  $i$ th cell will be free to move relative to each other. This relative motion cannot take place in the actual closed section, since the continuity of deformation of the section would then be broken at cut point  $i$ . The presence of the statically indeterminate shear-flow  $q_o$  at this point of the closed section ensures that the contiguous points do not undergo any relative motion and, thus, the continuity of the deformation is maintained. Once the distribution of shear flow ( $q_b$ ) in the imaginary open section is determined, a redundant shear flow ( $q_o$ ) of uniform intensity throughout individual cells can be superposed on it to obtain the actual shear flow ( $q_s$ ) in the closed section. Thus, the formal expression for the shear flow developed in cell  $i$  is

$$q_{s,i} = q_{o,i} + q_{b,i} \quad (2.14)$$

where  $q_{o,i}$  is the constant shear flow at the  $i^{\text{th}}$  cut required to close the gap, and  $q_{b,i}$  is the shear flow at any point in cell  $i$  which is given by Eq. 2.12.

The  $i^{\text{th}}$  cell of the multi-cell section is shown in Fig. 2.1. The shear forces  $Q_x$  and  $Q_y$  are assumed to act through the shear centre (see section 2.7). The curvilinear coordinates  $S_1, S_2, \dots, S_n$  of cells 1, 2,  $\dots$ , and  $n$ , respectively, are chosen to be positive in the anticlockwise direction, as shown in Fig. 2.1. The shear flows in the same direction are also positive, except in the webs where the downward flows are defined as positive.

The total complementary potential energy per unit length of the member

due to bending is

$$\begin{aligned}\Pi_c &= \int_A \frac{\sigma_{s,b}^2}{2E_1} dA + \int_A \frac{\tau_s^2}{2G} dA \\ &= \int_A \frac{\sigma_{s,b}^2}{2E_1} dA + \sum_i^n \int_{pl,mn} \frac{(q_{o,i} + q_{b,i})^2}{2Gt} ds + \sum_i^{n+1} \int_{lm} \frac{(q_{o,i} + q_{b,i} - q_{o,i-1})^2}{2Gt} ds\end{aligned}\quad (2.15)$$

By the use of the principle of minimum complementary potential energy, which states that  $\Pi_c$  must be a minimum with respect to each of the statically indeterminate shear flow  $q_{o,i}$ , it follows that

$$\frac{\partial \Pi_c}{\partial q_{o,i}} = 0 \quad (2.16)$$

Thus, a set of simultaneous equations may be written in the form

$$\begin{aligned}q_{o,1} \oint_1 \frac{dS_1}{t} - q_{o,2} \int_{1,2} \frac{dS_1}{t} + \oint_1 \frac{q_{b,1}}{t} dS_1 &= 0 \\ -q_{o,1} \int_{1,2} \frac{dS_2}{t} + q_{o,2} \oint_2 \frac{dS_2}{t} - q_{o,3} \int_{2,3} \frac{dS_2}{t} + \oint_2 \frac{q_{b,2}}{t} dS_2 &= 0 \\ \dots\dots\dots \\ -q_{o,n-1} \int_{n-1,n} \frac{dS_n}{t} + q_{o,n} \oint_n \frac{dS_n}{t} + \oint_n \frac{q_{b,n}}{t} dS_n &= 0\end{aligned}\quad (2.17)$$

where use has been made of the fact that, in the common wall of the cross-section,  $q_{b,i} = -q_{b,i+1}$  and  $dS_i = -dS_{i+1}$ .

Eqs. 2.17 can be written in matrix form as

$$[f]\{q_o\} = \{Dq\} \quad (2.18)$$

The elements of the flexibility matrix  $[f]$  are called flexibility influence coefficients which are the displacements due to the unit values of the redundants. Therefore,  $[f]$  depends only on the properties of the structure, and represents the flexibility of the released structure. The

flexibility influence coefficients can be expressed as

$$f_{ik} = - \int_{i,k} \frac{ds}{t} \quad \text{Integral along the common wall between cell i and cell k}$$

$$f_{ii} = \oint_i \frac{ds}{t} \quad \text{Contour integral along the circumference of cell i}$$
(2.19)

The vector  $\{Dq\}$  is the displacement vector in the released structure due to the shear flows  $q_b$ . It is expressed as

$$\{Dq\} = [Dq,1, Dq,2, \dots, Dq,n]^T$$
(2.20)

in which

$$Dq,i = - \oint_i \frac{q_{b,i}}{t} dS$$

$$= \bar{Q}_x \oint_i \bar{q}_{x,i} \frac{dS}{t} + \bar{Q}_y \oint_i \bar{q}_{y,i} \frac{dS}{t}$$
(2.21)

and where

$$\bar{q}_{x,i} = - \int_0^{S_i} t x dS_i = -S_{y,i}$$

$$\bar{q}_{y,i} = - \int_0^{S_i} t y dS_i = -S_{x,i}$$
(2.22)

The elements of the vector  $\{q_0\}$  are the redundant flows which can be obtained by solving Eq. 2.18

$$\{q_0\} = [f]^{-1} \{Dq\}$$
(2.23)

Although the positions of the cuts can be arbitrary from a theoretical point of view, their positions are quite important from a numerical point of view. In order to avoid an ill-conditioned system of equations, the cuts are preferably located near the centres of either the upper or lower walls of the cells. Generally, at these points, the final shear flows differ only slightly from those of the determinate structure. The resulting equations of consistent deformation are, therefore, well conditioned.

Let us suppose the multi-cell cross-section, with side cantilevers shown in Fig. 2.2, possesses  $n$  cells with two flanges parallel to the local  $x$  axis and  $n+1$  webs which are not necessarily vertical to the flanges. The resultant shear force acts through the shear centre. The values of open section flow  $(\bar{q}_x)$  due to unit shear force  $(\frac{Q_x}{I_{yy}} = 1)$  are expressed as follows,

$$\begin{aligned}
 (\bar{q}_x)_{1,1} &= (\bar{q}_x)_{n+1,n+2} = b_c t_c (x_o - \frac{1}{2} b_c) = \frac{1}{2} b_c (b_t + b_c) t_c \\
 (\bar{q}_x)_{i,i+1} &= -\frac{1}{2} b_{t,i} t_{t,i} (x_i + x_{i+1} + \frac{b_{t,i}}{2}) & (i=1,2,\dots,n) \\
 (\bar{q}_x)_{i+1,i+1} &= \frac{1}{2} b_{t,i} t_{t,i} (x_i + x_{i+1} - \frac{b_{t,i}}{2}) & (i=1,2,\dots,n) \\
 (\bar{q}_x)_{i,n+i+2} &= (\bar{q}_x)_{i,i+1} - (\bar{q}_x)_{i,i} & (i=1,2,\dots,n+1) \\
 (\bar{q}_x)_{n+i+2,n+i+2} &= (\bar{q}_x)_{i,n+i+2} - h_{c,i} (x_i + \frac{1}{2} h_{c,i} \cos \alpha_i) t_{h,i} & (i=1,2,\dots,n+1) \quad (2.24) \\
 (\bar{q}_x)_{n+3,2n+4} &= (\bar{q}_x)_{n+3,n+3} \\
 (\bar{q}_x)_{n+i+2,2n+i+2} &= (\bar{q}_x)_{n+i+1,2n+i+2} - b_{b,i-1} (x_{n+i+1} - \frac{1}{2} b_{b,i-1}) t_{b,i-1} & (i=2,3,\dots,n) \\
 (\bar{q}_x)_{n+i+2,2n+i+3} &= (\bar{q}_x)_{n+i+2,2n+i+2} + (\bar{q}_x)_{n+i+2,n+i+2} & (i=2,3,\dots,n) \\
 (\bar{q}_x)_{2n+3,3n+3} &= -(\bar{q}_x)_{2n+3,2n+3}
 \end{aligned}$$

where  $\cos \alpha_i$  is the direction cosine between the vector  $i, n+i+2$  and the  $x$  axis, and  $b_t = \sum_i^n b_{t,i} = x_1 - x_{n+1}$

The following expression is also available for checking the result,

$$(\bar{q}_x)_{2n+3,3n+3} = -(\bar{q}_x)_{2n+3,2n+3} = (\bar{q}_x)_{2n+2,3n+3} - b_{b,n} (x_{2n+2} - \frac{1}{2} b_{b,n}) t_{b,n} \quad (2.25)$$

The following expressions relate to the calculation of open section flow  $(\bar{q}_y)$  due to unit shear force  $(\frac{Q_y}{I_{xx}} = 1)$ ,

$$\begin{aligned}
 (\bar{q}_y)_{1,1} &= -(\bar{q}_y)_{n+1,n+2} = -b_c t_c y_o \\
 (\bar{q}_y)_{i,i+1} &= 0.5 b_{t,i} \cdot t_{t,i} \cdot y_o & (i=1,2,\dots,n) \\
 (\bar{q}_y)_{i+1,i+1} &= -0.5 b_{t,i} \cdot t_{t,i} \cdot y_o & (i=1,2,\dots,n) \\
 (\bar{q}_y)_{i,n+i+2} &= (\bar{q}_y)_{i,i+1} - (\bar{q}_y)_{i,i} & (i=1,2,\dots,n+1)
 \end{aligned}$$

$$\begin{aligned}
(\bar{q}_y)_{m,n+i+2} &= (\bar{q}_y)_{i,n+i+2} - \frac{1}{2}h_{c,i} \cdot t_{h,i} \left(\frac{1}{2}h - y_G\right) & (i=1,2,\dots,n+1) \\
(\bar{q}_y)_{n+i+2,n+i+2} &= (\bar{q}_y)_{i,n+i+2} - h_{c,i} \cdot t_{h,i} \left(\frac{1}{2}h - y_G\right) & (i=1,2,\dots,n+1) \\
(\bar{q}_y)_{n+3,2n+4} &= (\bar{q}_y)_{n+3,n+3} & \\
(\bar{q}_y)_{n+i+2,2n+i+2} &= (\bar{q}_y)_{n+i+1,2n+i+2} - b_{b,i-1} \cdot t_{b,i-1} (h - y_G) & (i=2,3,\dots,n) \\
(\bar{q}_y)_{n+i+2,2n+i+3} &= (\bar{q}_y)_{n+i+2,2n+i+2} + (\bar{q}_y)_{n+i+2,n+i+2} & (i=2,3,\dots,n) \\
(\bar{q}_y)_{2n+3,3n+3} &= -(\bar{q}_y)_{2n+3,2n+3} &
\end{aligned} \tag{2.26}$$

To check the result the following expression can be used,

$$(\bar{q}_y)_{2n+3,3n+3} = -(\bar{q}_y)_{2n+3,2n+3} = (\bar{q}_y)_{2n+2,3n+3} - b_{b,n} \cdot t_{b,n} (h - y_G) \tag{2.27}$$

where  $y_G$  is the vertical ordinate of the centroid from the top flange, and the subscripts in Eqs. 2.24 to 2.27 represent the node number and the plate number successively which identify the points considered, while the subscript 'm' represents the mid-point of the individual plate considered.

Once the distributions of  $\bar{q}_x$  and  $\bar{q}_y$  have been determined the displacement vector  $D_q$  may be obtained. For the sake of convenience we let  $\bar{Q}_x = Q_x/I_{yy} = 1$  and  $\bar{Q}_y = Q_y/I_{xx} = 1$ , and separate the displacement vector as the sum of the two vectors,

$$\{\bar{D}_q\} = \{\bar{D}_{qx}\} + \{\bar{D}_{qy}\} \tag{2.28}$$

where

$$\bar{D}_{qx,i} = \oint_i \bar{q}_{x,i} \frac{ds}{t} \tag{2.29a}$$

$$\bar{D}_{qy,i} = \oint_i \bar{q}_{y,i} \frac{ds}{t} \tag{2.29b}$$

Substitution of Eqs. 2.24 and 2.26 into Eq. 2.34 followed by integration gives

$$\begin{aligned}
\bar{D}_{qx,i} &= -\frac{b_{t,i}^3}{24} + [(\bar{q}_x)_{i,n+i+2} - \frac{1}{2}t_{h,i} \cdot h_{c,i} (x_i - \frac{1}{3}h_{c,i} \cos \alpha_i)] \frac{h_{c,i}}{t_{h,i}} \\
&\quad - [(\bar{q}_x)_{i+1,n+i+3} - \frac{1}{2}t_{h,i+1} h_{c,i+1} (x_{i+1} - \frac{1}{3}h_{c,i+1} \cos \alpha_{i+1})] \frac{h_{c,i+1}}{t_{h,i+1}}
\end{aligned}$$

$$+ [(\bar{q}_x)_{n+i+2,2n+i+3} - \frac{1}{2} b_{b,i} \cdot t_{b,i} \cdot (x_{n+i+2} - \frac{1}{3} b_{b,i})] \frac{b_{b,i}}{t_{b,i}}$$

$$(i=1,2,\dots,n) \quad (2.30a)$$

and,

$$\bar{D}_{qy,i} = [(\bar{q}_y)_{i,n+i+2} - h_{c,i} \cdot t_{h,i} \cdot (\frac{h}{6} - \frac{y_G}{2})] \frac{h_{c,i}}{t_{h,i}}$$

$$- [(\bar{q}_y)_{i+1,n+i+3} - h_{c,i+1} \cdot t_{h,i+1} \cdot (\frac{h}{6} - \frac{y_G}{2})] \frac{h_{c,i+1}}{t_{h,i+1}}$$

$$+ [(\bar{q}_y)_{n+i+2,2n+i+3} - \frac{1}{2} b_{b,i} \cdot t_{b,i} \cdot (h - y_G)] \frac{b_{b,i}}{t_{b,i}}$$

$$(i=1,2,\dots,n) \quad (2.30b)$$

After solving the  $n$  linearly-independent equations of consistent deformation, we may obtain the  $n$  corrective flows at the hypothetical cuts. The final shear flow can be interpreted as the algebraic sum of the shear flows  $q_b$  in the open section and  $n$  corrective, constant shear flows  $q_o$  applied independently in each cell. The formulae for calculating the actual shear flows can be expressed as:

$$(q_{s,x})_{i,j} = \bar{Q}_x [(\bar{q}_x)_{i,j} + (\bar{q}_{x,o})_{i-1}] \quad (i=1,2,\dots,n)$$

$$(q_{s,x})_{i,i+1} = \bar{Q}_x [(\bar{q}_x)_{i,i+1} + (\bar{q}_{x,o})_{i+1}] \quad (i=1,2,\dots,n)$$

$$(q_{s,x})_{i,n+i+2} = \bar{Q}_x [(\bar{q}_x)_{i,n+i+2} - (\bar{q}_{x,o})_{i-1} + (\bar{q}_{x,o})_i] \quad (i=1,2,\dots,n)$$

$$(q_{s,x})_{n+i+2,n+i+2} = \bar{Q}_x [(\bar{q}_x)_{n+i+2,n+i+2} - (\bar{q}_{x,o})_{i-1} + (\bar{q}_{x,o})_i] \quad (i=1,2,\dots,n)$$

$$(q_{s,x})_{n+i+2,2n+i+3} = \bar{Q}_x [(\bar{q}_x)_{n+i+2,2n+i+3} + (\bar{q}_{x,o})_i] \quad (i=1,2,\dots,n)$$

$$(q_{s,x})_{n+i+3,2n+i+3} = \bar{Q}_x [(\bar{q}_x)_{n+i+3,2n+i+3} + (\bar{q}_{x,o})_i] \quad (i=1,2,\dots,n)$$

$$(2.31)$$

and,

$$(q_{s,y})_{i,i} = \bar{Q}_y [(\bar{q}_y)_{i,i} + (\bar{q}_{y,o})_{i-1}] \quad (i=1,2,\dots,n)$$

$$(q_{s,y})_{i,i+1} = \bar{Q}_y [(\bar{q}_y)_{i,i+1} + (\bar{q}_{y,o})_{i+1}] \quad (i=1,2,\dots,n)$$

$$(q_{s,y})_{i,n+i+2} = \bar{Q}_y [(\bar{q}_y)_{i,n+i+2} - (\bar{q}_{y,o})_{i-1} + (\bar{q}_{y,o})_i] \quad (i=1,2,\dots,n)$$

$$(q_{s,y})_{m,n+i+2} = \bar{Q}_y [(\bar{q}_y)_{m,n+i+2} - (\bar{q}_{y,o})_{i-1} + (\bar{q}_{y,o})_i] \quad (i=1,2,\dots,n)$$

$$(q_{s,y})_{n+i+2,n+i+2} = \bar{Q}_y [(\bar{q}_y)_{n+i+2,n+i+2} - (\bar{q}_{y,o})_{i-1} + (\bar{q}_{y,o})_i] \quad (i=1,2,\dots,n)$$

$$(q_{s,y})_{n+i+2,2n+i+3} = \bar{Q}_y [(\bar{q}_y)_{n+i+2,2n+i+3} + (\bar{q}_{y,o})_i] \quad (i=1,2,\dots,n)$$

$$(q_{s,y})_{n+i+3,2n+i+3} = \bar{Q}_y [(\bar{q}_y)_{n+i+3,2n+i+3} + (\bar{q}_{y,o})_i] \quad (i=1,2,\dots,n)$$

$$(2.32)$$

in which,

$$(\bar{q}_{x,o})_o = (\bar{q}_{x,o})_{n+1} = (\bar{q}_{y,o})_o = (\bar{q}_{y,o})_{n+1} = 0,$$

$\bar{q}_{x,o}$  and  $\bar{q}_{y,o}$  are the redundant shear flows due to the shear forces  $\bar{Q}_x = 1$  and  $\bar{Q}_y = 1$  respectively.

The resultant shear flows in the cross-section are given by superposition as follows:

$$q_s = q_{s,x} + q_{s,y} , \quad (2.33a)$$

and the shear stresses in longitudinal loading

$$\tau_s = q_s / t \quad (2.33b)$$

### 2.3 Effects of shear lag

The planar assumption in the elementary theory of bending is invalid in the case of thin-walled structures owing to the action of in-plane shear strains in the flanges. Direct stresses are therefore redistributed in the flanges with the peak values, at the web-flange intersections, being greater than the stresses given by the elementary theory of bending. As explained previously this phenomenon is known as shear lag, and is indicated in Fig. 2.3. The action of shear strains in the flanges also results in the deflections obtained, using the elementary theory, being underestimated.

The prediction of the shear lag effect has been reported in many papers, such as the bar simulation method proposed by Evans and Taherian (31,138,32). The most convenient treatment associated with the present approach is the concept of an effective breadth of each flange to replace the actual breadth  $b_i$  to give the correct values of the maximum longitudinal stresses and of the deflections. The effective breadth can be written as (Fig. 2.3):

$$b_{e,i} = \frac{\int_{b_i} \sigma_{3,b} dS}{[\sigma_{3,b}]_{s=\pm b_i/2}} , \quad (2.34)$$

and the effective breadth ratio which is the ratio of the effective breadth of each flange to its actual breadth, as:

$$\psi_{ei} = \frac{b_{e,i}}{b_i} \quad (2.35)$$

Moffat and Dowling (93) initiated a parametric study of the effective breadth ratio by the finite element method using the rectangular third order extensional-flexural element. The results were incorporated in the Merrison design rules (18) and in the present British Standard BS 5400 (13). It was found by Moffatt and Dowling that the effective breadth factors can be treated in the design rules as independent of the cross-sectional shape. The total effective breadth of a flange associated with each web should be taken as the sum of the effective breadths of the portions of flange considered separately on each side of that web. Thus, the effective breadth of each portion shall be taken as  $\psi_{ei} b_i$  or  $0.85 \psi_{ec} b_c$  for parts between webs or for parts projecting beyond an outer web respectively (Fig. 2.4).

The most significant parameter influencing the effective breadth of a flange is the breadth of each portion to length ratio ( $b_i/2L$ ). The importance of this parameter can be seen from Table 2.1, which gives effective breadth ratios at the mid-span, quarter-span, and support sections for different support conditions. Moffat and Dowling have devised effective breadth ratios for simply-supported, cantilevered, propped-cantilevered and fixed-ended box beams shown in Table 2.1 (93,18,13). In the case of an internal span of a continuous girder, the values of  $\psi_e$  given for the fixed ended beams should be used and, for end spans of continuous beams the values of  $\psi_e$  given for the propped-cantilevered beams should be used. When adjacent spans are of unequal length, the value of  $\psi_e$  at the intermediate support may be taken as the mean of the values obtained at the support for each span considered separately.

In order to account for the effect of the orthotropy of a steel flange the stiffening factor  $\alpha$ , which is defined as the ratio of the cross-sectional area of the longitudinal stiffeners to the cross-sectional area of the associated flange plate within a breadth  $b_i$ , is also included in the tables. Table 2.1 provides effective breadth ratios for flanges having stiffening factors of 0 and 1, and it is recommended that other values should be obtained by linear interpolation or extrapolation.

Since the present stiffness analysis approach is able to assemble the stiffness matrix for varying sectional properties, the effective breadth ratio can be evaluated at each nodal section, in order to account for the fact that the effective breadth ratio varies along the span. The shear lag rules state that the values of  $\psi_e$  along a beam is assumed to vary linearly between the quoted values in Table 2.1.

The availability of effective breadth ratios described above enables the peak stress at a web-flange junction ( $\sigma_{z,m}$ ) to be calculated simply. However, in the design of a bridge flange, it may often be necessary to have an estimate of the longitudinal stresses in parts of the flange remote from the web-flange junction. Such stresses ( $\sigma_{z,b}$ ) may be estimated using the following formula (Ref. 18 and Fig. 2.5):

$$\sigma_{z,b} = \sigma_{z,m} \left[ 4 \left( \frac{x}{b_i} \right)^2 + \frac{(3\psi_e - 1)}{2} \left\{ 1 - 4 \left( \frac{x}{b_i} \right)^2 \right\} \right] \text{ for parts between webs,} \quad (2.36a)$$

or

$$\sigma_{z,b} = \sigma_{z,m} \left[ \left( \frac{x}{b_c} \right)^2 + \frac{(3\psi_e - 1)}{2} \left\{ 1 - \left( \frac{x}{b_c} \right)^2 \right\} \right] \text{ for projections,} \quad (2.36b)$$

where  $\sigma_{z,m}$  is the maximum stress at the web-flange intersection.

The validity of the treatment described in this section will be investigated and its adequacy assessed from numerical examples and model tests described in later chapters.

#### 2.4 Pure torsion of open and closed section members

Approximate expressions for shear stress distribution due to St. Venant torsion and the rate of twist in a thin-walled, open section member are based on those derived for a thin rectangular strip using the well-known membrane analogy (142). The shear stress distribution across the thickness of the section wall may be written as

$$\tau_v = 2Gn \frac{\partial \theta_{z,p}}{\partial z}, \quad (2.37)$$

where  $\theta_{z,p}$  is the twisting angle due to St. Venant torsion. The maximum values of  $\tau_v$  occur on the surfaces of the wall where  $n = \pm \frac{t}{2}$  and are

$$(\tau_v)_{\max} = \pm Gt \frac{\partial \theta_{z,p}}{\partial z} \quad (2.38)$$

The rate of twist  $\frac{\partial \theta_{z,p}}{\partial z}$  is expressed in terms of the torsional moment, the shear modulus  $G$  and the St. Venant torsional moment of inertia  $J_v$  by the following relationship,

$$M_{T,v} = GJ_v \frac{\partial \theta_{z,p}}{\partial z} \quad (2.39)$$

$$\text{where } J_v = \mu \frac{st^3}{3} \quad \text{or} \quad J_v = \frac{\mu}{3} \int_A t^3 ds \quad (2.40)$$

In Eq. 2.40 the second expression is used to calculate  $J_v$  if the cross-section has a variable wall thickness. Values of  $\mu$  for a variety of open sections have been determined experimentally and quoted in Ref. 107. In particular, many thin-walled sections can be considered as being composed of several rectangular sections monolithically connected together. It is suggested that  $\mu$  could be chosen as unity without significant error. Thus, the general formula for such a 'composite' member is

$$J_v = \sum_{i=1}^m \frac{l_i t_i^3}{3} \quad (\text{length}^4) \quad (2.41)$$

where  $m$  = total number of component rectangles forming a cross-section,  
 $l_i$  = length of each  $i^{\text{th}}$  component rectangle,  
 $t_i$  = thickness of each  $i^{\text{th}}$  component rectangle.

The product  $GJ_V$  is known as the St. Venant torsional rigidity of the member. Eqs. 2.37 and 2.38 may be rewritten in terms of the torsional moment by substituting for  $\frac{\partial \theta_{j,v}}{\partial z}$  from Eq. 2.39. Thus,

$$\tau_v = \frac{2M_{T,v}}{J_v} n \quad ; \quad (\tau_v)_{\max} = \pm \frac{M_{T,v} \cdot t}{J_v} \quad (2.42)$$

For a closed section member having  $n$  cells shown in Fig. 2.6, the shear stresses are usually given in terms of shear flows, i.e., shear stress times the wall thickness. In Fig. 2.7 consideration of the equilibrium of forces in the axial direction on a differential element taken from the wall of the section shows that

$$(\tau_B + \frac{\partial \tau_B}{\partial S} ds)t \cdot dz - \tau_B t dz = \frac{\partial(\tau_B t)}{\partial S} dz = 0 \quad (2.43)$$

Integration of this equation yields  $q_B = \tau_B t = \text{a constant}$ . It is seen that, although the shear stress may differ from wall to wall, it must have constant values  $q_{B,1}, q_{B,2}, \dots, q_{B,n}$  along the wall of each individual cell. These are referred to as Bredt's shear flows, and the corresponding torsional moment is Bredt's torsional moment.

Investigation of the axial equilibrium of forces on an element at a junction of the walls reveals a further restriction on the shear flow. If such an element is considered at junction  $i$  of the section, the free-body diagrams shown in Fig. 2.8 require that

$$q_{B,i} dz - q_{B,i-1} dz - q_{i-1,i}^B dz = 0$$

i.e.,

$$q_{i-1,i}^B = q_{B,i} - q_{B,i-1} \quad (2.44)$$

This shows that the shear flow in an interior wall can be considered to have been obtained by the algebraic superposition of the shear flows in the component cells. The convention for the sign of the shear flow is that adopted by Kollbruner and Basler (55). If the shear flow  $q_{B,i}$  is indicated around the  $i^{\text{th}}$  cell in a sense which is equivalent to the positive sense of rotation, i.e., a right-threaded screw rotation, then the shear flow  $q_{B,i}$  is positive. The shear flow  $q_{i-1,i}^B$  in the wall between cells  $i-1$  and  $i$  is positive when its direction is the same as  $q_{B,i}$ .

It is apparent that we are not able to determine the shear stress distribution by a straightforward consideration of the static equilibrium of forces, since there are  $n$  unknown constant values of shear flow for a multi-cell beam of  $n$  cells. Compatibility conditions must therefore be used for solving the  $n$  unknown constants. Let  $u_t = R_t \theta_{z,p}$  denote the tangential displacement of a point on the cross-section, where  $R_t$  is the distance from the twisting centre  $E_S$ , and  $\theta_{z,p}$  is the angle of rotation of the section in its plane (Fig. 2.9). Let  $w_{z,p}$  denote the associated longitudinal displacement in the  $z$ -direction (warping). Then the associated shear strain at a point on the mid-line of the wall of the section is given by

$$\gamma_{zs}^p = \frac{\partial w_{z,p}}{\partial s} + \frac{\partial u_t}{\partial z} = \frac{q_{B,i}}{Gt_j} \quad (2.45)$$

The condition of continuity of the axial displacements is expressed by the following equation

$$\oint_i \frac{\partial w_{z,p}}{\partial s} ds = 0 \quad (2.46)$$

which states that when proceeding around each individual cell, the initial and final warping must be equal. Integrating Eq. 2.45 around each cell, and substituting Eq. 2.46 into it and putting

$$\oint_i R_t ds = \Omega_i \quad \text{twice the enclosed area of the } i^{\text{th}} \text{ cell,} \quad (2.47)$$

we obtain the following expression

$$\oint_i \tau_B ds = G\Omega_i \frac{\partial \theta_{z,p}}{\partial z} \quad (2.48)$$

Extending Eq. 2.48 for each cell, introducing the coefficients  $f_{ik}$ ,  $f_{ji}$  which have been expressed in Eq. 2.19, and considering that the circulating shear flows, constant for each cell, oppose one another in the intermediate webs, we may obtain a set of flexibility equations

$$[f] \{ \bar{q}_B \} = \{ \Omega \} \quad (2.49)$$

where

$$\bar{q}_{B,i} = \frac{q_{B,i}}{G \frac{\partial \theta_{z,p}}{\partial z}} \quad (2.50)$$

is defined as the unit shear flow distribution function relating to pure torsion.

The total torsional moment is shared by the shear stresses distributed over the  $n$  cells and is therefore the sum of the individual moments for each cell,

$$\begin{aligned} M_{T,B} &= \int_A q_{B,i} R_t ds = \sum_{i=1}^n q_{B,i} \Omega_i \\ &= G \left( \sum_{i=1}^n \bar{q}_{B,i} \cdot \Omega_i \right) \frac{\partial \theta_{z,p}}{\partial z} \end{aligned} \quad (2.51)$$

We may put

$$M_{T,B} = GJ_B \frac{\partial \theta_{z,p}}{\partial z}, \quad (2.52)$$

and therefore

$$J_B = \oint \bar{q}_B R_t ds = \sum_{i=1}^n \bar{q}_{B,i} \Omega_i, \quad (2.53)$$

where  $J_B$  is referred to as the Bredt torsional moment of inertia ( $\text{length}^4$ ).

The shear flow of each cell is

$$q_{B,i} = G \bar{q}_{B,i} \frac{\partial \theta_{z,p}}{\partial z}, \quad (2.54a)$$

or 
$$q_{B,i} = \frac{M_{T,B}}{J_B} \bar{q}_{B,i}, \quad (2.54b)$$

For a single cell cross-section from Eq. 2.49 it is apparent that

$$\bar{q}_B = \frac{\Omega}{\oint \frac{dt}{s}}, \quad (2.55a)$$

$$J_B = \frac{\Omega}{\oint \frac{dt}{s}}, \quad (2.55b)$$

and

$$q_B = \frac{M_{T,B}}{\Omega}. \quad (2.55c)$$

The St. Venant torsional rigidity of the component elements of the cross-section may make a small contribution to the torsional characteristics of the entire section. The assumption of a constant shear stress  $\tau_B$  across the wall of a hollow cross-section is only an approximation. There is a difference between the maximum and the average shear stress (Fig. 2.10). If  $\Delta\tau$  is the difference, it may be considered to be the maximum shear stress in an imaginary open cross-section having the same specific rotation as the corresponding closed cross-section with the average shear stress  $\tau_B$ . This leads to the following relation,

$$\begin{aligned} M_{T,p} &= M_{T,V} + M_{T,B} = G(J_V + J_B) \frac{\partial \theta_{z,p}}{\partial z} \\ &= GJ_T \frac{\partial \theta_{z,p}}{\partial z} \end{aligned} \quad (2.56)$$

where  $M_{T,p}$  is the total pure torsional moment,

and  $J_T = J_V + J_B$  is the total torsional moment of inertia (length<sup>4</sup>).

It is also clear that

$$M_{T,y} = \frac{J_y}{J_T} \cdot M_{T,p}$$

$$M_{T,z} = \frac{J_z}{J_T} \cdot M_{T,p}$$
(2.57)

### 2.5 Deformation of cross-sections

For the moment we shall consider the deformation of cross-sections in the case of pure torsion. For cross-sections assumed to be undeformed the movement will be about a certain point in their own plane as for rigid bodies. The tangential displacement of a point on the cross-section is given by (Fig. 2.9)

$$u_t = R_t \theta_{z,p}$$
(2.58)

where  $R_t$  is the perpendicular distance from the centre of twist to the tangent to the mid-line of wall at the point considered, and  $\theta_{z,p}$  is the twisting angle of the section in its plane in pure torsion.

For an open section member we may derive the axial warping displacement expressing by using Wagner's assumption (147), which shows that

$$\gamma_{zs}^v = \frac{\partial w_{z,v}}{\partial s} + \frac{\partial u_t}{\partial z} = 0$$
(2.59)

where  $w_{z,v}$  denotes the axial or warping displacement in an open section member.

Substituting Eq. 2.58 in Eq. 2.59 and integrating once we obtain

$$w_{z,v} = w_{z,0} - \int_0^s R_t ds \cdot \frac{\partial \theta_{z,p}}{\partial z}$$

$$= - \omega_I \frac{\partial \theta_{z,p}}{\partial z} ,$$
(2.60)

in which the unit torsional warping function for an open section

$$\omega_I = \omega_{I,0} + \int_0^S R_t ds \quad (2.61)$$

is equal to twice the value of the area shaded in Fig. 2.11 and is also called the sectorial coordinate (in length<sup>2</sup>).

For a closed section, the warping displacement can be assumed to have the same basic transverse distribution as in the St. Venant torsion of an open section, i.e., the unit warping function is still defined as the negative warping per unit rate of the angle of twist,

$$w_{z,p} = - \hat{\omega}_I \frac{\partial \theta_{z,p}}{\partial z} \quad (2.62)$$

When we come to the shear strain at the mid-line of the section instead of using Wagner's assumption, we note that the shear strain can be equal to that obtained from the Bredt formula,

$$\gamma_{zs}^p = \frac{q_\theta}{Gt} = \frac{\partial w_{z,p}}{\partial s} + \frac{\partial u_t}{\partial z} \quad (2.63)$$

Substituting Eqs. 2.54a , 2.58 and 2.62 in Eq. 2.63, and after cancelling the common factor  $\frac{\partial \theta_{z,p}}{\partial z}$ , the result becomes

$$- \frac{\partial \hat{\omega}_I}{\partial s} + R_t = \frac{\bar{q}_\theta}{t} \quad (2.64)$$

Integrating Eq. 2.64 once we obtain

$$\hat{\omega}_I = \hat{\omega}_{I,0} + \int_0^S (R_t - \frac{\bar{q}_\theta}{t}) ds \quad (\text{length}^2) \quad (2.65a)$$

where  $\hat{\omega}_I$  is the unit torsional warping function for a closed section and is also called the reduced sectorial coordinate.

In particular, for an open section, in which  $\bar{q}_\theta = 0$ , we obtain

$$\hat{\omega}_I = \omega_I = \omega_{I,0} + \int_0^S R_t ds \quad (2.65b)$$

It is then obvious that we may have the same form of expression both for closed sections and open sections, except that it is necessary to use the reduced sectorial coordinate  $\hat{\omega}_1$  instead of the sectorial coordinate  $\omega_1$ .

For the determination of the sign of the sectorial coordinate the following remarks can be seen to apply. If we regard the differential element of the mid-line  $ds$  as a vector, whose direction is the same as that of the integration, and if this vector causes a right hand screw rotation about the pole, then the increment  $R_t ds$  is taken as positive (Fig. 2.11). The shear flow distribution function  $\bar{q}_B$  is also regarded as a vector. If the directional sense of  $\bar{q}_B$  agrees with the sense of integration then the increment  $\bar{q}_B ds$  is positive.

Furthermore, since axial restraints to warping always exist, the torsional behaviour of a member actually appears in the form of warping torsion. The influences of secondary shear stresses or warping shear stresses associated with the longitudinal warping stresses have to be taken into account in the warping torsion of closed section members. The total angle of twist with respect to the centre of twist can then be split into two components, namely the primary angle of twist  $\theta_{z,p}$  which varies linearly, and the secondary angle of twist  $\theta_{z,s}$ ,

$$\theta_z = \theta_{z,p} + \theta_{z,s} \quad (2.66)$$

Therefore, the twist per unit length in warping torsion is no longer equal to the change in the angle of twist as in the case of pure torsion.

By analogy with the assumption made by Bencoter (10) it is further assumed that the warping displacements vary over the cross-section in the same way as in pure torsion. Thus, the distribution of  $w_{z,t}$  at the cross-section is still proportional to  $\hat{\omega}_1$ , but the relationship is defined not by

the primary twist per unit length, but by the rate of the entire warping torsional rotation. Hence, we may write finally

$$w_{z,t} = - \hat{\omega}_I \frac{\partial \theta_z}{\partial z} \quad (2.67)$$

## 2.6 State of stress system of warping torsion

The torsional warping stresses are given by the following expression,

$$\sigma_I = E_1 \frac{\partial w_{z,t}}{\partial z} = -E_1 \hat{\omega}_I \frac{\partial^2 \theta_z}{\partial z^2} \quad (2.68)$$

where  $E_1 = E/1-\nu^2$  is the conversion modulus of elasticity.

Since the torsional warping stresses arise from the restraint on warping, this stress distribution must be self-equilibrating and must have a zero longitudinal force resultant and a zero moment resultant. To represent the global behaviour of the warping stresses a new type of 'force' which may be called the torsional warping bimoment is introduced

$$B_I = \int_A \sigma_I \hat{\omega}_I dA \quad (\text{force} \times \text{length}^2) \quad (2.69)$$

In contrast with a bending moment which may be represented by a force pair, a bimoment may be represented by an equilibrium moment pair.

By defining a new type of geometric property of the cross-section,

$$J_I = \int_A \hat{\omega}_I^2 dA \quad (\text{length}^6) \quad (2.70)$$

which is known as the torsional warping moment of inertia, we obtain from Eqs. 2.68, 2.69 and 2.70

$$B_I = -E_1 J_I \frac{\partial^2 \theta_z}{\partial z^2} \quad (2.71)$$

Substitution of Eq. 2.71 into Eq. 2.68 then gives

$$\sigma_I = \frac{B_I \hat{\omega}_I}{J_I} \quad (2.72)$$

To obtain an expression for the associated torsional warping shear stresses a differential element is cut out of the beam such that two planes  $dz$  apart lie perpendicular to the axis of the beam, and planes  $ds$  apart are parallel to the beam axis and perpendicular to the mid-line of the cross-section. The equilibrium condition for all forces acting on this element in the  $z$  direction gives the expression for torsional warping shear flow,

$$\begin{aligned} q_I &= q_I^0 - \int_0^S t \frac{\partial \sigma_I}{\partial z} ds \\ &= q_I^0 + E_1 \left( \int_0^S \hat{\omega}_I dA \right) \cdot \frac{\partial^3 \theta_z}{\partial z^3} \\ &= q_I^0 + E_1 \hat{S}_I \frac{\partial^3 \theta_z}{\partial z^3} \\ &= q_I^0 - \frac{B'_I}{J_I} \cdot \hat{S}_I \quad (\text{force/length}) \end{aligned} \quad (2.73)$$

The integral expression in Eq. 2.73 represents another cross-sectional function called the sectorial statical moment of area in warping torsion

$$\hat{S}_I = \int_0^S \hat{\omega}_I dA \quad (\text{length}^4) \quad (2.74)$$

and  $B'_I$  is the first derivative of the bimoment.

For an open section member, if the integration is started from the contour edge point, where  $q_I^0 = 0$ , we obtain

$$q_I = E_1 S_I \frac{\partial^3 \theta_z}{\partial z^3} = - \frac{B'_I}{J_I} S_I \quad (2.75)$$

where

$$S_I = \int_0^S \omega_I dA \quad (\text{length}^4) \quad (2.76)$$

It is apparent that the distribution of shear flow  $q_I$  is a particular problem for closed sections. The difference between Eq. 2.73 and that for open sections Eq. 2.75, lies in the presence of the term  $q_I^0$ , which cannot be determined from the equilibrium condition.

A way out of this difficulty, similar to one which we have already used, is obtained by cutting each cell of the given section to form an imaginary open section. The compatibility condition, which requires the uniqueness or periodicity of the function for normal displacement, should then be used for solving for the  $n$  unknown constants:

$$\oint_i \frac{\partial w_{z,t}}{\partial s} ds = 0$$

$$\text{Since } \frac{\partial w_{z,t}}{\partial s} = \gamma_{zs}^t - \frac{\partial u_t}{\partial z} = \gamma_{zs}^p + \gamma_{zs}^I - \frac{\partial u_t}{\partial z}, \quad (2.77)$$

and from Eq. 2.48 we have

$$\oint_i \left( \gamma_{zs}^p - \frac{\partial u_t}{\partial z} \right) ds = 0, \quad (2.78)$$

we can state the condition that the warping shear strain along each closed portion of the mid-line of the cross-section must be equal to zero

$$\oint_i \gamma_{zs}^I ds = 0, \quad (2.79a)$$

or

$$\oint_i \tau_I ds = \oint_i \frac{q_I}{t} ds = 0 \quad (2.79b)$$

By setting up condition Eq. 2.79b for each cell separately, and putting

$$\bar{q}_{I,i}^0 = \frac{q_{I,i}^0 \cdot J_I}{B_I'} \quad (\text{length}^4) \quad (2.80a)$$

as the unit shear flow function in warping torsion, i.e.,

$$q_{I,i}^0 = \frac{B_I'}{J_I} \bar{q}_{I,i}^0, \quad (2.80b)$$

and

$$\bar{S}_{I,i} = \oint_i \hat{S}_I \frac{ds}{t} \quad (\text{length}^4), \quad (2.80c)$$

we obtain a set of flexibility equations

$$[f] \{ \bar{q}_I^0 \} = \{ \bar{S}_I \} \quad (2.80)$$

where the flexibility coefficient matrix  $[f]$  is expressed as in Eq. 2.19.

It may be noted that the coefficient matrices in the systems of equations (2.18), (2.49) and (2.80) are the same. This is to be expected since they all represent the relative warping at the cuts due to unit redundant flows, regardless of the type of loading.

The total torsional moment with respect to the centre of twist is

$$\begin{aligned} M_T &= M_{T,\rho} + M_{T,I} \\ &= M_{T,v} + M_{T,B} + M_{T,I} \end{aligned} \quad (2.81)$$

where  $M_{T,\rho}$  is the primary torsional moment referred to the St. Venant shear stresses and/or the Bredt shear stresses,

$M_{T,v}$  is the St. Venant torsional moment component,

$M_{T,B}$  is the Bredt torsional moment component,

and  $M_{T,I}$  is the secondary or flexural torsional moment resulted from warping shear stresses.

We now try to find the relationship between the bimoment and the flexural torsional moment. For reasons of equilibrium, the warping shear stresses  $\frac{q_I}{t}$  are associated with the longitudinal warping stresses according to the expression,

$$\frac{\partial \sigma_I}{\partial z} t + \frac{\partial q_I}{\partial s} = 0 \quad (2.82)$$

On multiplying equilibrium condition (2.82) by  $\hat{\omega}_I ds$  and integrating over the whole cross-section, we obtain

$$\int_A \frac{\partial \sigma_I}{\partial z} \hat{\omega}_I dA + \int_A \frac{\partial q_I}{\partial s} \hat{\omega}_I ds = 0 \quad (2.83a)$$

or

$$B'_I + \int_A \frac{\partial q_I}{\partial s} \hat{\omega}_I ds = 0 \quad (2.83b)$$

Using the integration by parts the integral in the above expression can be transformed into

$$- \int_A q_I \frac{\partial \hat{\omega}_I}{\partial s} ds ,$$

so that we finally have

$$B'_I = \int_A q_I \frac{\partial \hat{\omega}_I}{\partial s} ds \quad (2.84)$$

Substitution of Eq. 2.65 into Eq. 2.84 gives

$$\begin{aligned} B'_I &= \int_A q_I R_t ds - \int_A q_I \bar{q}_B \frac{ds}{t} \\ &= \int_A q_I R_t ds \\ &= M_{T,I} \end{aligned} \quad (2.85)$$

i.e., the secondary or flexural torsional moment  $M_{T,I}$  equals the first derivative of the bimoment  $B'_I$ .

The torsional warping shear flow is then expressed as

$$q_I = \frac{M_{T,I}}{J_I} \bar{q}_I^o - \frac{M_{T,I}}{J_I} \hat{S}_I \quad (2.86)$$

By superposition with Bredt's shear flow we can finally obtain the total shear flow on the external wall of the section,

$$q_{T,i} = \frac{M_{T,B}}{J_B} \bar{q}_{B,i} + \frac{M_{T,I}}{J_I} \bar{q}_{I,i}^o - \frac{M_{T,I}}{J_I} \hat{S}_I \quad (2.87a)$$

where the subscript  $i$  shows the number of the cell bounded by this mid-line.

For points lying on the interior wall of the section the shear flow can be considered to have been obtained by the algebraic superposition of

the shear flows in the cells lying on either side of the mid-line separating them,

$$(q_T)_{i-1,i} = \frac{M_{T,B}}{J_B} (\bar{q}_{B,i} - \bar{q}_{B,i-1}) + \frac{M_{T,I}}{J_I} (\bar{q}_{I,i}^0 - \bar{q}_{I,i-1}^0) - \frac{M_{T,I}}{J_I} \hat{S}_I \quad (2.87b)$$

On the open portions of the section the shear flow is

$$q_T = - \frac{M_{T,I}}{J_I} \hat{S}_I \quad (2.87c)$$

For an open section member the shear flow is

$$q_T = - \frac{M_{T,I}}{J_I} S_I \quad (2.88)$$

where  $J_I = \int_A \hat{\omega}_I^2 dA$  and  $S_I = \int_0^S \hat{\omega}_I dA$ .

In particular, for a single cell cross-section we will have

$$q_T = \frac{M_{T,B}}{\Omega} + \frac{M_{T,I}}{J_I} \cdot \frac{\oint \hat{S}_I \frac{ds}{t}}{\oint \frac{ds}{t}} - \frac{M_{T,I}}{J_I} \hat{S}_I \quad (2.89)$$

The maximum shear stresses caused by torsion in the cross-section may be expressed as

$$(\tau_T)_{\max} = \frac{M_{T,V} \cdot t}{J_V} + \frac{M_{T,B}}{J_B} \cdot \frac{\bar{q}_B}{t} + \frac{M_{T,I}}{J_I} \cdot \frac{\bar{q}_I^0}{t} - \frac{M_{T,I}}{J_I} \cdot \frac{\hat{S}_I}{t} \quad (2.90)$$

## 2.7 Shear centre and twisting centre

We have introduced the term 'shear centre' or 'flexural centre' and the term 'twisting centre' or 'the centre of twist' in previous sections. More detailed consideration is given to them in this section.

The shear centre of a cross-section may be defined as the point in the cross-section through which shear loads must act to produce no twisting. In contrast to the definition of shear centre, we define the centre of twist as the point about which the section twists in the case of torsion without

bending. It may be shown by use of the reciprocal theorem that the shear centre must be identical with the centre of twist of the section subjected to torsion. We can see, therefore, that there is a two-fold physical significance attached to each of these centres.

According to the definition we can now locate the shear centre.

Let  $M_b$  denote the moment about a longitudinal axis through an arbitrary point due to the open section or determinate shear flow  $q_b$ . Referring to the Bredt-Batho formula, the torque developed by a constant shear flow  $(q_o)_i$  about some point is  $(q_o)_i \Omega_i$ , where  $\Omega_i$  is twice the enclosed area of cell  $i$ . Thus the total moment developed by the flows  $q_o$  is  $\sum_{i=1}^n (q_o)_i \Omega_i$ . It follows that the requirement of equilibrium of moments about a longitudinal axis is satisfied provided

$$Q \cdot e_s + M_b + \sum_{i=1}^n (q_o)_i \Omega_i = 0 \quad (2.91)$$

from which the distance  $e_s$ , which indicates the position of the shear centre, can be determined.

For the section under consideration shown in Fig. 2.2 which possesses a vertical axis of symmetry, the shear centre must lie on the local  $y$  axis at some distance from the top flange. If we apply shear load  $Q_x = 1$  through the shear centre, we may estimate the distribution of shear flows  $q_b$  and  $q_o$  produced by  $Q_x$  following the process described in section 2.2. Equating thereafter the moments about the mid-point of the top flange we have

$$y_s = -M_b - \sum_{i=1}^n (q_{x,o})_i \Omega_i \quad (2.92)$$

where  $y_s$  is the coordinate of the shear centre referred to the mid-point of the top flange in the cross-section, and

$$\Omega_i = (b_{t,i} + b_{b,i}) h \quad , \quad (2.93)$$

$$(q_{x,o})_i = \frac{1}{I_{yy}} (\bar{q}_{x,o})_i \quad (2.94)$$

The moment due to the determinate shear flow  $q_b$  can be expressed as

$$M_b = \frac{1}{I_{yy}} \left\{ \sum_{i=1}^k x_i h [2(\bar{q}_x)_{i,n+i+2} - (x_i + \frac{1}{3} h_{c,i} \cos \alpha_i) h_{c,i} \cdot t_{h,i}] + \sum_{i=1}^n [(\bar{q}_x)_{n+i+2,2n+i+3} \cdot h \cdot b_{b,i} - \frac{b_{b,i}^2}{2} \cdot h \cdot t_{b,i} (x_{n+i+2} - \frac{1}{3} b_{b,i})] \right\} \quad (2.95)$$

where  $k = \frac{n}{2}$  when the cell number  $n$  is even, and  $k = \frac{n+1}{2}$  when  $n$  is an odd number.

If we pose the problem as alternatively locating the twisting centre, it is necessary to establish the geometric relations for the sectorial coordinates  $\hat{\omega}_I$ . If the start of integration of Eq. 2.65 is chosen to be at a point where the warping displacement is assumed to be zero, the expression for sectorial coordinates may be written as

$$\hat{\omega}_I = \int_0^S (R_t - \frac{\bar{q}_B}{t}) ds \quad (2.96a)$$

or

$$\omega_I = \int_0^S R_t ds \quad (2.96b)$$

They are then called the normalized sectorial coordinates, and the integral origin is called the principal origin of integration.

Since the unit warping function arises as a basic distribution of normal stresses with warping restraint, the sectorial coordinates must satisfy the following three conditions

$$\int_A \omega_I dA = 0 \quad \text{or} \quad \int_A \hat{\omega}_I dA = 0 \quad (2.97a)$$

$$\int_A \omega_I \cdot x dA = 0 \quad \int_A \hat{\omega}_I \cdot x dA = 0 \quad (2.97b)$$

$$\int_A \omega_I \cdot y dA = 0 \quad \int_A \hat{\omega}_I \cdot y dA = 0 \quad (2.97c)$$

Eq. 2.97(a) might be used to determine the principal origin of integration where the warping displacement is zero. According to the definition Eqs. 2.97(b) and 2.97(c) could be used for determining the location of the

centre of twist. For this purpose the relationship between the sectorial coordinates, which are referred to two different poles A and B, is now determined (Fig. 2.12). Note that the local coordinate axes  $x, y$  pass through the centroid of the section, and if it is assumed that point A is located at the centre of twist of the section, point B represents an arbitrary pole of the sectorial coordinates.

Using Green's integral theorem, we may obtain the differential areas  $(d\hat{\omega}_I)_A$  and  $(d\hat{\omega}_I)_B$  in the forms of

$$\begin{aligned} d\hat{\omega}_{IA} &= (x - a_x)dy - (y - a_y)dx \\ d\hat{\omega}_{IB} &= (x - b_x)dy - (y - b_y)dx \end{aligned}$$

Noting that  $\bar{e}_x = a_x - b_x$ , and  $\bar{e}_y = a_y - b_y$ , we have

$$d\hat{\omega}_{IA} - d\hat{\omega}_{IB} = -\bar{e}_x dy + \bar{e}_y dx.$$

Integration of this equation with respect to  $S$  gives

$$\hat{\omega}_{IA} = \hat{\omega}_{IB} - \bar{e}_x \cdot y + \bar{e}_y \cdot x + c. \quad (2.98)$$

Hence substituting Eq. 2.98 into Eqs. 2.97(b) and 2.97(c) respectively we have, after integration,

$$\int_A \hat{\omega}_{IB} \cdot x \, dA - \bar{e}_x \int_A xy \, dA + \bar{e}_y \int_A x^2 \, dA + c \int_A x \, dA = 0 \quad (2.99)$$

$$\text{and} \quad \int_A \hat{\omega}_{IB} \cdot y \, dA - \bar{e}_x \int_A y^2 \, dA + \bar{e}_y \int_A xy \, dA + c \int_A y \, dA = 0$$

Since the axes  $x, y$  pass through the centroid of the section we have

$$\int_A x \, dA = \int_A y \, dA = 0$$

and, because from the equations

$$\begin{aligned} \int_A x^2 \, dA &= I_{yy}, & \int_A y^2 \, dA &= I_{xx}, & \int_A xy \, dA &= I_{xy}, \\ \int_A \hat{\omega}_{IB} \cdot x \, dA &= (\hat{S}_{\omega y})_B, & \int_A \hat{\omega}_{IB} \cdot y \, dA &= (\hat{S}_{\omega x})_B, \end{aligned}$$

Eqs. 2.99 become

$$\begin{aligned} (\hat{S}_{\omega x})_B - \bar{e}_x I_{xx} + \bar{e}_y I_{xy} &= 0 \\ (\hat{S}_{\omega y})_B - \bar{e}_x I_{xy} + \bar{e}_y I_{yy} &= 0 \end{aligned} \quad (2.100)$$

where  $\hat{S}_{\omega x}$  and  $\hat{S}_{\omega y}$  are specified as the sectorial products of inertia.

The solution of these two simultaneous equations gives the following two formulae:

$$\bar{e}_x = \frac{(\hat{S}_{\omega x})_B I_{yy} - (\hat{S}_{\omega y})_B I_{xy}}{I_{xx} I_{yy} - I_{xy}^2} \quad (2.101a)$$

$$\text{and } \bar{e}_y = -\frac{(\hat{S}_{\omega y})_B I_{xx} - (\hat{S}_{\omega x})_B I_{xy}}{I_{xx} I_{yy} - I_{xy}^2} \quad (2.101b)$$

i.e.,

$$a_x = b_x + \frac{(\hat{S}_{\omega x})_B I_{yy} - (\hat{S}_{\omega y})_B I_{xy}}{I_{xx} I_{yy} - I_{xy}^2} \quad (2.102a)$$

$$\text{and } a_y = b_y - \frac{(\hat{S}_{\omega y})_B I_{xx} - (\hat{S}_{\omega x})_B I_{xy}}{I_{xx} I_{yy} - I_{xy}^2} \quad (2.102b)$$

Substituting Eq. 2.98 into Eq. 2.97(a) we obtain

$$c = -\frac{1}{A} \int_A \hat{\omega}_{IB} dA \quad (2.103)$$

In the case where axes  $x$ ,  $y$  coincide with the principal axes of a section, we have  $I_{xy} = 0$  and hence formulae (2.101) are simplified into formulae (2.104) as follows:

$$\bar{e}_x = \frac{(\hat{S}_{\omega x})_B}{I_{xx}} \quad (2.104)$$

$$\text{and } \bar{e}_y = -\frac{(\hat{S}_{\omega y})_B}{I_{yy}}$$

For a uni-symmetrical section with  $y$  as the axis of symmetry the initial pole can be advantageously located on the  $y$  axis. Then because of the antisymmetry of the  $\hat{\omega}_I$  diagram, it follows that

$$\bar{e}_x = c = 0 \quad ,$$

$$\text{and } \bar{e}_y = -\frac{1}{I_{yy}} \int_A \hat{\omega}_{IB} \cdot x dA = -\frac{(\hat{S}_{\omega y})_B}{I_{yy}} \quad (2.105)$$

The twisting centre and the principal radius, therefore, both lie on the axis of symmetry. In particular, when a section has two axes of symmetry, then its centre of twist lies at its centroid and its principal radius lies on one of its axes of symmetry.

Bearing in mind that the shear centre and the twisting centre must be identical with each other for the section under consideration shown in Fig. 2.2, and choosing the integral origin at the mid-point of the top flange, we have

$$\bar{e}_y = y_s \quad (2.106)$$

Thus, the position of the shear centre and of the centre of twist can be located either by Eq. 2.92 or by Eq. 2.105. Numerical examples have shown that identical results are obtained from both equations. In practice, however, it is more convenient to use Eq. 2.105.

### 2.8 Basic differential equation for warping torsion

We consider now a differential element cut out of a beam subjected to a continuously distributed twisting moment  $m_{z,ext}$ . From the equilibrium condition, we obtain

$$\frac{\partial M_T}{\partial z} + m_{z,ext} = 0 \quad (2.107)$$

Since the total internal torsional moment is equal to the sum of the primary torsional moment and the secondary or flexural torsional moment, from Eqs. 2.56 and 2.85 we have

$$\begin{aligned} M_T &= M_{T,p} + M_{T,I} \\ &= GJ_T \frac{\partial \theta_{z,p}}{\partial z} - E_1 J_T \frac{\partial^3 \theta_z}{\partial z^3} \end{aligned} \quad (2.108)$$

From the generally valid relation

$$\tau_T = G \left( \frac{\partial w_{z,t}}{\partial s} + \frac{\partial u_t}{\partial z} \right),$$

we obtain by Eqs. 2.67 and 2.58

$$\tau_T = G \left( - \frac{\partial \hat{\omega}_T}{\partial s} \cdot \frac{\partial \theta_z}{\partial z} + R_t \frac{\partial \theta_{z,p}}{\partial z} \right). \quad (2.109)$$

Substitution of Eq. 2.96(a) in Eq. 2.109 gives

$$\tau_T = G \left[ - \left( R_t - \frac{\bar{q}_B}{t} \right) \frac{\partial \theta_z}{\partial z} + R_t \frac{\partial \theta_{z,p}}{\partial z} \right].$$

Using the equilibrium condition  $\int_A \tau_T R_t dA = M_T$ , we have

$$M_T = G \left[ - \left( \int R_t^2 dA - \oint \bar{q}_B R_t ds \right) \frac{\partial \theta_z}{\partial z} + \frac{\partial \theta_{z,p}}{\partial z} \int_A R_t dA \right] \quad (2.110)$$

Note that the integral  $\oint$  refers only to the closed part, whereas the integral  $\int_A$  should extend over the entire cross-sectional area.

Using Eq. 2.53 and putting

$$J_C = \int_A R_t^2 dA \quad (\text{length}^4) \quad (2.111)$$

which is called the central second moment of area, we have

$$M_T = G \left[ (J_B - J_C) \frac{\partial \theta_z}{\partial z} + J_C \frac{\partial \theta_{z,p}}{\partial z} \right]. \quad (2.112)$$

We then finally obtain the connection between the total twist and the primary twist as follows:

$$\frac{\partial \theta_{z,p}}{\partial z} = (1 - \mu_t) \frac{M_T}{GJ_B} + \mu_t \frac{\partial \theta_z}{\partial z}, \quad (2.113)$$

in which the coefficient

$$\mu_t = 1 - \frac{J_B}{J_C} \quad (2.114)$$

is called the warping shear parameter.

Substituting Eq. 2.113 in Eq. 2.108 and letting  $J_T \doteq J_B$  for cross-sections in which the closed portions are not small, we then obtain

$$M_T = - \frac{1}{\mu_t} E_I J_I \frac{\partial^3 \theta_z}{\partial z^3} + G J_T \frac{\partial \theta_z}{\partial z} \quad (2.115)$$

Differentiating Eq. 2.115 and substituting it in Eq. 2.108, we obtain the general differential equation for warping torsion

$$- \frac{1}{\mu_t} E_I J_I \frac{\partial^4 \theta_z}{\partial z^4} + G J_T \frac{\partial^2 \theta_z}{\partial z^2} = m_{z, \text{ext}} \quad (2.116)$$

In particular, for open section members  $J_B = 0$ , and thus  $\mu_t = 1$  accordingly

$$M_T = - E_I J_I \frac{\partial^3 \theta_z}{\partial z^3} + G J_T \frac{\partial \theta_z}{\partial z} \quad (2.117)$$

$$- E_I J_I \frac{\partial^4 \theta_z}{\partial z^4} + G J_T \frac{\partial^2 \theta_z}{\partial z^2} = m_{z, \text{ext}} \quad (2.118)$$

## 2.9 Calculation of sectional properties in bending and warping torsion

To calculate the normal and shear stresses due to bending and warping torsion in a thin-walled cross-section, with at least a vertical axis of symmetry to the flange (Fig. 2.2), the following geometrical variables relating to the cross-section are required:

- the vertical coordinate of the centroid from the top flange (length),  $y_G$ ,
- the vertical coordinate of the shear centre or the centre of twist from the top flange (length),  $y_S (\bar{e}_y)$ ,
- cross-sectional area (length<sup>2</sup>),  $A$ ,
- first moment of area of the partial cross-section about the x-axis (length<sup>3</sup>),  $S_x = \int_0^S y dA$ ,

- first moment of area of the partial cross-section about the y-axis (length<sup>3</sup>),  $S_y = \int_0^S x dA$ ,
- moment of inertia of the cross-section with respect to the x-axis (length<sup>4</sup>),  $I_{xx} = \int_A y^2 dA$ ,
- moment of inertia of the cross-section with respect to the y-axis (length<sup>4</sup>),  $I_{yy} = \int_A x^2 dA$ ,
- flexibility coefficients,  $f_{ij} = \oint_i \frac{ds}{t}$  or  $f_{ik} = -\int_{i,k} \frac{ds}{t}$ , in which the indices i and k relate to the cells lying on either side of the mid-line separating them,
- displacement vector due to unit shear force (length<sup>3</sup>),  $\bar{D}_{qx,i} = -\oint_i S_{y,i} \frac{ds}{t}$  and  $\bar{D}_{qy,i} = -\oint_i S_{x,i} \frac{ds}{t}$ ,
- twice the enclosed area of each cell (length<sup>2</sup>),  $\Omega_i$ ,
- the St. Venant torsional moment of inertia (length<sup>4</sup>),  $J_V = \sum_i^m \frac{\ell_i t_i^3}{3}$ ,
- the Bredt torsional moment of inertia for the closed portion of the section, (length<sup>4</sup>),  $J_B = \sum_i^n \bar{q}_{B,i} \Omega_i$ ,
- the total torsional moment of inertia in pure tension (length<sup>4</sup>),  $J_T = J_V + J_B$ ,
- the normalized sectorial coordinates (length<sup>2</sup>),  $\hat{\omega}_I = \int_0^S (R_t - \frac{\bar{q}_B}{t}) ds$ ,
- the torsional warping moment of inertia (length<sup>6</sup>),  $J_I = \int_A \hat{\omega}_I^2 dA$ ,
- the sectorial statical moment of area (length<sup>4</sup>),  $\hat{S}_I = \int_0^S \hat{\omega}_I dA$ ,
- the values of  $\bar{S}_{I,i} = \oint_i \hat{S}_I \frac{ds}{t}$  (length<sup>4</sup>),
- the central second moment of area (length<sup>4</sup>),  $J_C = \int_A R_t^2 dA$ ,
- the warping shear parameter,  $\mu_t = 1 - \frac{J_B}{J_C}$ .

The evaluation of some of the properties is a well known procedure, and some of them have already been discussed in detail in previous sections. In this section some supplementary formulae will be developed particularly

for calculating the geometric quantities used in the analysis of warping torsion.

We can see that in the course of determining these quantities, a certain number of definite integrals must be found. Such definite integrals can be expressed as follows (Fig. 2.13):

$$I = \int_{a_1}^{a_2} f(x)y(x)dx = \Omega y(x_G) \quad (2.119)$$

where  $y(x)$  is a linear function of the variable quantity  $x$ ,

$\Omega$  is the shaded area enclosed by the curve  $f(x)$  and  $a_1 < x < a_2$ ,

$x_G$  is the coordinate of the centroid  $G$ .

In particular, we now consider a straight element  $j$ - $k$  of the mid-line of the section. Let its wall thickness be  $t_j$  (Fig. 2.14). For this segment, let the ordinates  $\eta$  and  $\bar{\eta}$  of two different diagrams be given, whose form is linear. The integral

$$I_{jk} = \int_j^k \eta \bar{\eta} dF = t_j \int_j^k \eta \bar{\eta} dS$$

is then given by the expression

$$I_{jk} = \frac{l_j t_j}{6} [ \bar{\eta}_j (2\eta_j + \eta_k) + \bar{\eta}_k (2\eta_k + \eta_j) ] \quad (2.120a)$$

or

$$I_{jk} = \frac{l_j t_j}{6} [ \eta_j (2\bar{\eta}_j + \bar{\eta}_k) + \eta_k (2\bar{\eta}_k + \bar{\eta}_j) ] \quad (2.120b)$$

Eq. 2.120 may be simplified when  $\eta = \bar{\eta}$  to give

$$I_{jk} = \frac{l_j t_j}{3} (\eta_j^2 + \eta_k^2 + \eta_j \eta_k) \quad (2.121)$$

In the case in which  $\eta$  is a curvilinear line sometimes it is difficult to generate the position of the centroid. Thus it is advantageous to use Simpson's integration method. If  $\eta$  is a parabolic curve and  $\bar{\eta} = 1$  we may use the following formula with sufficient accuracy

$$I_{jk} = \int_j^k \eta \, ds = \frac{\ell_j}{6} (\eta_j + 4\eta_o + \eta_k) \quad (2.122)$$

where  $\eta_o$  is the ordinate at the midpoint.

In order to determine the position of the shear centre and to obtain the diagram of the reduced sectorial coordinates  $\hat{\omega}_I$ , the intersection of the y axis and the mid-line of the top flange B is chosen as the principal integral origin. The sectorial coordinates  $\hat{\omega}_{IB}$  of individual characteristic points (end nodes of the elements) can be calculated by the following expressions:

$$(\hat{\omega}_{IB})_o = - \sum_i^k (\bar{\tau}_B)_{m,i} (x_{i-1} - x_i) - (\bar{\tau}_B)_{m,k+1} \cdot x_k = -(\hat{\omega}_{IB})_{n+2}$$

where,  $k = \frac{n}{2}$  when n is an even number and  $k = \frac{n+1}{2}$  when n is an odd number (2.123)

$$(\hat{\omega}_{IB})_i = (\hat{\omega}_{IB})_{i-1} + (\bar{\tau}_B)_{m,i} (x_{i-1} - x_i) \quad (i=1,2,\dots,n+2)$$

$$(\hat{\omega}_{IB})_{n+i+2} = (\hat{\omega}_{IB})_i + x_i h - (\bar{\tau}_I)_{m,n+i+2} h_{c,i} \quad (i=1,2,\dots,n+1)$$

It should be noted that in the side cantilevers of the cross-section, both terms of the integral (2.96a) are equal to zero, so that the value of the sectorial coordinate is constant.

$$(\bar{\tau}_B)_{m,1} = (\bar{\tau}_B)_{m,n+2} = 0$$

$$(\bar{\tau}_B)_{m,i+1} = \bar{q}_{B,i} / t_{t,i} \quad (i=1,2,\dots,n)$$

$$(\bar{\tau}_B)_{m,n+i+2} = (\bar{q}_{B,j} - \bar{q}_{B,i-1}) / t_{h,i} \quad (i=1,2,\dots,n+1) \quad (2.124)$$

$$(\bar{\tau}_B)_{m,2n+i+3} = \bar{q}_{B,i} / t_{b,i} \quad (i=1,2,\dots,n)$$

in which  $\bar{q}_{B,0} = \bar{q}_{B,n+1} = 0$ , and n is the total number of the cells.

Applying the numerical integration shown in Eq. 2.120, we obtain from the diagram of  $\hat{\omega}_{IB}$  the quantity  $(\hat{S}_{\omega y})_B$  as

$$(\hat{S}_{\omega y})_B = \frac{1}{6} \sum_{i=1}^m \ell_i t_i [(\hat{\omega}_{IB})_j (2x_j + x_k) + (\hat{\omega}_{IB})_k (2x_k + x_j)] \quad (2.125)$$

where m is the total number of plate elements in the section,

$\ell_i$  is the length of the  $i^{\text{th}}$  element and  $t_i$  is its thickness.

Subscripts j and k indicate the number of the end nodes of the individual elements.

Using Eq. 2.105 we may obtain the coordinate  $y_s$  of the shear centre. The normalized reduced sectorial coordinates  $\hat{\omega}_I$  at individual nodes can then be evaluated by the following expressions:

$$\hat{\omega}_{I,0} = x_0 y_s - \sum_{i=1}^k (\bar{\tau}_B)_{m,i} (x_{i-1} - x_i) - (\bar{\tau}_B)_{m,k+1} \cdot x_k = -\hat{\omega}_{I,n+2}$$

where,  $k = \frac{n}{2}$  when  $n$  is an even number, and  $k = \frac{n+1}{2}$  when  $n$  is an odd number,

(2.126)

$$\hat{\omega}_{I,i} = \hat{\omega}_{I,i-1} - [y_s - (\bar{\tau}_B)_{m,i}] (x_{i-1} - x_i) \quad (i=1,2,\dots,n+2)$$

$$\hat{\omega}_{I,n+i+2} = \hat{\omega}_{I,i} + h \cdot x_i + y_s (x_{n+i+2} - x_i) - (\bar{\tau}_B)_{m,n+i+2} \cdot h_{c,i} \quad (i=1,2,\dots,n+1)$$

Using the diagram of normalized sectorial coordinates  $\hat{\omega}_I$  we obtain from Eq. 2.12. the value of  $J_I$  as

$$J_I = \frac{1}{3} \sum_{i=1}^m \ell_i t_i (\hat{\omega}_{I,j}^2 + \hat{\omega}_{I,k}^2 + \hat{\omega}_{I,j} \cdot \hat{\omega}_{I,k}) \quad (2.127)$$

In the same way as with open sections, we may calculate the  $\hat{S}_I$  diagram from the  $\hat{\omega}_I$  diagram. It should be noticed that all the cuts are located at the mid-points of the lower flange of the section (Fig. 2.15f). The formulae for calculating the values of  $\hat{S}_I$  at characteristic points are written as

$$(\hat{S}_I)_{0,1} = (\hat{S}_I)_{n+2,n+2} = 0$$

$$(\hat{S}_I)_{m,2n+i+3} = 0 \quad (i=1,2,\dots,n)$$

$$(\hat{S}_I)_{n+i+2,2n+i+3} = -\frac{1}{8} b_{b,i} t_{b,i} (3\hat{\omega}_{I,n+i+3} + \hat{\omega}_{I,n+i+2}) \quad (i=1,2,\dots,n)$$

$$(\hat{S}_I)_{n+i+3,2n+i+3} = \frac{1}{8} b_{b,i} t_{b,i} (3\hat{\omega}_{I,n+i+3} + \hat{\omega}_{I,n+i+2}) \quad (i=1,2,\dots,n)$$

$$(\hat{S}_I)_{n+3,n+3} = (\hat{S}_I)_{n+3,2n+4}$$

$$(\hat{S}_I)_{2n+3,2n+3} = -(\hat{S}_I)_{2n+3,3n+3}$$

$$(\hat{S}_I)_{n+i+2,n+i+2} = (\hat{S}_I)_{n+i+2,2n+i+3} - (\hat{S}_I)_{n+i+2,2n+i+2} \quad (i=2,3,\dots,n)$$

$$(\hat{S}_I)_{m,n+i+2} = (\hat{S}_I)_{n+i+2,n+i+2} - \frac{1}{8} h_{c,i} t_{h,i} (3\hat{\omega}_{I,n+i+2} + \hat{\omega}_{I,i}) \quad (i=1,2,\dots,n+1)$$

$$(\hat{S}_I)_{i,n+i+2} = (\hat{S}_I)_{n+i+2,n+i+2} - \frac{1}{2} h_{c,i} t_{h,i} (\hat{\omega}_{I,n+i+2} + \hat{\omega}_{I,i}) \quad (i=1,2,\dots,n+1)$$

$$(\hat{S}_I)_{m,1} = -\frac{1}{8} b_c t_c (3\hat{\omega}_{I,0} + \hat{\omega}_{I,1}) = (\hat{S}_I)_{m,n+2}$$

$$\begin{aligned}
(\hat{S}_I)_{1,1} &= -\frac{1}{2} b_c t_c (\hat{\omega}_{I,0} + \hat{\omega}_{I,1}) \\
(\hat{S}_I)_{i,i+1} &= (\hat{S}_I)_{i,i} + (\hat{S}_I)_{i,n+i+2} && (i=1,2,\dots,n+1) \\
(\hat{S}_I)_{m,i+1} &= (\hat{S}_I)_{i,i+1} - \frac{1}{8} b_{t,i} \cdot t_{t,i} (3\hat{\omega}_{I,i} + \hat{\omega}_{I,i+1}) && (i=1,2,\dots,n) \\
(\hat{S}_I)_{i+1,i+1} &= (\hat{S}_I)_{i,i+1} - \frac{1}{2} b_{t,i} \cdot t_{t,i} (\hat{\omega}_{I,i} + \hat{\omega}_{I,i+1}) && (i=1,2,\dots,n)
\end{aligned}
\tag{2.128}$$

To be able to determine the unit warping shear flow function  $\bar{q}_I^0$ , it is necessary to solve Eqs. 2.80. The coefficients are the same as those in Eqs. 2.49, from which we shall obtain the unit Bredt's shear flow function first. We here formulate the expressions for the free terms of Eqs. 2.80,

$$\begin{aligned}
\bar{S}_{I,i} &= \frac{b_{t,i}}{6 t_{t,i}} [(\hat{S}_I)_{i,i+1} + 4(\hat{S}_I)_{m,i+1} + (\hat{S}_I)_{i+1,i+1}] \\
&+ \frac{b_{b,i}}{6 t_{b,i}} [(\hat{S}_I)_{n+i+2,2n+i+3} + 4(\hat{S}_I)_{m,2n+i+3} + (\hat{S}_I)_{n+i+3,2n+i+3}] \\
&+ \frac{h_{c,i}}{6 t_{h,i}} [(\hat{S}_I)_{i,n+i+2} + 4(\hat{S}_I)_{m,n+i+2} + (\hat{S}_I)_{n+i+2,n+i+2}] \\
&- \frac{h_{c,i+1}}{6 t_{h,i+1}} [(\hat{S}_I)_{i+1,n+i+3} + 4(\hat{S}_I)_{m,n+i+3} + (\hat{S}_I)_{n+i+3,n+i+3}] \\
&(i=1,2,\dots,n)
\end{aligned}
\tag{2.129}$$

Note that in calculating the quantities  $\bar{q}_I^0$ , the sign convention adopted for Bredt's shear flow is used. For each individual cell, the positive directional sense is regarded as that which runs anticlockwise around the cell.

Finally, when considering the shear strain effect we shall calculate the central second moment of area  $J_c$ . The coordinates of the shear centre in the local coordinate system of the cross-section may be obtained as

$$\begin{aligned}
x_E &= 0 \\
y_E &= y_S - y_G
\end{aligned}
\tag{2.130}$$

The perpendicular distance from the shear centre to the individual element can be expressed by the coordinates of the two end nodes and of the shear centre,

$$R_t = \frac{x_j y_k + x_k y_E + x_E y_j - x_k y_j - x_E y_k - x_j y_E}{l_i} \quad (2.131)$$

We then have

$$J_C = \sum_{i=1}^m \frac{t_i (x_j y_k + x_k y_E - x_k y_j - x_j y_E)^2}{l_i} \quad (2.132)$$

where,  $m$  is the total number of elements,

$l_i$  is the length of the  $i^{\text{th}}$  element and  $t_i$  is its thickness, and the indices  $j$  and  $k$  are the number of the discrete nodes of the individual elements.

To understand the above process more clearly we give now a numerical example. The dimensions of the section and the subdivision of the section are given in Fig. 2.15(a) and Fig. 2.15(b).

The flexibility equations (2.81) become:

$$\begin{aligned} 5.6527 \bar{q}_{B,1} - 2 \bar{q}_{B,2} &= \frac{3}{2} a t_o \\ - 2 \bar{q}_{B,1} + 5.8333 \bar{q}_{B,2} - 2 \bar{q}_{B,3} &= 2 a t_o \\ - 2 \bar{q}_{B,2} + 5.6527 \bar{q}_{B,3} &= \frac{3}{2} a t_o \end{aligned}$$

Solving, we obtain

$$\begin{aligned} \bar{q}_{B,1} = \bar{q}_{B,3} &= 0.5105 a t_o \\ \bar{q}_{B,2} &= 0.6929 a t_o \end{aligned}$$

The unit warping shear stress function  $\bar{\tau}_B$  according to Eqs. 2.124 is shown in Fig. 2.15 (c), together with its directional sense.

The diagram  $\hat{\omega}_{IB}$  calculated by Eqs. 2.123 is shown in Fig. 2.15(d).

After evaluating  $I_{yy}$  and the integrals  $(\hat{S}_{\omega y})_B$  by Eq. 2.125, we obtain by Eq. 2.105 the position of the shear centre  $E_S$ .

$$y_s = \frac{6.2327}{13.2369} a = 0.4709 a$$

The coordinates of the shear centre about the  $xy$  coordinate system are

$$x_E = 0$$

$$y_E = 0.4709 a - 0.3109 a = 0.16 a$$

The  $\hat{\omega}_I$  diagram is then shown in Fig. 2.15(e). Using this diagram we obtain by integration the value of  $J_I$  as

$$J_I = 1.0414 \times 10^{-1} a^5 t_0$$

The  $\hat{S}_I$  diagram is shown in Fig. 2.15(f). Using this diagram we calculate the values for the free terms of the system of equations (2.81)

$$\bar{S}_{I,1} = 10.2081 \times 10^{-2} a^4$$

$$\bar{S}_{I,2} = 10.5993 \times 10^{-2} a^4$$

$$\bar{S}_{I,3} = 10.2081 \times 10^{-2} a^4$$

On solving the system of equations we obtain

$$\bar{q}_{I,1}^0 = 3.2332 \times 10^{-2} a^3 t_0$$

$$\bar{q}_{I,2}^0 = 4.0341 \times 10^{-2} a^3 t_0$$

$$\bar{q}_{I,3}^0 = 3.2332 \times 10^{-2} a^3 t_0$$

The  $\bar{q}_I^0$  diagram, with directions introduced, is shown in Fig. 2.15 (e).

Finally the  $\hat{S}_I - \bar{q}_I^0$  diagram is shown in Fig. 2.15(f).

Likewise we calculate the value of the central second moment of area

$$J_C = 3.46087 a^3 t_0$$

and the warping shear parameter

$$\mu_t = 1 - \frac{2 \times 1.5 \times 0.5105 + 2 \times 0.6929}{3.46087} = 0.1571$$

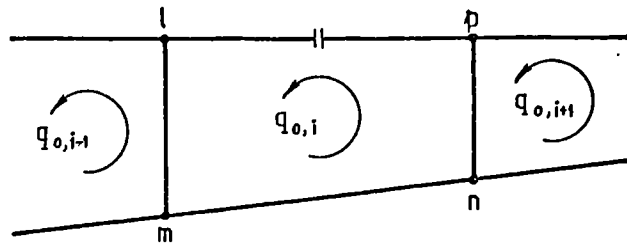


Fig. 2.1 Redundant shear flow in the  $i^{th}$  cell of an  $n$ -cell beam subjected to shear

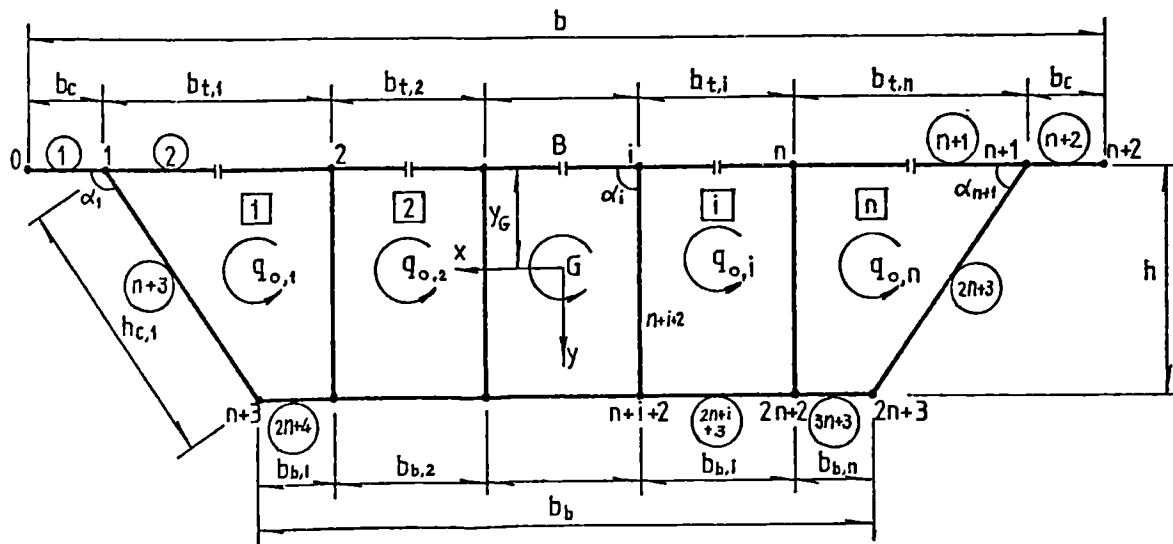


Fig. 2.2 Cell reference numbers

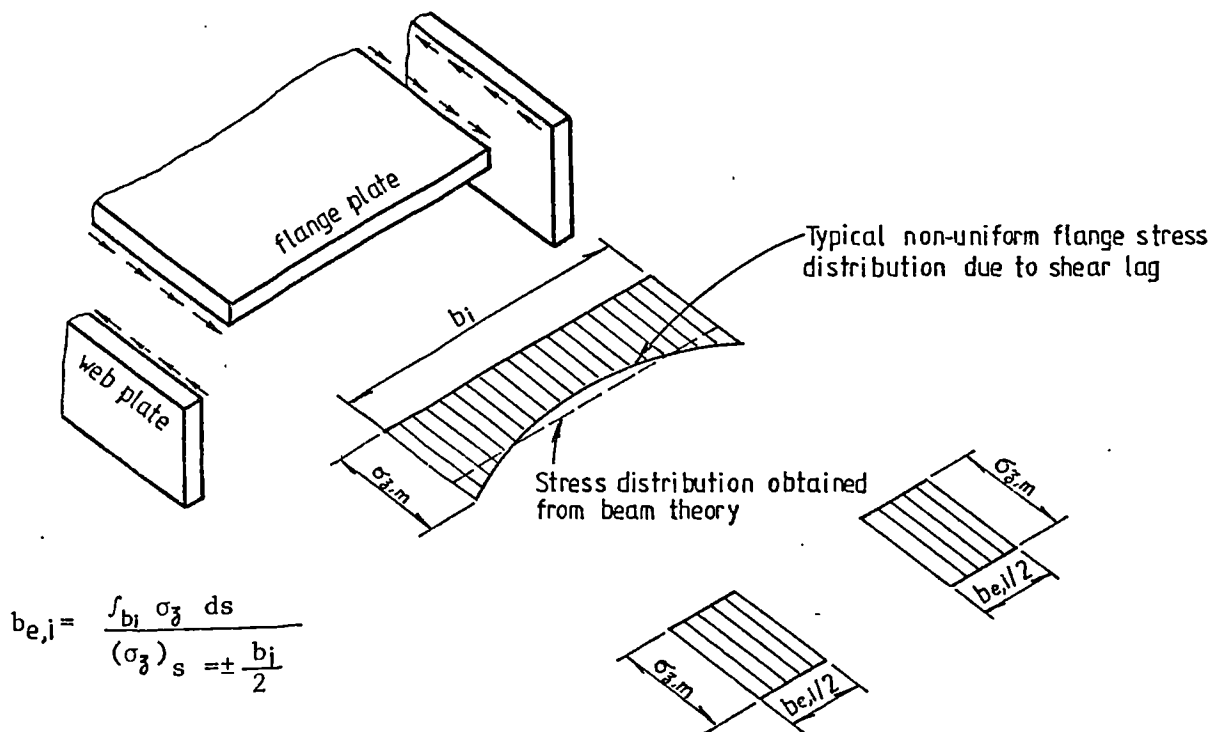


Fig. 2.3 Shear lag effects in flange plate

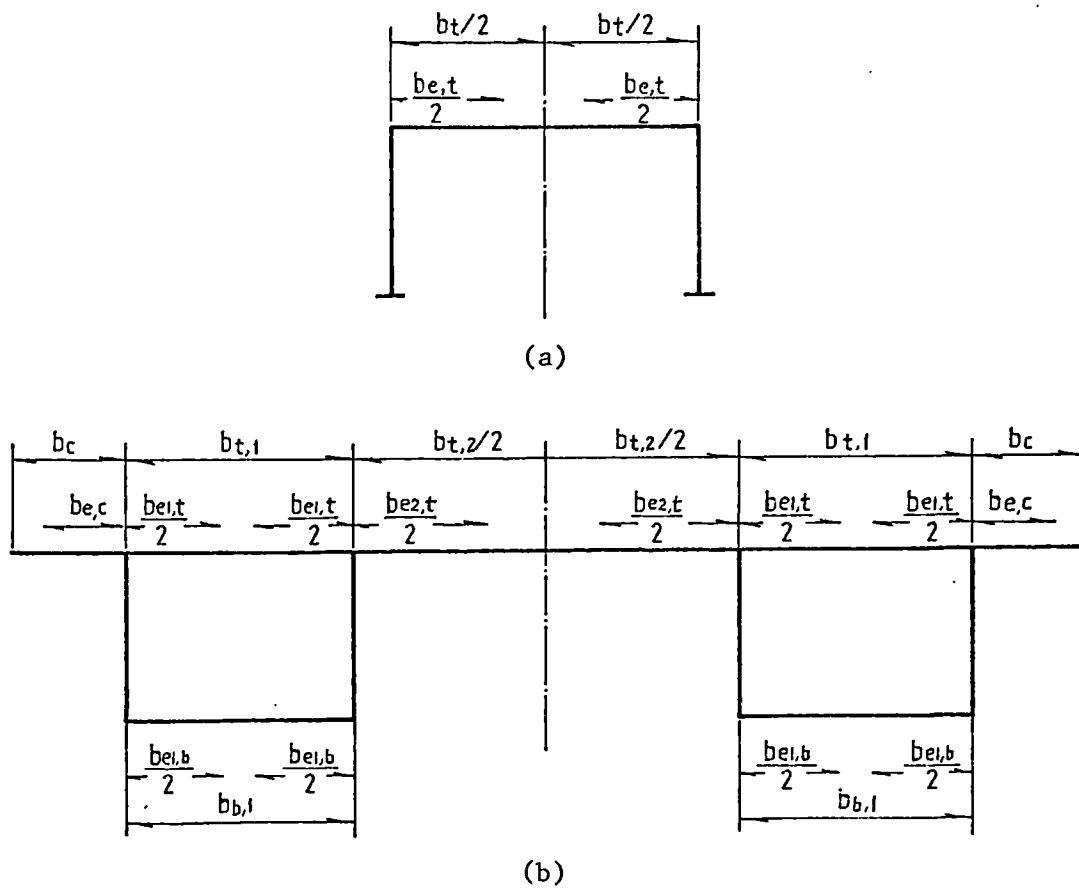


Fig. 2.4 Bridge cross-sections showing effective breadths of flange associated with each web

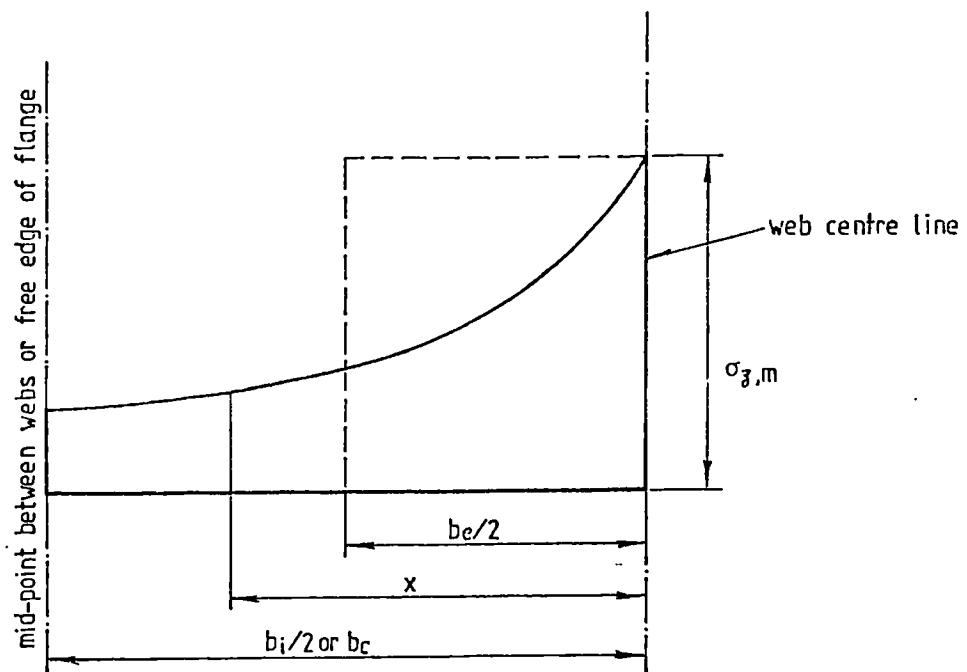
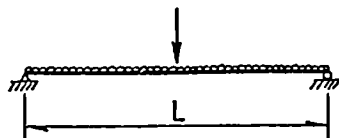
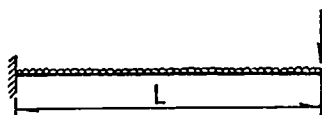


Fig. 2.5 Distribution of longitudinal flange stresses with allowance for shear lag

Table 2.1 Effective breadth ratios ( $\psi_e$ ) for use in design of box girdersTable 2.1 (a) Effective breadth ratios  $\psi_e$  for simply-supported girders

Effective breadth ratio	$\psi_e^U$						$\psi_e^D$					
Loading	Uniformly distributed load						Point loading at mid-span*					
Section considered	Mid-span		Quarter-span		Support-ends		Mid-span		Quarter-span		Support-ends	
$\alpha$ $b_i/2L$ or $b_c/L$	0	1	0	1	0	1	0	1	0	1	0	1
0	1.0	1.0	1.0	1.0	1.0	1.0	1.0	1.0	1.0	1.0	1.0	1.0
0.02	0.99	0.99	0.99	0.98	0.93	0.89	0.92	0.90	1.0	1.0	1.0	1.0
0.05	0.98	0.97	0.98	0.96	0.84	0.77	0.80	0.75	1.0	1.0	1.0	1.0
0.10	0.95	0.89	0.93	0.86	0.70	0.60	0.67	0.60	1.0	0.99	1.0	0.99
0.20	0.81	0.67	0.77	0.62	0.52	0.38	0.49	0.40	0.98	0.84	0.98	0.84
0.40	0.50	0.35	0.46	0.32	0.32	0.22	0.30	0.23	0.63	0.44	0.63	0.44
0.60	0.29	0.22	0.28	0.20	0.22	0.15	0.19	0.14	0.36	0.26	0.36	0.26
0.80	0.20	0.16	0.19	0.15	0.16	0.11	0.14	0.10	0.23	0.18	0.23	0.18
1.00	0.16	0.12	0.15	0.11	0.12	0.09	0.12	0.08	0.19	0.14	0.19	0.14

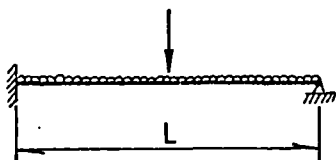
\*To be used only for point loads or reactions of significant magnitude; not for wheel loads or axle loads

Table 2.1 (b) Effective breadth ratios  $\psi_e$  for cantilevered girders

Effective breadth ratio	$\psi_e^U$						$\psi_e^D$					
Loading	Uniformly distributed load						Point loading at free end*					
Section considered	Fixed end		Quarter point near fixed end		Free end		Fixed end		Quarter point near fixed end		Free end	
$\alpha$ $b_i/2L$ or $b_c/L$	0	1	0	1	0	1	0	1	0	1	0	1
0	1.0	1.0	1.0	1.0	1.0	1.0	1.0	1.0	1.0	1.0	1.0	1.0
0.02	0.91	0.88	1.0	1.0	0.97	0.94	0.96	0.95	1.0	1.0	1.0	1.0
0.05	0.82	0.76	1.0	1.0	0.92	0.86	0.91	0.88	1.0	1.0	1.0	1.0
0.10	0.68	0.61	1.0	1.0	0.84	0.77	0.80	0.75	1.0	0.99	1.0	0.99
0.20	0.52	0.44	1.0	1.0	0.70	0.60	0.67	0.60	0.84	0.72	1.0	0.85
0.40	0.35	0.28	0.88	0.75	0.52	0.38	0.49	0.40	0.74	0.51	1.0	0.70
0.60	0.27	0.22	0.64	0.50	0.40	0.29	0.38	0.31	0.60	0.43	0.85	0.61
0.80	0.21	0.17	0.49	0.35	0.32	0.22	0.30	0.23	0.47	0.36	0.70	0.54
1.00	0.18	0.14	0.38	0.27	0.27	0.18	0.24	0.18	0.36	0.26	0.54	0.40

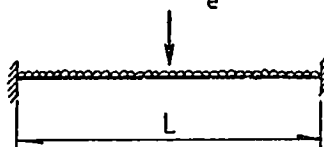
\*To be used only for point loads or reactions of significant magnitude; not for wheel loads or axle loads

contd.

Table 2.1 Effective breadth ratios ( $\psi_e$ ) for use in design of box girdersTable 2.1(c) Effective breadth ratios  $\psi_e$  for propped cantilevered girders

Effective breadth ratio	$\psi_e^U$						$\psi_e^P$					
Loading	Uniformly distributed load						Point loading at mid-span*					
Section considered	Fixed-end		Quarter-span near fixed-end		Propped-end		Fixed-end		Quarter-span near fixed-end		Propped-end	
$\alpha$ $b_f/2L$ or $b_c/L$	0	1	0	1	0	1	0	1	0	1	0	1
0	1.0	1.0	1.0	1.0	1.0	1.0	1.0	1.0	1.0	1.0	1.0	1.0
0.02	0.81	0.74	1.0	1.0	0.90	0.86	0.75	0.67	1.0	1.0	0.97	0.97
0.05	0.62	0.54	1.0	1.0	0.79	0.70	0.51	0.42	1.0	1.0	0.94	0.91
0.10	0.45	0.38	1.0	1.0	0.63	0.52	0.32	0.26	1.0	1.0	0.90	0.86
0.20	0.27	0.21	0.92	0.76	0.44	0.32	0.16	0.13	1.0	1.0	0.83	0.71
0.40	0.13	0.10	0.46	0.35	0.24	0.16	0.08	0.07	0.63	0.48	0.48	0.32
0.60	0.10	0.07	0.24	0.20	0.16	0.11	0.07	0.05	0.31	0.26	0.26	0.19
0.80	0.09	0.06	0.20	0.16	0.11	0.08	0.06	0.04	0.24	0.19	0.16	0.13
1.00	0.09	0.06	0.19	0.15	0.08	0.07	0.05	0.04	0.23	0.19	0.13	0.11

\*To be used only for point loads or reactions of significant magnitude; not for wheel loads or axle loads

Table 2.1(d) Effective breadth ratios  $\psi_e$  for fixed-ended girders

Effective breadth ratio	$\psi_e^U$						$\psi_e^P$					
Loading	Uniformly distributed load						Point loading at mid-span*					
Section considered	Mid-span		Quarter-span		Support-ends		Mid-span		Quarter-span		Support-ends	
$\alpha$ $b_f/2L$ or $b_c/L$	0	1	0	1	0	1	0	1	0	1	0	1
0	1.0	1.0	1.0	1.0	1.0	1.0	1.0	1.0	1.0	1.0	1.0	1.0
0.02	0.99	0.97	0.94	0.91	0.77	0.71	0.84	0.82	1.0	0.97	0.84	0.82
0.05	0.96	0.91	0.85	0.76	0.58	0.50	0.67	0.64	1.0	0.89	0.67	0.64
0.10	0.86	0.72	0.68	0.55	0.41	0.32	0.49	0.41	1.0	0.81	0.49	0.41
0.20	0.58	0.40	0.42	0.31	0.24	0.17	0.30	0.21	0.70	0.52	0.30	0.21
0.40	0.24	0.18	0.21	0.14	0.12	0.08	0.14	0.11	0.28	0.19	0.14	0.11
0.60	0.16	0.12	0.12	0.10	0.10	0.06	0.08	0.06	0.14	0.12	0.08	0.06
0.80	0.14	0.10	0.10	0.08	0.08	0.05	0.05	0.04	0.08	0.06	0.05	0.04
1.00	0.13	0.09	0.09	0.07	0.07	0.05	0.04	0.03	0.05	0.03	0.04	0.03

\*To be used only for point loads or reactions of significant magnitude; not for wheel loads or axle loads

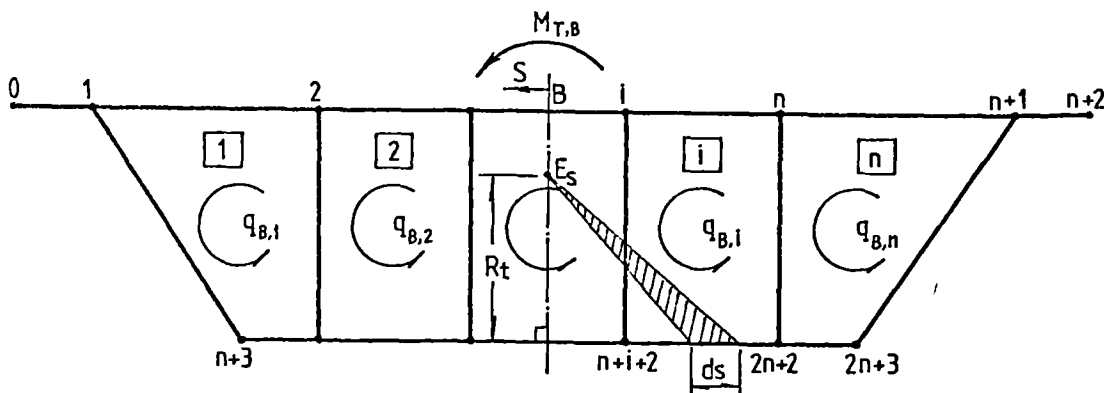


Fig. 2.6 Multi-cell beam subjected to a Bredt torsional moment  $M_{T,B}$

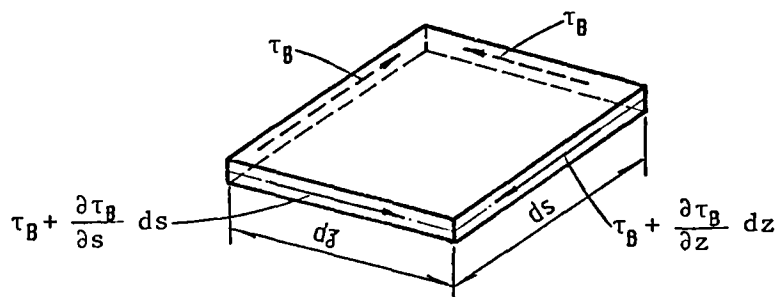


Fig. 2.7 Differential element subjected to Bredt's shear stresses

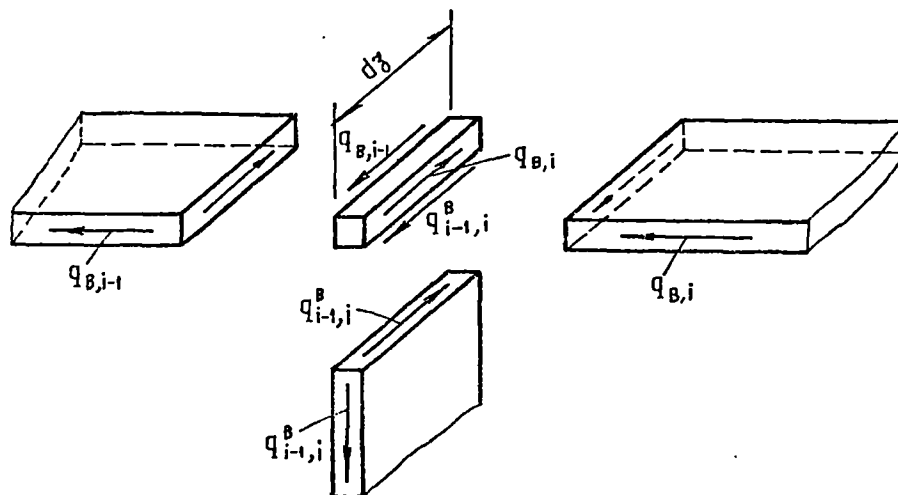


Fig. 2.8 Equilibrium of Bredt's shear flows at any junction of a multi-cell box beam

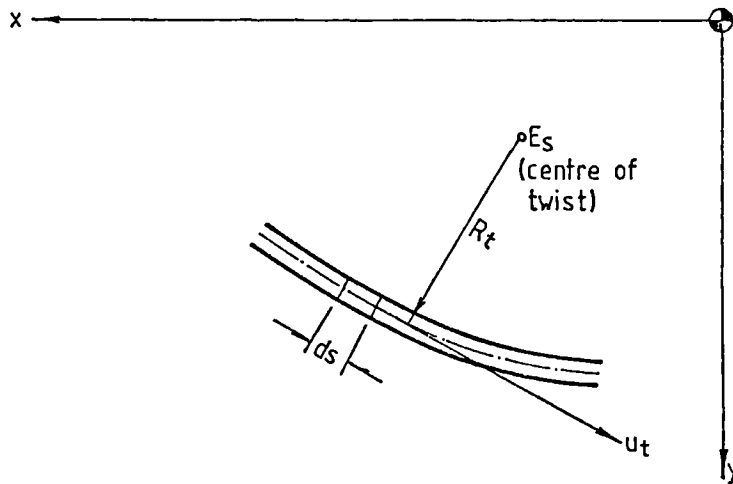


Fig. 2.9 Tangential displacement of cross-section

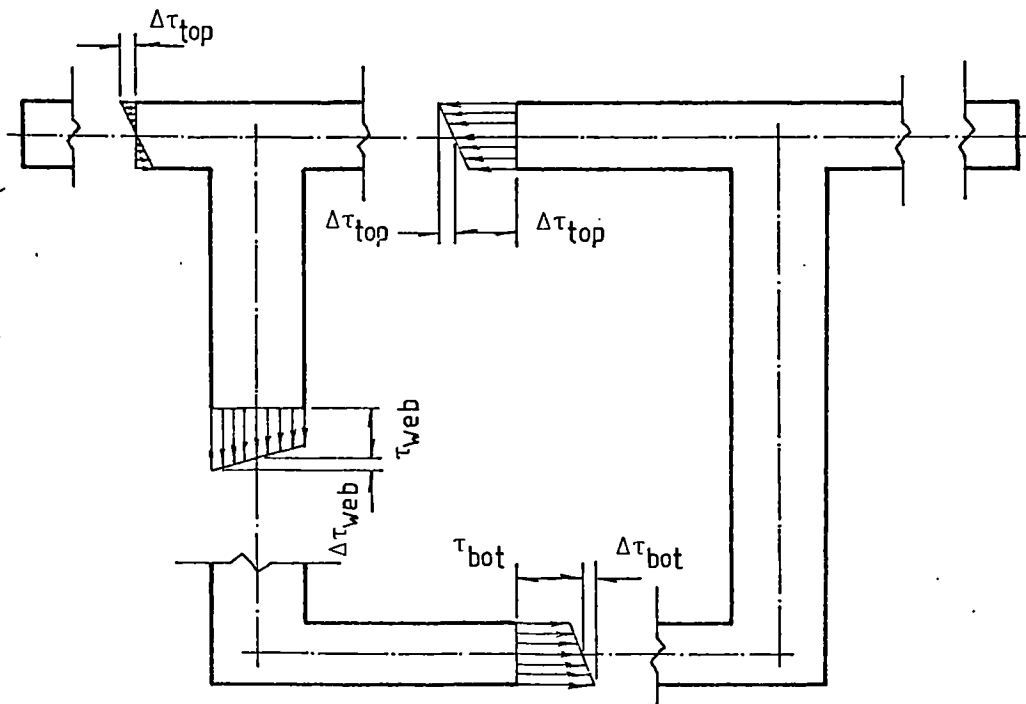


Fig. 2.10 Shear stress distribution due to pure torsion, considering linear variation of stress through thickness of wall

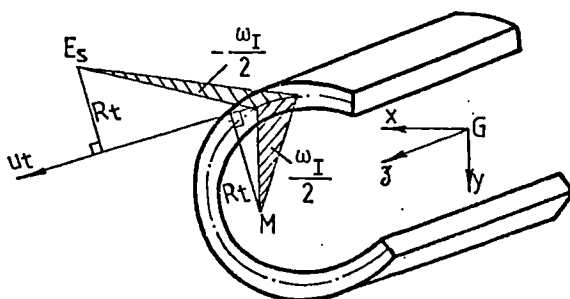


Fig. 2.11 Sectorial coordinate of an open section

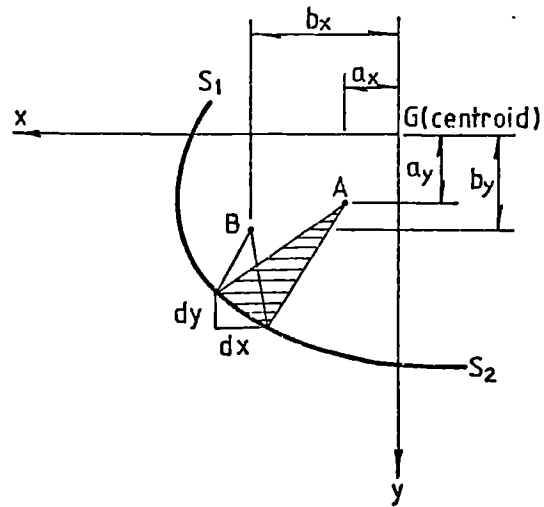


Fig. 2.12 Geometric relation for sectorial coordinates referred to different poles

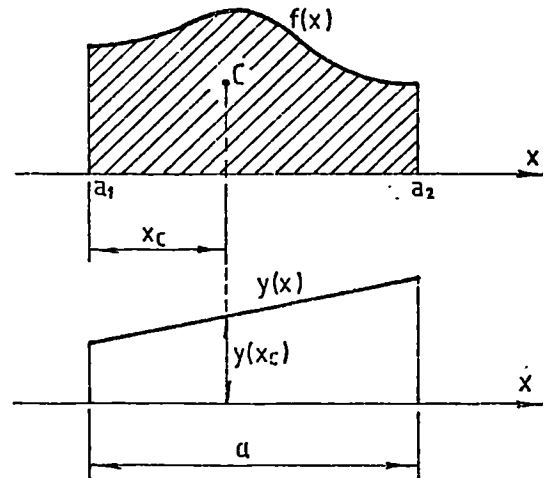


Fig. 2.13 Integral represented by area and centroid

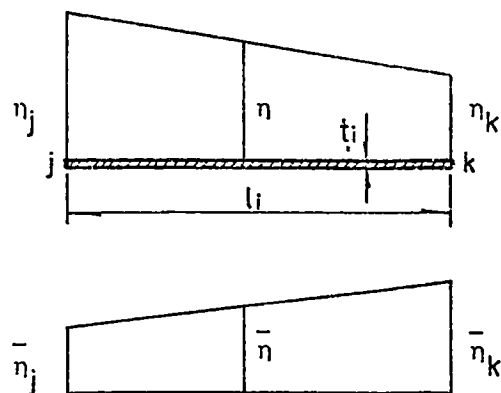
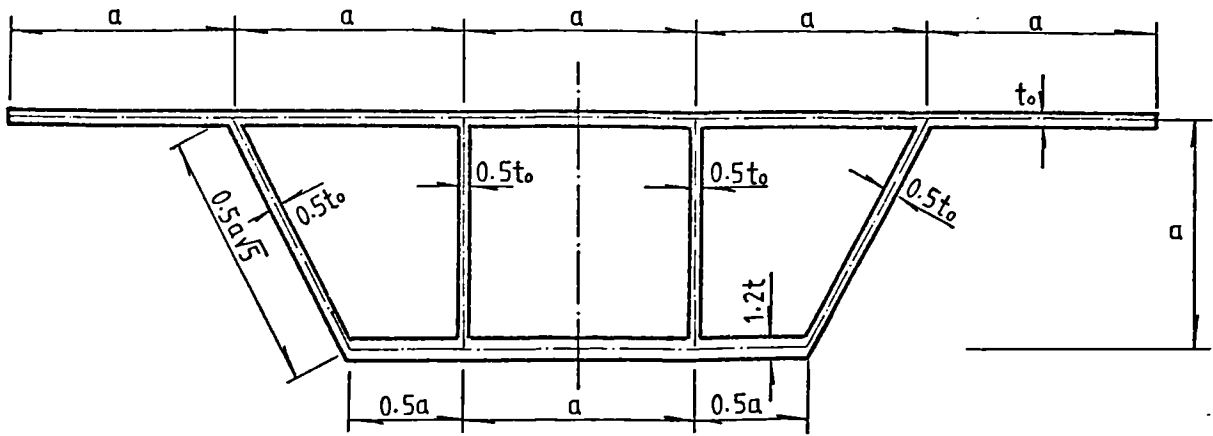
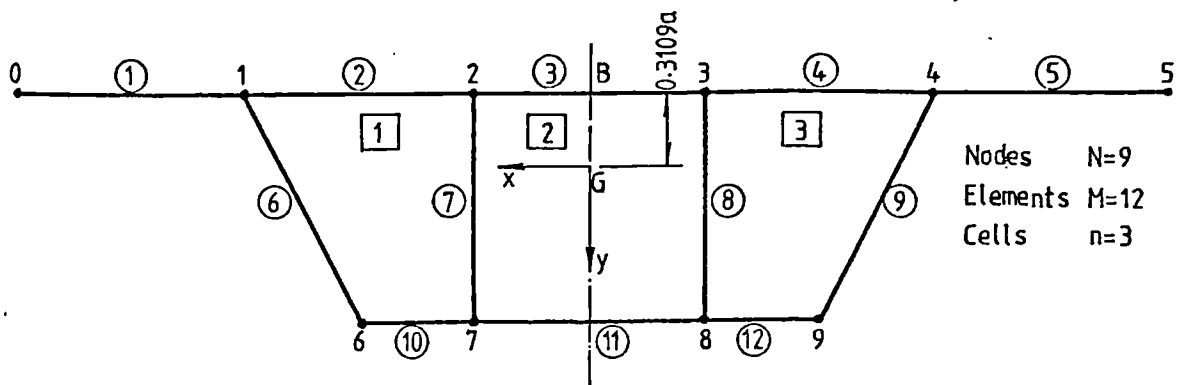


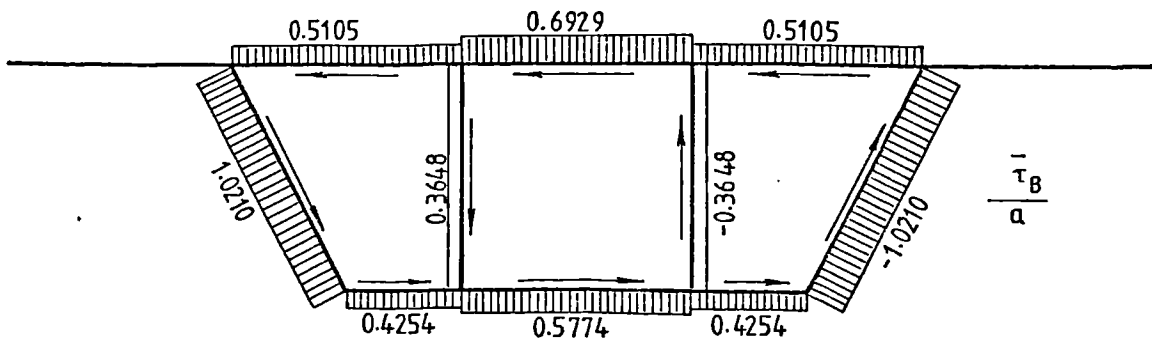
Fig. 2.14 Curvilinear integral along a straight element



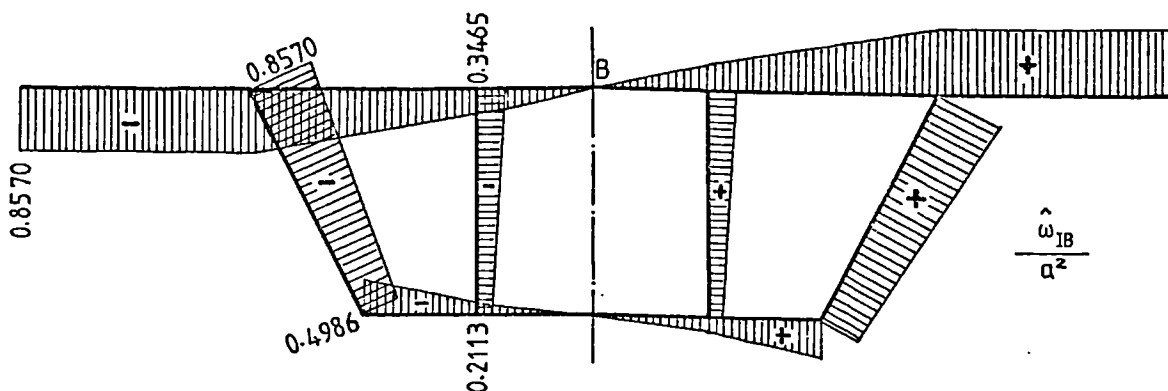
(a) Dimensions of cross-section



(b) Subdivision of the cross-section

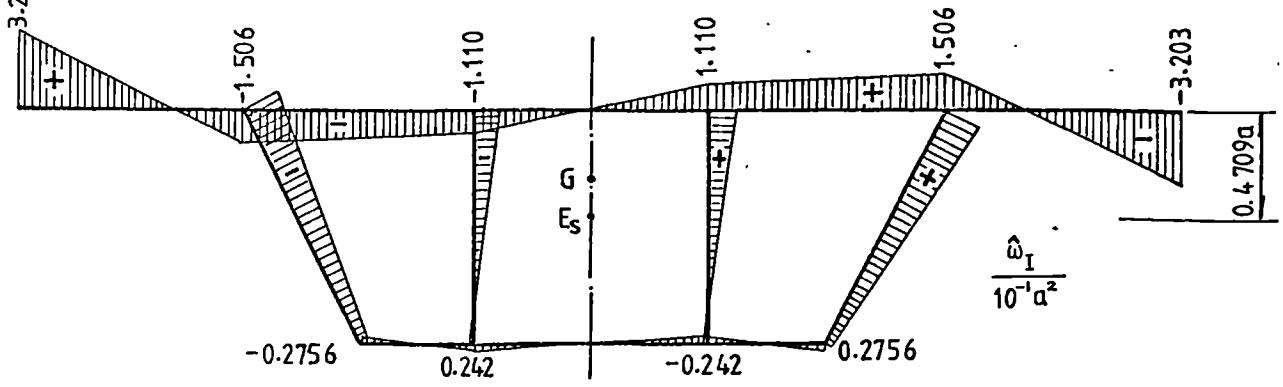


(c) Distribution of the shear stress function  $\bar{\tau}_B$

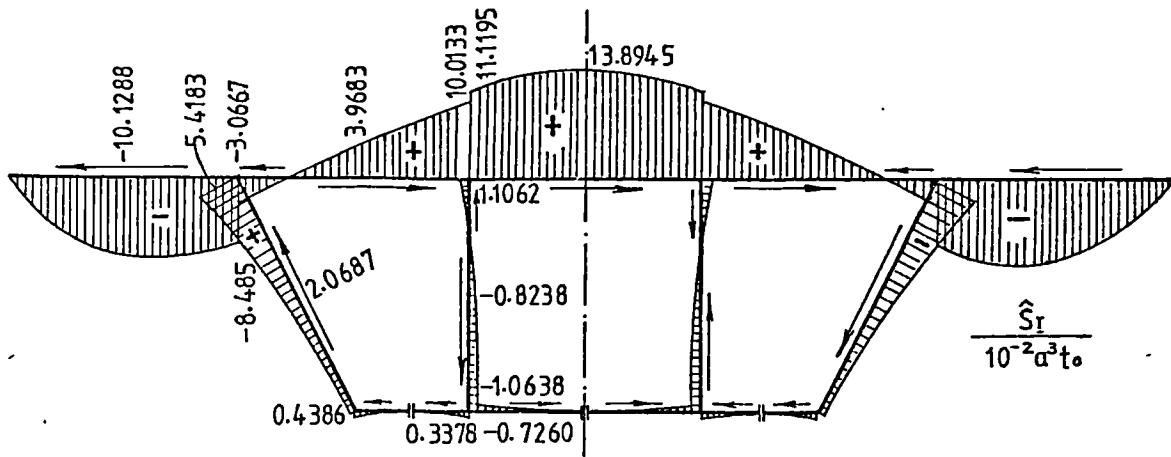


(d) Distribution of sectorial coordinates  $\hat{\omega}_{IB}$

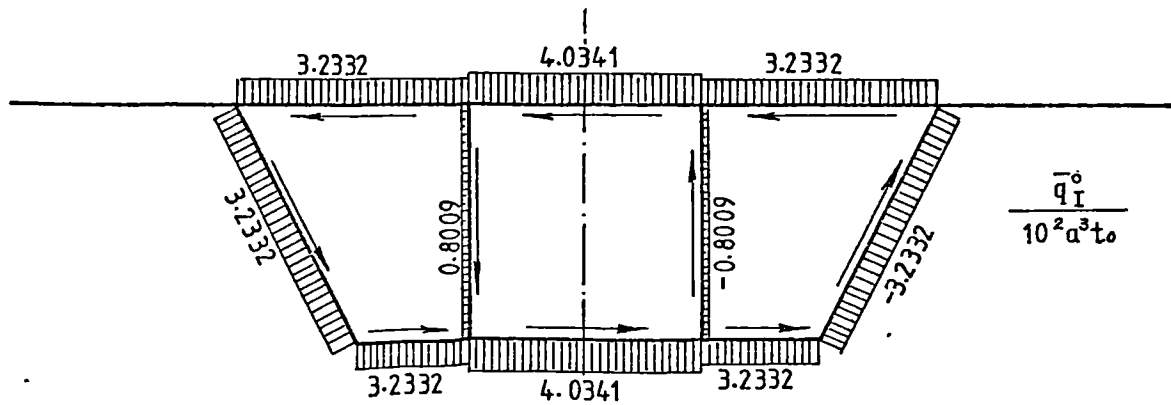
Fig. 2.15



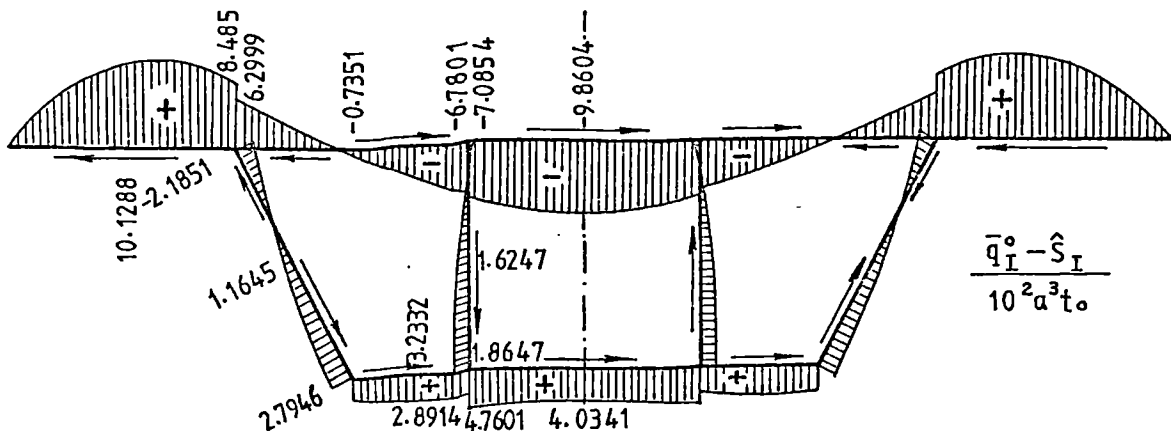
(e) Distribution of normalized sectorial coordinates  $\hat{\omega}_I$



(f) Distribution of the sectorial statical moment of area  $\hat{S}_I$



(g) Diagram of the unit warping shear flow function  $\bar{q}_I^0$



(h) Diagram of  $(\bar{q}_I^0 - \hat{S}_I)$

Fig. 2.15 Three-cell trapezoidal section beam

## CHAPTER 3

THE EFFECT OF CROSS-SECTIONAL DEFORMATION ON  
SINGLE-SPINED BOX BEAMS SUBJECTED TO TORSION3.1 Introduction

Thin-walled box spine-beams can be divided, according to their behaviour under torsion, into types with an infinitely rigid cross-section in their own plane and types with finite cross-sectional rigidity. Cross-sectional deformation of a single-spined box beam can be avoided by a sufficient number of stiff diaphragms or cross bracings. However, this measure not only increases the weight of material, but it also complicates the construction process in several ways. Moreover, it is also often required that free space be maintained inside the box. As a result, apart from support diaphragms which transmit the shear from the webs to the bearings, box beams are often designed with few intermediate diaphragms, or even without diaphragms. Stiffening may, in fact, be provided by an elastic bracing system on its own.

On the other hand, resistance of the cross-section to distortion also results from the longitudinal and transverse flexural stiffness of the component plates of the box. The transverse flexural stiffness provides the frame action of the box. The thicknesses of the walls of a box, however, or the transverse stiffening in the case of a steel box is normally not sufficient to prevent cross-sectional deformation when the box is subjected to torsion.

The state of stress of a deformed box beam (Fig. 3.1) is quite different from that of an undeformed beam, the analysis of which has been described. It must be realized that distortion of the cross-section is the main source of warping stresses and may form a significant addition to the ordinary bending stresses resulting from the symmetrical loading component. Moreover, the additional transverse bending stresses due to distortion of

the cross-section may be of the same order of magnitude as the longitudinal bending stresses, and are important in design practice. It is therefore essential to take account of distortional behaviour in the analysis of box beams in addition to considering bending and torsional effects.

The objective of this Chapter is to discuss the basic problems related to distortional effects under torsion. It will be considered that a box spine-beam is only a particular type of folded plate structure, which consists of a number of element plates that are stiffly interconnected together along their longitudinal edges and are arranged so as to form a closed section (Fig. 3.2). The theory presented in this section is accordingly based on the assumptions which are adopted in the ordinary folded plate analysis (29).

In contrast with box beams of rigid cross-section, the analysis of which has been described, the behaviour of deformable box beams is much more complicated. It is therefore intended only to deal with a bridge-girder type beam, the cross-section of which is symmetrical about the vertical axis, but for which the thicknesses of flanges and webs and the heights of webs may change. Furthermore, simplification also results in the neglect of shear deformation in the distortional warping analysis. A related study by Steinle (134) shows that neglecting the shear deformation can lead to an overestimate of maximum distortional warping stresses, and that the difference due to neglecting the shear deformation is localized near the point of application of the concentrated loading. Steinle and Dabrowski (21) recommend that the overestimate of distortional warping stresses should be accepted in practical design because of the simpler calculation involved when shear deformation is neglected.

Reference should be made to Chapter 1 with regard to coordinate systems and sign conventions. Index II will be used for those quantities which are

introduced in the distortional analysis, and which correspond to quantities in warping torsion. It is intended that the concepts described in this chapter will give a clear view of the effects of box beam and diaphragm proportions on the longitudinal warping and transverse flexural stresses induced by deformation of the cross-section. The content of this chapter is part of the theoretical basis involved in the later stiffness analysis procedure described in Chapter 4.

### 3.2 Distortional component of eccentric loading

External loads between the webs or on the side cantilevers of a box beam are transferred by flexure of the deck to the webs. Flexure of the deck would induce transverse bending stresses in the webs and consequently in the bottom flange of the girder. In design practice the stresses in the deck from this local bending effect may be calculated independently of the overall box beam analysis. Thus, for the global analysis of a box spine-beam, the loads not acting at webs can be approximated by statically equivalent loads applied at side webs.

Now let us consider a single-spined box beam with a trapezoidal periphery (Fig. 3.3a). The eccentric distributed loads  $p_x$  and  $p_y$  acting along the  $x$  and  $y$  axes respectively on the box beam, can be replaced by shear loads acting through the shear centre with distributed twisting moments  $m_{zH} = -p_x e_y$  and  $m_{yV} = p_y e_x$  (Fig. 3.3b,c). In practical analyses of box beams of deformable cross-section, it is often convenient further to separate the effects of torsion from the deformation of the cross-section.

The basic advantage of resolving the torsional loads into torsional and distortional components is that wherever the exact loading system may act we can always represent it as the sum:

$$\begin{aligned} \text{Exact loading system} = & \text{Statically equivalent loading system (corresponding} \\ & \text{to torsion)} \\ & + \\ & \text{Self-equilibrating loading system (corresponding to} \\ & \text{distortion),} \end{aligned}$$

where the statically equivalent loading system is in equilibrium with the external loads and satisfies the internal equilibrium conditions. The self-equilibrating loading system which has zero resultants, is compatible with the corresponding deformation pattern.

Accordingly, the antisymmetric pairs of loads resulting from the vertical and horizontal eccentric loading may be split into two groups of co-planar forces, consisting of the pure torsional load and a section-deforming load acting along the perimeter of the trapezoid, shown respectively in Figs. 3.4 and 3.5. The equivalent pure torsional forces may be obtained by integrating a constant shear flow given by the simple Bredt-Batho formula,  $q = m_z/\Omega$ , where  $\Omega$  denotes twice the value of the entire area enclosed within the perimeter of the trapezoid. Consequently, they are in equilibrium with the external twisting moments  $m_{zV}$  and  $m_{zH}$  respectively.

The section-deforming loads as shown in Fig. 3.4c and Fig. 3.5c can then be obtained from the following equilibrium conditions

$$\begin{aligned} (S_{c,1} + S_{c,2}) \sin\phi &= m_{zV}/b_t \\ S_{t,1} - S_{t,2} - 2(S_{c,1} + S_{c,2}) \cos\phi &= 0 \\ S_{b,1} - S_{b,2} &= 0 \end{aligned} \quad (3.1)$$

and,

$$\begin{aligned} \bar{S}_{t,1} + \bar{S}_{t,2} - (\bar{S}_{c,1} - \bar{S}_{c,2}) \cos\phi &= m_{zH}/h \\ \bar{S}_{b,1} + \bar{S}_{b,2} - (\bar{S}_{c,1} - \bar{S}_{c,2}) \cos\phi &= m_{zH}/h \\ \bar{S}_{c,1} - \bar{S}_{c,2} &= 0 \end{aligned} \quad (3.2)$$

Thus, we may obtain the vertical distortional component as

$$\begin{aligned} S_{t,2} &= \frac{b_b^2}{\Omega} \cdot \frac{m_{zV}}{b_t} \\ S_{b,2} &= \frac{b_t \cdot b_b}{\Omega} \cdot \frac{m_{zV}}{b_t} = \frac{b_t}{b_b} S_{t,2} \\ S_{c,2} &= \frac{h_c b_b}{\Omega} \cdot \frac{m_{zV}}{b_t} = \frac{h_c}{b_b} S_{t,2} \end{aligned} \quad (3.3)$$

and the horizontal distortional component as

$$\begin{aligned}\bar{S}_{t,2} &= \frac{b_b}{\Omega} m_{\bar{z}H} \\ \bar{S}_{b,2} &= \frac{b_t}{\Omega} m_{\bar{z}H} = \frac{b_t}{b_b} \bar{S}_{t,2} \\ \bar{S}_{h,2} &= \frac{h_c}{\Omega} m_{\bar{z}H} = \frac{h_c}{b_b} \bar{S}_{t,2}\end{aligned}\quad (3.4)$$

These two groups of distortional forces are self-equilibrating since the resultants of the forces adjacent to the box corners are equal and diametrically opposed to each other (Fig. 3.6). These resultants act along the diagonals of the box producing racking of the cross-section, and are evaluated from the following expressions

$$S_d = \frac{\sqrt{4h^2 + (b_t + b_b)^2}}{4b_b} \quad S_{t,2} = \frac{\sqrt{4h^2 + (b_t + b_b)^2}}{4\Omega} \frac{b_b}{b_t} m_{\bar{z}V} \quad (3.5)$$

and,

$$\bar{S}_d = \frac{\sqrt{4h^2 + (b_t + b_b)^2}}{4b_b} \quad \bar{S}_{t,2} = \frac{\sqrt{4h^2 + (b_t + b_b)^2}}{4\Omega} m_{\bar{z}H} \quad (3.6)$$

The vertical and horizontal components of the diagonal resultants are expressed as

$$S_V = \frac{h}{2b_b} S_{t,2} = \frac{h \cdot b_b}{2\Omega} \cdot \frac{m_{\bar{z}V}}{b_t} = \frac{b_b}{2(b_t + b_b)} \cdot \frac{m_{\bar{z}V}}{b_t} \quad (3.7)$$

$$S_H = \frac{b_t + b_b}{4b_b} S_{t,2} = \frac{b_b}{4h} \cdot \frac{m_{\bar{z}V}}{b_t}$$

and,

$$\bar{S}_V = \frac{h}{2b_b} \bar{S}_{t,2} = \frac{h}{2\Omega} m_{\bar{z}H} = \frac{1}{2(b_t + b_b)} m_{\bar{z}H} \quad (3.8)$$

$$\bar{S}_H = \frac{b_t + b_b}{4b_b} \bar{S}_{t,2} = \frac{b_t + b_b}{4\Omega} m_{\bar{z}H} = \frac{1}{4h} m_{\bar{z}H}$$

It can be seen from Fig. 3.6 that the distortional diagonal resultants which arise from a positive twisting load due to the horizontal eccentric loading, are in the opposite sense to the distortional diagonal resultants due to the vertical distortional component. Thus the positive horizontal twisting load accompanied by the positive vertical twisting load together reduce the distortional effect, but increase the twisting effect.

Each of the four distortional forces acting along the sides of a trapezoid or acting along the diagonals of the trapezoid together, are defined as a generalized distortional force. It should be noted that the term generalized force is used to denote a group of forces that are defined in direction and relative magnitude. Thereafter, the group can be specified by a single number. Note also that each of these two groups of distortional forces provide equal and opposite couples of magnitude  $m_{dV} = \frac{b_b}{2b_t} m_{zV}$  and  $m_{dH} = -\frac{1}{2} m_{zH}$  respectively. We can then define the distortional moment as

$$m_d = m_{dV} + m_{dH} = \frac{1}{2} \left( \frac{b_b}{b_t} m_{zV} - m_{zH} \right) \quad (3.9)$$

to represent the generalized distortional force. In the case of a rectangular cross-section with  $b_t = b_b$ , then

$$m_d = \frac{1}{2} (m_{zV} - m_{zH}) \quad (3.10)$$

The effect on distortion of sloping the webs is clear from Eq. 3.9 in that the deformation of the cross-section reduces as the slope increases. This is because the bottom flange is shorter and hence, more stiff. On the other hand, the torsional shear stresses are increased.

We should now consider the effect of loads applied at the cantilever portion of the cross-section as shown in Fig. 3.7a. If a thick flange is used almost all the cantilever fixed moment is taken by the flange. The cantilevers can be equivalent to the mechanism shown in Fig. 3.7c. The

distortional loading and transverse moments on the walls of the box increase in the same proportion as the torsional load increases, so that the distortional moment is

$$m_{dv} = \frac{Py}{2} \cdot \frac{b_b}{b_t} \cdot e_x \quad (3.11)$$

On the other hand if thick webs are used almost all the fixed moment is taken by the webs which are equivalent to the mechanism shown in Fig. 3.7d. The distortional moment can then be calculated as

$$m_{dv} = \frac{Py}{2} \left( \frac{b_b}{2} - b_x \right) \quad (3.12)$$

In fact the cantilevers are part of the frame of the whole box and the cantilever fixed moment is taken partly by the web and partly by the top flange. If we specify the ratio of the distributed moment in the top flange to the applied fixed moment as the distribution factor  $\zeta_d$ , the distortional moment due to the vertical eccentric load acting at the cantilever portion, can be expressed as

$$\begin{aligned} m_{dv} &= \frac{Py}{2} \left[ \frac{b_b}{b_t} (e_x - b_x) + \frac{b_b}{b_t} \zeta_d b_x - (1 - \zeta_d) b_x \right] \\ &= \frac{Py}{2} \left[ \frac{b_b}{b_t} e_x - \left( 1 + \frac{b_b}{b_t} \right) (1 - \zeta_d) b_x \right] \end{aligned} \quad (3.13a)$$

or

$$m_{dv} = \frac{Py}{2} \left[ \alpha_d e_x - (1 + \alpha_d) (1 - \zeta_d) b_x \right] \quad (3.13b)$$

where  $\alpha_d = b_b/b_t$  is the ratio of the width of the bottom flange to the top flange.

It is apparent from Eq. 3.13 that when  $\zeta_d = 1$  or  $\zeta_d = 0$  we may obtain the same results as in Eq. 3.11 and Eq. 3.12 respectively. If the bottom corners of the box are assumed supported horizontally and vertically, the distribution factor  $\zeta_d$  due to a unit fixed moment can be obtained from the analysis of a frame formed from a unit slice of the box beam.

### 3.3 Deformation of single-spined box beam

A single-spined box beam with a deformable cross-section is deformed under torsion into the shape shown in Fig. 3.8. The corner points of the cross-section are horizontally and vertically displaced by the components  $\bar{u}_t$ ,  $\bar{u}_b$  and  $\bar{v}_t$ ,  $\bar{v}_b$  respectively. The displacements  $\bar{u}_t$  and  $\bar{v}_t$  are generally not identical with  $\bar{u}_b$  and  $\bar{v}_b$  respectively because of the effect of the different stiffness exerted by the upper and lower flanges.

The relationship between the displacements  $\bar{u}_t$ ,  $\bar{u}_b$ ,  $\bar{v}_t$  and  $\bar{v}_b$  characterizing the deformation of the cross-section, will be fixed using the condition that the compatibility of the cross-section is preserved.

The tangent displacement to the side webs may be expressed in two ways, i.e.,

$$\bar{v}_h = \bar{v}_t \sin\phi + \bar{u}_t \cos\phi \quad (3.14)$$

or

$$\bar{v}_h = \bar{v}_b \sin\phi - \bar{u}_b \cos\phi \quad (3.15)$$

where  $\phi$  is the angle of the top flange with respect to the inclined side web.

By comparing these two equations we have

$$\bar{v}_t \sin\phi + \bar{u}_t \cos\phi = \bar{v}_b \sin\phi - \bar{u}_b \cos\phi ,$$

and consequently

$$\bar{v}_b = \bar{v}_t + \frac{\bar{u}_t + \bar{u}_b}{\operatorname{tg}\phi} \quad (3.16)$$

It can be seen from Eq. 3.16 that the displacement components are interrelated. It can also be seen that for a rectangular cross-section  $\bar{v}_b$  must equal  $\bar{v}_t$ .

The rotation angle for the side web can be expressed as

$$\begin{aligned}\phi_{\bar{z}} &= \frac{(\bar{u}_t \sin\phi - \bar{v}_t \cos\phi) + (\bar{v}_b \cos\phi + \bar{u}_b \sin\phi)}{h_c} \\ &= \frac{(\bar{u}_t + \bar{u}_b) \sin^2\phi + (\bar{v}_b - \bar{v}_t) \sin\phi \cos\phi}{h}\end{aligned}\quad (3.17)$$

Substituting Eq. 3.16 into Eq. 3.17 we have

$$\phi_{\bar{z}} = \frac{\bar{u}_t + \bar{u}_b}{h} \quad (3.18)$$

Hence all the rotation angles of the webs due to deformation of the cross-section are identical with each other and have the magnitude calculated by Eq. 3.18.

The shape of the cross-sectional deformation shown in Fig. 3.8 indicates that the upper and lower flanges rotate by angles  $\psi_{\bar{z},t}$  and  $\psi_{\bar{z},b}$  respectively, which are not generally identical with each other. These horizontal rotation angles can be expressed with relation to the vertical translations of the corner points as

$$\psi_{\bar{z},t} = \frac{2\bar{v}_t}{b_t} \quad (3.19)$$

and

$$\psi_{\bar{z},b} = \frac{2\bar{v}_b}{b_b} \quad (3.20)$$

Substitution of Eq. 3.16 and Eq. 3.18 into Eq. 3.20 gives

$$\psi_{\bar{z},b} = \frac{b_t}{b_b} \psi_{\bar{z},t} + \frac{2h}{b_b \operatorname{tg}\phi} \phi_{\bar{z}} \quad (3.21)$$

Thus, we are now able to define the distortional angle as the characteristic quantity for representing the cross-sectional deformation. It is given by the rotation of the top flange of the cross-section related to the inclined side web and can be expressed as

$$\gamma_d = \psi_{\bar{z},t} + \phi_{\bar{z}} = \frac{2\bar{v}_t}{b_t} + \frac{\bar{u}_t + \bar{u}_b}{h} \quad (3.22)$$

Substituting Eq. 3.14 into Eq. 3.22 we then obtain

$$\gamma_d = \frac{\bar{u}_t + \bar{u}_b}{h} + \frac{2}{b_t} \left( \frac{\bar{v}_h}{\sin\phi} - \bar{u}_t \cot\phi \right) \quad (3.23)$$

where  $\bar{u}_t$ ,  $\bar{u}_b$  and  $\bar{v}_h$  are the tangent displacements to the sides of the box associated with distortion.

Corresponding to the definition of the generalized distortional moment, the unit value of a distortional angle will be provisionally defined as the generalized distortional displacement which represents the group of distortional displacements producing a unit quantity of work when operated on by a unit generalized distortional force.

It can be seen that if cross-sectional deformation is not constant along the beam, it causes not only the motions in the plane of the cross-section, but also out-of-plane displacements of the cross-section. These additional warping displacements are called distortional warping displacements, and are associated with in-plane bending of flanges and webs.

The component of displacement in the plane of the cross-section which is directed along the tangent  $ds$  to the mid-line of the walls will be denoted by  $u_t(\zeta, S)$ , and the warping displacement (i.e., that in the  $z$ -direction) by  $w_z(\zeta, S)$ . In the torsion theory of thin-walled beams, the tangent displacement  $u_t$  is found directly from the product of the twisting radius and the rotation of the whole cross-section. However, in the present case the term is found from the displacement of the cross-section associated with distortion. In other words,  $u_t(\zeta, S)$  may be expressed as the product of a distribution function  $V_S(S)$  of the tangential displacement and the measure of distortion  $\gamma_d$  expressed in Eq. 3.23 and shown in Fig. 3.8, i.e.

$$u_{t,d} = V_S(S) \gamma_d(z) \quad (3.24)$$

To develop an approximate theory neglecting shear deformation, it may be assumed that the in-plane motion is accompanied by sufficient out-of-plane displacement (warping) to annul the average shear strains in the plate which form the cross-section. This can be expressed as

$$\frac{\partial u_{t,d}}{\partial z} + \frac{\partial w_{z,d}}{\partial s} = 0 \quad (3.25)$$

After substituting Eq. 3.24 into Eq. 3.25 and integrating it we obtain

$$w_{z,d} = w_{z,0} - \gamma'_d(z) \int_0^S V_S(S) ds \quad (3.26)$$

Since the origin of the curvilinear coordinate  $S$  lies on the vertical axis of symmetry of the cross-section, and the distribution of the longitudinal displacement is antisymmetric about this axis, we have  $w_{z,0} = 0$ . Thus, we finally obtain

$$\begin{aligned} w_{z,d} &= - \gamma'_d(z) \int_0^S V_S(S) ds \\ &= - \omega_{II}(S) \gamma'_d(z) \end{aligned} \quad (3.27)$$

where

$$\omega_{II}(S) = \int_0^S V_S(S) ds \quad (3.28)$$

indicates the distribution of the longitudinal displacement and is defined as the unit distortional warping function and has dimensions of  $L^2$ .

It thereby becomes possible to follow the analogy between the section properties and functions which have been considered here with the corresponding quantities in warping torsion. This will be shown in detail in the following sections.

#### 3.4 Distribution of normal and shear stresses over the cross-section

The warping displacements are not, in general, constant along the axis of the box beam. Longitudinal stresses thus arise from the constraint of

warping. If, in turn, these warping stresses vary along the beam, shear stresses are required by considerations of longitudinal equilibrium. These shear stresses in the planes of the plates also change from section to section.

Differentiating Eq. 3.27 once we can have

$$\epsilon_{z,d} = \frac{\partial w_{z,d}}{\partial z} = -\omega_{II}(S) \frac{\partial^2 \gamma_d}{\partial z^2}, \quad (3.29)$$

and the distortional warping stresses are then given by

$$\sigma_{II} = E_1 \frac{\partial w_{z,d}}{\partial z} = -E_1 \omega_{II}(S) \frac{\partial^2 \gamma_d}{\partial z^2} \quad (3.30)$$

Since the distortional forces are in a self-equilibrating system, the warping normal stresses  $\sigma_{II}$  must also form a system in equilibrium as in warping torsion; they produce no normal force  $N_z$ , no bending moments  $M_x$  and  $M_y$ , and the conditions

$$\int_A \sigma_{II} dA = \int_A \sigma_{II} x dA = \int_A \sigma_{II} y dA = 0 \quad (3.31)$$

should be satisfied. To represent the resultant of the distortional warping stresses we may define, by means of the analogy to the warping torsion, the distortional bimoment as

$$B_{II} = \int_A \sigma_{II} \omega_{II} dA \quad (3.32)$$

which has dimensions of  $FL^2$ .

By substituting Eq. 3.30 into Eq. 3.32 we have

$$B_{II} = -E_1 J_{II} \frac{\partial^2 \gamma_d}{\partial z^2} \quad (3.33)$$

where

$$J_{II} = \int_A \omega_{II}^2 dA \quad (3.34)$$

and is called the distortional warping moment of inertia.

From Eqs. 3.30 and 3.33 we may finally obtain

$$\sigma_{II} = \frac{B_{II}}{J_{II}} \omega_{II} = f_{II} \omega_{II} \quad (3.35)$$

It is apparent that this expression is analogous to the normal stress formulation in warping torsion theory.

For the section with a vertical axis of symmetry shown in Fig. 3.9a the warping stress pattern has a linear variation across each element plate as shown in Fig. 3.9b, which is based on the plane assumption of ordinary folded plate theory. Because of the antisymmetry of the diagram of  $\omega_{II}$ , the conditions  $\int_A \omega_{II} dA = 0$  and  $\int_A \omega_{II} y dA = 0$  are satisfied.

From the linear variation of  $\omega_{II}$  we may define

$$\alpha_i = \frac{\omega_{II,i}}{\omega_{II,1}} = \frac{x_j}{x_1} \quad (i=0,1,2,\dots,n+2) \quad (3.36a)$$

$$\lambda_j = \frac{\omega_{II,n+i+2}}{\omega_{II,n+3}} = \frac{x_{n+i+2}}{x_{n+3}} \quad (i=1,2,\dots,n+1) \quad (3.36b)$$

$$\beta = - \frac{\omega_{II,n+3}}{\omega_{II,1}} \quad (3.36c)$$

and

$$\alpha_{b,i} = \frac{\omega_{II,n+i+2}}{\omega_{II,1}} = \frac{\omega_{II,n+i+2}}{\omega_{II,n+3}} \cdot \frac{\omega_{II,n+3}}{\omega_{II,1}} = -\lambda_i \beta \quad (i=1,2,\dots,n+1) \quad (3.36d)$$

where  $x_0, x_1, \dots, x_{2n+3}$  are the  $x$  coordinates related to the local coordinate system.

Thus, the ratio of  $\omega_{II}$  at the two ends of individual webs can be obtained as

$$\begin{aligned} \frac{\omega_{II,n+i+2}}{\omega_{II,i}} &= \frac{\omega_{II,n+i+2}}{\omega_{II,n+3}} \cdot \frac{\omega_{II,n+3}}{\omega_{II,1}} \cdot \frac{\omega_{II,1}}{\omega_{II,i}} = \lambda_i (-\beta) \left( \frac{1}{\alpha_i} \right) \\ &= -\beta \frac{\lambda_i}{\alpha_i} \\ &= \beta \psi_i \end{aligned} \quad (3.37)$$

where

$$\psi_i = -\frac{\lambda_i}{\alpha_i} = -\frac{x_{n+i+2}}{x_{n+3}} \cdot \frac{x_1}{x_i} = -\frac{b_t}{b_b} \cdot \frac{x_{n+i+2}}{x_i} \quad (i=1,2,\dots,n+1) \quad (3.38)$$

In order to establish equations of equilibrium and hence the relationships between interior forces, free body diagrams of web and flange elements are considered (Fig. 3.10). Normal stresses in the elements in the longitudinal direction may be replaced by bending moments  $M(z)$  and normal forces  $N(z)$ ; shear stresses on the planes of elements being replaced by shear forces  $Q(z)$ . Interior forces  $\bar{g}$ ,  $\bar{q}$ ,  $\bar{n}$  between the individual webs and flanges in their axes of contact, and transverse moments per unit width  $m_{db}$ , represent transverse flexural distortion stresses. Actually interior force  $\bar{g}$  is neglected in the present approach.

We may now obtain the ratio  $\beta$  from the condition  $\int_A \sigma_{xx} dA = 0$ :

1) The moment with respect to the  $y$  axis of symmetry due to the normal stresses at the upper flange is

$$M_t = \frac{b_c t_c}{3} [\alpha_0(2x_0 + x_1) + \alpha_1(2x_1 + x_0)] + \sum_{i=1}^n \frac{b_{t,i} t_{t,i}}{6} [\alpha_i(2x_i + x_{i+1}) + \alpha_{i+1}(2x_{i+1} + x_i)] \quad (3.39)$$

2) The moment with respect to the  $y$  axis of symmetry due to the normal stresses at the lower flange is

$$M_b = -\beta \sum_{i=1}^n \frac{b_{b,i} t_{b,i}}{6} [\lambda_i(2x_{n+i+2} + x_{n+i+3}) + \lambda_{i+1}(2x_{n+i+3} + x_{n+i+2})] = -\beta \bar{M}_b \quad (3.40a)$$

where

$$\bar{M}_b = \sum_{i=1}^n \frac{b_{b,i} t_{b,i}}{6} [\lambda_i(2x_{n+i+2} + x_{n+i+3}) + \lambda_{i+1}(2x_{n+i+3} + x_{n+i+2})] \quad (3.40b)$$

3) The moment with respect to the y axis of symmetry due to the normal stresses at the webs

$$\begin{aligned} M_h &= \sum_{i=1}^{n+1} \frac{h_{c,i} t_{h,i}}{6} [\alpha_i (2x_i + x_{n+i+2}) - \lambda_i \beta (2x_{n+i+2} + x_i)] \\ &= \bar{M}_{h,1} - \beta \bar{M}_{h,2} \end{aligned} \quad (3.41a)$$

where

$$\bar{M}_{h,1} = \sum_{i=1}^{n+1} \frac{h_{c,i} t_{h,i}}{6} \alpha_i (2x_i + x_{n+i+2}) \quad (3.41b)$$

and

$$\bar{M}_{h,2} = \sum_{i=1}^{n+1} \frac{h_{c,i} t_{h,i}}{6} \lambda_i (2x_{n+i+2} + x_i) \quad (3.41c)$$

From the equilibrium condition  $M_t + M_b + M_h = 0$ , we then obtain

$$\beta = \frac{M_t + \bar{M}_{h,1}}{\bar{M}_b + \bar{M}_{h,2}} \quad (3.42)$$

For the single cell section shown in Fig. 3.11 we have from Eqs. 3.39. to 3.42

$$\beta = \frac{\alpha_o^3 b_t^2 t_t + 2h_c t_h (b_t + \frac{b_b}{2})}{b_b^2 t_b + 2h_c t_h (b_b + \frac{b_t}{2})} \quad (3.43)$$

In particular, for a single cell rectangular section with  $b_t = b_b$  and  $h_c = h$ , from Eq. 3.43 we can obtain the following formulae which have been shown in (135):

$$\beta = \frac{\alpha_o^* + 3}{\alpha_b^* + 3} \quad (3.44)$$

where

$$\begin{aligned} \alpha_o^* &= \alpha_o^3 \frac{b_t}{h} \frac{t_t}{t_h} \\ \alpha_b^* &= \frac{b_t}{h} \frac{t_b}{t_h} \end{aligned} \quad (3.45)$$

$$\text{and } \alpha_o = \frac{b}{b_t}$$

We will now continue using the ordinary folded plate analysis process to set out the relation between normal warping stresses and displacements. In order to arrive at a general solution, the individual plates are first considered separately, as a result of which the compatibility condition along an edge is established.

As we have defined them, the displacements tangential to the side web plates are designated by  $\bar{v}_h$ . The horizontal displacement of the upper flange plate is designated by  $\bar{u}_t$ , while the horizontal displacement of the lower flange plate in the opposite direction is  $\bar{u}_b$ . We may express the displacements  $\bar{u}_t$ ,  $\bar{u}_b$  and  $\bar{v}_h$  in terms of  $f_{II} = B_{II}/J_{II}$ , neglecting the effect of shear deformation.

Hence, we have, for the side web plate

$$\bar{v}_h'' = -\frac{M_h}{E_1 I_h} = -\frac{W_h}{E_1 I_h} \cdot \frac{M_h}{W_h} \quad (3.46a)$$

where

$$I_h = \frac{1}{12} h_c^3 t_h$$

$$W_h = \frac{h_c^2}{6} t_h$$

thus

$$\bar{v}_h'' = -\frac{2}{E_1 h_c} \cdot \frac{M_h}{W_h} \quad (3.46b)$$

We will now express  $M_h$  in terms of  $f_{II}$

$$M_h = -\frac{\omega_{II,1} - \omega_{II,n+3}}{2} f_{II} W_h = -\frac{(1+\beta)}{2} \omega_{II,1} f_{II} W_h \quad (3.47)$$

Substituting Eq. 3.47 into Eq. 3.46b we obtain

$$\bar{v}_h'' = \frac{1+\beta}{E_1 h_c} \cdot \omega_{II,1} f_{II} \quad (3.48)$$

Similar relations may also be derived for  $\bar{u}_t$  and  $\bar{u}_b$ . Summarising,

we have

$$\begin{aligned}\bar{v}_h'' &= \frac{\omega_{II,1}}{E_1} \cdot \frac{1+\beta}{h_c} \cdot f_{II} \\ \bar{u}_t'' &= \frac{\omega_{II,1}}{E_1} \cdot \frac{2}{b_t} \cdot f_{II} \\ \bar{u}_b'' &= \frac{\omega_{II,1}}{E_1} \cdot \frac{2\beta}{b_b} \cdot f_{II}\end{aligned}\tag{3.49}$$

Differentiating the geometrical relation Eq. 3.23 twice and substituting Eqs. 3.49 into it, we then have

$$\begin{aligned}\gamma_d'' &= \frac{\bar{u}_t'' + \bar{u}_b''}{h} + \frac{2}{b_t} \left( \frac{\bar{v}_h''}{\sin\phi} - \bar{u}_t'' \cot\phi \right) \\ &= \frac{\omega_{II,1}}{E_1 h} \cdot \frac{2}{b_t} \cdot f_{II} - \frac{\omega_{II,1}}{E_1} \cdot \frac{4 \cot\phi}{b_t^2} f_{II} + \frac{\beta \omega_{II,1}}{E_1 h} \cdot \frac{2}{b_b} \cdot f_{II} + \frac{\omega_{II,1}}{E_1 h_c \sin\phi} \cdot \frac{2}{b_t} \cdot (1+\beta) f_{II} \\ &= \frac{\omega_{II,1} f_{II}}{E_1 h b_t^2 b_b} [ 2b_t b_b - 4h b_b \cot\phi + 2b_t^2 \beta + 2b_t b_b (1+\beta) ] \\ &= \frac{\omega_{II,1} f_{II}}{E_1 h b_t^2 b_b} [ 2b_t b_b - 2(b_t - b_b) b_b + 2b_t^2 \beta + 2b_t b_b + 2b_t b_b \beta ] \\ &= \frac{\omega_{II,1} f_{II}}{E_1 h b_t^2 b_b} [ 2b_b^2 + 2b_t^2 \beta + 2b_t b_b + 2b_t b_b \beta ] \\ &= \frac{2(b_t + b_b)(\beta b_t + b_b)}{E_1 h b_t^2 b_b} \omega_{II,1} f_{II}\end{aligned}\tag{3.50}$$

Substitution of the above expression into Eq. 3.30 gives

$$\sigma_{II,1} = - \frac{2(b_t + b_b)(\beta b_t + b_b)}{h b_t^2 b_b} \omega_{II,1}^2 f_{II}\tag{3.51}$$

From Eq. 3.35 we have

$$\sigma_{II,1} = f_{II} \omega_{II,1}\tag{3.52}$$

By comparison of Eq. 3.51 with Eq. 3.52 we finally obtain

$$\omega_{II,1} = - \frac{hb_t^2 b_b}{2(b_t + b_b)(\beta b_t + b_b)} \quad (\text{length}^2) \quad (3.53)$$

By using Simpson's integration method, the distortional moment of inertia  $J_{II}$  is evaluated as

$$\begin{aligned} J_{II}/\omega_{II,1}^2 &= \frac{2b_c t_c}{3} (\alpha_0^2 + \alpha_1^2 + \alpha_0 \alpha_1) + \sum_{i=1}^n \frac{b_{t,i} t_{t,i}}{3} (\alpha_i^2 + \alpha_{i+1}^2 + \alpha_i \alpha_{i+1}) \\ &+ \sum_{i=1}^n \frac{b_{b,i} t_{b,i}}{3} (\alpha_{b,i}^2 + \alpha_{b,i+1}^2 + \alpha_{b,i} \alpha_{b,i+1}) \\ &+ \sum_{i=1}^n \frac{h_{c,i} t_{h,i}}{3} (\alpha_i^2 + \alpha_{b,i}^2 + \alpha_i \alpha_{b,i}) \\ &= \frac{2b_c t_c}{3} (\alpha_0^2 + \alpha_1^2 + \alpha_0 \alpha_1) + \sum_{i=1}^n \frac{b_{t,i} t_{t,i}}{3} (\alpha_i^2 + \alpha_{i+1}^2 + \alpha_i \alpha_{i+1}) \\ &+ \sum_{i=1}^n \frac{\beta^2 b_{b,i} t_{b,i}}{3} (\lambda_i^2 + \lambda_{i+1}^2 + \lambda_i \lambda_{i+1}) \\ &+ \sum_{i=1}^{n+1} \frac{h_{c,i} t_{h,i}}{3} (\alpha_i^2 + \beta^2 \lambda_i^2 - \beta \alpha_i \lambda_i) \end{aligned} \quad (3.54)$$

For a single cell rectangular section, from Eqs. 3.53 and 3.54 we can obtain

$$\omega_{II,1} = - \frac{b_t h}{4(1+\beta)} \quad (3.55)$$

and

$$J_{II} = \frac{b_t^2 h^3 t_h}{48} \left[ \frac{3 + 2(\alpha_0^* + \alpha_b^*) + \alpha_0^* \alpha_b^*}{6 + (\alpha_0^* + \alpha_b^*)} \right] \quad (3.56)$$

where,  $\alpha_0^*$  and  $\alpha_b^*$  are shown in expressions (3.45).

The associated in-plane shear stresses caused by the constraint of warping are determined from the condition of equilibrium

$$t \frac{\partial \sigma_{II}}{\partial z} dz ds + t \frac{\partial \tau_{II}}{\partial s} dz ds = 0 \quad (3.57a)$$

or

$$t \frac{\partial \sigma_{II}}{\partial z} + \frac{\partial q_{II}}{\partial s} = 0 \quad (3.57b)$$

Substituting Eq. 3.35 into Eq. 3.57b and integrating we obtain

$$q_{II} = q_{II}^o - \frac{B'_{II}}{J_{II}} S_{II} \quad (3.58)$$

where

$$S_{II} = \int_0^S \omega_{II} dA = \int_0^S \omega_{II} t ds \quad (\text{length}^4) \quad (3.59)$$

is called the distortional statical moment of area.

The constant of integration in Eq. 3.58 is determined from the compatibility condition

$$\phi_i \gamma_{\beta s}^{II} ds = 0 \quad (3.60a)$$

or

$$\phi_i \tau_{II} ds = \phi_i \frac{q_{II}}{t} ds = 0 \quad (3.60b)$$

By establishing the compatibility condition (3.60b) for each cell separately, and putting

$$\bar{q}_{II,i}^o = \frac{q_{II,i}^o J_{II}}{B'_{II}} \quad (\text{length}^4) \quad (3.61a)$$

as the unit distortional shear flow function,

i.e.,

$$q_{II,i}^o = \frac{B'_{II}}{J_{II}} \bar{q}_{II,i}^o \quad (3.61b)$$

and defining

$$\bar{S}_{II,i} = \phi_i S_{II} \frac{ds}{t} \quad (\text{length}^4)$$

we may obtain a set of flexibility equations

$$[f] \{ \bar{q}_{II}^o \} = \{ \bar{S}_{II} \} \quad (3.62)$$

where the flexibility coefficient matrix  $[f]$  is expressed as in Eqs. 2.19.

$$\{\bar{q}_{\text{II}}^{\circ}\} = \begin{Bmatrix} \bar{q}_{\text{II},1}^{\circ} \\ \bar{q}_{\text{II},2}^{\circ} \\ \vdots \\ \bar{q}_{\text{II},n}^{\circ} \end{Bmatrix} \quad \{\bar{S}_{\text{II}}\} = \begin{Bmatrix} \bar{S}_{\text{II},1} \\ \bar{S}_{\text{II},2} \\ \vdots \\ \bar{S}_{\text{II},n} \end{Bmatrix} \quad (3.63)$$

After solving the set of flexibility equations (3.62), by superposition we can finally obtain the total shear flow on the walls of the section

$$q_{\text{II}} = \frac{B'_{\text{II}}}{J_{\text{II}}} \hat{S}_{\text{II}} \quad (3.64)$$

where

$$\hat{S}_{\text{II}} = \bar{q}_{\text{II}}^{\circ} - S_{\text{II}} \quad (3.65)$$

is called the reduced distortional statical moment of area.

It should be borne in mind that for points lying on the interior walls of the section the unit shear flow function is obtained by the algebraic superposition of the constant shear flows in the cells lying on either side of the midline separating them, i.e.,

$$(\bar{q}_{\text{II}}^{\circ})_{i-1,i} = \bar{q}_{\text{II},i}^{\circ} - \bar{q}_{\text{II},i-1}^{\circ} \quad (3.66)$$

On the open portions of the section the unit shear flow function equals zero.

For a general single-spined box beam shown in Fig. 3.9a, we may calculate the  $S_{\text{II}}$  diagram from the  $\omega_{\text{II}}$  diagram (Fig. 3.9b). Noting that all the imaginary cuts are located at the mid-points of the bottom flange of the section (see Figs. 3.11d and 3.12d). The formulae for calculating the values of  $S_{\text{II}}$  at characteristic points are written as

$$\begin{aligned} (S_{\text{II}})_{0,1} &= (S_{\text{II}})_{n+2,n+2} = 0 \\ (S_{\text{II}})_{m,2n+i+3} &= 0 \quad (i=1,2,\dots,n) \\ (S_{\text{II}})_{n+i+2,2n+i+3} &= -\frac{1}{8} b_{b,i} t_{b,i} (3\omega_{\text{II},n+i+2} + \omega_{\text{II},n+i+3}) \quad (i=1,2,\dots,n) \\ (S_{\text{II}})_{n+i+3,2n+i+3} &= \frac{1}{8} b_{b,i} t_{b,i} (3\omega_{\text{II},n+i+3} + \omega_{\text{II},n+i+2}) \quad (i=1,2,\dots,n) \end{aligned}$$

$$\begin{aligned}
(S_{II})_{n+3,n+3} &= (S_{II})_{n+3,2n+4} \\
(S_{II})_{2n+3,2n+3} &= (S_{II})_{2n+3,3n+3} \\
(S_{II})_{n+i+2,n+i+2} &= (S_{II})_{n+i+2,2n+i+3} - (S_{II})_{n+i+2,2n+i+2} \quad (i=2,3,\dots,n) \\
(S_{II})_{m,n+i+2} &= (S_{II})_{n+i+2,n+i+2} - \frac{1}{8} h_{c,i} t_{h,i} (3\omega_{II,n+i+2} + \omega_{II,i}) \quad (i=1,2,\dots,n+1) \\
(S_{II})_{i,n+i+2} &= (S_{II})_{n+i+2,n+i+2} - \frac{1}{2} h_{c,i} t_{h,i} (\omega_{II,n+i+2} + \omega_{II,i}) \quad (i=1,2,\dots,n+1) \\
(S_{II})_{m,1} &= -\frac{1}{8} b_c t_c (3\omega_{II,o} + \omega_{II,1}) = (S_{II})_{m,n+2} \\
(S_{II})_{1,1} &= -\frac{1}{2} b_c t_c (\omega_{II,o} + \omega_{II,1}) \\
(S_{II})_{i,i+1} &= (S_{II})_{i,i} + (S_{II})_{i,n+i+2} \quad (i=1,2,\dots,n+1) \\
(S_{II})_{m,i+1} &= (S_{II})_{i,i+1} - \frac{1}{8} b_{t,i} t_{t,i} (3\omega_{II,i} + \omega_{II,i+1}) \quad (i=1,2,\dots,n) \\
(S_{II})_{i+1,i+1} &= (S_{II})_{i,i+1} - \frac{1}{2} b_{t,i} t_{t,i} (\omega_{II,i} + \omega_{II,i+1}) \quad (i=1,2,\dots,n)
\end{aligned} \tag{3.67}$$

where  $n$  is the total number of cells in the section. For the above indices, the first subscript represents the node number, and the second represents the element number, while the subscript  $m$  indicates the mid-point of the individual elements.

The expressions for the free terms of Eqs. 3.62 can be written as

$$\begin{aligned}
\bar{S}_{II,i} &= \frac{b_{t,i}}{6 t_{t,i}} [(S_{II})_{i,i+1} + 4(S_{II})_{m,i+1} + (S_{II})_{i+1,i+1}] \\
&+ \frac{b_{b,i}}{6 t_{b,i}} [(S_{II})_{n+i+2,2n+i+3} + 4(S_{II})_{m,2n+i+3} + (S_{II})_{n+i+3,2n+i+3}] \\
&+ \frac{h_{c,i}}{6 t_{h,i}} [(S_{II})_{i,n+i+2} + 4(S_{II})_{m,n+i+2} + (S_{II})_{n+i+2,n+i+2}] \\
&- \frac{h_{c,i+1}}{6 t} [(S_{II})_{i+1,n+i+3} + 4(S_{II})_{m,n+i+3} + (S_{II})_{n+i+3,n+i+3}] \\
&(i = 1, 2, \dots, n)
\end{aligned} \tag{3.68}$$

The sign convention adopted here is the same as that described in Chapter 2.

We give now two numerical examples to illustrate the calculation of sectional properties and the distribution of warping stresses.

Example 3.1 Single-cell box beam with trapezoidal section

The dimensions of the cross-section and the subdivision of the section are given in Fig. 3.11a and Fig. 3.11b:

(a) Unit distortional warping function  $\omega_{II}$

The cross-sectional parameters are calculated as follows:

$$\alpha_0 = 2, \quad \alpha_1 = 1, \quad \alpha_2 = -1, \quad \alpha_3 = -2$$

$$\lambda_1 = 1, \quad \lambda_2 = -1$$

$$\psi_1 = -1, \quad \psi_2 = -1$$

$$\beta = \frac{2^3 \cdot a^2 \cdot t_0 + 2 \times 0.7159a \times 0.5 t_0 (a + \frac{0.7a}{2})}{0.7^2 a^2 \cdot 1.2 t_0 + 2 \times 0.7159a \times 0.5 t_0 (0.7a + \frac{0.5}{a})}$$

$$= 6.2$$

$$\alpha_{b,1} = -6.2$$

$$\alpha_{b,2} = 6.2$$

The value of the unit distortional warping function at the upper corner point is

$$\omega_{II,1} = -\frac{0.7a \times a^2 \times 0.7a}{2(a + 0.7a)(6.2a + 0.7a)} = -2.0887 \times 10^{-2} a^2$$

The diagram of  $\omega_{II}$  is shown in Fig. 3.11c.

(b) Distortional warping moment of inertia  $J_{II}$

By integrating the diagram of  $\omega_{II}$  we may obtain

$$\begin{aligned} \frac{2}{3} \times 0.5a t_0 (0.041774^2 + 0.020887^2 + 0.041774 \times 0.020887) a^4 &= 0.001018 a^5 t_0 \\ \frac{1}{3} \times a t_0 (0.020887^2) a^4 &= 0.000145 a^5 t_0 \\ \frac{2}{3} \times 0.7159a \times 0.5 t_0 (0.020887^2 + 0.1294994^2 - 0.020887 \times 0.1294994) a^4 &= 0.003461 a^5 t_0 \\ \frac{1}{3} \times 0.7a \times 1.2 t_0 (0.1294994^2) a^4 &= 0.004696 a^5 t_0 \\ J_{II} &= 0.00932 a^5 t_0 \end{aligned}$$

(c) Reduced distortional statical moment of area  $\hat{S}_{II} = \bar{q}_{II}^o - S_{II}$

Using Eqs. 3.67 we first calculate the values of  $S_{II}$ :

$$(S_{II})_{0,1} = (S_{II})_{3,3} = 0$$

$$(S_{II})_{m,6} = 0$$

$$(S_{II})_{4,6} = -\frac{1}{8} \times 0.7a \times 1.2t_0 (3 \times 0.1294994 - 0.1294994)a^2 = -2,7195 \times 10^{-2} a^3 t_0$$

$$(S_{II})_{5,6} = -\frac{1}{8} \times 0.7a \times 1.2t_0 (-3 \times 0.1294994 + 0.1294994)a^2 = -2.7195 \times 10^{-2} a^3 t_0$$

$$(S_{II})_{4,4} = -2.7195 \times 10^{-2} a^3 t_0$$

$$(S_{II})_{5,5} = 2.7195 \times 10^{-2} a^3 t_0$$

$$(S_{II})_{m,4} = -0.027195a^3 t_0 - \frac{1}{8} \times 0.7159a \times 0.5t_0 (3 \times 0.1294994 - 0.020887)a^2 = -4.3643 \times 10^{-2} a^3 t_0$$

$$(S_{II})_{1,4} = -0.027195a^3 t_0 - \frac{1}{2} \times 0.7159a \times 0.5t_0 (0.1294994 - 0.020887)a^2 = -4.6634 \times 10^{-2} a^3 t_0$$

$$(S_{II})_{m,5} = 4.3643 \times 10^{-2} a^3 t_0$$

$$(S_{II})_{2,5} = 4.6634 \times 10^{-2} a^3 t_0$$

$$(S_{II})_{m,1} = -\frac{1}{8} \times 0.5a \times t_0 (-3 \times 0.041774 - 0.020887)a^2 = 0.9138 \times 10^{-2} a^3 t_0$$

$$(S_{II})_{1,1} = -\frac{1}{2} \times 0.5a \times t_0 (-0.041774 - 0.020887)a^2 = 1.5665 \times 10^{-2} a^3 t_0$$

$$(S_{II})_{1,2} = 1.5665 \times 10^{-2} a^3 t_0 - 4.6634 \times 10^{-2} a^3 t_0 = -3.0969 \times 10^{-2} a^3 t_0$$

$$(S_{II})_{m,2} = -0.030969 a^3 t_0 - \frac{1}{8} a t_0 (-3 \times 0.020887 + 0.020887) = -2.5747 \times 10^{-2} a^3 t_0$$

$$(S_{II})_{2,2} = -3.0969 \times 10^{-2} a^3 t_0$$

$$(S_{II})_{2,3} = -3.0969 \times 10^{-2} a^3 t_0 + 4.6634 \times 10^{-2} a^3 t_0 = 1.5665 \times 10^{-2} a^3 t_0$$

$$(S_{II})_{m,3} = 0.9138 \times 10^{-2} a^3 t_0$$

For a single cell box the constant shear flow can be obtained from

$$\bar{q}_{II}^o = \frac{\oint \frac{S_{II}}{t} ds}{\oint \frac{ds}{t}}$$

in which

$$\begin{aligned} \oint \frac{S_{II}}{t} ds &= \frac{a}{6t_0} (-0.030969 - 4 \times 0.025747 - 0.030969) a^3 t_0 + \frac{0.7a}{6 \times 1.2t_0} (-2 \times 0.027195) a^3 t_0 \\ &+ \frac{2 \times 0.7159a}{6 \times 0.5t_0} (-0.046634 - 4 \times 0.043643 - 0.027195) a^3 t_0 \\ &= -0.1513 a^4 \end{aligned}$$

$$\oint \frac{ds}{t} = \frac{a}{t_0} + \frac{2 \times 0.7159a}{0.5t_0} + \frac{0.7a}{1.2t_0} = 4.44693a/t_0$$

Thus, we have

$$\bar{q}_{II}^o = \frac{-0.1513a^4}{4.44693 \frac{a}{t_0}} = -0.034023 a^3 t_0$$

Finally, the  $\hat{S}_{II} = \bar{q}_{II}^o - S_{II}$  diagram with arrows showing the direction is given in Fig. 3.11f.

### Example 3.2 Three-cell box beam with trapezoidal section

The dimensions of the cross-section are shown in Fig. 3.12a. To use the formulae derived we subdivide the section into individual plate elements interconnected at discrete nodes (see Fig. 3.12b).

The calculation is carried out as follows:

(a) Unit distortional warping function  $\omega_{II}$

Using Eqs. 3.36 and 3.38 we calculate the cross-sectional parameters first:

$$\alpha_0 = \frac{2.5}{1.5} = 1.6667, \quad \alpha_1 = 1, \quad \alpha_2 = \frac{0.5}{1.5} = 0.3333,$$

$$\alpha_3 = -0.3333, \quad \alpha_4 = -1, \quad \alpha_5 = -1.6667$$

$$\lambda_1 = 1, \quad \lambda_2 = 0.5, \quad \lambda_3 = -0.5, \quad \lambda_4 = -1$$

$$\psi_1 = -1, \quad \psi_2 = -1.5, \quad \psi_3 = -1.5, \quad \psi_4 = -1.$$

$$\bar{M}_t = \frac{at_0}{3} [1.6667(2 \times 2.5a + 1.5a) + (2 \times 1.5a + 2.5a)]$$

$$+ \frac{at_0}{3} [(2 \times 1.5a + 0.5a) + 0.3333(2 \times 0.5a + 1.5a)] + \frac{at_0}{6} [2 \times 0.3333(2 \times 0.5a - 0.5a)]$$

$$= 6.9445 a^2 t_0$$

$$\bar{M}_b = \frac{0.5ax1.2t_0}{3} [(2xa + 0.5a) + 0.5(2x0.5a + a)] + \frac{ax1.2t_0}{6} [2x0.5(2x0.5a - 0.5a)]$$

$$= 0.8 a^2 t_0$$

$$\bar{M}_{h,1} = \frac{0.5\sqrt{5}ax0.5t_0}{3} (2x1.5a+a) + \frac{ax0.5t_0}{3} \times 0.3333(2x0.5a+0.5a)$$

$$= 0.8287 a^2 t_0$$

$$\bar{M}_{h,2} = \frac{0.5\sqrt{5}a \times 0.5t_0}{3} (2xa+1.5a) + \frac{ax0.5t_0}{3} \times 0.5(2x0.5a+0.5a)$$

$$= 0.7772 a^2 t_0$$

$$\beta = \frac{6.9445 + 0.8287}{0.8 + 0.7772} = 4.93$$

$$\alpha_{b,1} = -4.93, \quad \alpha_{b,2} = -2.465, \quad \alpha_{b,3} = 2.465, \quad \alpha_{b,4} = 4.93$$

$$\omega_{II,1} = -\frac{a(3a)^2 \times 2a}{2(3a+2a)(4.93 \times 3a+2a)} = -1.0721 \times 10^{-1} a^2$$

Thus the diagram of  $\omega_{II}$  can be shown as in Fig. 3.12c.

(b) Distortional warping moment of inertia  $J_{II}$

By integrating the diagram of  $\omega_{II}$  we obtain the distortional warping moment of inertia

$$J_{II} = 0.38455 a^5 t_0$$

(c) Reduced distortional statical moment of area  $\hat{S}_{II} = \bar{q}_{II}^0 - S_{II}$

By using Eqs. 3.67 the diagram of the distortional statical moment of area  $S_{II}$  is presented in Fig. 3.12d.

In accordance with Eq. 3.68 we may further calculate the free terms of Eqs. 3.62. The set of flexibility equations may then be set:

$$\begin{aligned} 5.6527 \bar{q}_{II,1}^0 - 2 \bar{q}_{II,2}^0 &= -0.1438 a^3 t_0 \\ -2 \bar{q}_{II,1}^0 + 5.8333 \bar{q}_{II,2}^0 - 2 \bar{q}_{II,3}^0 &= -1.1715 a^3 t_0 \\ -2 \bar{q}_{II,2}^0 + 5.6527 \bar{q}_{II,3}^0 &= -0.1438 a^3 t_0 \end{aligned}$$

Solving, we obtain

$$\begin{aligned}\bar{q}_{\text{II},1}^0 &= \bar{q}_{\text{II},3}^0 = -0.12471 a^3 t_0 \\ \bar{q}_{\text{II},2}^0 &= -0.28819 a^3 t_0\end{aligned}$$

The  $\hat{S}_{\text{II}} = \bar{q}_{\text{II}}^0 - S_{\text{II}}$  diagram with arrows showing the direction introduced is given in Fig. 3.12f.

### 3.5 Resistance of cross-section to distortion

It has already been shown that the distortion of the cross-sectional shape of a box beam is, in general not uniform along the axis of the beam. Longitudinal warping stresses and associated shear stresses arise from constraint to warping.

Considering as a free body an element of the girder in the form of a closed frame of unit length (Fig. 3.13), the gradient of the in-plane shear and distortional loading subject the plate element to transverse flexure. The pattern of deformation is similar to that of a Vierendeel frame having an elevation identical to the cross-section of the box beam. Thus the frame action of the cross-section caused by the flexural stiffness of the walls results in another partial resistance to deformation, which adds to the resistance caused by the constraint of warping.

From the general equilibrium condition shown in Eq. 3.57b, we may have

$$\int_A \frac{\partial \sigma_{\text{II}}}{\partial z} \omega_{\text{II}} dA + \int_A \frac{\partial q_{\text{II}}}{\partial s} \omega_{\text{II}} ds = 0 \quad (3.69)$$

i.e.,

$$B'_{\text{II}} = - \int_A \frac{\partial q_{\text{II}}}{\partial s} \omega_{\text{II}} ds \quad (3.70)$$

And integration by parts of the integral on the right gives

$$B'_{II} = \int_A q_{II} \frac{\partial \omega_{II}}{\partial s} ds \quad (3.71)$$

Substituting Eq. 3.28 and Eq. 3.24 into Eq. 3.71 we then obtain

$$B'_{II} = \frac{\int_A q_{II} u_{t,d} ds}{\gamma_d(z)} \quad (3.72)$$

From the principal of virtual work and the definition of the distortional moment, it is clear that we have

$$B'_{II} = M_d \quad (\text{force} \times \text{length}) \quad (3.73)$$

This means that the interior distortional moment is identical to the first derivative of the distortional bimoment  $B_{II}$ .

Now, the resistance of the cross-section to deformation due to frame action is examined. We define the effective frame stiffness of the section per unit length as the resisting component which is required to correspond to a unit distortional angle. This is determined with the aid of the following energy equation.

The internal energy per unit length is given by the general expression  $\frac{1}{2} k_d \gamma_d^2$ , while the external energy in terms of the distortional angle and the distortional moment is equal to  $\frac{1}{2} M_d \gamma_d$ .

Hence

$$\frac{1}{2} k_d \gamma_d^2 = \frac{1}{2} M_d \gamma_d$$

so that

$$k_d = E_t J_d = \frac{M_d}{\gamma_d} \quad (3.74)$$

where

$k_d$ (force) is termed distortional frame stiffness of the section per unit length,

$J_d$  which has units of  $L^2$  is defined as the distortional second moment

of area and is equal to  $1/E_1$  times frame stiffness.

Physically the distortional frame stiffness can be evaluated by analysis of a frame with the shape and dimensions of a unit length of the box beam. The frame is constrained horizontally and vertically at the lower corner points as shown in Fig. 3.14, and is loaded by diagonal forces with unit horizontal components, i.e.,

$$\begin{aligned} S_H &= 1 \\ S_V &= \frac{2}{b_t + b_b} \\ S_d &= \frac{\sqrt{4h^2 + (b_t + b_b)^2}}{b_t + b_b} \end{aligned} \quad (3.75)$$

The deformed shape of the frame slice is shown in Fig. 3.15. If we ignore the axial deformation of the individual plate elements, we will have

$$u_1 \cos \phi - v_1 \sin \phi = v_2 \sin \phi - u_2 \cos \phi = 0 \quad (3.76)$$

The rotation angle for the left side web can be expressed as

$$\gamma_{h1} = - \frac{u_1 \sin \phi + v_1 \cos \phi}{h_c} \quad (3.77)$$

Substitution of Eq. 3.76 into Eq. 3.77 gives

$$\begin{aligned} \gamma_{h1} &= - \frac{u_1 \sin^2 \phi + v_1 \sin \phi \cos \phi}{h_c \sin \phi} = - \frac{u_1 (\sin^2 \phi + \cos^2 \phi)}{h} \\ &= - \frac{u_1}{h} \end{aligned} \quad (3.78)$$

Similarly we can write down the rotation angle for the right side web as

$$\gamma_{h2} = - \frac{u_2}{h} \quad (3.79)$$

Thus,

$$\gamma_h = \gamma_{h1} = \gamma_{h2} = - \frac{u_1 + u_2}{2h} \quad (3.80)$$

We use Eq. 3.80 instead of Eq. 3.78 or Eq. 3.79, since in using the computer stiffness method for plane frames, axial deformation is also included.

The horizontal rotation angle may be written as

$$\gamma_t = \frac{v_2 - v_1}{b_t} \quad (3.81)$$

Thus the total distortional angle can be expressed as

$$\begin{aligned} \gamma_d &= \gamma_h + \gamma_t = -\frac{u_1 + u_2}{2h} + \frac{v_2 - v_1}{b_t} \\ &= \frac{-b_t(u_1 + u_2) + 2h(v_2 - v_1)}{2hb_t} \end{aligned} \quad (3.82)$$

Since the corresponding distortional moment is  $M_d = 2h$ , from Eq. 3.74 we can calculate the frame stiffness

$$k_d = \frac{4h^2 b_t}{-b_t(u_1 + u_2) + 2h(v_2 - v_1)} \quad (\text{force}) \quad (3.83)$$

and the distortional second moment of area is

$$J_d = \frac{4h^2 b_t}{E_1 [-b_t(u_1 + u_2) + 2h(v_2 - v_1)]} \quad (\text{length}^2) \quad (3.84)$$

where  $u_1$ ,  $u_2$ , and  $v_1$ ,  $v_2$  are the horizontal and vertical displacements respectively at the upper corner points of the section, and the sign convention follows the local coordinate system shown in Fig. 3.15.

In particular, for a single-cell box beam if we ignore axial and shear deformations, and assume that the effect of the slope angle of the side web with respect to the flange is insignificant we may analyse the frame slice directly by the influence coefficient method neglecting the vertical displacements of the upper corner points (see Fig. 3.16).

Releasing the frame at the mid-point of the upper flange, from the conditions of symmetry and antisymmetry, it is evident that we can clarify the redundants as

$$X_1 = 0$$

$$X_2 = 0$$

Placing a pair of unit loads at the released position gives the  $\bar{M}_3$  diagram (Fig. 3.17a). The bending moment diagram due to external forces is shown in Fig. 3.17b.

The influence coefficients can be calculated as

$$\begin{aligned} \delta_{33} &= \int_A \frac{\bar{M}_3^2}{D} ds \\ &= \frac{b_t^3}{12D_t} + \frac{b_b^3}{12D_b} + \frac{(b_t^2 + b_t b_b + b_b^2) h_c}{6D_h} \\ \Delta_{3p} &= -\frac{1}{6} \left[ \frac{(b_t + 2b_b) h_c}{D_h} + \frac{h \cdot b_b^2}{D_b} \right] \end{aligned}$$

From the compatibility condition

$$\delta_{33} X_3 + \Delta_{3p} = 0$$

we therefore obtain

$$X_3 = \frac{2h \frac{D_t}{D_h} [(b_t + b_b) h_c \frac{D_b}{D_h} + b_b^2]}{\frac{D_b}{D_h} b_t^3 + \frac{D_t}{D_h} b_b^3 + 2h_c (b_t^2 + b_t b_b + b_b^2) \frac{D_t D_h}{D_h^2}} \quad (3.85)$$

where  $D_t$ ,  $D_b$  and  $D_h$  are the transverse flexural rigidity of the top and bottom flanges and side webs respectively.

The horizontal displacement at the junction of the upper flange and the side web is

$$\delta_H = \frac{h^2 b_b}{6D_h} \left[ 2 \cdot \frac{h_c}{b_b} + \frac{D_h}{D_b} \right] - \frac{h}{12D_h} \left[ (b_t + 2b_b) h_c + \frac{D_h}{D_b} b_b^2 \right] X_3$$

We then finally obtain the frame stiffness of the section per unit length as

$$k_d = \frac{2h}{\gamma_d} = \frac{2h^2}{\delta_H} = \frac{24D_h}{\eta_1 h} \quad (3.86)$$

where

$$\eta_1 = \frac{\frac{2}{h} \left( b_t^3 b_b + 2h_c b_t^3 \frac{D_b}{D_h} + 2h_c b_b b_t^2 \frac{D_t}{D_h} + 3b_t^2 h_c^2 \frac{D_t D_b}{D_h^2} \right)}{\frac{D_b}{D_h} b_t^3 + \frac{D_t}{D_h} b_b^3 + 2h_c (b_t^2 + b_t b_b + b_b^2) \frac{D_t D_b}{D_h^2}} \quad (3.87)$$

For a rectangular section with  $b_t = b_b = b$  and  $h_c = h$ , we may obtain  
(135)

$$\eta_1 = 1 + \frac{2 \frac{b}{h} + 3 \frac{I_b + I_t}{I_h}}{\frac{I_b + I_t}{I_h} + 6 \frac{h}{b} \frac{I_t I_b}{I_h^2}} \quad (3.88)$$

where  $I_t$ ,  $I_b$  and  $I_h$  are the plate moments of inertia per unit length of the top flange, the bottom flange and webs respectively.

A frame analysis using the influence coefficient method produces, however, for complicated cross-sections a procedure rather too complex. It is more convenient to use the computer stiffness method for plane frames. A supplemental program, PRFRAN, to the main analytical program has been written based on the theory of plane frames (see Appendix II) for calculating the frame stiffness at discrete cross-sections. To operate this program the input consists of local coordinates of the junctions of the individual plate elements located on the section considered, the cross-sectional area and the transverse flexural rigidity of the plate elements.

The transverse flexural rigidity of an individual plate element is denoted by  $D$ . For an unstiffened thin plate

$$D = \frac{Et^3}{12(1-\nu^2)} \quad (3.89)$$

in which  $\nu$  = Poisson's ratio.

For transversely stiffened plates,  $D$  may be evaluated as described in the American Institute of Steel Construction (AISC) Orthotropic Plate Deck Bridge Manual (25). An approximate expression for the effective width of plate acting with one transverse stiffener is suggested by Wright et al (150) as

$$d_o = \frac{d \tanh(5.6 \frac{d}{a})}{\frac{5.6d}{a} (1-\nu^2)} \quad (3.90)$$

in which (for Eq. 3.90 only)  $d$  = the stiffener spacing,  $d_o$  = the effective width of plate, and  $a$  = the span of the plate in the transverse direction. Eq. 3.90 is obtained by fitting curves given in the AISC Manual and assuming that the plate bends with a line of inflection at midspan. Transverse flexural rigidity is obtained by computing the moment of inertia of the stiffener acting with the width of the plate,  $d_o$  and using  $D = E_1 I/d$ .

For a nonhomogeneous section, such as a steel box beam with a composite reinforced concrete deck, it is assumed that the thickness  $t$  and the rigidity  $D$  are appropriately transformed by the use of some notional Young's modulus  $E$ .

### 3.6 Calculation of transverse bending stresses and the properties of diaphragms

After analysing the frame of unit length loaded by diagonal forces with unit horizontal components, using the computer stiffness method, we may obtain the end moments and the shear forces of the individual plate elements. They may be used as the influence quantities of the transverse interior forces per unit length at the section considered and are denoted by  $\bar{m}_{db}$  and  $\bar{q}_{db}$  respectively. We can then obtain the transverse distortional bending moments

and distortional shear forces per unit length at the junctions of individual plate elements by using the following expressions

$$m_{db} = \bar{m}_{db} \cdot \frac{\gamma_d}{\bar{\gamma}_d} \quad (3.91)$$

$$q_{db} = \bar{q}_{db} \cdot \frac{\gamma_d}{\bar{\gamma}_d}$$

where  $\bar{\gamma}_d$  is the influence distortional angle calculated from Eq. 3.82 in the Vierendeel frame loaded by diagonal forces with unit horizontal components.  $\gamma_d$  is the actual distortional angle at the section considered.

The sign convention is that adopted in the conventional displacement method. It states that the end moments are considered positive if they are clockwise, and the shear force at one end of a plate element is positive when it rotates clockwise relative to the other end (see Appendix II).

For a single cell box beam we can obtain the corner moments of the top and bottom slabs from a frame analysis as

$$m_{db}^t = \frac{E_1 J_d \gamma_d}{4} (1 + \eta_2) \quad (3.92a)$$

and

$$m_{db}^b = \frac{E_1 J_d \gamma_d}{4} (1 - \eta_2) \quad (3.92b)$$

where

$$\eta_2 = \frac{(2b_t - b_b) b_b^2 \frac{D_t}{D_h} - \frac{D_b}{D_h} b_t^3 - 2h_c (b_t b_b - b_b^2) \frac{D_t D_b}{D_h^2}}{\frac{D_b}{D_h} b_t^3 + \frac{D_t}{D_h} b_b^3 + 2h_c (b_t^2 + b_t b_b + b_b^2) \frac{D_t D_b}{D_h^2}} \quad (3.93)$$

For a single-cell rectangular section with  $b_t = b_b = b$  and  $h_c = h$ , we have the following expression which has been given in (134)

$$\eta_2 = \frac{1 - \frac{I_b}{I_t}}{1 + \frac{I_b}{I_t} + 6 \frac{h}{b} \cdot \frac{I_b}{I_h}} \quad (3.94)$$

The transverse bending moment diagram for a single-cell box beam is given in Fig. 3.18. Note that the moments are plotted on the tensile sides of the plates.

So far we have considered only the transverse distortional bending stresses  $\sigma_{db,1}$  due to the antisymmetrical component of load. In fact, the multicell box beam is another instance for which the symmetrical component of load also produces transverse stresses  $\sigma_{db,2}$ . Thus, the final influence values from the computer frame analyses should be obtained by superposition of these two loading cases

$$\bar{\sigma}_{db} = \bar{\sigma}_{db,1} + \bar{\sigma}_{db,2} \quad (3.95)$$

where  $\bar{\sigma}_{db,1}$  and  $\bar{\sigma}_{db,2}$  are the influence values of the transverse distortional bending stresses due to antisymmetrical and symmetrical components of load respectively. This may be illustrated from the numerical example in Fig. 3.19 (see also in Chapter 8), where it can be seen that the stress  $\sigma_{db,2}$  due to the symmetrical component is a significant proportion of the total stress. By increasing the number of cells the stresses  $\sigma_{db}$  are increased, yet the deflections and warping stresses are not significantly changed.

The transverse stresses due to the distortion of the cross-section can be of the same order as the longitudinal stresses associated with longitudinal bending and torsional and distortional warping. In such a case, the Poisson's ratio effect in transverse bending can generate longitudinal stresses which are not negligible in comparison with the longitudinal bending stresses and torsional and distortional warping stresses. As an approximation we may obtain the longitudinal bending moments of the plates per unit width by multiplying the transverse bending moments by Poisson's ratio, i.e.,

$$m_{lb} = \nu m_{db} \quad (3.96)$$

The approximation can be confirmed by model tests (see References 83, -134 and Chapter 8).

Although it is desirable not to use intermediate diaphragms in box bridge girders, it is apparent that additional longitudinal warping stresses and transverse bending stresses due to deformation of the cross-sections, reduce the advantages anticipated from the high torsional stiffness of the box beam. A proper provision of diaphragms is preferable in bridge girders. Thus, diaphragms are sometimes not only located at supports, but also along the span at regular spacings. According to the different construction forms there are three types of diaphragms (Fig. 3.20):

- 1) Plate diaphragms
- 2) Braced frame - diagonal cross bracing, V-type bracing or inverted V-type bracing,
- 3) Ring stiffening.

A diaphragm is a planar figure having membrane and plate bending stiffness, connected to the box beam (either in the corners only or along its whole perimeter). In fact the out-of-plane stiffness of a diaphragm is negligible compared with the warping resistance of the plates composing the box beam. Thus, in an analysis of box beams, the diaphragm is usually assumed to be rigid in its own plane and absolutely flexible in a direction perpendicular to that plane. Therefore, the effect of diaphragm properties on box beams is determined only by evaluating the corresponding transverse distortional stiffness. This is defined as the distortional moment that will produce a unit transverse distortion of the diaphragm.

The transverse bracing system can be regarded as a stiff jointed frame composed of perimeter plate elements of unit length and stiffened by braces. Although Wright et al. (150) and Billington (11) have given a list of formulae for calculating the distortional stiffness of transverse bracing

systems, it is still convenient to follow the computer frame analysis process described in the preceding section.

The distortional stiffness due to ring stiffening can be calculated from the same frame analysis process when the transverse flexural rigidity  $D$  of an individual plate element is replaced by the  $EI$  of the relevant stiffener plus the associated effective width of plate which may be calculated from Eq. 3.90.

For a plate diaphragm of uniform thickness  $t_p$ , the unit length can be thought of as the idealized thickness of the diaphragm. Since the flexural stiffness about the axis normal to the plate is assumed to be infinite, the diaphragm stiffness can be found from an analysis of an end-loaded tapered cantilever with span  $h$  considering shear strain only. Denoting by  $y_1$  the deflection due to shear, we obtain for any cross-section the following expression for the slope (141).

$$\frac{dy_1}{dx} = \frac{\alpha V}{GA} \quad (3.97)$$

in which  $V/A$  is the average shear stress,  $G$  is the modulus in shear and  $\alpha$  is a numerical factor by which the average shear stress must be multiplied in order to obtain the shear stress at the centroid of the cross-section. In the case considered we adopt  $\alpha = 1$  (107). Using Simpson's integration method we obtain

$$\begin{aligned} y_{1,t} &= \frac{h}{6G} \left( \frac{1}{A_b} + \frac{8}{A_t + A_b} + \frac{1}{A_t} \right) \\ &= \frac{h(b_t^2 + 10b_t b_b + b_b^2)}{6Gt_p b_t b_b (b_t + b_b)} \end{aligned} \quad (3.98)$$

So that the transverse distortional stiffness is

$$k_d = E_1 J_d = \frac{h}{\gamma_d} = \frac{6Gt_p b_t b_b (b_t + b_b) h}{b_t^2 + 10 b_t b_b + b_b^2} \quad (3.99)$$

For a rectangular section with  $b_t = b_b = b$ , we obtain

$$k_d = Gbht_p = \frac{E}{2(1 + \nu)} bht_p \quad (3.100)$$

It should be noted that diaphragms are assumed to be located at longitudinal discrete nodes only. Therefore, the diaphragm stiffnesses are easy to include in the stiffness matrix.

### 3.7 Single-spined box beams curved in plan

Considering a single-spined box beam curved in plan, it is assumed that the cross-sectional dimensions are small in relation to the radius of curvature. Numerical results based on the finite element method and the BEF analogy (15) show that in a curved box beam the transverse distortional stresses due to the antisymmetrical component of the load, are similar to those in an equivalent straight box beam with a span equal to the developed length of the centre line of the curved box beam. In accordance with this structural behaviour, the transverse frame analysis at nodal sections for curved box beams can be simplified.

At each nodal section, a one-way frame having a unit arc dimension in the longitudinal direction is taken, as shown in Fig. 3.21. This unit dimension is measured at the mid-width of the box beam. The dimensions of a typical frame are shown in Fig. 3.22. It can be seen that the longitudinal dimension of the frame is  $1 + 0.5 \frac{b}{R}$  at the outer edge of the beam, and  $1 - 0.5 \frac{b}{R}$  at the inner edge, where  $b$  is the width of the flange in the radial direction and  $R$  is the radius of curvature of the beam measured to the centre of the flange.

To simplify the transverse frame analysis, the real frame shown in Fig. 3.22 is replaced by an equivalent frame shown in Fig. 3.23, where the plate elements having curved web plates are replaced by equivalent flat

rectangular members. The individual plates are then considered to have a width equal to the average of the outer and inner edge dimensions of the plate. The width of the equivalent web plates, for instance, in a multicell boxbeam as shown in Fig. 3.9 is determined by

$$b_{n+i+2} = 1 - \frac{x_i + x_{n+i+2}}{2R} \quad (i=1,2,\dots,n+1) \quad (3.101)$$

where  $n$  is the total number of cells,

$x_i$  and  $x_{n+i+2}$  are the local  $x$ -coordinates of the end nodes of the web plate elements respectively.

The equivalent frame may then be analysed by the plane frame program. For a box beam having a radius of curvature of a practical magnitude, the simplified procedure can be adopted with little loss of accuracy but with a substantial saving in computational effort.

Additional distortional forces occur in boxbeams curved in plan due to the radial component of the longitudinal bending stresses. The radial component,  $\sigma_R$ , of the longitudinal bending stress,  $\sigma_{z,b}$ , for unit length of the box is given by

$$\sigma_R = \frac{\sigma_{z,b}}{R} \quad (3.102)$$

where  $R$  is the radius of curvature which is positive when the centre of curvature is on the positive side of the  $x$  axis.

The system of radial forces shown in Fig. 3.24 can be replaced by an horizontal force acting through the shear centre and a torsional moment. Thus, the additional distortional moment per unit length can be expressed as

$$m_{dR} = 0.5 \int_A \frac{M_x y}{I_{xx} R} [y - (y_S - y_G)] dA \quad (3.103)$$

where  $M_x$  is the longitudinal bending moment about the  $x$  axis of a positive section,

$I_{xx}$  is the moment of inertia of the entire cross-section about the horizontal centroidal axis,

$y$  is the coordinate of a point on the centroid of the walls, referred to the neutral axis  $x$  of bending of the cross-section,

$y_s$  is the vertical coordinate indicating the position of the centre from the mid-line of the top flange, calculated by Eq. 2.92 or Eq.2.105,

$y_g$  is the vertical coordinate of the centroid from the top flange,

$R$  is the radius of curvature.

It is preferable to use Simpson's integration method to evaluate the integral in Eq. 3.103 for a general multicellular section shown in Fig. 3.9

$$m_{dR} = \frac{M_x}{12 I_{xx} R} \sum_{i=1}^m [ 2(y_j^2 + y_j y_k + y_k^2) - 3(y_s - y_g)(y_j + y_k) ] \ell_i A_{z,i} \quad (3.104)$$

where  $m$  is the total number of plate elements which form the cross-section,  $y_j$  and  $y_k$  are the vertical coordinates of two end nodes of the  $i^{\text{th}}$  plate element,

$A_{z,i}$  is the area per unit width of the  $i^{\text{th}}$  plate element.

The longitudinal bending moments in statically-determinate box beams are independent of the torsional moments. In the case of curved box beams under statically-indeterminate conditions, the bending moments  $M_x$  are not given at the outset (and the equivalent distortional loading is not known in advance) and are themselves affected by the cross-sectional deformation. Generally, the distribution of bending and torsional moments in curved box beams may be approximated, initially assuming non-deformable cross-sections, by the use of the stiffness analysis program. The distortional loading is then treated as the sum of the distortional component of the loading and the additional distortional component of the radial forces given by Eq. 3.103. The interaction between the bending and torsional moments influenced by

the deformation of the cross-section can then be included by a further iterative procedure which will be discussed in later sections.

### 3.8 Basic differential equation for distortion

In order to implement the stiffness analysis procedure we here follow an energy argument leading to the governing differential equation.

The strain energy corresponding to the distortional warping stresses may be written as

$$\begin{aligned}
 U_1 &= \frac{1}{2} \int_V \sigma_{II} \epsilon_{\beta}^2 dV = \frac{E_1}{2} \int_V \epsilon_{\beta}^2 dV \\
 &= \frac{E_1}{2} \int_l \left[ \int_A \omega_{II}^2(z) dA \right] [\gamma_d''(z)]^2 dz \\
 &= \frac{E_1}{2} \int_l J_{II} [\gamma_d''(z)]^2 dz \tag{3.105}
 \end{aligned}$$

The energy required to distort a frame formed by a length  $dz$  of the box is

$$dU_2 = \frac{1}{2} k_d \gamma_d^2(z) dz, \tag{3.106}$$

thus,

$$U_2 = \frac{1}{2} \int_l k_d \gamma_d^2(z) dz \tag{3.107}$$

The potential energy of the external generalized distortional force is

$$V = - \int_l m_d(z) \gamma_d(z) dz \tag{3.108}$$

The total potential energy is given by

$$\begin{aligned}
 W &= U + V \\
 &= \frac{E_1}{2} \int_l J_{II} [\gamma_d''(z)]^2 dz + \frac{1}{2} \int_l k_d [\gamma_d(z)]^2 dz - \int_l m_d \gamma_d(z) dz \tag{3.109}
 \end{aligned}$$

or

$$W = \int_l F(z, \gamma_d, \gamma_d', \gamma_d'') dz \tag{3.110}$$

where

$$F(z, \gamma_d, \gamma_d', \gamma_d'') = \frac{E_1}{2} J_{II} (\gamma_d'')^2 + \frac{k_d}{2} (\gamma_d)^2 - m_d \gamma_d \quad (3.111)$$

According to the principle of the stationary value of the total potential energy, we have

$$\delta W = 0 \quad (3.112)$$

The Euler-Lagrange equation is used to obtain the first variation of the total potential energy, thus

$$\frac{\partial F}{\partial \gamma_d} - \frac{\partial}{\partial z} \left( \frac{\partial F}{\partial \gamma_d'} \right) + \frac{\partial^2}{\partial z^2} \left( \frac{\partial F}{\partial \gamma_d''} \right) = 0 \quad (3.113)$$

Thus we obtain the basic differential equation as

$$E_1 J_{II} \frac{\partial^4 \gamma_d}{\partial z^4} + k_d \gamma_d = m_d \quad (3.114a)$$

or

$$\frac{\partial^4 \gamma_d}{\partial z^4} + 4 \lambda_{II}^4 \gamma_d = \frac{m_d}{E_1 J_{II}} \quad (3.114b)$$

where

$$\lambda_{II} = \sqrt[4]{\frac{k_d}{4E_1 J_{II}}} \quad (3.115)$$

is called the distortional decay coefficient.

For a curved box beam Eq. 3.114b should include the effect due to the radial component of the longitudinal bending stresses. It then takes the form

$$\frac{\partial^4 \gamma_d}{\partial z^4} + 4 \lambda_{II}^4 \gamma_d = \frac{1}{E_1 J_{II}} \left( \mu_d \frac{M_x}{R} + m_d \right) \quad (3.116)$$

where  $R$  is the radius of curvature, and

$\mu_d$  is the initial curvature multiplication factor.

From Eq. 3.103 we have

$$\mu_d = \frac{0.5}{I_{xx}} \int_A y [y - (y_s - y_g)] dA \quad (3.117)$$

It can be seen that the basic differential equation for distortion is identical in form to that for beams on elastic foundations. The physical basis of the analogy is the fact that the transverse bending strength of the box beam provides a continuous elastic support for the webs, which therefore behave like beams on elastic foundations. Although an analytical procedure based on the BEF analogy has been given (150, 11), a more efficient finite element technique will be introduced in following chapter for the solution of the differential equation.

### 3.9 Interaction between bending, torsion and distortion

We denote the centroid of the box section by G and take it as the origin of the local x, y axes as shown in Fig. 3.25. The bending-torsional characteristic displacements in the cross-sectional plane can be expressed in terms of the lateral and vertical translations  $u(z)$  and  $v(z)$  of the point G and the twisting angle  $\theta_z$  with respect to the shear centre and the deformation of its contour, i.e., the distortional angle  $\gamma_d$ . The longitudinal displacement  $w_z(x, y, z)$  in the z direction consists of those due to bending, torsion and distortion.

For a straight prismatic box beam the fundamental equations governing the force-displacement relationships can be summarized as follows:

$$\begin{aligned} - \frac{1}{\mu_x} E_1 I_{yy} \frac{\partial^4 u}{\partial z^4} &= p_x \\ - \frac{1}{\mu_y} E_1 I_{xx} \frac{\partial^4 v}{\partial z^4} &= p_y \\ - \frac{1}{\mu_t} E_1 J_I \frac{\partial^4 \theta_z}{\partial z^4} + GJ_T \frac{\partial^2 \theta_z}{\partial z^2} &= m_{z, \text{ext}} \\ E_1 J_{II} \frac{\partial^4 \gamma_d}{\partial z^4} + k_d \gamma_d &= m_d \end{aligned} \quad (3.118)$$

for which  $\mu_x$  and  $\mu_y$  are the shear deformation parameters.

From the above equations it would seem that each of the bending, torsional and distortional actions is independent of the others and can be treated separately. However, strictly speaking this independence is valid only for a straight prismatic boxbeam with bi-symmetrical cross-sections (70). Apart from special cases such as curved boxbeams or multi-spined boxbeams, there is some interaction between bending, torsion and distortion.

The interaction between distortion and bending-torsion is really a difficult problem. Lie (70,71) tried to solve this problem, but his results were limited to a single-cell prismatic boxbeam only. Since the main advantage of the basic technique in this thesis is its simplicity, all modifications have been governed by the need to retain this simplicity and, consequently, the economy of the solution procedure. Considering this special requirement, a numerical iterative procedure, which has been suggested by Billington (11), is adopted here.

At first, we introduce the rotational angle of the top flange  $\psi_z$  and the rotational angle of the side web  $\phi_z$  (Fig. 3.25). The relationship between these two rotational angles and the twisting angle  $\theta_z$  and the distortional angle  $\gamma_d$  can be expressed approximately as

$$\theta_z = \frac{1}{2} (\phi_z + \psi_z), \quad \gamma_d = \psi_z - \phi_z \quad (3.119a)$$

or

$$\psi_z = \theta_z + \frac{1}{2} \gamma_d, \quad \phi_z = \theta_z - \frac{1}{2} \gamma_d \quad (3.119b)$$

From Eq. (3.119b) the distortional angle can be thought of as a rotation of the flange which is additive to the twisting angle. An increase in twist is equivalent to a decrease in torsional stiffness and the influence of distortion is to reduce the effective torsional rigidity of the

cross-section. Consequently, we may define the rotation  $\psi_{\bar{z}}$  as the effective twisting angle, and the torsional stiffness reduction factor is given by

$$\xi_d = \frac{\theta_{\bar{z}}}{\psi_{\bar{z}}} \quad (3.120)$$

Substituting Eq. 3.120 into Eqs. 3.118 and assuming that the torsional stiffness reduction factor is constant along the  $z$  axis, we have

$$\begin{aligned} - \frac{1}{\mu_x} E_1 I_{yy} \frac{\partial^4 u}{\partial z^4} &= P_x \\ - \frac{1}{\mu_y} E_1 I_{xx} \frac{\partial^4 v}{\partial z^4} &= P_y \\ - \frac{\xi_d}{\mu_t} E_1 J_I \frac{\partial^4 \psi_{\bar{z}}}{\partial z^4} + \xi_d G J_T \frac{\partial^2 \psi_{\bar{z}}}{\partial z^2} &= m_{\bar{z}, \text{ext}} \\ E_1 J_{II} \frac{\partial^4 \gamma_d}{\partial z^4} + k_d \gamma_d &= m_d \end{aligned} \quad (3.121)$$

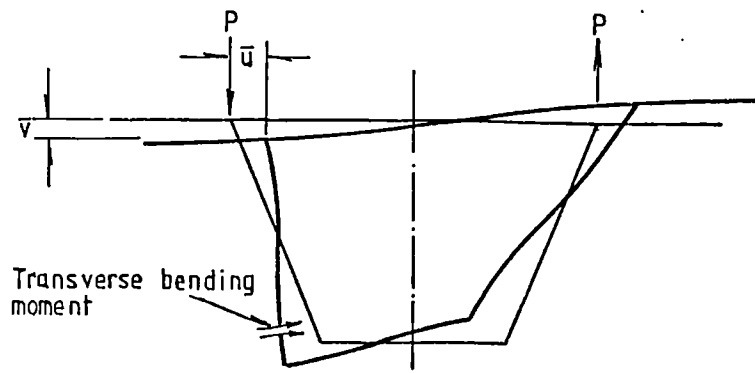
It is apparent that the third equation in this set of equations is identical in form to the original torsional governing differential equation, but uses reduced torsional rigidities instead of full torsional rigidities. This mathematical analogy provides the basis for an iterative process which leads to the modified solution considering the interaction between distortion and bending-torsion.

The compatibility condition considered is that the effective twisting angle should be equal to the sum of the half distortional angle ( $\frac{1}{2} \gamma_d$ ) and the actual twisting angle  $\theta_{\bar{z}}$  given by multiplying  $\psi_{\bar{z}}$  by the torsional stiffness reduction factor. The compatibility criterion can be expressed by the following equation

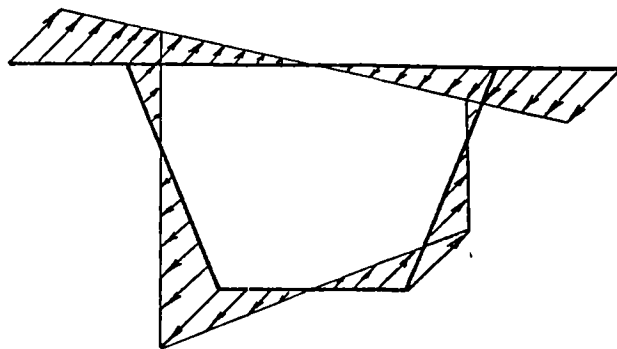
$$\psi_{\bar{z}, i+1} - \psi_{\bar{z}, i} = 0 \quad (3.122)$$

It is shown by numerical studies that the changes in torsional

stiffness are not sensitive to the magnitude of torsional moments. Thus in many cases no reduction is necessary in order to obtain accuracy sufficient for design, and that in such cases an overestimate is made for torsional moments and hence distortional stresses. In most cases two or three successive reductions of the torsional stiffness are sufficient to calculate the effects of distortion for the loading case considered.

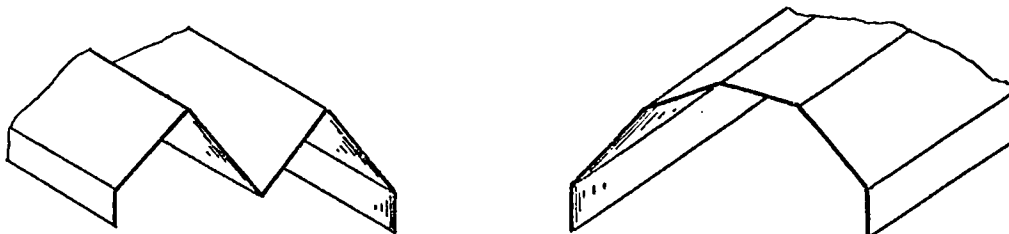


(a) Deformation of cross-section

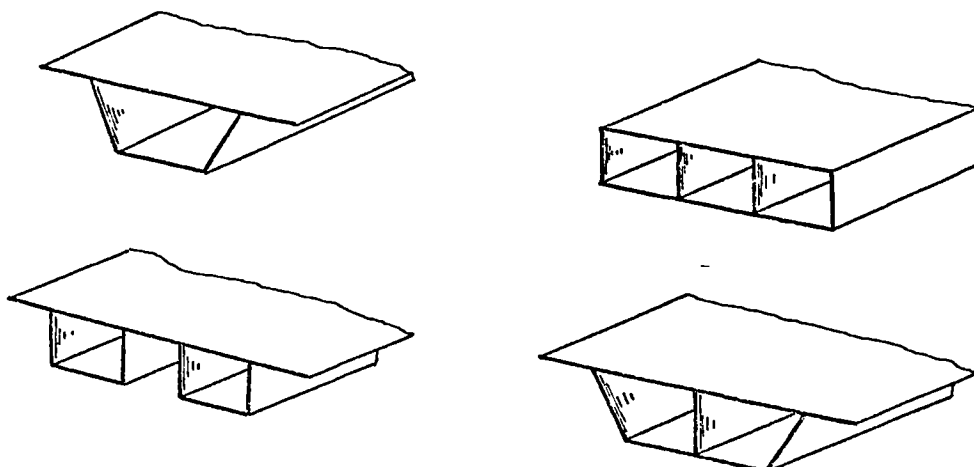


(b) Warping stress pattern

Fig. 3.1 Response of boxbeam of deformable cross-section to torsional load

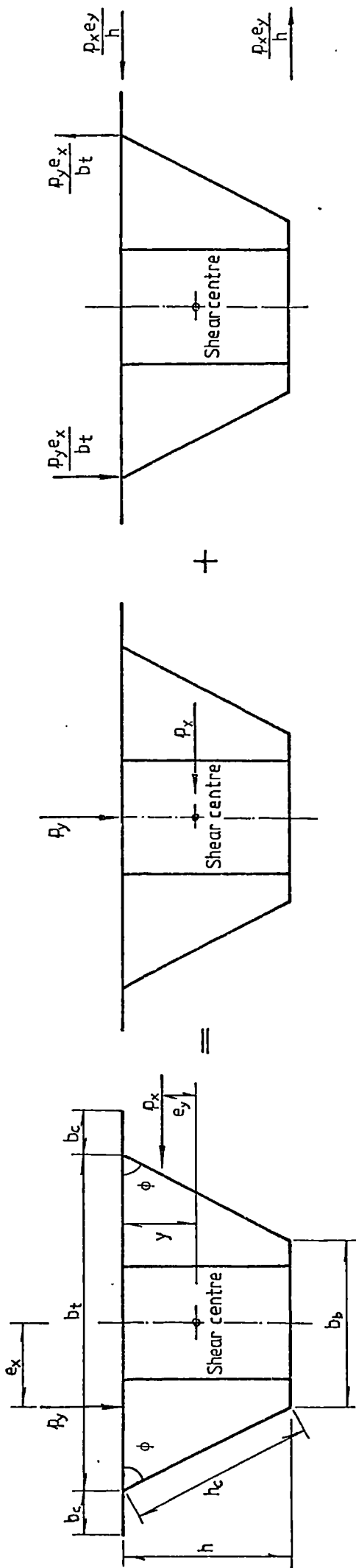


(a) Folded plates



(b) Box spine-beams

Fig. 3.2 Typical folded plate and boxbeam cross-sections

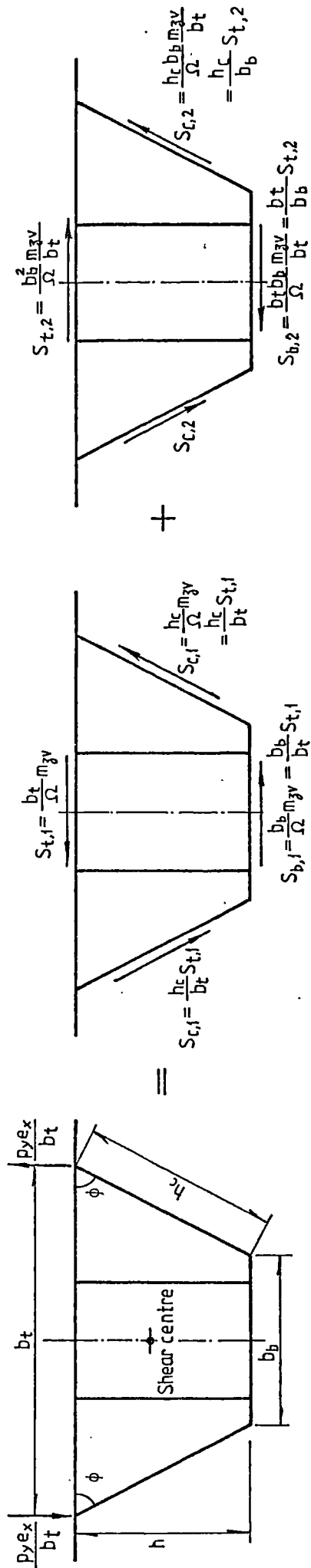


(a) Eccentric Loads

(b) Bending Loads

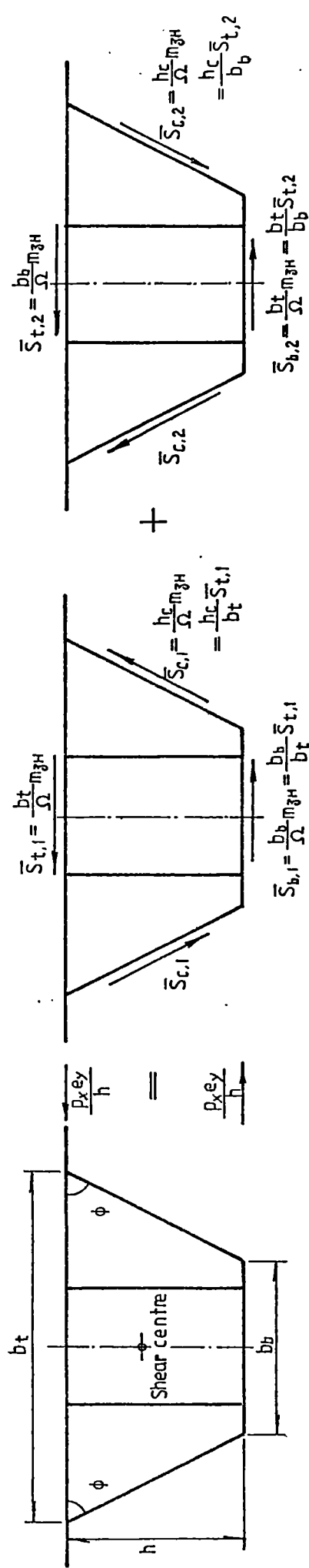
(c) Twisting Loads

Fig. 3.3 Bending and Twisting Components of Eccentric Loads



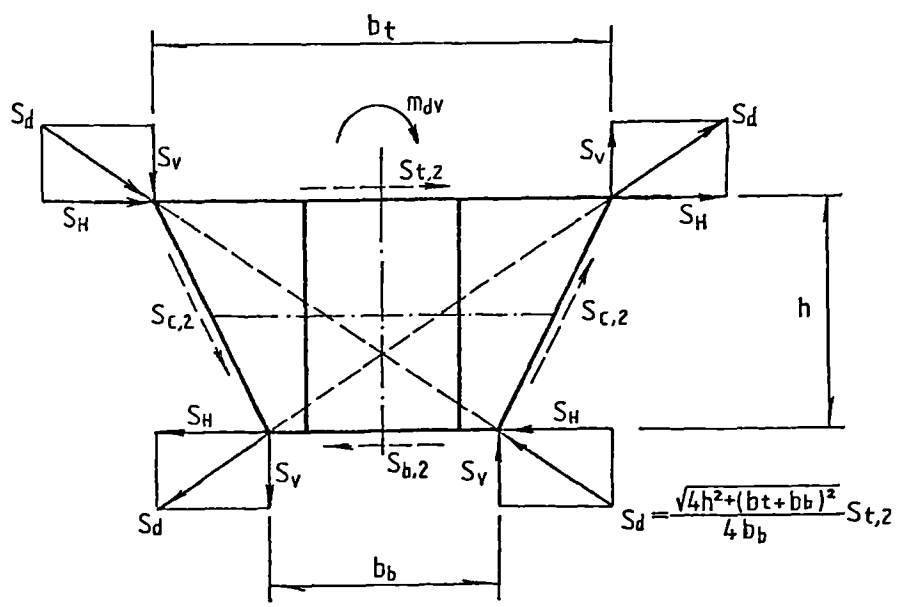
(a) Vertical antisymmetrical loading (b) Equivalent vertical torsional component (c) Vertical distortional component

Fig. 3.4 Components of vertical antisymmetrical loading

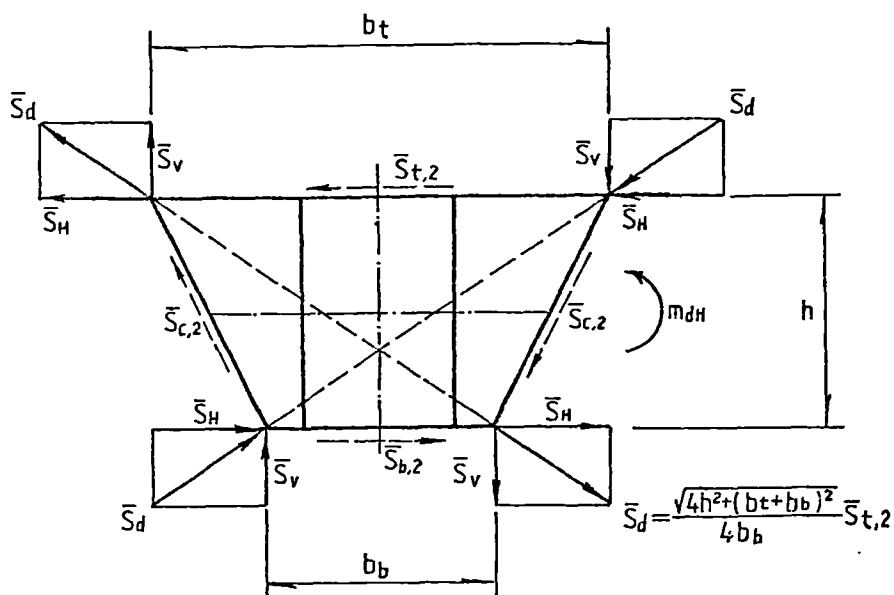


(a) Horizontal antisymmetrical loading (b) Equivalent horizontal torsional component (c) Horizontal distortional component

Fig. 3.5 Components of horizontal antisymmetrical loading

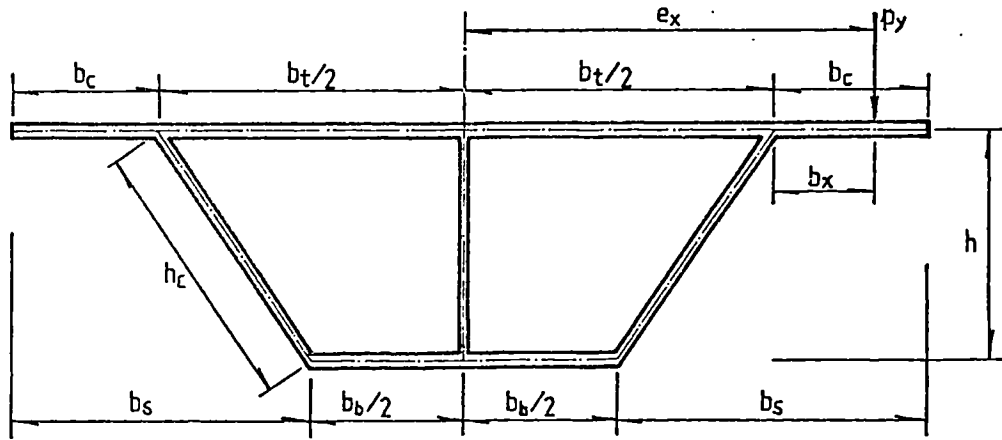


(a) Vertical distortional component resolved at box corners

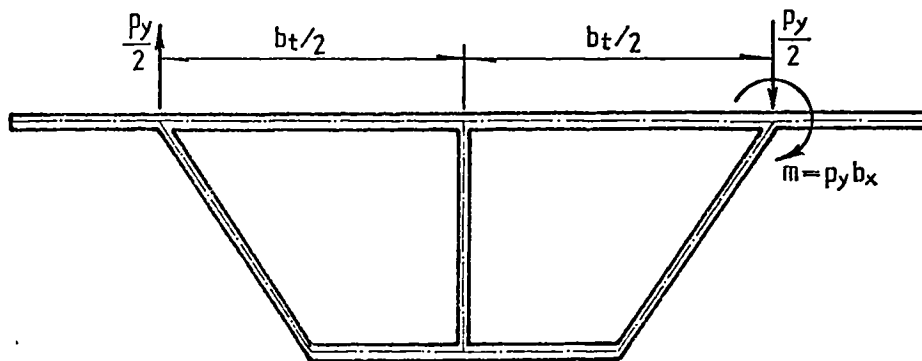


(b) Horizontal distortional component resolved at box corners

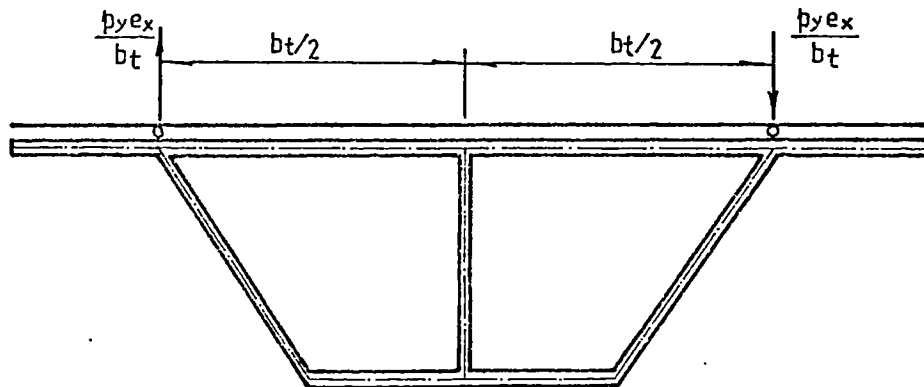
Fig. 3.6 Distortional component resolved at box corners



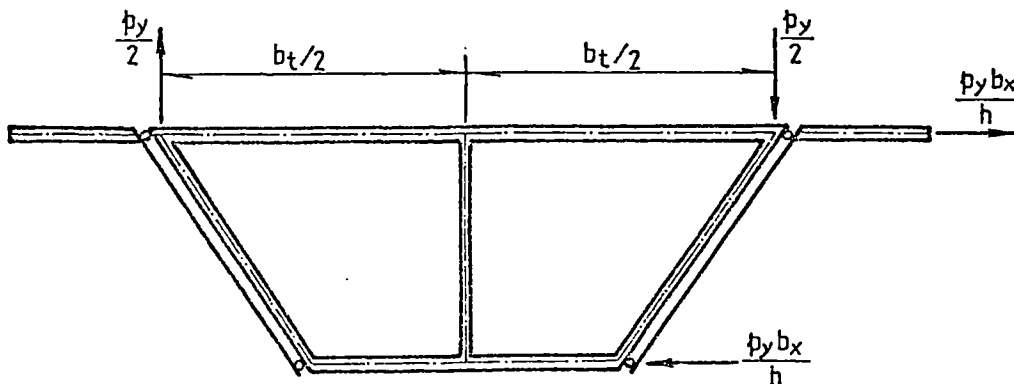
(a) Eccentric loading applied at the cantilever portion



(b) Equivalent twisting load

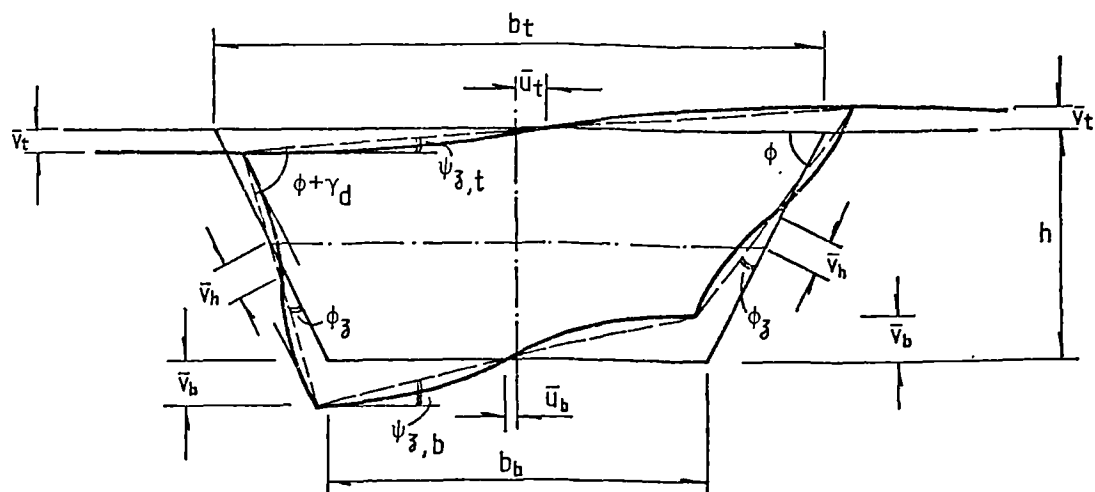


(c) Equivalent twisting load for thick flanges

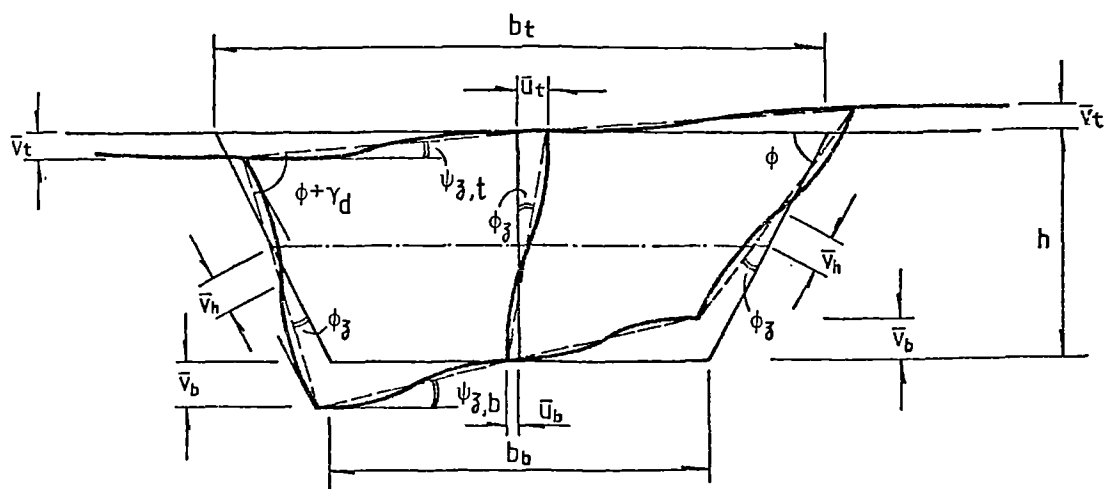


(d) Equivalent twisting load for thick webs

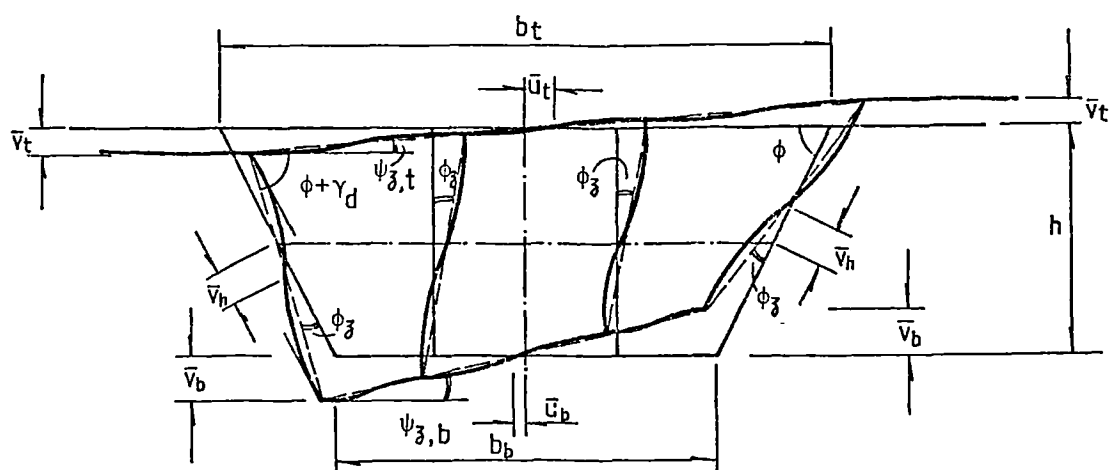
Fig. 3.7 Distortional force with load on cantilever



(a) Single-cell box

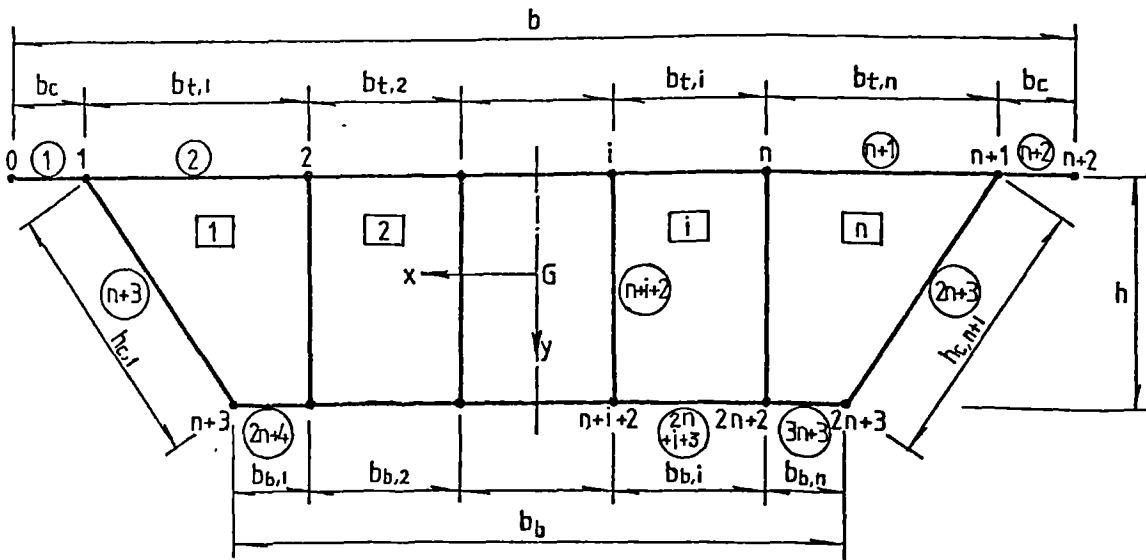


(b) Double-cell box

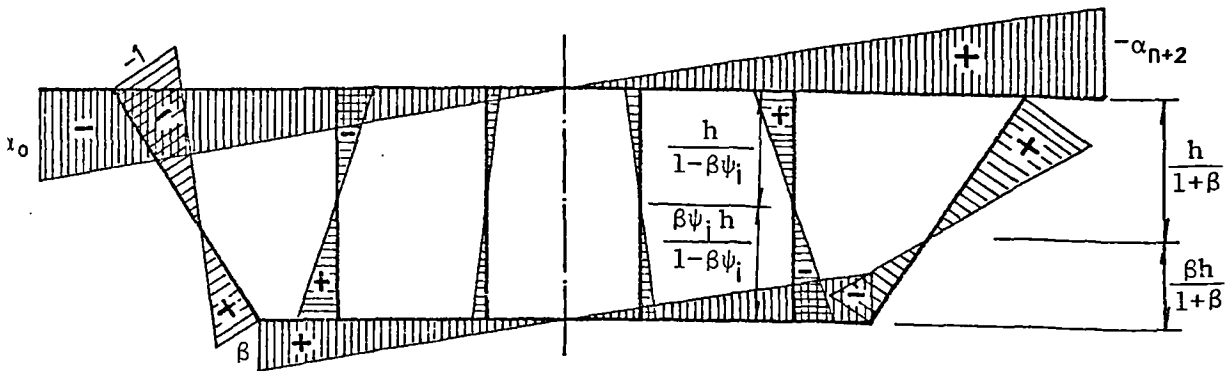


(c) Triple-cell box

Fig. 3.8 Deformation of uni-symmetrical box spine-beam



(a) Subdivision of cross-section



(b) Normalized unit warping  $\omega_{II}/|\omega_{II,1}|$

Fig. 3.9 Distribution of distortional warping stresses of a box beam with a vertical axis of symmetry

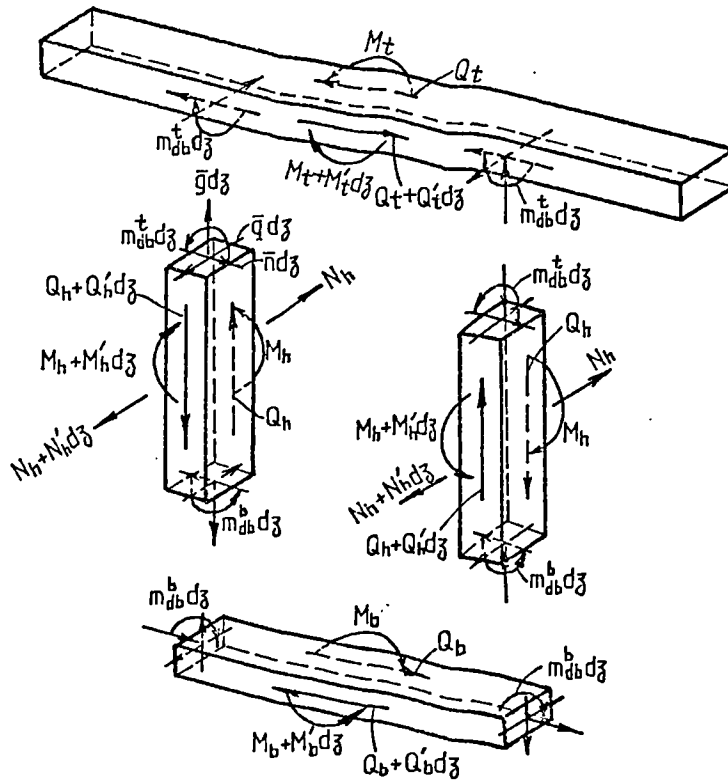


Fig. 3.10 Forces which work on elements of webs and flanges

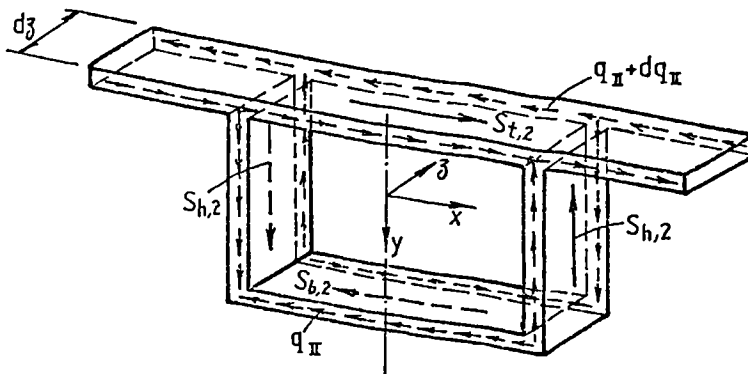
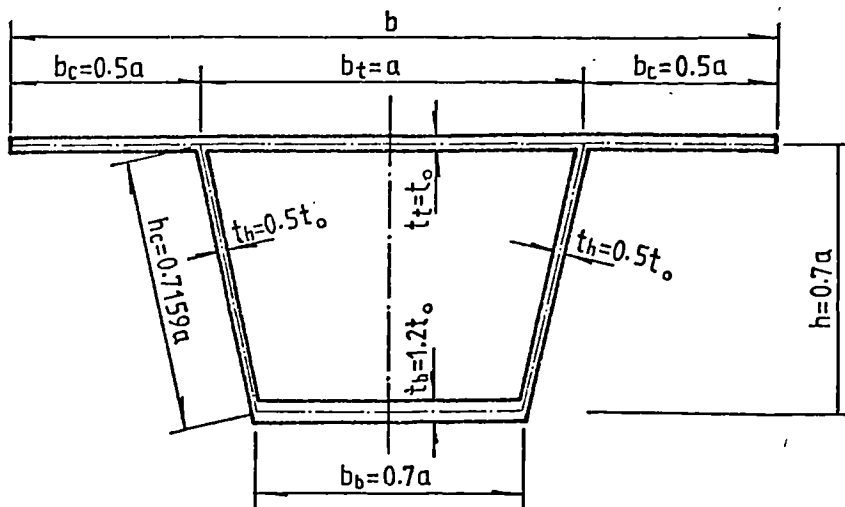
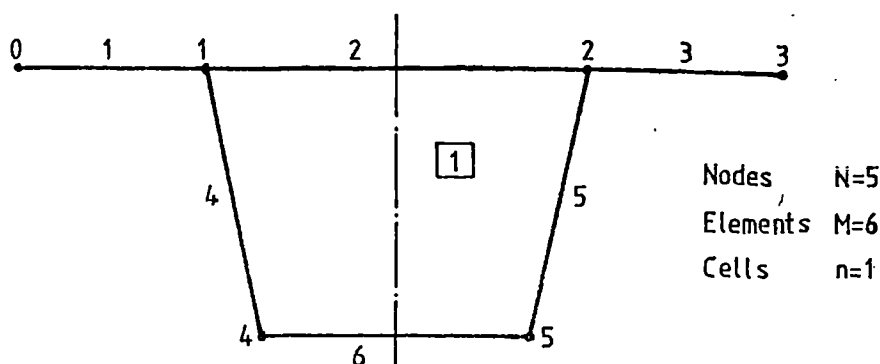


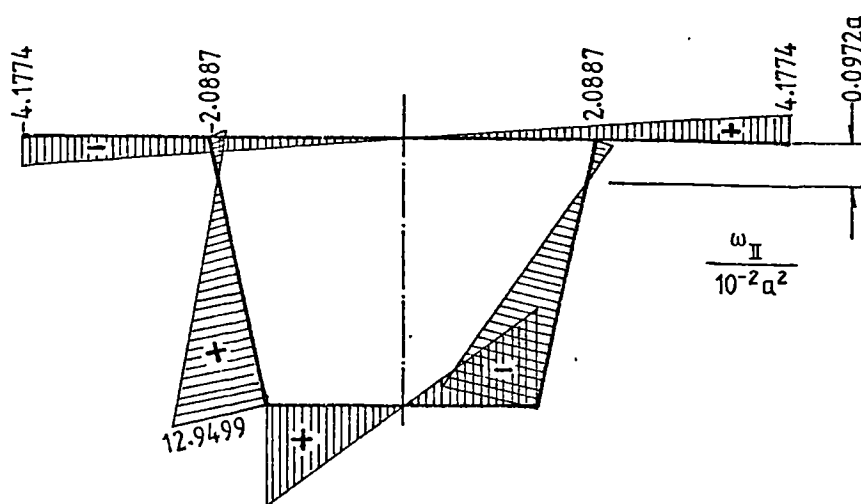
Fig. 3.13 Element of box beam with form of elementary frame



(a) Dimensions of cross-section

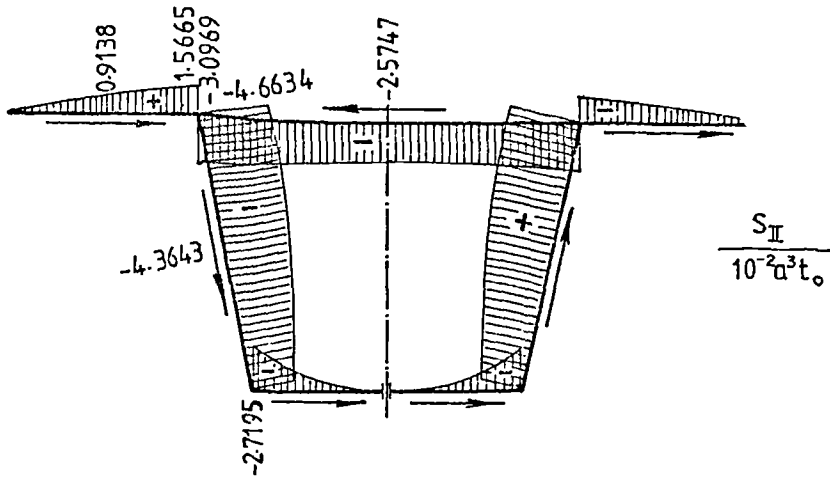


(b) Subdivision of the cross-section

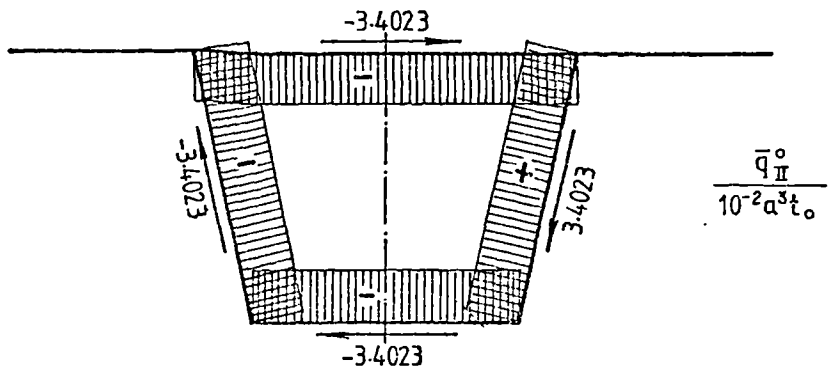


(c) Distribution of distortional warping function  $\omega_{II}/10^{-2}a^2$

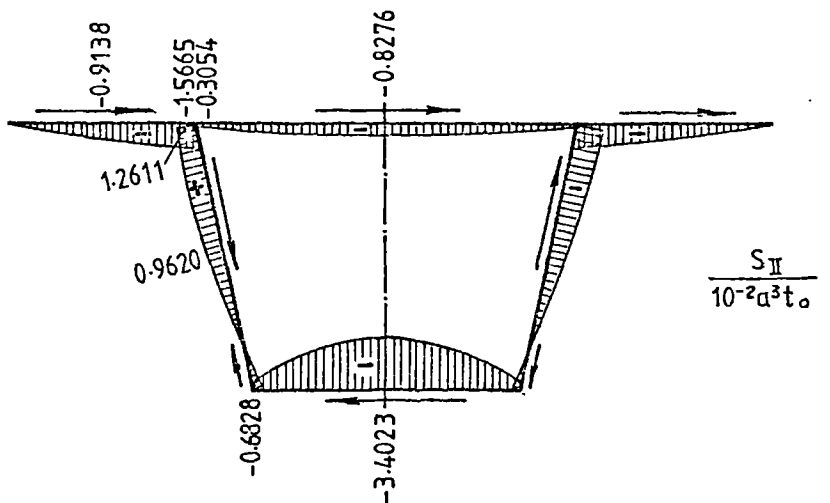
Fig. 3.11 Distribution of distortional warping stresses in a single-cell box beam



(d) Distribution of distortional statical moment of area  $S_{II}$

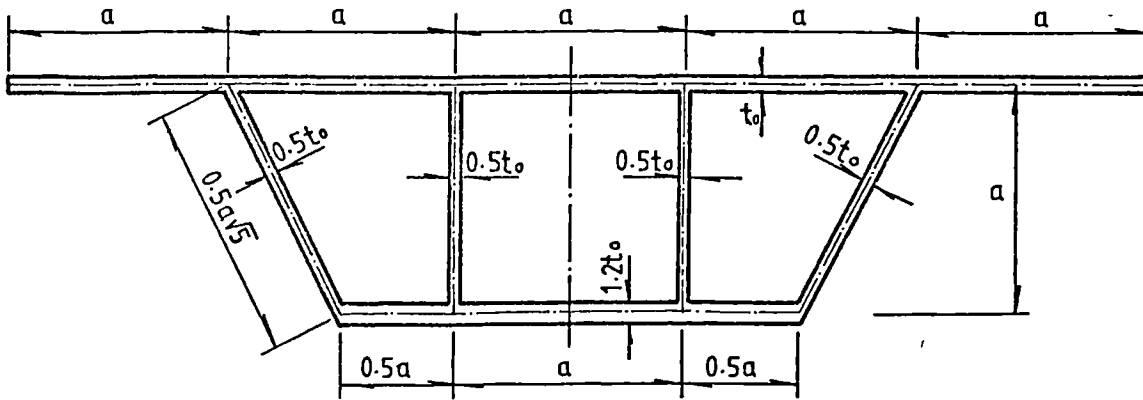


(e) Diagram of the unit distortional shear flow function  $\bar{q}_{II}^0$

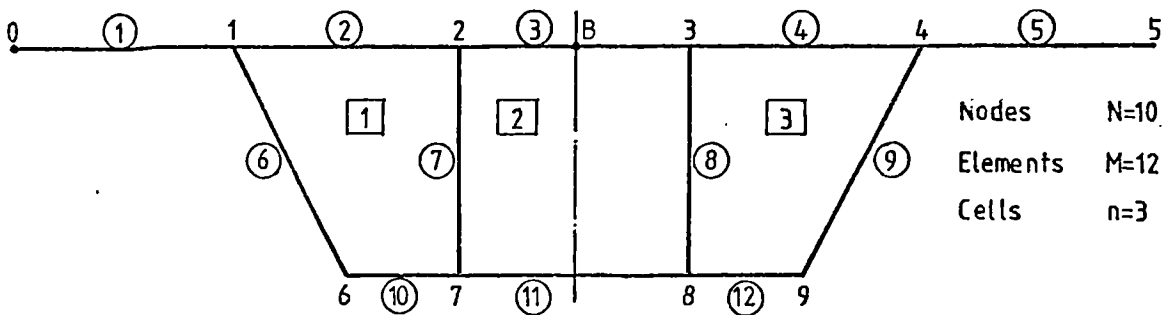


(f) Diagram of the reduced distortional statical moment of area  $\hat{S} = \bar{q}_{II}^0 - S_{II}$

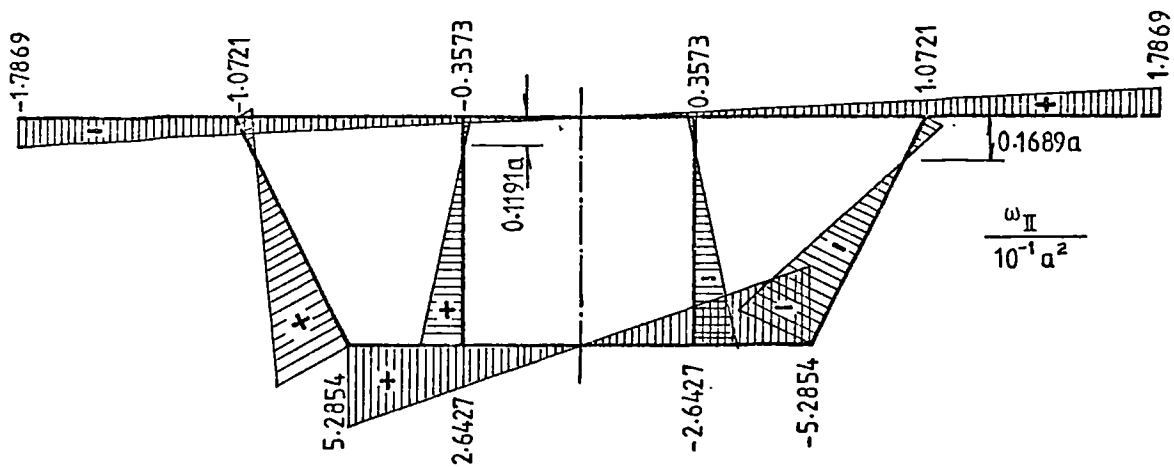
Fig. 3.11 Distribution of distortional warping stresses in a single-cell box beam



(a) Dimensions of cross-section

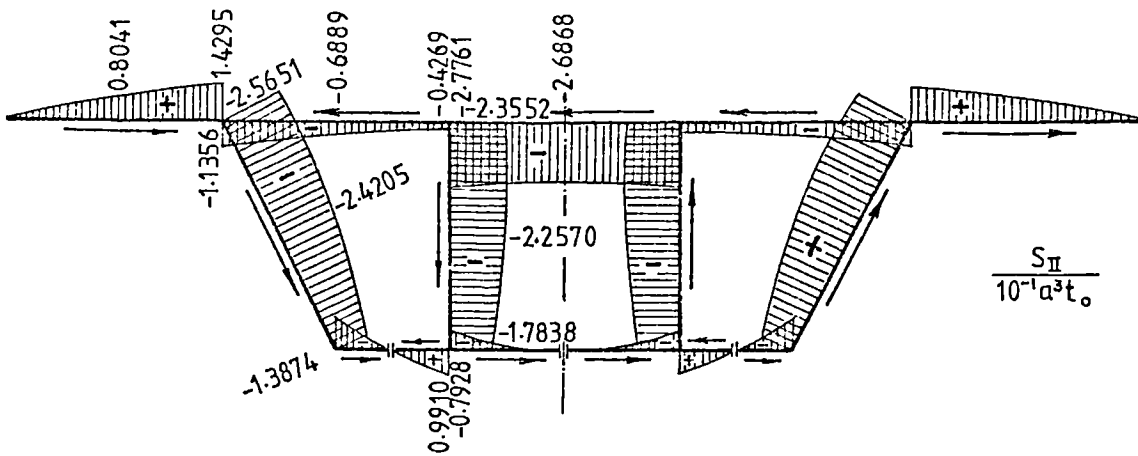


(b) Subdivision of the cross-section

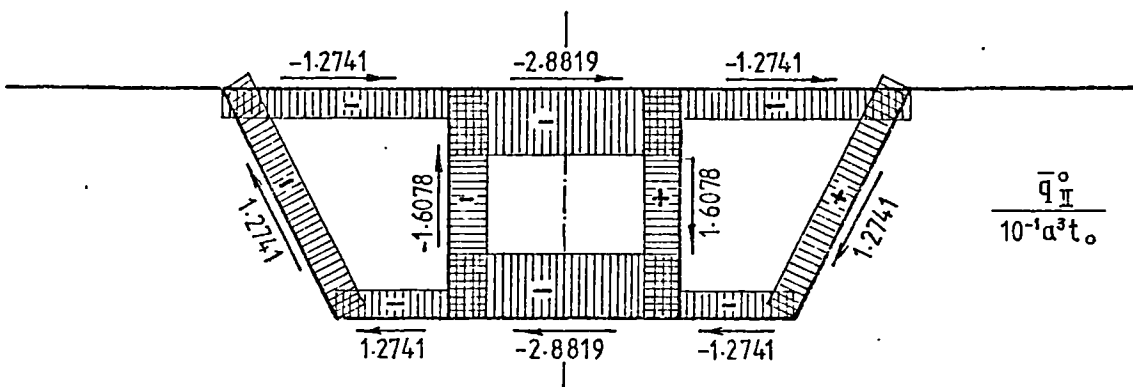


(c) Distribution of unit distortional warping function  $\omega_{II}$

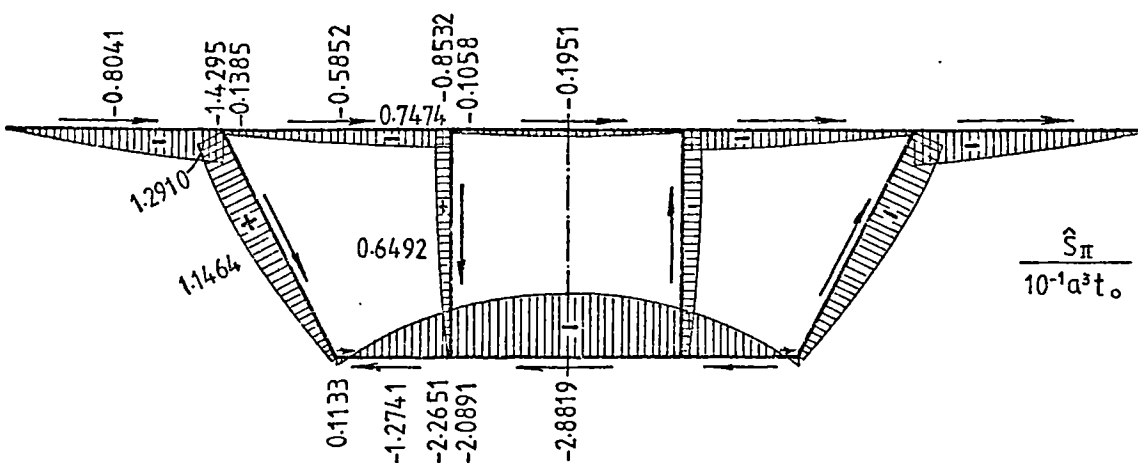
Fig. 3.12 Distribution of distortional warping stresses in a triple-cell box beam



(d) Distribution of distortional statical moment of area  $S$



(e) Diagram of the unit distortional shear flow function  $\bar{q}_{II}^0$



(f) Diagram of the reduced distortional statical moment of area

$$\hat{S}_{II} = \bar{q}_{II}^0 - S_{II}$$

Fig. 3.12 Distribution of distortional warping stresses in a triple-cell boxbeam

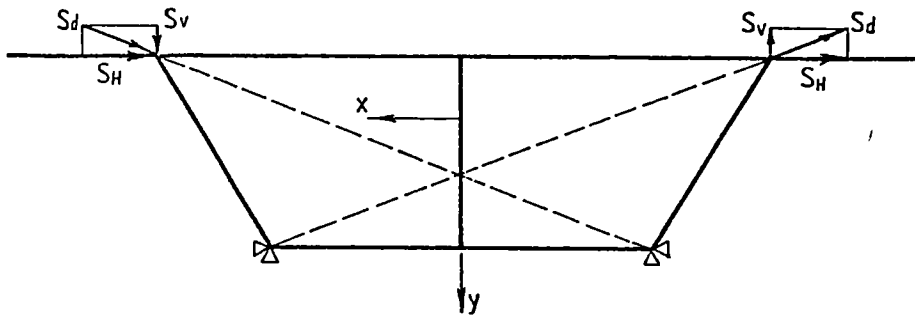


Fig. 3.14 Plane frame for assessing frame stiffness of unit length

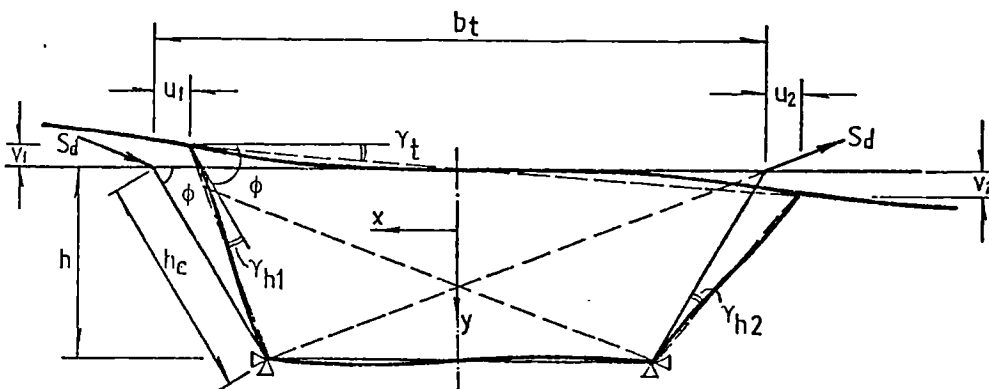


Fig. 3.15 Deformation of the plane frame

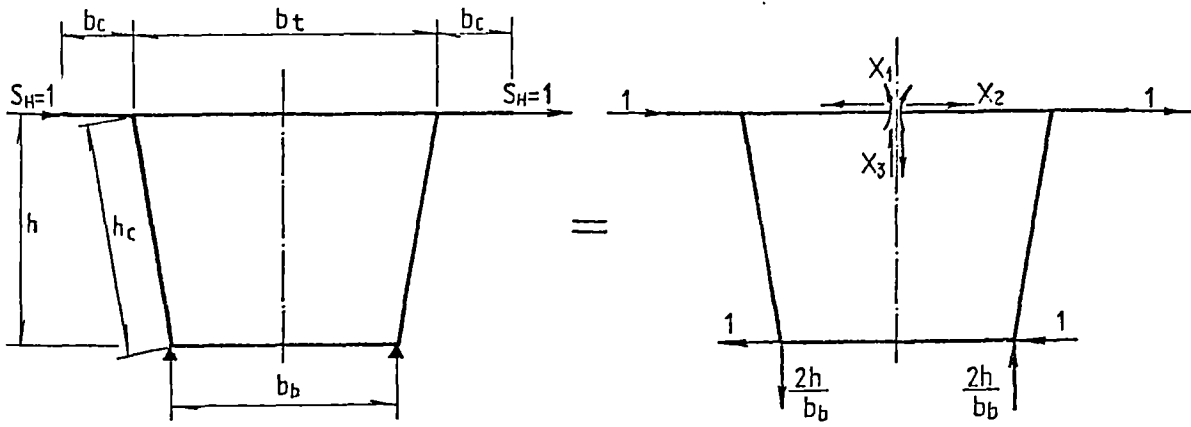
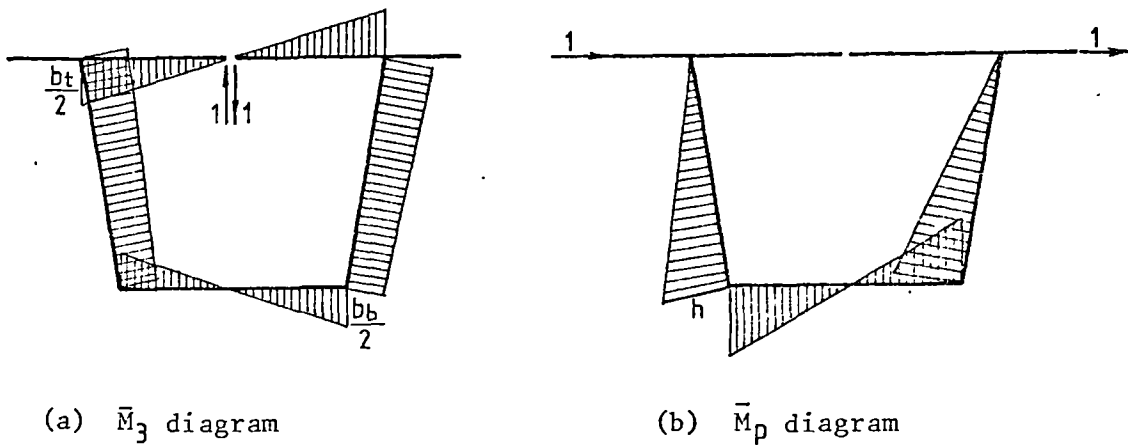


Fig. 3.16 Vierendeel frame of single-cell box



(a)  $\bar{M}_3$  diagram

(b)  $\bar{M}_p$  diagram

Fig. 3.17 Bending moment diagrams of released structure

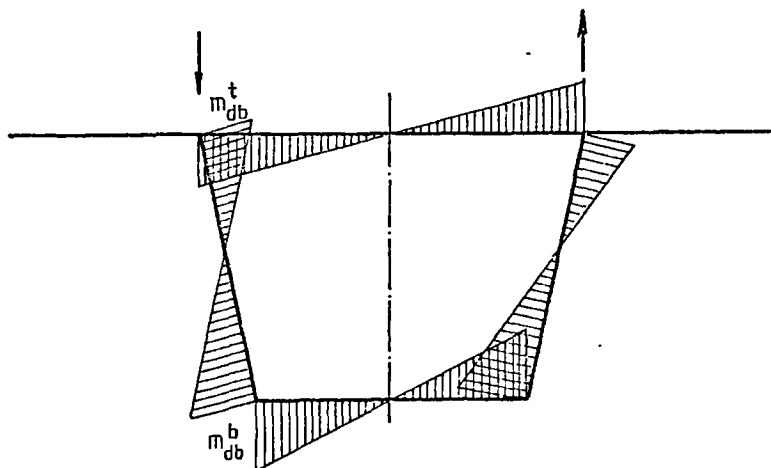
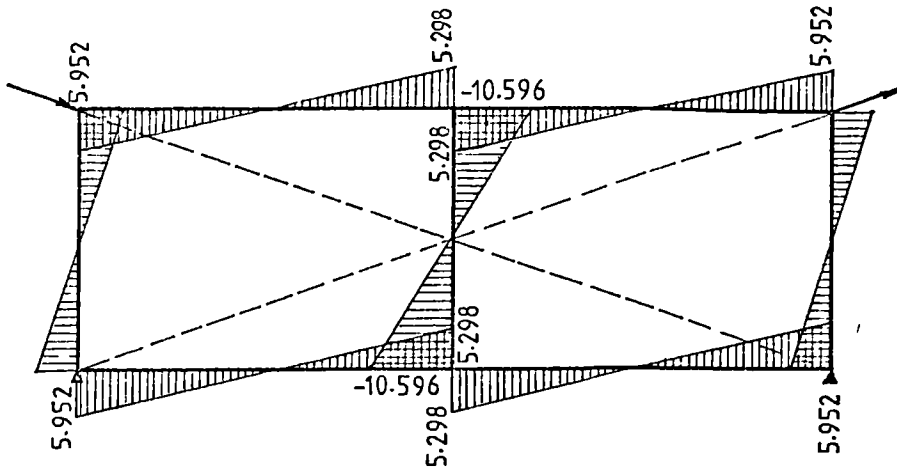
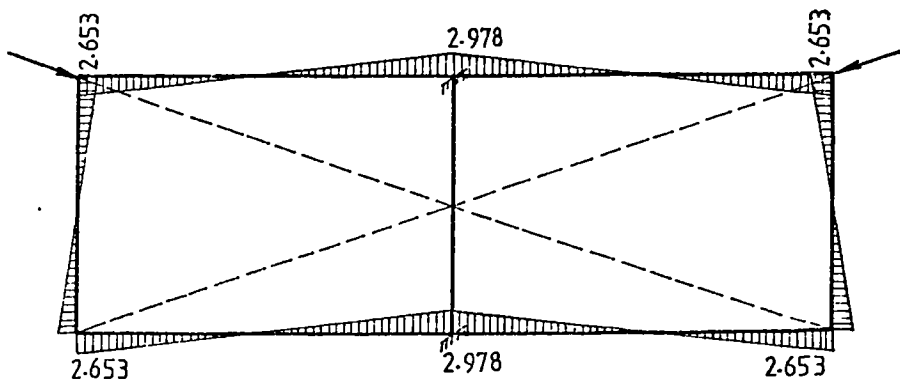


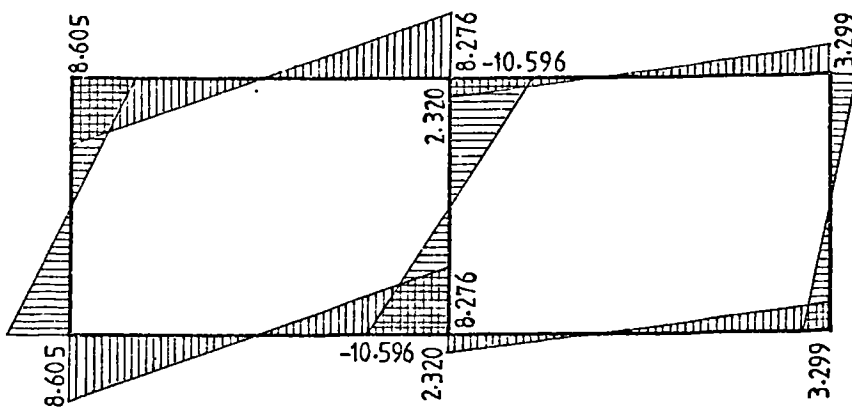
Fig. 3.18 Diagram of transverse distortional bending moments



(a) Influence values of transverse bending moments due to anti-symmetrical component

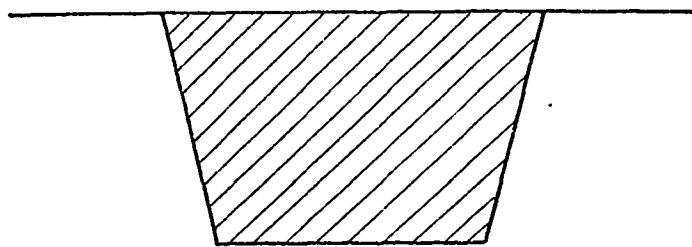


(b) Influence values of transverse bending moments due to symmetrical component

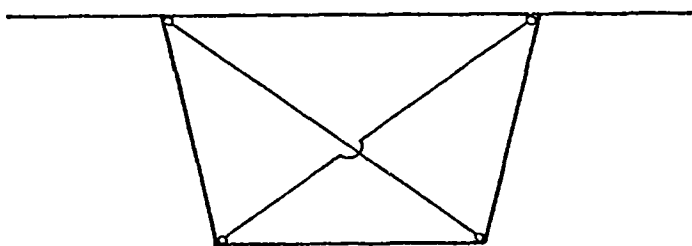


(c) Composition of the influence values

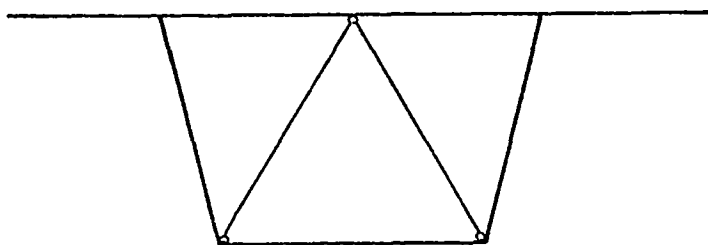
Fig. 3.19 Influence values of transverse bending moments in a double-cell box beam



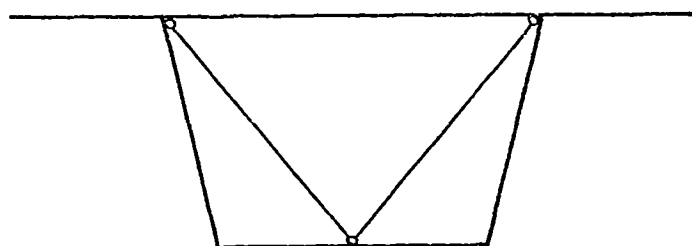
(a) Plate diaphragm



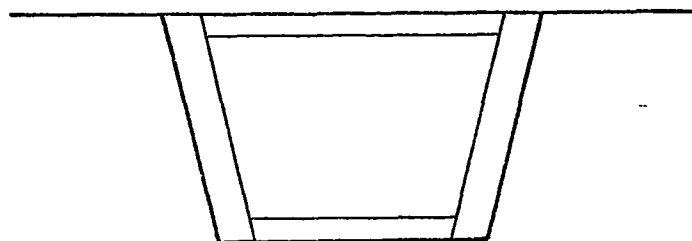
(b) Diagonal cross bracing



(c) Inverted V-type bracing



(d) V-type bracing



(e) Ring stiffening

Fig. 3.20 Different types of diaphragms

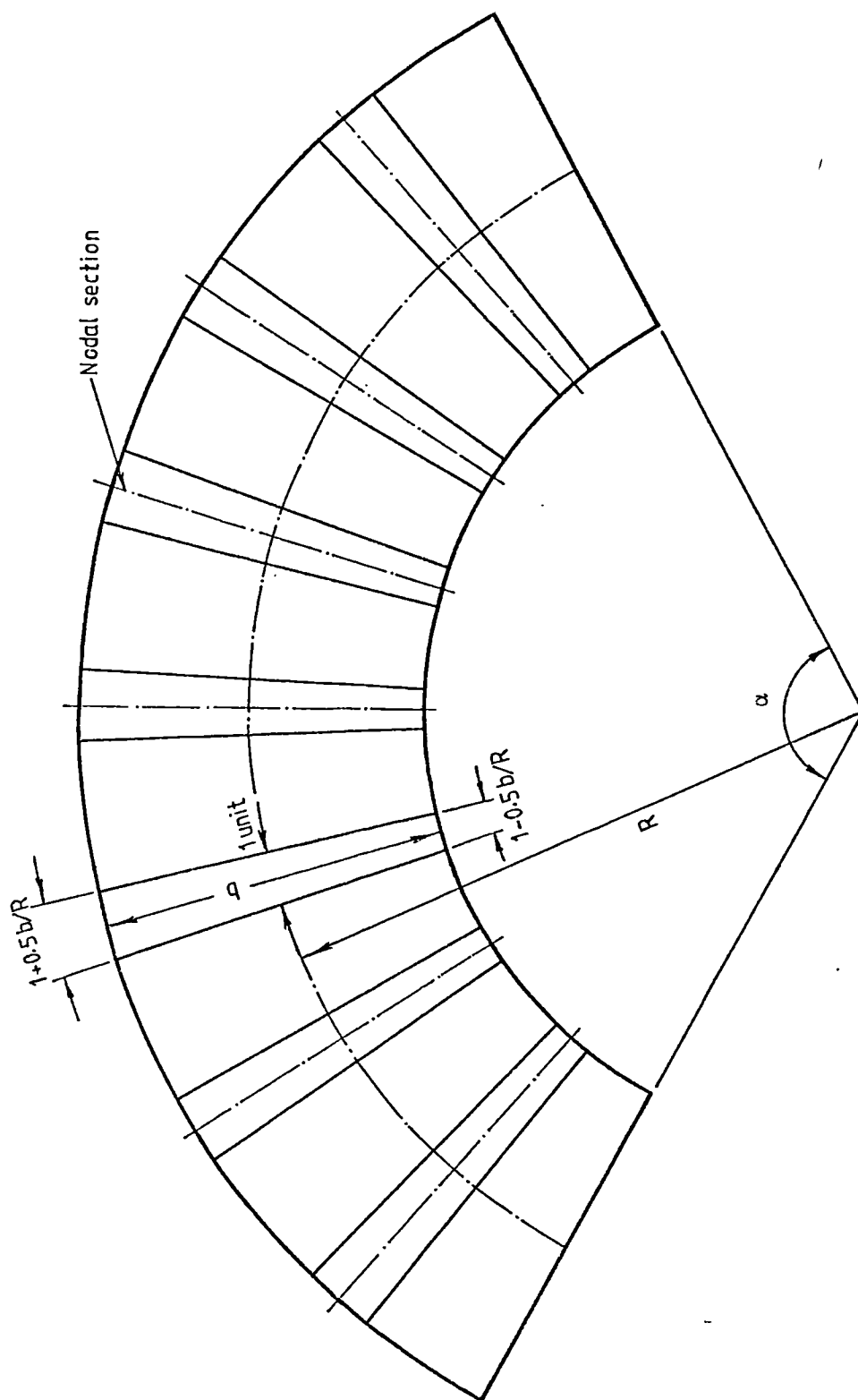


Fig. 3.21 Typical frame strips considered during transverse frame analysis

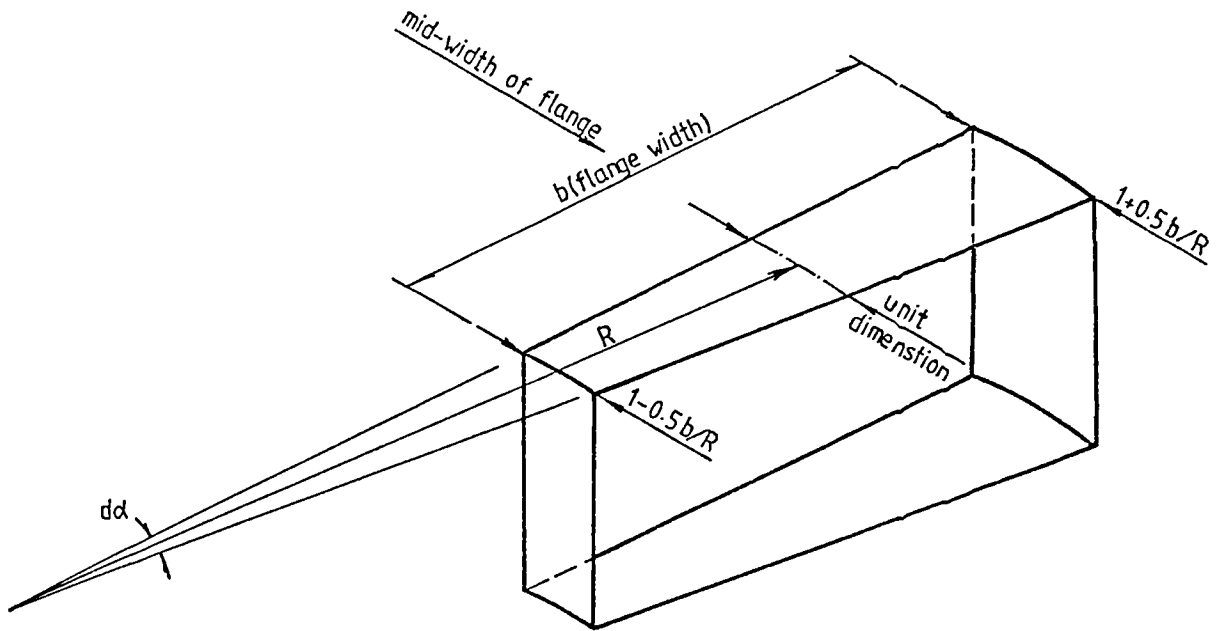


Fig. 3.22 Typical frame considered at a modal section in the transverse frame analysis

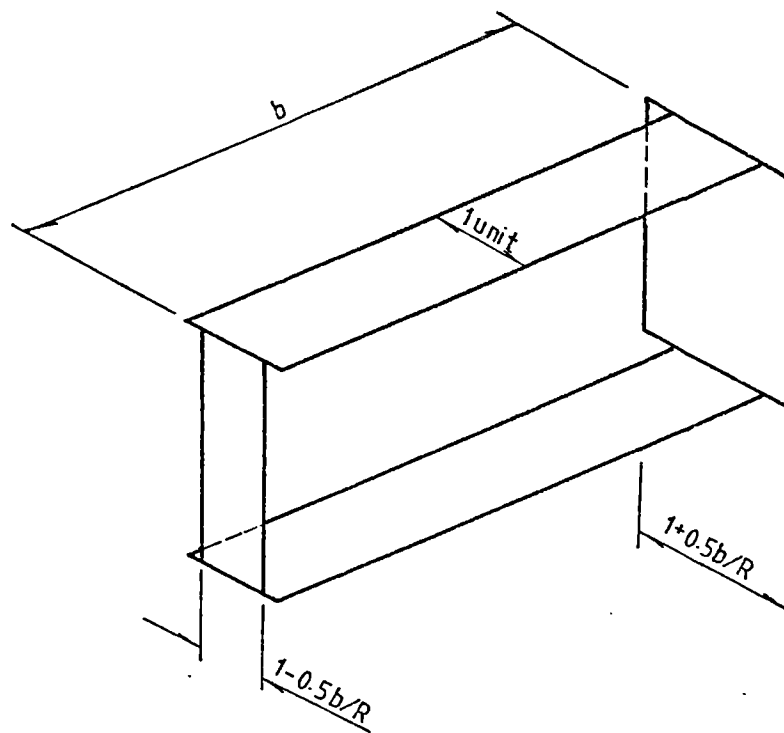


Fig. 3.23 Simplified equivalent transverse frame

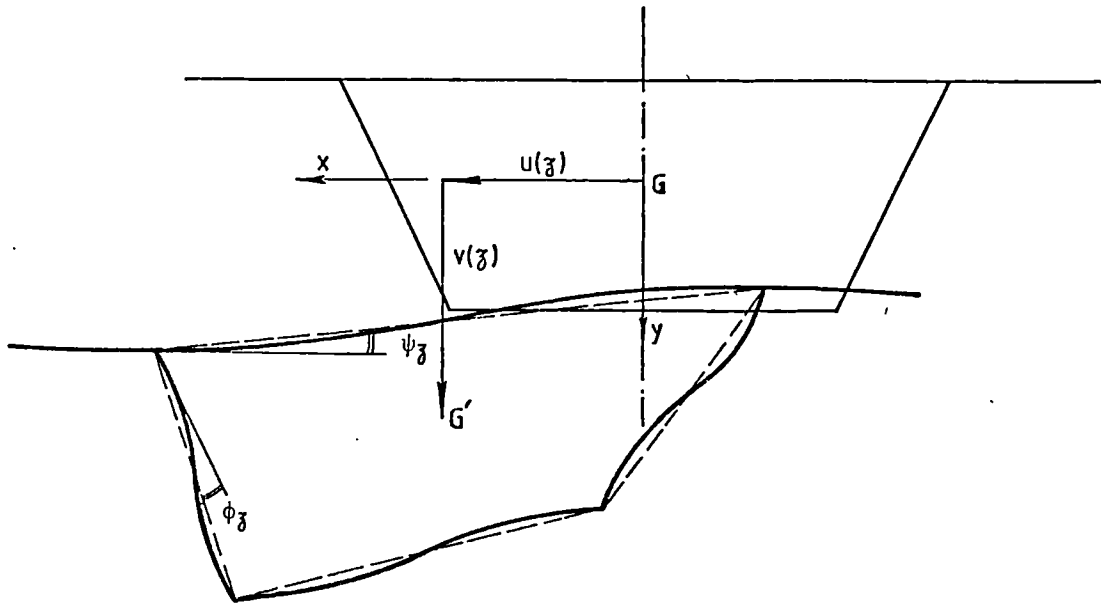


Fig. 3.25 Displacements in the cross-sectional plane

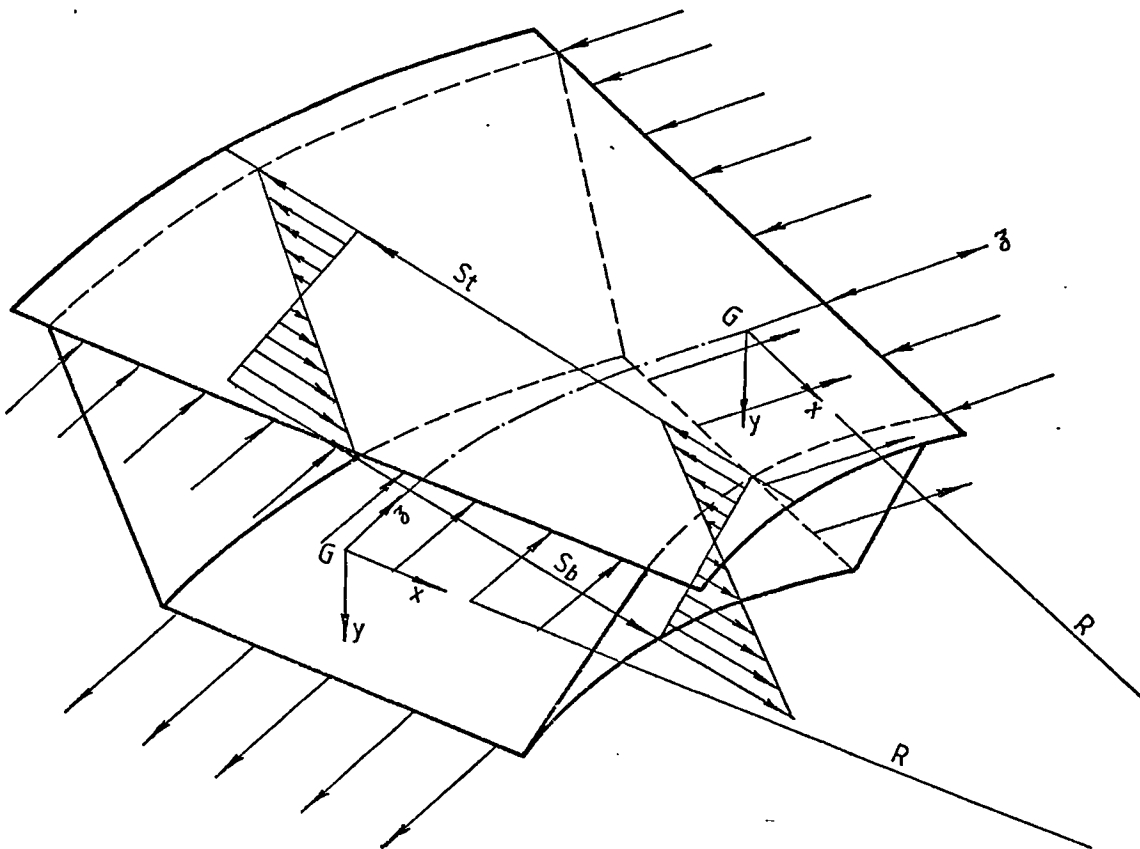


Fig. 3.24 Distortional forces due to bending moments in curved boxes

## CHAPTER 4

## A ONE DIMENSIONAL FINITE ELEMENT FAMILY

4.1 Introduction

Although a continuous structure is in reality three-dimensional, a reduced one-dimensional form has certain simplifying advantages in many instances. However, the conventional truss or beam type elements are oversimplified to represent box spine-beam bridges. Thus, associated structural effects such as warping and distortion should be included in the one-dimensional element formulation.

The main objective of this chapter is to present a family of special one-dimensional sub-parametric elements which may be used for global bridge deck analysis; especially for the preliminary elastic analysis of a variety of general box-type bridge decks, such as box spine-beams, multi-box girders and articulated bridge decks. The available elements included in the family can be specified as

- two-node truss elements;
- inclined cable elements with catenary action;
- two-node solid beam elements;
- three-node solid beam elements;
- thin-walled beam elements with rigid sections;
- thin-walled box beam elements with deformable sections.

The thin-walled box beam element can be regarded as a general beam element in this family. In addition to the usual six degrees of freedom at each node, represented by the three displacements and the three rotations, three more degrees of freedom have been incorporated in the formulation, to account for the warping and distortion effects which occur in box beams. The additional degrees of freedom are designated as the rate of twisting angle,

the distortional angle of the cross-section and the rate of the distortion. The element formulation is available for structures with variable cross-sections as well as with curved geometric shape.

Since all the other elements included in the family can be realized as a reduced form of the general box beam element, it seems convenient to include here only the procedure derived with respect to the thin-walled box beam element. The other elements can then be obtained from the general form.

It should be noted that the additional degrees of freedom for the general beam element cannot be transformed from one coordinate system to another. These types of elements can only be used in cases where the assembly of general beam elements forms a single continuous curvilinear or rectilinear lines. As a result the global treatment of the additional degrees of freedom can then correspond with the local system. It is apparent that this limitation can be complied with for most girder bridges.

A basis for constructing a finite element approximation is the principle of minimum potential energy, which involves a displacement field  $u$ . According to this principle the increment of the total potential energy due to any admissible displacements requires

$$\Delta\Pi = 0. \quad (4.1)$$

The total potential energy increment  $\Delta\Pi$  can be expressed as

$$\Delta\Pi = \int_V \Delta\varepsilon^T D \varepsilon \, dV - \int_V \Delta\varepsilon^T D \varepsilon_0 \, dV + \int_V \Delta\varepsilon^T \sigma_0 \, dV - \int_V \Delta u^T b \, dV - \int_A \Delta u^T S \, dA - \sum \Delta u^T P \quad (4.2)$$

where  $\varepsilon$  is the strain tensor,  $\varepsilon_0$  is the initial strain tensor,  $\sigma_0$  is the vector of initial residual stresses,  $D$  is the elasticity matrix,  $b$  is the vector of body forces,  $S$  is the vector of surface tractions,  $P$  is the vector of external concentrated forces,  $V$  is the volume and  $A$  is the surface area.

After some manipulation we can finally obtain the general form of the stiffness equation (80)

$$K\delta = F , \quad (4.3)$$

where  $K$  is defined as the stiffness matrix,  $\delta$  is the generalized nodal displacement vector and  $F$  is the vector of nodal forces.

The theory presented in this chapter is the basis for the development of the necessary programming for the linear elastic solution of bridge decks. The extension of the family to multi-box structures will be discussed in Chapter 6, and the non-linear behaviour of the cable elements arising from catenary action will be dealt with in Chapter 7. These analytical facilities will all be incorporated into the program CUBAS, developed in this thesis (see Appendix I).

## 4.2 Geometric definition

### 4.2.1 Geometric definition of a thin-walled box beam element

Consider a thin-walled box beam element with the variable cross-sections of Fig. 4.1. The external edges of the element may be curved, yet the sections of the element are generated by straight lines. The element sections are specified to have at least one axis of symmetry with respect to their widths, though this is not a necessary condition for the other type of elements in the family.

The locus of centroids of the cross-sections is defined as the element axis, and the cross-sections are assumed to be normal to this axis. Although for a thin-walled box beam element the element axis may be distinct from the flexural axis (line of shear centres), they are assumed to be parallel to each other. We should bear in mind that the torsional characteristics are actually related to the flexural axis of the element.

The element has two nodes located on the centroids of the end sections and an additional internal node located at the middle of the element axis. Two coordinate schemes are used in the element formulation: the Cartesian orthogonal coordinate system  $x, y, z$  and the natural coordinate system  $\xi, \eta, \zeta$ . The origin of the normalized coordinate system  $\xi, \eta, \zeta$  lies at the middle point of the element axis (Fig. 4.1). It is assumed that  $\zeta$  varies between  $-1$  and  $+1$  on the respective faces of the element. The geometry of the element axis is then defined as a mapped image of a parent straight element. The length  $l$  of the element is mapped to a length of 2 in the unit system.

#### 4.2.2 Definition of the local orthogonal coordinate system

The local coordinate system along the element axis is defined as follows (Fig. 4.2).

The origin of the coordinate system is located at the centroid of the cross-section, and the orientation of the local axes is assumed to coincide with the principal axes of the cross-section. The local  $z$  axis is tangential to the element axis running from node 1 towards node 2, and for straight elements it coincides with the element axis. The local  $y$  axis normally represents the axis of symmetry with respect to the width. The local  $x$  axis can then be specified as forming a right-handed orthogonal system.

A suitable method for describing the orientation of the local  $y$  axis is to give the global coordinates of two points that lie in one of the principal axes of the section. In most cases the mid-points of the bottom flanges are specified by the geometrical and environmental requirements. Thus it is convenient to define the global coordinates of the centroid  $G$  and the mid-point of the bottom flange  $P_0$  for specifying the orientation of the local  $y$  axis. A unit vector in the local  $y$  direction is given by the

vector difference of  $\vec{r}_p$  and  $\vec{r}_g$

$$\hat{y} = \frac{\vec{r}_p - \vec{r}_g}{\overline{GP}_o}, \quad (4.3a)$$

$$\text{or } \hat{y} = \cos(X.y) \cdot \hat{i} + \cos(Y.y) \cdot \hat{j} + \cos(Z.y) \cdot \hat{k}, \quad (4.3b)$$

where  $\hat{i}$ ,  $\hat{j}$  and  $\hat{k}$  are unit vectors in the global X, Y, Z directions respectively, and the direction cosines are given by

$$\cos(X.y) = \frac{X_p - X_g}{\sqrt{(X_p - X_g)^2 + (Y_p - Y_g)^2 + (Z_p - Z_g)^2}},$$

$$\cos(Y.y) = \frac{Y_p - Y_g}{\sqrt{(X_p - X_g)^2 + (Y_p - Y_g)^2 + (Z_p - Z_g)^2}}, \quad (4.4)$$

$$\cos(Z.y) = \frac{Z_p - Z_g}{\sqrt{(X_p - X_g)^2 + (Y_p - Y_g)^2 + (Z_p - Z_g)^2}}.$$

The vector in the z direction can be defined as

$$\vec{z} = \frac{\partial X}{\partial \zeta} \cdot \hat{i} + \frac{\partial Y}{\partial \zeta} \cdot \hat{j} + \frac{\partial Z}{\partial \zeta} \cdot \hat{k}. \quad (4.5)$$

From Eq. 4.5 a unit vector defined in the z direction is given by

$$\hat{z} = \frac{\vec{z}}{|\vec{z}|} = \frac{\frac{\partial X}{\partial \zeta} \hat{i} + \frac{\partial Y}{\partial \zeta} \hat{j} + \frac{\partial Z}{\partial \zeta} \hat{k}}{\sqrt{\left(\frac{\partial X}{\partial \zeta}\right)^2 + \left(\frac{\partial Y}{\partial \zeta}\right)^2 + \left(\frac{\partial Z}{\partial \zeta}\right)^2}} \quad (4.6)$$

The local  $\hat{x}$  is perpendicular to the local  $\hat{y}$  and  $\hat{z}$ , and forms a right handed system, thus

$$\hat{x} = \hat{y} \times \hat{z}, \quad (4.7a)$$

or

$$\hat{x} = \frac{[\cos(Y.y)\frac{\partial Z}{\partial \zeta} - \cos(Z.y)\frac{\partial Y}{\partial \zeta}]\hat{i} + [\cos(Z.y)\frac{\partial X}{\partial \zeta} - \cos(X.y)\frac{\partial Z}{\partial \zeta}]\hat{j} + [\cos(X.y)\frac{\partial Y}{\partial \zeta} - \cos(Y.y)\frac{\partial X}{\partial \zeta}]\hat{k}}{\sqrt{\left(\frac{\partial X}{\partial \zeta}\right)^2 + \left(\frac{\partial Y}{\partial \zeta}\right)^2 + \left(\frac{\partial Z}{\partial \zeta}\right)^2}} \quad (4.7b)$$

In most cases it is convenient for the analysis of bridge structures to fix the global Y axis as normal to the level plane, i.e., the XZ plane is parallel to the levelling base. The global Z axis normally orientates along the direction of the span. Three special orientations, which appear mostly in practical bridge constructions, should be mentioned here:

1. The principal planes yz of the element are parallel to the YZ plane.

In this case the local x axis is orientated following the global X axis, and we have

$$\hat{x} = \hat{i} \quad (4.8)$$

The unit vector along the local z axis is then given by

$$\hat{z} = \frac{\frac{\partial Y}{\partial \zeta} \hat{j} + \frac{\partial Z}{\partial \zeta} \hat{k}}{\sqrt{\left(\frac{\partial Y}{\partial \zeta}\right)^2 + \left(\frac{\partial Z}{\partial \zeta}\right)^2}} \quad (4.9)$$

The unit vector in the local y axis can be designated by the vector product

$$\begin{aligned} \hat{y} &= \hat{z} \times \hat{x} \\ &= \frac{\frac{\partial Y}{\partial \zeta} \hat{j} \times \hat{i} + \frac{\partial Z}{\partial \zeta} \hat{k} \times \hat{i}}{\sqrt{\left(\frac{\partial Y}{\partial \zeta}\right)^2 + \left(\frac{\partial Z}{\partial \zeta}\right)^2}} \end{aligned} \quad (4.10)$$

From the definition of the global axes it can be seen that

$$\begin{aligned} \hat{j} \times \hat{i} &= -\hat{k} , \\ \hat{k} \times \hat{i} &= \hat{j} . \end{aligned} \quad (4.11)$$

Substitution of Eq. 4.11 into Eq. 4.10 gives

$$\hat{y} = \frac{\frac{\partial Z}{\partial \zeta} \hat{j} - \frac{\partial Y}{\partial \zeta} \hat{k}}{\sqrt{\left(\frac{\partial Y}{\partial \zeta}\right)^2 + \left(\frac{\partial Z}{\partial \zeta}\right)^2}} \quad (4.12)$$

2. The principal planes xz of the element are parallel to the XZ plane.

The local y axis now orientates in the same direction as the global Y axis, which is defined as

$$\hat{y} = \hat{j} \quad (4.13)$$

The unit vector in the z direction is

$$\hat{z} = \frac{\frac{\partial X}{\partial \zeta} \hat{i} + \frac{\partial Z}{\partial \zeta} \hat{k}}{\sqrt{\left(\frac{\partial X}{\partial \zeta}\right)^2 + \left(\frac{\partial Z}{\partial \zeta}\right)^2}} \quad (4.14)$$

The unit vector in the local x axis is given by

$$\begin{aligned} \hat{x} &= -\hat{z} \times \hat{y} \\ &= \frac{\frac{\partial Z}{\partial \zeta} \hat{i} - \frac{\partial X}{\partial \zeta} \hat{k}}{\sqrt{\left(\frac{\partial X}{\partial \zeta}\right)^2 + \left(\frac{\partial Z}{\partial \zeta}\right)^2}} \end{aligned} \quad (4.15)$$

3. The principal planes yz of the element are parallel to the XY plane.

The local x axis is now defined as:

$$\hat{x} = \hat{k} \quad (4.16)$$

The unit vector in the local z direction is given by

$$\hat{z} = \frac{\frac{\partial X}{\partial \zeta} \hat{i} + \frac{\partial Y}{\partial \zeta} \hat{j}}{\sqrt{\left(\frac{\partial X}{\partial \zeta}\right)^2 + \left(\frac{\partial Y}{\partial \zeta}\right)^2}} \quad (4.17)$$

The unit vector in the local  $y$  axis can be obtained by the vector product

$$\begin{aligned}\hat{y} &= \hat{z} \times \hat{x} \\ &= \frac{\frac{\partial Y}{\partial \zeta} \hat{i} - \frac{\partial X}{\partial \zeta} \hat{j}}{\sqrt{\left(\frac{\partial X}{\partial \zeta}\right)^2 + \left(\frac{\partial Y}{\partial \zeta}\right)^2}}\end{aligned}\quad (4.18)$$

For these three special cases, after specifying the position of the centroid, there is then no need to define another reference point located at the middle of the bottom flange. This will certainly be advantageous for the analysis.

#### 4.3 Displacement field and degrees of freedom

##### 4.3.1 Displacement field due to axial loading and bending

The classical thin-beam theory based on the Bernoulli-Euler assumption, in which normals to the neutral axis before deformation remain straight and normal to the neutral axis after deformation, excludes any shear deformations. However, the transverse shear deformation may be important in cases of thick beams and beams of sandwich construction. Thus, it is preferable to develop an element formulation which can be used to analyse either thin beams or beams in which transverse shear deformation effects are not negligible.

In shear deformation, certain warping of the section occurs, and this effect is shown in Fig. 4.4. The modified plane assumption, which states that the cross-sections of the beam remain plane after deformation but not necessarily normal to the element axis, should now be adopted. Rotations  $\theta_x$  and  $\theta_y$  can thus be considered as average rotations and a correction will be made subsequently to allow for non-uniform shear distribution. In

Fig. 4.4 the angle  $\phi_x$  denotes the average shear deformation and for both the x and y directions.

$$\begin{Bmatrix} \theta_x \\ \theta_y \end{Bmatrix} = \begin{Bmatrix} \frac{\partial w_z}{\partial y} + \phi_x \\ -\frac{\partial w_z}{\partial x} + \phi_y \end{Bmatrix} \quad (4.19)$$

where  $\partial w/\partial y$  or  $\partial w/\partial x$  is the slope of the neutral axis and  $\phi$  is an extra rotation due to the transverse shear effects. For avoiding the difficulties which arise in satisfying the  $C_1$ - continuity requirement and having the ability to reproduce shear deformations, independent translations and rotations are used. The result is that only  $C_0$ - continuity is required of the shape functions.

As the strains in the direction normal to the beam axis are assumed to be negligible, and according with the plane assumption (Fig. 4.3) the displacement throughout the element can be uniquely defined by the three translations  $u, v, w$  on the beam axis and the two rotations  $\theta_x, \theta_y$  about the x and y axes respectively. This can be written in matrix form as

$$\mathbf{u}_t = \begin{Bmatrix} u_x \\ v_y \\ w_z \end{Bmatrix} = \begin{Bmatrix} u \\ v \\ w - x\theta_y + y\theta_x \end{Bmatrix} \quad (4.20)$$

#### 4.3.2 Displacement field due to warping torsion and distortion

Since the type of element to be considered is that in which the walls are thin, it is convenient to describe the state of torsional and distortional displacements using the generalized coordinate system  $(z, S)$ . The three displacement components of a point on the wall are shown as the

tangential displacement  $u_t$ , the normal displacement  $v_n$  and the axial displacement  $w_z$ . The displacements  $u_t$  and  $v_n$  are in the plane of the cross-section under consideration, and  $w_z$  is normal to the section. The positive direction of the tangential displacement component  $u_t$  is identical to the positive direction of the curvilinear coordinate  $S$ . The positive direction of the axial displacement component follows the positive direction of the  $z$  axis. The three displacement components  $u_t$ ,  $v_n$  and  $w_z$  comprise a right-handed orthogonal system which is shown in Fig. 4.5.

Following the warping torsion theory and the distortion theory described in the preceding chapters, the three displacement components can be related to the twisting angle and the distortional angle of the cross-section as

$$\begin{aligned} u_t &= R_t \theta_z + V_s(S) \gamma_d \\ v_n &= 0 \cdot \theta_z + V_n(S) \gamma_d \\ w_z &= -\hat{\omega}_I \frac{\partial \theta_z}{\partial z} - \omega_{II} \frac{\partial \gamma_d}{\partial z} \end{aligned}$$

or in matrix notation

$$\mathbf{u}_b = \begin{Bmatrix} u_t \\ v_n \\ w_z \end{Bmatrix} = \begin{bmatrix} R_t & 0 & V_s & 0 \\ 0 & 0 & V_n & 0 \\ 0 & -\hat{\omega}_I & 0 & -\omega_{II} \end{bmatrix} \begin{Bmatrix} \theta_z \\ \theta'_z \\ \gamma_d \\ \gamma'_d \end{Bmatrix} \quad (4.21)$$

where  $\theta_z$  is the angle of twist,  $\theta'_z$  is the rate of twist,  $\gamma_d$  is the distortional angle,  $\gamma'_d$  is the rate of distortion,  $R_t$  is the perpendicular distance from the shear centre to the tangent to the mid-line of the wall,  $V_s(S)$  is the distribution function of the tangential displacement in distortion,

$V_n(S)$  is the distribution function of the normal displacement in distortion,

$\hat{\omega}_I$  is the unit torsional warping function, and

$\omega_{II}$  is the unit distortional warping function.

#### 4.3.3 Degrees of freedom

We know that the displacement field of an element can be related to the relevant displacement parameters on the element axis. Thus, the generalized displacement field in the local coordinate system is expressed as (Fig. 4.6)

$$\{\bar{u}\} = [u \quad v \quad w \quad \theta_x \quad \theta_y \quad \theta_z \quad \varphi \quad \gamma_d \quad \psi_d]^T \quad (4.22)$$

where  $\varphi = \frac{\partial \theta_z}{\partial z}$  and  $\psi_d = \frac{\partial \gamma_d}{\partial z}$

The total number of unknown displacements of a free joint with respect to the global coordinate system, i.e. the degrees of freedom, amount to nine

$$\{\bar{\delta}\} = [U \quad V \quad W \quad \phi_x \quad \phi_y \quad \phi_z \quad \varphi \quad \gamma_d \quad \psi_d]^T \quad (4.23)$$

where  $U$ ,  $V$  and  $W$  are the translations along the global  $X$ ,  $Y$  and  $Z$  axes respectively, and  $\phi_x$ ,  $\phi_y$  and  $\phi_z$  are the rotations about the global  $X$ ,  $Y$  and  $Z$  axes respectively (Fig. 4.7). Hence, the total number of degrees of freedom for a thin-walled box beam element is twenty-seven, nine at each of the three nodes.

For a thin-walled beam element with a rigid cross-section the number of unknown displacements at a node are reduced to seven, and the total number of degrees of freedom of the element is twenty-one,

$$\{\bar{u}\} = [u \quad v \quad w \quad \theta_x \quad \theta_y \quad \theta_z \quad \varphi]^T \quad (4.24a)$$

$$\text{and } \{\bar{\delta}\} = [U \quad V \quad W \quad \Phi_x \quad \Phi_y \quad \Phi_z \quad \psi]^T \quad (4.24b)$$

For a solid beam, since we ignore the warping freedom and since deformation of the cross-section is not permitted according to the rigid section assumption, there are only six unknown displacements at each node:

$$\{\bar{u}\} = [u \quad v \quad w \quad \theta_x \quad \theta_y \quad \theta_z]^T \quad (4.25a)$$

$$\text{and } \{\bar{\delta}\} = [U \quad V \quad W \quad \Phi_x \quad \Phi_y \quad \Phi_z]^T \quad (4.25b)$$

The truss element is defined as a fairly slender element with frictionless pin joints. Only one unknown displacement exists at a node in the local system, whereas the movement of a free node in the global coordinate system is defined by three translations

$$\{\bar{u}\} = \{w\} \quad (4.26a)$$

$$\text{and } \{\bar{\delta}\} = [U \quad V \quad W]^T \quad (4.26b)$$

Thus, the total number of degrees of freedom for a truss element is six.

#### 4.4 Strain components and stress resultants

##### 4.4.1 Strains and stress resultants due to axial loading and bending

The strains in the case of bending at a point in the element domain can be expressed as

$$\epsilon_b = \begin{Bmatrix} \gamma_{x\bar{z}}^b \\ \gamma_{y\bar{z}}^b \\ \epsilon_{\bar{z},b} \end{Bmatrix} = \begin{Bmatrix} \frac{\partial w_{\bar{z}}}{\partial x} + \frac{\partial u_x}{\partial z} \\ \frac{\partial w_{\bar{z}}}{\partial y} + \frac{\partial v_y}{\partial z} \\ \frac{\partial w_{\bar{z}}}{\partial z} \end{Bmatrix} \quad (4.27)$$

where  $\gamma_{x\bar{z}}^b$ ,  $\gamma_{y\bar{z}}^b$  and  $\epsilon_{\bar{z},b}$  are the shear strains and axial strain respectively.

Substitution of Eq. 4.20 in Eq. 4.27 gives

$$\epsilon_b = \begin{Bmatrix} \gamma_{x\bar{z}}^b \\ \gamma_{y\bar{z}}^b \\ \epsilon_{\bar{z},b} \end{Bmatrix} = \begin{Bmatrix} -\theta_y + \frac{\partial u}{\partial z} \\ \theta_x + \frac{\partial v}{\partial z} \\ \frac{\partial w}{\partial z} - x \frac{\partial \theta_y}{\partial z} + y \frac{\partial \theta_x}{\partial z} \end{Bmatrix} \quad (4.28)$$

Eq. 4.28 can be written as

$$\epsilon_b = \begin{bmatrix} 1 & 0 & 0 & 0 & 0 \\ 0 & 1 & 0 & 0 & 0 \\ 0 & 0 & 1 & y & x \end{bmatrix} \bar{\epsilon}_b \quad (4.29)$$

where

$$\bar{\epsilon}_b = \begin{Bmatrix} -\theta_y + \frac{\partial u}{\partial z} \\ \theta_x + \frac{\partial v}{\partial z} \\ \frac{\partial w}{\partial z} \\ \frac{\partial \theta_x}{\partial z} \\ -\frac{\partial \theta_y}{\partial z} \end{Bmatrix} \quad (4.30)$$

Thus, Eq. 4.29 gives the strains at any point in terms of the displacement of a point on the element axis.

The corresponding stress components at a point in the element domain can be obtained in the linear-elastic case as

$$\begin{Bmatrix} \tau_{x\bar{z}}^b \\ \tau_{y\bar{z}}^b \\ \sigma_{\bar{z},b} \end{Bmatrix} = D_b \begin{Bmatrix} \gamma_{x\bar{z}}^b \\ \gamma_{y\bar{z}}^b \\ \epsilon_{\bar{z},b} \end{Bmatrix} \quad (4.31)$$

where the elasticity matrix is given by

$$D_b = \begin{bmatrix} G & 0 & 0 \\ 0 & G & 0 \\ 0 & 0 & E \end{bmatrix} \quad (4.32)$$

in which  $E_1 = \frac{E}{1-\nu^2}$  and  $G = \frac{E}{2(1+\nu)}$ .

Substituting Eq. 4.29 and Eq. 4.32 into the integral expansion of Eq. 4.2, we obtain

$$\int_V \Delta \epsilon_b^T D_b \epsilon_b dV = \int_{-l/2}^{+l/2} \Delta \epsilon_b^T \bar{\sigma}_b dz \quad (4.33)$$

$$\text{where } \bar{\sigma}_b = \bar{D}_b \bar{\epsilon}_b \quad (4.34)$$

and

$$\begin{aligned} \bar{D}_b &= \int_A \begin{bmatrix} 1 & 0 & 0 \\ 0 & 1 & 0 \\ 0 & 0 & 1 \\ 0 & 0 & y \\ 0 & 0 & x \end{bmatrix} \begin{bmatrix} G & 0 & 0 \\ 0 & G & 0 \\ 0 & 0 & E_1 \end{bmatrix} \begin{bmatrix} 1 & 0 & 0 & 0 & 0 \\ 0 & 1 & 0 & 0 & 0 \\ 0 & 0 & 1 & y & x \end{bmatrix} dA \\ &= \int_A \begin{bmatrix} G & 0 & 0 & 0 & 0 \\ 0 & G & 0 & 0 & 0 \\ 0 & 0 & E_1 & E_1 y & E_1 x \\ 0 & 0 & E_1 y & E_1 y^2 & E_1 xy \\ 0 & 0 & E_1 x & E_1 xy & E_1 x^2 \end{bmatrix} dA \quad (4.35) \end{aligned}$$

Integrating over the region A and since the x and y axes are the principal axes of the cross-section, this gives

$$\int_A E_1 x dA = 0, \quad \int_A E_1 y dA = 0, \quad \int E_1 xy dA = 0, \quad I_{xx} = \int_A y^2 dA$$

and  $I_{yy} = \int_A x^2 dA$ . Hence we obtain

$$\bar{D}_b = \begin{bmatrix} GA & 0 & 0 & 0 & 0 \\ 0 & GA & 0 & 0 & 0 \\ 0 & 0 & E_1 A & 0 & 0 \\ 0 & 0 & 0 & E_1 I_{xx} & 0 \\ 0 & 0 & 0 & 0 & E_1 I_{yy} \end{bmatrix} \quad (4.36a)$$

where  $A$  is the cross-sectional area and  $I_{xx}$ ,  $I_{yy}$  are the moments of inertia with respect to the  $x$  and  $y$  axes respectively.

In order to account more accurately for the shear strain energy due to non-uniform shear distribution, an effective shear cross-sectional area should be introduced (100). Thus, Eq. 4.36(a) can be further developed in the form

$$\bar{D}_b = \begin{bmatrix} GA_{sx} & 0 & 0 & 0 & 0 \\ 0 & GA_{sy} & 0 & 0 & 0 \\ 0 & 0 & E_1 A & 0 & 0 \\ 0 & 0 & 0 & E_1 I_{xx} & 0 \\ 0 & 0 & 0 & 0 & E_1 I_{yy} \end{bmatrix} \quad (4.36b)$$

where  $A_{sx}$  and  $A_{sy}$  represent the beam effective shear cross-sectional areas in the  $x$ -direction and the  $y$ -direction respectively.

The effective shear areas can be expressed as

$$A_{sx} = \frac{1}{F_{s,x}} \cdot A$$

and

$$A_{sy} = \frac{1}{F_{s,y}} \cdot A$$

where  $F_s$  is defined as the shear-deformation factor, which depends on the form of the cross-section (107). For a rectangular section,  $F_s = \frac{6}{5}$ , for a solid circular section,  $F_s = \frac{10}{9}$ , for a thin-walled hollow circular section,

$F_s = 2$ , and for an I or box section having flanges and webs of uniform thickness,

$$F_s = \left[ 1 + \frac{3(D_2^2 - D_1^2)D_1}{2D_2^3} \left( \frac{t_2}{t_1} - 1 \right) \right] \frac{4D_2^2}{10r^2} \quad (4.38)$$

where  $D_1$  = distance from neutral axis to the nearest surface of the flange,

$D_2$  = distance from neutral axis to extreme fiber,

$t_1$  = thickness of web (or webs in box beams)

$t_2$  = width of flange

$r$  = radius of gyration of section with respect to the neutral axis.

If the I or box beam has flanges of nonuniform thickness, it may be replaced by an "equivalent" section whose flanges, having uniform thickness, have the same width and area as those of the actual sections. Approximate results may be obtained for I or box beams taking the effective shear area as the cross-sectional area of the web plates only (30).

The stress vector  $\bar{\sigma}_b$  represents the conventional stress resultants for a beam, i.e., shear forces, axial force and bending moments (Fig. 4.6)

$$\bar{\sigma}_b = [Q_x \quad Q_y \quad N_z \quad M_x \quad M_y]^T \quad (4.39)$$

The generalized strain vector  $\bar{\epsilon}_b$  represents the shear strains, the axial strain and the curvatures.

#### 4.4.2 Strains and stress resultants due to warping torsion

From the specification of the displacement field described in 4.3.2, the strains due to torsion at a point in the element domain can be expressed as (see also Chapter 2):

$$\epsilon_t = \begin{Bmatrix} \gamma_{\beta s}^t \\ \epsilon_{\beta, t} \end{Bmatrix} = \begin{Bmatrix} \phi_I \frac{\partial \theta_\beta}{\partial z} \\ -\hat{\omega}_I \frac{\partial^2 \theta_\beta}{\partial z^2} \end{Bmatrix} \quad (4.40)$$

Eq. 4.40 can be written as

$$\epsilon_t = \begin{bmatrix} \phi_I & 0 \\ 0 & \hat{\omega}_I \end{bmatrix} \bar{\epsilon}_t \quad (4.41)$$

where the generalized strain vector due to torsion is

$$\bar{\epsilon}_t = \begin{Bmatrix} \frac{\partial \theta_3}{\partial z} \\ -\frac{\partial^2 \theta_3}{\partial z^2} \end{Bmatrix} \quad (4.42)$$

For the present we may neglect the strain energy due to the secondary shear stresses associated with the normal warping stresses, and we consider only the primary torsional shear strain. We can see later that a warping shear parameter might be used for considering approximately the effects of secondary shear stresses. Thus, the function  $\phi_I$  may be given as

$$\phi_I = \begin{cases} 2y_n & \text{for the St. Venant part of the shear strain} \\ \frac{\bar{q}_B}{t} & \text{for the Bredt part of the shear strain} \end{cases} \quad (4.43)$$

where  $y_n$  is the normal coordinate to the mid-line of the wall,

$\bar{q}_B$  is the unit Bredt shear flow function,

$t$  is the thickness of the wall.

The corresponding stress components are given by

$$\sigma_t = \begin{Bmatrix} \tau_{3s}^t \\ \sigma_{3,t} \end{Bmatrix} = D_t \begin{Bmatrix} \gamma_{3s}^t \\ \epsilon_{3,t} \end{Bmatrix} \quad (4.44)$$

where the elasticity matrix

$$D_t = \begin{bmatrix} G & 0 \\ 0 & E_1 \end{bmatrix} \quad (4.45)$$

Substitution of Eq. 4.41 and Eq. 4.45 into the strain energy expression gives

$$\int_V \Delta \varepsilon_t D_t \varepsilon_t dV = \int_{-l/2}^{+l/2} \Delta \bar{\varepsilon}_t \bar{\sigma}_t dz \quad (4.46)$$

where the generalized stress vector is

$$\bar{\sigma}_t = \bar{D}_t \bar{\varepsilon}_t \quad (4.47)$$

The generalized torsional elasticity matrix can be expressed as

$$\begin{aligned} \bar{D}_t &= \int_A \begin{bmatrix} \phi_I & 0 \\ 0 & \hat{\omega}_I \end{bmatrix} \begin{bmatrix} G & 0 \\ 0 & E_1 \end{bmatrix} \begin{bmatrix} \phi_I & 0 \\ 0 & \hat{\omega}_I \end{bmatrix} dA \\ &= \int_A \begin{bmatrix} G\phi_I^2 & 0 \\ 0 & E_1 \hat{\omega}_I^2 \end{bmatrix} dA \end{aligned} \quad (4.48)$$

Integrating the terms in the matrix over the whole region A we have

$$\int_A E_1 \hat{\omega}_I^2 dA = E_1 J_I, \quad (4.49)$$

and

$$\int_A G \phi_I^2 dA = \int_A G \left( \frac{q_B}{t} \right)^2 dA + \int_A 4Gy_n^2 dA \quad (4.50)$$

From the compatibility condition shown in Eq. 2.46 we obtain

$$\int_A q_B \frac{\partial \hat{\omega}_I}{\partial S} \frac{dA}{t} = 0 \quad (4.51)$$

The total Bredt torsional moment is evaluated as

$$M_{T,B} = \int_A q_B R_t ds \quad (4.52)$$

Substitution of Eqs. 2.54(a), 2.64 and 4.51 into Eq. 4.52 gives alternatively the Bredt torsional moment as

$$M_{T,B} = G \int_A \left( \frac{q_B}{t} \right)^2 dA \cdot \frac{\partial \theta_{J,P}}{\partial z} \quad (4.53)$$

From the definition of the Bredt torsional moment of inertia, we

then have

$$J_B = \int_A \left( \frac{\bar{q}_B}{t} \right)^2 dA \quad (4.54)$$

In addition, the second integral on the right hand side of Eq. 4.50 can be expressed as

$$\int_A 4y_n^2 dA = \sum_A \frac{4}{3} \ell \cdot 2 \left( \frac{t}{2} \right)^3 = \frac{1}{3} \sum_A \ell t^3 = J_V \quad (4.55)$$

Thus, we have

$$\int_A G \phi_I^2 dA = G(J_B + J_V) = GJ_T \quad (4.56)$$

Hence, we can write the generalized torsional elasticity matrix as

$$\bar{D}_t = \begin{bmatrix} GJ_T & 0 \\ 0 & E_1 J_I \end{bmatrix} \quad (4.57)$$

where  $J_T$  is the total torsional moment of inertia, and  $J_I$  is the torsional warping moment of inertia.

Note that in the case of a thin-walled closed section beam the deformational influence due to the warping shear stresses must not be neglected. The generalized elasticity matrix has now to be modified in such a way that the vector product Eq. 4.46 gives the same internal work in the manner of the governing differential equation listed in Chapter 2. Thus, we finally obtain the generalized torsional elasticity matrix as

$$\bar{D}_t = \begin{bmatrix} GJ_T & 0 \\ 0 & \frac{1}{\mu_t} E_1 J_I \end{bmatrix} \quad (4.58)$$

in which the coefficient  $\mu_t$  is known as the warping shear parameter, and is expressed as in Eq. 2.114.

It is obvious that the generalized stress vector represents the torsional stress resultants, which are the torsional moment and the torsional bimoment (Fig. 4.6)

$$\bar{\sigma}_t = [M_T \quad \frac{1}{\mu_t} B_I]^T \quad (4.59)$$

The generalized strain vector  $\bar{\epsilon}_t$  indicates the rate of the twisting angle, and the second derivative of the twisting angle. It can be seen that if the rate of twist is constant only pure torsion appears.

#### 4.4.3 Strains and stress resultants due to distortion

It is convenient to express the generalized distortional strains and stresses in the manner described in Chapter 3. The strain energy increment due to distortion includes two parts:

1) the strain energy increments due to the internal work done by the distortional warping stresses

$$\begin{aligned} \int_V \Delta \epsilon_{\bar{\beta},d}^T E_1 \epsilon_{\bar{\beta},d} dV &= \int_{-l/2}^{+l/2} \Delta \left( -\frac{\partial^2 \gamma_d}{\partial z^2} \right) \int_A E_1 \omega_{II}^2 dA \left( -\frac{\partial^2 \gamma_d}{\partial z^2} \right) dz \\ &= \int_{-l/2}^{+l/2} \Delta \left( -\frac{\partial^2 \gamma_d}{\partial z^2} \right) B_{II} dz, \end{aligned} \quad (4.60)$$

2) the strain energy increment associated with the transverse frame action of the box, i.e., due to the internal work done by the transverse bending stresses

$$\begin{aligned} \int_V \Delta \epsilon_{db}^T E_1 \epsilon_{db} dV &= \int_{-l/2}^{+l/2} \Delta \gamma_d E_1 J_d \gamma_d dz \\ &= \int_{-l/2}^{+l/2} \Delta \gamma_d M_d dz, \end{aligned} \quad (4.61)$$

where  $\gamma_d$  is the distortional angle,  $M_d$  is the generalized distortional moment, and  $B_{II}$  is the distortional bimoment.

We may rewrite the above expression in matrix notation as

$$\int_V \Delta \epsilon_d^T \mathbf{D}_d \epsilon_d dV = \int_{-l/2}^{+l/2} \Delta \bar{\epsilon}_d^T \bar{\sigma}_d dz \quad (4.62)$$

where the generalized distortional strain vector is

$$\bar{\epsilon}_d = \left[ \gamma_d \quad -\frac{\partial^2 \gamma_d}{\partial z^2} \right] \quad (4.63)$$

and the generalized elasticity matrix is

$$\bar{\mathbf{D}}_d = \begin{bmatrix} E_1 J_d & 0 \\ 0 & E_1 J_{\Pi} \end{bmatrix} \quad (4.64)$$

in which  $J_d$  is the distortional second moment of area, and  $J_{\Pi}$  is the distortional warping moment of inertia.

The generalized stress vector  $\bar{\sigma}_d$  represents the distortional stress resultants, i.e., the distortional moment and the distortional bimoment (Fig. 4.6)

$$\bar{\sigma}_d = [M_d \ B_{\Pi}]^T \quad (4.65)$$

#### 4.4.4 Generalized stress-strain relation

To conclude the derivations, the constitutive relation of linear elasticity is of the form

$$\bar{\sigma} = \bar{\mathbf{D}} \bar{\epsilon} \quad (4.66)$$

where the generalized stress vector (Fig. 4.6) is

$$\bar{\sigma} = [Q_x \ Q_y \ N_z \ M_x \ M_y \ M_T \ \frac{1}{\mu_t} B_I \ M_d \ B_{\Pi}]^T, \quad (4.67)$$

and the generalized elasticity matrix is

$$\bar{\mathbf{D}} = \begin{bmatrix} GA_{sx} & 0 & 0 & 0 & 0 & 0 & 0 & 0 & 0 \\ 0 & GA_{sy} & 0 & 0 & 0 & 0 & 0 & 0 & 0 \\ 0 & 0 & E_1 A & 0 & 0 & 0 & 0 & 0 & 0 \\ 0 & 0 & 0 & E_1 I_{xx} & 0 & 0 & 0 & 0 & 0 \\ 0 & 0 & 0 & 0 & E_1 I_{yy} & 0 & 0 & 0 & 0 \\ 0 & 0 & 0 & 0 & 0 & GJ_T & 0 & 0 & 0 \\ 0 & 0 & 0 & 0 & 0 & 0 & \frac{1}{\mu_t} E_1 J_I & 0 & 0 \\ 0 & 0 & 0 & 0 & 0 & 0 & 0 & E_1 J_d & 0 \\ 0 & 0 & 0 & 0 & 0 & 0 & 0 & 0 & E_1 J_{II} \end{bmatrix} \quad (4.68)$$

The generalized strain vector is

$$\bar{\boldsymbol{\epsilon}} = \begin{bmatrix} -\theta_y + \frac{\partial u}{\partial z} \\ \theta_x + \frac{\partial v}{\partial z} \\ \frac{\partial w}{\partial z} \\ \frac{\partial \theta_x}{\partial z} \\ -\frac{\partial \theta_y}{\partial z} \\ \frac{\partial \theta_z}{\partial z} \\ -\frac{\partial^2 \theta_z}{\partial z^2} \\ \gamma_d \\ -\frac{\partial^2 \gamma_d}{\partial z^2} \end{bmatrix} \quad (4.69)$$

#### 4.5 Transformation of nodal displacements

For the purpose of assembling the element stiffness which will be

shown in further sections, it is necessary to transform the nodal displacements relative to the local coordinate system to displacements with respect to the global system.

Referring to Fig. 4.7, let the resultant vector of translation components of any point on the element axis be  $\vec{d}$  and the resultant vector of rotation components of the section be  $\vec{\phi}$ . These can be given in terms of global components as

$$\begin{aligned}\vec{d} &= U \hat{i} + V \hat{j} + W \hat{k} \\ \vec{\phi} &= \phi_x \hat{i} + \phi_y \hat{j} + \phi_z \hat{k}\end{aligned}\tag{4.70}$$

The translation components  $u$ ,  $v$ ,  $w$ , and the rotation components  $\theta_x$ ,  $\theta_y$ ,  $\theta_z$  with respect to the local  $x$ ,  $y$ ,  $z$  axes respectively can be obtained by scalar products as

$$\begin{aligned}u &= \vec{d} \cdot \hat{x} & \theta_x &= \vec{\phi} \cdot \hat{x} \\ v &= \vec{d} \cdot \hat{y} & \theta_y &= \vec{\phi} \cdot \hat{y} \\ w &= \vec{d} \cdot \hat{z} & \theta_z &= \vec{\phi} \cdot \hat{z}\end{aligned}\tag{4.71}$$

After substituting from Eq. 4.70 into Eq. 4.71, we can have

$$\begin{aligned}u &= U \hat{i} \cdot \hat{x} + V \hat{j} \cdot \hat{x} + W \hat{k} \cdot \hat{x} \\ v &= U \hat{i} \cdot \hat{y} + V \hat{j} \cdot \hat{y} + W \hat{k} \cdot \hat{y} \\ w &= U \hat{i} \cdot \hat{z} + V \hat{j} \cdot \hat{z} + W \hat{k} \cdot \hat{z} \\ \theta_x &= \phi_x \hat{i} \cdot \hat{x} + \phi_y \hat{j} \cdot \hat{x} + \phi_z \hat{k} \cdot \hat{x} \\ \theta_y &= \phi_x \hat{i} \cdot \hat{y} + \phi_y \hat{j} \cdot \hat{y} + \phi_z \hat{k} \cdot \hat{y} \\ \theta_z &= \phi_x \hat{i} \cdot \hat{z} + \phi_y \hat{j} \cdot \hat{z} + \phi_z \hat{k} \cdot \hat{z}\end{aligned}\tag{4.72}$$

where,  $\hat{i} \cdot \hat{x}$ ,  $\hat{j} \cdot \hat{x}$  and  $\hat{k} \cdot \hat{x}$  are the direction cosines of the local  $x$  axis relative to the global coordinate system;  $\hat{i} \cdot \hat{y}$ ,  $\hat{j} \cdot \hat{y}$  and  $\hat{k} \cdot \hat{y}$  those of the  $y$  axis, and  $\hat{i} \cdot \hat{z}$ ,  $\hat{j} \cdot \hat{z}$  and  $\hat{k} \cdot \hat{z}$  those of the local  $z$  axis.

According to the single continuous assumption, the warping displacement mode and the transverse distortion mode should be transformed with unity (156).

Hence, the local displacement field  $\bar{\mathbf{u}}$  can be expressed in terms of the global displacement field

$$\bar{\mathbf{u}} = \lambda \bar{\delta} \quad (4.73)$$

where  $\lambda$  is termed the transformation matrix.

The transformation matrices  $\lambda$  for different types of elements are expressed respectively as:

1. The truss element

$$\lambda = [ \hat{i} \cdot \hat{z} \quad \hat{j} \cdot \hat{z} \quad \hat{k} \cdot \hat{z} ] \quad (4.74a)$$

2. The solid beam element

$$\lambda = \begin{bmatrix} \hat{i} \cdot \hat{x} & \hat{j} \cdot \hat{x} & \hat{k} \cdot \hat{x} & 0 & 0 & 0 \\ \hat{i} \cdot \hat{y} & \hat{j} \cdot \hat{y} & \hat{k} \cdot \hat{y} & 0 & 0 & 0 \\ \hat{i} \cdot \hat{z} & \hat{j} \cdot \hat{z} & \hat{k} \cdot \hat{z} & 0 & 0 & 0 \\ 0 & 0 & 0 & \hat{i} \cdot \hat{x} & \hat{j} \cdot \hat{x} & \hat{k} \cdot \hat{x} \\ 0 & 0 & 0 & \hat{i} \cdot \hat{y} & \hat{j} \cdot \hat{y} & \hat{k} \cdot \hat{y} \\ 0 & 0 & 0 & \hat{i} \cdot \hat{z} & \hat{j} \cdot \hat{z} & \hat{k} \cdot \hat{z} \end{bmatrix} \quad (4.74b)$$

3. The thin-walled beam element with rigid section

$$\lambda = \begin{bmatrix} \hat{i} \cdot \hat{x} & \hat{j} \cdot \hat{x} & \hat{k} \cdot \hat{x} & 0 & 0 & 0 & 0 \\ \hat{i} \cdot \hat{y} & \hat{j} \cdot \hat{y} & \hat{k} \cdot \hat{y} & 0 & 0 & 0 & 0 \\ \hat{i} \cdot \hat{z} & \hat{j} \cdot \hat{z} & \hat{k} \cdot \hat{z} & 0 & 0 & 0 & 0 \\ 0 & 0 & 0 & \hat{i} \cdot \hat{x} & \hat{j} \cdot \hat{x} & \hat{k} \cdot \hat{x} & 0 \\ 0 & 0 & 0 & \hat{i} \cdot \hat{y} & \hat{j} \cdot \hat{y} & \hat{k} \cdot \hat{y} & 0 \\ 0 & 0 & 0 & \hat{i} \cdot \hat{z} & \hat{j} \cdot \hat{z} & \hat{k} \cdot \hat{z} & 0 \\ 0 & 0 & 0 & 0 & 0 & 0 & 1 \end{bmatrix} \quad (4.74c)$$

## 4. The thin-walled box beam element

$$\lambda = \begin{bmatrix} \hat{i} \cdot \hat{x} & \hat{j} \cdot \hat{x} & \hat{k} \cdot \hat{x} & 0 & 0 & 0 & 0 & 0 & 0 \\ \hat{i} \cdot \hat{y} & \hat{j} \cdot \hat{y} & \hat{k} \cdot \hat{y} & 0 & 0 & 0 & 0 & 0 & 0 \\ \hat{i} \cdot \hat{z} & \hat{j} \cdot \hat{z} & \hat{k} \cdot \hat{z} & 0 & 0 & 0 & 0 & 0 & 0 \\ 0 & 0 & 0 & \hat{i} \cdot \hat{x} & \hat{j} \cdot \hat{x} & \hat{k} \cdot \hat{x} & 0 & 0 & 0 \\ 0 & 0 & 0 & \hat{i} \cdot \hat{y} & \hat{j} \cdot \hat{y} & \hat{k} \cdot \hat{y} & 0 & 0 & 0 \\ 0 & 0 & 0 & \hat{i} \cdot \hat{z} & \hat{j} \cdot \hat{z} & \hat{k} \cdot \hat{z} & 0 & 0 & 0 \\ 0 & 0 & 0 & 0 & 0 & 0 & 1 & 0 & 0 \\ 0 & 0 & 0 & 0 & 0 & 0 & 0 & 1 & 0 \\ 0 & 0 & 0 & 0 & 0 & 0 & 0 & 0 & 1 \end{bmatrix} \quad (4.74d)$$

The direction cosines are given by the following expressions:

$$\begin{aligned} \hat{i} \cdot \hat{y} &= \cos Xy = (X_p - X) / \sqrt{(X_p - X)^2 + (Y_p - Y)^2 + (Z_p - Z)^2} \\ \hat{j} \cdot \hat{y} &= \cos Yy = (Y_p - Y) / \sqrt{(X_p - X)^2 + (Y_p - Y)^2 + (Z_p - Z)^2} \\ \hat{k} \cdot \hat{y} &= \cos Zy = (Z_p - Z) / \sqrt{(X_p - X)^2 + (Y_p - Y)^2 + (Z_p - Z)^2} \\ \hat{i} \cdot \hat{x} &= \cos Xx = \left( \cos Yy \frac{\partial Z}{\partial \xi} - \cos Zy \frac{\partial Y}{\partial \xi} \right) / \sqrt{\left( \frac{\partial X}{\partial \xi} \right)^2 + \left( \frac{\partial Y}{\partial \xi} \right)^2 + \left( \frac{\partial Z}{\partial \xi} \right)^2} \\ \hat{j} \cdot \hat{x} &= \cos Yx = \left( \cos Zy \frac{\partial X}{\partial \xi} - \cos Xy \frac{\partial Z}{\partial \xi} \right) / \sqrt{\left( \frac{\partial X}{\partial \xi} \right)^2 + \left( \frac{\partial Y}{\partial \xi} \right)^2 + \left( \frac{\partial Z}{\partial \xi} \right)^2} \\ \hat{k} \cdot \hat{x} &= \cos Zx = \left( \cos Xy \frac{\partial Y}{\partial \xi} - \cos Yy \frac{\partial X}{\partial \xi} \right) / \sqrt{\left( \frac{\partial X}{\partial \xi} \right)^2 + \left( \frac{\partial Y}{\partial \xi} \right)^2 + \left( \frac{\partial Z}{\partial \xi} \right)^2} \\ \hat{i} \cdot \hat{z} &= \cos Xz = \frac{\partial X}{\partial \xi} / \sqrt{\left( \frac{\partial X}{\partial \xi} \right)^2 + \left( \frac{\partial Y}{\partial \xi} \right)^2 + \left( \frac{\partial Z}{\partial \xi} \right)^2} \\ \hat{j} \cdot \hat{z} &= \cos Yz = \frac{\partial Y}{\partial \xi} / \sqrt{\left( \frac{\partial X}{\partial \xi} \right)^2 + \left( \frac{\partial Y}{\partial \xi} \right)^2 + \left( \frac{\partial Z}{\partial \xi} \right)^2} \\ \hat{k} \cdot \hat{z} &= \cos Zz = \frac{\partial Z}{\partial \xi} / \sqrt{\left( \frac{\partial X}{\partial \xi} \right)^2 + \left( \frac{\partial Y}{\partial \xi} \right)^2 + \left( \frac{\partial Z}{\partial \xi} \right)^2} \end{aligned} \quad (4.75)$$

In the case where the principal planes yz of the element are parallel to the YZ plane, the direction cosines are simplified to

$$\begin{aligned}
\hat{i} \cdot \hat{x} &= 1 \\
\hat{j} \cdot \hat{x} &= \hat{k} \cdot \hat{x} = \hat{i} \cdot \hat{y} = \hat{i} \cdot \hat{z} = 0 \\
\hat{j} \cdot \hat{y} &= \hat{k} \cdot \hat{z} = \frac{\partial Z}{\partial \zeta} \bigg/ \sqrt{\left(\frac{\partial Y}{\partial \zeta}\right)^2 + \left(\frac{\partial Z}{\partial \zeta}\right)^2} \\
-\hat{k} \cdot \hat{y} &= \hat{j} \cdot \hat{z} = \frac{\partial Y}{\partial \zeta} \bigg/ \sqrt{\left(\frac{\partial Y}{\partial \zeta}\right)^2 + \left(\frac{\partial Z}{\partial \zeta}\right)^2}
\end{aligned} \tag{4.76}$$

When the principal planes  $xz$  of the element are parallel to the  $XZ$  plane, we may express the direction cosines as

$$\begin{aligned}
\hat{j} \cdot \hat{y} &= 1 \\
\hat{i} \cdot \hat{y} &= \hat{k} \cdot \hat{y} = \hat{j} \cdot \hat{x} = \hat{j} \cdot \hat{z} = 0 \\
\hat{i} \cdot \hat{x} &= \hat{k} \cdot \hat{z} = \frac{\partial Z}{\partial \zeta} \bigg/ \sqrt{\left(\frac{\partial X}{\partial \zeta}\right)^2 + \left(\frac{\partial Z}{\partial \zeta}\right)^2} \\
\hat{i} \cdot \hat{z} &= -\hat{k} \cdot \hat{x} = \frac{\partial X}{\partial \zeta} \bigg/ \sqrt{\left(\frac{\partial X}{\partial \zeta}\right)^2 + \left(\frac{\partial Z}{\partial \zeta}\right)^2}
\end{aligned} \tag{4.77}$$

When the principal planes  $yz$  of the element are parallel to the  $XY$  plane, the direction cosines are

$$\begin{aligned}
\hat{k} \cdot \hat{x} &= 1 \\
\hat{i} \cdot \hat{x} &= \hat{j} \cdot \hat{x} = \hat{k} \cdot \hat{y} = \hat{k} \cdot \hat{z} = 0 \\
\hat{i} \cdot \hat{y} &= \hat{j} \cdot \hat{z} = \frac{\partial Y}{\partial \zeta} \bigg/ \sqrt{\left(\frac{\partial X}{\partial \zeta}\right)^2 + \left(\frac{\partial Y}{\partial \zeta}\right)^2} \\
-\hat{j} \cdot \hat{y} &= \hat{i} \cdot \hat{z} = \frac{\partial X}{\partial \zeta} \bigg/ \sqrt{\left(\frac{\partial X}{\partial \zeta}\right)^2 + \left(\frac{\partial Y}{\partial \zeta}\right)^2}
\end{aligned} \tag{4.78}$$

#### 4.6 Sub-parametric formulation

We now follow the standard displacement method which is given in Reference 155 to establish the relevant sub-parametric formulae.

##### 4.6.1 Shape functions for mapping the element geometry

It has been shown that the normalized coordinates can be distorted

to a new, curvilinear set when plotted in a Cartesian space (155). Hence a most convenient method of mapping the geometrical shape of the one-dimensional element is to use the interpolation function with natural coordinate  $\zeta$ . Thus, for each element, we have

$$G = MG^e \quad (4.79)$$

where  $G$  represents the geometrical function of the element,  $G^e$  lists the nodal values of the geometrical function, and  $M$  is the geometrical shape function given in terms of the natural coordinates.

A special form of transformation, referred to as hierarchical mapping is adopted here (80). The hierarchical shape functions are defined in terms of the natural coordinate  $\zeta$  as

$$\begin{aligned} M_j &= \frac{1}{2}(1 + \zeta_0) & \text{for } i=1 \text{ and } 2 \\ M_j &= (1 - \zeta^2) & \text{for } i=3 \end{aligned} \quad (4.80)$$

where  $\zeta_0 = \zeta \zeta_j$

The hierarchical shape functions take account of the variables specifying the departure from linearity. Thus, the same shape functions apply for the geometrical mapping of both the straight elements defined by two end-nodes only, and the curvilinear elements defined by two end-nodes as well as a mid-node.

Using the hierarchical mapping defined by Eq. 4.80 the global coordinates and the characteristic sectional properties of any point on the element axis may be given in terms of the corresponding nodal values

as





It has already been established that the potential energy functional due to warping torsion and distortion contains second derivatives of the unknown functions, and the physical problem is characterized by fourth order differential equations. Continuity conditions between elements have now to be imposed not only on the unknown quantities themselves but also on their derivatives. This is the so-called  $C_1$ -continuity problem (155).

When the displacement function and its slope are prescribed at the nodes, the general interpolation function can be expressed as

$$f = \bar{N}_{11} f_1 + \bar{N}_{12} \left( \frac{\partial f}{\partial z} \right)_1 + \bar{N}_{21} f_2 + \bar{N}_{22} \left( \frac{\partial f}{\partial z} \right)_2 + \bar{N}_{31} f_3 + \bar{N}_{32} \left( \frac{\partial f}{\partial z} \right)_3 \quad (4.86)$$

where  $f_i$  is the value of the unknown function at node  $i$  and  $\left( \frac{\partial f}{\partial z} \right)_i$  is its first derivative.

In order to differentiate the interpolation function with respect to the Cartesian coordinate  $z$ , it is necessary to use the rule of partial differentiation. For a one-dimensional problem the derivative is replaced by

$$\frac{\partial f}{\partial z} = \frac{\partial f}{\partial \zeta} \cdot \frac{\partial \zeta}{\partial z} = J^{-1} \frac{\partial f}{\partial \zeta} \quad (4.87)$$

where the Jacobian factor  $J$  can be expressed, from the definition of the  $z$  axis, as

$$J = \frac{\partial z}{\partial \zeta} = \sqrt{\left( \frac{\partial X}{\partial \zeta} \right)^2 + \left( \frac{\partial Y}{\partial \zeta} \right)^2 + \left( \frac{\partial Z}{\partial \zeta} \right)^2} \quad (4.88)$$

Differentiating Eq. 4.86 once we obtain

$$\frac{\partial f}{\partial z} = J^{-1} \left[ \frac{\partial \bar{N}_{11}}{\partial \zeta} f_1 + \frac{\partial \bar{N}_{12}}{\partial \zeta} \left( \frac{\partial f}{\partial z} \right)_1 + \frac{\partial \bar{N}_{21}}{\partial \zeta} f_2 + \frac{\partial \bar{N}_{22}}{\partial \zeta} \left( \frac{\partial f}{\partial z} \right)_2 + \frac{\partial \bar{N}_{31}}{\partial \zeta} f_3 + \frac{\partial \bar{N}_{32}}{\partial \zeta} \left( \frac{\partial f}{\partial z} \right)_3 \right] \quad (4.89)$$

Since three discrete nodes are specified in each box beam element,

a fifth order polynomial expression would be appropriate

$$\bar{N} = A_1 + A_2 \zeta + A_3 \zeta^2 + A_4 \zeta^3 + A_5 \zeta^4 + A_6 \zeta^5, \quad (4.90)$$

and

$$\frac{\partial \bar{N}}{\partial \zeta} = A_2 + 2A_3 \zeta + 3A_4 \zeta^2 + 4A_5 \zeta^3 + 5A_6 \zeta^4. \quad (4.91)$$

Noting that  $\bar{N}_{i1} = 1$  and  $\frac{\partial \bar{N}_{i2}}{\partial \zeta} = 1$  at node  $i$  but is zero at other nodes,

we can obtain the shape functions as

$$\begin{aligned} \bar{N}_{11} &= \frac{\zeta^2}{4} (4 - 5\zeta - 2\zeta^2 + 3\zeta^3) \\ \bar{N}_{12} &= \frac{J_1}{4} \zeta^2 (1 - \zeta)(1 - \zeta^2) \\ \bar{N}_{21} &= \frac{\zeta^2}{4} (4 + 5\zeta - 2\zeta^2 - 3\zeta^3) \\ \bar{N}_{22} &= \frac{J_2}{4} \zeta^2 (1 + \zeta)(\zeta^2 - 1) \\ \bar{N}_{31} &= (1 - \zeta^2)^2 \\ \bar{N}_{32} &= J_3 \zeta (1 - \zeta^2)^2 \end{aligned} \quad (4.92)$$

where  $J_1$ ,  $J_2$  and  $J_3$  are the Jacobian factors at the three nodes of the element.

#### 4.6.3 Displacement field

The global displacement at any point on the beam axis in terms of the nodal values are given by

$$\bar{\delta} = \left\{ \begin{array}{c} U \\ V \\ W \\ \phi_x \\ \phi_y \\ \phi_z \\ \vartheta \\ \gamma_d \\ \psi_d \end{array} \right\} = \sum_{i=1}^3 \left[ \begin{array}{cccccccccc} N_i & 0 & 0 & 0 & 0 & 0 & 0 & 0 & 0 & 0 \\ 0 & N_i & 0 & 0 & 0 & 0 & 0 & 0 & 0 & 0 \\ 0 & 0 & N_i & 0 & 0 & 0 & 0 & 0 & 0 & 0 \\ 0 & 0 & 0 & \bar{N}_{i1} & 0 & 0 & \bar{N}_{i2}(\hat{i}\hat{z}) & 0 & 0 & 0 \\ 0 & 0 & 0 & 0 & \bar{N}_{i1} & 0 & \bar{N}_{i2}(\hat{j}\hat{z}) & 0 & 0 & 0 \\ 0 & 0 & 0 & 0 & 0 & \bar{N}_{i1} & \bar{N}_{i2}(\hat{k}\hat{z}) & 0 & 0 & 0 \\ 0 & 0 & 0 & \frac{\partial \bar{N}_{i1}}{\partial z}(\hat{i}\hat{z}) & \frac{\partial \bar{N}_{i1}}{\partial z}(\hat{j}\hat{z}) & \frac{\partial \bar{N}_{i1}}{\partial z}(\hat{k}\hat{z}) & \frac{\partial \bar{N}_{i2}}{\partial z} & 0 & 0 & 0 \\ 0 & 0 & 0 & 0 & 0 & 0 & 0 & \bar{N}_{i1} & \bar{N}_{i2} & 0 \\ 0 & 0 & 0 & 0 & 0 & 0 & 0 & \frac{\partial \bar{N}_{i1}}{\partial z} & \frac{\partial \bar{N}_{i2}}{\partial z} & 0 \end{array} \right] \left\{ \begin{array}{c} U \\ V \\ W \\ \phi_x \\ \phi_y \\ \phi_z \\ \vartheta \\ \gamma_d \\ \psi_d \end{array} \right\}_i \quad (4.93)$$

Substitution of Eqs. 4.93 and 4.74 into Eq. 4.73 gives

$$\bar{\mathbf{u}} = \left[ \begin{array}{c} u \\ v \\ w \\ \theta_x \\ \theta_y \\ \theta_z \\ \psi \\ \gamma_d \\ \psi_d \end{array} \right] = \sum_{i=1}^3 \left[ \begin{array}{cccccccccc} N_i \hat{i}\hat{x} & N_i \hat{j}\hat{x} & N_i \hat{k}\hat{x} & 0 & 0 & 0 & 0 & 0 & 0 & 0 \\ N_i \hat{i}\hat{y} & N_i \hat{j}\hat{y} & N_i \hat{k}\hat{y} & 0 & 0 & 0 & 0 & 0 & 0 & 0 \\ N_i \hat{i}\hat{z} & N_i \hat{j}\hat{z} & N_i \hat{k}\hat{z} & 0 & 0 & 0 & 0 & 0 & 0 & 0 \\ 0 & 0 & 0 & \bar{N}_{i1} \hat{i}\hat{x} & \bar{N}_{i1} \hat{j}\hat{x} & \bar{N}_{i1} \hat{k}\hat{x} & 0 & 0 & 0 & 0 \\ 0 & 0 & 0 & \bar{N}_{i1} \hat{i}\hat{y} & \bar{N}_{i1} \hat{j}\hat{y} & \bar{N}_{i1} \hat{k}\hat{y} & 0 & 0 & 0 & 0 \\ 0 & 0 & 0 & \bar{N}_{i1} \hat{i}\hat{z} & \bar{N}_{i1} \hat{j}\hat{z} & \bar{N}_{i1} \hat{k}\hat{z} & 0 & 0 & 0 & 0 \\ 0 & 0 & 0 & \frac{\partial \bar{N}_{i1}}{\partial z} \hat{i}\hat{z} & \frac{\partial \bar{N}_{i1}}{\partial z} \hat{j}\hat{z} & \frac{\partial \bar{N}_{i1}}{\partial z} \hat{k}\hat{z} & \bar{N}_{i2} & 0 & 0 & 0 \\ 0 & 0 & 0 & 0 & 0 & 0 & 0 & \bar{N}_{i1} & \bar{N}_{i2} & 0 \\ 0 & 0 & 0 & 0 & 0 & 0 & 0 & \frac{\partial \bar{N}_{i1}}{\partial z} & \frac{\partial \bar{N}_{i2}}{\partial z} & 0 \end{array} \right] \left[ \begin{array}{c} U \\ V \\ W \\ \Phi_x \\ \Phi_y \\ \Phi_z \\ \psi \\ \gamma_d \\ \psi_d \end{array} \right] \quad (4.94)$$

Reducing the unnecessary high order terms we can finally obtain

$$\bar{\mathbf{u}} = [\bar{N}_1 \bar{N}_2 \bar{N}_3] \bar{\delta}^e = \bar{N} \bar{\delta}^e \quad (4.95)$$

where the displacement shape function matrix  $\bar{N}$  is of the order  $9 \times 27$ , and its submatrices are expressed as

$$\bar{N}_i = \left[ \begin{array}{cccccccccc} N_i \hat{i}\hat{x} & N_i \hat{j}\hat{x} & N_i \hat{k}\hat{x} & 0 & 0 & 0 & 0 & 0 & 0 & 0 \\ N_i \hat{i}\hat{y} & N_i \hat{j}\hat{y} & N_i \hat{k}\hat{y} & 0 & 0 & 0 & 0 & 0 & 0 & 0 \\ N_i \hat{i}\hat{z} & N_i \hat{j}\hat{z} & N_i \hat{k}\hat{z} & 0 & 0 & 0 & 0 & 0 & 0 & 0 \\ 0 & 0 & 0 & N_i \hat{i}\hat{x} & N_i \hat{j}\hat{x} & N_i \hat{k}\hat{x} & 0 & 0 & 0 & 0 \\ 0 & 0 & 0 & N_i \hat{i}\hat{y} & N_i \hat{j}\hat{y} & N_i \hat{k}\hat{y} & 0 & 0 & 0 & 0 \\ 0 & 0 & 0 & \bar{N}_{i1} \hat{i}\hat{z} & \bar{N}_{i1} \hat{j}\hat{z} & \bar{N}_{i1} \hat{k}\hat{z} & \bar{N}_{i2} & 0 & 0 & 0 \\ 0 & 0 & 0 & \frac{\partial \bar{N}_{i1}}{\partial z} \hat{i}\hat{z} & \frac{\partial \bar{N}_{i1}}{\partial z} \hat{j}\hat{z} & \frac{\partial \bar{N}_{i1}}{\partial z} \hat{k}\hat{z} & \frac{\partial \bar{N}_{i2}}{\partial z} & 0 & 0 & 0 \\ 0 & 0 & 0 & 0 & 0 & 0 & 0 & \bar{N}_{i1} & \bar{N}_{i2} & 0 \\ 0 & 0 & 0 & 0 & 0 & 0 & 0 & \frac{\partial \bar{N}_{i1}}{\partial z} & \frac{\partial \bar{N}_{i2}}{\partial z} & 0 \end{array} \right] \quad (4.96)$$

( $i=1, 2, 3$ )

#### 4.6.4 Strains

With displacements known at all points within the element the 'strains' at any point can be determined. From Eq. 4.69 the strains can be written in matrix notation as

$$\bar{\epsilon} = L \bar{u} \quad (4.97)$$

where L is a suitable linear operator

$$L = \begin{bmatrix} \frac{\partial}{\partial z} & 0 & 0 & 0 & -1 & 0 & 0 & 0 & 0 \\ 0 & \frac{\partial}{\partial z} & 0 & 1 & 0 & 0 & 0 & 0 & 0 \\ 0 & 0 & \frac{\partial}{\partial z} & 0 & 0 & 0 & 0 & 0 & 0 \\ 0 & 0 & 0 & \frac{\partial}{\partial z} & 0 & 0 & 0 & 0 & 0 \\ 0 & 0 & 0 & 0 & -\frac{\partial}{\partial z} & 0 & 0 & 0 & 0 \\ 0 & 0 & 0 & 0 & 0 & \frac{\partial}{\partial z} & 0 & 0 & 0 \\ 0 & 0 & 0 & 0 & 0 & 0 & -\frac{\partial}{\partial z} & 0 & 0 \\ 0 & 0 & 0 & 0 & 0 & 0 & 0 & 1 & 0 \\ 0 & 0 & 0 & 0 & 0 & 0 & 0 & 0 & -\frac{\partial}{\partial z} \end{bmatrix} \quad (4.98)$$

Using Eq. 4.95, the above Eq. 4.97 can be approximated as

$$\bar{\epsilon} = \bar{B} \bar{\delta}^e \quad (4.99)$$

where the strain matrix

$$\bar{B} = L\bar{N} = [\bar{B}_1 \quad \bar{B}_2 \quad \bar{B}_3] \quad (4.100)$$

is of the order 9 x 27, and its submatrices are obtained by the multiplication of matrices

$$\bar{B}_i = \begin{bmatrix} \frac{\partial N_i}{\partial z} \hat{i}\cdot\hat{x} & \frac{\partial N_i}{\partial z} \hat{j}\cdot\hat{x} & \frac{\partial N_i}{\partial z} \hat{k}\cdot\hat{x} & -N_i \hat{i}\cdot\hat{y} & -N_i \hat{j}\cdot\hat{y} & -N_i \hat{k}\cdot\hat{y} & 0 & 0 & 0 \\ \frac{\partial N_i}{\partial z} \hat{i}\cdot\hat{y} & \frac{\partial N_i}{\partial z} \hat{j}\cdot\hat{y} & \frac{\partial N_i}{\partial z} \hat{k}\cdot\hat{y} & N_i \hat{i}\cdot\hat{x} & N_i \hat{j}\cdot\hat{x} & N_i \hat{k}\cdot\hat{x} & 0 & 0 & 0 \\ \frac{\partial N_i}{\partial z} \hat{i}\cdot\hat{z} & \frac{\partial N_i}{\partial z} \hat{j}\cdot\hat{z} & \frac{\partial N_i}{\partial z} \hat{k}\cdot\hat{z} & 0 & 0 & 0 & 0 & 0 & 0 \\ 0 & 0 & 0 & \frac{\partial N_i}{\partial z} \hat{i}\cdot\hat{x} & \frac{\partial N_i}{\partial z} \hat{j}\cdot\hat{x} & \frac{\partial N_i}{\partial z} \hat{k}\cdot\hat{x} & 0 & 0 & 0 \\ 0 & 0 & 0 & -\frac{\partial N_i}{\partial z} \hat{i}\cdot\hat{y} & -\frac{\partial N_i}{\partial z} \hat{j}\cdot\hat{y} & -\frac{\partial N_i}{\partial z} \hat{k}\cdot\hat{y} & 0 & 0 & 0 \\ 0 & 0 & 0 & \frac{\partial \bar{N}_{i1}}{\partial z} \hat{i}\cdot\hat{z} & \frac{\partial \bar{N}_{i1}}{\partial z} \hat{j}\cdot\hat{z} & \frac{\partial \bar{N}_{i1}}{\partial z} \hat{k}\cdot\hat{z} & \frac{\partial \bar{N}_{i2}}{\partial z} & 0 & 0 \\ 0 & 0 & 0 & -\frac{\partial^2 \bar{N}_{i1}}{\partial z^2} \hat{i}\cdot\hat{z} & -\frac{\partial^2 \bar{N}_{i1}}{\partial z^2} \hat{j}\cdot\hat{z} & -\frac{\partial^2 \bar{N}_{i1}}{\partial z^2} \hat{k}\cdot\hat{z} & -\frac{\partial^2 \bar{N}_{i2}}{\partial z^2} & 0 & 0 \\ 0 & 0 & 0 & 0 & 0 & 0 & 0 & \bar{N}_{i1} & \bar{N}_{i2} \\ 0 & 0 & 0 & 0 & 0 & 0 & 0 & -\frac{\partial^2 \bar{N}_{i1}}{\partial z^2} & -\frac{\partial^2 \bar{N}_{i2}}{\partial z^2} \end{bmatrix}$$

(i=1, 2, 3) (4.101)

The derivatives of the shape functions with respect to Cartesian coordinates  $z$  are related by

$$\frac{\partial N_i}{\partial z} = J^{-1} \frac{\partial N_i}{\partial \zeta} \quad (4.102)$$

$$\text{and } \frac{\partial^2 N_i}{\partial z^2} = \frac{\partial J^{-1}}{\partial \zeta} \frac{\partial N_i}{\partial z} + (J^{-1})^2 \frac{\partial^2 N_i}{\partial \zeta^2} \quad (4.103)$$

$$\text{where } J^{-1} = 1 / \sqrt{\left(\frac{\partial X}{\partial \zeta}\right)^2 + \left(\frac{\partial Y}{\partial \zeta}\right)^2 + \left(\frac{\partial Z}{\partial \zeta}\right)^2} \quad (4.104)$$

and

$$\frac{\partial J^{-1}}{\partial \zeta} = - \left[ \frac{\partial X}{\partial \zeta} \cdot \frac{\partial^2 X}{\partial \zeta^2} + \frac{\partial Y}{\partial \zeta} \cdot \frac{\partial^2 Y}{\partial \zeta^2} + \frac{\partial Z}{\partial \zeta} \cdot \frac{\partial^2 Z}{\partial \zeta^2} \right] \left[ \left(\frac{\partial X}{\partial \zeta}\right)^2 + \left(\frac{\partial Y}{\partial \zeta}\right)^2 + \left(\frac{\partial Z}{\partial \zeta}\right)^2 \right]^{-\frac{3}{2}} \quad (4.105)$$

We can now obtain the derivatives of the shape functions with respect

to natural coordinates  $\zeta$  directly from Eqs. 4.85 and 4.92

$$\begin{aligned}\frac{\partial N_1}{\partial \zeta} &= \zeta - \frac{1}{2} \\ \frac{\partial N_2}{\partial \zeta} &= \zeta + \frac{1}{2}\end{aligned}\tag{4.106}$$

$$\begin{aligned}\frac{\partial N_3}{\partial \zeta} &= -2\zeta \\ \frac{\partial^2 N_1}{\partial \zeta^2} &= 1 \\ \frac{\partial^2 N_2}{\partial \zeta^2} &= 1\end{aligned}\tag{4.107}$$

$$\frac{\partial^2 N_3}{\partial \zeta^2} = -2$$

and

$$\begin{aligned}\frac{\partial \bar{N}_{11}}{\partial \zeta} &= \frac{1}{4} (8\zeta - 15\zeta^2 - 8\zeta^3 + 15\zeta^4) \\ \frac{\partial \bar{N}_{12}}{\partial \zeta} &= \frac{J_1}{4} (2\zeta - 3\zeta^2 - 4\zeta^3 + 5\zeta^4) \\ \frac{\partial \bar{N}_{21}}{\partial \zeta} &= \frac{1}{4} (8\zeta + 15\zeta^2 - 8\zeta^3 - 15\zeta^4) \\ \frac{\partial \bar{N}_{22}}{\partial \zeta} &= \frac{J_2}{4} (-2\zeta - 3\zeta^2 + 4\zeta^3 + 5\zeta^4) \\ \frac{\partial \bar{N}_{31}}{\partial \zeta} &= -4\zeta + 4\zeta^3 \\ \frac{\partial \bar{N}_{32}}{\partial \zeta} &= J_3 (1 - 6\zeta^2 + 5\zeta^4)\end{aligned}\tag{4.108}$$

and

$$\begin{aligned}
 \frac{\partial^2 \bar{N}_{11}}{\partial \zeta^2} &= \frac{1}{4} (8 - 30\zeta - 24\zeta^2 + 60\zeta^3) \\
 \frac{\partial^2 \bar{N}_{12}}{\partial \zeta^2} &= \frac{J_1}{4} (2 - 6\zeta - 12\zeta^2 + 20\zeta^3) \\
 \frac{\partial^2 \bar{N}_{21}}{\partial \zeta^2} &= \frac{1}{4} (8 + 30\zeta - 24\zeta^2 - 60\zeta^3) \\
 \frac{\partial^2 \bar{N}_{22}}{\partial \zeta^2} &= \frac{J_2}{4} (-2 - 6\zeta + 12\zeta^2 + 20\zeta^3) \\
 \frac{\partial^2 \bar{N}_{31}}{\partial \zeta^2} &= -4 + 12\zeta^2 \\
 \frac{\partial^2 \bar{N}_{32}}{\partial \zeta^2} &= J_3 (-12\zeta + 20\zeta^3)
 \end{aligned} \tag{4.109}$$

From Eqs. 4.80 and 4.81 we can obtain

$$\begin{aligned}
 \frac{\partial X}{\partial \zeta} &= \frac{1}{2} (X_2 - X_1) - 2\zeta \Delta X \\
 \frac{\partial Y}{\partial \zeta} &= \frac{1}{2} (Y_2 - Y_1) - 2\zeta \Delta Y \\
 \frac{\partial Z}{\partial \zeta} &= \frac{1}{2} (Z_2 - Z_1) - 2\zeta \Delta Z
 \end{aligned} \tag{4.110}$$

Substituting from Eq. 4.110 into Eq. 4.88 we have

$$\begin{aligned}
 J_1 &= \frac{1}{2} \sqrt{(X_2 - X_1 + 4\Delta X)^2 + (Y_2 - Y_1 + 4\Delta Y)^2 + (Z_2 - Z_1 + 4\Delta Z)^2} \\
 J_2 &= \frac{1}{2} \sqrt{(X_2 - X_1 - 4\Delta X)^2 + (Y_2 - Y_1 - 4\Delta Y)^2 + (Z_2 - Z_1 - 4\Delta Z)^2} \\
 J_3 &= \frac{1}{2} \sqrt{(X_2 - X_1)^2 + (Y_2 - Y_1)^2 + (Z_2 - Z_1)^2}
 \end{aligned} \tag{4.111}$$

in which

$$\begin{aligned}
 \Delta X &= X_3 - \frac{1}{2} (X_1 + X_2) \\
 \Delta Y &= Y_3 - \frac{1}{2} (Y_1 + Y_2) \\
 \Delta Z &= Z_3 - \frac{1}{2} (Z_1 + Z_2)
 \end{aligned} \tag{4.112}$$

#### 4.7 Element stiffness matrix and equivalent nodal forces

The virtual increment of the displacement field can be approximated by

$$\Delta \bar{\mathbf{u}} = \bar{\mathbf{N}} \Delta \bar{\delta}^e \quad (4.113)$$

Accordingly the increment in strains is given as

$$\Delta \bar{\boldsymbol{\epsilon}} = \bar{\mathbf{B}} \Delta \bar{\delta}^e \quad (4.114)$$

Ignoring the initial strain and initial stress system, Eq. 4.1 becomes

$$\int_{-1/2}^{+1/2} \Delta \bar{\boldsymbol{\epsilon}}^T \bar{\mathbf{D}} \bar{\boldsymbol{\epsilon}} dz - \int_V \Delta \bar{\mathbf{u}}^T \bar{\mathbf{F}} dV = 0 \quad (4.115)$$

where  $\bar{\mathbf{F}}$  is the applied force vector.

Substitution of Eqs. 4.99, 4.113 and 4.114 into Eq. 4.115 gives

$$(\Delta \bar{\delta}^e)^T \int_{-1/2}^{+1/2} \bar{\mathbf{B}}^T \bar{\mathbf{D}} \bar{\mathbf{B}} dz \bar{\delta}^e - (\Delta \bar{\delta}^e)^T \int_{\text{vol}} \bar{\mathbf{N}}^T \bar{\mathbf{F}} dV = 0 \quad (4.116)$$

Since the virtual displacement  $\Delta \bar{\delta}^e$  is arbitrary, Eq. 4.116 can be written as

$$\mathbf{K}^e \bar{\delta}^e = \mathbf{F}^e \quad (4.117)$$

where  $\mathbf{K}^e$  is the element stiffness matrix and is expressed, on substituting for  $dz$  from Eq. 4.88, by

$$\mathbf{K}^e = \int_{-1/2}^{+1/2} \bar{\mathbf{B}}^T \bar{\mathbf{D}} \bar{\mathbf{B}} dz = \int_{-1}^{+1} J \bar{\mathbf{B}}^T \bar{\mathbf{D}} \bar{\mathbf{B}} d\zeta \quad (4.118)$$

The element stiffness matrix of the box beam element is of the order 27 x 27. Subsequently it follows the dimensions of 21 x 21, 18 x 18, 12 x 12 and 6 x 6 for the thin-walled beam element, the three-node solid beam element, the two-node beam element and the two-node truss element respectively. The integration of the stiffness coefficient is carried out exclusively by the Gauss-Legendre quadrature. Thus, Eq. 4.118 can be evaluated numerically by

$$K^e = \sum_{i=1}^n H_i (\bar{B}^T \bar{D} \bar{B} \sqrt{(\frac{\partial X}{\partial \zeta})^2 + (\frac{\partial Y}{\partial \zeta})^2 + (\frac{\partial Z}{\partial \zeta})^2})_i \quad (4.119)$$

where  $H_i$  is the weight coefficient and  $n$  is the number of sampling points (155).

It can be seen that exact integration of the element stiffness should be facilitated by three-point Gaussian quadrature for the axial and bending contribution, and six-point quadrature for the torsional and distortional contribution. We know that the Bernoulli-Euler hypothesis has been modified here to include shear deformations. The rotations due to bending are then interpreted as shear strains. A great excess of shear strain is therefore stored by the element. This problem can be overcome by using the reduced integration method (45, 80, 153). Thus, the two-point integration procedure which exactly integrates the bending contribution, but underintegrates the shear contribution, is used instead of three-point integration. This greatly improves the element performance and yields accurate results for both thick and thin beam situations.

As shown in Eq. 4.116 the general form of the consistent nodal loads is written as

$$F^e = \int_V \bar{N}^T \bar{F} dV \quad (4.120)$$

We consider here only the solutions due to gravity loads, uniformly distributed loads and the point loads (Fig. 4.8)

$$F^e = \{F^e\}^{B.F.} + \{F^e\}^{D.F.} + \{F^e\}^{P.F.} \quad (4.121)$$

The consistent force vector due to gravity loads can be expressed as

$$\{F^e\}^{B.F.} = \int_{-L/2}^{+L/2} \bar{N}^T b \rho A dz \quad (4.122a)$$

where  $\rho$  is the specific weight of the material of the element, and  $A$  is the cross-sectional area which varies following Eq. 4.81.

Since we have fixed the global Y axis normal to the level plane, we may express the body force vector as

$$\mathbf{b} = [\hat{j} \cdot \hat{x} \quad \hat{j} \cdot \hat{y} \quad \hat{j} \cdot \hat{z} \quad 0 \quad 0 \quad \hat{j} \cdot \hat{x}(y_g - y_s) \quad 0 \quad -\frac{1}{2} \hat{j} \cdot \hat{x}(y_g - y_s) \quad 0]^T \quad (4.123)$$

where  $\hat{j} \cdot \hat{x}$ ,  $\hat{j} \cdot \hat{y}$  and  $\hat{j} \cdot \hat{z}$  are the direction cosines of the Y axis relative to the local x, y and z axes respectively,  $y_g$  indicates the position of the centroid measured from the top flange, and  $y_s$  is the position of the shear centre evaluated by Eq. 2.105.

The consistent force vector due to distributed forces is written as

$$\begin{aligned} \{\mathbf{F}^e\}^{\text{D.F.}} &= \int_{-L/2}^{+L/2} \bar{\mathbf{N}}^T \mathbf{q}^e dz \\ &= \sum_{i=1}^n H_i (\bar{\mathbf{N}}^T \mathbf{q}^e \sqrt{(\frac{\partial X}{\partial \zeta})^2 + (\frac{\partial Y}{\partial \zeta})^2 + (\frac{\partial Z}{\partial \zeta})^2})_i \end{aligned} \quad (4.124)$$

where the distributed force vector is (Fig. 4.8)

$$\mathbf{q}^e = [p_x \quad p_y \quad p_z \quad m_{x,\text{ext}} \quad m_{y,\text{ext}} \quad m_{z,\text{ext}} \quad b_I \quad m_D \quad b_{II}]^T \quad (4.125)$$

The distributed components per unit length are all related to the local coordinate system of the cross-section, and are assumed to be constant along the element.

The statically equivalent nodal forces due to the applied concentrated forces can be expressed as

$$\{\mathbf{F}\}^{\text{P.F.}} = \sum \bar{\mathbf{N}}^T \mathbf{P} \quad (4.126)$$

Any point load applied on an element is specified in terms of its global components. The point of application of the concentrated load is defined by the natural coordinate  $\zeta$  and the local coordinates x and y.

The concentrated force vector is then (Fig. 4.8)

$$\mathbf{P} = [\bar{P}_x \quad \bar{P}_y \quad \bar{P}_z \quad \bar{M}_x \quad \bar{M}_y \quad \bar{M}_z \quad 0 \quad \bar{M}_D \quad 0]^T \quad (4.127)$$

The components of the force vector in Eq. 4.127 are calculated by the following expressions:

$$\begin{aligned}
 \bar{P}_x &= P_x (\hat{i} \cdot \hat{x})_z + P_y (\hat{j} \cdot \hat{x})_z + P_z (\hat{k} \cdot \hat{x})_z \\
 \bar{P}_y &= P_x (\hat{i} \cdot \hat{y})_z + P_y (\hat{j} \cdot \hat{y})_z + P_z (\hat{k} \cdot \hat{y})_z \\
 \bar{P}_z &= P_x (\hat{i} \cdot \hat{z})_z + P_y (\hat{j} \cdot \hat{z})_z + P_z (\hat{k} \cdot \hat{z})_z \\
 \bar{M}_x &= M_{x,ext}(\hat{i} \cdot \hat{x})_z + M_{y,ext}(\hat{j} \cdot \hat{x})_z + M_{z,ext}(\hat{k} \cdot \hat{x})_z + \bar{P}_z \cdot y \\
 \bar{M}_y &= M_{x,ext}(\hat{i} \cdot \hat{y})_z + M_{y,ext}(\hat{j} \cdot \hat{y})_z + M_{z,ext}(\hat{k} \cdot \hat{y})_z + \bar{P}_z \cdot x \\
 \bar{M}_z &= M_{x,ext}(\hat{i} \cdot \hat{z})_z + M_{y,ext}(\hat{j} \cdot \hat{z})_z + M_{z,ext}(\hat{k} \cdot \hat{z})_z + \bar{P}_y \cdot x - \bar{P}_x (y - y_s + y_g) \\
 \bar{M}_d &= \frac{1}{2} \left[ \frac{b_b}{b_t} \cdot \bar{P}_y x + \bar{P}_x (y - y_s + y_g) \right], \quad |x| \leq b_t/2, \quad \text{or} \\
 \bar{M}_d &= \frac{1}{2} \left[ \frac{b_b}{b_t} \cdot \bar{P}_y x - \left(1 + \frac{b_b}{b_t}\right) (1 - \zeta_d) b_x + \bar{P}_x (y - y_s + y_g) \right], \quad |x| > b_t/2,
 \end{aligned} \tag{4.128}$$

where  $b_x = x - b_t/2$  ( $x > 0$ ), or  $b_x = x + b_t/2$  ( $x < 0$ ),

and  $\zeta_d$  is the distribution factor which can be obtained from the analysis of a frame formed from a unit slice of the box beam.

#### 4.8 Boundary conditions

Using the basic equilibrium and compatibility conditions, we can finally obtain the well known stiffness equation as shown in Eq. 4.3. The structure stiffness matrix is formed from the assembly of the individual elements of the structure. However, without substitution of a minimum number of prescribed displacements, or boundary conditions, the complex stiffness matrix  $K$  is singular. The minimum number of prescribed displacement components should be equal to the maximum degrees of freedom of a typical free joint in the system.

For some conventional support conditions used in bridge construction the following holds true:

1. If the beam is fixed at the support, no deformation arises in the support cross-section, and therefore the following may be written

$$\begin{aligned}
 \left. \begin{aligned} u &= v = w = 0 \\ \theta_x &= \theta_y = \theta_z = 0 \end{aligned} \right\} &\implies & \left. \begin{aligned} U &= V = W = 0 \\ \phi_x &= \phi_y = \phi_z = 0 \end{aligned} \right\} \\
 \varphi &= 0 \\
 \gamma_d &= 0 \\
 \psi_d &= 0
 \end{aligned} \tag{4.129}$$

2. If the support cross-section is connected by a pinned support and is braced by a rigid diaphragm, and yet is free to warp, then the independent boundary conditions are

$$\begin{aligned}
 u = v = w = 0 &\implies U = V = W = 0 \\
 \theta_z &= 0 \\
 \gamma_d &= 0
 \end{aligned}$$

3. If the cross-section is supported by a linear roller which is orientated perpendicularly to the longitudinal axis, and also is braced by a rigid diaphragm, but is free to warp, the boundary conditions may be adjusted to

$$\begin{aligned}
 u = v &= 0 \\
 \theta_z &= 0 \\
 \gamma_d &= 0
 \end{aligned}$$

4. If the free end cross section of a cantilever is braced by a diaphragm to resist its transverse deformation only, yet is free to warp, only one boundary condition applies and that is

$$\gamma_d = 0 \tag{4.132}$$

From the above conditions, it is obvious that in some cases such as curved bridges or structures with inclined supports the imposed restrictions at the boundaries are in the local xyz directions. It would be very unlikely that the orientation of a single global coordinate system would comply with this requirement. Thus, further modification of the structures stiffness

equation should be made for dealing with the boundary conditions.

The complete stiffness matrix of a skeletal structure prior to the introduction of the boundary conditions would have the following pattern:

$$\begin{bmatrix} K_{11} & K_{12} \cdots K_{1i} \cdots K_{1n} \\ K_{21} & K_{22} \cdots \cdots K_{2n} \\ \vdots & \vdots \cdots \vdots \cdots \vdots \\ K_{i1} & K_{i2} \cdots K_{ij} \cdots K_{in} \\ \vdots & \vdots \cdots \vdots \cdots \vdots \\ K_{n1} & K_{n2} \cdots K_{ni} \cdots K_{nn} \end{bmatrix} \begin{Bmatrix} \bar{\delta}_1 \\ \bar{\delta}_2 \\ \vdots \\ \bar{\delta}_i \\ \vdots \\ \bar{\delta}_n \end{Bmatrix} = \begin{Bmatrix} F_1 \\ F_2 \\ \vdots \\ F_i \\ \vdots \\ F_n \end{Bmatrix} \quad (4.133)$$

If the prescribed displacements in the directions of the local frame are specified at the  $i^{\text{th}}$  joint of the structure, from Eq. 4.73 we have

$$\begin{bmatrix} K_{11} & K_{12} \cdots K_{1i}(\lambda_i)^{-1} \cdots K_{1n} \\ K_{21} & K_{22} \cdots \cdots \cdots \\ \vdots & \vdots \cdots \vdots \cdots \vdots \\ K_{i1} \cdots \cdots K_{ij}(\lambda_i)^{-1} \cdots K_{in} \\ \vdots & \vdots \cdots \vdots \cdots \vdots \\ K_{ni} \cdots \cdots K_{ni}(\lambda_i)^{-1} \cdots K_{nn} \end{bmatrix} \begin{Bmatrix} \bar{\delta}_1 \\ \bar{\delta}_2 \\ \vdots \\ u_i \\ \vdots \\ \bar{\delta}_n \end{Bmatrix} = \begin{Bmatrix} F_1 \\ F_2 \\ \vdots \\ F_i \\ \vdots \\ F_n \end{Bmatrix} \quad (4.134)$$

Since the premultiplication of the  $i^{\text{th}}$  row on both sides by  $\lambda_i$  would not disturb the equality, and noticing that in orthogonal coordinate systems,  $\lambda_i \lambda_i^T = I$ , Eq. 4.134 finally becomes

$$\begin{bmatrix} K_{11} & K_{12} \cdots K_{1i} \lambda_i^T \cdots K_{1n} \\ K_{21} & K_{22} \cdots \cdots \cdots \\ \vdots & \vdots \cdots \vdots \cdots \vdots \\ \lambda_i K_{i1} & \lambda_i K_{i2} \cdots \lambda_i K_{ij} \lambda_i^T \cdots \lambda_i K_{in} \\ \vdots & \vdots \cdots \vdots \cdots \vdots \\ K_{n1} \cdots \cdots K_{ni} \lambda_i^T \cdots K_{nn} \end{bmatrix} \begin{Bmatrix} \bar{\delta}_1 \\ \bar{\delta}_2 \\ \vdots \\ u_i \\ \vdots \\ \bar{\delta}_n \end{Bmatrix} = \begin{Bmatrix} F_1 \\ F_2 \\ \vdots \\ \lambda_i F_i \\ \vdots \\ F_n \end{Bmatrix} \quad (4.135)$$

where  $\lambda_i$  is the transformation matrix at the  $i^{\text{th}}$  node and is related to the element specifying the local coordinate system.

Now, the boundary conditions specified by the local coordinate system can be introduced to Eq. 4.135 by simply erasing the corresponding rows and columns. If there is more than one node at which the local boundary conditions are defined, the above procedure must then be repeated for each of these nodes.

In certain cases, alternative treatment for boundary conditions may be the use of appropriate springs at support nodes. Note that the spring support stiffnesses are given in a local coordinate system which can produce large off-diagonal terms when the transformation to the global system is done. These terms can influence the solution accuracy of the equilibrium equations. Thus, it is still preferable to use the technique indicated in Eq. 4.135.

#### 4.9 Internal forces at the ends of the individual elements

The solution of Eq. 4.3 yields the displacement field  $\delta$  at the nodes of the structure. Although the internal forces can be related to the discrete nodal displacements by combining Eqs. 4.66 and 4.99

$$\bar{\sigma} = \bar{D} \bar{B} \bar{\delta}^e, \quad (4.136)$$

it is advantageous to use the following formulae for recovering the internal forces at the respective faces of each element:

$$\bar{\sigma}_{\zeta=-1} = \lambda_{\zeta=-1} \{ [K_{11}^e \ K_{12}^e \ K_{13}^e] \bar{\delta}^e - F_1^e \} \quad (4.137a)$$

and

$$\bar{\sigma}_{\zeta=+1} = \lambda_{\zeta=+1} \{ [K_{21}^e \ K_{22}^e \ K_{23}^e] \bar{\delta}^e - F_2^e \} \quad (4.137b)$$

where  $K_{11}^e, K_{12}^e, \dots, K_{23}^e$  are the submatrices of the element stiffness matrix, the subscript numbers 1, 2 and 3 indicate the end-nodes and the mid-node of the element respectively, and  $F_1^e, F_2^e$  are the equivalent nodal forces produced by the external forces applied on the element considered.

The secondary or flexural torsional moment due to the warping shear stresses can be calculated from

$$M_{T,I} = M_T - \mu_t G J_T \sum_{i=1}^3 \left[ \frac{\bar{N}_{i1}}{\partial z} \hat{i} \cdot \hat{z} + \frac{\bar{N}_{i1}}{\partial z} \hat{j} \cdot \hat{z} + \frac{\bar{N}_{i1}}{\partial z} \hat{k} \cdot \hat{z} + \frac{\bar{N}_{i2}}{\partial z} \right] \begin{Bmatrix} \phi_x \\ \phi_y \\ \phi_z \\ \phi \end{Bmatrix}_i \quad (4.138)$$

and the primary torsional moment is

$$M_{T,p} = M_T - M_{T,I} \quad (4.139)$$

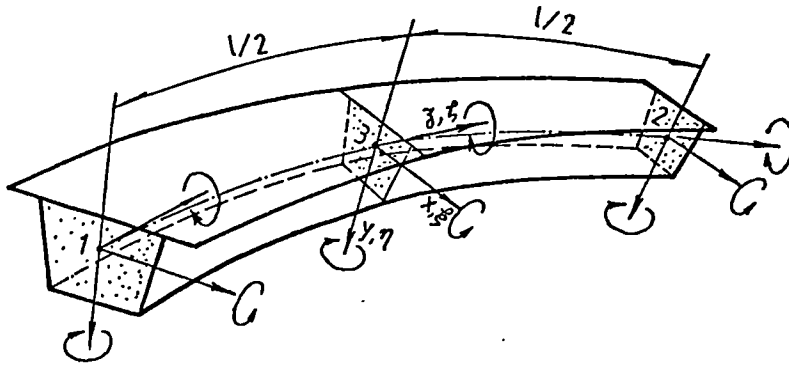


Fig. 4.1 Thin-walled box beam element with three nodes

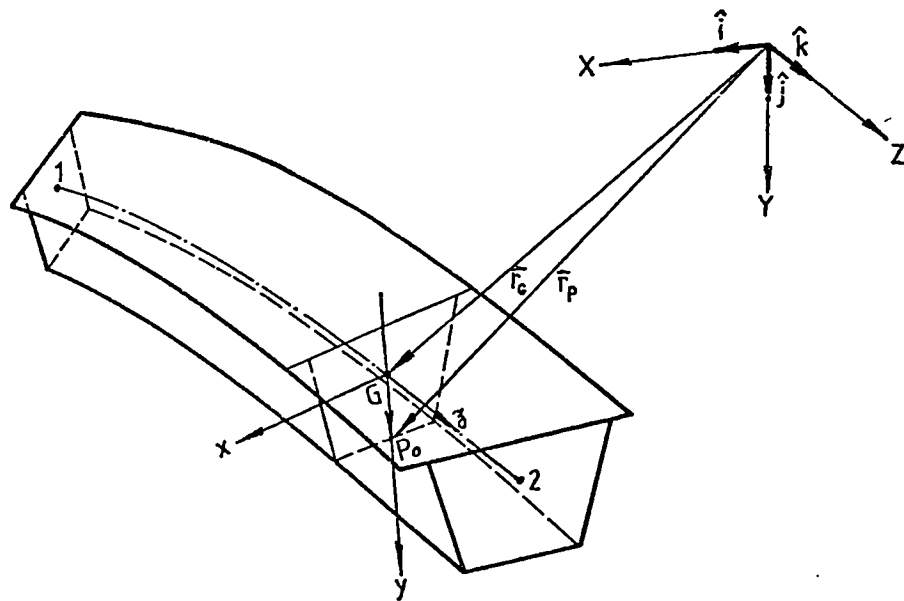


Fig. 4.2 Definition of local coordinate system

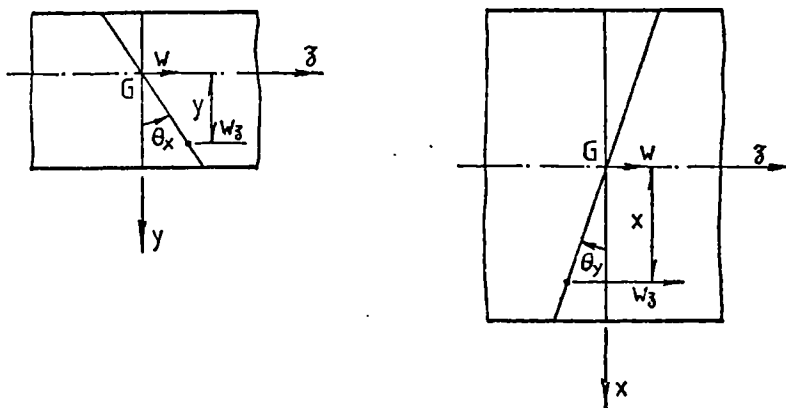


Fig. 4.3 Positive  $\theta_x$  and  $\theta_y$  (right-hand screw rule)

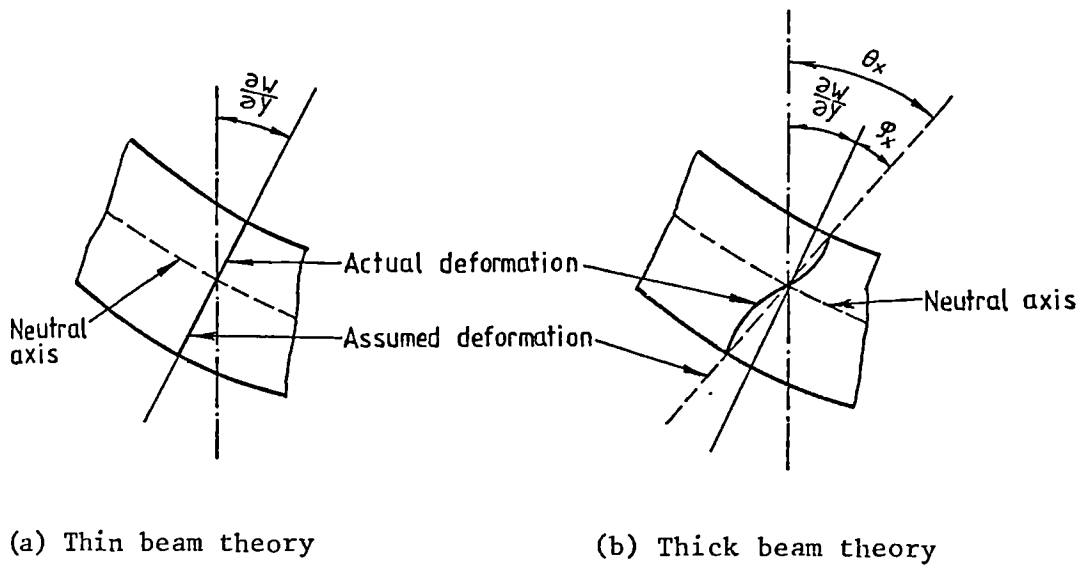


Fig. 4.4 Cross-sectional deformation of beam

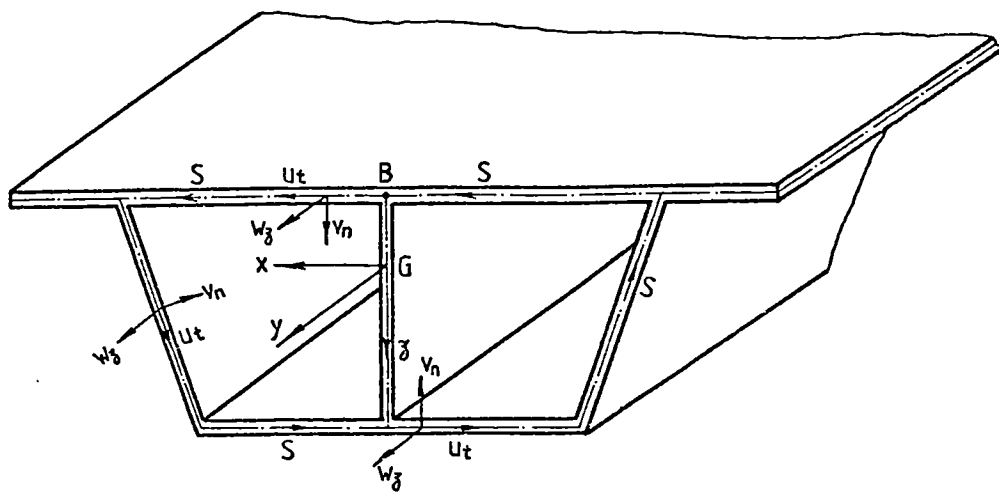


Fig. 4.5 Displacement field in generalized coordinate system

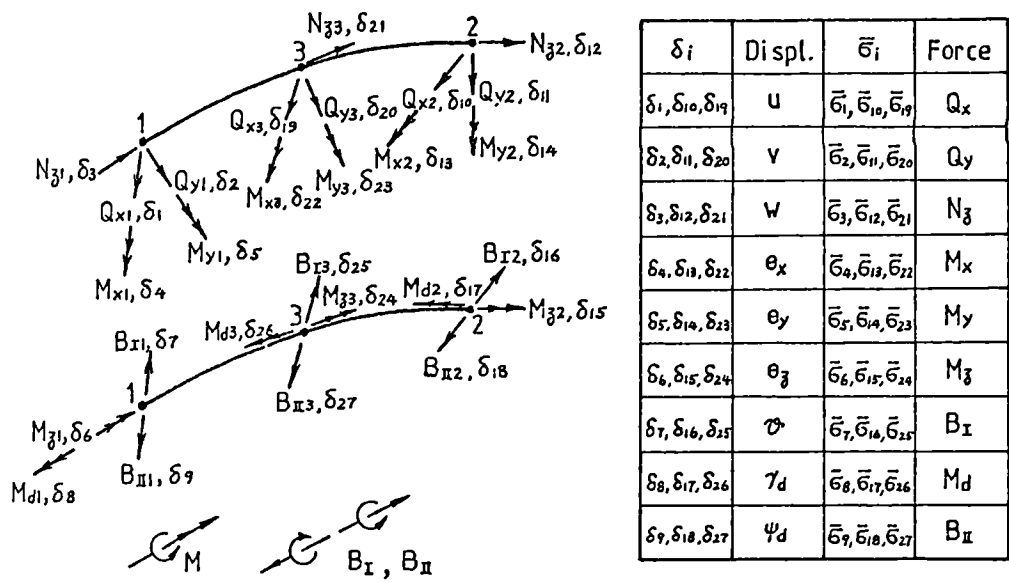


Fig. 4.6 Generalized Forces and Displacements

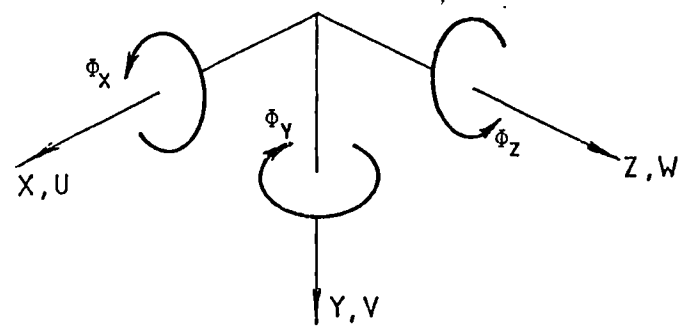


Fig. 4.7 Translations and Rotations in Global System

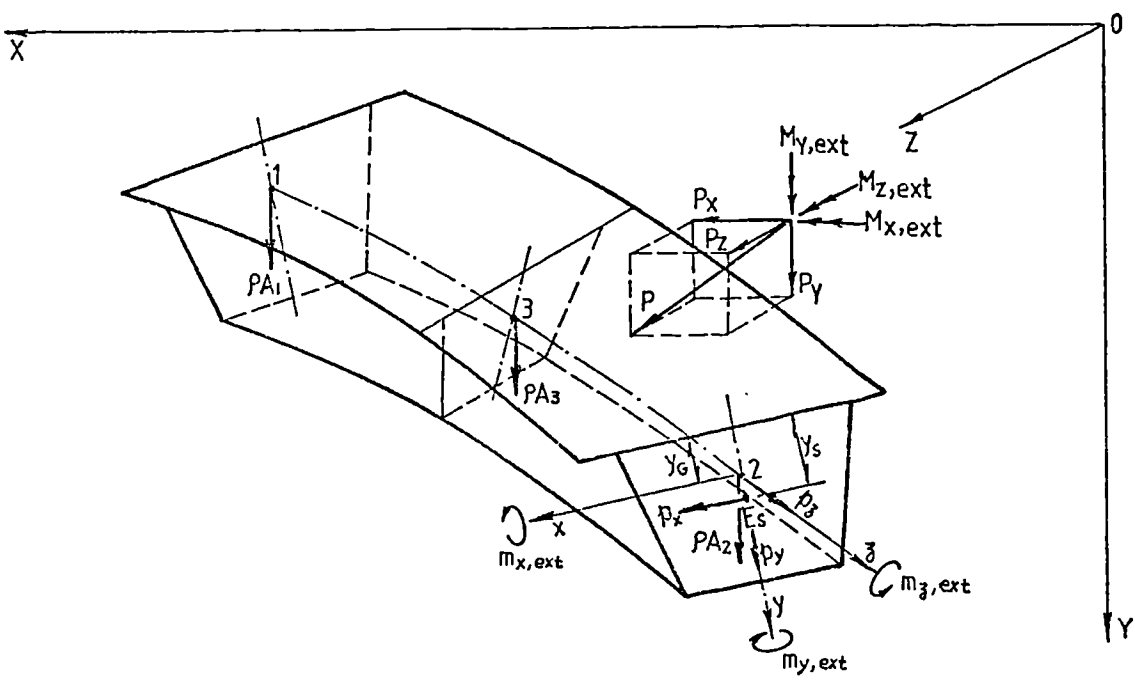


Fig. 4.8 Applied forces (bimoments and distortional moments are not shown)

## CHAPTER 5

## NUMERICAL EXAMPLES AND APPLICATIONS

5.1 Introduction

The objectives of this Chapter are first to demonstrate the reliability of the present analytical method relative to other methods or experimental studies and secondly to show its versatility.

A number of initial problems were analysed to check the theory as well as the computational procedure, CUBAS, and some of the results are reported herein. A subsequent series of applications of the analysis to cases of different types of box beam was investigated to establish the validity and generality of the proposed formulation. The influence of the number of diaphragms between supports on the warping stresses and transverse distortional bending stresses was also investigated.

5.2 Numerical examples5.2.1 A deep cantilever beam

The first problem to be considered was a relatively deep beam, Fig. 5.1. It was subjected to both uniformly distributed and concentrated loads. The beam was idealized either with two-node beam elements or with three-node beam elements for various discretizations. The deflections and bending moments are plotted for both loading cases (Figs. 5.1 and 5.2). The results agree very closely with the Engineer's theory of bending (141). Tip displacement results for several discretizations are also presented in Table 5.1. It can be seen that the three-node beam element results are vastly superior to the two-node beam elements especially for the case of concentrated load.

### 5.2.2 L-type cantilever load

The structure in Fig. 5.3 was analysed with a 4 element mesh using three-node beam elements and was subjected to both uniformly distributed and concentrated loads. The variations of displacements, bending moments and torsions are plotted in Figs. 5.3, 5.4, 5.5 and 5.6. These results demonstrate that the bending moments in the beam BC have been accurately transferred to torsion. The tip displacements in both loading cases include three components which can be calculated individually as follows:

Bending displacements,

$$\delta_B = 2 \times \frac{P_y \ell^3}{3EI_{xx}} = 0.28294146 \quad (\text{for concentrated load}),$$

$$\delta_B = 2 \times \frac{p_y \ell^4}{8EI_{xx}} + \frac{p_y \ell^4}{3EI_{xx}} = 2.47573777 \quad (\text{for distributed load}),$$

Shear displacements,

$$\delta_s = 2F_{s,y} \frac{P_y \ell}{GA} = 0.00589463 \quad (\text{for concentrated load}),$$

$$\delta_s = 2F_{s,y} \frac{p_y \ell^2}{GA} = 0.05894628 \quad (\text{for distributed load}),$$

Torsional displacements,

$$\delta_T = \frac{M_T \ell^2}{GJ_T} = 0.53051524 \quad (\text{for concentrated load}),$$

$$\delta_T = \frac{M_T \ell^2}{GJ_T} = 2.65257618 \quad (\text{for distributed load}).$$

Thus, their sums equal 0.81935 and 5.18726 respectively, which are identical to the computer solutions presented.

### 5.2.3 A semi-circular beam

The structure was subjected to a concentrated load and was idealized with a 4 element mesh using three-node beam elements. The variations of deflections, bending moments and torsions are plotted in Fig. 5.7. These

results demonstrate that the three-node beam elements can accurately accommodate very large curvatures, and the additional deflection due to shear which plays a significant part in the total deflection for this particular case.

#### 5.2.4 Dome structure

The dome structure shown in Fig. 5.8 was analysed using the three-node beam element. Since the structure is axi-symmetric, only one beam was analysed. A 4 element mesh was used to model the curve. The results are shown in Fig. 5.9, which correlate very closely with the solutions obtained using semiloof beam elements (95).

### 5.3 Application to the analysis of single-spined box beams

#### 5.3.1 A simply-supported box beam subjected to an eccentric live point load

To verify the validity of the inclusion of warping and distortion effects in the element formulation, a simply-supported box beam example given by Maisel and Roll (83) was considered first. The span  $L$  is 30 m and the diaphragms are located only at the ends where there is full torsional and distortional restraint. The diaphragms are assumed to offer no resistance to warping. At midspan there is a live point load of 1000 kN over one web as an approximate idealization of one bogie of an HB vehicle. Thin-walled box beam elements were used with an 8 element mesh to analyse the beam. Fig. 5.10 shows the geometry and loading, and Fig. 5.11 gives the bending moment, shear force and torsional moment diagrams due to live load.

Torsional warping as well as distortional warping effects are shown in Figs. 5.12 and 5.13 respectively. The torsional warping theory of Kollbrunner, Hajdin and Heilig (59, 57, 42), and the distortional warping theory based on the beam-on-elastic-foundation analogy, neglecting shear

deformation, (135, 134, 150), were used to obtain the solutions of Eq. 2.116 and Eq. 3.114 for comparison. The results agree very closely with the results of finite element method.

### 5.3.2 A fixed-ended box beam subjected to an eccentric live point load

As a second example, consider the beam and loading previously illustrated in Fig. 5.10, with the end conditions changed to fixed-ends, i.e., full restraint of bending, torsion and distortion. The live load torsional warping effects are shown in Fig. 5.14, and the distortion along the beam of internal stress resultants due to cross-sectional deformation is shown in Fig. 5.15. As in the case of the simply-supported beam, the finite element results are very close to the differential equation solutions.

As shown in Figs. 5.12 and 5.14, the total internal resistive torsional moment of a box beam is made up of a combination of St. Venant and Bredt shear stresses and torsional warping shear stresses. Note that the sum of their magnitudes remains constant at  $M_{z,ext}/2$  along each half span. In addition, the torsional warping stresses are highly localized in the longitudinal direction, as indicated in Figs. 5.12 and 5.14. However, the distortional warping stresses, shown in Figs. 5.13 and 5.15, are less localized longitudinally provided only magnitude is considered and the reversal of the sign of the solutions is ignored.

### 5.3.3 Simply-supported box beam example given by Vlasov

The third example examined is a simply-supported box beam considered initially by Vlasov (146). The span of the beam is 10 m, the depth 1200 mm and the width 700 mm. The wall thickness is 10 mm for vertical plates and 16 mm for horizontal plates. Poisson's ratio is assumed to be zero. The beam is loaded by a uniformly distributed load of 100 kg/m (981 N/m) applied in the plane of one of the vertical plates. Only one thin-walled box beam

element was used for each half of the beam. The maximum stresses for the cases of symmetrical and antisymmetrical load are shown in Figs. 5.16(a) and 5.16(b) respectively. Fig. 5.16(c) shows the composition of the stresses. Mikkola and Paavola in Ref. 90 have analysed the same problem using a special type of finite element with a twenty-element mesh. Both Vlasov's and Mikkola's results are shown in parentheses for comparison.

#### 5.3.4 Simply-supported box beam example given by Křistek

Another simply-supported box beam with a span of 262.47 ft (80.05 m), discussed by Křistek (63), is further considered. Mikkola and Paavola have also provided results for the same beam (90).

The cross-section and the uniformly distributed loading are shown in Fig. 5.17(a). The Young's modulus is taken as 4500 kip/sq.in ( $31.05 \text{ kN/mm}^2$ ), and Poisson's ratio as 0.15. The example was solved by the method described in this thesis using two box beam elements for each half of the beam whereas 10 elements were necessary in Mikkola's and Paavola's method in Ref. 90. The deformed shape of the cross-section at midspan is shown in Fig. 5.17(b). Figs. 5.17(c) and Fig. 5.17(d) show the longitudinal warping stresses and transverse bending moment diagrams at midspan respectively. The results from Ref. 63 and Ref. 90 are also given in parentheses in each figure. The agreement between the results obtained by the different methods is quite satisfactory.

#### 5.3.5 Sawko and Cope's simply-supported box girder model

A simply-supported box girder model with cantilever slabs, fabricated from perspex sheets, was tested by Sawko and Cope (20, 118, 119). The span of the model was 60 in. (1524 mm) and the cross-section was as shown in Fig. 5.18. An asymmetrical point load of 224 lb (0.9968 kN) producing torsional effects applied at midspan above the web was considered. The same

problem has also been considered or referred to in Refs. 50, 85 and 90. Since these existing results vary considerably, it is difficult to make a satisfactory comparison. Thus, we here recalculate this problem by using, for further comparison, the LUSAS finite element system (79, 80).

The finite elements chosen in the LUSAS system are the flat thin shell box elements (SHI6) each with six nodes, taking account of both membrane (in-plane) and flexural (out-of-plane) deformations. In order to ensure that the boundary conditions are the same for the present study four node thin shell box elements (SHI4) are also employed as the diaphragms resisting torsional and distortional deformations of the cross-sections at the end supports. The finite element idealization of the model is shown in Fig. 5.19 in which 84 elements are used.

Eight thin-walled box beam elements were used for the whole beam in the present study. Mikkola and Paavola (90) however, calculated the same box girder using a thirty element mesh. In order to consider the shear lag effect, effective breadth ratios are used from Table 2.1 (93, 13, 18).

Fig. 5.20 displays the deformed shape of the cross-section at midspan. Good agreement between the present results and the LUSAS results is evident. The longitudinal membrane stresses are shown in Fig. 5.21(a), and the longitudinal warping stresses and the transverse bending stresses at the outer surface at midspan are shown in Fig. 5.21(b) and Fig. 5.21(c) respectively. A close agreement for practical engineering purposes is evident between the results obtained from the box beam elements and from the LUSAS program.

#### 5.3.6 Tapered box girder models given by Křistek

The box girder analyses and experiments carried out by Křistek (62) to illustrate the two steps in his elastic procedure, were selected as a further example to verify the present work.

Křistek did the experiments on tapered celluloid box girder models with fixed ends. The models are shown in Figs. 5.22 and 5.23. The span of the first model is 24 in. (610 mm), and the width is 1.6 in. (40.6 mm), while the depth varied parabolically from 3.2 in. (81.3 mm) to 7.2 in. (182.9 mm). The second beam had a span of 48 in. (1220 mm), a width of 4 in. (102 mm), and a depth which varied parabolically from 4.7 in. (119 mm) at the supports to 3.2 in. (81.3 mm) at midspan. The wall thicknesses were constant at 0.12 in. (3.05 mm) throughout both models. The modulus of elasticity was 500,000 psi ( $3.45 \text{ kN/mm}^2$ ) and Poisson's ratio was 0.33.

In the first step of Křistek's analysis, the box was assumed to have no transverse distortion. The stiffness of the cross-section for the first model was ensured by means of diagonal cross braces at regular intervals. The girder was loaded at both ends by couples, the value of which was 125 in.-lb (14.13 m-N) and the ends were fixed to prevent warping.

In the present study an analysis was carried out using 15 thin-walled beam elements. The variation of the longitudinal warping stresses in one of the corners is plotted in Fig. 5.24 together with results obtained by Křistek (62).

The second step of Křistek's method consisted of analysing the box girder for transverse distortion. The girder was loaded by a pair of distributed loads along the diagonal of the box. The load had a constant vertical component of 0.716 lb/in. (125 N/m) and its horizontal component varied parabolically from 0.609 lb/in. (106.5 N/m) at the supports to 0.895 lb/in. (156.6 N/m) at midspan.

Three elements for each half of the beam were used in the present solution. Bažant and El Nimeire (9) also used the same models as illustrative examples. The vertical deflections at the corner point for all the comparable methods are given in Table 5.2, together with Křistek's experimental

results. Graphical comparisons are also shown in Fig. 5.25. Agreement was found to be good.

### 5.3.7 A double-cell box beam under twisting loads

The distortional and torsional behaviour of a box beam with a trapezoidal double-cell cross-section has been demonstrated by the analysis of a simply-supported prestressed concrete bridge given by Richmond (104, 106). The span of the box beam is 200 ft (61 m) and the trapezoidal cross section is shown in Fig. 5.26(a). Twisting loads of 40 kips (178 kN) are applied at midspan. The modulus of elasticity is  $3 \times 10^6$  kip/sq.in. ( $20.7 \text{ kN/mm}^2$ ) for  $G/E = \frac{1}{2}$ .

Eight thin-walled box beam elements were used for the present analysis. Finite element analysis by means of the LUSAS program was also carried out for comparison. Figs. 5.26(b), 5.26(c) and 5.26(d) show the solution of the example compared with the stresses and deflections of a finite element solution using thin shell elements. It can be seen that fairly good results are given by the present study compared with the finite shell element analysis.

### 5.3.8 A two-span 3-cell box-bridge given by Scordelis and Davis

Fig. 5.27(a) shows a two-span three-cell box-bridge with no overhangs but with rigid diaphragms provided at all support sections. The cross-section of the 3-cell structure is depicted in Fig. 5.27(b). A 1000 lb (4450 N) line force, concentrated over 1 ft (305 mm) longitudinally and applied over one exterior web at the centre of each span, comprised the loading. The material properties are also indicated in Fig. 5.27.

The bridge was first analysed by Scordelis and Davis (126) to study the efficiency of the computer programs which they had developed using the folded plate theory compared with the finite element and finite segment

approaches. The two span box bridge has also been analysed by Loo and Cusens using the program COSBOB based on the finite strip approach(77). For the present method, separate computer analyses were performed again by the finite element method with either a thin-walled box beam element mesh or a thin shell element mesh. Results by the LUSAS program are considered exact for purposes of comparison in order to assess the relative accuracy of the present method. Longitudinal symmetry of loading permitted treatment of only one fixed-simple span by the two methods. The concentrated line load is simulated by a narrow patch load. Eight box beam elements were used for the present study, while a total number of 140 shell elements were used for the LUSAS analysis.

Vertical deflections at the top of the loaded web are shown in Fig. 5.28. The vertical deflections are generally the least sensitive of the results obtained and the present approach produced deflections comparing favourably with those of the finite shell element analysis.

The longitudinal distribution of longitudinal in-plane stresses near the box corner is plotted in Fig. 5.29 for each of the two analyses. A typical plot of the transverse slab moments is shown in Fig. 5.30. Although the breadth of the box-bridge in relation to its length is not suitable for approximating the substructure as a single-spined beam, the figures indicate general agreement among results for the two methods except in the vicinity of the concentrated load. The thin-walled beam solution appears to underestimate the stresses under the applied load.

#### 5.3.9 A simply-supported single-box girder bridge curved in plan

As a final example, this box-bridge illustrates the versatility of the present theory for describing the structural behaviour of box beams including those of curved spine-beam bridges. The curved box-bridge was

initially presented by Meyer to illustrate the validity of the curved strip theory and of the computer program CURSTR (87). By means of the program CURSTR it is possible to analyse prismatic folded plate structures curved in plane and simply-supported along their straight radial edges.

The dimensions of the curved box girder are shown in Fig. 5.31(a). The modulus of elasticity is  $432 \times 10$  kip/sq.ft ( $20.69 \text{ kN/mm}^2$ ), and the Poisson's ratio is 0.15. The girder is subjected to a single concentrated 1 kip (4.45 kN) load at midspan over the outer web.

The present analysis was carried out by using box beam elements with an eight element mesh. The state of stress in the curved single-box girder bridge is plotted in Fig. 5.31(b) and Fig. 5.31(c) together with the values obtained by computer programs LUSAS and CURSTR respectively. It can be seen that fairly good results are given by the present study. The only significant difference in transverse moments is in the region of the local disturbance at point loads. The difference in transverse bending moments between the present study and the finite element solution is due to local plate bending of the cantilever.

#### 5.4 Box beam diaphragms

In the present analysis of box beams, the diaphragm is assumed to be rigid in its own plane and absolutely flexible normal to that plane. Thus, the diaphragm prevents the deformation of shape of the cross-section in which it is placed, but does not induce any bimoment effects.

Diaphragms may be classified according to their position into support diaphragms and intermediate ones. Accordingly, they have a somewhat different effect on the behaviour of the box beam.

The support diaphragms prevent deformation of the cross-sectional shape

at supports, and consequently reduce significantly the transverse distortional bending stresses and the longitudinal normal stresses which are caused by torsion accompanied by a deformation of the cross-sectional shape. The intermediate diaphragms also reduce the deformability of the cross-sectional shape, but their influence manifests itself differently both with regard to longitudinal warping stresses and also to transverse distortional bending stresses.

An analysis based on the box beam given by Krístek (Example 5.3.4) was carried out with different numbers of rigid diaphragms located between end supports. The relative values of the longitudinal warping stresses and transverse distortional bending stresses vary in accordance with the number of intermediate diaphragms in the curve shown in Fig. 5.32. All values in the diagram refer to the values for the girder which is provided with rigid support diaphragms only and is used as the datum for comparison. The transverse distortional bending stresses as well as the warping stresses decrease rapidly with an increasing number of rigid diaphragms between supports.

Actually, on the basis of the calculations for many practical and possible cases of box beams with different numbers of intermediate diaphragms, carried out by Krístek, there are four different types of curves showing the influence of the number of diaphragms between supports on the warping stresses and transverse distortional bending stresses (Ref. 63 and Fig. 5.33).

The type of curve in each case depends on the length of the box beam and on the dimensions of the cross-section. For a symmetrical rectangular cross-section Krístek gave the following formula for determining a critical distance of transverse rigid diaphragms, for which the warping stresses are maximum (63).

$$L_{cr} \doteq 0.844 \sqrt{[b_t^2 h^2 (ht_h + b_t t_t) (\frac{h}{t_h^3} + \frac{b_t}{t_t^3})]} \quad (5.1)$$

On the basis of the known value of  $L_{cr}$  it is possible to decide which type of behaviour (see Fig. 5.32) a box beam under consideration exhibits. The following approximate rules may be obtained (63):

Fig. 5.32(a) corresponds to  $L \leq L_{cr}$ ,

Fig. 5.32(b) corresponds to  $L_{cr} < L < 2L_{cr}$ ,

Fig. 5.32(c) corresponds to  $L \approx 2L_{cr}$ ,

Fig. 5.32(d) corresponds to  $2L_{cr} < L < 3L_{cr}$ .

### 5.5 Conclusion

The various applications successfully presented in this chapter demonstrate that the general one-dimensional finite element system has been implemented correctly. The results have been compared with analytical solutions or with other types of elements such as flat thin shell elements. Good agreement generally exists between the results obtained. The thin-walled box beam element together with a transverse frame analysis give an economical approach for the analysis of straight or curved single-spined box beams with variable cross-sections and different boundary conditions having sufficient accuracy for preliminary design purposes. Additional verification for the present approach, using model test results, will be presented in Chapter 8.

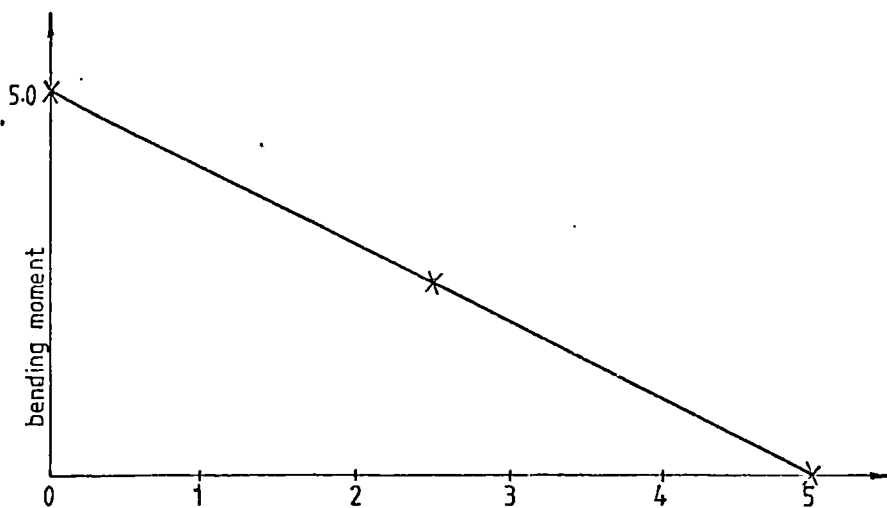
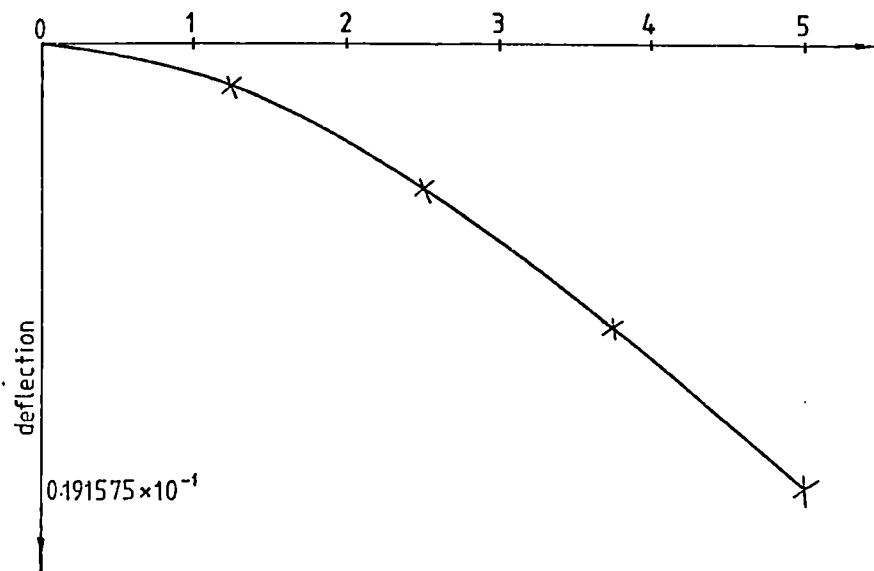
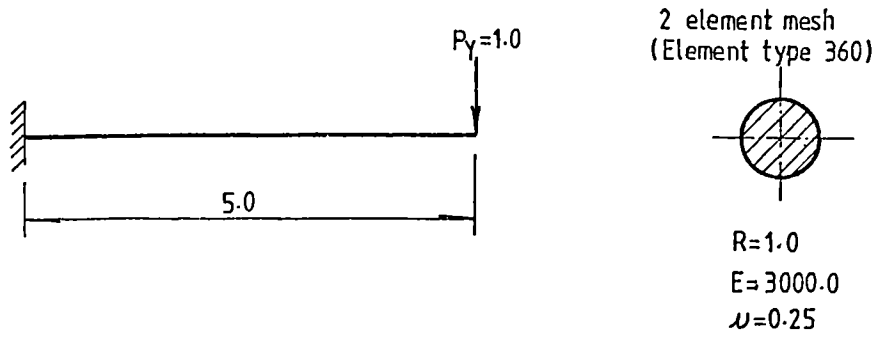


Fig. 5.1 A deep cantilever beam subjected to concentrated load

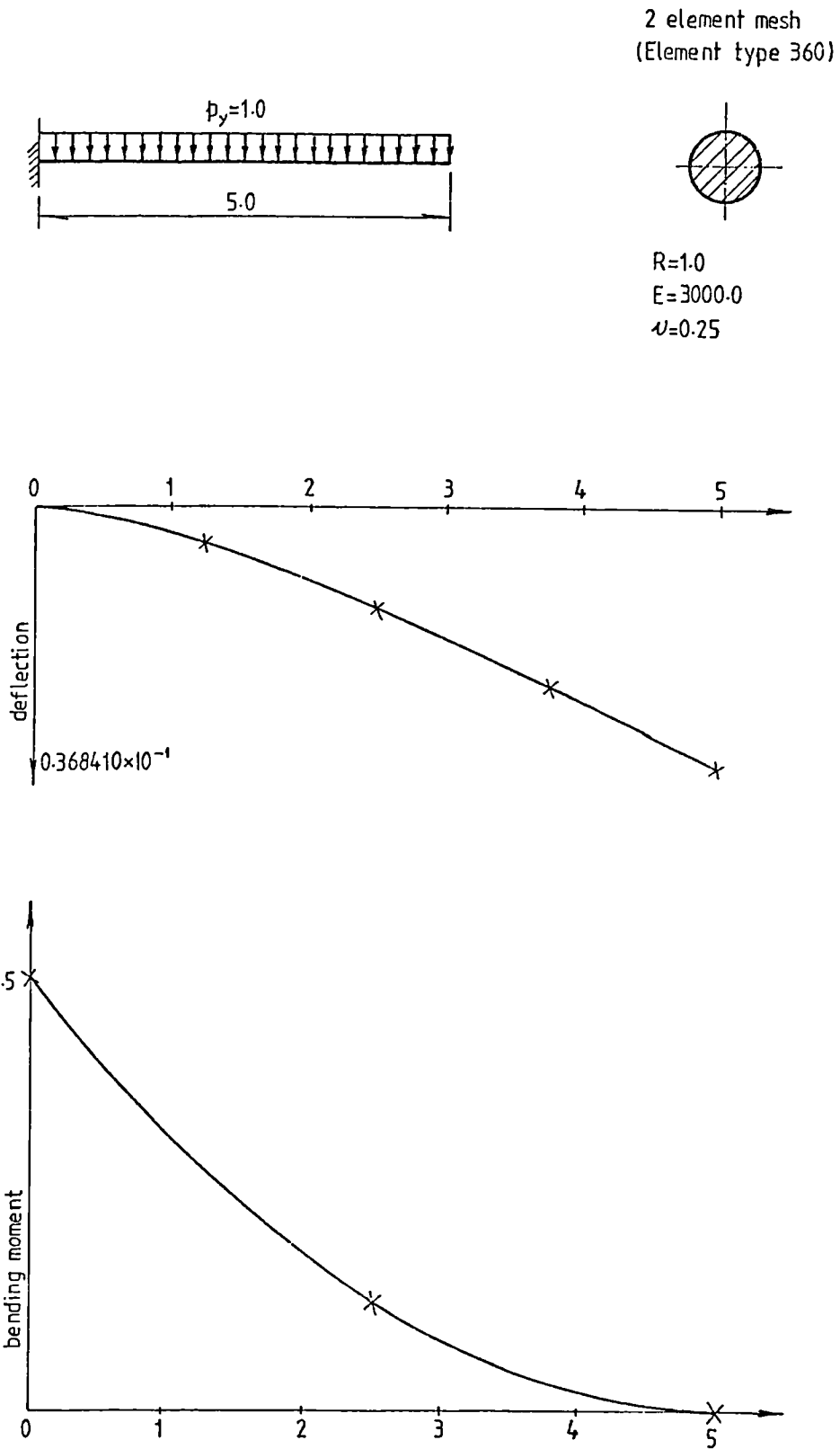


Fig. 5.2 A deep cantilever beam subjected to uniformly distributed load

Number of elements	Concentrated load case		Uniformly distributed load case	
	Tip displacement two-node beam element	Tip displacement three-node beam element	Tip displacement two-node beam element	Tip displacement three-node beam element
1	0.01474	0.01916	0.03684	0.03684
2	0.01805	0.01916	0.03684	0.03684
4	0.01888	0.01916	0.03684	0.03684
8	0.01909	0.01916	0.03684	0.03684
16	0.01914	0.01916	0.03684	0.03684
Solutions from the Engineer's theory of bending	$\delta_B = \frac{P_y \ell^3}{3E_{I_{xx}}} = 0.017684$ $\delta_S = \frac{P_y \ell}{F_{sY} GA} = 0.001474$ $\delta = \delta_B + \delta_S = 0.01916$		$\delta_B = \frac{P_y \ell^4}{8E_{I_{xx}}} = 0.0331572$ $\delta_S = \frac{1}{2} \frac{P_y \ell^2}{F_{sY} GA} = 0.0036841$ $\delta = \delta_B + \delta_S = 0.03684$	

Table 5.1 Tip displacement for a deep cantilever beam

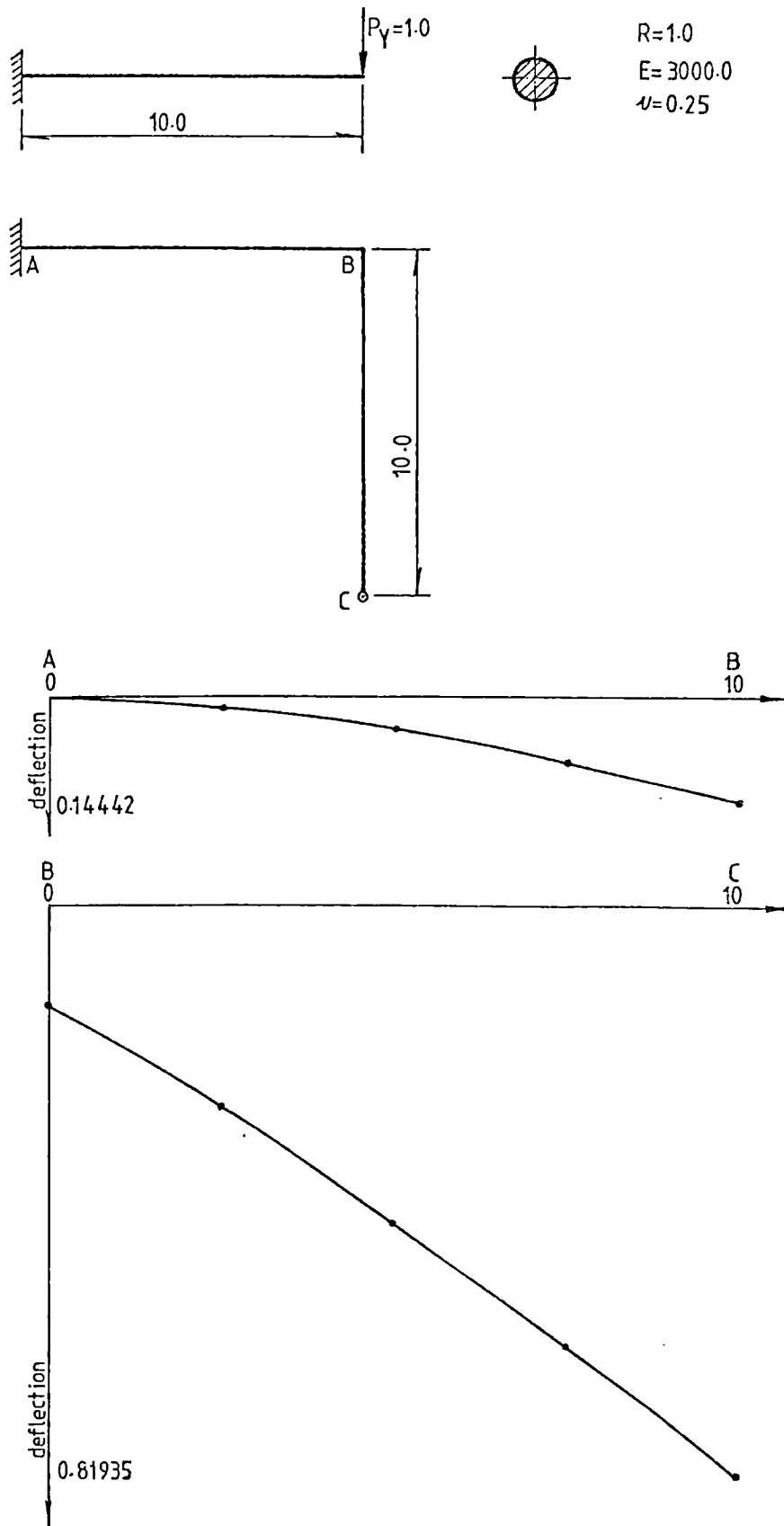


Fig. 5.3 Deflections of an L-type frame subjected to concentrated load

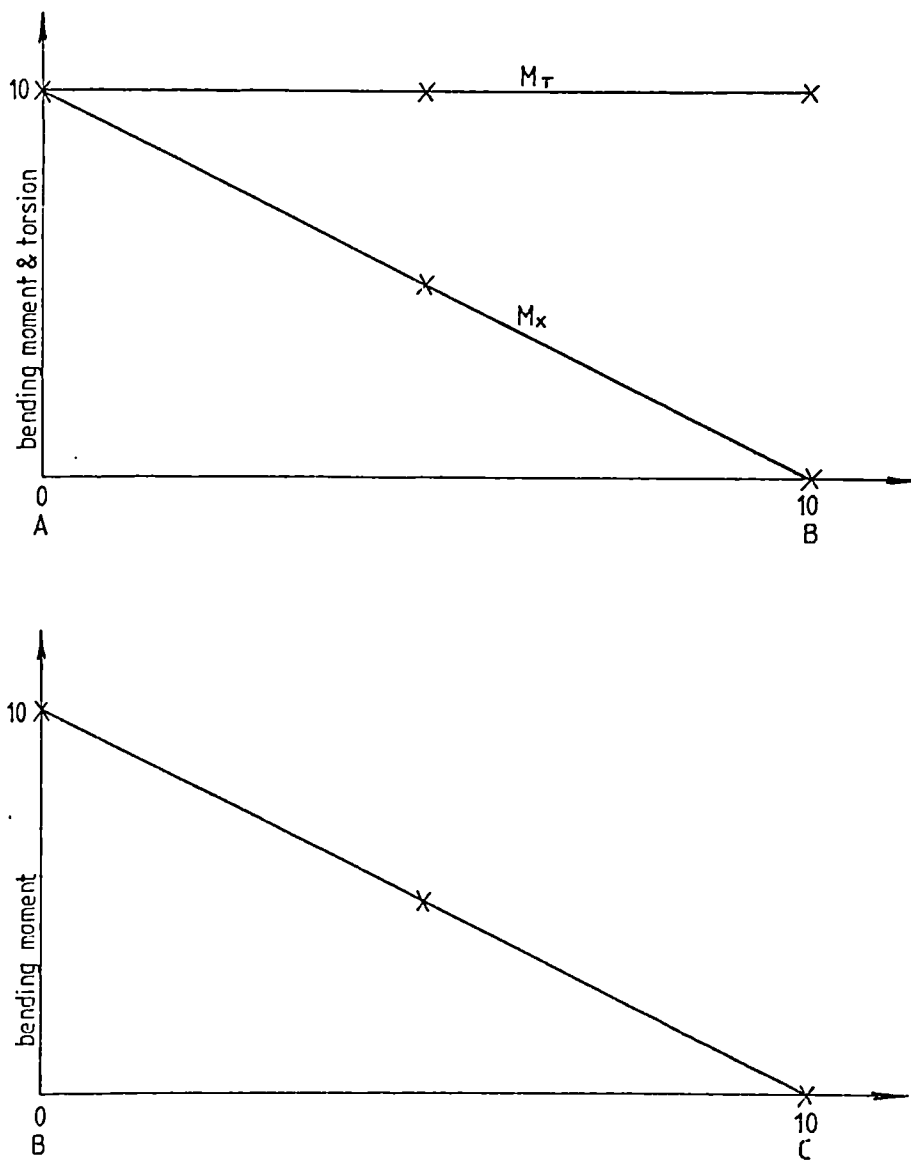


Fig. 5.4 Bending moment and torsion of an L-type frame subjected to concentrated load

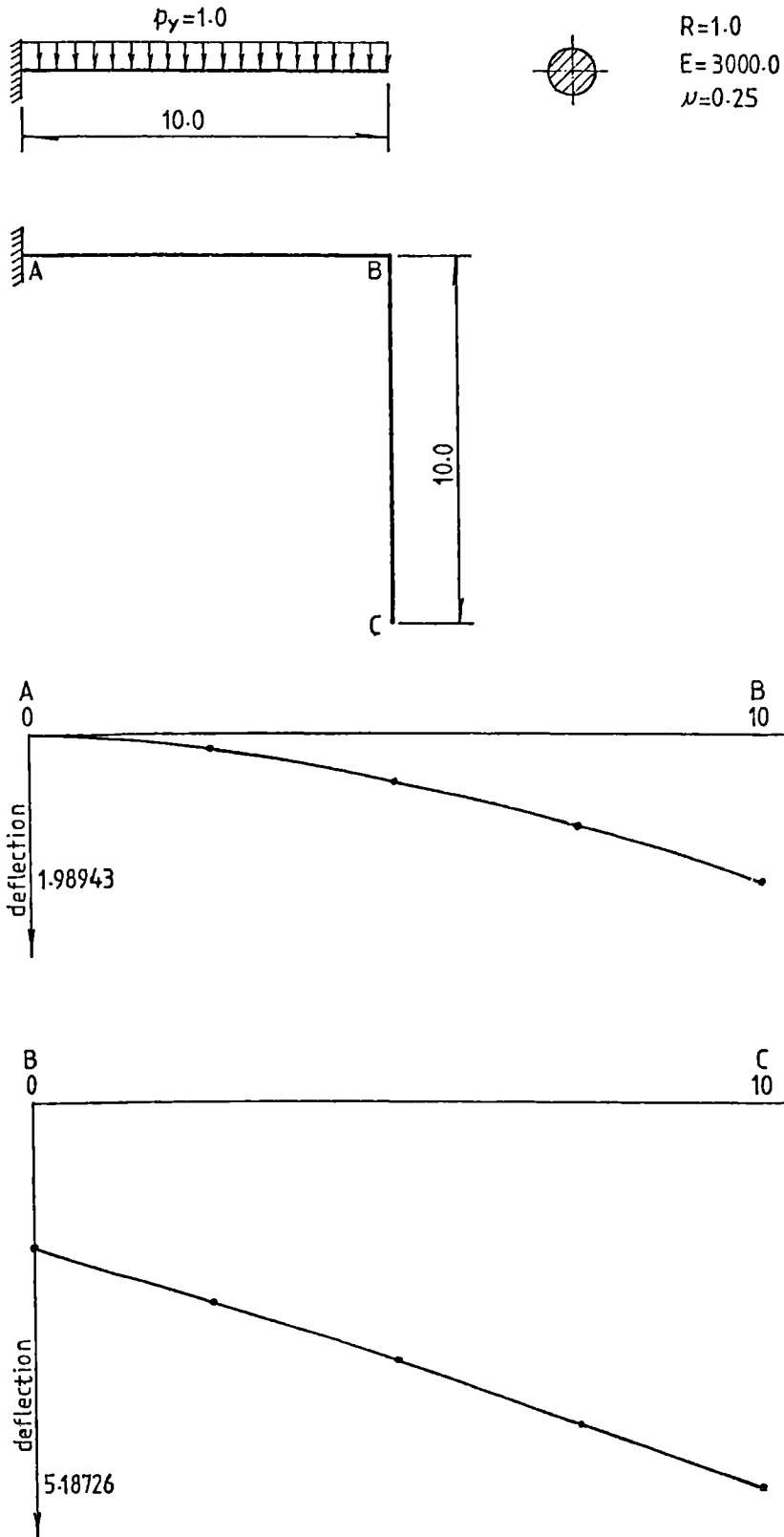
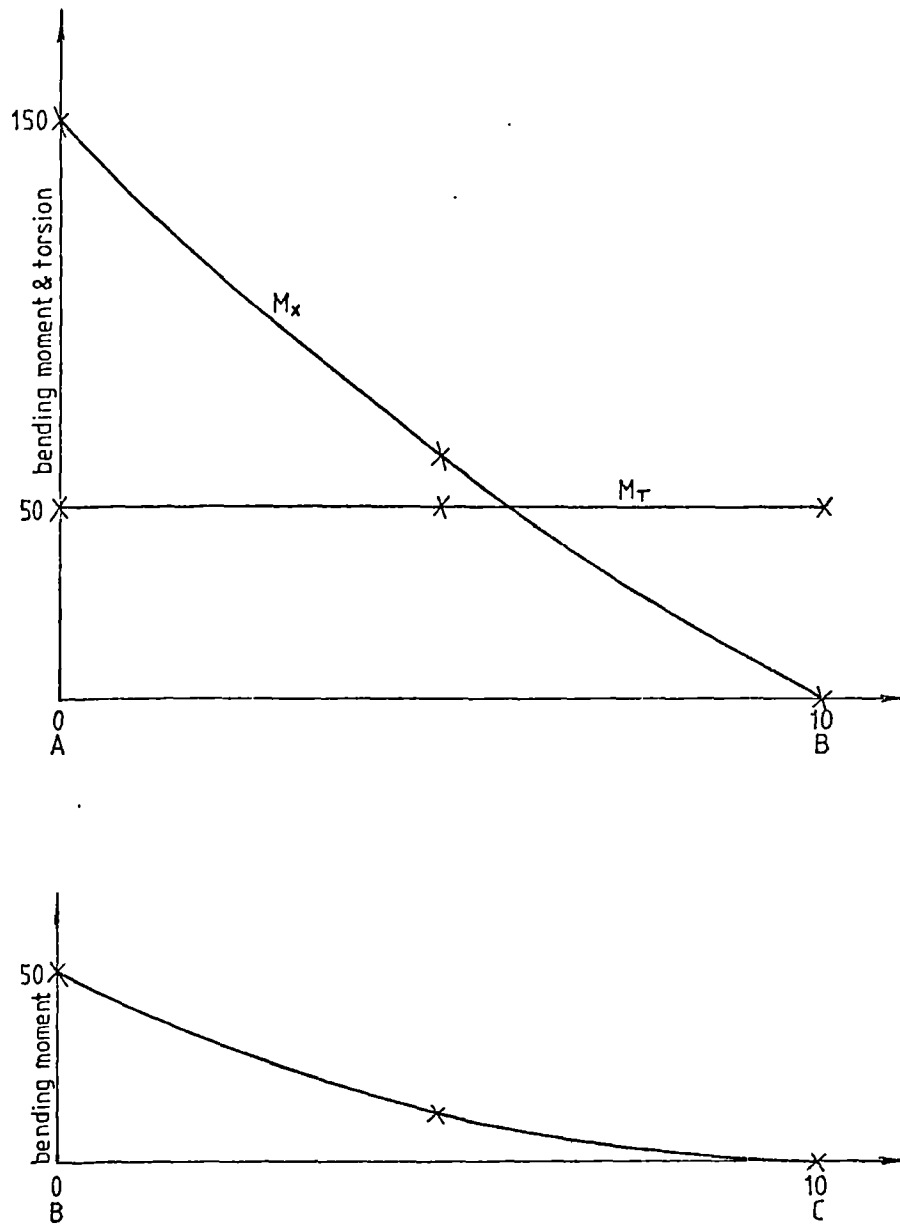


Fig. 5.5 Deflections of an L-type frame subjected to uniformly distributed load



ig. 5.6 Bending moment and torsion of an L-type frame subjected to uniformly distributed load

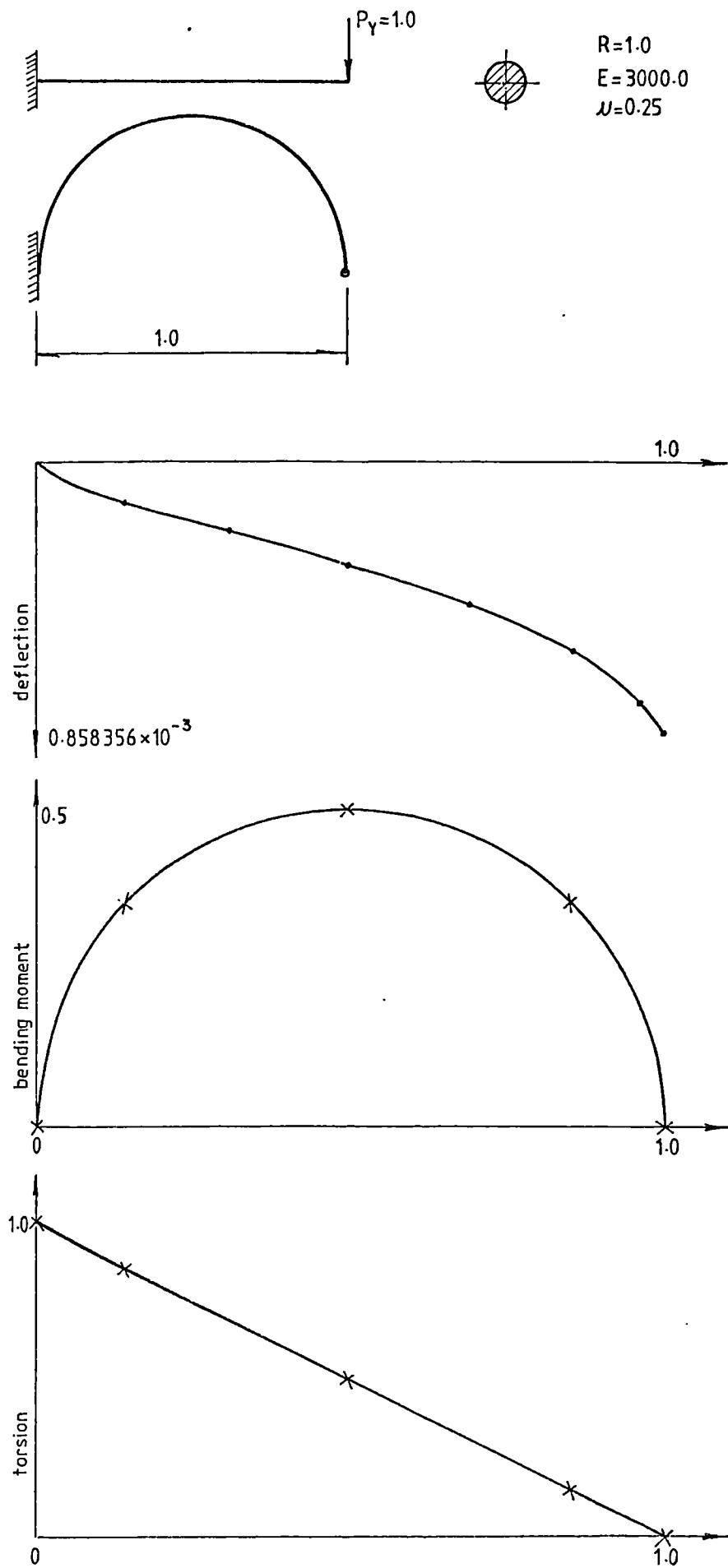


Fig. 5.7 A semi-circular beam subjected to concentrated load

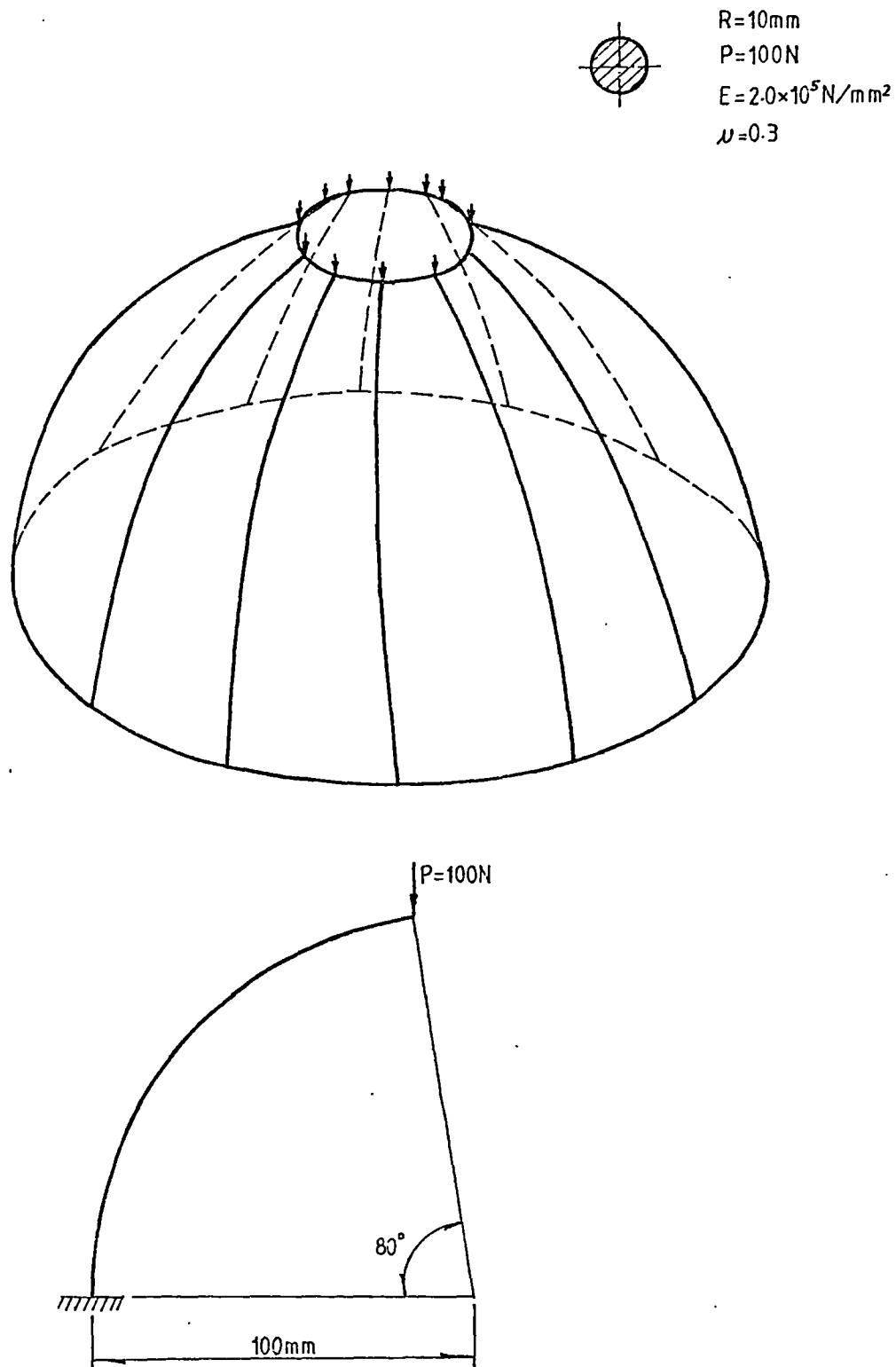


Fig. 5.8 A dome structure

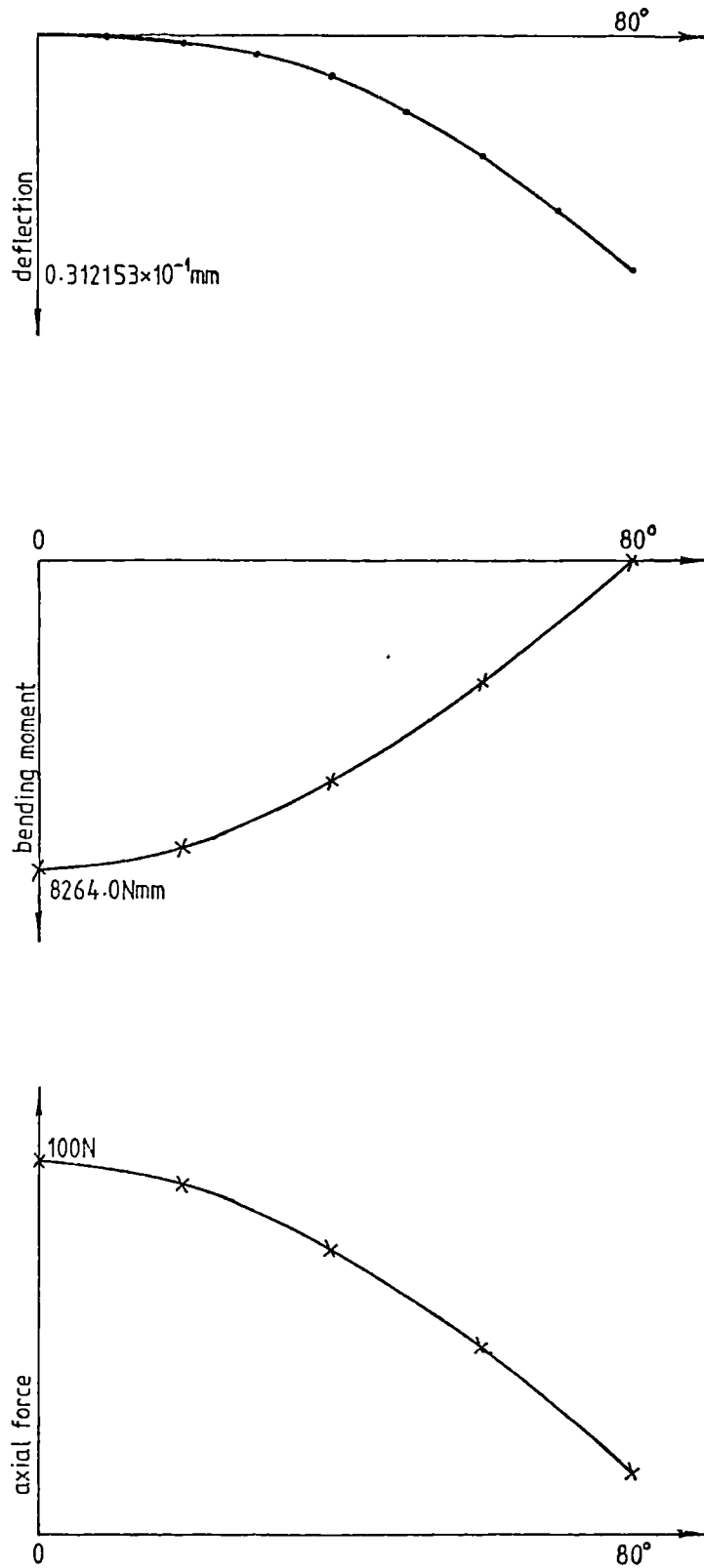
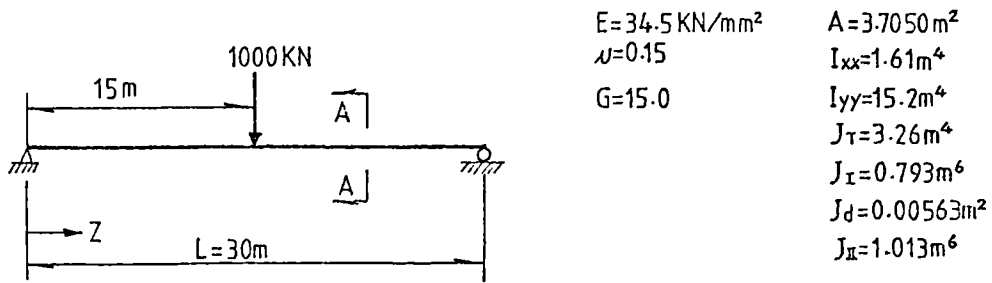
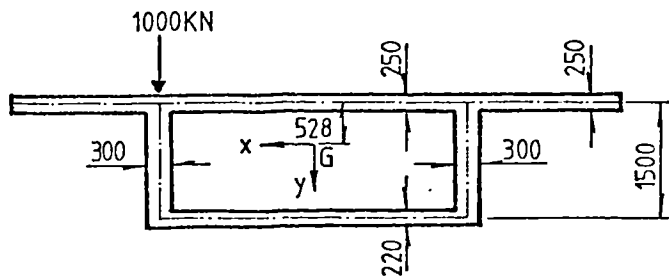


Fig. 5.9 Variations of the deflections, bending moments and axial forces of a dome structure

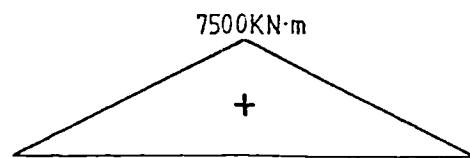


(a) Elevation of beam

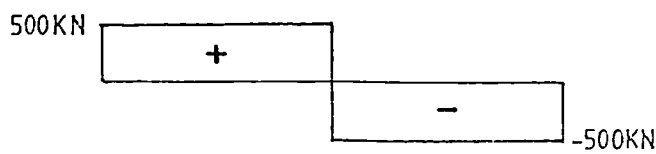


(b) Section A-A (Dimensions in mm)

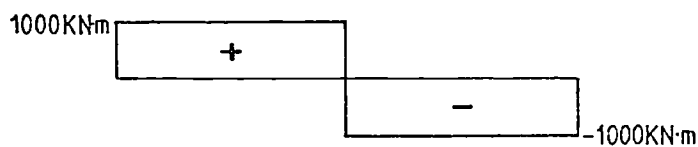
Fig. 5.10 Loading and geometry



(a) Bending moment diagram

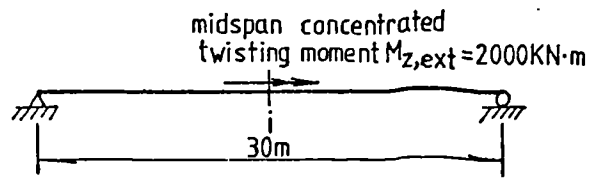


(b) Shear force diagram

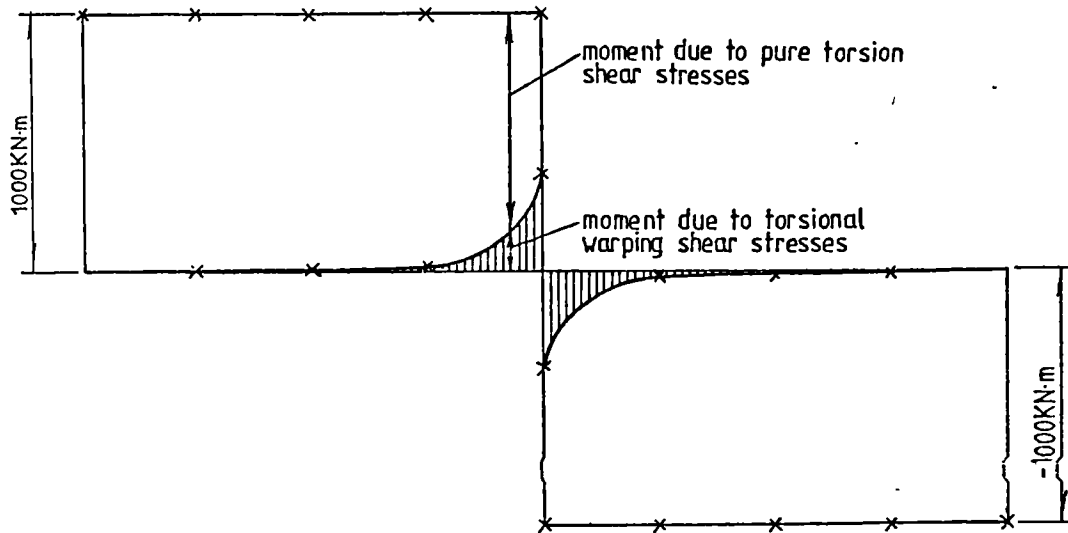


(c) Torsional moment diagram

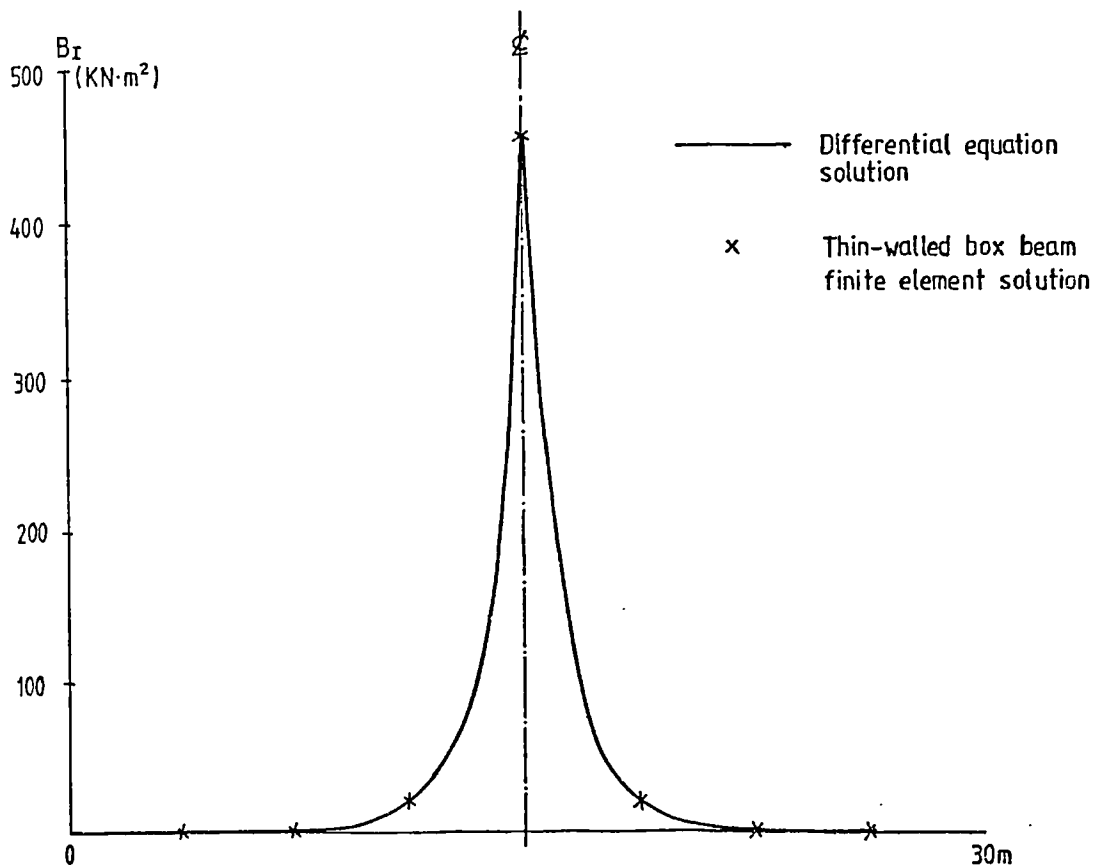
Fig. 5.11 Bending moment, shear force and torsional moment diagrams due to live load



(a) Elevation of beam  
(Torsional restraint at supports but no warping restraint)

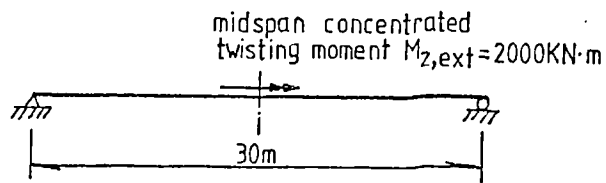


(b) Distribution along beam of internal torsional moments



(c) Torsional warping bimoment distribution along beam

Fig. 5.12 Distribution along beam of internal stress resultants due to warping torsion



(a) Elevation of beam  
(Distortional restraint at supports but no warping restraint)

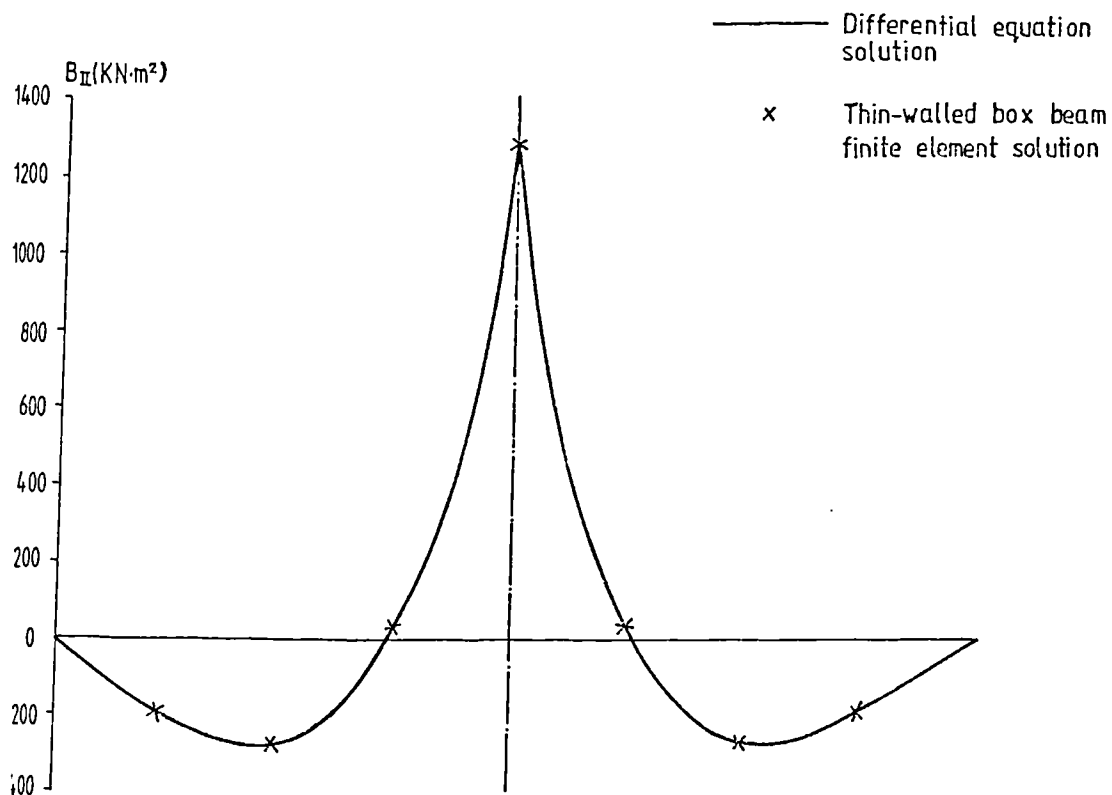
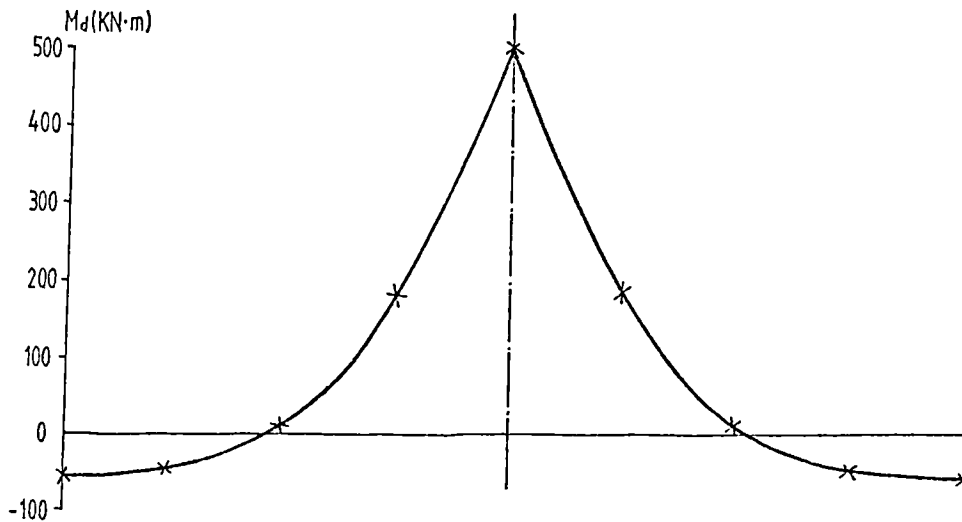
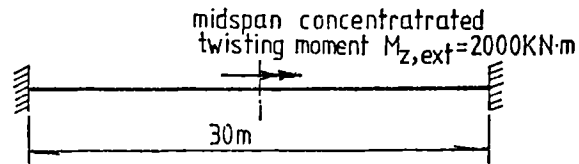
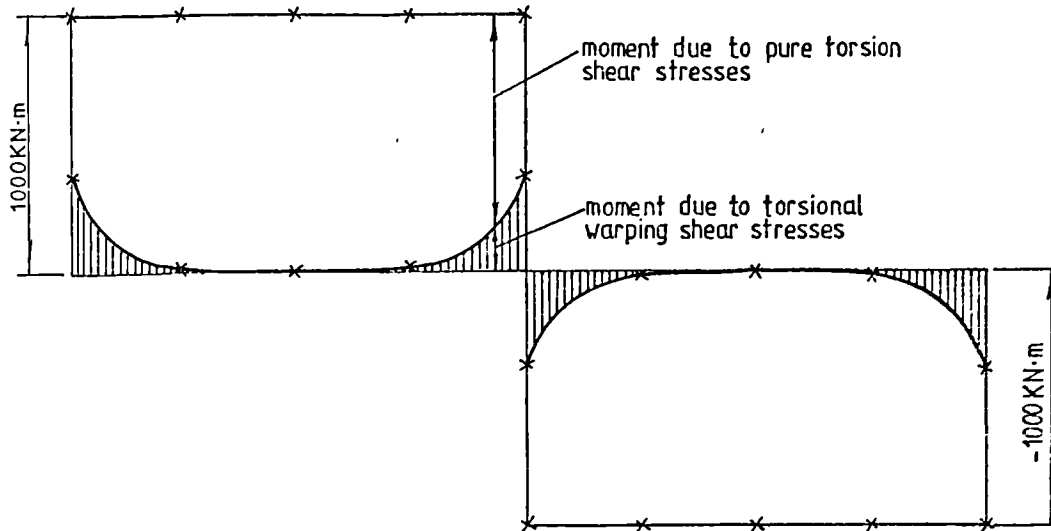


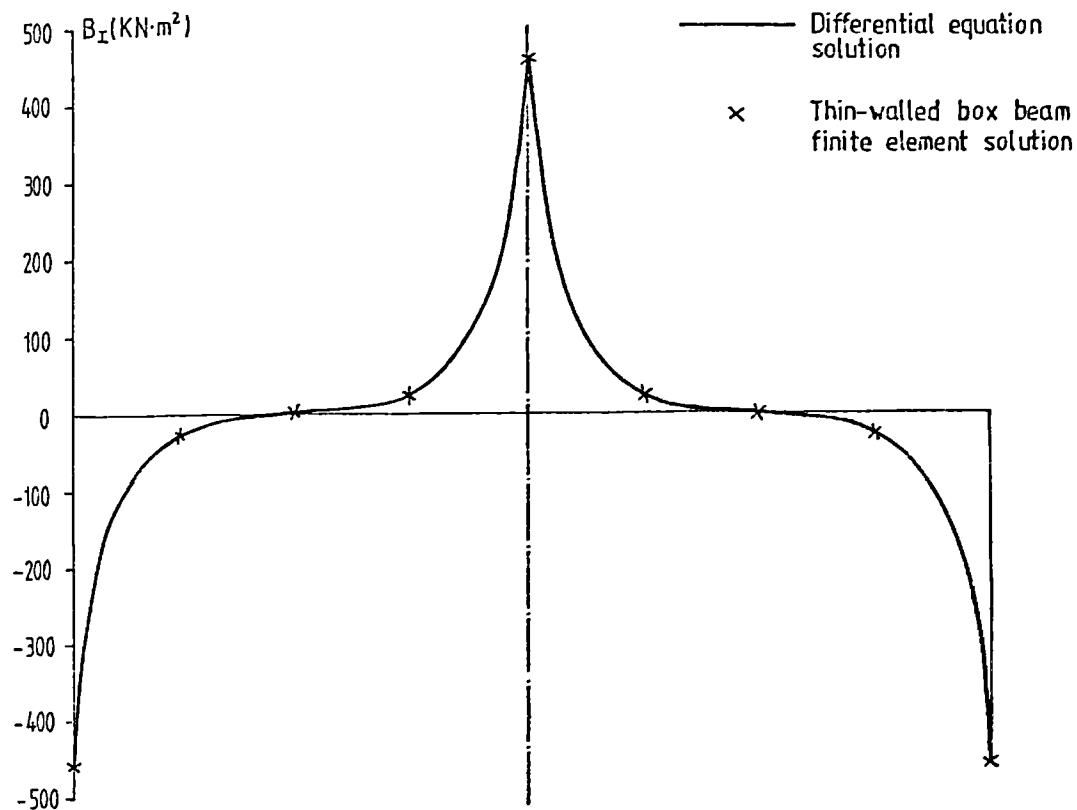
Fig. 5.13 Distribution along beam of internal stress resultants due to deformation of the cross-section



(a) Elevation of beam  
(Full torsion and warping restraint at both supports)

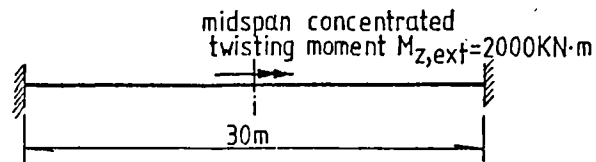


(b) Distribution along beam of internal torsional moment

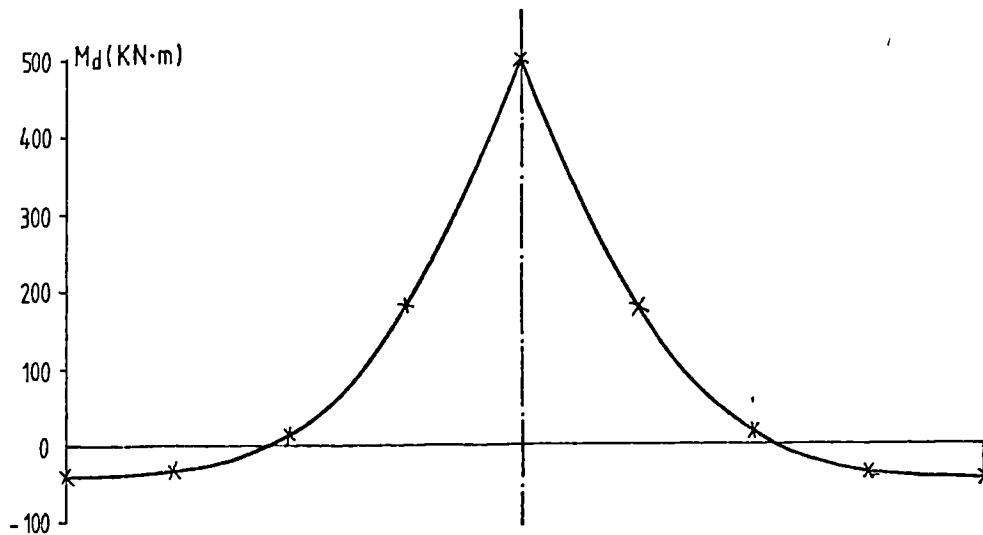


(c) Torsional warping bimoment distribution along beam

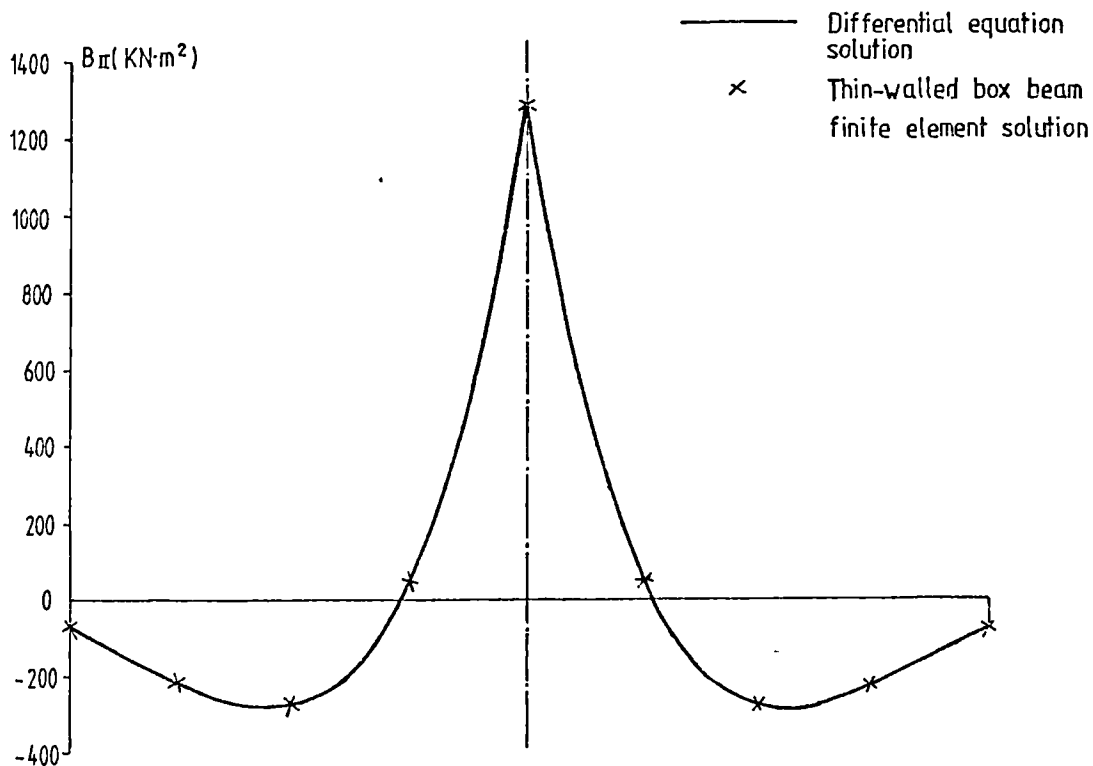
Fig. 5.14 Distribution along beam of internal stress resultants due to warping torsion



(a) Elevation of beam  
(Full distortion and warping restraint at both supports)



(b) Distortional moment ( $B'_{II}$ ) distribution along beam



(c) Distortional bimoment distribution along beam

Fig. 5.15 Distribution along beam of internal stress resultants due to deformation of the cross-section

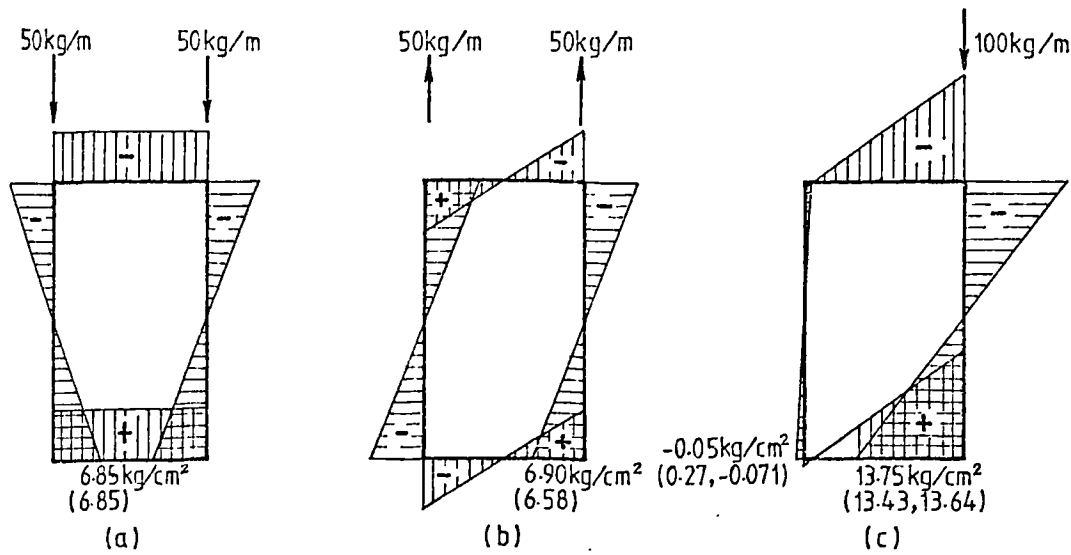


Fig. 5.16 Results for example from Ref. 146:

- (a) Longitudinal stresses due to symmetrical load at mid-span;
- (b) Longitudinal warping stresses due to antisymmetric load at midspan;
- (c) The total longitudinal stresses at midspan.

Values in parentheses are from Ref. 146 and Ref. 90 (1kg=9.81N)

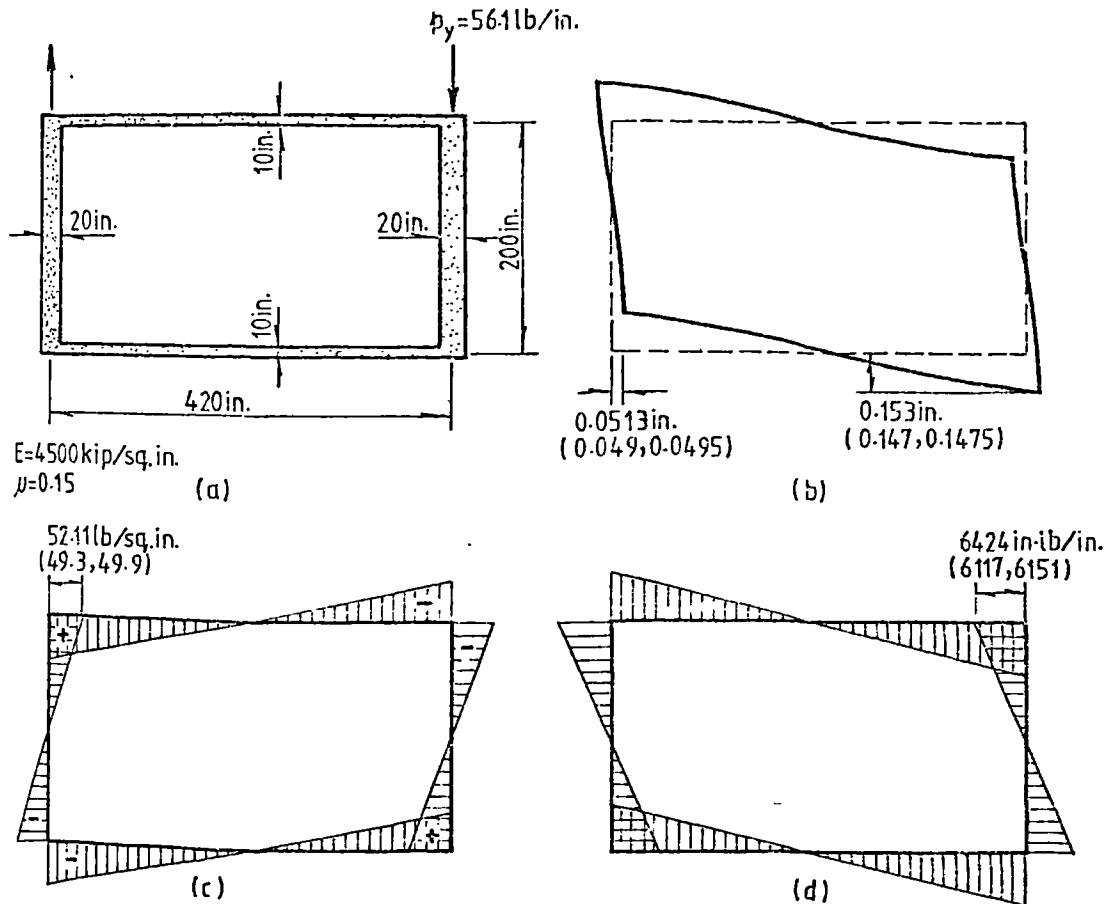
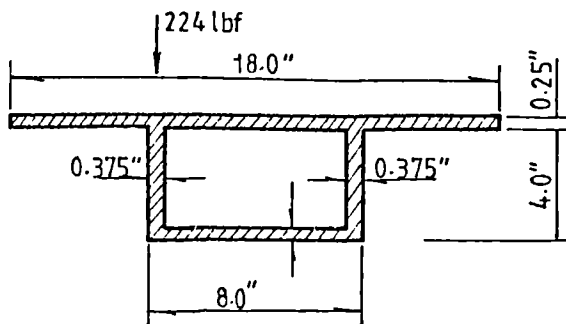


Fig. 5.17 Results for example from Ref. 63: (a) Cross-section and loading; (b) Shape and displacement of the deformed cross-section at midspan; (c) Longitudinal warping stresses in the cross-section at midspan; (d) Transverse bending moments at midspan. Values in parentheses are from Refs. 63 and 90 respectively. (1 in. = 25.4 mm; 1 lbf = 4.45N; 1 kip = 4.45 kN).



$E=3.9 \times 10^5$  psi  
 $\nu=0.40$

Fig. 5.18 Cross-section of Sawko and Cope's box girder model  
 (1 in. = 25.4 mm; 1 lbf. = 4.45 N)

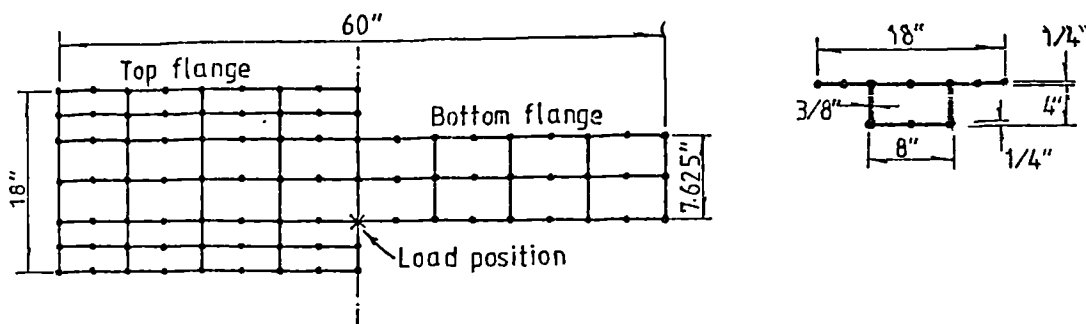


Fig. 5.19 Idealization of Sawko and Cope's box girder model using thin shell finite elements  
 (1 in. = 25.4 mm; 1 lbf. = 4.45 N)

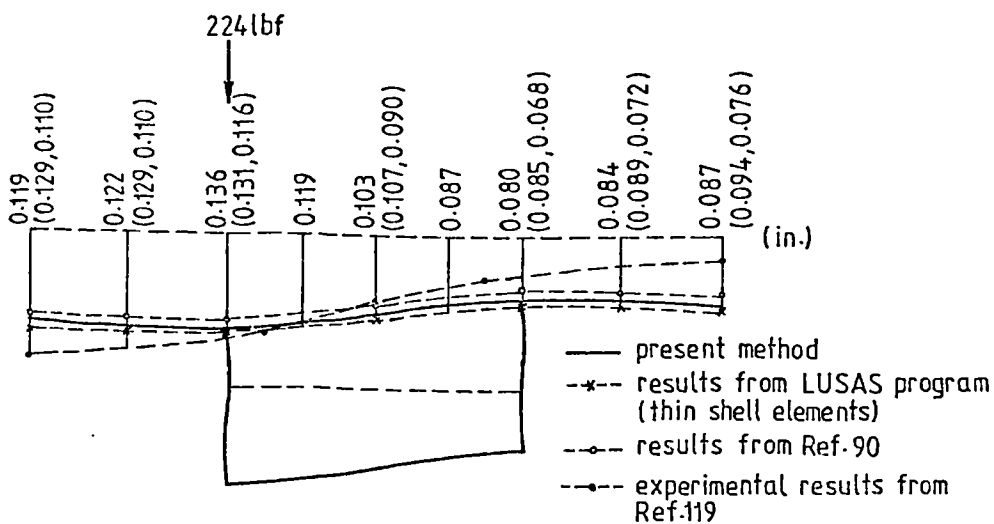
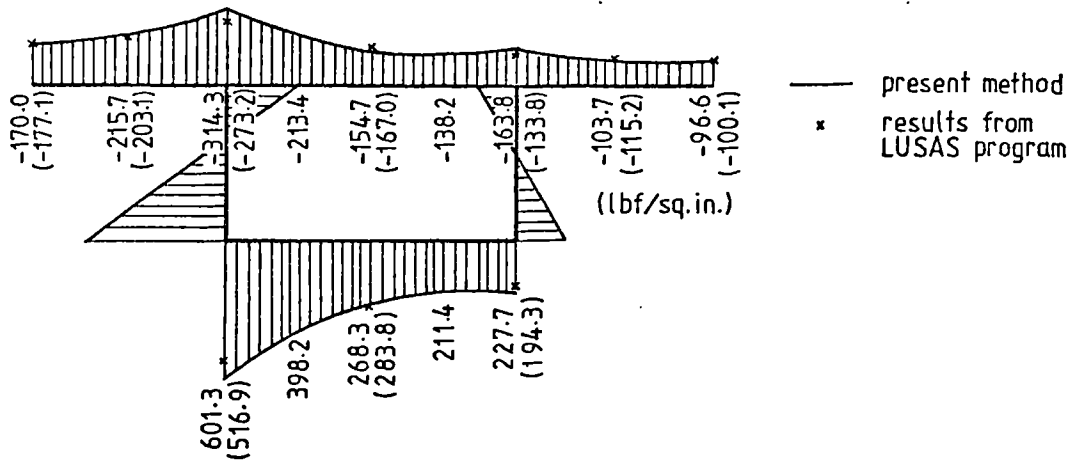
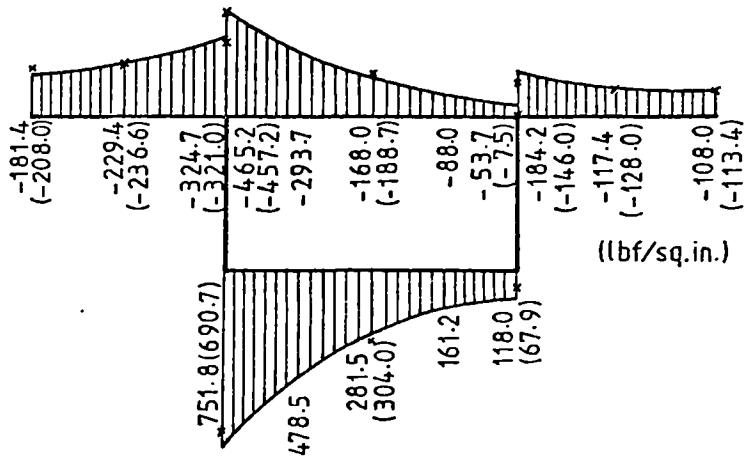


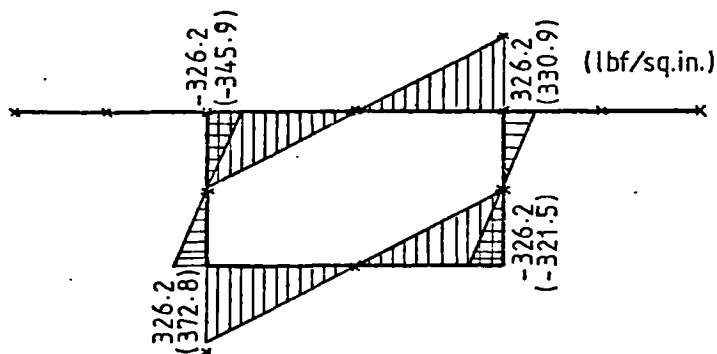
Fig. 5.20 Shape of Deformed Cross-Section at Midspan  
 (1 in. = 25.4mm; 1 lbf. = 4.45 N)



(a) Longitudinal membrane stresses at midspan

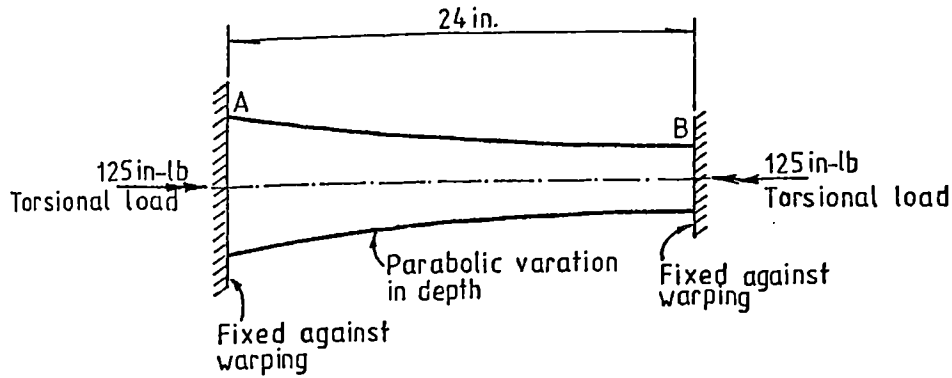


(b) Longitudinal warping stresses at outer face at midspan



(c) Transverse bending stresses at midspan

Fig. 5.21 Results for case of eccentric point load  
(1 in. = 25.4 mm; 1 lbf. = 4.45 N)



(a) Elevation

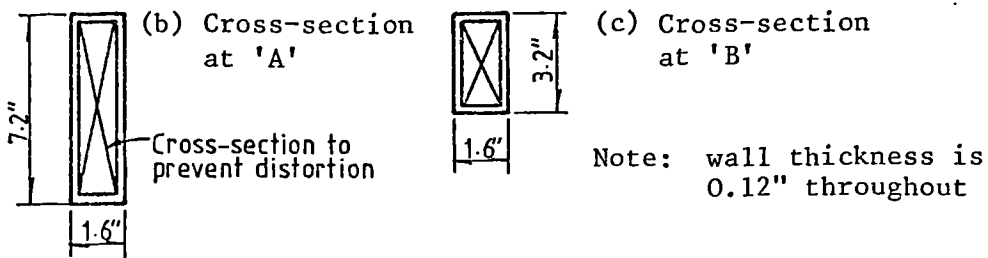
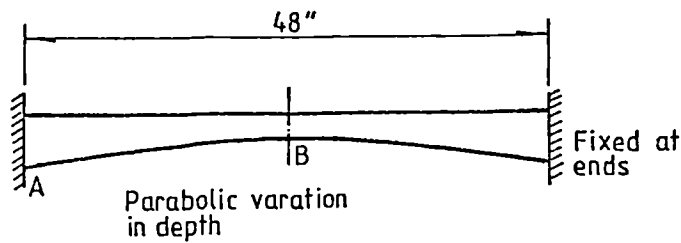
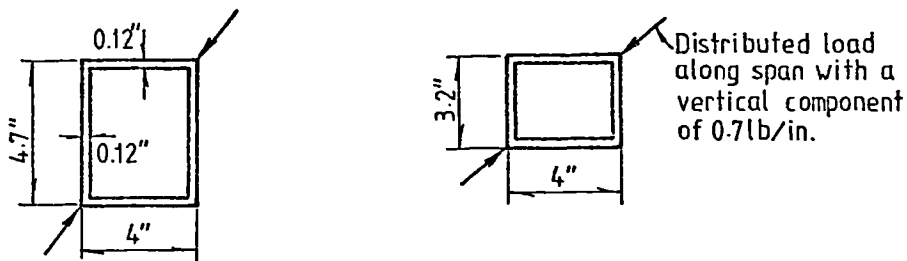


Fig. 5.22 Experimental model used by Křistek to check first step of his analysis method  
(1 in. = 25.4 mm; 1 lbf. = 4.45 N)



(a) Elevation



(b) Cross-section at 'A'

(b) Cross-section at 'B'

Fig. 5.23 Experimental model used by Křistek to check second step of his analysis method  
(1 in. = 25.4 mm; 1 lbf. = 4.45 N)

Table 5.2 Deflections of nodal edges of tapered box girder compared with results from Refs. 9, 62 and 90.

Distance from support, in inches	Present method	Measured deflections from Ref.62	Computed deflections from Ref.62	Computed deflections from Ref.9	Computed deflections from Ref.90
(1)	(2)	(3)	(4)	(5)	(6)
0	0	0	0	0	0
4	0.0799	0.075	0.068	0.074	0.0734
8	0.2716	0.351	0.332	0.348	0.3476
12	0.5027	0.556	0.541	0.550	0.5511
16	0.7105	0.741	0.739	0.740	0.7402
20	0.8508	0.859	0.869	0.859	0.8600
24	0.9000	0.907	0.916	0.907	0.9073

Deflections are in inches  $\times 10^{-2}$

Note: 1 in. = 25.4 mm

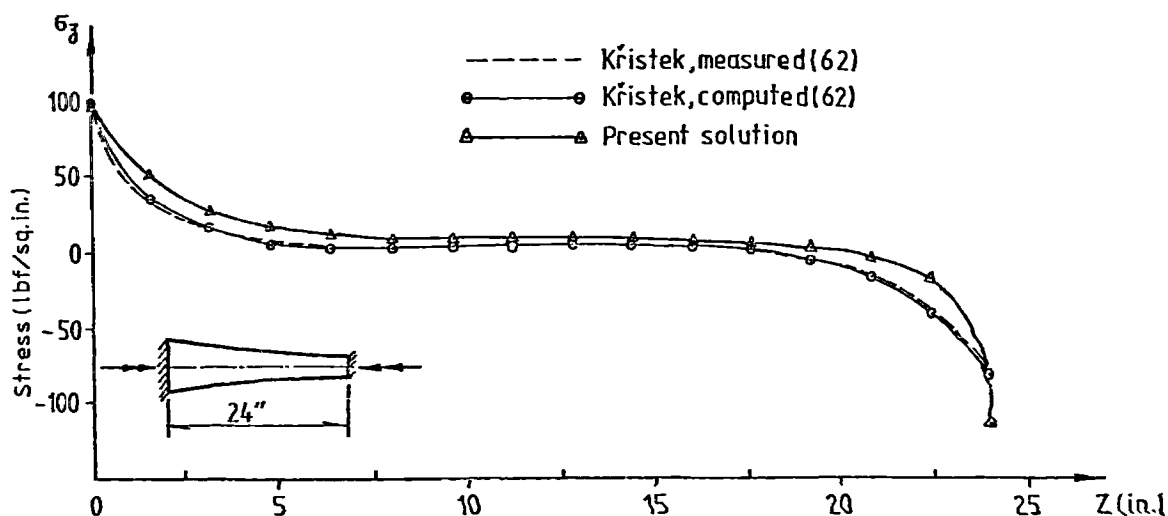


Fig. 5.24 Comparison of Longitudinal Warping Stresses along Span from Present Solution with Křistek's First Step Analysis and Test Data (1 in. = 25.4 mm; 1 lb./sq.in. = 6.9 kN/m<sup>2</sup>)

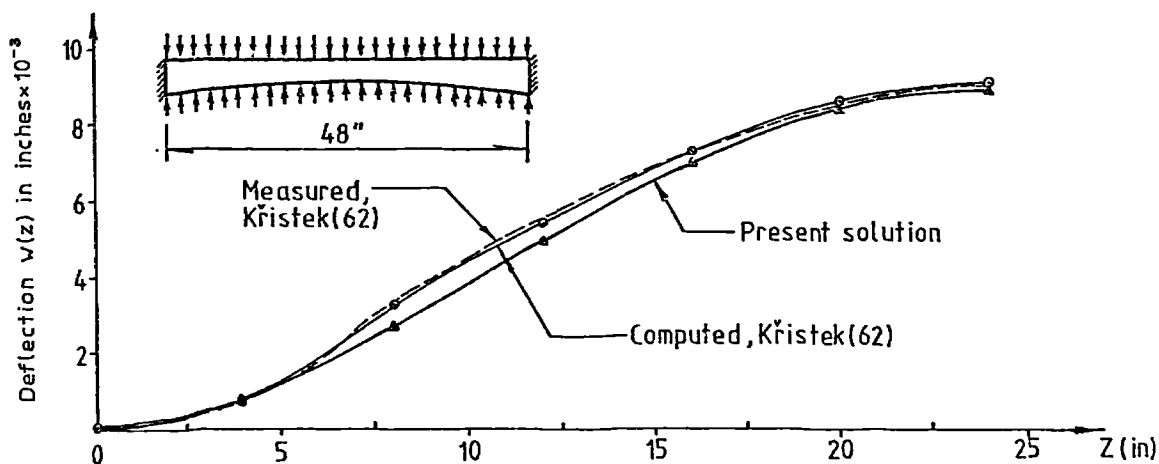
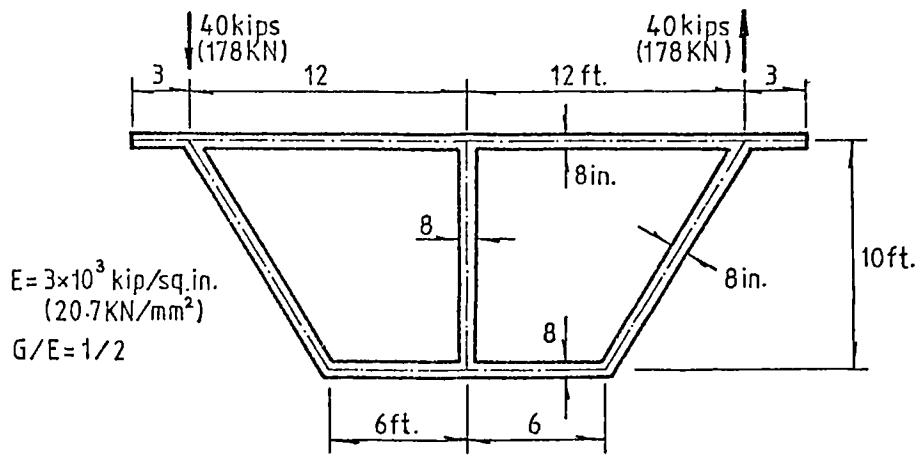
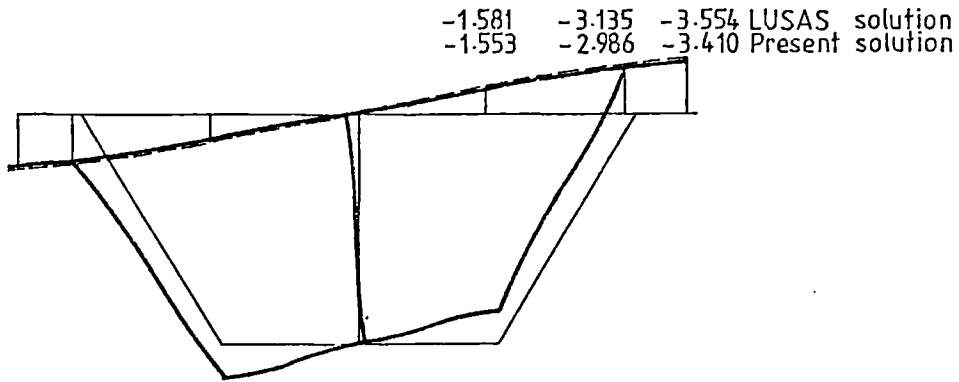


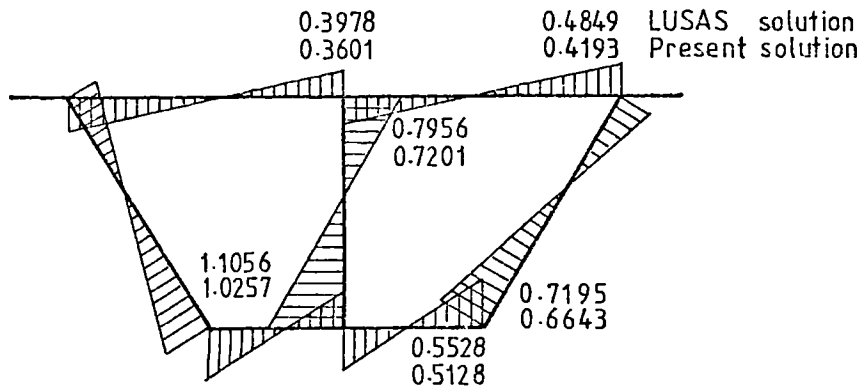
Fig. 5.25 Comparison of Vertical Deflection in Second Step of Křistek's Analysis (1 in. = 25.4 mm)



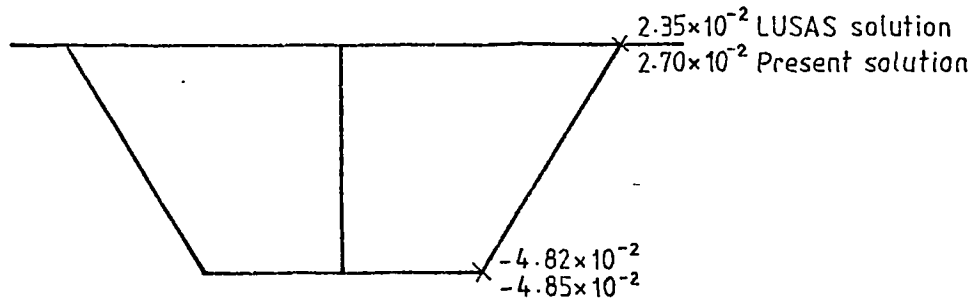
(a) Cross-section and loading



(b) Deflections at midspan ( $10^{-2}$  in.)

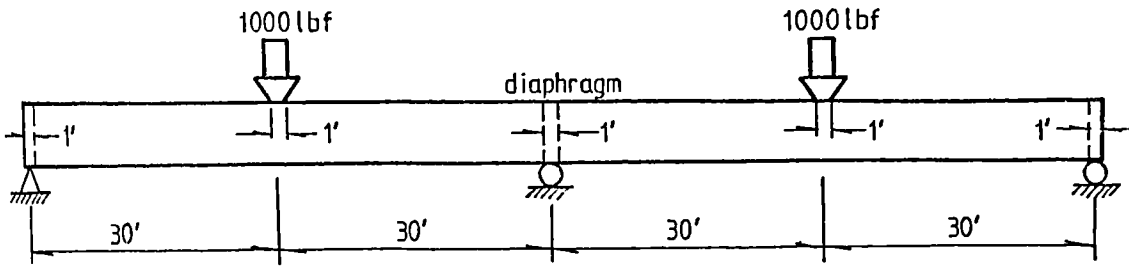


(c) Transverse bending moments at midspan (kip.in./in.)

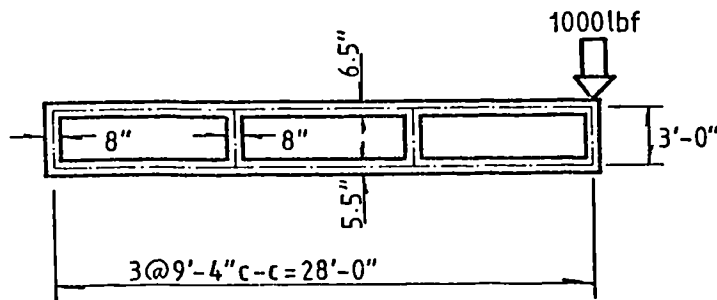


(d) Warping stresses at midspan (kip /in<sup>2</sup> )

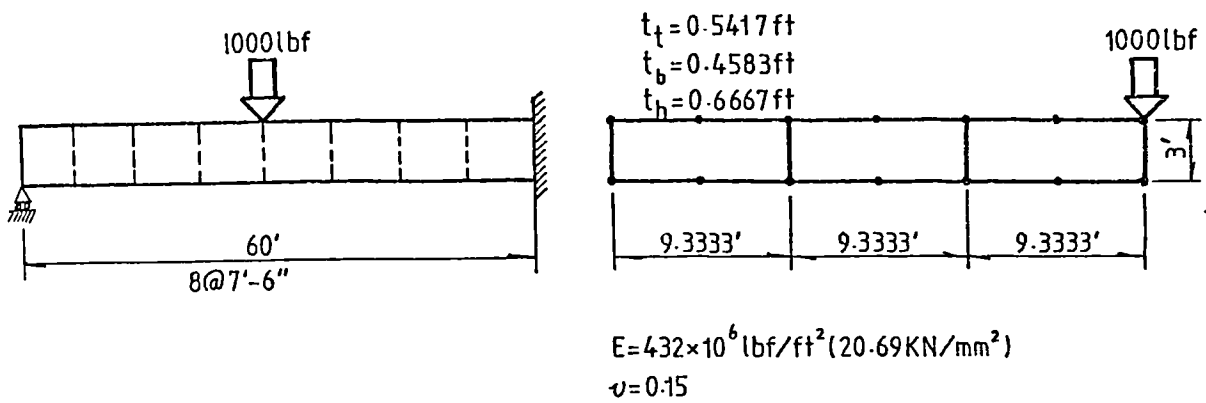
Fig. 5.26 A double cell boxbeam under twisting loads  
 (1 in. = 25.4 mm; 1 ft. = 0.305 m; 1 kip/in<sup>2</sup> = 6.9 N/mm<sup>2</sup>)



(a) Bridge elevation and loading position



(b) Typical transverse section



(c) Three-dimensional finite element model

Fig. 5.27 Two-span continuous box bridge  
(1 ft. = 0.305 m; 1 lbf. = 4.45 N)

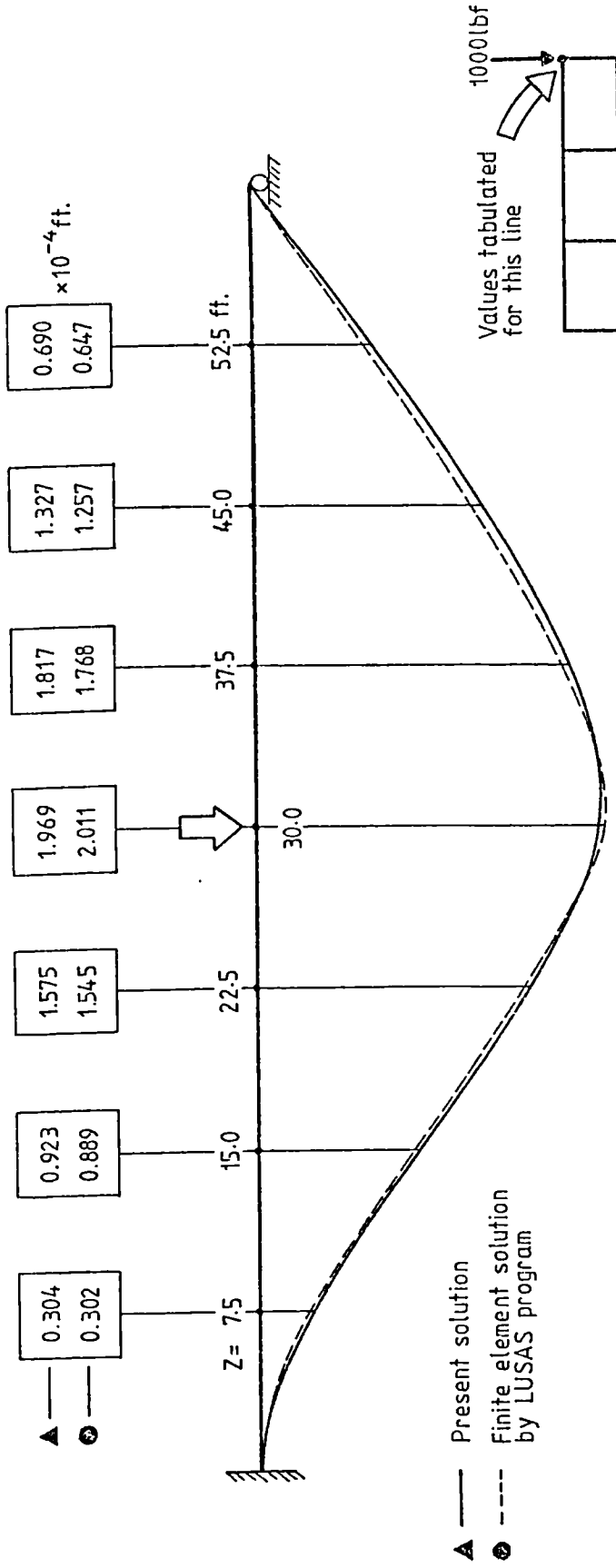


Fig. 5.28 Vertical deflection along longitudinal line at top of outer web  
 (1 ft. = 0.305 m; 1 lbf. = 4.45 N)

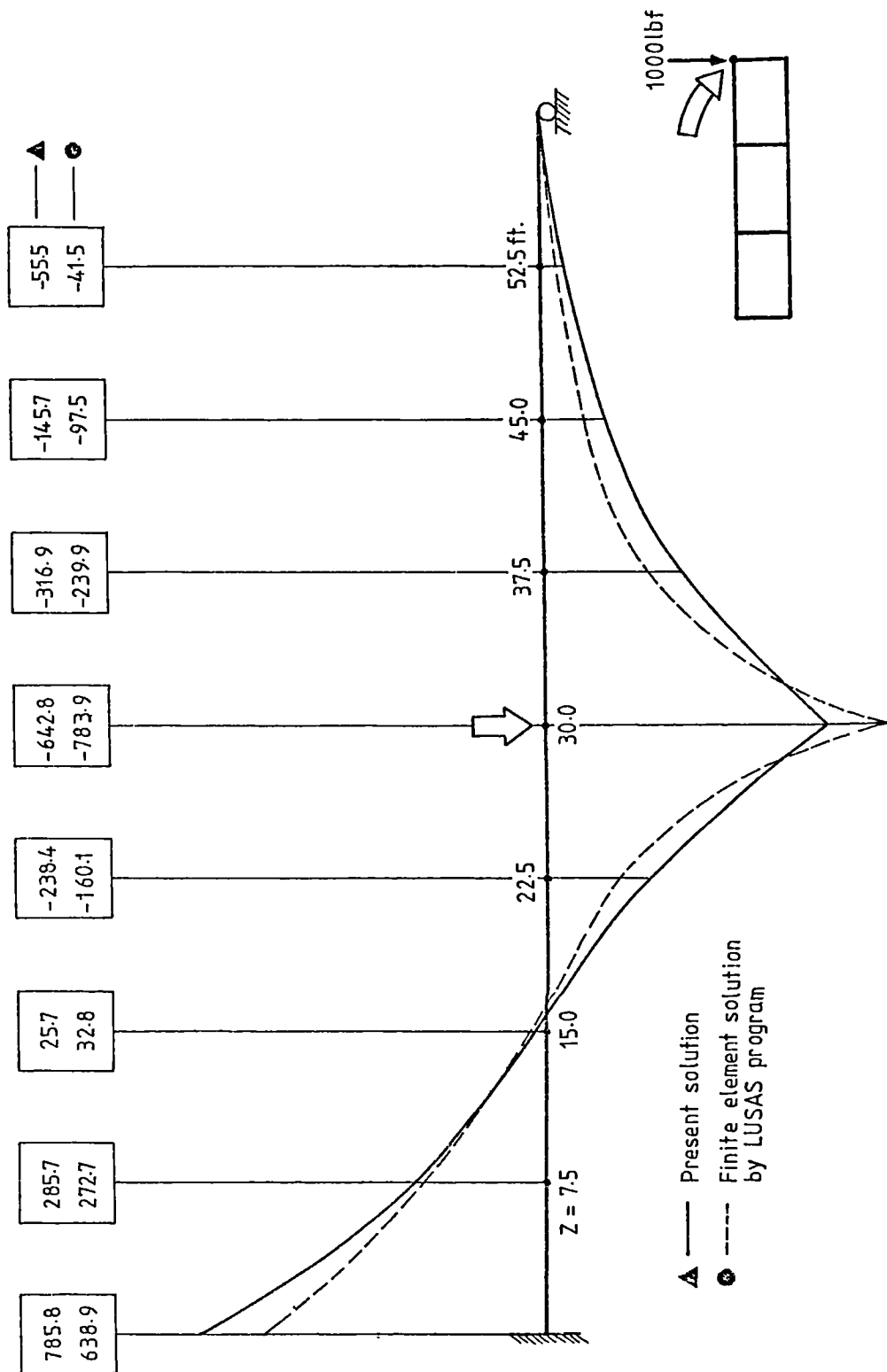


Fig. 4.29 Longitudinal distribution of longitudinal stress (psf) in top slab over loaded side web  
 (1 ft = 0.305 m; 1 lbf/sq.ft. = 47.9 N/m<sup>2</sup>)

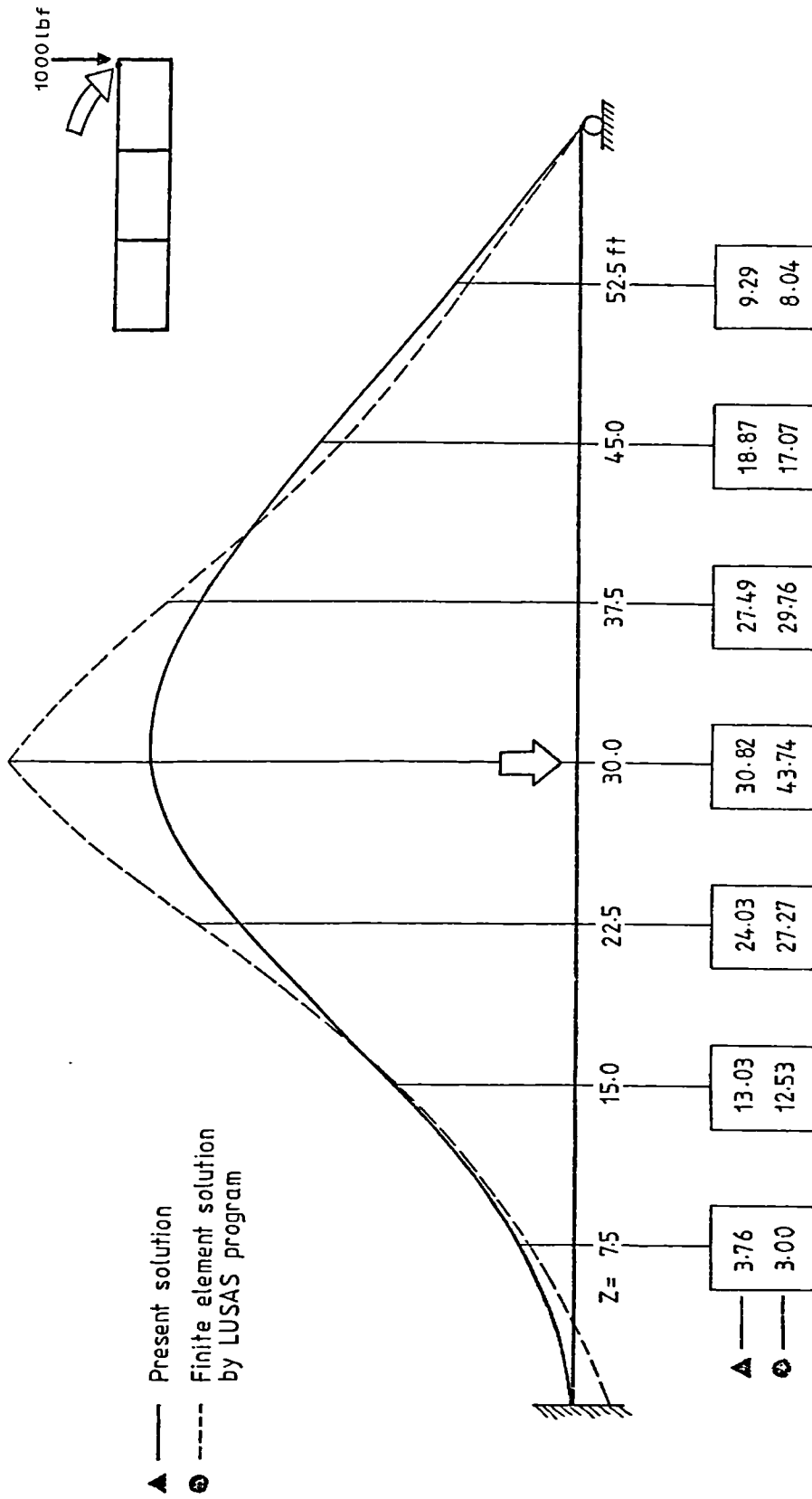
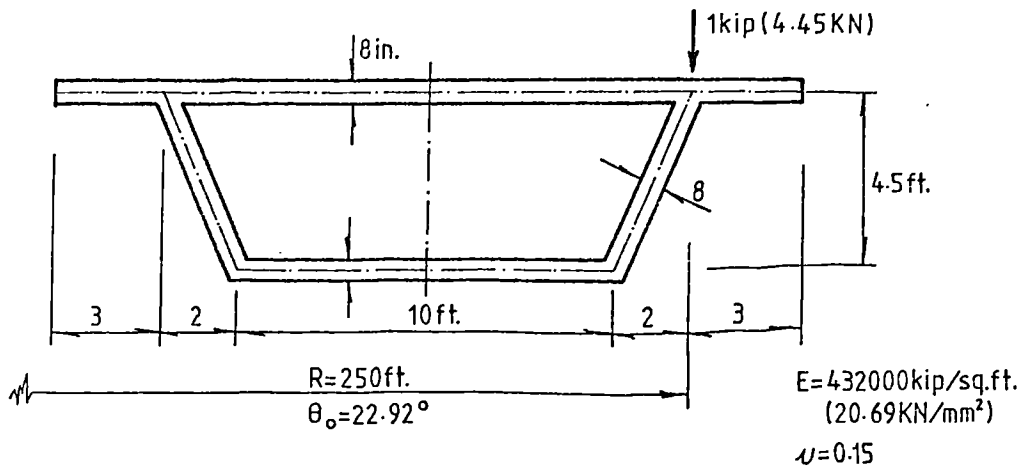
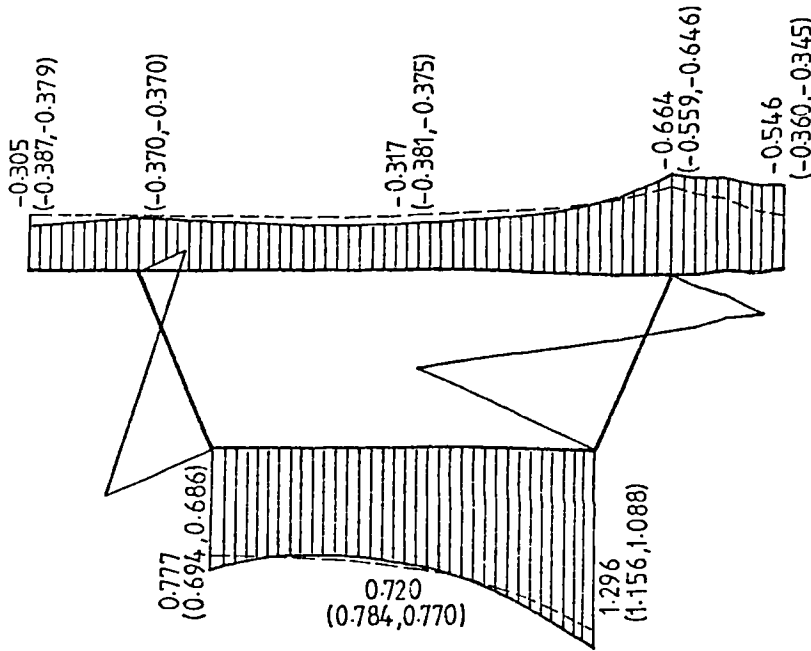


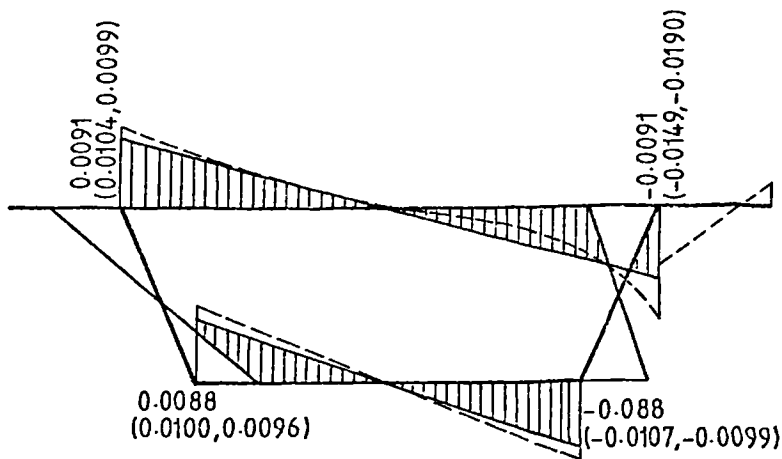
Fig. 5.30 Longitudinal distribution of transverse bending moment (ft-lb/ft) in top slab over loaded side web (1 ft = 0.305 m; 1 lbf = 4.45 N)



(a) Cross-section and loading



(b) Longitudinal normal stresses at midspan (kip/sq.ft.)



(c) Transverse bending moments at midspan(k-ft/ft)

Fig. 5.31 A single-cell curved box girder example (The values in parentheses are from LUSAS program and CURSTR program respectively)  
 (1 ft. = 0.305 m; 1 kip/sq.ft. = 47.9 kN/m<sup>2</sup>)

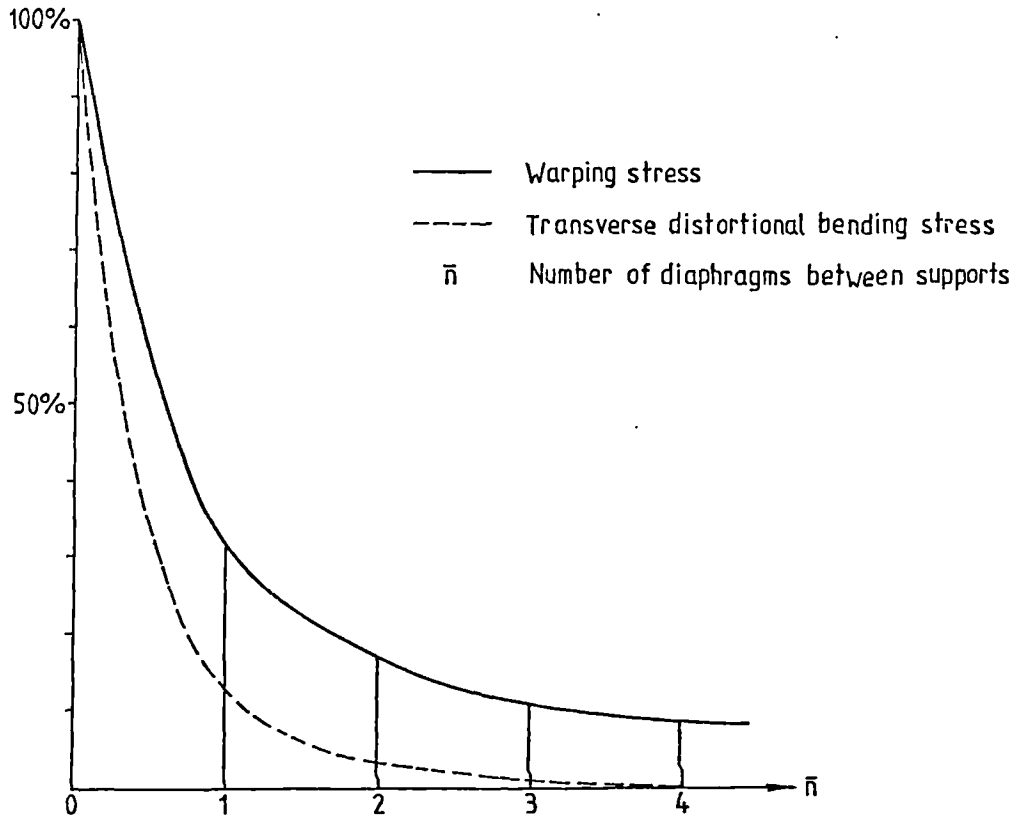


Fig. 5.31 Influence of the number of diaphragms between supports on the state of stresses in the box beam given by Krístek (63).

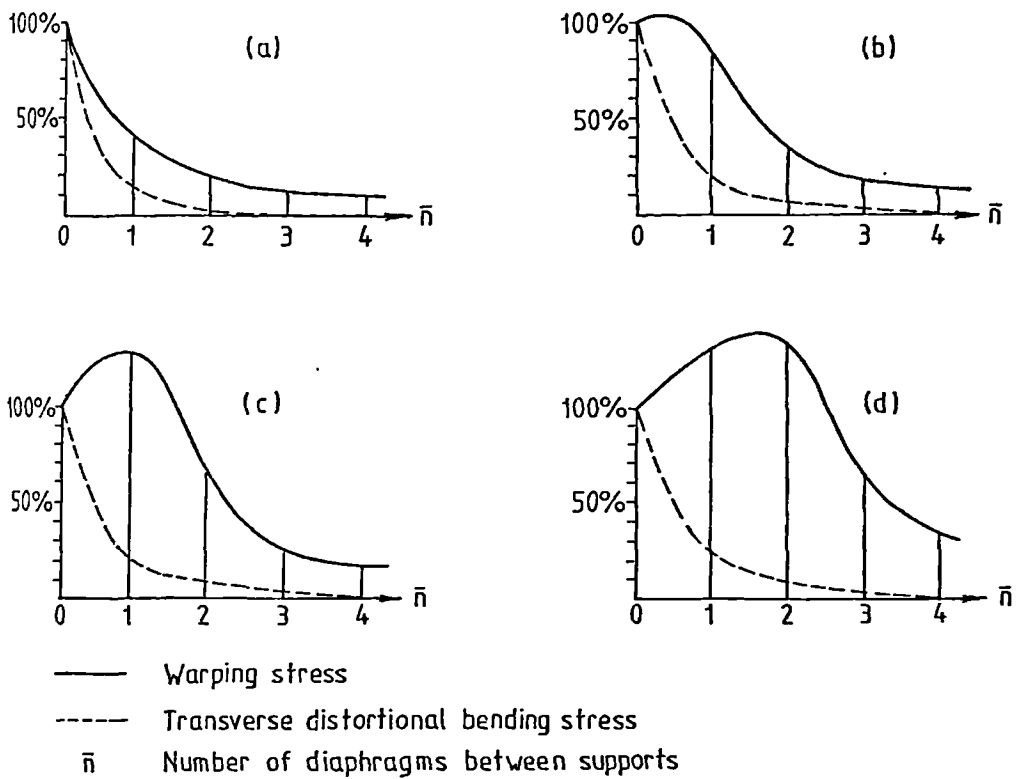


Fig. 5.32 Influence of the number of diaphragms between supports on the warping stress and transverse distortional bending stresses

## CHAPTER 6

A FINITE ELEMENT - GRILLAGE APPROACH TO THE ANALYSIS OF  
MULTIBOX BRIDGE STRUCTURES6.1 General

The box-section forming the spine provides the main source of strength in a single-spined box beam bridge. However, as may be expected there is a limit to the breadth over which the strength of a single spine may be economically effective. In practical bridge construction, the full width required may then be provided by multi-spined or twin superstructures. The term 'twin' is used to denote two nearly identical superstructures side by side, placed on common piers or with each of the pair having an independent system of piers. The twin superstructures may be completely independent but the halves are often joined by simple precast elements spanning between the two. In some cases, the gap between is filled with in-situ concrete although transverse flexural continuity is not assumed in the analysis. By contrast, the multi-spined superstructure is obviously beneficial under unevenly distributed live loading since it reduces both the bending moment on individual spines and the difference in deflections between neighbouring spines. As a result, a multi-spined superstructure should be generally adopted in preference to twin single piers.

Swann has stated (136), as a general rule for concrete box spine-beam bridges, that single-spined structures are suited to decks of breadth less than about 18 m and multi-spined or twin superstructures are suited to decks of breadth greater than this, Fig. 6.1. A survey of 173 concrete box spine-beam bridges given by Swann shows that of the total, 53 are single-spined having a single cell, 59 are single spined having multicells, and the remainder, 61, are multi-spined with a number of twin structures.

A substantial number of multi-spined steel box-bridges have also been constructed. A similar survey of data obtained from 62 steel box-bridges compiled for the Merrison Committee Parametric Studies report (35) reveals that 15 were single cell, 4 were multicells and 43 were multi-spined.

In addition, the use of composite box girder bridge decks has gained in popularity in the small to medium span range. A composite box girder bridge deck consists of a number of pre-fabricated steel boxes or precast-prestressed boxes with an in-situ composite concrete slab, Fig. 6.2. The concrete slab acts as the transverse distributing medium in the bridge deck. The torsion rigidity of the component boxes obviates the necessity of using intermediate diaphragms. It can be seen that composite box girder bridges can be placed in the same category as that of multi-spined box beams, which are basically composed of several box girders connected by a continuous top flange only.

Furthermore, short and medium span bridge decks are often erected by laying out precast-prestressed hollow box beams side by side and connecting them with in-situ concrete fill, Fig. 6.3. Since the joints will have very small and uncertain transverse bending stiffnesses and torsional stiffness it is often assumed in design that the joints act as pure shear keys, and the bridge deck as an articulated plate bridge.

In general we can use the term multibox structures to designate multi-spined box beams, or composite box girder bridge decks, or even articulated cellular bridge decks, having cross-sections with several separate boxes.

An analytical approach in the form of a one-dimensional discrete system with reference to single-spined superstructures, has been presented in previous chapters. It is clear that for the method to be of general use to the designer, it must also be applicable to multibox structures. At

first sight this type of superstructure seems unlikely to be idealized by a one-dimensional discrete system. However, an interconnected grillage of beams (37, 73, 114, 115, 116, 121, 148, 41, 30) can, with care, be made to yield an adequate representation of structures which clearly behave in a three-dimensional mode. This measure of flexibility, combined with economy in computing, input preparation and interpretation time, makes grillage analysis a popular and widely used method in the bridge design offices.

In this chapter a method based on a finite element-grillage approach, using the general one-dimensional finite element system derived for the analysis of multibox structures, is proposed. Guidance is given on the geometric layout of grillage beams to represent the actual structure, and on the establishment of equivalent element properties. An iterative procedure proposed initially by Billington (11) is incorporated into the computer program to account for distortional effects in a deformable multibox structure. Modification of the stiffness matrix due to the effect of shear keys is also formulated.

The method is used to investigate a typical twin-box structure, and also to investigate the load distribution of some articulated cellular bridge decks. Validation is proved by comparison with three-dimensional finite element results or with other analytical solutions.

## 6.2 Grillage idealization of multi-spined box beams

As a first step in a grillage analysis, the actual continuum structure must be idealized as a two-dimensional arrangement composed of discrete one-dimensional elements. The interaction between longitudinal and transverse force system takes place at nodal points. Restraints may be applied at any joint and elements framing into a joint can be at any angle. It should be borne in mind at all stages of calculation that the grillage

idealization is not a direct representation of the real physical structure; nevertheless, it can be made, with care, to reflect an adequate distribution of displacements and internal forces within the structure.

Logically, the longitudinal grillage members should be placed coincident with the physical boxes, i.e., single equivalent elements along individual spine axes. Thus, internal forces in the grillage members directly represent those in the spines of the structure. This idealization leads to a higher degree of accuracy than one where the members are placed coincident with the longitudinal webs in the deck (30, 41). It also considerably reduces the total number of longitudinal elements. Additional longitudinal members of low stiffness are sometimes located along the edges of deck cantilevers or along the midline of the slab between neighbouring boxes to assist load description.

In order to provide a representation of the transverse bending action, transverse grillage members, intersecting the longitudinal members, must be used. There will invariably be transverse diaphragms at the supports and there may be diaphragms within the spans. Obviously, transverse grillage members must be incorporated along the line of each diaphragm in a structure. In bridge construction, the spacing of the transverse diaphragms may be considerably greater than that of the distance between boxes. In such a case, additional transverse elements placed between the transverse diaphragms, are needed to reflect the load-sharing characteristics of the deck.

Experience shows that very close spacing of transverse elements permits a detailed study of the structure, but is expensive and does not necessarily make the characteristic behaviour of the grillage any closer to that of the actual structure. On the other hand, very wide spacing results in inaccuracy of load transference and excessively large discontinuities in internal forces at the joints. Some guidance given by West (148) is that

transverse element should be placed at intervals not exceeding twice the spacing of longitudinal elements. For the present analysis of multi-spined box beams, it is preferable to stipulate that the spacing should not exceed twice the breadth between the outer webs of neighbouring box-spines. It is also recommended that normally the spacing of transverse grillage elements should be not less than this breadth or not less than the spacing of longitudinal elements.

Notice that the fictitious transverse medium between the box-spines consists only of the deck slab itself. However, across the width of the box additional stiffening is present due to the frame action of the box cells. Different grillage elements with high stiffness are then used across the width of the box so that the transverse grillage elements, which represent the slab between individual boxes, have the correct span and stiffness properties.

Although the one-dimensional discrete system will invariably change the even internal force system of a real three-dimensional structure so that it is abrupt and centred on nodal points, the accuracy of the grillage method, within acceptable limits, may be justified by physical reasons. First of all, in a thin-walled structure the use of an effective width of top slab for calculating the flexural section property evades problems which would otherwise arise from incompatibility of the longitudinal bending. Secondly, since the connecting slab between boxes does not increase the total torsional stiffness appreciably, the discontinuity of the warping restraint within the top plate is not expected to cause significant error in the solution. Thirdly, the load-sharing capacity between individual spines depends mainly on the transverse bending action of the top slab and of the diaphragms, and this action can be represented adequately by the transverse interconnected elements.

As an example, a finite element-grillage discretization for a twin-box beam is shown in Fig. 6.4. The idealization consists of a single line of longitudinal elements along the centre line of each box with transverse elements to represent the boxes and top slab as well as the support diaphragms. Three-node beam elements are used to simulate the transverse action of the boxes, with the mid-nodes of these elements coincident with the box axes. Cantilevered transverse slab members can also be used beyond the outer half of the box, though they are not very necessary in the calculations.

The computer program presented in this thesis permits the application of point loads and distributed loads on the elements. Since the grillage approach is expected only to produce a global response to the structural action, it implies that external loads are always statically distributed to longitudinal elements so that deck distortion and local bending of transverse elements are not confused.

In accordance with this principle, when the applied loads locate within the width of the individual box spines, they are considered as eccentric loads acting directly at corresponding longitudinal elements. Whilst for loads applied on the connecting slab between neighbouring box spines or on the side cantilevers, it is sufficiently accurate to replace the loads by statically equivalent loads distributed to pairs of neighbouring longitudinal grillage elements.

### 6.3 Determination of grillage element properties

Grillage element properties depend upon the positioning of the elements. Fig. 6.4 shows the division of the deck into longitudinal beams by cuts through the slab midway between adjacent spines. By splitting the deck in this way, the longitudinal grillage elements coincide with the individual box-spines. Thus, the sectional properties for these longitudinal

equivalents are calculated from a complete box with its associated top slab, and obviously no computational difficulties need be anticipated using the formulae derived in previous chapters.

It should be borne in mind that shear lag has a significant effect on distribution of bending stresses. This can be estimated by considering the flange to have a reduced 'effective width' over which the stress is uniform, as is outlined in Chapter 2. Using the full effective width of the flange and assuming that it can act with the webs, the beam stiffness can then be established.

In most cases of multi-spined box beam bridges, at any cross-section of a bridge, the longitudinal grillage elements will have the same sectional properties with vertical axes of symmetry. Consequently, the individual horizontal neutral axes will appear at the same level as the neutral axis of the deck as a whole. However, in some cases the sectional sizes of the side cantilevers will be slightly different from the half intervals. Thus, by cutting the deck along the slab midway between neighbouring spines, the side box-spines will be unsymmetrical and the level of neutral axes will vary across the width of the deck. For simplification it is assumed that the neutral axes of all longitudinal elements are coincident with that of the gross cross-section. Moreover, the side box-spines are also treated as having cross-sections with vertical axes of symmetry for evaluating the warping properties. Numerical experience has shown that calculated results are close to a three-dimensional finite element analysis.

Within the net spacing of the neighbouring box-spines the transverse medium consists only of the deck slab itself. No difficulties are experienced in calculating the sectional properties. When a transverse grillage element represents a diaphragm as well as some width of the top and bottom slabs, the inertia and shear stiffness should include that of the diaphragm.

The width of slab considered to act with the diaphragm should be the flange width reduced by shear lag, as given in Chapter 2. The remainder of the slabs are attributed to neighbouring transverse grillage members, which have very low shear stiffness to allow for distortion.

The determination of the equivalent stiffness for the transverse grillage elements is not immediately obvious. The structural action of the medium is somewhat complex since no through diaphragms are present. Transverse distribution of loading is achieved by the distortion of cell walls as in a Vierendeel girder. For simulating this 'frame' type of action it is convenient to analyse a frame with the shape and dimensions of a unit length of the deck. This can be done by using the plane frame computer program PFRAN (Appendix II).

Fig. 6.5(a) shows a slice of half of an individual box-spine. Under the action of a unit pure bending moment the webs remain undistorted and flexure is achieved by extension of the top flange and compression of the bottom flange. The equivalent moment of inertia of a transverse grillage element is therefore calculated as

$$I_{xx} = \frac{b_t^2}{8E_1\delta_B} \quad (\text{per unit length}) \quad (6.1)$$

where  $\delta_B$  is the bending deflection in the direction of the local  $y$  axis at the corner node above the outer web of the box-spine.

For assessing an effective cross-sectional area which results in shear deflections approximating to those of Vierendeel, the frame is constrained as in Fig. 6.5(b), so that it cannot rotate, and is subjected to a unit distortional shear force  $S$ . By equating the shear stiffness  $S/\delta_S$  to  $0.5A_{sy}G/b_t$  the equivalent shear area of the grillage element can be determined as

$$A_{sy} = \frac{b_t}{2G\delta_S} \quad (\text{per unit length}) \quad (6.2)$$

where  $\delta_s$  is the shear deflection at the corner node in the local y-direction.

The torsional inertia of a fictitious transverse element within the neighbouring outer webs represents the resistance of the top slab to torque and is calculated by

$$J_T = \frac{1}{3} t^3 \quad (\text{per unit length}) \quad (6.3)$$

where  $t$  is the thickness of the top slab.

The torsional stiffness of a transverse grillage member across the box-spine arises from the opposed shears in the *top and bottom* slabs represented by that member. The torsion constant is the same as two layers within a solid slab giving (41)

$$J_T = \frac{2h^2 t_t t_b}{t_t + t_b} \quad (\text{per unit length}) \quad (6.4)$$

where  $t_t$  and  $t_b$  are the thicknesses of the top and bottom flange respectively, and  $h$  is the depth of the cross-section.

#### 6.4 An iterative process for assessing distortional effects

Economic considerations dictate that the use of thin walls and the elimination of intermediate diaphragms may lead to significant deformability of the box-section. Thus it has been necessary to consider the distortion of the transverse cross-sections. With regard to the structural action arising from deformation of the cross-sections, the grillage assemblage has no adequate mechanism with which to represent directly the distortional effects. Additional deflections of the box corners which result from deformation have been simulated by using an equivalent shear area of the transverse grillage member calculated to produce the same displacements as

the box when subjected to shear forces. However, the top flange, which connects the individual boxes and completes the entire cross-section, rotates not only through the pure twisting angle but also through an addition of half of the distortional angle (Fig. 3.25). The rotation of the top flange can then be regarded as equivalent to the effective torsional angle of the cross-section. This has a significant effect on the stress distribution in the deformable multi-spined superstructure.

For assessing the rotational angle, which results from deformation, additional to the pure twisting angle, the reduced torsional stiffness referred to as the effective torsional stiffness of the box-section, can be used in the analysis. This structural treatment leads to an iterative procedure utilising the proposed grillage approach with reduced torsional stiffness for the longitudinal box beam elements to make allowance for deformation of the cross-section. Thus, compatibility of deformations and continuity of rotation are ensured between adjacent elements.

The following iterative procedure, which yields the final solution, is convenient for programming:

- Step 1 Carry out a grillage analysis of the multi-spined structure assuming that the longitudinal elements have the full torsional stiffness as given in Chapter 2.
- Step 2 Carry out a distortional analysis of each box-spine with distortional loading associated with the member end forces given by Step 1.
- Step 3 At key sections compare the sum of twisting angle and half of the distortional angle with the effective torsional angle given by the grillage analysis.

Step 4 Calculate the new torsional stiffness equal to the full torsional stiffness multiplied by the reduction factor  $\xi_d$  which is given by

$$\xi_{d,i+1} = \frac{\xi_{d,i} (\psi_z)_i}{\xi_{d,i} (\psi_z)_i + \frac{1}{2} (\gamma_d)_i} \quad (6.5)$$

where  $\psi_z$  is the effective torsional angle and the subscript  $i$  indicates the iterative circulation.

Step 5 Carry out a further grillage analysis with the new reduced torsional stiffness.

Step 6 Carry out a distortional analysis of each box-spine with distortional loading associated with the member end forces given by Step 5.

Step 7 Repeat Steps 3 to 6 until the following compatibility criterion is obtained at Step 3

$$(\psi_z)_i = \xi_{d,i} (\psi_z)_i + \frac{1}{2} (\gamma_d)_i \quad (6.6)$$

The above iterative analysis yields the correct distribution of displacements and internal forces, and experience has shown that the iterative process converges very quickly. Thus we may specify in the program that normally after four circulations the iteration will be stopped and the output accepted. This measure will decrease relatively the computing time and still provide sufficient accuracy for design purposes.

Since the continuous structure is idealized by discrete, skeletal grillage elements, the distribution of the internal forces for the longitudinal elements has discontinuities at the joints due to interaction with the transverse elements. Where all the elements meeting at a joint are physical beams, there will be a genuine step in the diagram of stress

resultants at this point and the actual output of values from the program should be used. If any of the transverse grillage beams are hypothetical and represent sections of slab, the 'true' diagram of the internal forces can be assumed for the purpose of design to pass through the average value of the internal forces on the two sides of each joint. Note that the distribution of bimoments and distortional moments are not affected by the transverse grillage elements.

The transverse bending moments of the top and bottom slabs within the box-spines are derived from the distortion of the cross-section proportioned to the plane frame analysis. The transverse bending moments of the top slabs between the box-spines are obtained directly from the grillage analysis. The local effects occurring in the top slab are evaluated independently and are added to the moments from distortion.

#### 6.5 Numerical example of a composite twin-box beam

A simply-supported composite twin-box beam discussed by Billington (11) is used to verify the validity of the proposed finite element-grillage approach. The dimensions of the twin-box structure are shown in Fig. 6.6. The cross-section consists of two open-topped steel boxes with a composite reinforced concrete deck. The four webs are equally spaced at 8 ft. (2440 mm) centres and a concentrated load of 1000 LBF (4.45 kN) is applied above an outer web at midspan. The modulus of elasticity for the steel is  $3.0 \times 10^7$  lb/sq.in. (207 kN/mm<sup>2</sup>), and for the concrete is  $40 \times 10^6$  lb/sq.in. (27.6 kN/mm<sup>2</sup>). Poisson's ratio is taken as 0.30 for steel, and 0.20 for concrete. The modular ratio for calculating the sectional properties referred to bending is

$$m_E = \frac{E_{st}}{E_{co}} \times \frac{1 - \nu_{co}^2}{1 - \nu_{st}^2} = 7.912 \quad (6.7)$$

and the modular ratio for calculating the sectional properties referred to torsion is

$$m_G = \frac{E_{St}}{E_{Co}} \times \frac{1 + \nu_{Co}}{1 + \nu_{St}} = 6.923 \quad (6.8)$$

The idealization used for the grillage analysis is shown in Fig. 6.8 and consists of a single line of longitudinal elements along the centre line of each box with transverse elements to represent the boxes and the slab. Three-node beam elements with high stiffness evaluated from a transverse frame analysis are used across the width of the box to simulate the transverse action. The sectional properties of each element are given in Table 6.1. The final iteration for the grillage analysis gave the values of  $GJ_T/17.38$  for the loaded box and  $GJ_T/18.60$  for the unloaded box.

The three-dimensional finite element analysis was performed using the LUSAS program for comparison. The mesh selected for the analysis consisted of rectangular flat thin shell box elements (Fig.6.7). Billington also carried out a three-dimensional finite element 'shell' analysis using the ICSAS (Imperial College Structural Analysis System) program.

The deformable shape of the cross-section at midspan obtained from the grillage analysis together with the results calculated by LUSAS is plotted in Fig. 6.9. Agreement between the grillage analysis and the FE results are found to be good. Fig. 6.10 shows a comparison of the longitudinal stresses with the FE results, and the transverse flexural distortion stresses for the load case with the corresponding FE results are given in Fig. 6.11. The stress results indicate that the grillage approach with an iterative process gives results of sufficient accuracy for design purposes.

#### 6.6 Analysis of articulated cellular bridge decks

An articulated deck is a pseudo-slab form of construction. The deck is formed of precast prestressed beams each of which has incorporated in it

some transverse shear steel, at the time of casting. Transverse continuity is then obtained by making concrete joints between the beams. The deck will distribute load almost entirely by shear, since it will have very little bending stiffness and torsional stiffness at the joints.

The articulated bridge deck can be analysed by orthotropic plate theory formulated by Guyon and Massonet and developed by other investigators such as Spindel (132). Křistek (63, 64) has also presented a solution based on elasticity, for structures composed of box beams connected by hinges. Since existing analytical methods lack the ability to deal with skew supports and continuity, and the full three-dimensional finite element analysis requires too much computing time, Sawko and Swaminadhan (122, 137) developed a rectangular quasi-slab element which is specified as a six-node grillage element. The element has a single degree of freedom at each node including vertical displacements at the four corners of each element and two rotations along the longitudinal centre line. The derivation of the element stiffness matrix is based on both the finite element and grillage concepts.

In fact the grillage approach proposed in this Chapter is also applicable, without any difficulties, *to the analysis of articulated bridge decks with stiff as well as deformable cross-sections and to skew and continuous spans.* As described in previous sections, the distortional effects can be simulated by a shear area analogy obtained from transverse Vierendeel frame analysis. The only modification necessary for the transverse elemental stiffness is the releasing of the member end moments which will be zero at the positions of shear keys.

The analytical procedure is similar to the static condensation process described in Ref. 155. We use the three-node beam elements to represent the component boxes transversely in which the mid-node is always coincident with the box axis and the width of each element is equal to the centre to

centre distance of the shear keys between the beams. The sequence of the degrees of freedom is rearranged and the subscript 'r' is used to denote the released degrees of freedom and 'f' the remaining degrees of freedom of the element  $i$ . The equilibrium equations for the element  $i$  can be written in terms of released and remained displacements as

$$\begin{bmatrix} k_{ff} & k_{fr} \\ k_{rf} & k_{rr} \end{bmatrix} \begin{Bmatrix} \delta_f \\ \delta_r \end{Bmatrix} = \begin{Bmatrix} f_f \\ f_r \end{Bmatrix} \quad (6.9)$$

where

$$\delta_f = [u_1, v_1, w_1, u_2, v_2, w_2, u_3, v_3, w_3]^T \quad (6.10)$$

and

$$\delta_r = [\theta_{x1}, \theta_{y1}, \theta_{z1}, \theta_{x2}, \theta_{y2}, \theta_{z2}, \theta_{x3}, \theta_{y3}, \theta_{z3}]^T \quad (6.11)$$

Solving for  $\delta_r$  in terms of  $\delta_f$  from the released condition

$$[k_{rf} \quad k_{rr}] \begin{Bmatrix} \delta_f \\ \delta_r \end{Bmatrix} = 0 \quad (6.12)$$

we have

$$\delta_r = -k_{rr}^{-1} \cdot k_{rf} \delta_f \quad (6.13)$$

Substituting from Eq. 6.11 for  $\delta_r$  in Eq. 6.9 gives

$$[k_{ff} - k_{fr}k_{rr}^{-1}k_{rf}] \{\delta_f\} = \{f_f - k_{fr}k_{rr}^{-1}f_r\} \quad (6.14)$$

or

$$[k_{ff} - R] \{\delta_f\} = \{f_f - k_{fr}k_{rr}^{-1}f_r\} \quad (6.15)$$

where  $R$  is the released matrix which is given by

$$[R] = k_{fr}k_{rr}^{-1}k_{rf} \quad (6.16)$$

Eq. 6.15 can be written as

$$[k_R] \{\delta_f\} = \{f_R\} \quad (6.17)$$

where

$$[k_R] = k_{ff} - R \quad (6.18)$$

and

$$\{f_R\} = f_f - k_{fr} k_{rr}^{-1} f_r \quad (6.19)$$

Only  $k_R$  and  $f_R$  are then transformed to the global coordinate system and added to the structure stiffness matrix and load vector.

The formulae derived have been incorporated into the computer program CUBAS. The degree of accuracy of the present method is tested by comparing the results obtained by the computer program CUBAS with the methods of Swaminadhan (122, 137) and Kristek (64) on a right bridge deck for point load. The geometry of the deck and the mesh arrangement are shown in Fig. 6.12. Figs. 6.13 to 6.15 show the deflections, moments and torsion diagrams for deformable cross sections. It can be seen that in all cases the agreement between the different approaches is very good.

The present method can deal with fixed and continuous support conditions without difficulty. A single 18 metre span was analysed with three different sets of end conditions as shown in Fig. 6.16, and referred to as simple-simple, simple-fixed and fixed-fixed. These various end conditions will give a range of results intended to demonstrate the versatility of the finite element-grillage method for analysing continuous decks. The mesh arrangement used is shown in Fig. 6.17.

Table 6.2 shows the midspan deflections for the various support conditions under central and eccentric point loading. The mid span moments are given in Tables 6.3 and 6.4. Results obtained by Swaminadhan (137) are also listed in the tables with parentheses. Again excellent agreement between the two methods is apparent. It can also be seen from these tables that the total moment predicted at a section by the analysis differs from the theoretical total moment (shown at the bottom of Tables 6.3 and 6.4)

by less than 1.0%. These observations for the three types of edge conditions appear to confirm the validity of the approach for the analysis of continuous structures.

Swaminadhan also used his method to investigate a skew articulated bridge deck model (137). Although no comparable results are shown here between the two methods, it follows that the present method would be able to predict the behaviour of a skew articulated bridge deck with the same degree of accuracy.

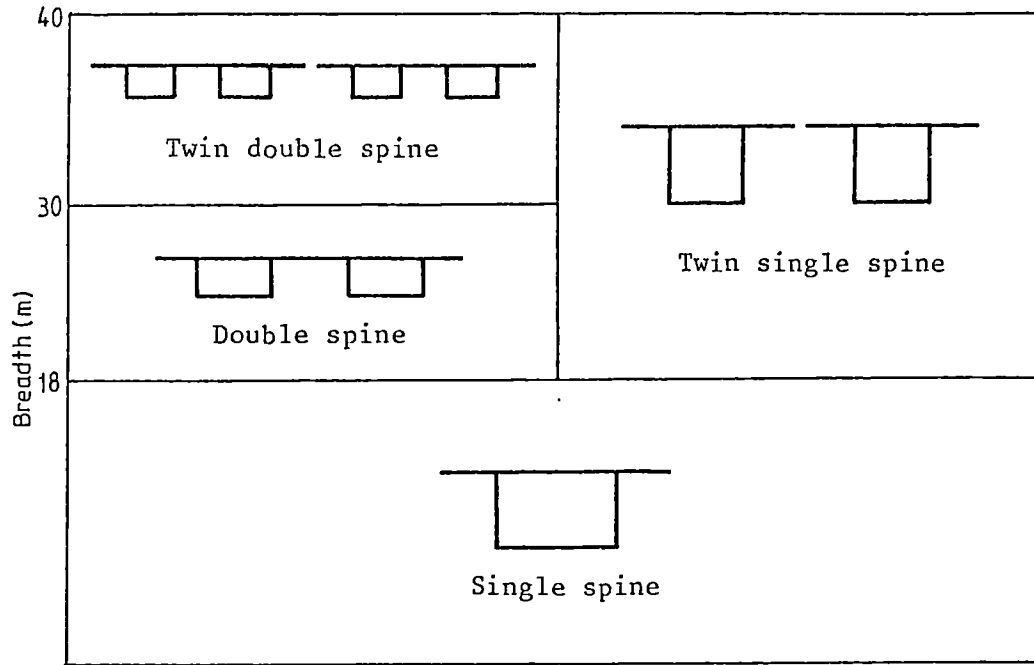
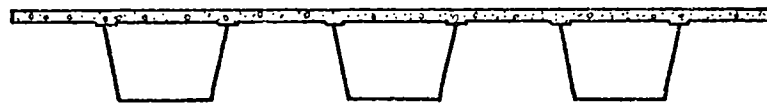


Fig. 6.1 Breadths for different cross-sections



(a) Thin plate steel boxes



(b) Precast-prestressed boxes

Fig. 6.2 Bridges with composite slab over individual boxes

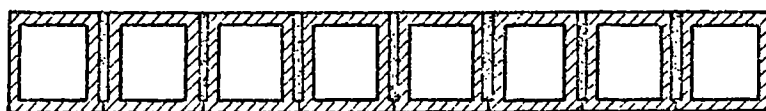
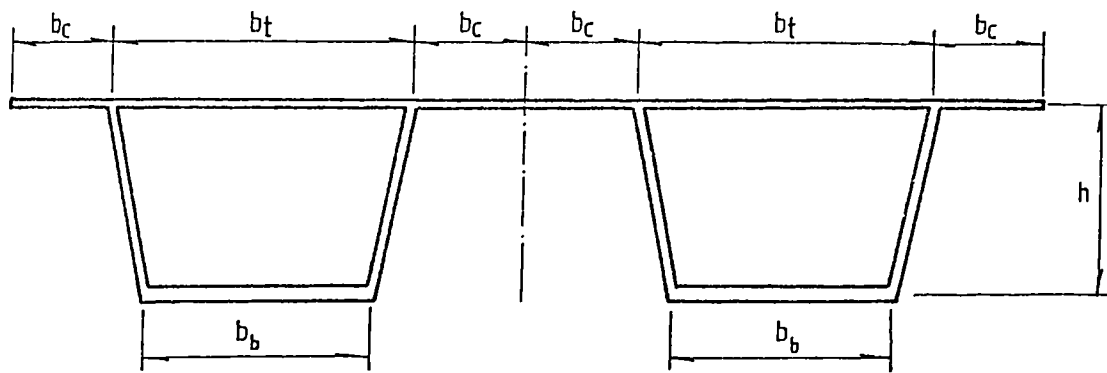
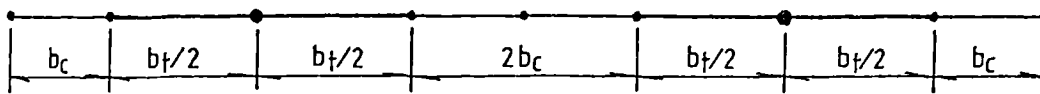


Fig. 6.3 Articulated cellular bridge deck



(a) Deck cross-section



(b) Grillage cross-section

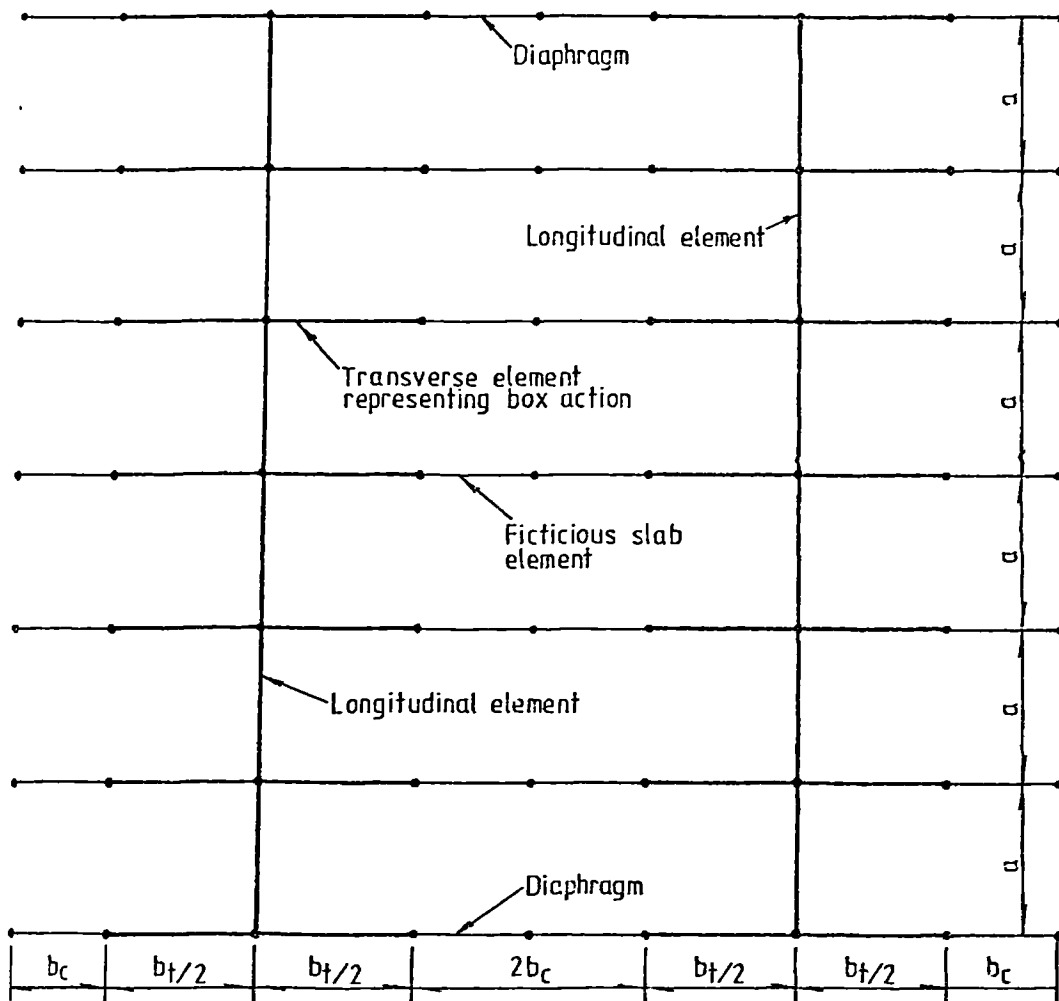
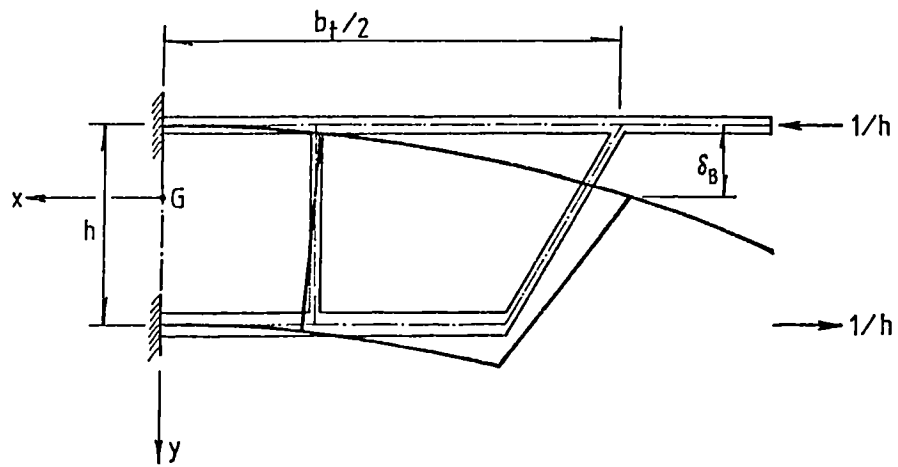
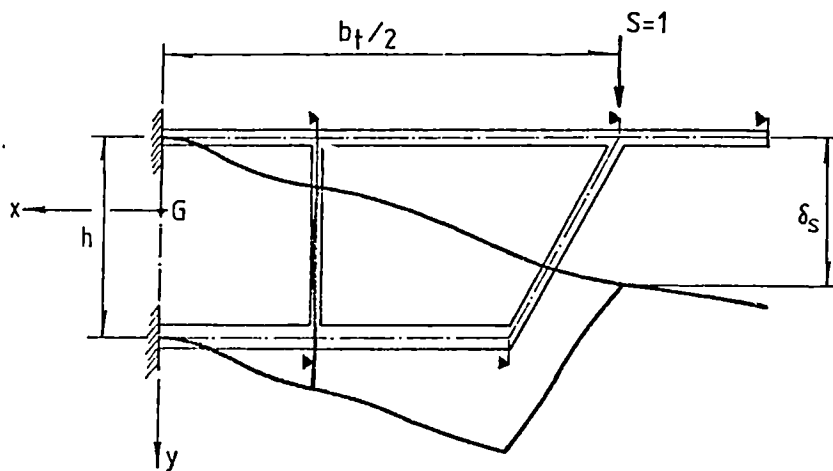
(c) Grillage plan  $\frac{a}{2b_c} \leq 2$ 

Fig. 6.4 Finite element-grillage idealization



(a) Bending deformation mode



(b) Shearing deformation mode

Fig. 6.5 Transverse action of box-spine

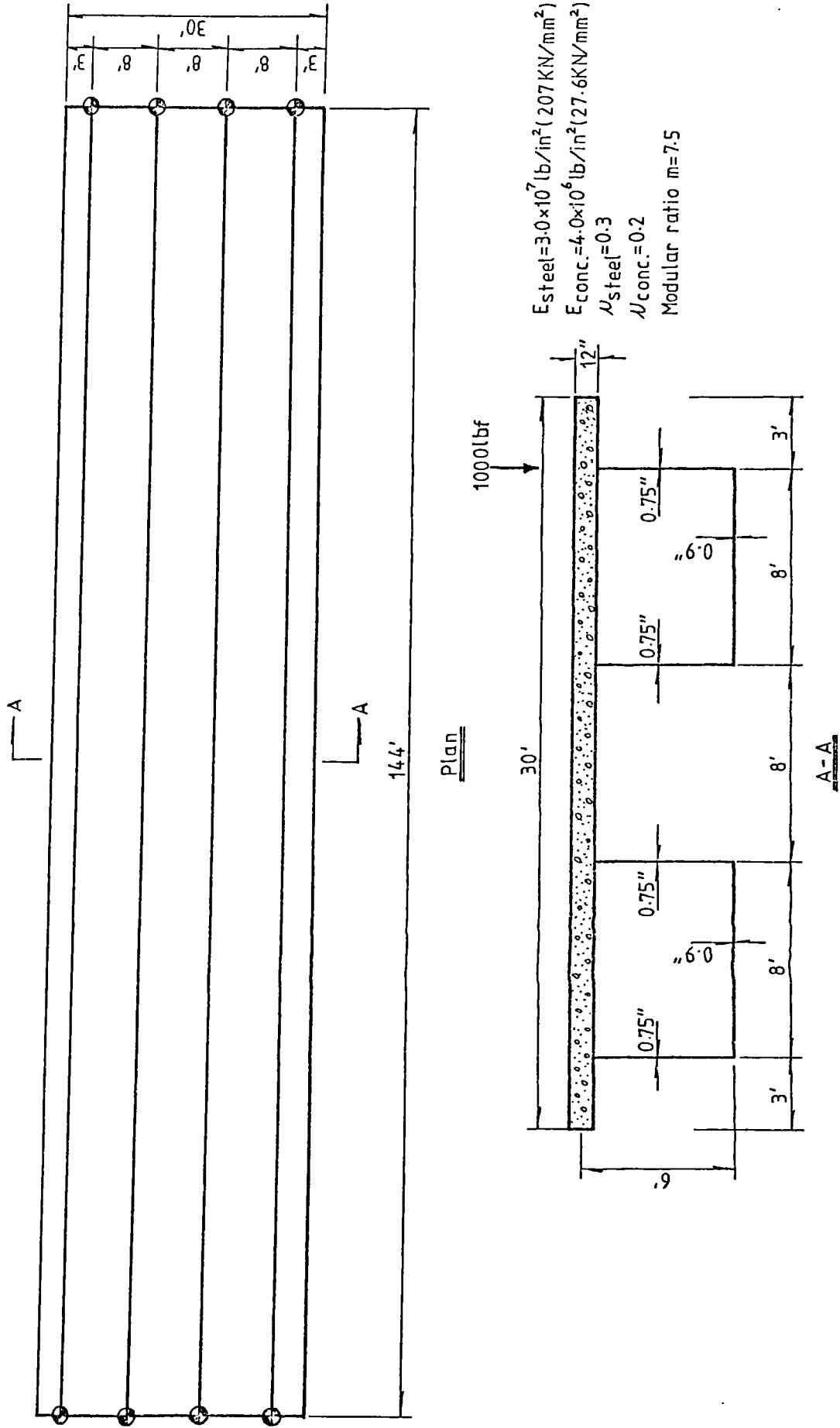


Fig. 6.6 Dimensions and loading of twin-box beam example (1 ft = 0.305 m; 1 in. = 25.4 mm, 1 lbf = 4.45 N)

Element Type	Bending moment of inertia ( $I_{xx}$ ) in <sup>4</sup>	Effective shear area ( $A_{sy}$ ) in <sup>2</sup>	Torsional moment of inertia ( $J_T$ ) in <sup>4</sup>	Torsional warping moment of inertia ( $J_I$ ) in <sup>6</sup>	Distortional second moment of area ( $J_d$ ) in <sup>4</sup>	Distortional warping moment of inertia ( $J_{IT}$ ) in <sup>6</sup>
Longitudinal (midspan section)	373938.94	114.54	623133.33	38831733.81	0.00872	148669585.0
Transverse box	28810034.64	7.41	663344.53	—	—	—
Transverse slab	1965.62	136.50	8985.70	—	—	—

Table 1 Sectional properties for the analysis of a twin-box beam example  
(1 in. = 25.4 mm)

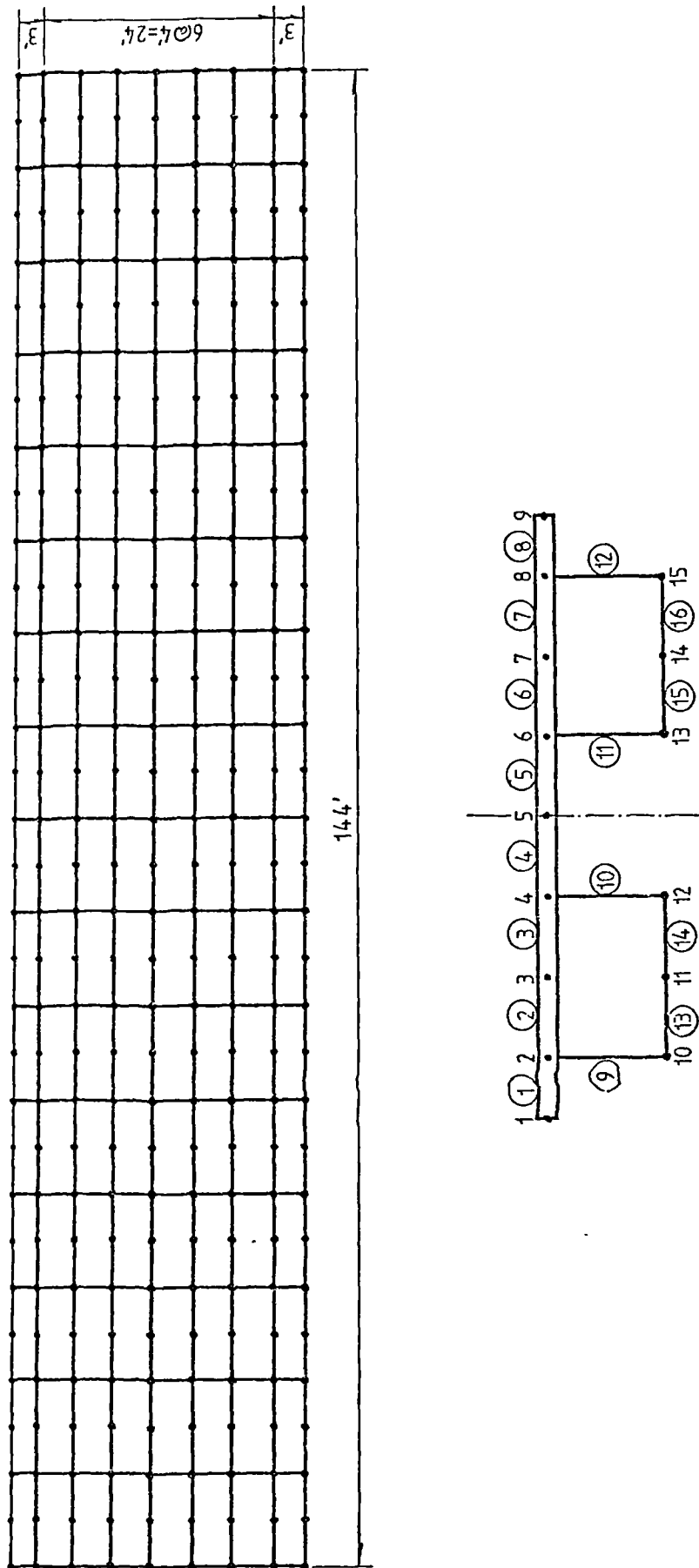


Fig. 6.7 Finite element mesh for twin-box beam example (1 ft. = 0.305 m)

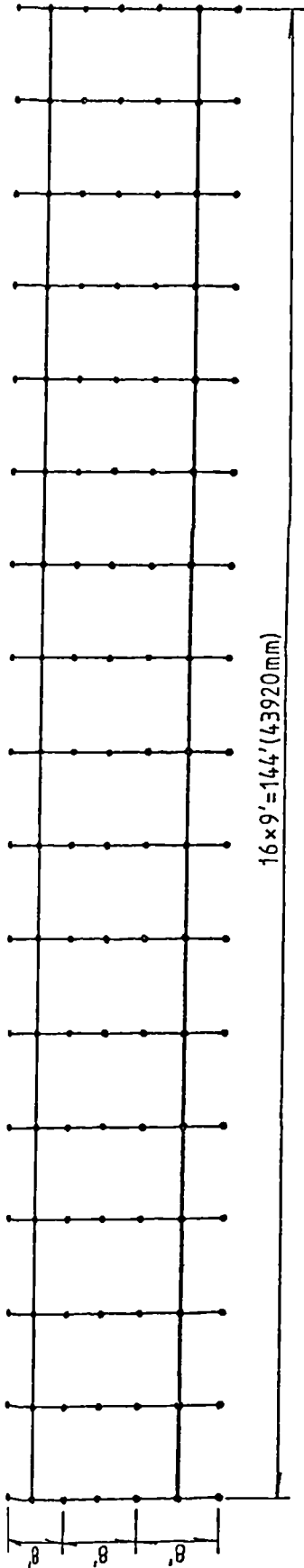


Fig. 6.8 Finite element-grillage mesh for twin-box beam example (1 ft. = 0.305 m)

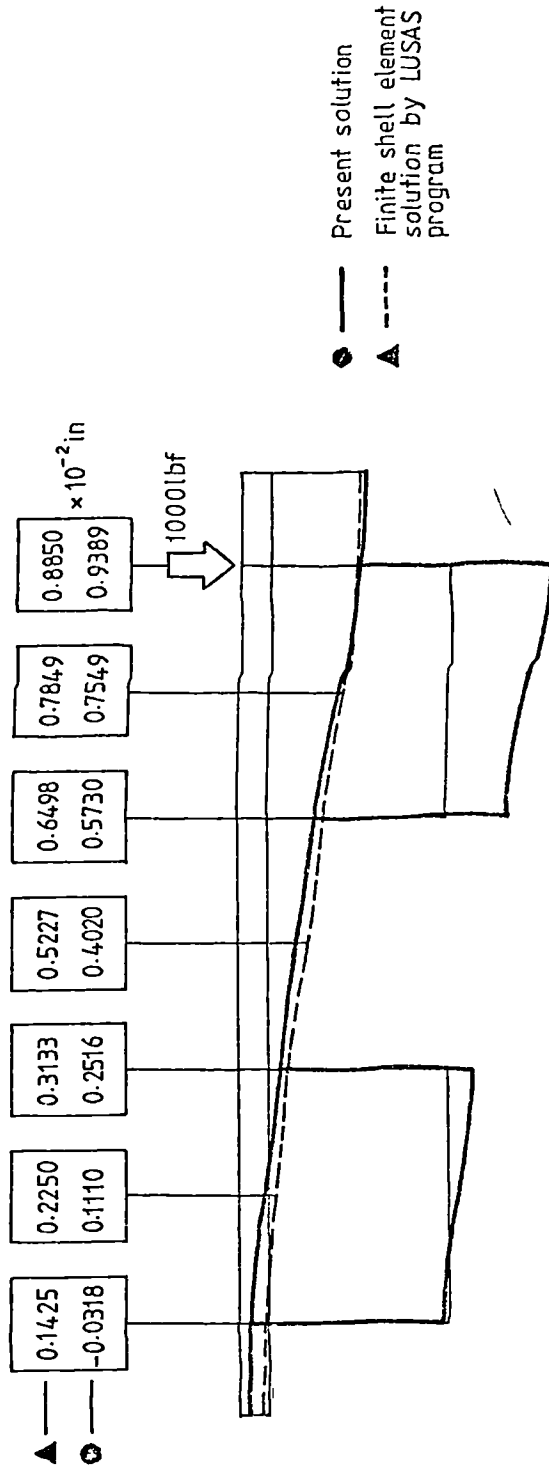
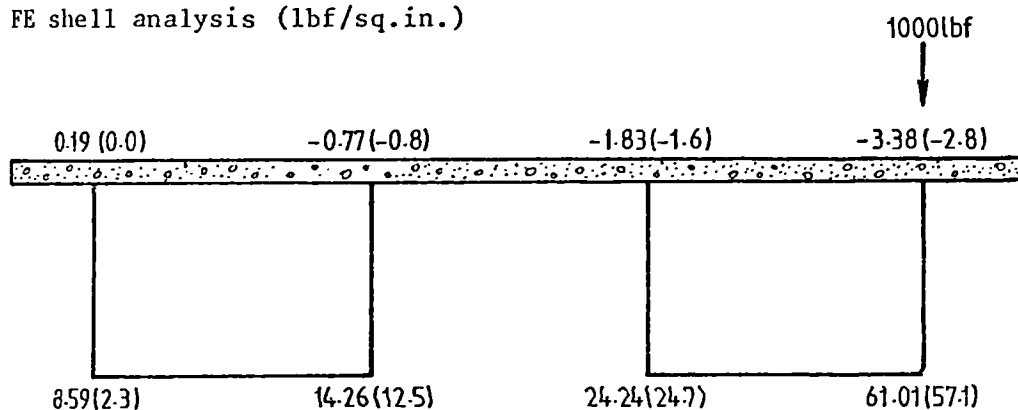


Fig. 6.9 Deflections at midspan in twin-box beam example for a concentrated load applied above an outer web at midspan (1 in. = 25.4 mm, 1 lbf = 4.45 N)

FE shell analysis (lbf/sq.in.)



FE-Grillage analysis (lbf/sq.in.)

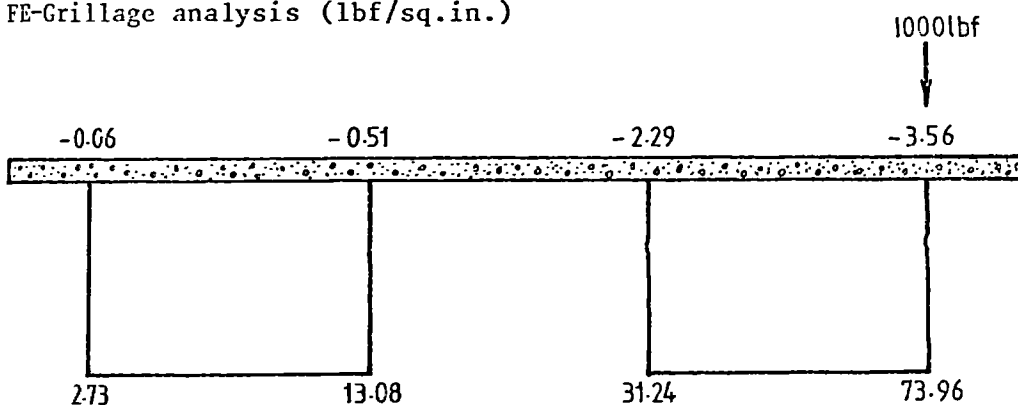
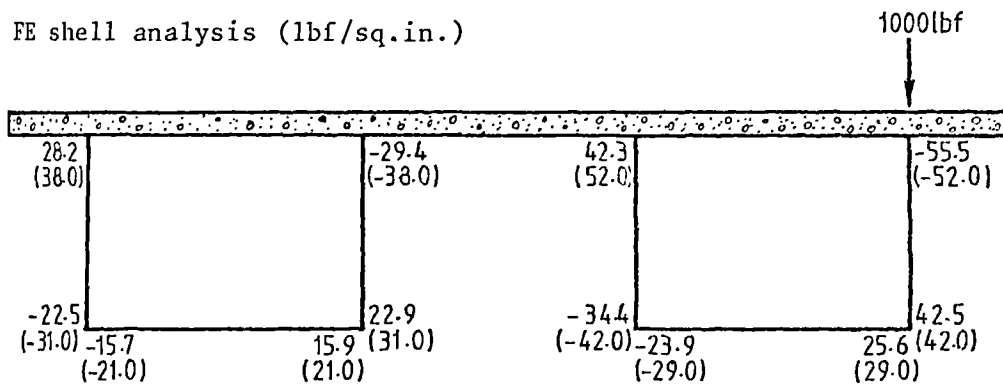


Fig. 6.10 Comparison of longitudinal stresses in twin-box beam example for a concentrated load applied above an outer web at midspan (Values in parentheses are given by Billington<sup>11</sup>) (1 in. = 25.4 mm, 1 lbf = 4.45 N, 1 lbf/sq.in. = 6.9 kN/m<sup>2</sup>)

FE shell analysis (lbf/sq.in.)



FE-Grillage analysis (lbf/sq.in.)

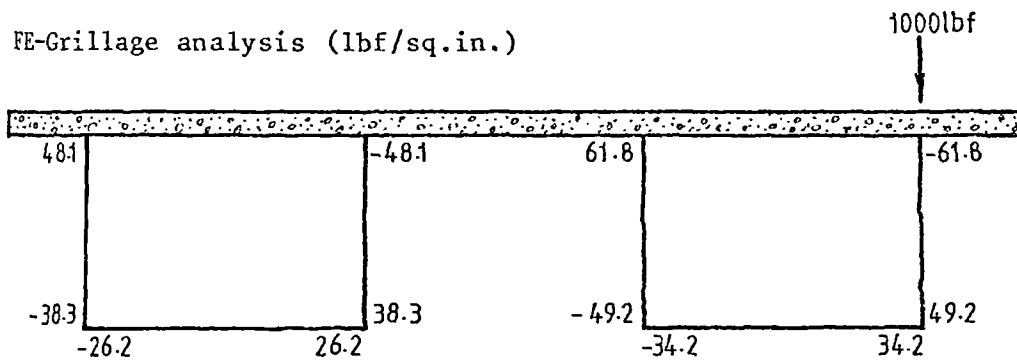


Fig. 6.11 Comparison of transverse distortional bending stresses in twin-box beam example for a concentrated load applied above an outer web at midspan (Values in parentheses are given by Billington<sup>11</sup>)  
(1 in. = 25.4 mm, 1 lbf. = 4.45 N, lbf/sq.in. = 6.9 kN/m<sup>2</sup>)

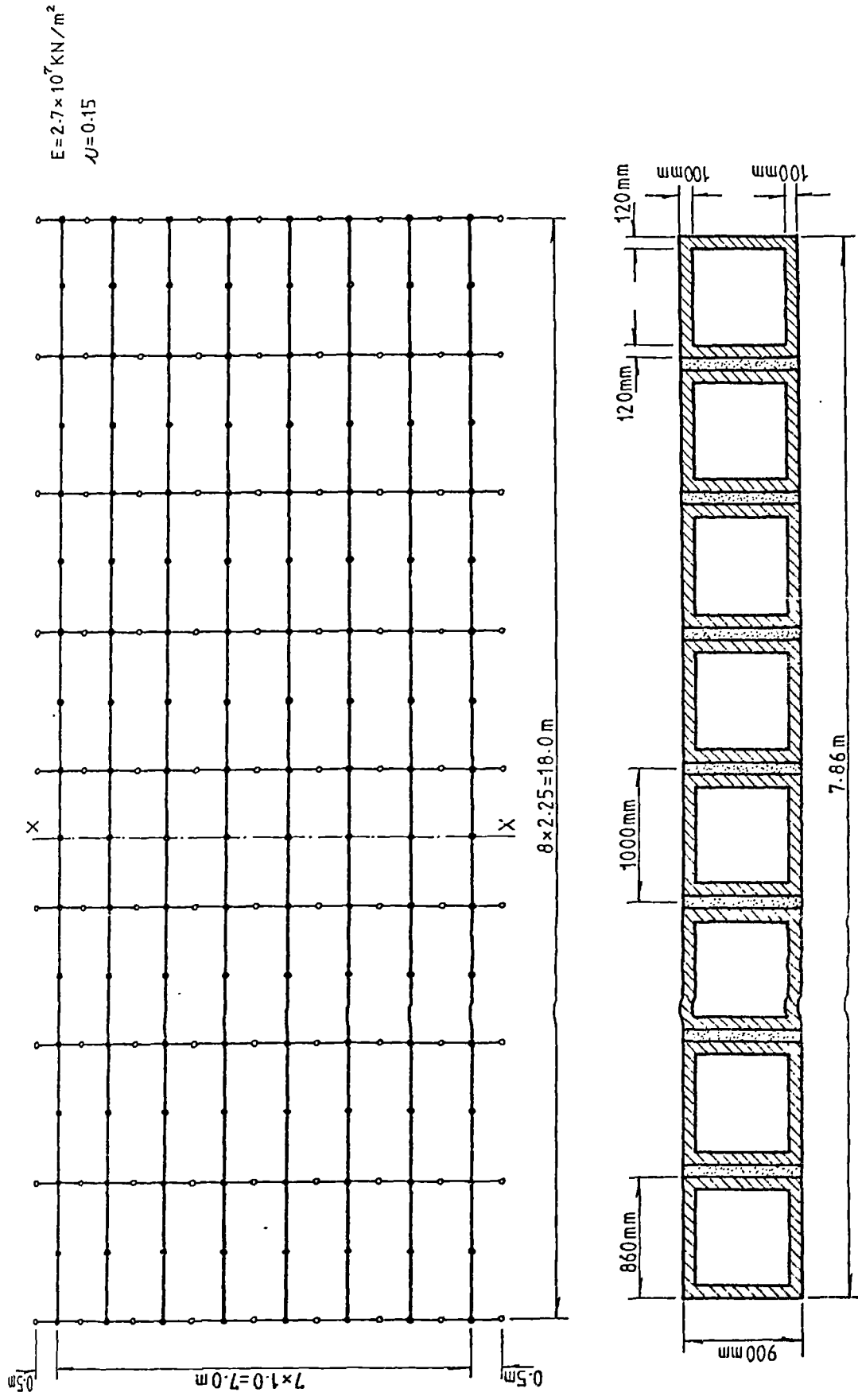


Fig. 6.12 Geometry of Deck and Mesh Arrangement

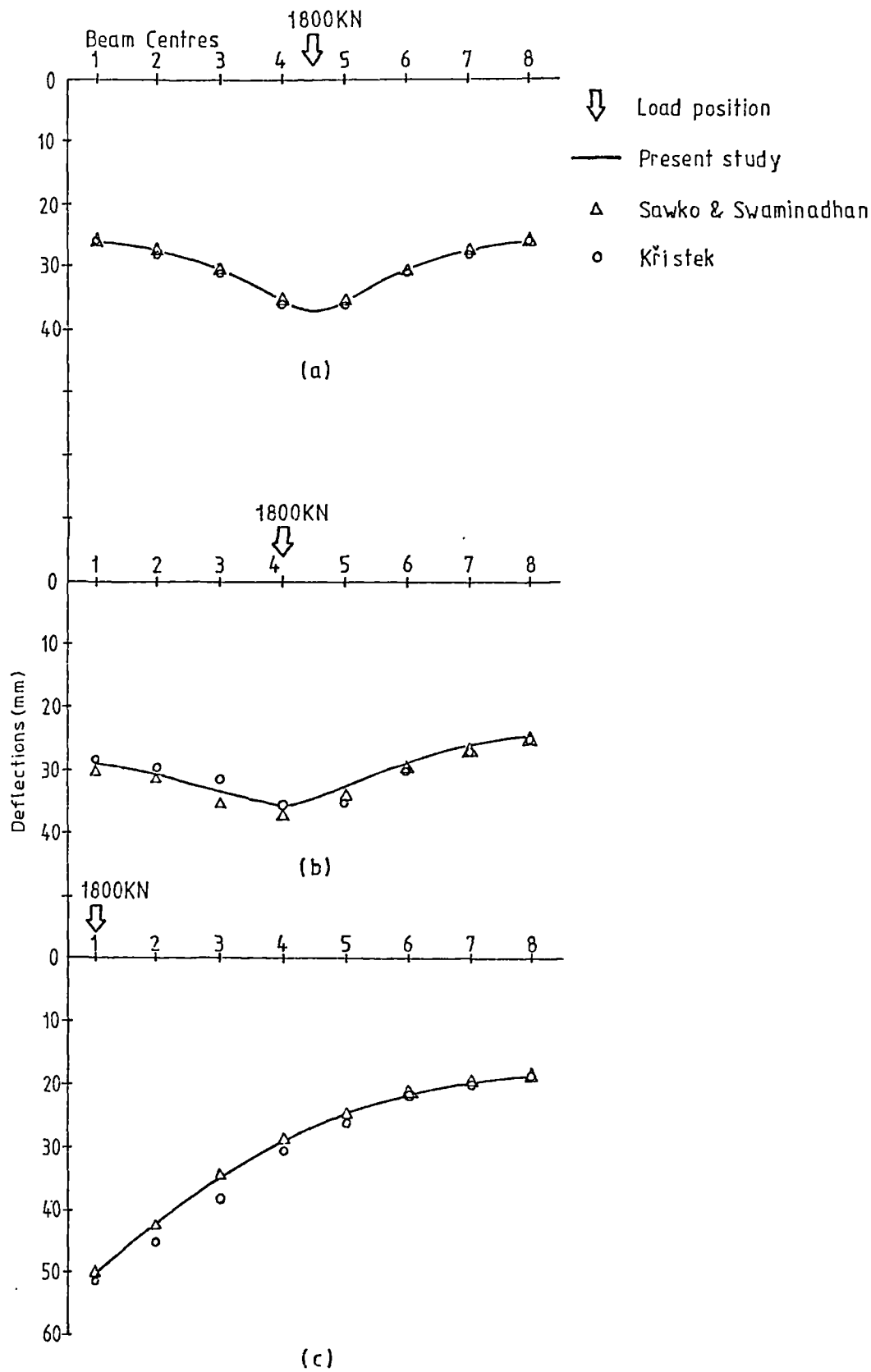


Fig. 6.13 Deflections at Midspan for Right Bridge Deck with Eight Cells

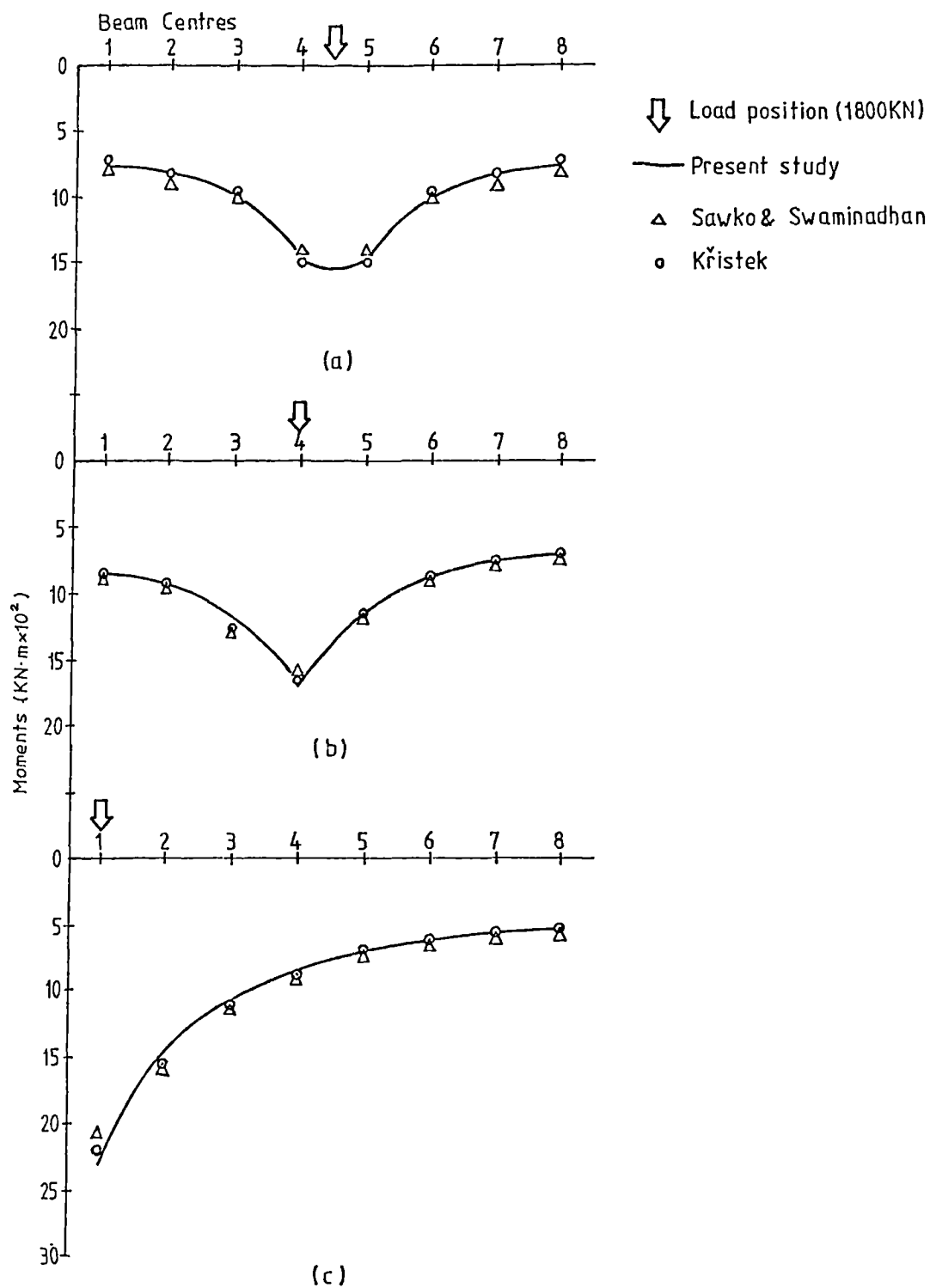


Fig. 6.14 Moments at Midspan for Right Bridge Deck with Eight Cells

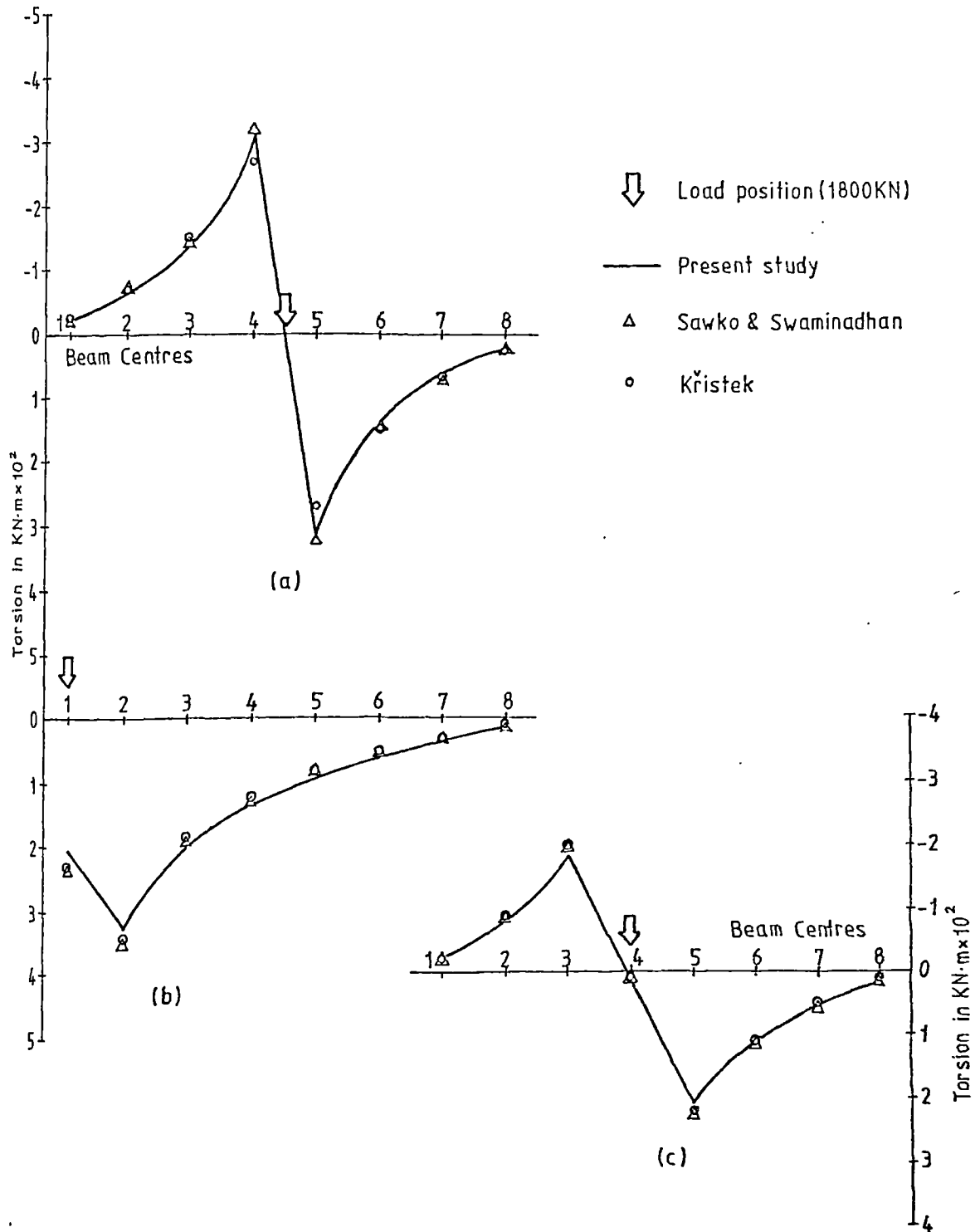


Fig. 6.15 Torsion near Midspan on Section 'XX' for Right Bridge Deck with Eight Cells

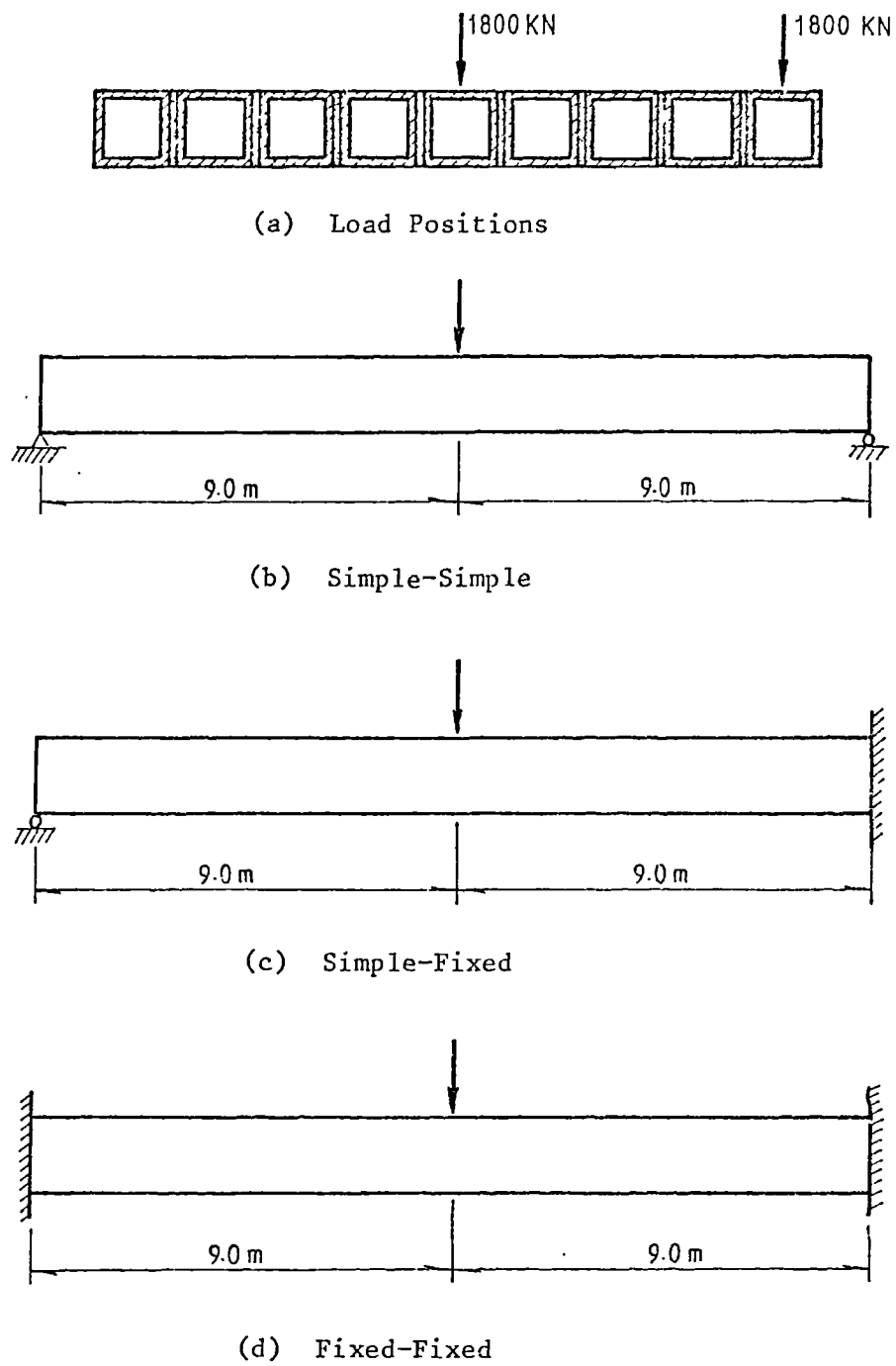


Fig. 6.16 Loading and End Support Conditions

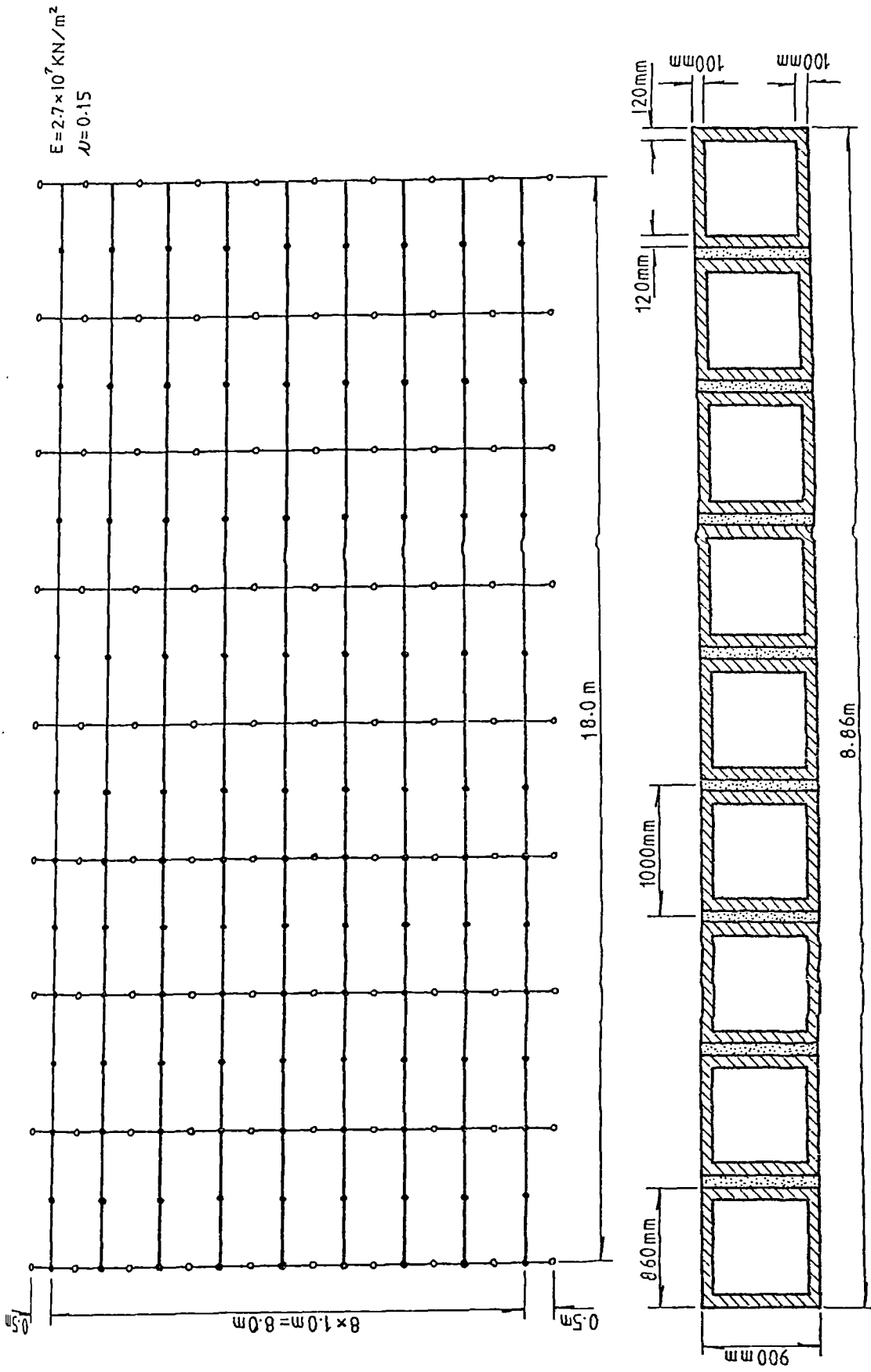


Fig. 6.17 Geometry and Mesh Arrangement for Right Bridge Deck with Nine Cells

Beams Supports	1	2	3	4	5	6	7	8	9
SIMPLE- SIMPLE	22.72 (22.63)	23.89 (23.84)	26.34 (26.35)	30.35 (30.42)	33.28 (32.90)	30.35 (30.42)	26.34 (26.35)	23.89 (23.84)	22.72 (22.63)
SIMPLE- FIXED	8.40 (8.60)	9.38 (9.60)	11.49 (11.77)	15.12 (15.51)	17.88 (17.83)	15.12 (15.51)	11.49 (11.77)	9.38 (9.60)	8.40 (8.60)
FIXED- FIXED	3.85 (4.04)	4.67 (4.88)	6.50 (6.77)	9.82 (10.21)	12.43 (12.40)	9.82 (10.21)	6.50 (6.77)	4.67 (4.88)	3.85 (4.04)

(a) Midspan Vertical Deflections (mm) for Central Loading

Beams Supports	1	2	3	4	5	6	7	8	9
SIMPLE- SIMPLE	48.84 (48.72)	41.17 (41.43)	33.21 (33.32)	27.23 (27.22)	22.72 (22.63)	19.38 (19.25)	17.02 (16.87)	15.52 (15.35)	14.79 (14.61)
SIMPLE- FIXED	29.33 (29.56)	22.54 (23.10)	15.95 (16.30)	11.48 (11.75)	8.40 (8.60)	6.30 (6.46)	4.91 (5.04)	4.07 (4.18)	3.67 (3.77)
FIXED- FIXED	21.26 (21.53)	15.11 (15.67)	9.49 (9.86)	6.02 (6.28)	3.85 (4.04)	2.50 (2.64)	1.67 (1.79)	1.21 (1.30)	1.00 (1.08)

(b) Midspan Vertical Deflections (mm) for Eccentric Loading

Table 6.2 Midspan Vertical Deflections

Beam Nos. Sup- port	Section	1	2	3	4	5	6	7	8	9	Total Moment
		Simple	Mid-span	655.52 (672.72)	701.68 (727.14)	810.51 (857.46)	1072.21 (1132.83)	1620.16 (1319.70)	1072.21 (1132.83)	810.51 (857.46)	
Simple-Fixed	Mid-span	315.69 (339.48)	361.50 (392.89)	469.89 (521.64)	731.31 (795.62)	1279.19 (981.99)	731.31 (795.62)	469.89 (521.64)	361.50 (392.89)	315.69 (339.48)	5036 (5081)
	Sup- port	447.85 (423.53)	508.37 (485.44)	644.40 (630.05)	915.27 (921.65)	1096.27 (1116.10)	915.27 (921.65)	644.40 (630.05)	508.37 (485.44)	447.85 (423.53)	6128 (6037)
Fixed-Fixed	Mid-span	202.41 (226.72)	247.91 (279.27)	355.93 (406.72)	617.13 (679.56)	1164.94 (865.46)	617.13 (679.56)	355.43 (406.72)	247.91 (279.27)	202.41 (226.72)	4012 (4050)
	Sup- port	244.12 (226.72)	296.17 (279.27)	416.42 (406.72)	667.92 (679.56)	839.04 (865.46)	667.92 (679.56)	416.42 (406.72)	296.17 (279.27)	244.12 (226.72)	4088 (4050)

BEAM MOMENTS (kN-M)	
	SUPPORT
SIMPLE-SIMPLE	8100
SIMPLE-FIXED	6075
FIXED-FIXED	4050

Table 6.3 Distribution of Longitudinal Moments for Central Loading (1800 kN)

Beam Nos.	Beam Nos.										TOTAL MOMENT
	1	2	3	4	5	6	7	8	9	10	
Simple-Sup	2276.67 (2036.20)	1445.69 (1551.60)	1030.97 (1099.30)	805.39 (839.43)	655.52 (672.72)	551.81 (560.43)	481.22 (485.29)	437.02 (438.73)	415.71 (416.39)	8100 (8100)	
	1879.79 (1639.20)	1055.50 (1162.80)	653.63 (725.58)	445.61 (485.12)	315.69 (339.48)	231.59 (247.25)	177.76 (188.95)	145.70 (159.45)	130.71 (138.37)	5036 (5081)	
Simple-Fixed	1827.52 (1864.20)	1354.11 (1357.90)	901.14 (878.35)	627.53 (599.12)	447.85 (423.53)	328.68 (309.86)	251.63 (237.14)	205.56 (193.84)	184.02 (173.61)	6128 (6037)	
	1730.10 (1485.10)	910.03 (1014.10)	516.31 (586.71)	319.53 (358.87)	202.41 (226.72)	130.78 (147.12)	87.53 (99.29)	63.04 (72.18)	51.98 (59.93)	4012 (4050)	
Fixed-Fixed	1443.55 (1485.10)	1007.51 (1014.10)	606.09 (586.71)	381.69 (358.87)	244.12 (226.72)	158.60 (147.12)	106.49 (99.29)	76.83 (72.18)	63.41 (59.93)	4088 (4050)	

BEAM MOMENTS (kN-M)	MIDSPAN		SUPPORT
	SIMPLE-SIMPLE	8100	0
SIMPLE-FIXED	5063	6075	
FIXED-FIXED	4050	4050	

Table 6.4 Distribution of Longitudinal Moments for Eccentric Loading (1800 kN)

## CHAPTER 7

## STATIC ANALYSIS OF CABLE-STAYED BRIDGES

7.1 Introductory remarks

As a practical application of the one-dimensional finite element family to the analysis of bridge decks, in this chapter we will discuss the static analysis of cable-stayed bridges. Despite the fact that the concept and practical application of cable-stayed systems have been attractive to engineers and builders for centuries (98), a successful implementation has been realized only recently, with the introduction of high-strength steels, progress in structural analysis and model studies, and the development of electronic computers. Ever since the first modern cable-stayed bridge, the Strömsund Bridge, was completed in Sweden in 1955, the number of applications of this type of bridge has grown rapidly. This indicates its competitiveness in medium and long span bridge construction.

The cable-stayed bridge consists of a stiffened girder at deck level, rigidly supported on abutments and piers and elastically supported at intermediate points by inclined cables. The cables are suspended from towers located at interior supports. In contrast with conventional suspension bridges, the essential feature of this type of bridge is that the reactions from the cables are transferred directly to the bridge deck (Fig. 7.1). Thus, the deck in a cable-stayed bridge is subjected to the combined effects of both axial forces and bending moments.

The cable-stayed bridge is a highly statically indeterminate space structure which is difficult and tedious to analyse. Most of the existing analytical methods approximate the real structure to a two-dimensional plane frame. This approach is relevant only to the single-plane system in which torsional forces acting on the deck would have to be superimposed on the

girder. If the bridge girder is suspended along its edges, the additional torsional resistance provided by the stayed cables is rather significant. In spite of its complexity, an analysis taking into account the three-dimensional space action is then necessary.

The complexity of the analysis is caused not only by the necessity of considering the space action, but also by the fact that the cable-stayed bridge displays a nonlinear structural behaviour. The nonlinearity is due to large displacements, bending moment-axial force interaction and the catenary action of the inclined cables. The structural problem is then a geometrically nonlinear problem together with the non-linear material of the cables. In addition, the creep of the concrete and the relaxation of the cable may also induce nonlinearity in the analysis. For a nonlinear structure, the principle of superposition does not apply and consequently, it is not possible to determine stresses and displacements by superposition of influence lines as in the case of linear bridge systems. The analysis of a cable-stayed bridge should be carried out by loading the system with its full dead and live loads.

The objective of this chapter is to apply the one-dimensional finite element family developed in this thesis to a plane or spatial frame model of the cable-stayed structure combining it with a Newton-Raphson iterative scheme. Firstly, a review of different structural forms which can be used for the cables, the decks and the towers, is made. The existing methods of analysis are then briefly introduced. A detailed derivation of an equivalent modulus of elasticity of the inclined cable, considering the catenary action, is given. A stiffness analysis based on the one-dimensional finite element system and on the Newton-Raphson algorithm has then been devised. Finally, a numerical example and a practical construction are investigated to confirm the validity of the present study.

## 7.2 Geometric configuration of cable-stayed bridges

The cable-stayed bridge has a large variety of different geometrical configurations. The variety is shown in the span arrangements, the types and geometric configurations of the cables, the superstructure types, the tower configurations and placement etc. The combination of these different features lends itself to versatility in relation to the environmental requirements and the optimisation of design.

It is not the object of this thesis to attempt to present an extensive study of all aspects of the structural features involved in design, but for the sake of understanding the following analytical process, a general description concerning possible structural forms is made.

### 7.2.1 Span arrangements

The span arrangements of cable-stayed bridges can be categorized as of three basic types: two spans, symmetrical or asymmetrical, Fig. 7.2; three spans, Fig. 7.3; or multiple spans, Fig. 7.4.

A partial survey of existing bridges (97) indicates that, for the two-span asymmetrical bridge structure, the length of the longer span ranges from 0.60 - 0.70 of the total length. In three-span structures the ratio of centre span length is of the order of 0.55. An investigation of bridges with multiple spans indicates that the spans are normally of equal length, with the exception of the flanking spans which are adjusted to connect with the approach span or abutments.

To avoid high longitudinal bending moments in the towers and to use a system which brings mainly vertical loads to the foundation, Leonhardt (69) proposed two alternative multispan cable-stayed bridge structures shown in Fig. 7.5.

### 7.2.2 Stay geometry

There are two basic arrangements for the positions of cables in space, viz. the single-plane system and the two-plane system (Fig. 7.6). For very wide bridges with combined railway and highway traffic 3 or 4 cable planes might be chosen.

The single-plane arrangement consists of one vertical plane of cables normally located on the longitudinal centre line of the structure. A variation of this arrangement occurs when the vertical plane of the cables is positioned laterally from the longitudinal centre line of the structure.

In the two-plane system the cables may lie in two vertical or oblique planes. The latter is recommended for very long spans where the tower has to be very high and needs the lateral stiffness given by the triangular frame effect.

According to the various longitudinal cable arrangements, there are four basic systems that are normally used (Fig. 7.7): 1. The radiating or converging system where all the cables are spaced along the girder and are attached at a common point on the tower; 2. The harp system where the cables are parallel to each other and are spaced along the girder and the tower; 3. The fan system where the cables are spaced along the girder and the tower but are not parallel to each other; 4. The star system where the cables are spaced along the tower and converged at a common point on the girder. Within the four basic systems a number of variations are available.

A tabular summary of the various arrangements is presented in Fig. 7.8. A recent tendency is for a large number of stays to be used with spacings at the deck anchorage of only 8 to 15m. The beam girder then behaves mainly as the compressive chord member of a cantilever structure suspended from the towers by inclined stay cables (69).

### 7.2.3 Superstructure types

Basically there are two types of girder: the stiffening truss and the solid web type. In practice, the stiffening truss is seldom used. Cross-sections of solid web steel girders are shown in Fig. 7.9a. Of these the box girder type with an orthotropic deck is most widely used.

In recent years a number of cable-stayed bridges have also been built with reinforced or prestressed concrete girders. These bridges are economical, possess high stiffness and exhibit relatively small deflections. The damping effect of these monolithic structures is very high and vibrations are relatively small. Typical cross-sections of this system are shown in Fig. 7.9b.

The proportion of the girder depth to the length of span varies from 1:40 to 1:100. In multi-stay-cable systems, the depth of the longitudinal girder is almost independent of the main span and should be chosen to be small. Furthermore, if the girder is suspended along its edges, a simple concrete slab or an orthotropic steel plate with massive edge ribs or hollow edge girders is sufficient (Fig. 7.10).

### 7.2.4 Tower types

Cable-stayed bridge towers are designed to suit the site and design conditions, as well as for aesthetic considerations and to suit cable geometry. The various possible types of tower construction are illustrated in Fig. 7.12, which shows that they may take the form of

1. Single towers (Fig. 7.11a and b),
2. Twin towers (Fig. 7.11d),
3. Rectangular or trapezoidal portal frames (Fig. 7.11e),
4. A-shaped frames (Fig. 7.11f),
5. Diamond-shaped towers (Fig. 7.11g),
6. Inverted Y-shaped tower (Fig. 7.11c).

The height of the towers influences the necessary amount of cable steel and the longitudinal compressive forces in the bridge deck. Tower height normally rises to about  $0.2L$  up to  $0.25L$ , where  $L$  is the length of the span.

### 7.3 Brief review of some of the existing analytical methods

Various analytical methods have been devised, based on computer applications, to consider the linear and nonlinear behaviour of cable-stayed bridge systems. Most papers published on the static behaviour of cable-stayed bridges related only to the simplified idealization of a two-dimensional plane frame structure.

The transfer matrix method, also referred to as the reduction method, which was developed in Germany, has been applied to the analysis of cable-stayed bridges by Tang (139). An iterative process which treats all nonlinear terms as imaginary external loads, considers both the nonlinear behaviour of girders and towers as well as the special force-deformation relationships of the cables and is suitable for computer programming.

Trotsky and Lazar (143) used a flexibility approach to obtain analytical data for comparison with experimental results. Lazar (65) also proposed the standard stiffness method for carrying out a two-dimensional frame analysis. The general computer programs employed, e.g. FRAN, STRESS, STRUDL, are adjusted through methods (19, 86, 91, 112) which take into account the nonlinearity due to large displacements, axial force-bending moment interaction and cable catenary action. When the Southern Crossing Bridge across San Francisco Bay was being designed in 1972, a space frame idealization was proposed by Baron and Lien (7).

A mixed force-displacement method was developed by Stafford Smith (131). As one of the exceptions to consider the space behaviour of cable-

stayed bridges, Smith extended his approach to the analysis of double-plane cable-stayed bridges and treated the deck as a plate.

An attempt was made by Goschy (38,40) to give an analytical method for a twisted cable-stayed bridge. The approach is based on the theory of thin-walled structures, developed by Vlasov (146). The structure is considered as a three-dimensional system consisting of a stiffening girder supported by inclined cables.

Kajita and Cheung (53) studied the linear analysis of a double plane cable-stayed bridge by the finite element method, in which the bridge deck was divided into a number of shell elements and the whole structure treated as a three dimensional system. A computer program has been developed which can deal with various saddle types for the cables and also various types of connections between the tower and the deck.

#### 7.4 Behaviour of catenary-stayed cables

The actual shape of a perfectly flexible cable hanging freely under its own weight and tensioned at both ends is a kind of curve known as the catenary. The end displacement of the cable under an axial load depends not only on the cross-sectional area and the modulus of elasticity of the cable but to a certain extent on the cable sag. As a result, the cable does not behave linearly and it is necessary to adopt a corrective technique to account for the nonlinear effect.

To facilitate the analysis of cable-stayed bridges, all cables are assumed to be straight members and are represented geometrically by their chord. The tension forces calculated are also assumed to act along the chord lines. For small sag ratios the error is within acceptable limits for design purposes. In addition, cables are also assumed to remain in tension.

This assumption is reasonable because all the cables must be relatively highly stressed under dead load in order to act as effective supports for the bridge girder.

For representing the nonlinear effect due to the change of sag several methods have been proposed by various authors who suggest the use of an equivalent modulus of elasticity for the cable (26, 39, 145). The basic principle in the analysis for the cable tension force is that the behaviour of the straight substitute member with an equivalent modulus of elasticity is nearly identical to that of the catenary curved cable. The most popular proposal uses an expression for the equivalent modulus of elasticity given by Ernst (26):

$$E_{eq} = \frac{E}{1 + [(\rho L)^2 / 12 \sigma_y^3] E} \quad (7.1)$$

where  $E_{eq}$  = equivalent modulus of elasticity,

$E$  = modulus of elasticity of the cable material,

$\rho$  = specific weight of the cable,

$L$  = horizontal length of the cable,

$\sigma_y$  = tensile stress in the cable.

For protection against corrosion, the cables are normally wrapped with glass fibre tissue drenched in polyethylene or polyurethane. An alternative proposition is to coat the cable by a prestressed concrete tube after erection. As a result, the cables are no longer perfectly flexible and a certain bending stiffness may exist. The stiffened cables are termed semi-stiffened cables (128). We here devise a more general formula for the evaluation of the equivalent modulus of elasticity involving not only the tensile stiffness but also the bending stiffness due to the coating.

Let us now consider an inclined cable with hinged ends subjected to uniformly distributed load (Fig. 7.12). The simple beam moment of the cable

under load component  $q_1$  is given by

$$M_s = -EI \frac{d^2 v}{dz^2} \quad (7.2)$$

From the basic principles of static equilibrium the cable moment can be determined by

$$M_s = M_c + M_q \quad (7.3)$$

$$\text{where } M_c = -T \cdot v \quad (7.4a)$$

$$\text{and } M_q = \frac{q_1 z}{2} (\ell - z) \quad (7.4b)$$

Substitution of Eqs. 7.3 and 7.4 into Eq. 7.2 gives the basic differential equation for the cable,

$$\frac{d^2 v}{dz^2} - \alpha_c^2 v = \frac{q_1}{2EI} (z^2 - \ell z) \quad (7.5)$$

$$\text{where } \alpha_c^2 = T/EI, \quad (7.6)$$

and  $T$  is the tensile force of the cable along the chord.

By solving this second order nonhomogeneous linear equation with constant coefficients we have

$$v = \frac{q_1}{T} \cdot \frac{1}{\alpha_c^2} \cdot \left[ \frac{\text{ch} \alpha_c \left( \frac{\ell}{2} - z \right)}{\text{ch} \frac{\alpha_c \ell}{2}} - 1 \right] - \frac{q_1}{2T} (z^2 - \ell z) \quad (7.7)$$

The cable length is

$$S = \int_0^\ell \sqrt{1 + \left( \frac{dv}{dz} \right)^2} dz \quad (7.8a)$$

and by using the curtailed form of Taylor's series expansion, we may write

$$S = \ell + \frac{1}{2} \int_0^\ell \left( \frac{dv}{dz} \right)^2 dz \quad (7.8b)$$

Differentiating Eq. 7.7 once and substituting into Eq. 7.8(b),  
the cable length can then be expressed as

$$S = l + \frac{1}{2} \left( \frac{q_1 l}{T} \right)^2 l \left[ \frac{5\text{sh}\alpha_c l - 3\alpha_c l - 2\alpha_c l \text{ch}\alpha_c l}{(1 + \text{ch}\alpha_c l) \cdot (2l)^3} + \frac{1}{12} \right] \quad (7.9)$$

The differentiation of Eq. 7.9 yields

$$dS = \left\{ 1 + \frac{G^2}{T^2} \left[ \frac{1}{2} \cdot \frac{5\text{sh}\alpha_c l - 3\alpha_c l - 2\alpha_c l \text{ch}\alpha_c l}{(1 + \text{ch}\alpha_c l)(\alpha_c l)^3} \right] + \frac{1}{24} + \frac{1}{2} \frac{4\alpha_c l - 15}{(\alpha_c l)^3} \right\} dl -$$

$$\frac{G^2 l}{T^3} \left\{ \frac{1}{12} + \frac{5\text{sh}\alpha_c l - 3\alpha_c l - 2\alpha_c l \text{ch}\alpha_c l}{(1 + \text{ch}\alpha_c l)(\alpha_c l)^3} - \frac{1}{4} \cdot \frac{4\alpha_c l - 15}{(\alpha_c l)^3} \right\} dT \quad (7.10)$$

$$\text{where } G = q_1 l = \rho A l \cos \beta_c = w_g l \cos \beta_c = w_g L \quad (7.11)$$

According to Hooke's law, the elongation of the cable due to the  
change of the tensile force T is approximated by

$$\frac{dS}{dT} = \frac{S}{EA} \quad (7.12)$$

where A is the sectional area of the cable.

The axial deformation of the chord due to the change of the tensile  
force T may be expressed similarly by using the apparent modulus of  
elasticity,

$$\frac{dl}{dT} = \frac{l}{E_{eq} \cdot A} \quad (7.13)$$

Substituting Eqs. 7.12 and 7.13 into Eq. 7.10, using the chord length  
as the length of the cable, and assuming  $e^{-\alpha l} = 0$ , we finally obtain an  
expression for the equivalent modulus of elasticity in the form

$$E_{eq} = \frac{E}{1 + \frac{(w_g L)^2 AE}{T^3} \left[ \frac{1}{12} - \frac{3\alpha_c l - 35/4}{(\alpha_c l)^3} \right]} \quad (7.14)$$

If we substitute  $I = 0$  into Eq. 7.14, we may obtain directly the well known Ernst formula for the flexible cable

$$E_{eq} = \frac{E}{1 + [(w_g L)^2 A E / 12 T^3]} \quad (7.15)$$

where  $L$  is the horizontal component of the chord length, and  $w_g$  is the weight per unit length of the cable.

Since the stiffness of the cable-stayed bridge depends largely upon the tensile stiffness of the stayed cables, the utilization of semi-stiffened cables will improve the structural behaviour of the whole bridge to some extent. However, there are difficulties in actual construction, so it is still seldom used practically. It is also apparent both from Eq. 7.14 and 7.15 that the analysis becomes an iterative process requiring several determinations of cable stresses and the corresponding equivalent moduli of elasticity until a convergence of the values is achieved.

#### 7.5 Stiffness method of analysis with approximate nonlinear considerations

Since cable-stayed bridges are generally large and important structures used for long spans, many alternative structural forms need to be compared and many load cases have to be considered. It does not seem a realistic solution to use the three-dimensional finite element plate or shell analysis (53) for design purposes. Although the cable-stayed system in modern bridge engineering has a large variety of geometrical configurations as shown in Figs. 7.2 - 7.12, a linear statical analysis can be carried out without any difficulties by using the present one-dimensional finite element family. The structure can be modelled as either a plane frame or as a spatial frame according to the accuracy required. By choosing relevant types of elements available in the family of elements, deformations due to shear, distortion and warping of the girder section can be considered.

The difficulties arising in the statical analysis of cable-stayed bridges are those associated with particular considerations of nonlinear features. As stated in previous sections, the cable-stayed system is so flexible that the deflections both from the deck and from the towers change significantly the orientation of the stayed cables and consequently the horizontal and vertical components of the cable forces. These changes introduce, in the deck, new axial forces and bending moments which cannot be deduced through any conventional linear analytical method. Accordingly, bending moment-axial force interaction also needs to be taken into account in the analysis. Thus, the problem is that of a structure with large displacements; this transforms it into a geometrically non-linear problem. In addition, because of the sag change, the cables do not behave linearly. Thus some of the elements of the structure have a non-linear behaviour which cannot be related directly to the deflections of the deck and the towers. For these reasons, the structural problem becomes a geometrically nonlinear problem with a non-linear material.

Whether the displacements (or strains) are large or small, equilibrium conditions between internal and external forces have to be satisfied. Following the minimum potential energy process, the nonlinear equilibrium equations become (149, 155)

$$\bar{R}(\delta) = \int_1 \bar{B}^T \bar{\sigma} dz - F = 0 \quad (7.16)$$

where  $\bar{R}$  represents the sum of external and internal generalized forces, in which the integration is carried out over the whole length  $l$  of the element, the strain matrix  $\bar{B}$  is defined from the general definition of strain as

$$d\bar{\epsilon} = \bar{B} d\delta \quad (7.17)$$

the stress resultants  $\bar{\sigma}$  are written in terms of the elasticity matrix  $\bar{D}$  and the strain vector  $\bar{\epsilon}$  as

$$\bar{\sigma} = \bar{D}\bar{\epsilon} \quad (7.18)$$

and  $\mathbf{F}$  is a vector of equivalent nodal forces due to the external forces.

The solution for the nonlinear equations (7.16) is based on the Newton-Raphson method involving a series of solutions to linear incremental equilibrium equations (Fig. 7.13). If an initial estimation of the total displacements is  $\delta_i$  for which  $\bar{R}(\delta_i) \neq 0$ , then the value of  $\bar{R}$  for an increment  $\Delta\delta_i$  in  $\delta_i$  is given by Taylor's series expansion of  $\bar{R}$  about  $\delta_i$  ignoring third and succeeding terms as follows:

$$\bar{R}(\delta_i + \Delta\delta_i) = \bar{R}(\delta_i) + \frac{\partial \bar{R}(\delta_i)}{\partial \delta_i} \Delta\delta_i + \dots$$

which can be written as

$$\bar{R}(\delta_i + \Delta\delta_i) = \bar{R}(\delta_i) + \mathbf{K}_T \Delta\delta_i \tag{7.19}$$

where  $\mathbf{K}_T$  is called the tangent stiffness matrix evaluated at  $\delta = \delta_i$ .

It can be seen that problems involving geometric nonlinearity arise both from non-linear strain-displacement relations, and from finite changes in geometry. Assuming that the curvature is small, the large deformation strain (Green-Lagrange strain) is defined in terms of the displacements as

$$\bar{\epsilon} = \left\{ \begin{array}{l} -\theta_y + \frac{\partial u}{\partial z} \\ \theta_x + \frac{\partial v}{\partial z} \\ \frac{\partial w}{\partial z} \\ \frac{\partial \theta_x}{\partial z} \\ -\frac{\partial \theta_y}{\partial z} \\ \frac{\partial \theta_z}{\partial z} \\ -\frac{\partial^2 \theta_z}{\partial z^2} \\ \gamma_d \\ -\frac{\partial^2 \gamma_d}{\partial z^2} \end{array} \right\} + \left\{ \begin{array}{l} \left( \frac{\partial w}{\partial z} \right) \left( \frac{\partial w}{\partial x} \right) \\ \left( \frac{\partial w}{\partial z} \right) \left( \frac{\partial w}{\partial y} \right) \\ \frac{1}{2} \left[ \left( \frac{\partial u}{\partial z} \right)^2 + \left( \frac{\partial v}{\partial z} \right)^2 + \left( \frac{\partial w}{\partial z} \right)^2 \right] \\ 0 \\ 0 \\ 0 \\ 0 \\ 0 \\ 0 \end{array} \right\} \tag{7.20a}$$

or

$$\bar{\epsilon} = \bar{\epsilon}_0 + \bar{\epsilon}_L \tag{7.20b}$$

Furthermore, a particle  $p$  on the beam axis in an initial undeformed position is identified by the Lagrangian coordinates:

$$\{X\} = [X, Y, Z]^T, \quad (7.21)$$

and the same particle is identified in the final deformed position  $p$  by the Eulerian coordinates:

$$\{\bar{X}\} = [\bar{X}, \bar{Y}, \bar{Z}]^T, \quad (7.22)$$

where a bar above an item ( $\bar{\quad}$ ) denotes reference to the deformed position of the element. A bar omitted signifies reference to the initial undeformed position. Coordinates are with respect to fixed Cartesian axes, i.e., the global coordinate system.

If the displacements  $u$  of the particle  $p$  in deforming to  $p'$  are given a function of  $\{X\}$  or  $\{\bar{X}\}$  by

$$u(X) = u(\bar{X}) = [U, V, W]^T \quad (7.23)$$

then the final coordinates are given by

$$\{\bar{X}\} = \{X\} + \{u\} \quad (7.24)$$

It can be seen that the cable-stayed superstructure mainly performs as a truss system, and that the bending moments in the stiffening girder depend largely on the magnitude of deflection of the stiffening girder at the locations of cable attachments. The deformations of the system change the angle of inclination of the cable with respect to the chord of the girder and consequently lead to the redistribution of the stresses in the girder. This means that for a cable-stayed bridge the 'change in geometry' effect is more important than the relative magnitudes of the linear and non-linear strain-displacement terms. Hence, as an approximation we may ignore the non-linear portion in the Green-Lagrange strain vector, i.e.,

$$\bar{\epsilon} = \bar{\epsilon}_0 \quad (7.25)$$

Thus the tangential stiffness matrix is equivalent to the conventional stiffness matrix which is used in any small displacement-small strain analysis, but is also a function of the current value of the displacements. It can then be expressed as (155)

$$K_T = K_0(\delta_j) \quad (7.26)$$

in which  $K_0$  represents the usual, small displacements stiffness matrix.

As tested designs indicate, the change of stresses, considering the influence of deformations on cable-stayed systems, does not exceed a few percent (34). The error produced by neglecting the whole nonlinear behaviour of the cable-stayed bridge may increase however, according to Wintergerst, up to 12.4% (65). The relatively small influence of the deformation of the whole system on the magnitudes of the computed forces in the members of the structure, justifies the application of an approximate method of analysis. Tang (139) and Lazar (65) have adopted a similar approach in their analytical processes.

Moreover, all the two-node elements in the present family are assumed to remain straight after deformation, which is reasonable only when the axial force is small in comparison with the Euler load (112). Thus, it is advantageous to use the three-node elements for the idealization of cable-stayed bridges. Since the bowed shape of the element after deformation can be mapped by the changed coordinates of the three nodes, the interaction between bending moment and axial force can be approximately considered.

From Eqs 7.19 and 7.26 the linearized approximation for the relation between the residual force vector  $R_i$  and the resulting increment in nodal displacements  $\Delta\delta_j$ , necessary to achieve equilibrium, is

$$\Delta\delta_j = K_0^{-1}(\delta_j)R_i \quad (7.27)$$

from which a new approximation to the total displacements is obtained as,

$$\delta_{i+1} = \delta_i + \Delta\delta_i, \quad (7.28a)$$

$$\text{or } \delta_{i+1} = \delta_i + K_o^{-1}(\delta_i) \cdot R_i, \quad (7.28b)$$

$$\text{where } R_i = F - K_o(\delta_i) \cdot \delta_i \quad (7.29)$$

is the residual load vector.

Thus we only need to solve at each step a linear system of equations defined by the tangential stiffness matrix,  $K_o$ , computed on the deformed structure. In order to find a complete equilibrium path,  $R_i$  is applied as a series of incremental loads. The residual load vector has two terms: The first one is formed by the external loads currently applied on the structure, and the second one is the sum at each node of the end forces of all the elements which are connected to this node. These forces have to be projected over the global coordinate directions and to do this, the current orientation of each element has to be considered. Iterations continue within a load increment until  $R$  satisfies a given convergence criterion.

The non-linearity in the response of cable stays does not affect the analytical method which has just been described. The only difficulty is in evaluating the cable tension at each iteration. The well-known Ernst formula Eq. 7.15 or Eq. 7.14, which determines the equivalent cable modulus due to the sag effect, can be used to compute at any moment the tangent stiffness of the cable. However, Eqs. 7.14 and 7.15 are based on a constant value of force or stress, i.e., a zero force or stress increment. They cannot give an accurate value of cable tension after each iteration which is what is needed to compute the nodal forces to be used in Eq. 7.28. The cable tension can be determined through an independent iterative procedure which has been described in Fig. 7.14, using the secant modulus in each iteration which can be expressed by (97):

$$E_{eq} = \frac{E}{1 + \left[ \frac{(w_g L)^2 (T_i + T_{i+1}) A \cdot E}{24 T_i^2 T_{i+1}^2} \right]} \quad (7.30)$$

In this equation  $E$  is the cable material modulus,  $L$  is the horizontal projected length of the cable,  $w_g$  is the weight per unit length of the cable,  $A$  the cross-sectional area of the cable and  $T_i$  and  $T_{i+1}$  are the cable tensions corresponding to two consecutive steps in the Newton-Raphson process.

The problem which arises in computing the secant modulus is that  $T_{i+1}$  is not known. A first estimate of cable tension,  $T_{i+1}^1$ , can be determined by using the tangent modulus corresponding to a cable tension equal to  $T_i$ . Once  $T_{i+1}^1$  is known, the secant modulus corresponding to the interval  $T_i$ ,  $T_{i+1}^1$  is determined according to Eq. 7.29 and a new estimation of cable tension,  $T_{i+1}^2$ , is computed. This process is repeated until satisfactory convergence is reached. Convergence is obtained quickly and three iterations are usually sufficient in most cases.

In addition, cable-stayed bridges are structures in which initial stresses are very important and have to be considered when a non-linear analysis is to be performed. The initial stresses are usually known, since they are introduced during the erecting stages. It is possible to adjust the axial forces in the cables to assign the erected *dead load stresses* to compensate for extreme live load stresses and to achieve more effective use of material. For example, the cable tension can be defined in such a way that each cable supports the dead weight of its corresponding girder length.

In order to apply the Newton-Raphson iteration to analyse the response of the complete bridge structure to any live load, the complete set of member forces which are left after the end of the construction process has to be given as initial data to start the nonlinear analysis. To achieve equilibrium conditions all the dead loads have to be idealized by a system of nodal loads. These are added to the nodal live loads to form the nodal load vector to be considered in the nonlinear analysis (Eq. 7.28). The

initial member forces together with the member forces due to live load, which are found after iteration, after being projected along the global coordinate directions, will form the nodal auxiliary force vector to be used in Eq. 7.28. Then a new distribution of member forces will be obtained, since the initial forces are resolved at any iteration according to the current orientation of each element.

#### 7.6 Numerical example and analysis of Santai cable-stayed bridge

A numerical example given by M.C. Tang (139, 140) will be used to verify the nonlinear analytical process described in the previous section. The dimensions of the cable-stayed bridge and the basic specifications are shown in Fig. 7.15(a). For evaluating the stresses of the bridge under dead load Tang selected the statically determinate base system as shown in Fig. 7.15(b), and assigned the following values to M:

$$M_5 \text{ tower} = 0 ,$$

$$M_6 \text{ girder} = -50,000 \text{ ft-kips } (-67862.5 \text{ kN-m}),$$

$$M_{11} \text{ girder} = -20,000 \text{ ft-kips } (-27145.0 \text{ kN-m}),$$

$$M_{16} \text{ girder} = -10,000 \text{ ft-kips } (-13572.5 \text{ kN-m}).$$

Thus, the stress state of the bridge under dead load is established, whereby the cable tension is determined as follows:

$$T_{\text{left}} = 9680 \text{ kips } (43076 \text{ kN}) , T_{\text{right}} = 11500 \text{ kips } (51175 \text{ kN})$$

For nonlinear analysis due to uniform live load of a magnitude of 8.0 kips per linear ft. (116.72 kN/m), the initial stress state of the system under dead load, is assigned as shown in Fig. 7.15(c). The whole structure is idealized using eighteen three-node beam elements and two cable elements. The bending moment diagram due to live load is shown in Fig. 7.15(d) and the results of the analysis are shown in Table 7.1. It can be seen that the results obtained from the present approach are very close to those

calculated by Tang (139) using the reduction method (or referred to as the transfer-matrix method). By comparing the results of different iterations listed in Table 7.1, we can see how the nonlinearity affects the stresses.

As a further practical engineering example, the Santai cable-stayed bridge, which spans the Pujiang River in China, has been analysed using the present one-dimensional finite element family. The bridge was designed previously by the author and was completed in 1981.

Santai bridge is a 3 span (56.0 + 128.0 + 56.0 m) cable-stayed concrete highway bridge with a suspended span of 16 m in the centre. The overall dimensions of the bridge are shown in Fig. 7.16, and a general view of it can be seen from Figure 1.

The prestressed concrete girder has a twin box-section connected by monolithic slab and transverse diaphragms at the supports and cable anchorages. The girder has a constant depth of 2.0 m, except near the fixed end where it varies linearly from 2.0 m to 2.20 m within a distance of 13.20 m. The overall width of the girder is 10.50 m, and the total length 241.06 m. At the towers, the girder is fixed to the piers as well as to the towers. At each end abutment the girder is held down against uplift from the cables by two pairs of hinged support bars that allow for temperature movement. The overall dimensions of a typical section and elevation of the girder are given in Figs. 7.17 and 7.18 respectively. Also, detailed figures are listed in Table 7.2.

The concrete girder is stayed by two-plane cables at 9 m intervals. The cables are arranged in a pattern commonly called the 'Fan' type. From the top area of each tower where the cables are anchored without using saddles, five pairs of cables radiate to the respective anchorages at the side of the

roadway. The cables are composed of 5 mm dia. steel wires with an ultimate strength of about  $16000 \text{ kg/cm}^2$  ( $1.57 \text{ kN/mm}^2$ ). The composition of each cable is shown in Table 7.3.

The dimensions of the reinforced concrete towers and piers are shown in Figs. 7.19 and 7.20 respectively. Erection of the bridge was carried out by the free cantilever balanced casting method with a segmental length of 3.0 m. The girder was post-tensioned longitudinally during the erecting stage.

Before the actual opening of the bridge static loading tests, which can be seen from Figures 2, 3 and 4, were carried out. The different vehicle loading positions are shown in Figs. 7.21 to 7.24.

For comparison with the measured values obtained from the loading tests, the bridge has been analysed using the model represented in Fig. 7.25. The model is three-dimensional and is composed of 61 elements and 80 node points. It can be seen that the entire structure can be separated into two individual parts by the suspended span in the static analysis.

Since the diaphragms are sufficient to retain the shape of the whole cross section, the twin-box girder is represented by single longitudinal thin-walled beam elements along the longitudinal centre-line of the roadway. Each element of the model has the same properties as the corresponding member of the prototype. At the anchorage positions, the transverse beam elements which perform like rigid arms extend to the locations of the cable anchorages. The cables are represented by cable elements which are assumed to be straight in the linear analysis, and are considered to be a catenary supporting its own dead weight in the nonlinear study. The tower and the pier are divided into 12 elements using three-node solid beam elements.

Young's moduli of elasticity taken for the analysis are as follows:

$$\begin{aligned}
 E_{\text{cable}} &= 2.0 \times 10 \text{ kg/cm}^2 \text{ (196.2 kN/mm}^2\text{)}, \\
 E_{\text{girder}} &= 3.5 \times 10 \text{ kg/cm}^2 \text{ (34.335 kN/mm}^2\text{)}, \\
 E_{\text{tower}} &= 3.3 \times 10 \text{ kg/cm}^2 \text{ (32.373 kN/mm}^2\text{)}, \\
 E_{\text{pier}} &= 3.1 \times 10 \text{ kg/cm}^2 \text{ (30.411 kN/mm}^2\text{)}.
 \end{aligned}$$

The Poisson's ratio of the concrete is taken as 0.167. The cable tension due to dead load was determined in the erecting calculation as:

Side Span		Mid-Span
$T_1 = 90.17$ (884.57 kN)	,	$T_1 = 78.32$ (768.32 kN)
$T_2 = 120.09$ (1178.08 kN)	,	$T_2 = 114.60$ (1124.23 kN)
$T_3 = 180.87$ (1774.33 kN)	,	$T_3 = 180.30$ (1768.74 kN)
$T_4 = 192.24$ (1885.87 kN)	,	$T_4 = 197.31$ (1935.61 kN)
$T_5 = 211.20$ (2071.87 kN)	,	$T_5 = 223.67$ (2194.20 kN)

A few influence lines for the Santai Birdge are given in Figs. 7.26 and 7.27. They are merely representative of those required in design, from which the critical positions of the vehicles can be determined. The calculated deflections with measured values under vehicle loading in position 1 are shown in Table 7.4 and Fig. 7.28. A comparison of the transverse distribution of vertical deflection due to eccentric loading at typical sections between the theoretical solutions and the tested values can be seen from Fig. 7.29. A summary of the comparison of measured and calculated values is given in Table 7.5. The agreement between theory and test in general is good, and it verifies that the one-dimensional finite element family presented here can be used adequately for the design of cable-stayed bridges.

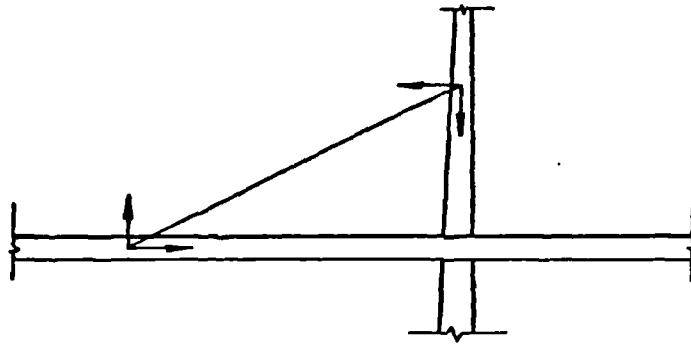
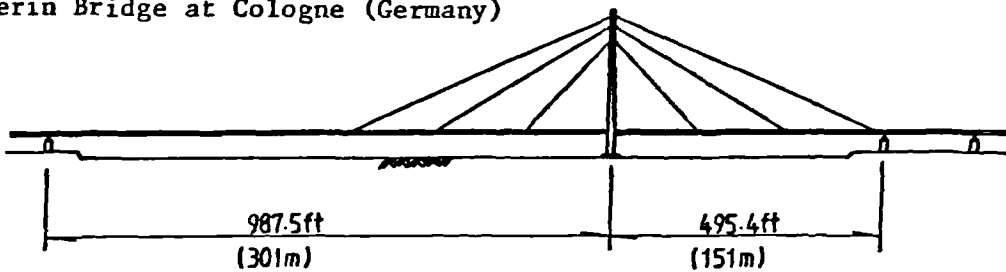
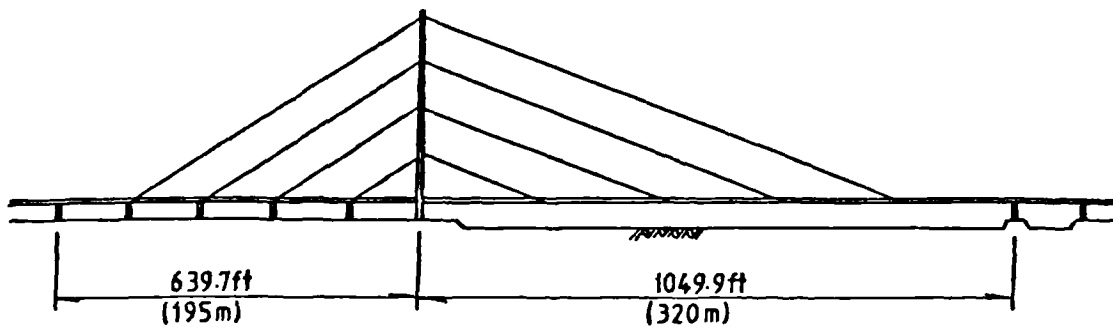


Fig. 7.1 Cable Tension Inducing Shear and Compression in Tower and Girder

Severin Bridge at Cologne (Germany)



Knie Bridge (Germany)



Batman Bridge (Australia)

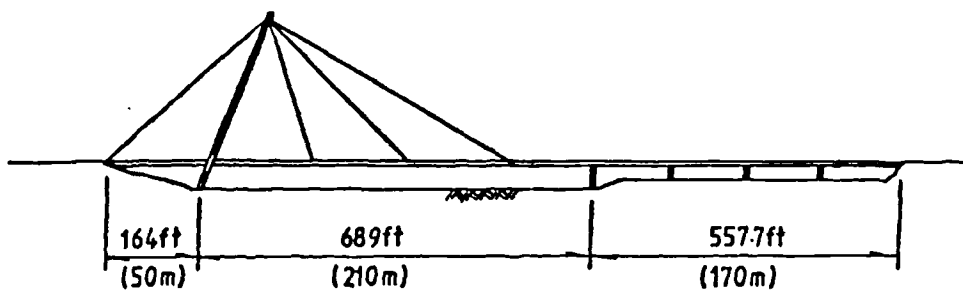
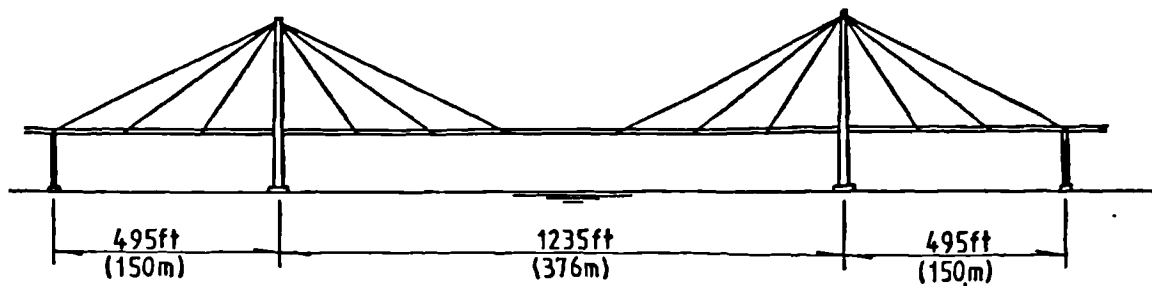
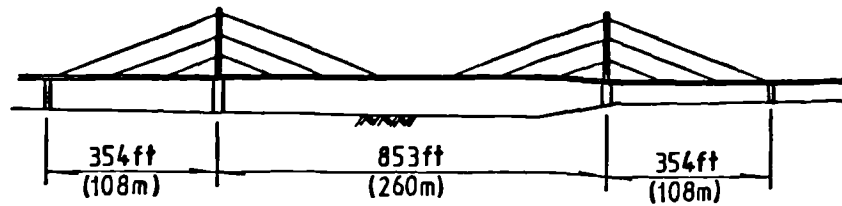


Fig. 7.2 Examples of Two-Span Cable-Stayed Bridge Structures

Luling Bridge Louisiana (U.S.A.)



North Bridge Düsseldorf (Germany)



Point Meules Bridge (France)

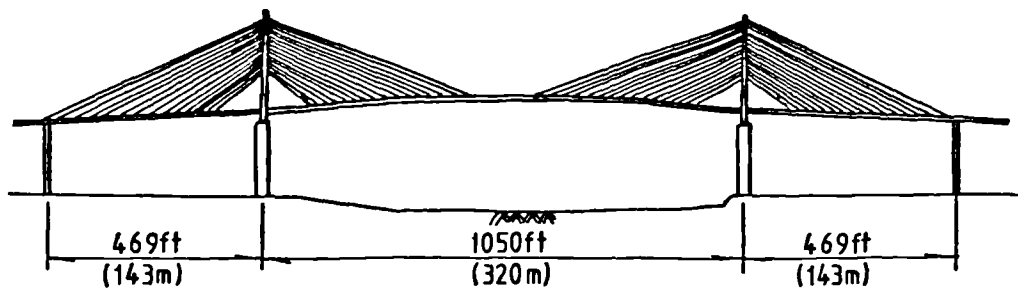
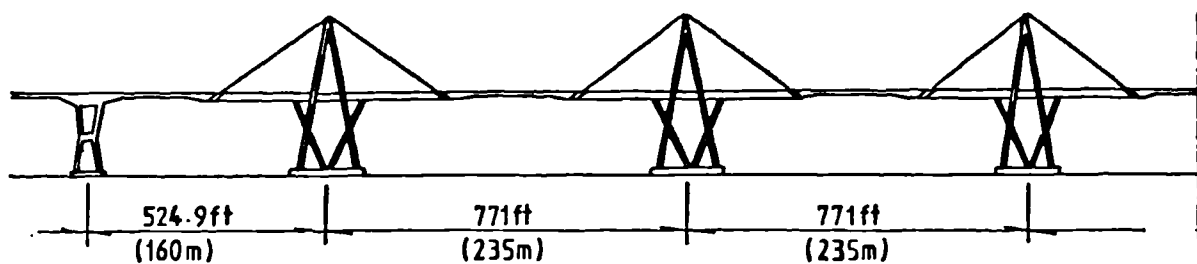


Fig. 7.3 Examples of Three-Span Cable-Stayed Bridge Structures

Maracaibo (Venezuela)



Ganga Bridge (India, not built)

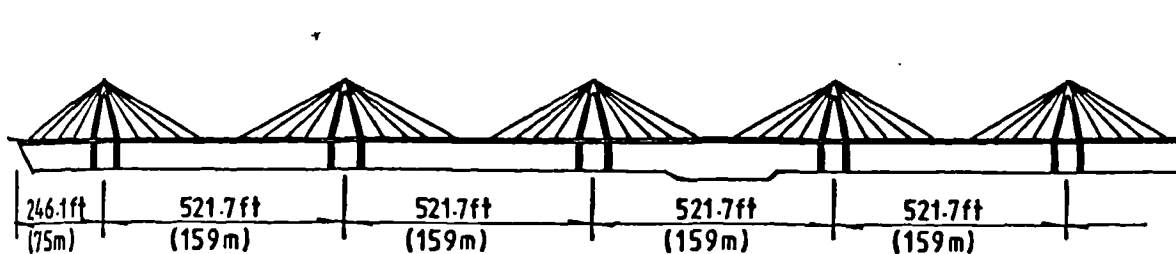


Fig. 7.4 Examples of Multispan Cable-Stayed Bridge Structures

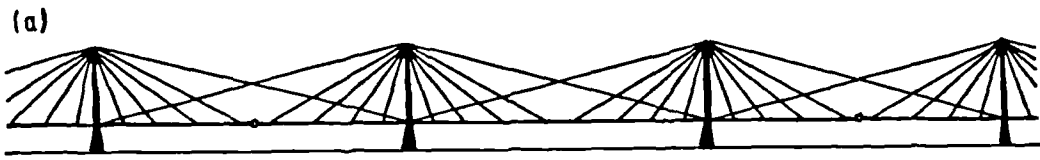


Fig. 7.5 Multispan Cable-Stayed Bridges

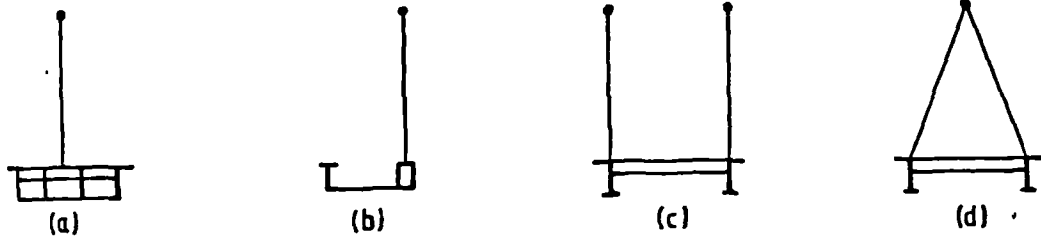
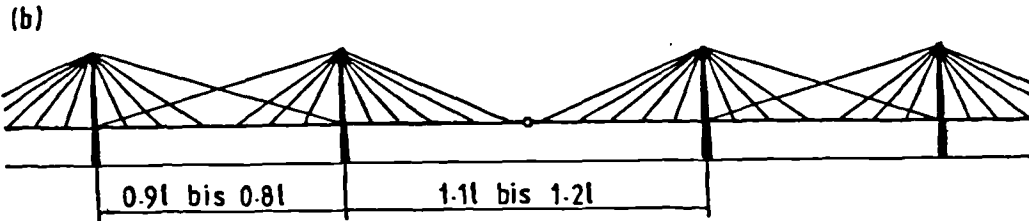


Fig. 7.6 Transverse Cable Arrangement: (a) Single Plane-Vertical; (b) Single Plane-Vertical/Lateral; (c) Double Plane-Vertical; (d) Double Plane-Sloping

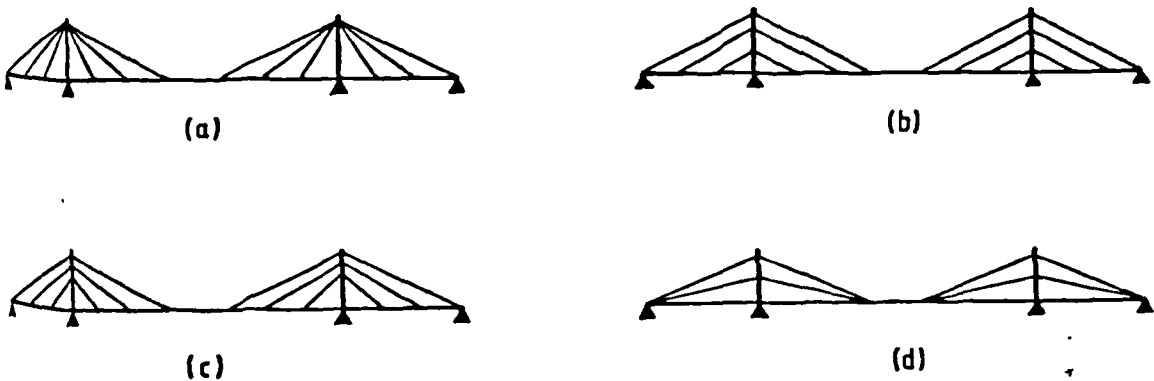


Fig. 7.7 Longitudinal Cable-Arrangements: (a) Radiating; (b) Harp; (c) Fan; (d) Star.

STAY SYSTEM	SINGLE					DOUBLE					TRIPLE					MULTIPLE					COMBINED						
	1	2	3	4	5	1	2	3	4	5	1	2	3	4	5	1	2	3	4	5	1	2	3	4	5		
1 CONVERGING or RADIATING																											
2 HARP																											
3 FAN																											
4 STAR																											

Fig. 7.8 Systems of Cable Arrangement

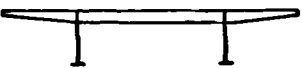
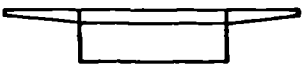
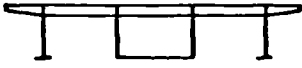
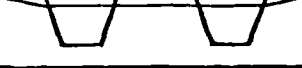
Types of main girder		
Arrangement		Deck cross-section
1	Twin I girder	
2	Single rectangular box girder	
3	Central box girder and side single web girders	
4	Single twin box girder and sloping struts	
5	Single trapezoidal box girder	
6	Twin rectangular box girder	
7	Twin trapezoidal box girder	

Fig. 7.9a Types of steel main girder

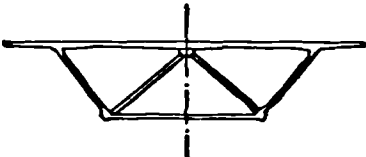
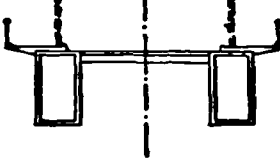
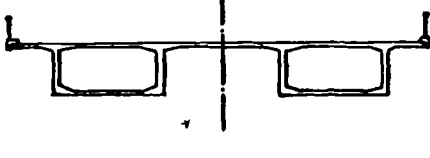
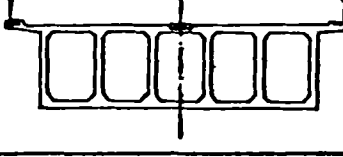
Types of girder		Deck cross-section
1	Single box girder (Brotonne Bridge, France)	
2	Twin box girder (River Parana Bridge, Argentina)	
3	Twin box girder (River Waal Bridge, Holland)	
4	Multiple box girder (Polcevera Viaduct, Italy)	

Fig. 7.9b Reinforced and Prestressed Concrete Girders

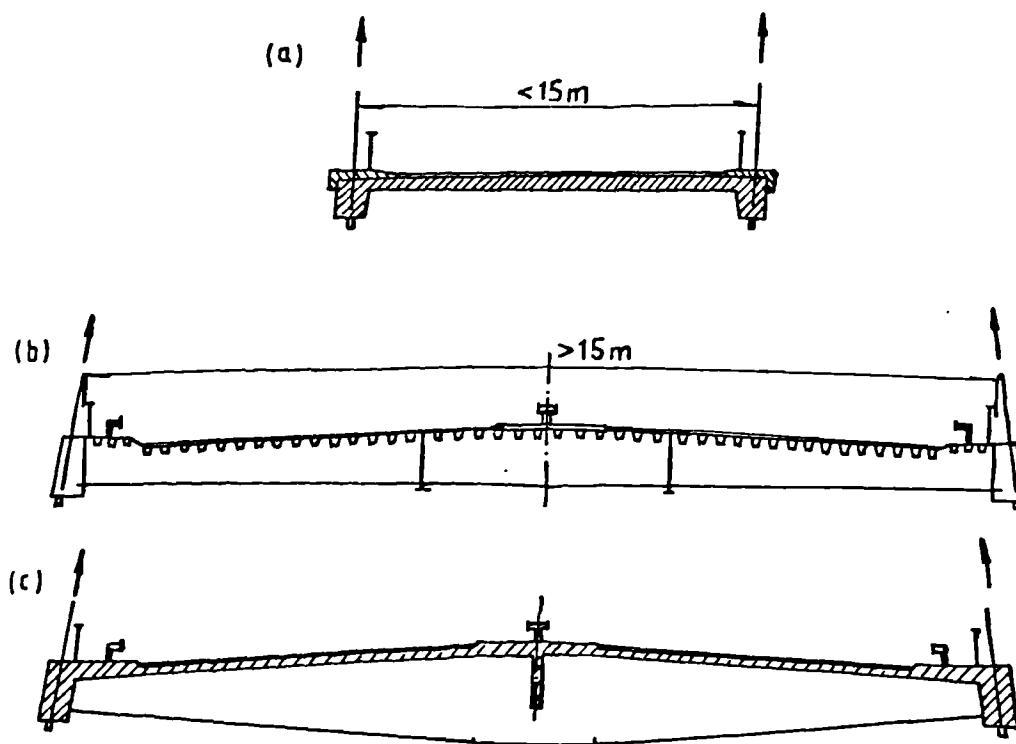


Fig. 7.10a Cross-section of a concrete bridge with a width  $b < 15$  m  
 7.10b,c Cross-section of concrete or steel bridge width  $b > 15$  m

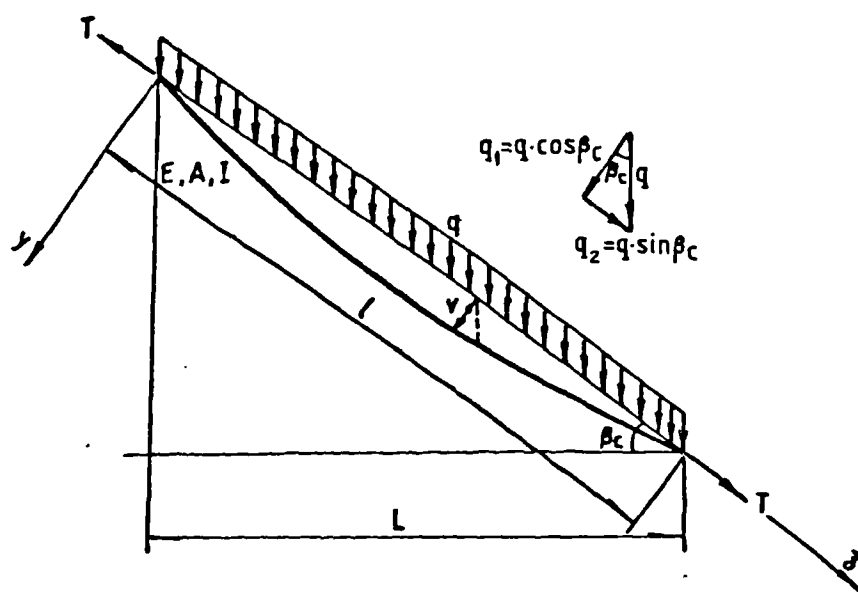
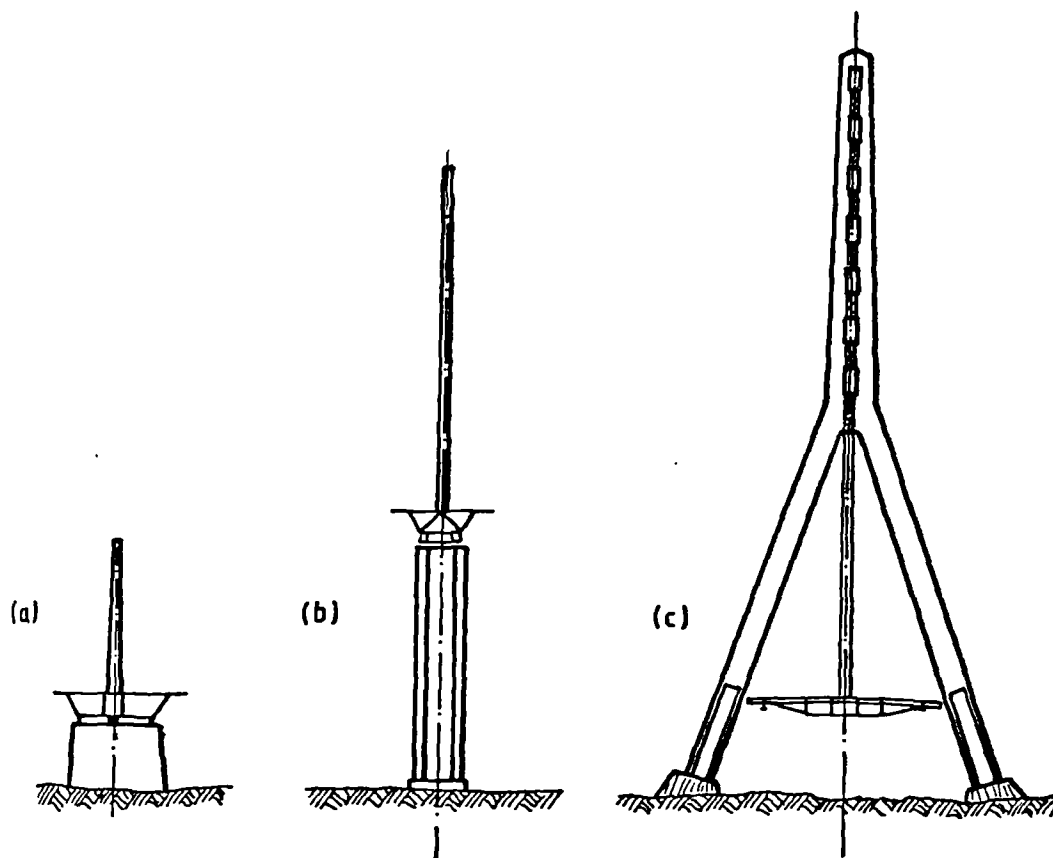
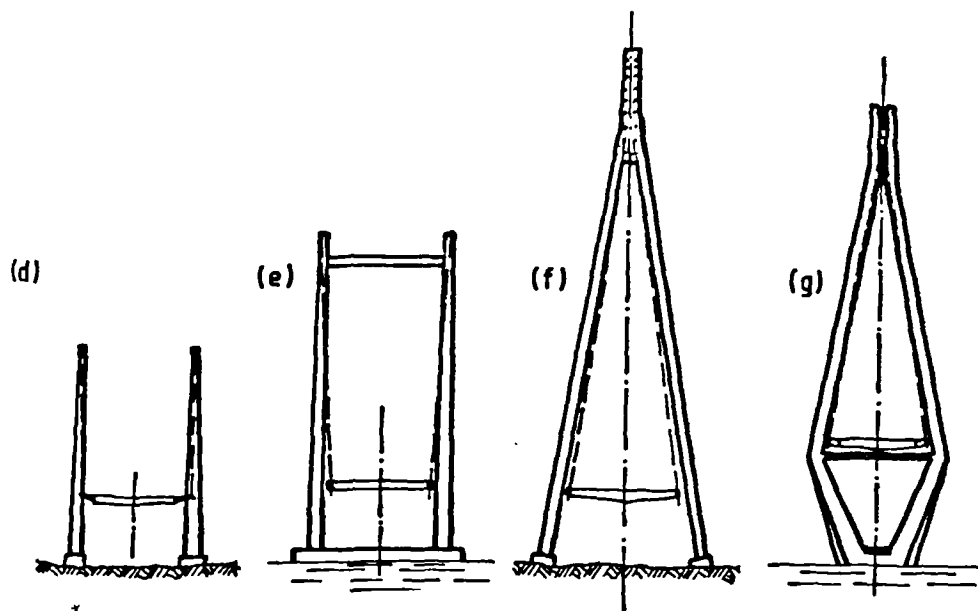


Fig. 7.12 Uniformly loaded cable



One cable plane - tower shapes



Two cable planes - tower shapes

Fig. 7.11 Different solutions for the towers

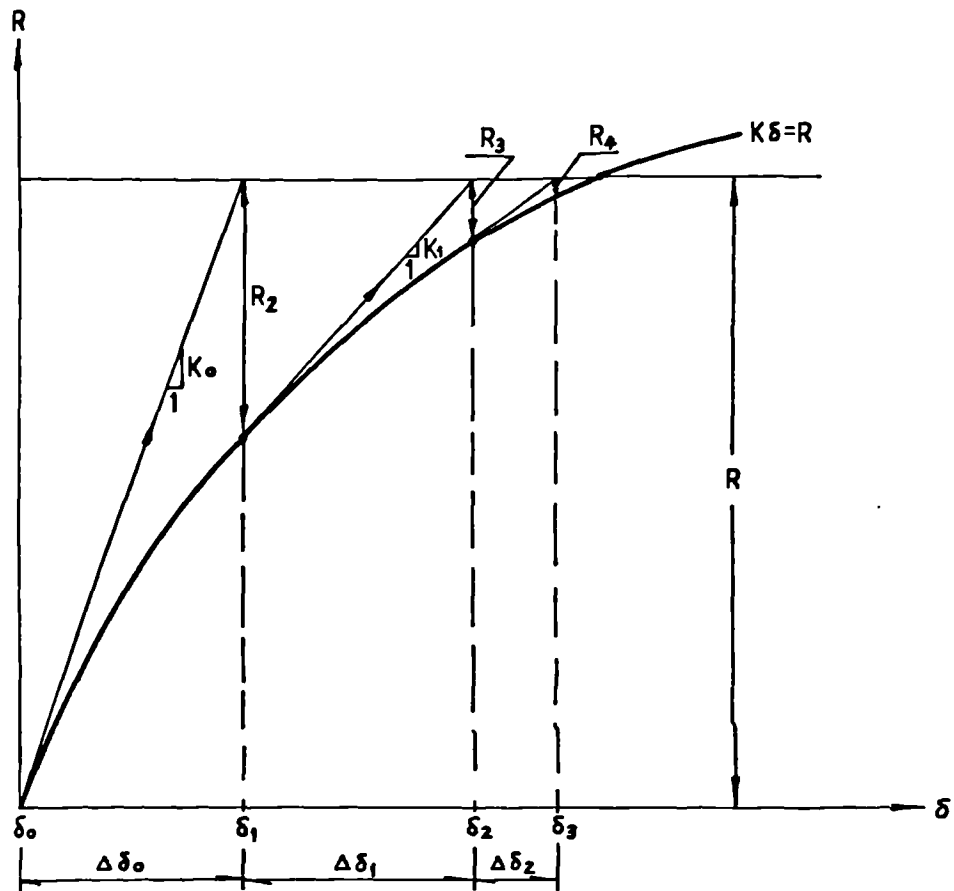


Fig. 7.13 Newton-Raphson method

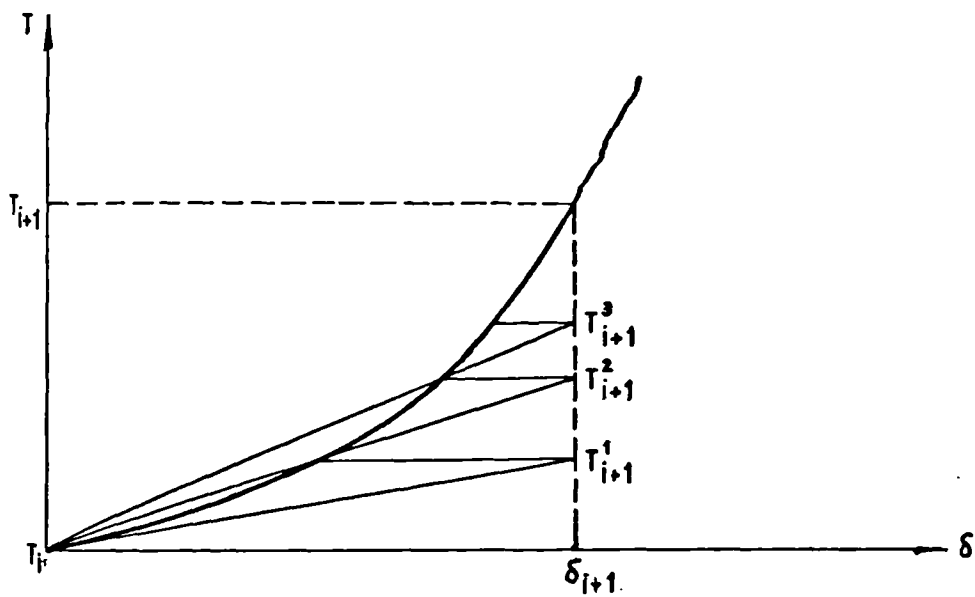
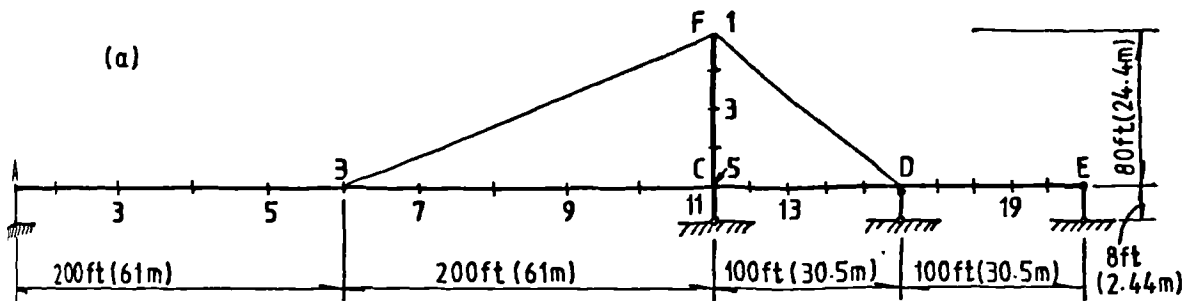


Fig. 7.14 Determination of the tensile force of the cable



Specifications: modulus of elasticity = 4000000 ksf (191.6 KN/mm<sup>2</sup>);  
 girder -  $I = 45.0 \text{ ft}^4 (0.3894 \text{ m}^4)$ ;  $A = 8.0 \text{ sq.ft.} (0.7442 \text{ m}^2)$ ;  
 tower - above girder:  $I = 20.0 \text{ ft}^4 (0.1731 \text{ m}^4)$ ;  $A = 3.0 \text{ sq.ft.} (0.2791 \text{ m}^2)$ ;  
 below girder:  $I = 200.0 \text{ ft}^4 (1.731 \text{ m}^4)$ ;  $A = 10.0 \text{ sq.ft.} (0.9303 \text{ m}^2)$ ;  
 cables -  $A = 1.10 \text{ sq.ft.} (0.1023 \text{ m}^2)$ ;  
 dead load of girder = 16.0 kips per lin.ft. (233.44 KN/m);  
 live load of girder = 8.0 kips per lin. ft. (116.72 KN/m).

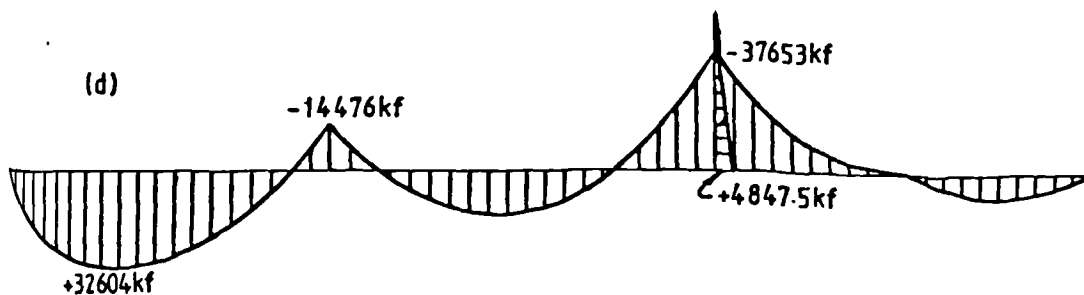
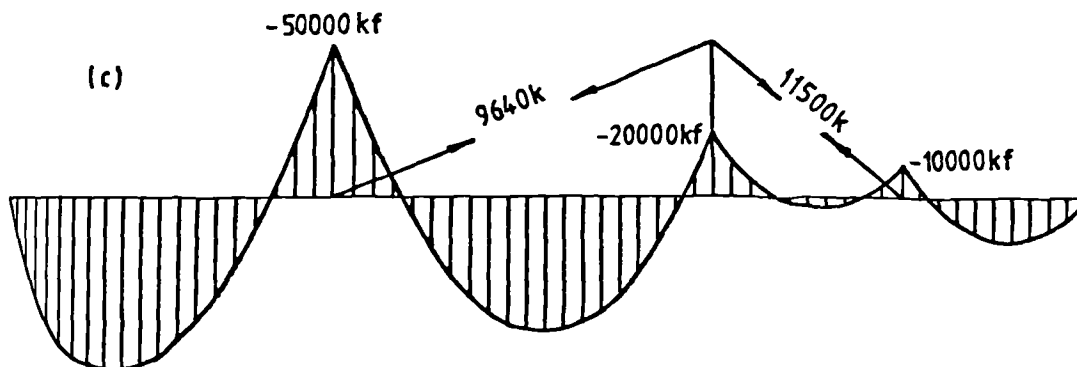
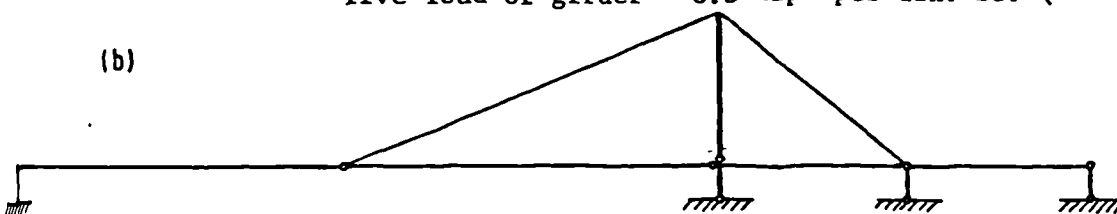


Fig. 7.15 Example given by Man-Chung Tang (139,140)  
 (1k = 4.45 KN, 1 kf = 1.35725 KN-m)

Table 7.1 Results of analysis and influence of nonlinearity

Stage	Linear behaviour	1st iteration	2nd iteration	3rd iteration	4th iteration	Difference as a percentage	Results given in (139)
(a) Axial forces of cables, in kips ( 1 kip = 4.45 kN )							
Cables							
left	4191.658	4335.789	4233.872	4230.876	4230.968	+0.94	
right	5059.026	5068.200	5118.107	5115.925	5116.0741	+1.13	
(b) Bending moment in kip-feet ( 1 kip-feet = 1.35725 kN-m)							
Girder							
3	32673	32361	33826	32111	32134	-1.65	32800
5	14147	14147	13148	13167	13150	-7.05	14400
7	6691	6860	7265	7545	7539	+12.67	8850
11	-37283	-37597	-37872	-38072	-38101	+2.19	-37500
13	-10747	-10710	-11930	-12102	-12128	+12.85	-11700
Tower							
3	2343	2151	2864	2974	2991	+27.66	2940
5	4686	4385	4981	5068	5077	+8.34	5000
(c) Deflection, in feet ( 1 foot = 0.305 m)							
Girder							
3	1.191	1.192	1.176	1.171	1.171	-1.68	1.165
5	1.408	1.370	1.354	1.353	1.353	-3.91	1.354
7	1.155	1.105	1.120	1.125	1.125	-2.60	1.126
10	0.296	0.296	0.310	0.312	0.313	+5.74	0.308
13	-0.066	-0.066	-0.072	-0.073	-0.073	+10.61	-0.074
Tower							
1	0.262	0.262	0.268	0.269	0.269	+2.67	0.265
3	0.172	0.172	0.181	0.182	0.182	+5.81	0.180

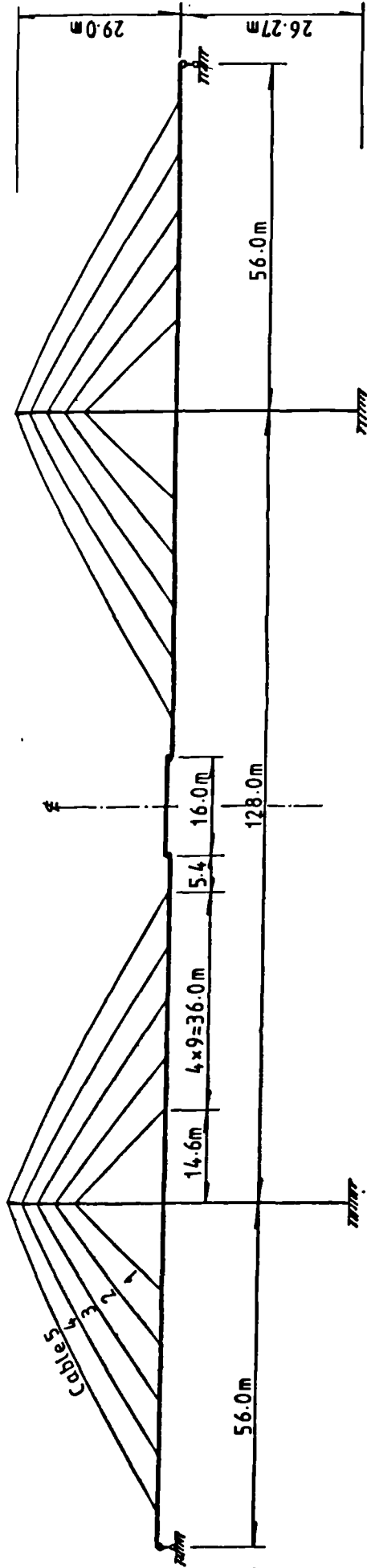


Fig. 7.16 General arrangement of Santai Bridge, China

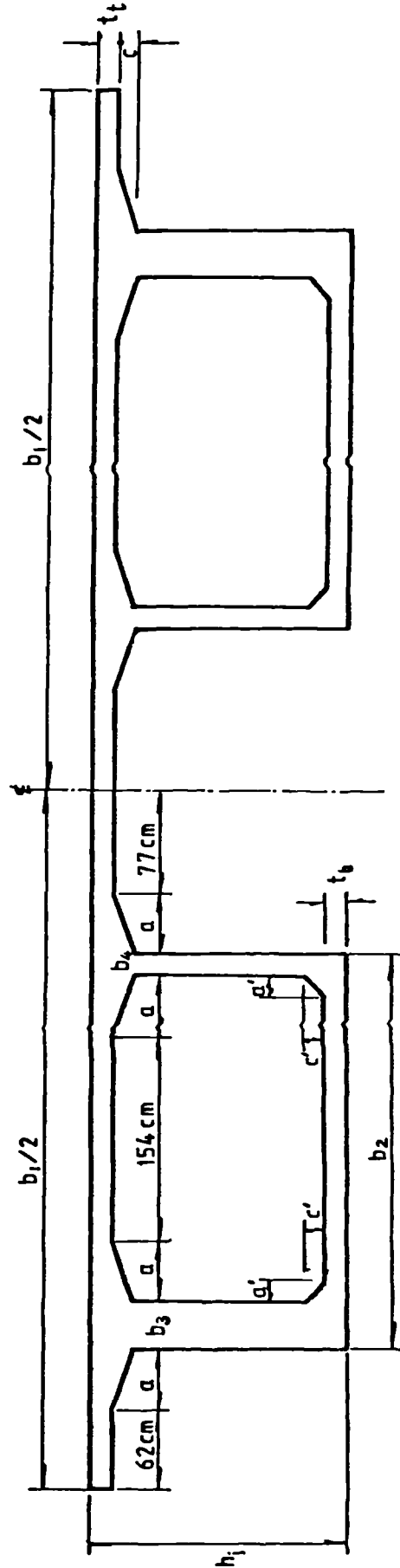


Fig. 7.17 Cross-section of the stiffening girder

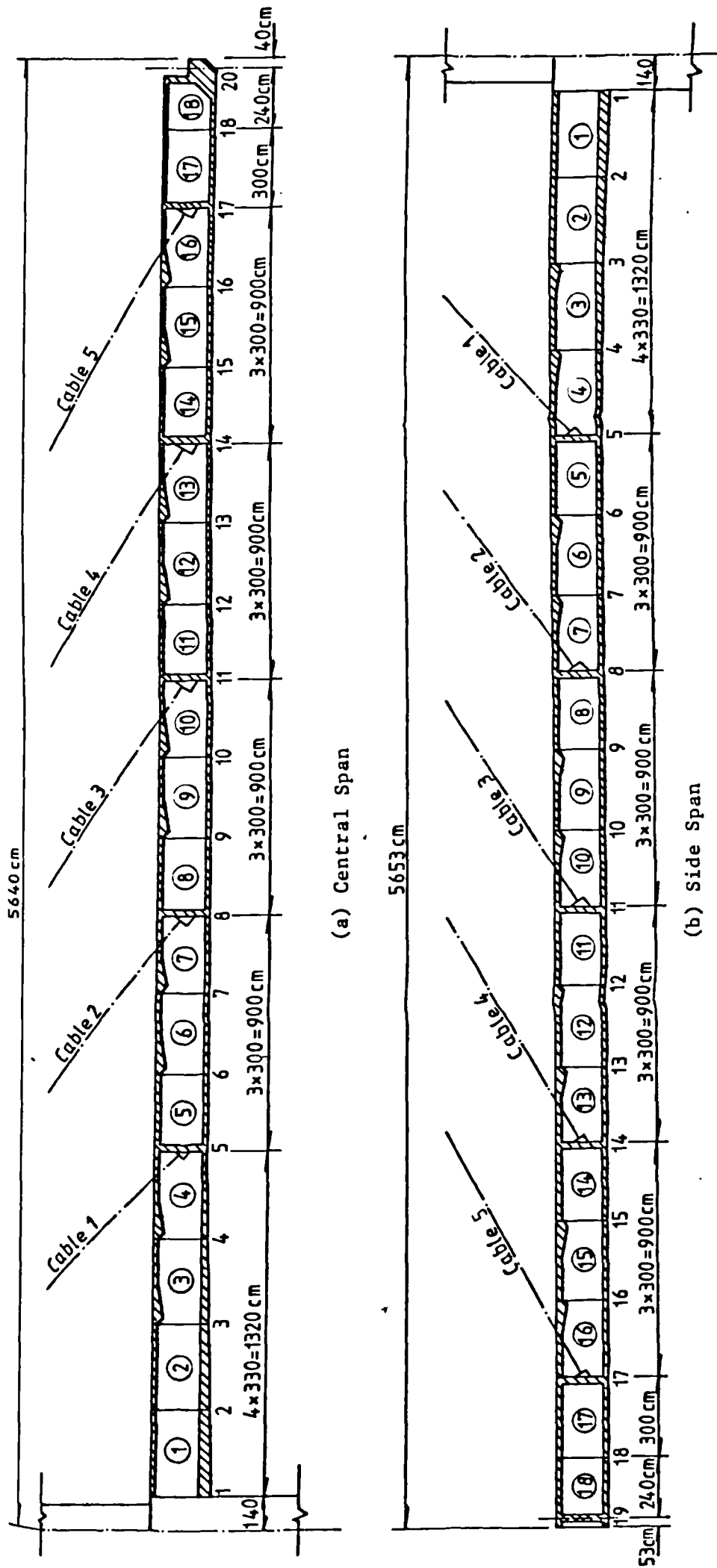


Fig. 7.18 Elevation of the stiffening girder

Table 7.2 Detailed dimensions of the cross-sections (in cm, 1 cm = 10 mm)

No. of sec. \ Dimen- sions	$h_j$	$t_t$	$t_b$	$b_1$	$b_2$	$b_3$	$b_4$	$a$	$c$	$a'$	$c'$
1	220	18	38	525	296	36	16	45	15	15	15
2	215	18	33	525	296	36	16	45	15	15	15
3	210	18	28	525	296	36	16	45	15	15	15
4	205	18	23	525	296	36	16	45	15	15	15
5-18 19-21	200	18	18	525	296	36	16	45	15	15	15
20	100	-	-	428	428	-	-	-	-	-	-

Table 7.3 Composition of the stayed cables

Items \ No. of cable	1	2	3	4	5
Number of strands of the cables	5	5	7	7	9
Number of wires in each strand	36	36	36	36	36
Number of wires in each cable	180	180	252	252	324
Sectional area for each cable ( $\text{mm}^2$ )	3534	3534	4948	4948	6362

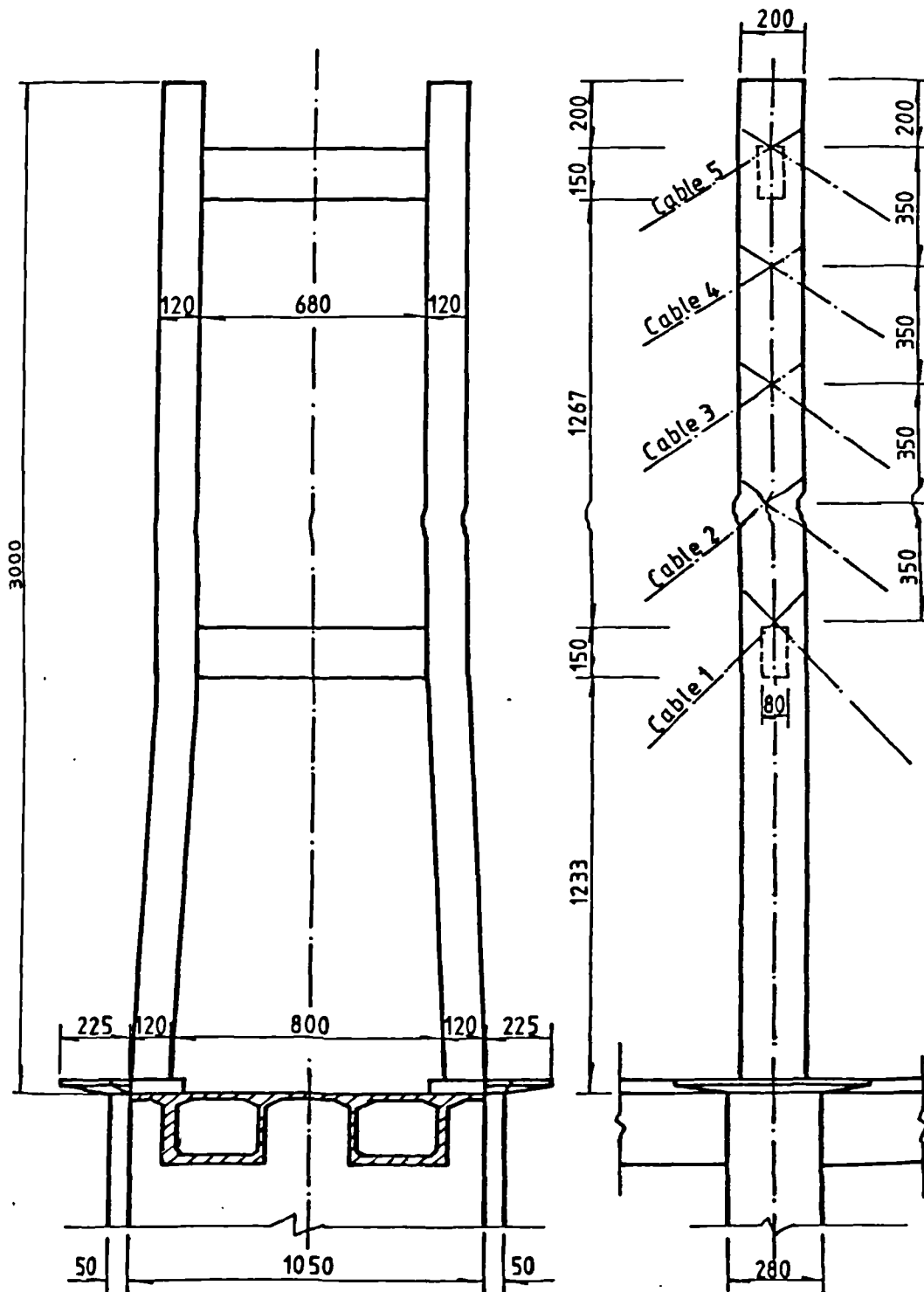


Fig. 7.19 Tower system of Santai Bridge (Dimensions in cm)

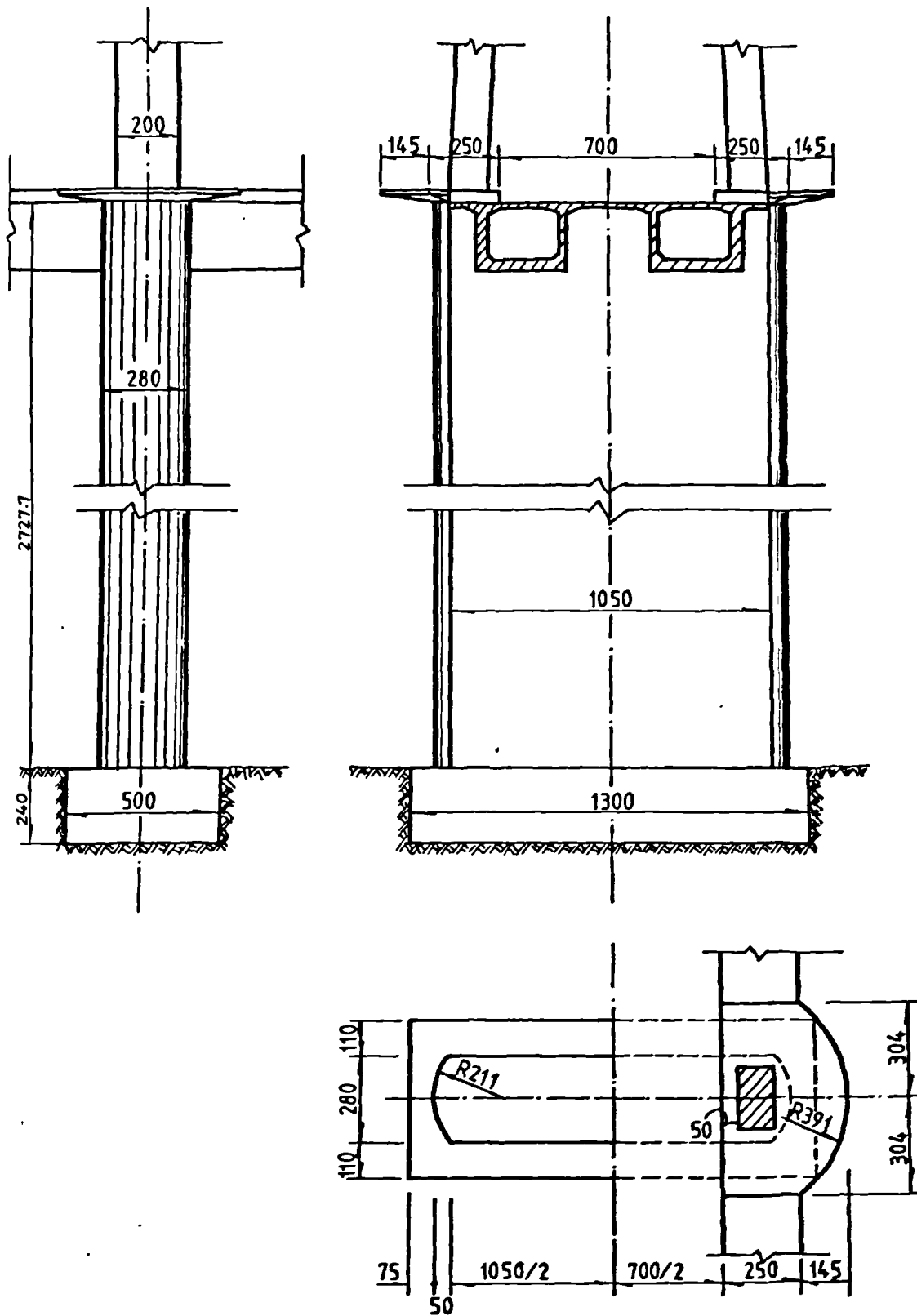


Fig. 7.20 Pier System of Santai Bridge (Dimensions in cm)

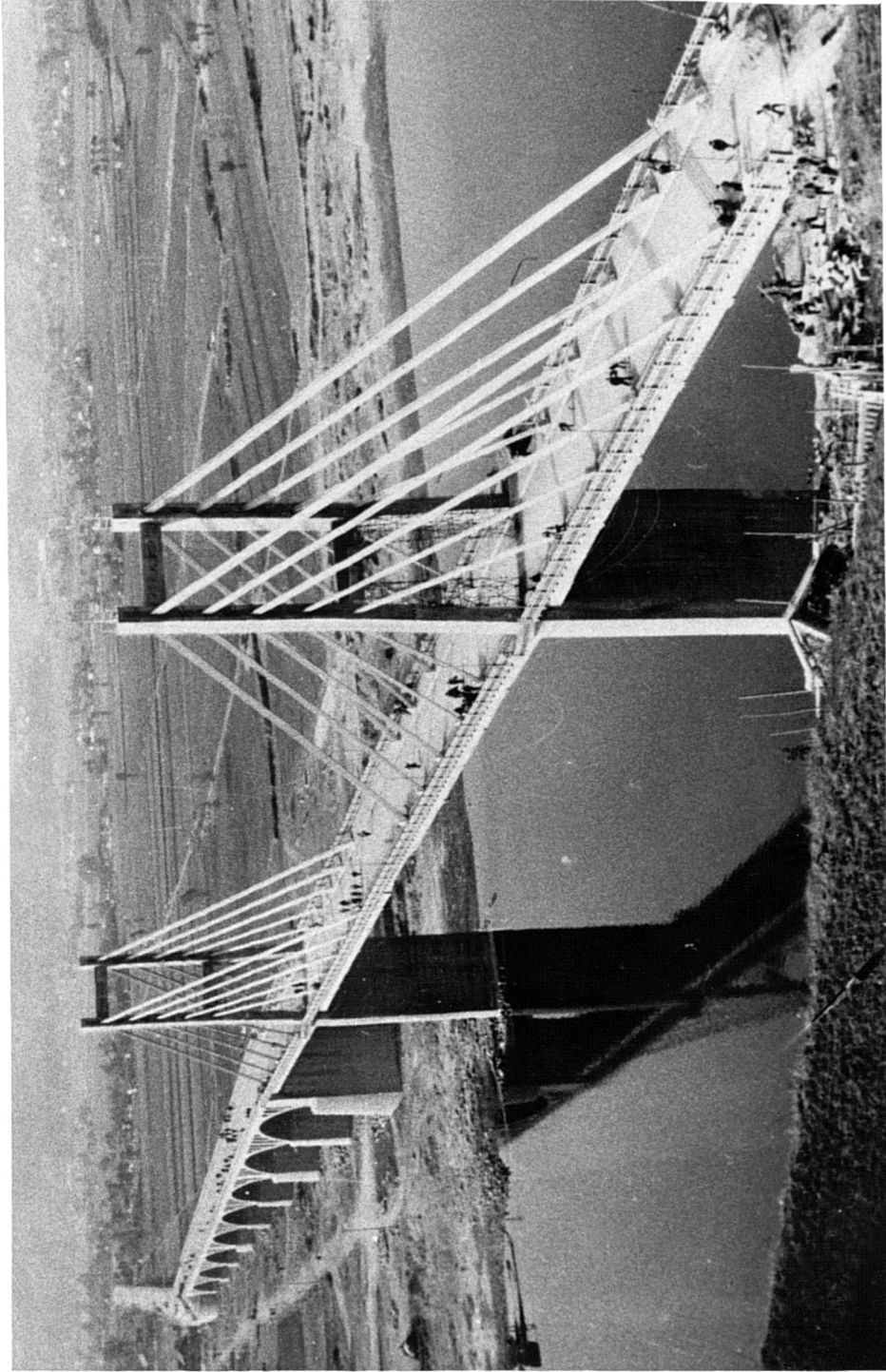


Figure 1 View of Santai Bridge, China



Figure 2 View of loading test

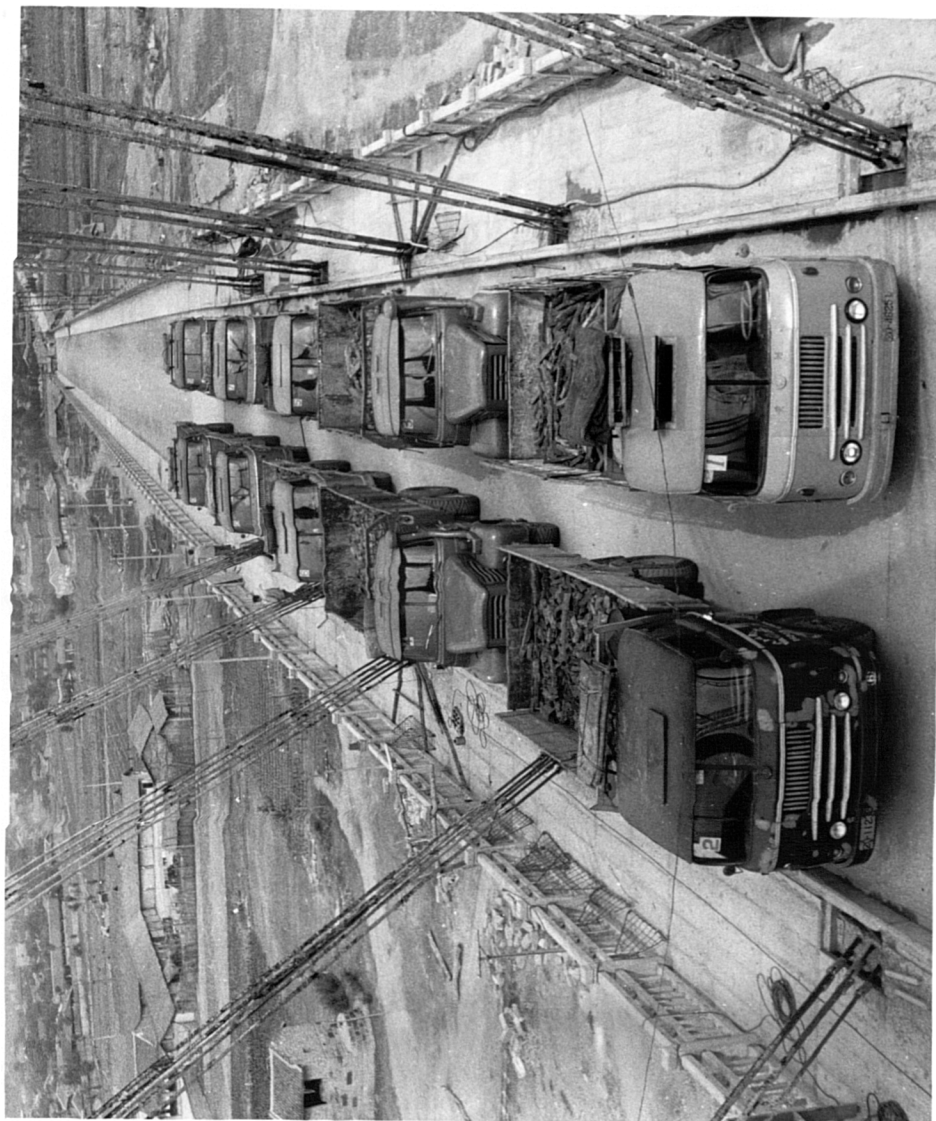


Figure 3 View of symmetrical loading test

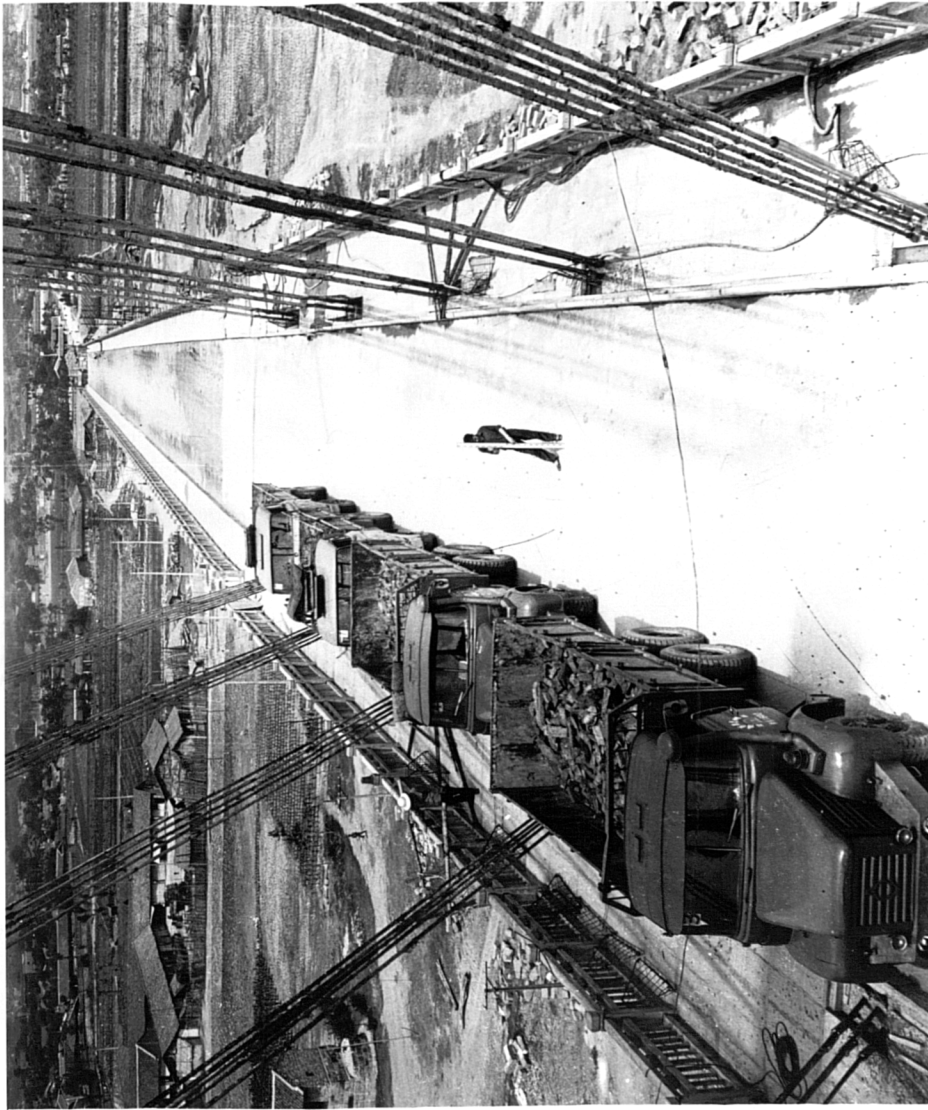
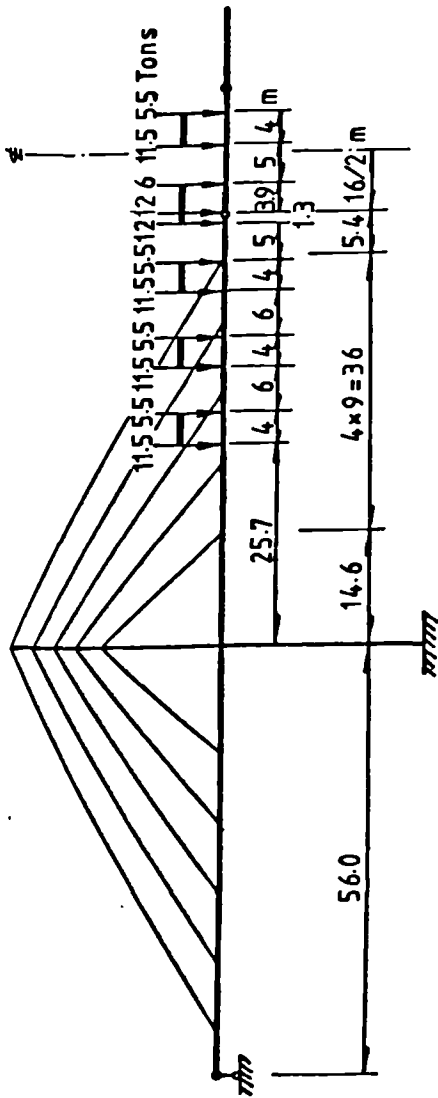


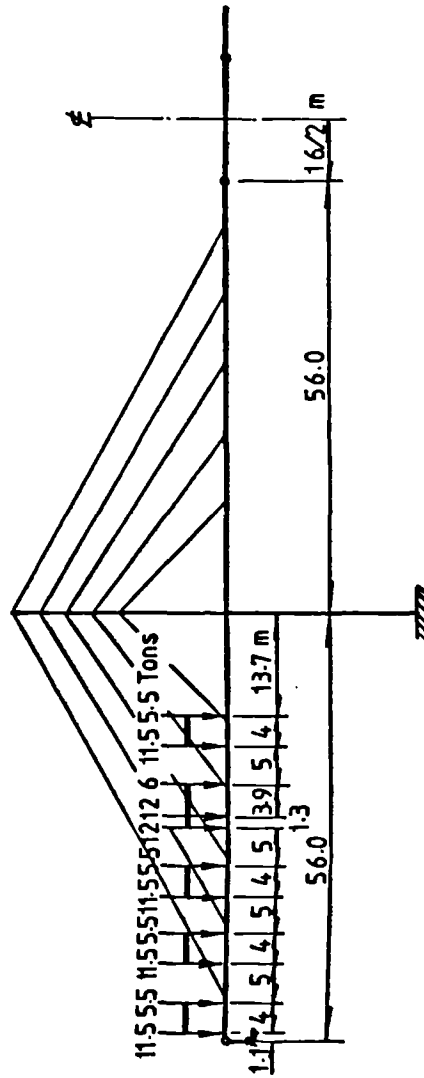
Figure 4 View of asymmetrical loading test



(a) Longitudinal position of vehicle

(b) Vehicle central positions

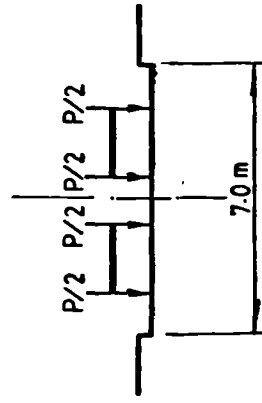
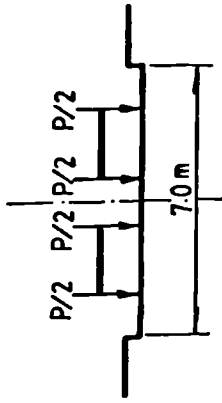
Fig. 7.21 Loading position 1 (1 ton = 9.81 kN)

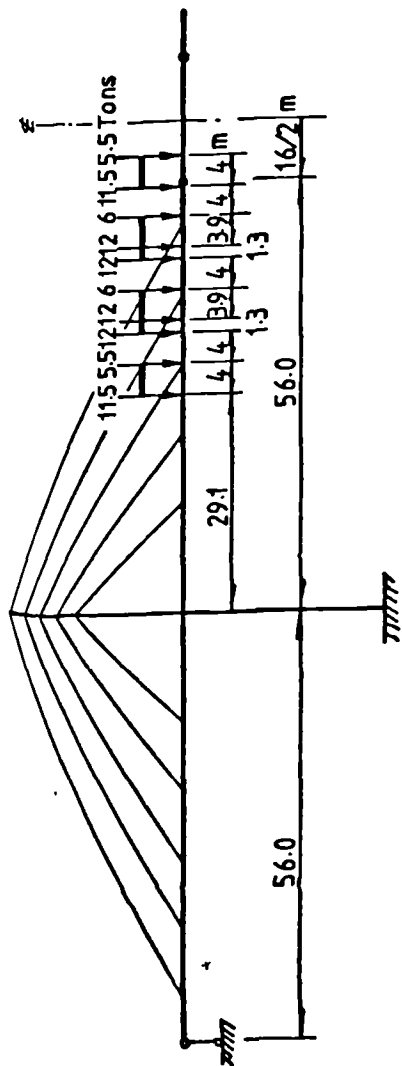


(a) Longitudinal position of vehicle

(b) Vehicle central positions

Fig. 7.22 Loading position 2 (1 ton = 9.81 kN)

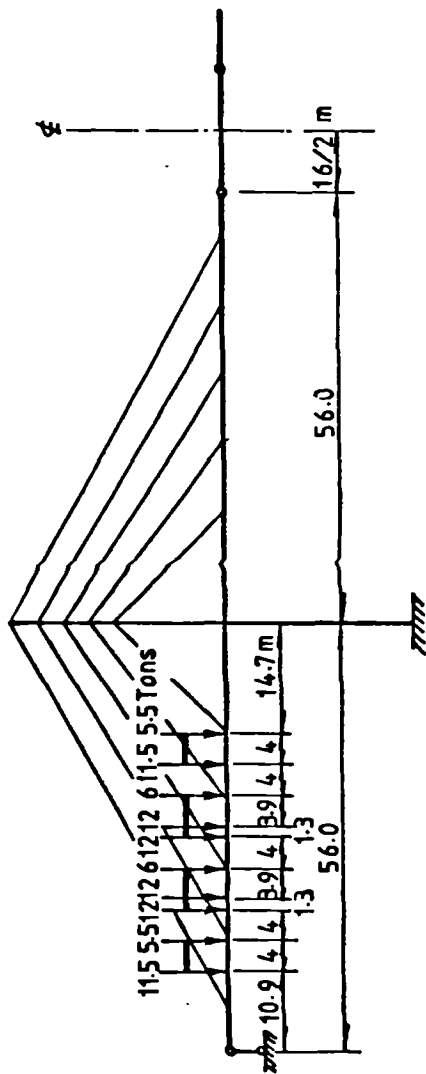




(a) Longitudinal position of vehicle

Fig. 7.23 Loading position 3 (1 ton = 9.81 kN)

(b) Vehicle eccentric positions



(a) Longitudinal position of vehicle

Fig. 7.24 Loading position 4 (1 ton = 9.81 kN)

(b) Vehicle eccentric positions

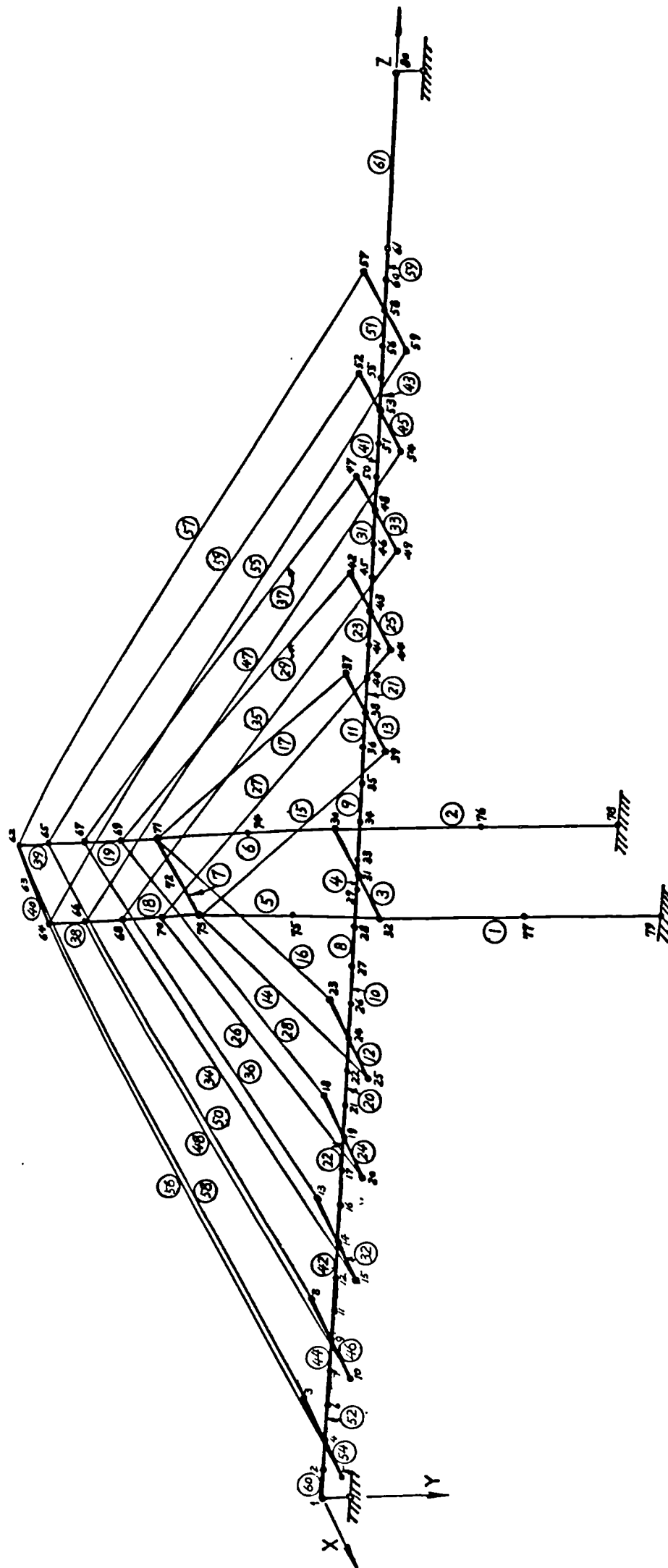
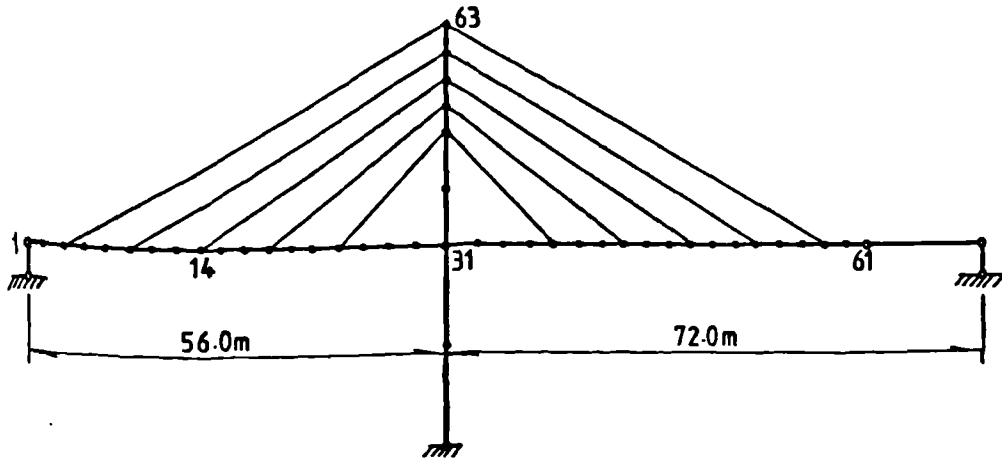
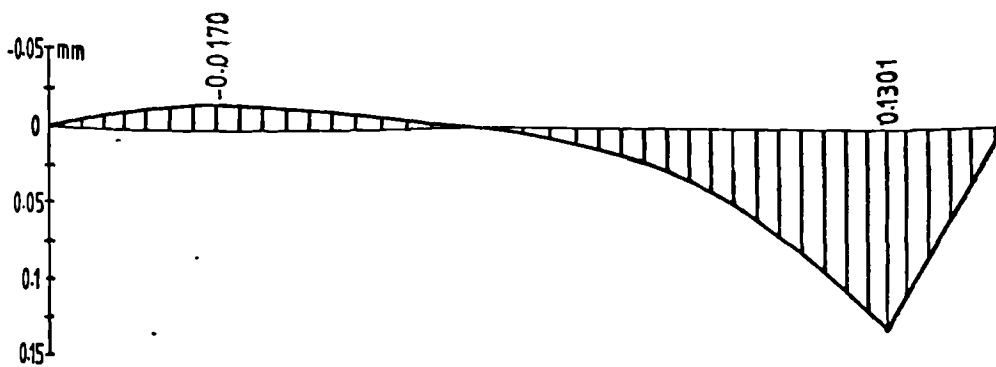


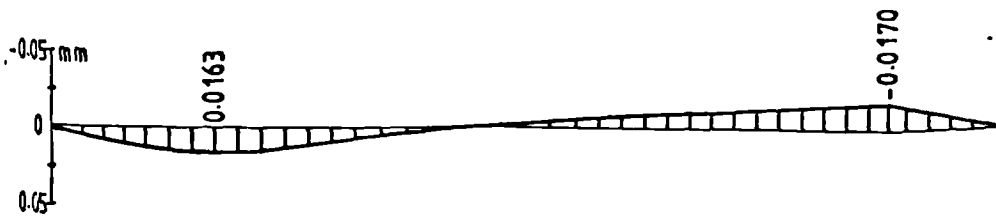
Fig. 7.25 Analytical model of Santai Bridge



(a) List of selected nodes



(b) Deflection of girder : Node 61

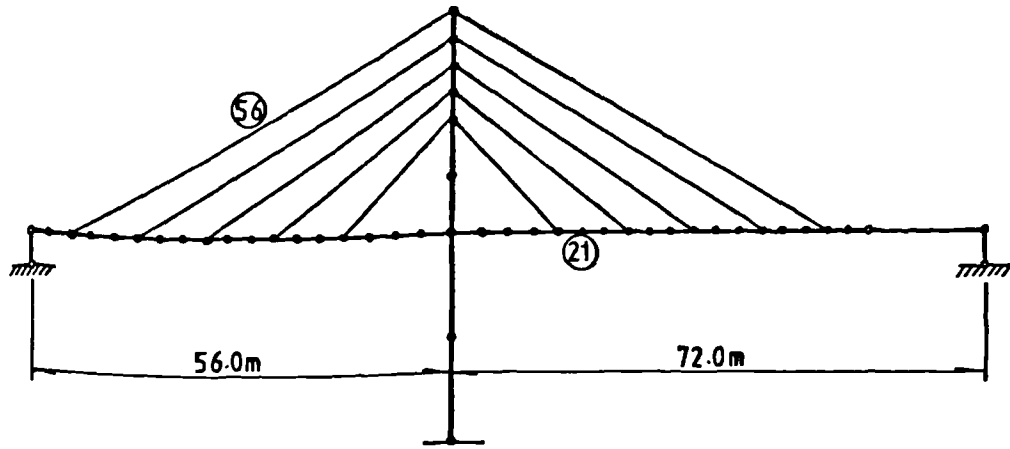


(c) Deflection of girder : Node 14

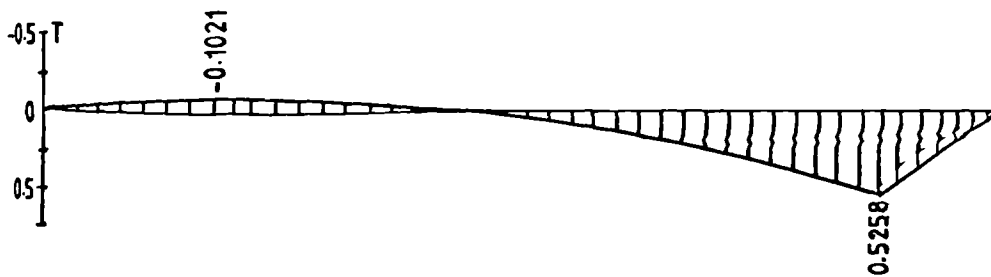


(d) Horizontal deflection of tower : Node 63

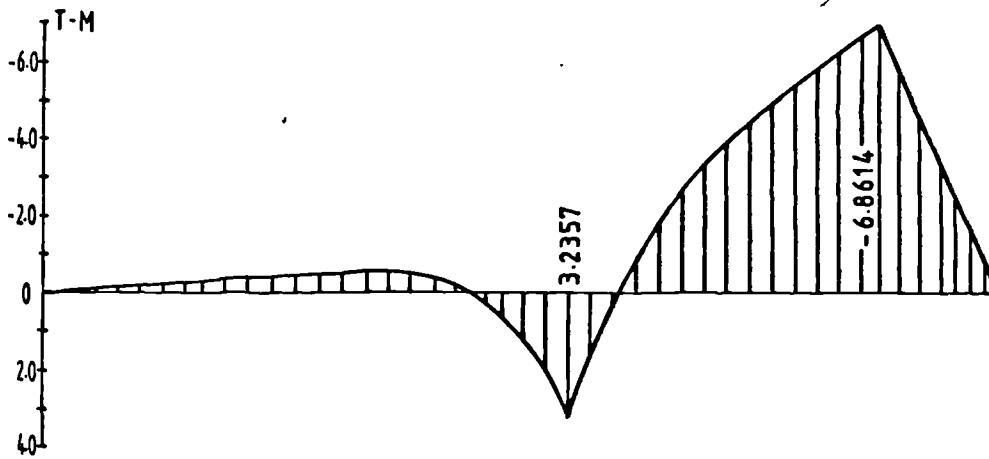
Fig. 7.26 Typical influence lines of deflection



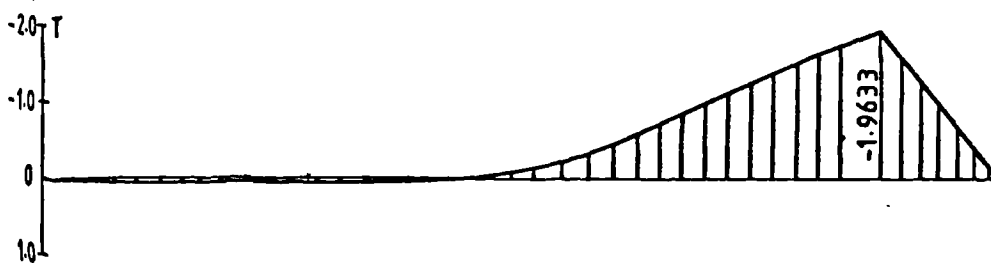
(a) List of selected members



(b) Force in cable : Member 56



(c) Moment in girder : Member 21



(d) Axial force in girder : Member

Fig. 7.27 Typical influence lines of internal forces  
 (1 T = 9.81 kN, 1 T-M = 9.81 kN·m)

Table 7.4 Deflections of the girder due to loading position 1 (in mm)

Side spans	Cross-sections		1	2	3	4	5	6	7	8	9	10	11	12	13	14	15	16	17	18	19 or 20
		Measured deflections	Calculated deflections	-0.10	-0.30	-0.60	-0.90	-1.10	-1.40	-1.50	-1.70	-1.80	-1.80	-1.90	-1.70	-1.60	-1.50	-1.30	-1.00	-0.70	-0.40
	Measured deflections	Calculated deflections	0.20	0.40	0.90	1.05	1.65	2.20	2.65	3.45	4.00	4.65	5.60	6.40	7.25	8.10	9.15	10.05	11.05	12.05	12.85
Midspan	Measured deflections	Calculated deflections	0.116	0.413	0.786	1.240	1.782	2.354	3.001	3.717	4.500	5.342	6.242	7.203	8.215	9.278	10.392	11.545	12.732	13.830	14.938

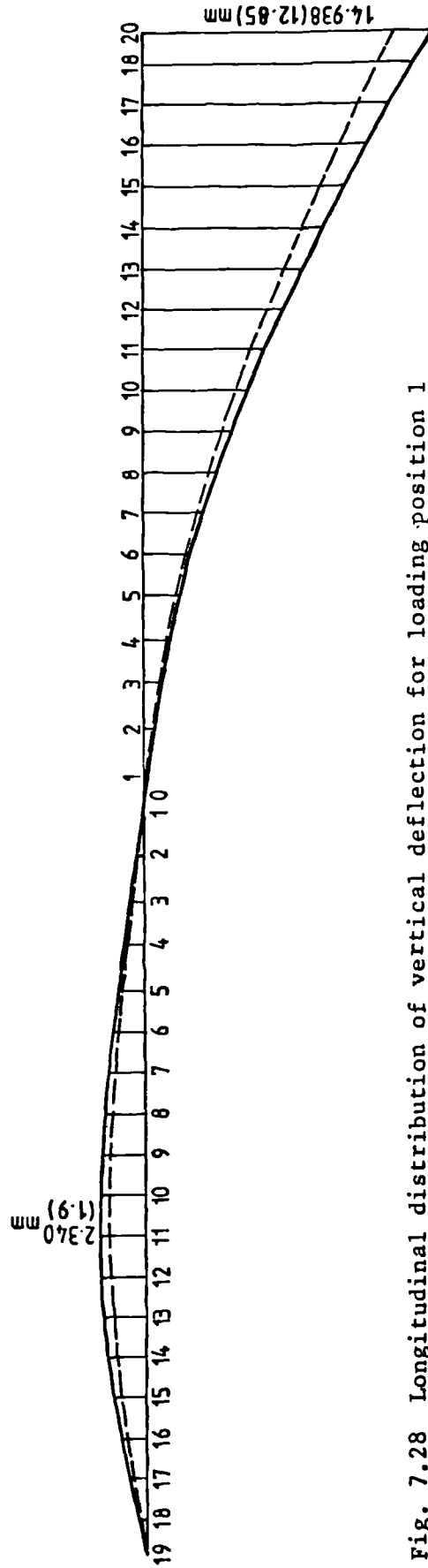
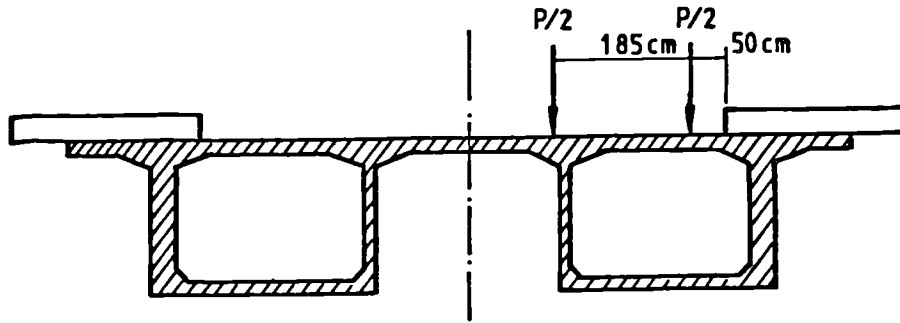
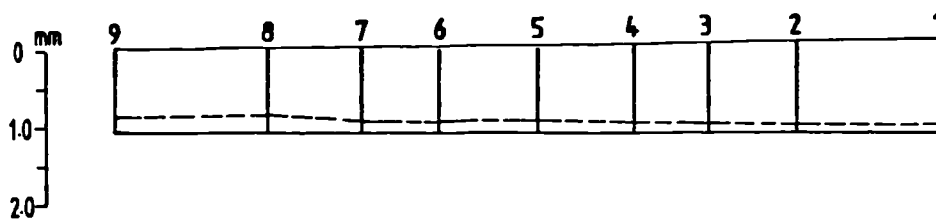


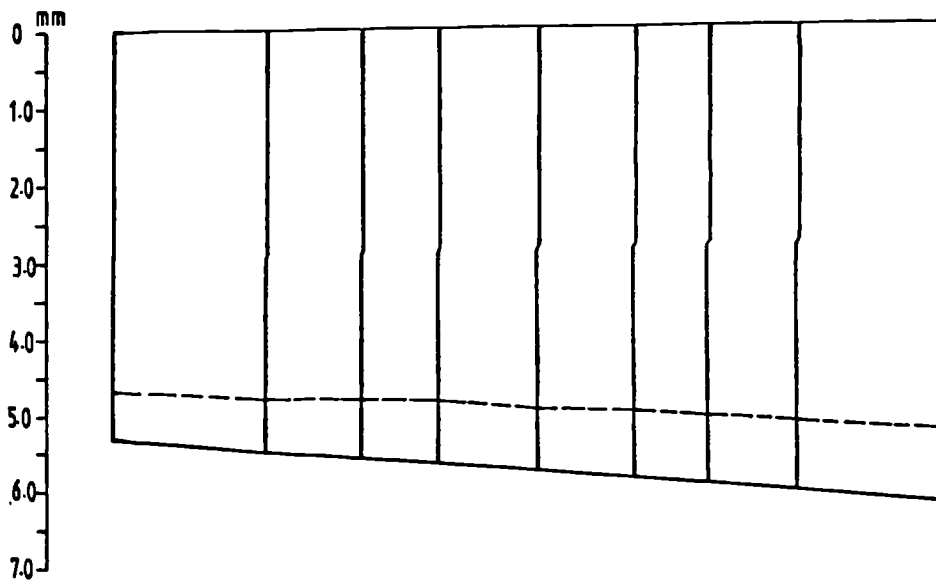
Fig. 7.28 Longitudinal distribution of vertical deflection for loading position 1



(a) Cross-section of the girder



(b) Section 9 of the side-span for loading position 4



(c) Section 16 of mid-span for loading position 3

——— calculated deflection  
 - - - - - measured deflection

Fig. 7.29 Transverse distribution of vertical deflection

Table 7.5 Comparison of measured and calculated values

Sections	Loading position	Measured values	Calculated values	Difference, as a percentage	
(a) Axial forces of cables, in kg (1 kg = 9.81 N)					
Cables					
Side-span	3	(1)	23470	24945	+6.3
	4	(1)	32990	37911	+14.9
	5	(1)	57030	65414	+14.7
Mid-span	3	(1)	27650	29979	+8.4
	4	(1)	36890	41960	+13.7
	5	(1)	55830	66283	+18.7
(b) Mean stresses at bottom reinforcement, in kg/cm <sup>2</sup> (1kg/cm <sup>2</sup> = 0.0981 N/mm <sup>2</sup> )					
Girder					
Sidespan					
9	(2)	+197	+219	+11.2	
Midspan					
5	(1)	-289	-271	-6.2	
(c) Deflection, in mm					
Girder					
Sidespan					
11	(1)	1.90	2.340	+23.2	
Midspan					
20	(1)	12.85	14.938	+16.2	
Tower					
top	(1)	42.0	49.0	+16.7	

## CHAPTER 8

## EXPERIMENTAL INVESTIGATION

8.1 Objectives of the experimental investigation

Although the beam models have been tested by previous investigators, notably Roll and Aneja (4, 111), Steinle (134), Křistek (62), Billington and Dowling (11, 12), Evans and Al-Rifaie (2, 3, 28), Moffatt and Lim (94), and Sawko and Cope (118, 119), it was considered that a comprehensive experimental investigation of a specific geometrical and material nature was necessary. The results of this could then be related to the theoretical research work. However, model research is expensive and time-consuming, and accordingly only four linearly-elastic box beam models representing different structural forms were carefully chosen and tested to investigate the static response of deformable box beams subjected to bending as well as to twisting loads. Details of the four models were as follows,

- Model 1 - straight cantilever single cell box beam,
- Model 2 - curved cantilever single cell box beam with side cantilevers,
- Model 3 - two-span continuous double cell box beam,
- Model 4 - simply supported twin-box beam with trapezoidal cross-sections.

Model 1 has been introduced mainly to verify the use of additional degrees of freedom which represent warping and distortion. Models 2 and 3 have been used to verify the extension of the proposed analysis to structures with initial curvatures in plan or with cross-sections other than single cells. Model 4 has been tested to confirm the procedure for the numerical analysis of multibox structures described in Chapter 6.

To summarize, the objectives of the experimental research were two fold. In the first place, it was necessary to assess the validity and versatility of the proposed theoretical methods by means of comparison with

existing analytical solutions and also with results of model tests. Then, secondly, it was necessary to be able to observe the real behaviour of the models during an experiment so that an understanding of the structural action could be obtained which would assist the development of the theory in different structural cases.

All experiments were conducted in the linear elastic range. As an exception, once the elastic response had been recorded, Model 3 was continuously loaded until failure. The ultimate load and mechanism of failure (Figure 13) were obtained for other purposes.

## 8.2 Description of model structures

### 8.2.1 Dimensions and fabrication of the models

For the sake of convenience, and in the interests of accuracy, Models 1, 2 and 4 were constructed from mild steel plates, whilst Model 3 was constructed in prestressed concrete.

The dimensions and construction of the individual models are shown in Figs. 8.2, 8.3, 8.4 and 8.6 respectively. General information about the cross-sections of the models is shown in Fig. 8.1 and tabulated in Table 8.1. The steel plate thickness of the models was measured at several positions and the average thickness of each member was determined and recorded in Table 8.1. It should be noted that for the steel models, the flange width/thickness ratios for both top and bottom flanges were approximately 60-100. The models are, therefore, extremely thin-walled according to Vlasov's definition (146). Furthermore, there were no diaphragms within the span. Thus ensuring that the warping and distortional effects were rather significant when the models were subjected to eccentric loading. However, the flange width/thickness ratio of the prestressed concrete model was approximately 13 which is within the usual range for prestressed concrete box beams governed by local bending effects.

The steel plate used for the manufacture of Model 1 was cut from cold rolled mild steel sheet having a thickness of 3.12 mm. The flat steel plate was folded around a specially prepared former and was welded along one interconnected edge to form a hollow rectangular section. This hollow segment was then welded at one end to a 610 x 610 x 20 mm steel plate which was later connected by 3/4" bolts to a reaction frame.

The radius of curvature to the centre line of Model 2 was 3000 mm providing an R/L ratio of 2.0. The model was fabricated from mild steel plate having a thickness of 3.46 mm. The flanges were cut to shape and the web plates were bent from a flat steel plate to follow the profile of the edges of the bottom flange. The webs were attached to the bottom flange by means of welding, as shown in Figure 9. The open U channel was then welded on to the top flange to form the closed section. Finally the curved box beam was also welded at one end to a 610 x 610 x 20 mm steel plate and was subsequently connected to the reaction frame by 3/4" bolts.

The remaining twin-box steel model was designed to have a simply supported span of 1500 mm. The top flange thickness was designed to be greater than the top flange thicknesses of the existing steel models in order to be able to transfer the structural action from one box to the other. Thus, the top flange was formed from mild steel plate having a thickness of 5.0 mm and the other plates (bottom flanges and webs) had thicknesses of 3.0 mm. The two trapezoidal channels were folded by using single steel sheet. They were then welded to the monolithic top flange. The support diaphragms in the trapezoidal boxes had a thickness of 5 mm. There were no diaphragms between the two boxes.

Model 3 was a two-span continuous beam, and each span was precast in micro-concrete separately. After setting each of the box beams on concrete piers, the intermediate diaphragm was cast to form the continuity.

The model was prestressed using 9 Nos. 5 mm unbonded high tensile steel wires. Fig. 8.5 shows the steel arrangement of the model

### 8.2.2 Material property

The modulus of elasticity of the model steel was measured by the flexure of cantilever calibration beams and was calculated from the following expression,

$$E = k \frac{P}{\delta} \quad (8.1)$$

where  $P$  is the concentrated load applied at the tip of the cantilever beam,  
 $\delta$  is the measured deflection of the calibration beam,  
 $k$  is a proportionality factor depending on the dimensions of the beam and the position of measurement.

The observed load-deflection curves for the beams with different thicknesses are shown in Fig. 8.7. The average value of the modulus of elasticity calculated from the bending tests was found to be  $196.2 \text{ kN/mm}^2$  ( $2.0 \times 10^4 \text{ kg/cm}^2$ ).

An experimental value of Poisson's ratio for the steel plate was obtained from bending tests on special cantilever beams, Fig. 8.8. T pattern uniaxial strain gauges or biaxial rosette gauges were located on the top and bottom surfaces of the cantilever beams. By comparing both the longitudinal and transverse strains recorded, Poisson's ratio could be obtained. The average Poisson's ratio calculated from bending tests was found to be 0.27.

The modulus of elasticity for the concrete model was found to be  $29 \text{ kN/mm}^2$  from compressive and bending tests. Poisson's ratio for the concrete was determined to be 0.18.

### 8.2.3 Instrumentation

The models were instrumented to provide experimental values of the displacements and strains in two directions at right angles within the models. The instrumentation was concentrated at sections which were considered to have significant structural action. In general, at least one section in each of the models was fully instrumented.

The vertical and horizontal displacements in Model 1 were measured with dial gauges graduated in units of 0.002 mm. Experience has shown that the sensitivity is sufficient for measuring the deflections of this type of model. However, in view of the extensive instrumentation on the remaining models, it was considered essential to read the deflections electronically rather than visually. Therefore special transducers (Potentiometer, Type 8FLP10, Japan) were used for the remaining three models. The transducers were wired into four arm full bridge circuits in an automatic data logger to record the deflections; calibration resolution showing that one digit reading from the data logger was approximately equivalent to a deflection of 0.00265 mm. The layout of the dial gauges or transducers for the models is shown in Fig. 8.9.

For comparison with displacement values obtained from dial gauges in Model 1, an optical instrument (the Hilger & Watts Angle-Dekkor Mark III) was used for measuring directly the rotated angle of the deformed vertical web.

The Angle-Dekkor is essentially an auto-collimating telescope fitted with measuring graticules to measure, simultaneously, angular displacements of up to 60 x 60 minutes in two planes. When the telescope is accurately set vertical to the clean surface-plate, the reflected cross-lines of the target graticule appear superimposed on the scales of the measuring graticule, and in focus with them. The movement of the cross-lines of the reflected

image gives a direct reading to 0.5 minutes of arc. The arrangement as used in the test of this optical system is shown in Figure 8.

Longitudinal and transverse strains for the first model shown in Fig. 8.2 were recorded by means of T.M.L. electrical resistance strain gauges having a gauge length of 6 mm and a gauge factor of 2.11. The strain gauges were arranged in a T-pattern on the outer surfaces where stresses were required both in the longitudinal as well as the transverse directions. A total of 112 of these strain gauges were located at the  $1/8$ ,  $1/4$ ,  $3/8$ ,  $1/2$ ,  $5/8$ ,  $3/4$  and  $7/8$  span cross-sections to record the strain readings. The position of the gauges at a cross-section is indicated in Fig. 8.10(a).

Biaxial rosette gauges having a gauge length of 6 mm and a gauge factor of 2.095 were used for Models 2 and 4. In most locations the rosette gauges were bonded to both sides of the box walls in order to separate in-plane and flexural components of stresses. A total of 72 rosette gauges were located at  $1/8$ ,  $1/2$  and  $7/8$  arc length cross-sections for the curved cantilever model, and 38 rosette gauges were bonded at midspan cross-section for the twin-box beam model. The gauge positions located at sections considered for these two models are shown in Figs. 8.10(b) and 8.10(c) respectively.

Since the main purpose of Model 3 was to obtain the ultimate load behaviour of this structure for another research student, the model was not as comprehensively instrumented for the author's purpose as it would otherwise have been. Thus, there were no strain record points set up within the two span continuous concrete box beam model.

Two data logging systems were used for the tests - a 100 channel Compulog II and a 200 channel Compulog IV. The 100 channel logger was used

for Models 1 and 2, and the 200 channel system was used for Model 4.

The supports of Model 3 and 4 were instrumented by load cells so that the support reactions could be measured. The load cells were calibrated using a proving ring. This gave a calibration of approximately 1 digit reading equivalent to a force of 3.2 N(0.7 lbf.). The load cells were pre-compressed by tightening the bolts of the support reaction frames so that both tensile and compressive reactions could be recorded (Figures 10 and 13), and they were then connected to a four-arm full bridge circuits in an automatic data logger to record the reactions.

#### 8.2.4 Loading system and testing procedure

In accordance with the objectives of the model research, the elastic behaviour of the models was determined by applying point loads. The load conditions applied to the models are listed in Table 8.2.

Special reaction frames were constructed and 5 ton (44.5 kN) hydraulic jacks were used for the application of the point loading. To apply a pair of point loads, the two 5 ton (44.5 kN) jacks were connected by a hydraulic hose to a hand pump through a tee connector. As a result, the pressure applied to the models by the two jacks was confirmed to be identical and simultaneous. For the test on the concrete model, a 30 ton (267 kN) hydraulic jack was used to apply two point loads by a steel distributing beam. All the jacks and pressure gauges were calibrated by proving rings before the tests were carried out.

The test procedure adopted for each of the four models was similar. Having assembled the model, loading system and apparatus for measuring the deflections and strains, preliminary tests were carried out on each model to check the operation of the system and instrumentation.

Each load case test consisted of taking readings for the following sequence of loads:

OO LL OO LL OO

where O represents one set of readings at zero load,

L represents one set of readings with the load applied to the model.

This sequence includes two complete loading cycles, which allows duplicate readings to be taken. Overall views of the models and the layout of the instrumentation and loading system can be seen in Figures 7 to 14.

### 8.3 Experimental and theoretical results

The results of the tests conducted on the four elastic models are presented in this section. A comparison between the results obtained experimentally and the results derived from theoretical studies is given. No attempt has been made to reproduce all the information obtained from the tests, but representative results which illustrate particular aspects of the structural behaviour are included. The behaviour of the individual models is studied with particular attention being given to the torsion and distortion of the box sections, the cross-sectional distributions of longitudinal and transverse bending stresses and the deflections.

Before the actual comparison of experimental and theoretical results is carried out, the methods used to obtain the results are discussed individually. The magnitude of the load considered as a basis of comparison in each of the tests is given in Table 8.2.

#### 8.3.1 Calculation of the experimental results

The incremental values of deflection and strain were recorded throughout each loading cycle and the average of the two cycles was obtained.

Only the average values of displacement and strain corresponding to the maximum load were compared with the theoretical results.

The observed deflections at each point considered were obtained directly, after multiplying the differences between readings at zero load and readings at the applied final load by the calibration factor for the transducers. The longitudinal distributions of the deflections and/or the transverse distributions of the deflections at typical cross-sections were then plotted or tabulated. To illustrate the existence of additional degrees of freedom which represent warping and distortion, the distributions of the torsional angles as well as the distortional angles for Model 1 were evaluated and plotted.

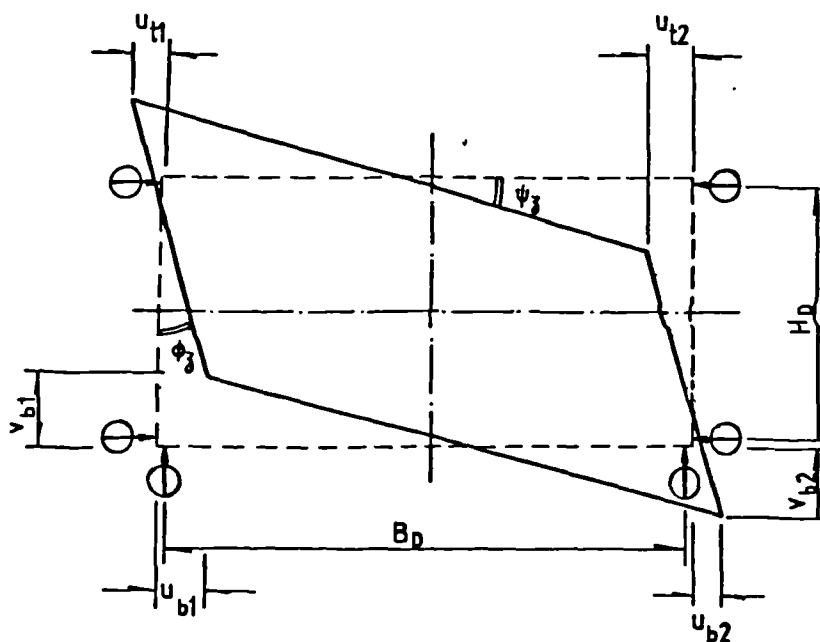


Fig. 8.11 The rotations of the flanges and webs due to the twisting load

The horizontal displacements of the top and bottom flange plates are designated by  $u_{t1}$ ,  $u_{t2}$ ,  $u_{b1}$  and  $u_{b2}$  respectively. Similarly, the vertical deflections of the webs are designated by  $v_{b1}$  and  $v_{b2}$  respectively (see Fig.8.11).

Thus, we can evaluate the angle of rotation of the flange from the observed deflections by

$$\psi_{\bar{z}} = \frac{v_{b,1} - v_{b,2}}{B_0} \quad (8.2)$$

and the angle of rotation of the web from the dial gauge readings by

$$\phi_{\bar{z}} = \frac{(u_{b1} - u_{t1}) + (u_{b2} - u_{t2})}{2H_0} \quad (8.3)$$

However, the angle of rotation of the web could be measured more accurately using the Angle-Dekkor.

Furthermore, from the geometric relationship we have,

$$\psi_{\bar{z}} = \frac{1}{2} \gamma_D + \theta_{\bar{z}} \quad (8.4a)$$

and

$$\phi_{\bar{z}} = \frac{1}{2} \gamma_D - \theta_{\bar{z}} \quad (8.4b)$$

From Eqs. 8.4 we may then obtain the torsional and distortional angles by measuring the angles of rotation of the walls, *i.e.*

$$\theta_{\bar{z}} = \frac{1}{2} (\psi_{\bar{z}} - \phi_{\bar{z}}) \quad (8.5a)$$

and

$$\gamma_D = \psi_{\bar{z}} + \phi_{\bar{z}} \quad (8.5b)$$

The strains were measured in the longitudinal (tangential) and transverse (radial) directions on the outer and/or inner surface of a plate at the points considered, as shown previously in Fig. 8.10. The stresses  $\sigma_{\bar{z}}$  on each surface at a point could then be calculated from orthogonal strain readings  $\epsilon_{\bar{z}}$  and  $\epsilon_s$  according to the relationships:

$$\sigma_{\bar{z}} = \frac{E}{(1 - \nu^2)} (\epsilon_{\bar{z}} + \nu\epsilon_s) \quad (8.6a)$$

$$\sigma_s = \frac{E}{(1 - \nu^2)} (\epsilon_s + \nu\epsilon_z) \quad (8.6b)$$

where  $E$  is Young's modulus

$\nu$  is Poisson's ratio.

The subscripts (z) and (s) denoting the longitudinal (tangential) and transverse (radial) directions respectively.

In practice, gauges or rosettes identical with those used in testing were fixed to a compensating cantilever beam (Fig. 8.8) subjected to known stresses and of the same material as the test model. The required stresses were obtained directly in terms of the known compensating stress and the measured resistance changes (89). Cross-sensitivity, gauge factor and constants of elasticity of the test piece cancel out under these conditions and errors due to inaccurate assumptions of their values are avoided.

The resolution of a strain gauge is related to the strains in the test piece by

$$\rho_z = (\delta R/R) = \frac{F}{1 - n\nu_0} (\epsilon_z + n\epsilon_s) \quad (8.7)$$

where  $R$  is the resistance of the strain gauge,

$F$  is the gauge factor,

$n$  is the cross-sensitivity factor,

$\nu_0$  is the calibration value of Poisson's ratio.

Two gauges are fixed in any z,s-direction to a test surface and two gauges from the batch are fixed in the same manner in the L,c-direction to a compensating bar. If the separate gauge signals or their sums and differences are indicated by appropriate bridge circuits, then from Eq. 8.7 and using Hook's law we have

$$\rho_L + \rho_c = \frac{F(1 \pm n)}{1 - n\nu_0} \cdot \frac{1 \mp \nu'}{E'} \sigma_L \quad (8.8)$$

$$\rho_z + \rho_s = \frac{F(1 \pm n)}{1 - n\nu_0} \cdot \frac{1 \mp \nu}{E} (\sigma_z \mp \sigma_s)$$

Hence

$$\sigma_z + \sigma_s = \frac{\rho_z + \rho_s}{\rho_L + \rho_C} \cdot \frac{E}{E'} \cdot \frac{1 + \nu'}{1 + \nu} \cdot \sigma_L \quad (8.9)$$

or, if the compensating bar is of the same material as the test piece,

$$\sigma_z + \sigma_s = \frac{\rho_z + \rho_s}{\rho_L + \rho_C} \cdot \sigma_L \quad (8.10a)$$

i.e.,

$$\sigma_z = \frac{\sigma_L}{\rho_L^2 - \rho_C^2} (\rho_L \cdot \rho_z - \rho_C \cdot \rho_s) \quad (8.10b)$$

$$\sigma_s = \frac{\sigma_L}{\rho_L^2 - \rho_C^2} (\rho_L \cdot \rho_s - \rho_C \cdot \rho_z)$$

where,  $E$  is the Young's modulus of the test piece,  $E'$  is the Young's modulus of the compensating bar, and  $\nu$ ,  $\nu'$  are the Poisson's ratios of the test piece and the compensating bar respectively. The subscripts  $z$ ,  $s$  denote the mutually perpendicular directions in the test piece, and  $L$ ,  $c$  the longitudinal and transverse directions of the compensating bar.

From Eqs. 8.10 the required stresses  $\sigma_z$ ,  $\sigma_s$  are thus completely determined by the four gauge readings and the known *compensating stress*  $\sigma_L$ ; the five constants  $F$ ,  $n$ ,  $\nu_0$ ,  $E$ ,  $\nu$  cancelling out. The accuracy now depends only on the gauge readings.

Knowing the stresses in the longitudinal (tangential) and transverse (radial) directions on both surfaces, the transverse moments and longitudinal direct stresses were then obtained as:

transverse moment per unit length

$$m_s = \left( \frac{\sigma_{s,b} - \sigma_{s,t}}{2} \right) \frac{t^2}{6}$$

and longitudinal membrane stresses

$$\sigma_{\bar{y}} = \frac{\sigma_{\bar{y},b} + \sigma_{\bar{y},t}}{2}$$

The subscripts t and b denoting the top and bottom surfaces respectively of the plate under consideration.

Since there were no gauges fixed on the inner surfaces of the plates, the longitudinal membrane stresses for Model 1 could be evaluated approximately by

$$\sigma_{\bar{y}} = \frac{E}{1 - \nu^2} \epsilon_{\bar{y}} \quad (8.11a)$$

or

$$\sigma_{\bar{y}} = \frac{\sigma_L}{\rho_L^2 - \rho_C^2} \rho_L \cdot \rho_{\bar{y}} \quad (8.12b)$$

### 8.3.2 Theoretical solutions

The models were analysed by the finite element method of analysis using both thin-walled box beam elements and three-dimensional thin shell elements facilitated in LUSAS.

The general theory has been derived and discussed in previous chapters. The theoretical results predicted by the present study were obtained by using the CUBAS computer program which will be described in Appendix I. The general beam idealization of the individual models is shown in Fig. 8.12. The properties of the box beam sections, without considering the shear lag effect, are listed in Table 8.3. In practice, the bending moments of inertia  $I_{xx}$  used in the computing, were evaluated by considering the effective width of the flanges from the relevant tables listed in Chapter 2, which have been suggested by Moffat and Dowling (93).

For each loading condition the output of the computer program gave displacement components and stress resultants at each node. The longitudinal

and/or transverse displacement distributions and the stresses could then be obtained theoretically at each gauge section for the individual loading conditions.

For the purpose of comparison, three-dimensional finite element analyses were also carried out. The LUSAS computer program (79) was utilized to obtain the theoretical results for each model test. The detail theoretical background for the LUSAS system can be found in Ref. 80.

The extensional-flexural quadrilateral elements with six nodes named SHI6 were chosen for idealizing the boxes and the lower order quadrilateral elements with four nodes named SHI4 were used for representing the diaphragms. The flat thin shell box element idealization for each of the four elastic models is shown in Figs. 8.13, 8.14, 8.15 and 8.16 respectively. For obtaining the convergence results and also for the sake of convenience when comparing with the experimental results, fine meshes for the flange plates and along the length of the beams were used. Since the in-plane displacement field represented exactly the beam action in the cell walls, only a single element over the depth of a web was involved (80). It should be noted that, although the web elements are cylindrically-curved plates in the curved cantilever box beam model, they are treated in practice as flat rectangular elements because of the limitation of the available elements in the computer program.

### 8.3.3 Comparison of the theoretical and experimental results for the models

The values obtained from the experimental tests on the four models will now be compared with those predicted by the general beam and three-dimensional finite element methods. The loading conditions for the models are listed in Table 8.2.

### 8.3.3.1 Presentation of results for Model 1 — straight cantilever box beam model

The twisting angles and distortional angles along the box beam were evaluated from the observed values of displacements (Table 8.3 and 8.4). The comparisons of the distributions of the twisting angles as well as the distortional angles along the beam are listed in Table 8.4 together with the plots shown in Figs. 8.17 and 8.18. The close agreement of the theoretical solutions with those obtained experimentally indicates that the additional degrees of freedom which represent the warping and distortional actions can be presented accurately by thin-walled box beam finite elements.

In Fig. 8.19 the vertical deflections of the bottom flange at  $7/8$  span and midspan cross-sections are plotted and tabulated. Good agreement is also shown between the observed values and the calculated values both from the thin shell box element idealization and the thin-walled box beam element idealization. The deformed shape of the cross-section at the tip of the beam can be seen visually from the photograph of Figure 15.

The values of longitudinal warping stresses and transverse bending stresses on the outer surface around the  $3/4$  span cross-section and midspan cross-section of the model are plotted in Figs. 8.20 and 8.21. Table 8.3 gives a detailed comparison of the observed and calculated stresses in the top flange near the web. The stress comparison in the case of Model 1 has shown that the additional stress system arising from the warping torsion and distortion effects can be predicted sufficiently accurately for straight single-spined box beams by a one-dimensional finite element analysis using thin-walled box beam elements. Attention should also be drawn to the fact that the calculated stress results from beam elements and shell elements are in close agreement.

### 8.3.3.2 Presentation of results for Model 2—curved cantilever box beam model

In the comparison of results obtained from the tests on Model 2, the vertical deflections at various positions across the top flange at the  $7/8$  arc length cross-section from the fixed end, are shown in Fig. 8.23. The comparison shows that the theoretical values obtained by thin-walled box beam elements with the reduced torsional stiffness described in Chapter 3 are in close agreement with those measured in both loading cases. In this case the three-dimensional finite element solution is not in close agreement with either the experimental results or the results obtained using the thin-walled box beam element. Yet, the deformed shapes are basically the same as the experimental ones.

The deformed shapes of the tip cross-section can be seen from Figures 16 and 17. By using photogrammetric techniques the distortional angle of the tip section was measured as 0.01649 radians for the two-point load case and 0.04448 radians for the one-point load case. The corresponding values calculated by general beam theory were 0.01649 radians and 0.04597 radians respectively. The observed model results are in very close agreement with the calculated results.

Typical examples of the comparison between the experimental stresses and those obtained from the finite element methods are given in Figs. 8.24 and 8.25. Here the longitudinal membrane stresses at the  $1/8$  arc length cross-section, and transverse bending stresses for the outer surfaces at the  $7/8$  arc length cross-section have been plotted.

It may be noted that from Figs. 8.24 and 8.25 the radial stresses obtained by the finite element method using either shell elements or beam elements are in reasonable agreement with those obtained experimentally. The tangential (longitudinal) stresses, however, do not compare so well.

In general, the finite element values are higher than the experimental ones, but it should also be noted that the theoretical results from the present approach are closer to the experimental values than in the case of the three-dimensional finite element analysis. The shapes of the tangential stress plots are basically the same as those of the experimental results.

#### 8.3.3.3 Presentation of results for Model 3—two-span continuous box beam model

The results obtained from Model 3 represented only the elastic behaviour of this structure. Since no devices were employed to measure the strains on concrete surfaces, only a comparison of experimental and theoretical deflections has been established.

In Fig. 8.26 the vertical deflection at the bottom of the side web along the continuous box beam is plotted and tabulated. Close agreement has been shown between the theoretical values and the observed results. As a typical comparison the measured transverse distribution of the vertical deflection across the bottom flange at the mid-span cross-section of the loaded span, together with the results calculated from finite element methods is shown in Fig. 8.27.

The values of longitudinal stress resultants and transverse bending moments around the mid-span cross-section of the model are plotted in Figs. 8.28 and 8.29 respectively. A comparison of the finite element shell analysis and the finite element beam analysis for the longitudinal stresses at the mid-span cross-section of the loaded span is shown in Fig. 8.30. This indicates that close agreement between these two theoretical approaches occur not only for the displacement results but also for the stresses.

8.3.3.4 Presentation of results for Model 4 — simply supported twin-box beam model

The observed deflections across the top flange at the mid-span cross-section for two symmetrical concentrated loads totalling 40 kN applied above the two inner webs at 7/16 of the span, together with those evaluated from the finite element analyses, are plotted and tabulated in Fig. 8.31. In addition, the shape of the deformed cross-section at midspan due to a concentrated load of 20 kN applied above one of the inner webs at 7/16 span has been shown in Fig. 8.32. It is interesting to note that the results due to symmetrical loading may be obtained from those due to asymmetrical loading by the superposition principle.

The comparison presented in Fig. 8.31 shows that the maximum deflection calculated by the finite element-grillage method with a reduced torsional stiffness factor of 1/7.90 for the symmetrical loading case is within 7% of the experimental value, an accuracy quite adequate for design purposes. For the asymmetrical loading case, however, the agreement between the deflections obtained from the experiment and from the finite element-grillage calculation with reduced factor of 1/7.91 for the loaded box and of 1/8.05 for the unloaded box, shown in Fig. 8.32, is not good; although the deformed shapes are largely the same. The theoretical results obtained from finite element analysis using thin shell elements indicate that, in general, it gives results of greater stiffness than those obtained from measurement as well as from the finite element-grillage analysis.

The longitudinal stresses on the outer surface at the mid-span cross-section from the three-dimensional finite element, the experimental and the finite element-grillage results are shown in Figs. 8.33 and 8.34. Stresses for both loading cases are in adequate agreement in the loaded box. It is also interesting to note that the finite element-grillage approach results in an overestimate of the stresses in the loaded box, and

an underestimate of the stresses in the unloaded box.

Figs. 8.35 and 8.36 indicate the comparison of transverse bending stresses at the mid-span cross-section for both loading cases. Although the theoretical results and the observed values are not in very close agreement, the discrepancy between theory and experiment in the loaded box for both loading cases, is acceptable for primary design purposes.

The reactions measured by the load cells in both loading cases are shown on a plan of the structure in Figs. 8.37 and 8.38 together with the values calculated from finite element analyses. The sum of the measured reactions was 1.79% lower than the total applied for the symmetrical loading case, whereas the total applied load gave the lesser value of 1.65% for asymmetrical loading.

#### 8.4 Summary and conclusions of the results obtained from the experimental work

A series of comprehensive model investigations was carried out in an indirect manner, i.e., the models were used mainly to assess the validity of the proposed theory. Also, the experimental tests enabled the real structural behaviour of the box spine-beams with deformable cross-sections to be observed. Thus an understanding of the structural action was obtained which effectively assisted the development of the theory.

In the previous section, the theoretical and experimental results obtained have been compared and discussed. From this comparison and also from the comparison between the results given by the thin-walled beam elements and the flat thin-shell elements, several conclusions can be established and these may be summarized as follows:

1. From the close agreement of the experimental and theoretical values for Models 1 and 3 it can be concluded that thin-walled box beam

elements which have additional nodal variables can be used to predict the global behaviour of straight single-spined box beams with sufficient accuracy.

2. The results obtained experimentally from Model 2 have illustrated the behaviour of curved box beams. This study showed that if deformation of the cross-section is permitted, the initial curvature greatly increases the rigid deflections of the girder. This confirms that the interaction between the bending and torsional effects is significantly influenced by the cross-sectional deformation. However, the transverse distortional response of the curved box beam is not very different from an equivalent straight box beam with a span equal to the developed length of the centre line of the curved box.

Furthermore, experimental results have verified that additional distortional forces occur in box beams curved in plan due to the radial component of the longitudinal bending stresses. They must be included in the distortional calculation even when the applied loads are symmetrical about the cross-section axes.

3. The investigated structural response of the curved model has shown that the radial and tangential stresses obtained from thin-walled box beam elements were overestimated but the theory predicted well the distribution and sense of the stresses. Thus the general beam theory can be used to analyse deformable box spine-beams curved in plan with adequate accuracy for design purposes.

4. The finite element-grillage method developed within this thesis for multi-spined box beams, consists essentially of making reductions to the torsional stiffness properties of the longitudinal members of the grillage to allow for the apparent increased rotations about the

longitudinal axis due to distortion of the cross-section. The results obtained from Model 4 compared with the theoretical solutions indicate that a finite element-grillage analysis gives an adequate assessment of the displacements and stresses in the case of the loaded box. In practice, the monolithic top flange would be much stiffer than that in the model. The analysis should therefore be more accurate when applied to a real multi-spined box beam.

5. From the observed distribution of longitudinal normal stresses across the model cross-sections, the effective breadth treatment of shear lag, which is based on Moffatt's work (93), has been qualitatively verified.

6. The longitudinal warping stresses which arise from constrained torsional warping and distortional warping can form a significant addition to the ordinary bending stresses and must be considered in design. Distortion is the main source of warping stresses and torsional warping stresses are generally of secondary importance in practical box beam structures. Maximum distortional warping stresses for the models were found to be 22% - 70% of the ordinary bending stresses, whilst the torsional warping stresses were only 1% - 7% of the bending stresses.

7. Transverse distortional bending stresses in deformable box beams are extremely sensitive to the transverse cross-sectional properties. They may be of the same order as the longitudinal bending stresses under the same loading. Consequently, transverse distortional bending can generate significant longitudinal stresses due to the Poisson's ratio effect and are by no means negligible in comparison with the longitudinal bending stresses. The experimental stress results, when compared with those obtained theoretically, verify that the longitudinal bending moments of individual plates can be approximated by the corresponding transverse bending moments multiplied by Poisson's ratio (83).

8. The multicell box is another instance in which the symmetrical component of load produces transverse bending stresses. This is illustrated for Model 3 in Fig. 8.31, where it can be seen that the bending stress due to the symmetrical components is a significant portion of the total stress, while the deflections and warping stresses are not significantly changed.

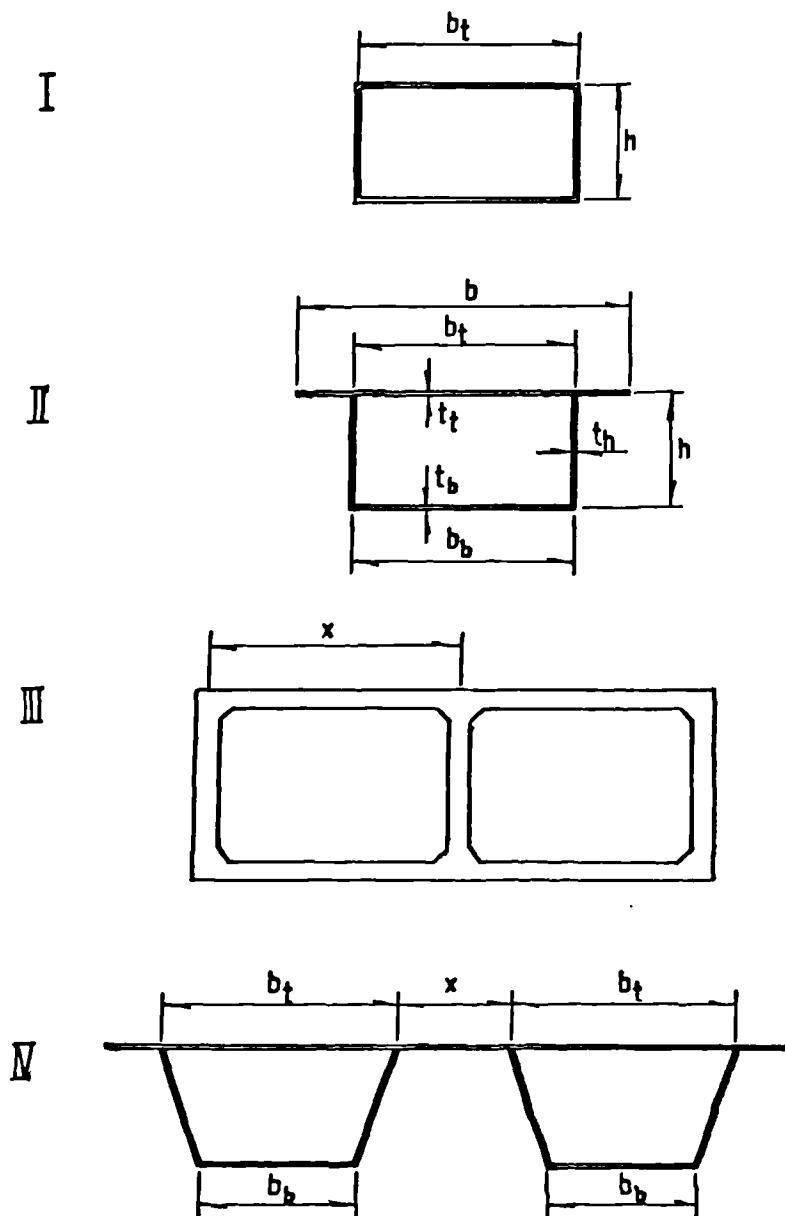


Fig. 8.1 Model cross-sections. Dimensions are given in Table 8.1

Table 8.1 Centreline dimensions and wall thicknesses of cross-sections shown in Fig. 8.1

Section Number	$b_t$ (mm)	$b_b$ (mm)	$b$ (mm)	$h$ (mm)	$x$ (mm)	$t_t$ (mm)	$t_b$ (mm)	$t_h$ (mm)
I	300	300	300	150	—	3.18	3.18	3.18
II	300	300	450	150	—	3.46	3.46	3.46
III	660	660	660	225	330	25	25	30
IV	300	200	900	154	150	5.0	3.0	3.0

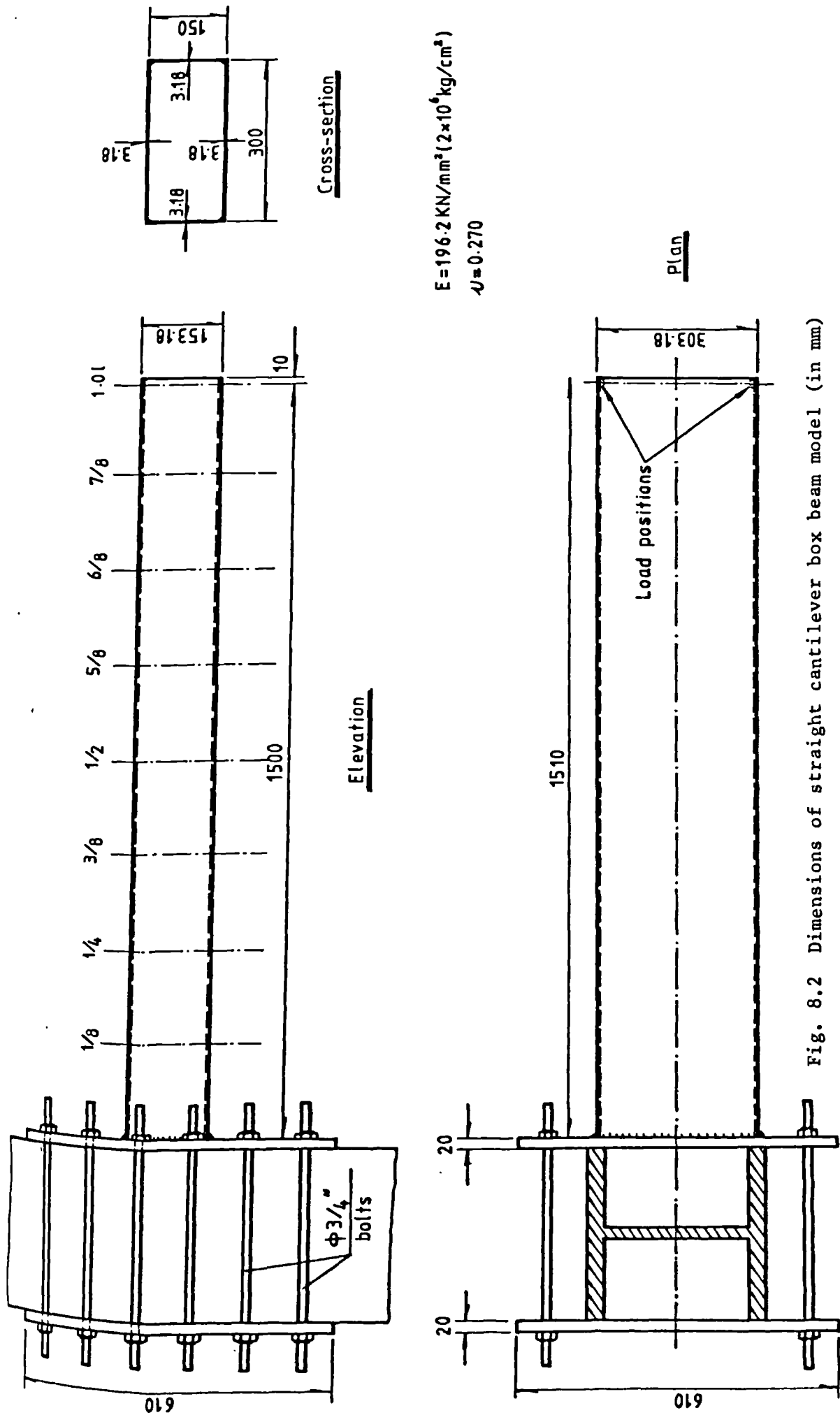


Fig. 8.2 Dimensions of straight cantilever box beam model (in mm)

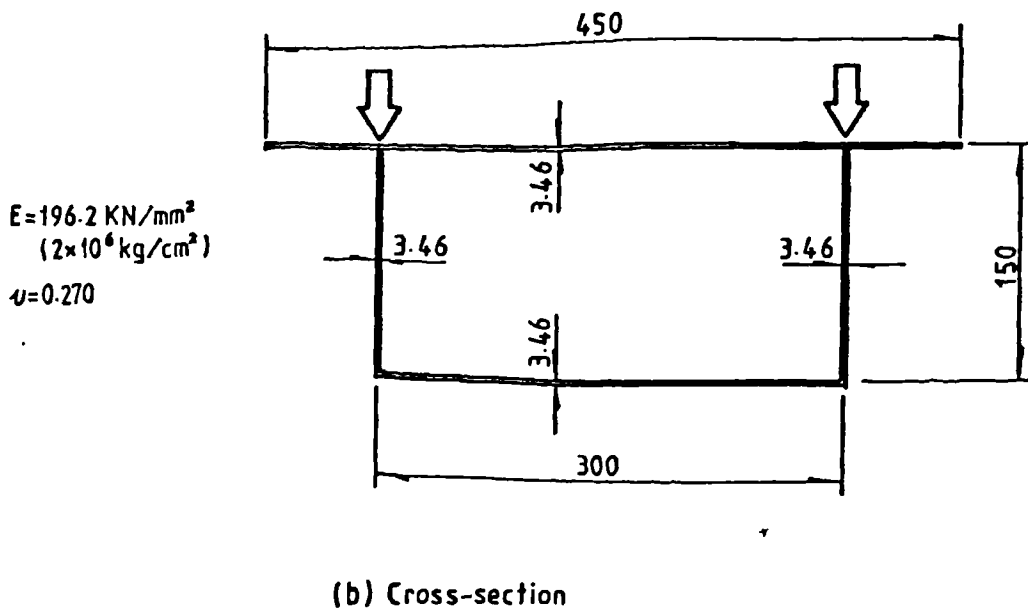
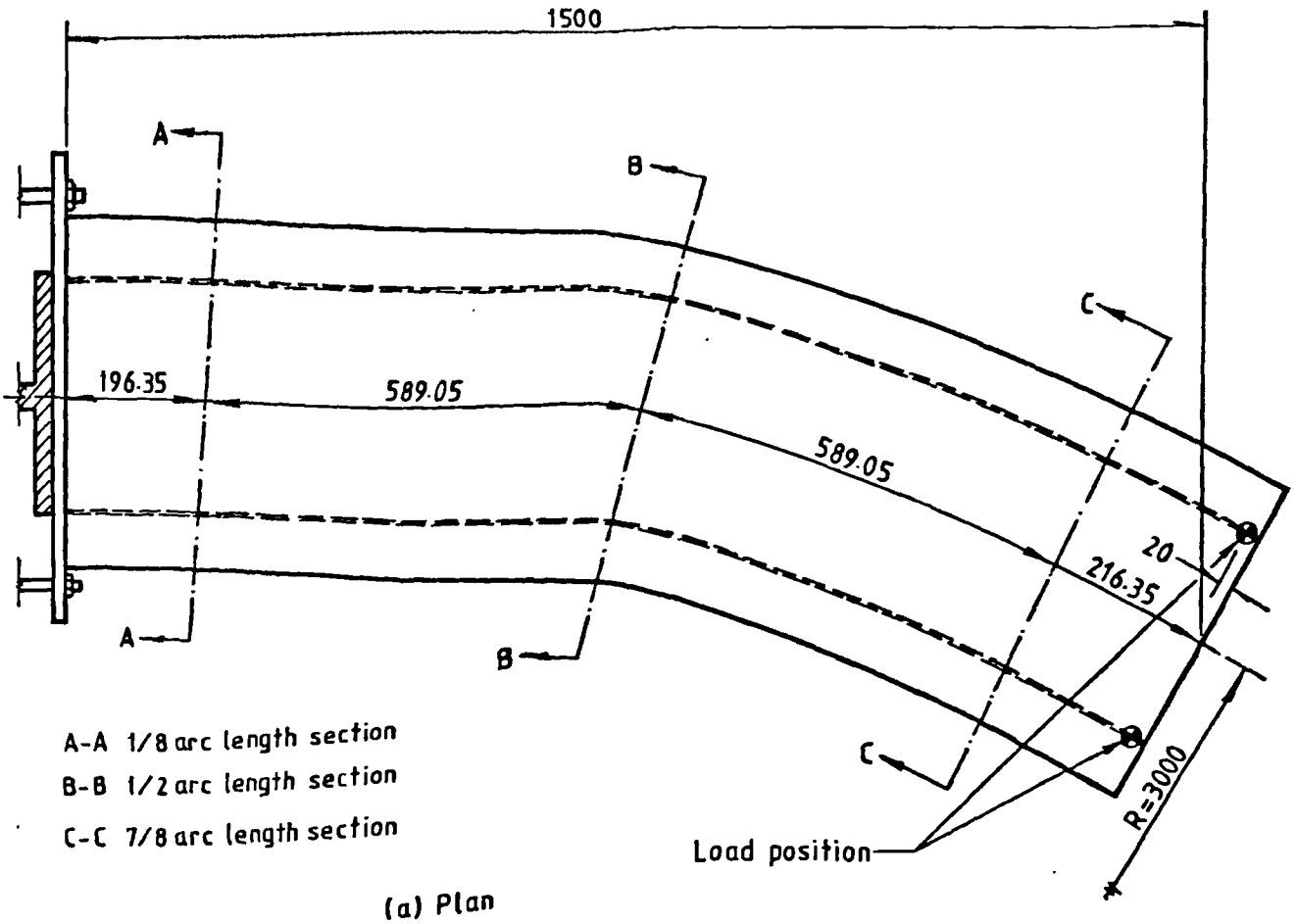
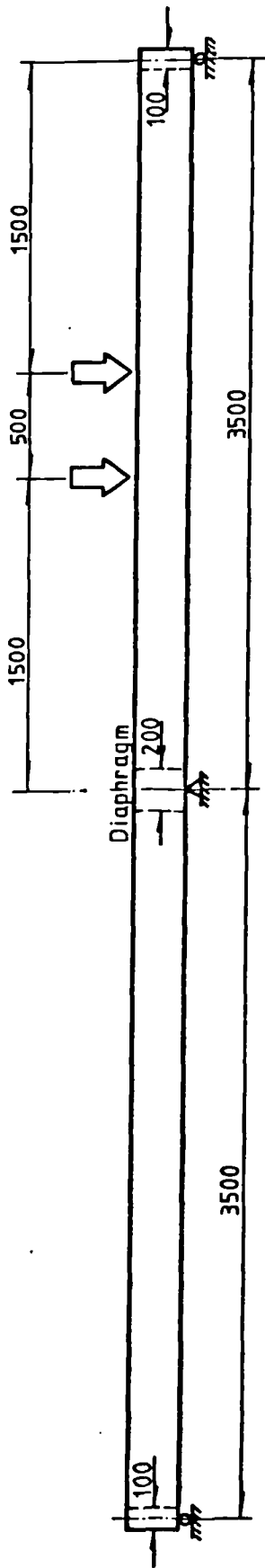
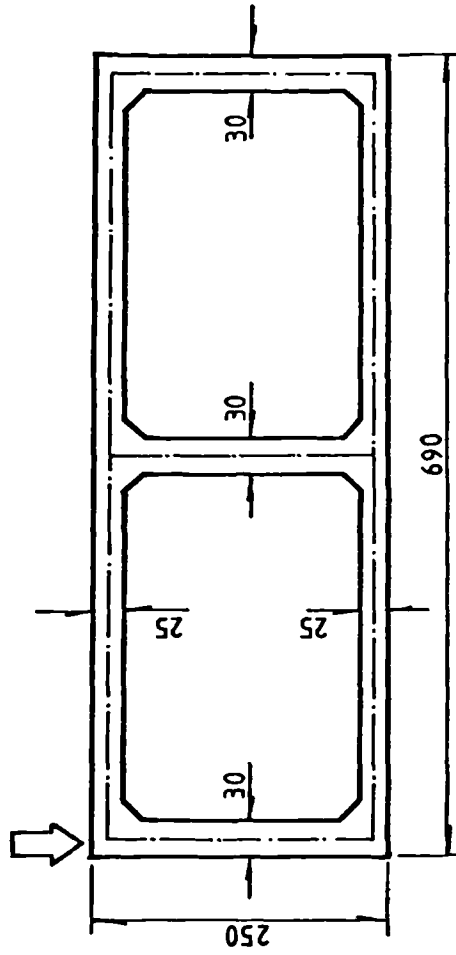


Fig. 8.3 Structural details of curved box beam model (in mm)



(a) Longitudinal elevation



(b) Cross-section

$E = 29 \text{ KN/mm}^2$   
 $\nu = 0.18$

Fig. 8.4 Two span continuous box beam model (in mm)

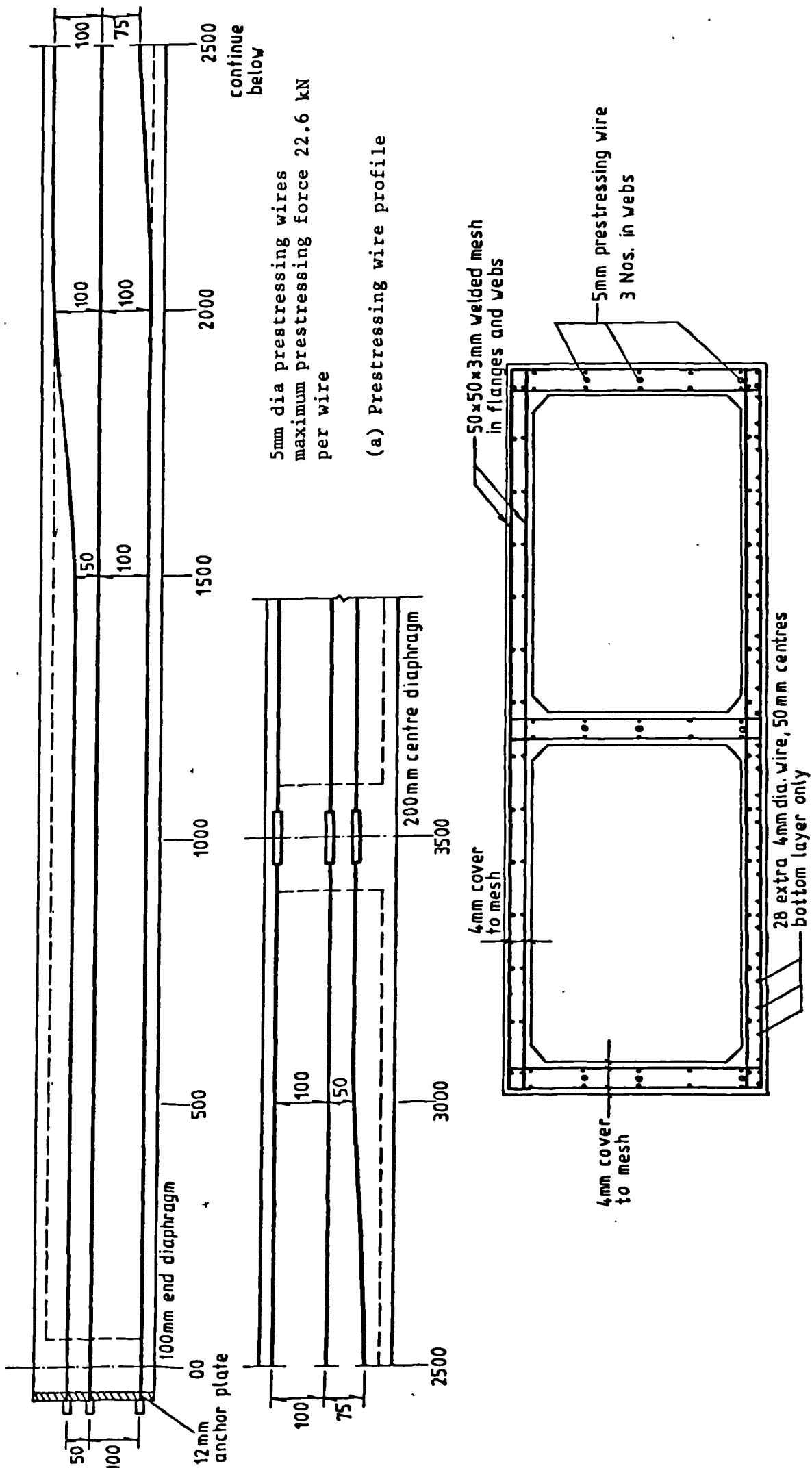


Fig. 8.5 Continuous box beam reinforcement

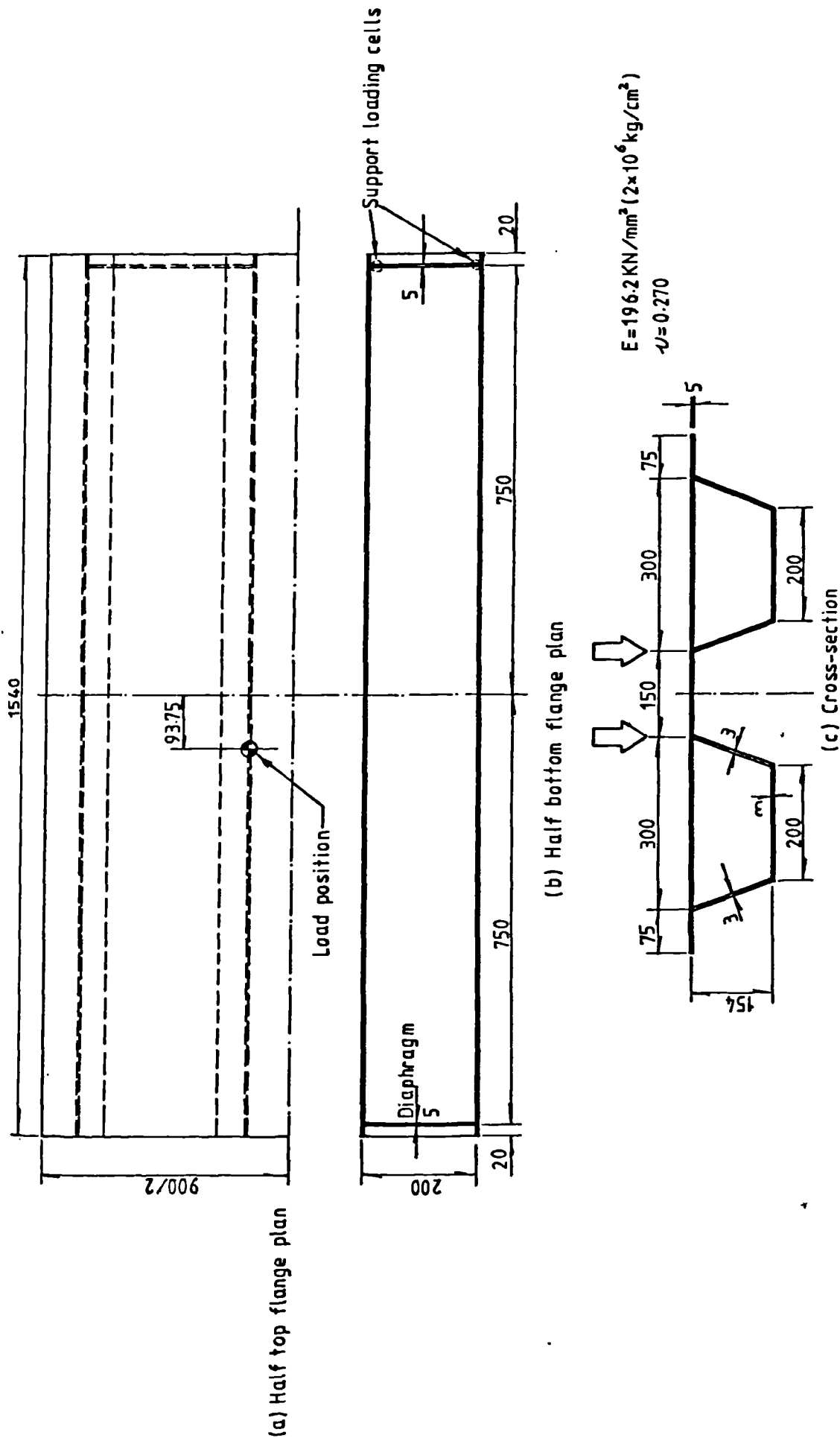


Fig. 8.6 Simply supported twin-box beam model (in mm)

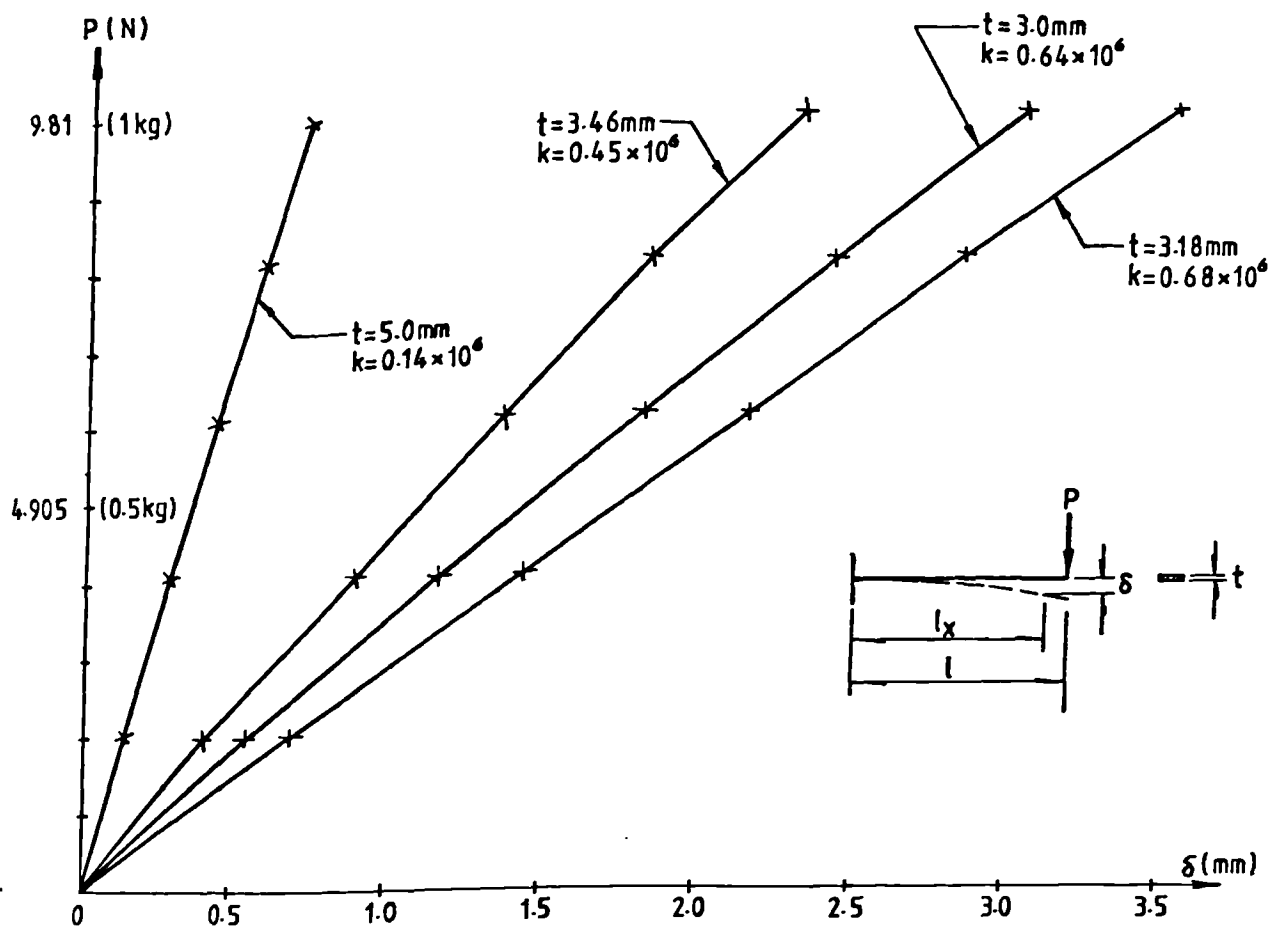


Fig. 8.7 Load/Deflection curves obtained on model steel material

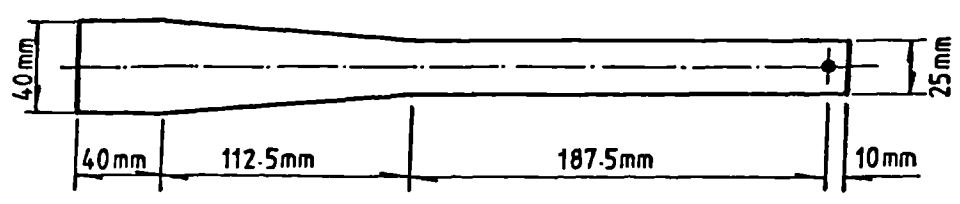
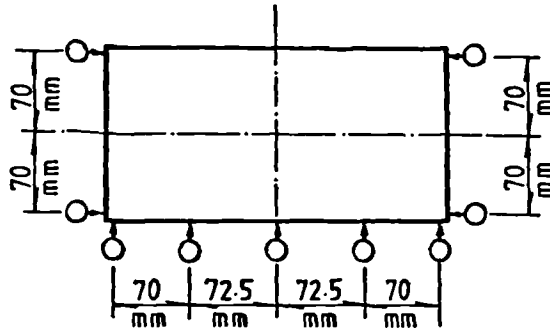
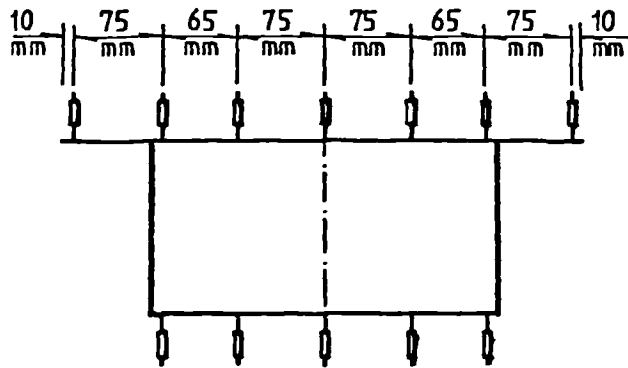


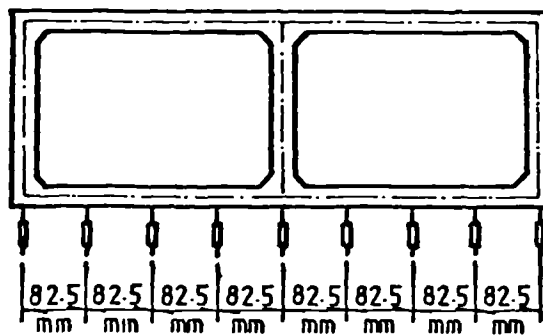
Fig. 8.8 Calibration beam with constant strain portion



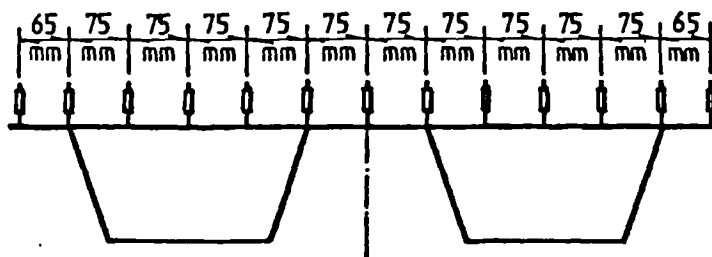
- (a) Dial gauge positions for straight cantilever model at  $1/4$ ,  $3/8$ ,  $1/2$ ,  $5/8$ ,  $6/8$  and  $7/8$  span cross-sections respectively



- (b) Transducer positions for curved cantilever model at  $1/2$  and  $7/8$  arc length cross-sections respectively

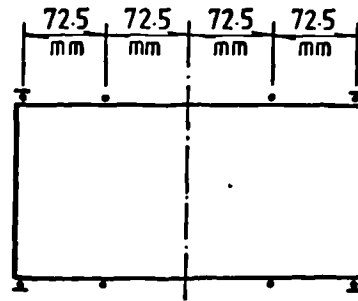


- (c) Transducer positions for continuous box beam model at midspan cross-section of the loaded span



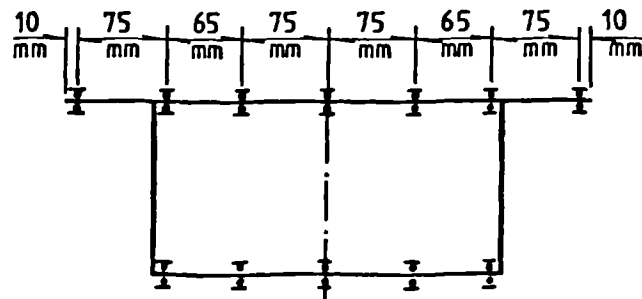
- (d) Transducer positions for twin-box beam model at midspan cross-section

Fig. 8.9 Positions of deflection gages for the models

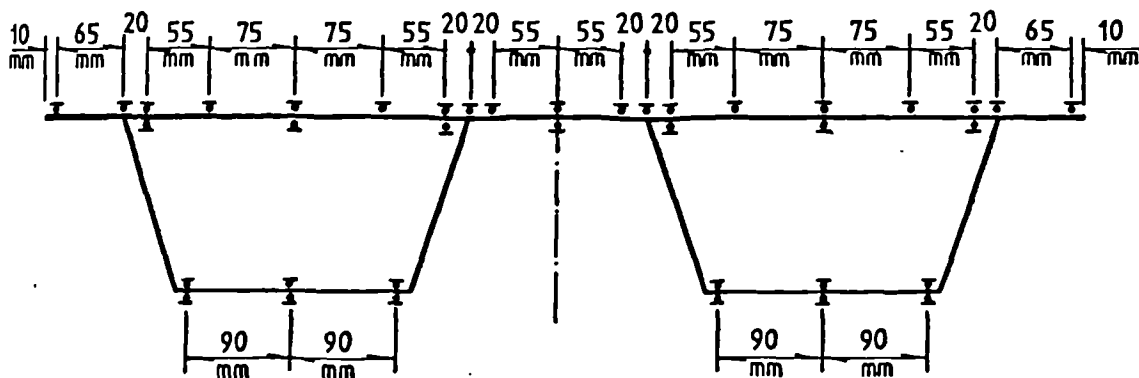


- Longitudinal strain gauge
- Transverse strain gauge

(a) Strain gauge positions for straight cantilever model at  $1/8$ ,  $1/4$ ,  $3/8$ ,  $1/2$ ,  $5/8$ ,  $3/4$  and  $7/8$  span cross-sections respectively



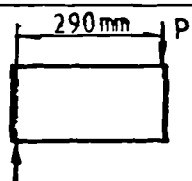
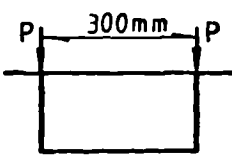
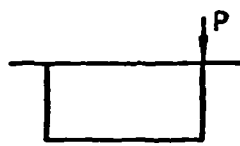
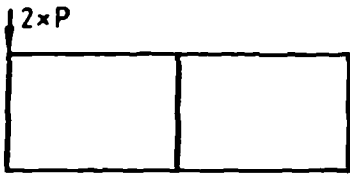
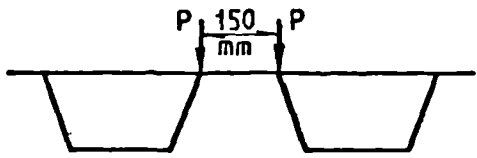
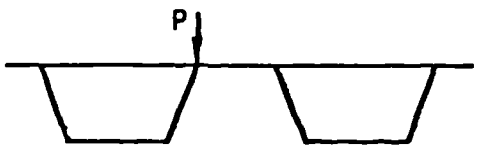
(b) Strain gauge positions for curved cantilever model at  $1/8$ ,  $1/2$  and  $7/8$  arc length cross-sections respectively



(c) Strain gauge positions for twin-box beam model at midspan cross-section

Fig. 8.10 Strain gauge positions for the models.

Table 8.2 Loading cases

Test	Type of Loading		Values
	Cross-section	Plan	
1		A pair of opposite point loads at tip ends to form the concentrated torque	$P = 4905 \text{ N}$ (500kg)
2		Point loads at tip end	$P = 3924 \text{ N}$ (400kg)
3		Point load at tip end	$P = 7848 \text{ N}$ (800kg)
4		Point loads near midspan of the loaded span (see Fig.8.4)	$P = 10 \text{ KN}$ (1019kg)
5		Point loads at 7/16 span	$P = 20 \text{ KN}$ (2038kg)
6		Point load at 7/16 span	$P = 20 \text{ KN}$ (2038kg)

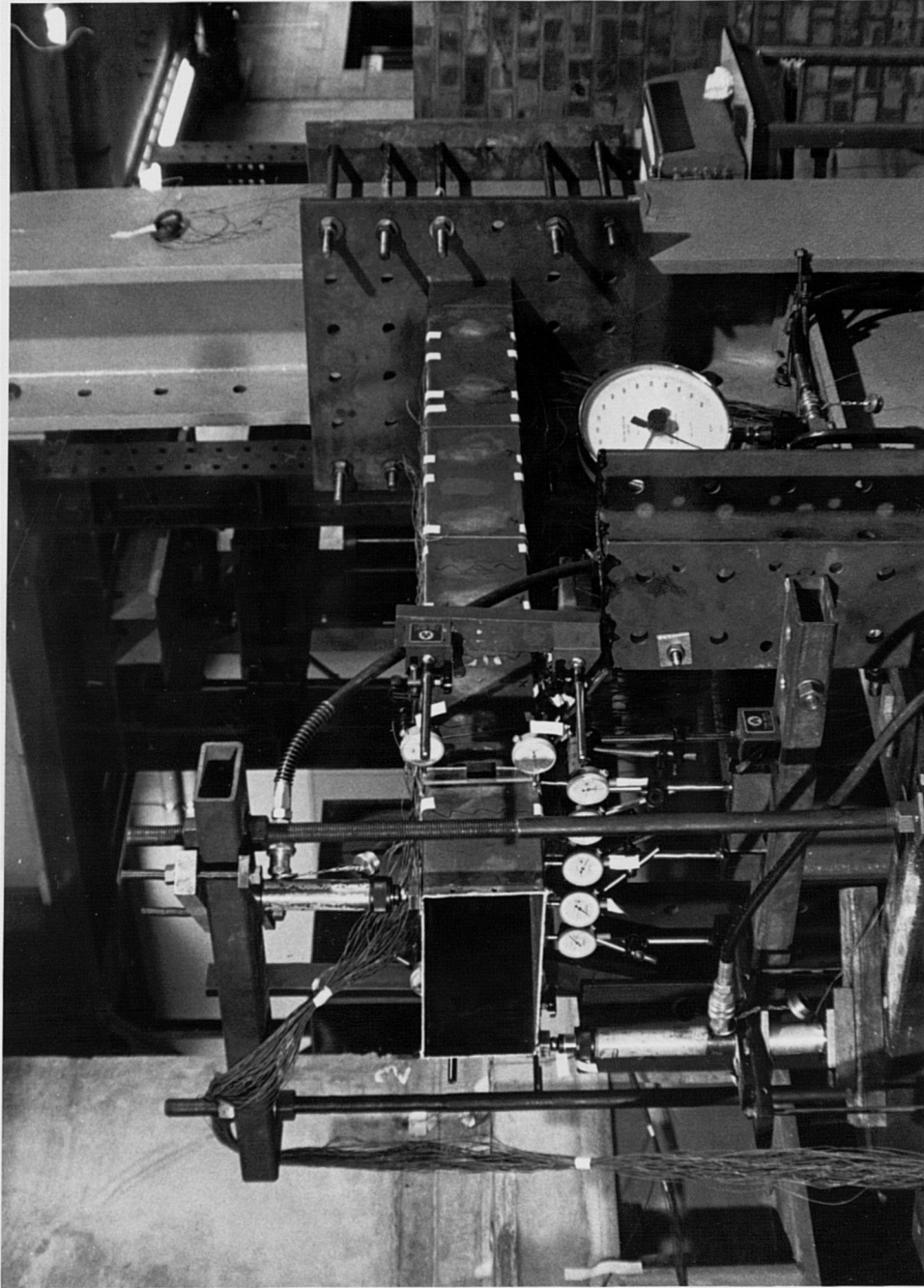


Figure 5. A general view of the steel cantilever box beam model

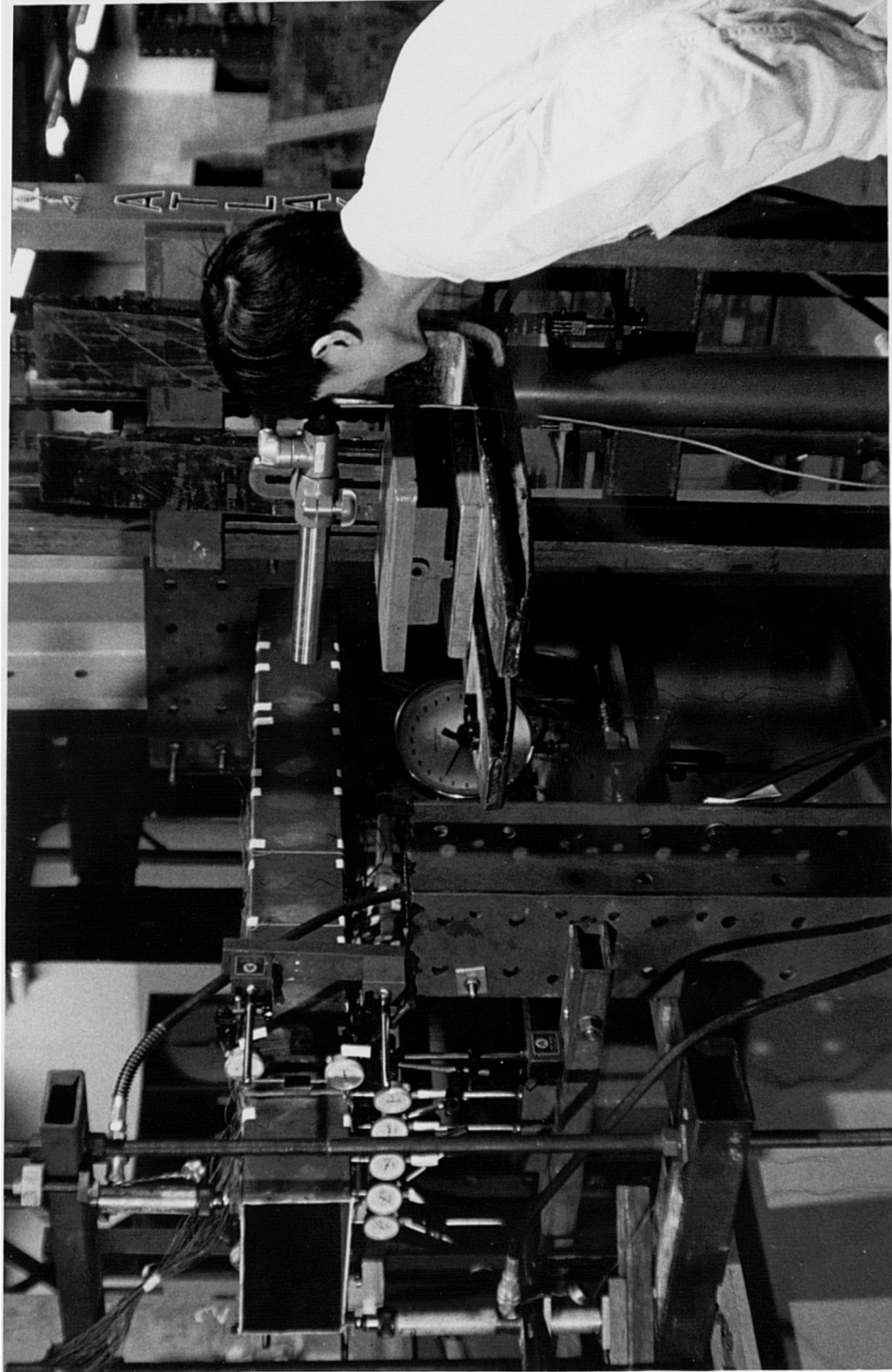


Figure 6. A view of using Angle Dekkor optical device

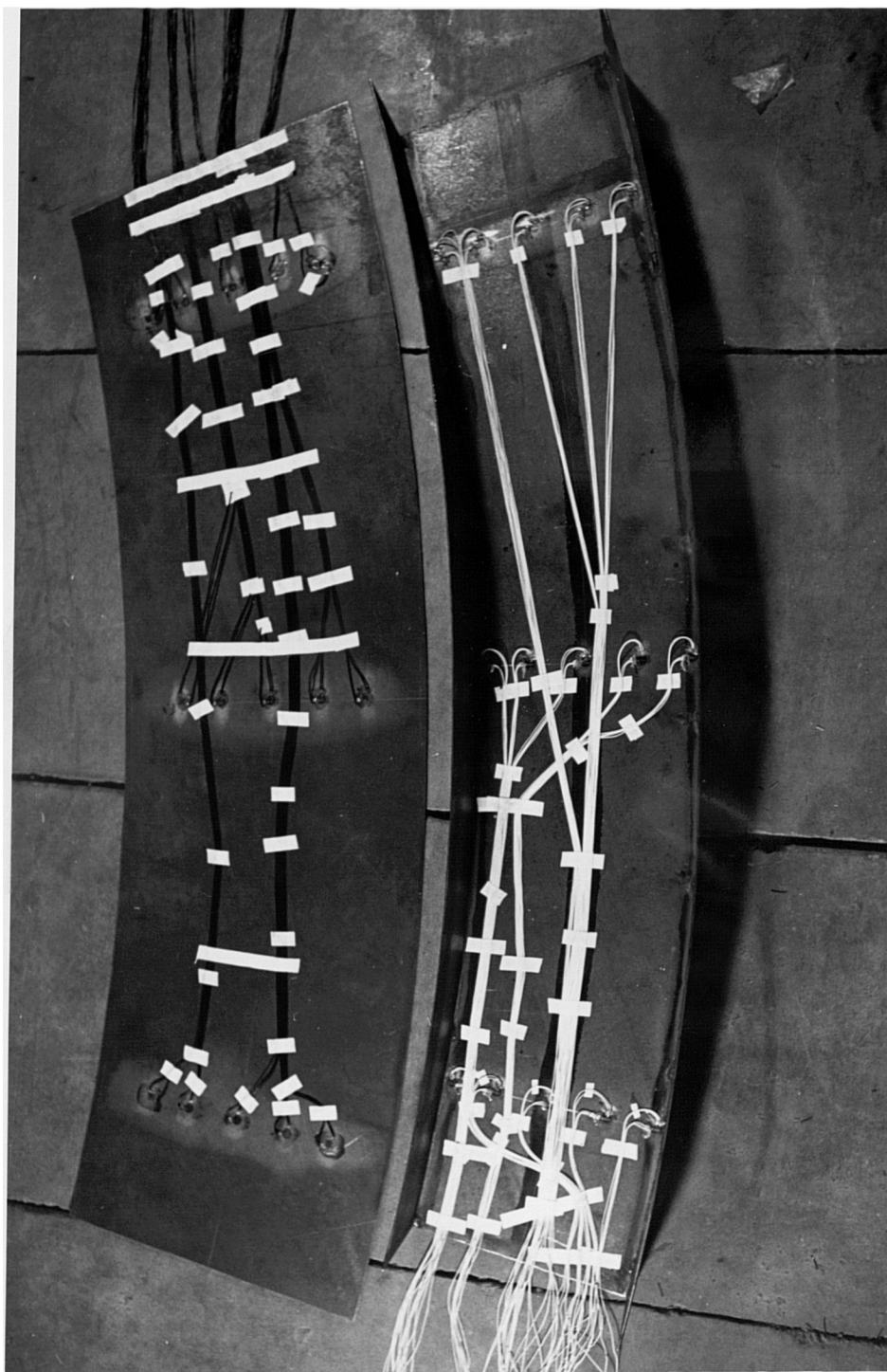


Figure 7 A view of the top flange and the open U channel of the curved box beam model

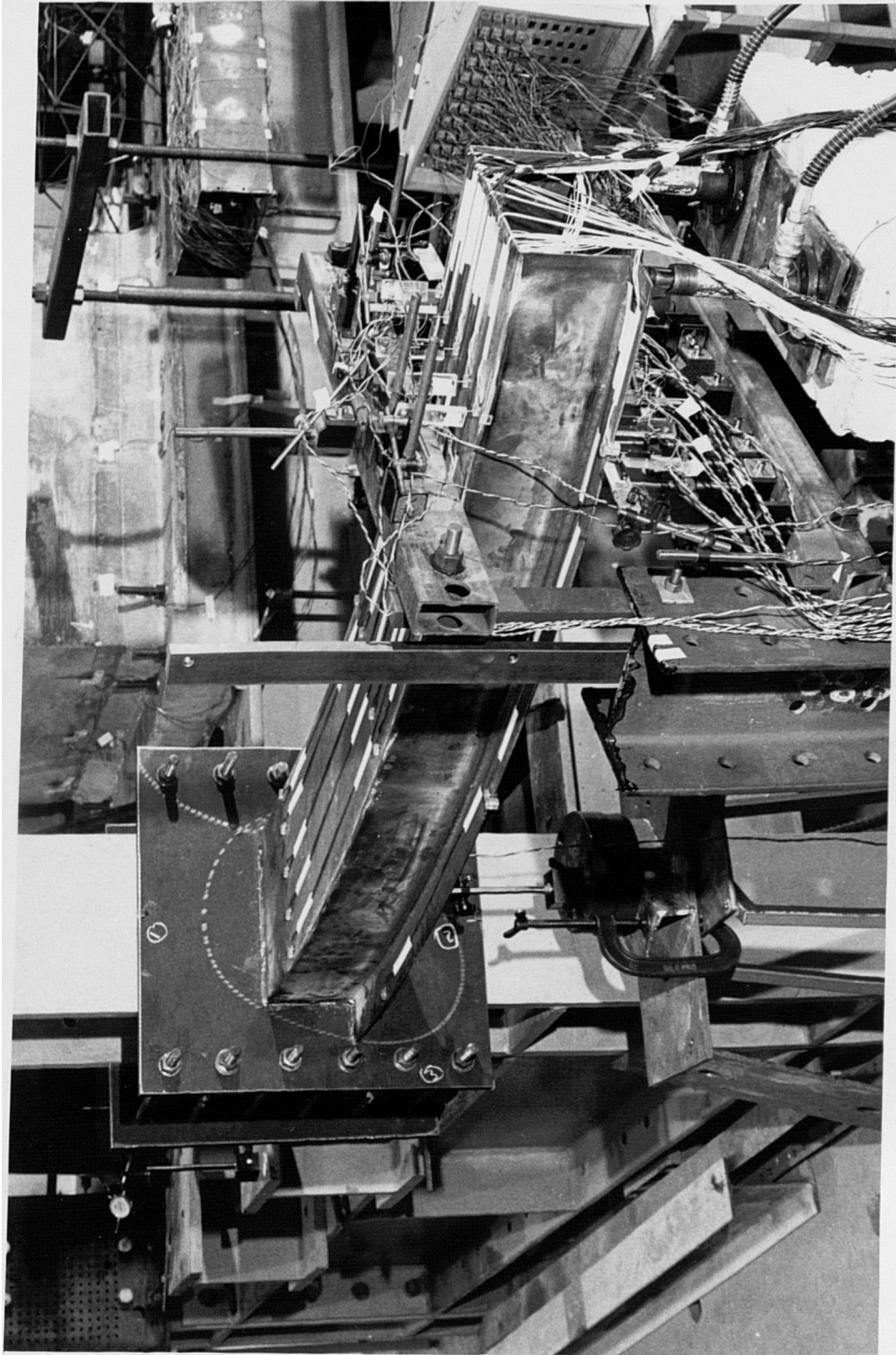


Figure 8 A general view of the steel cantilever box beam model curved in plan

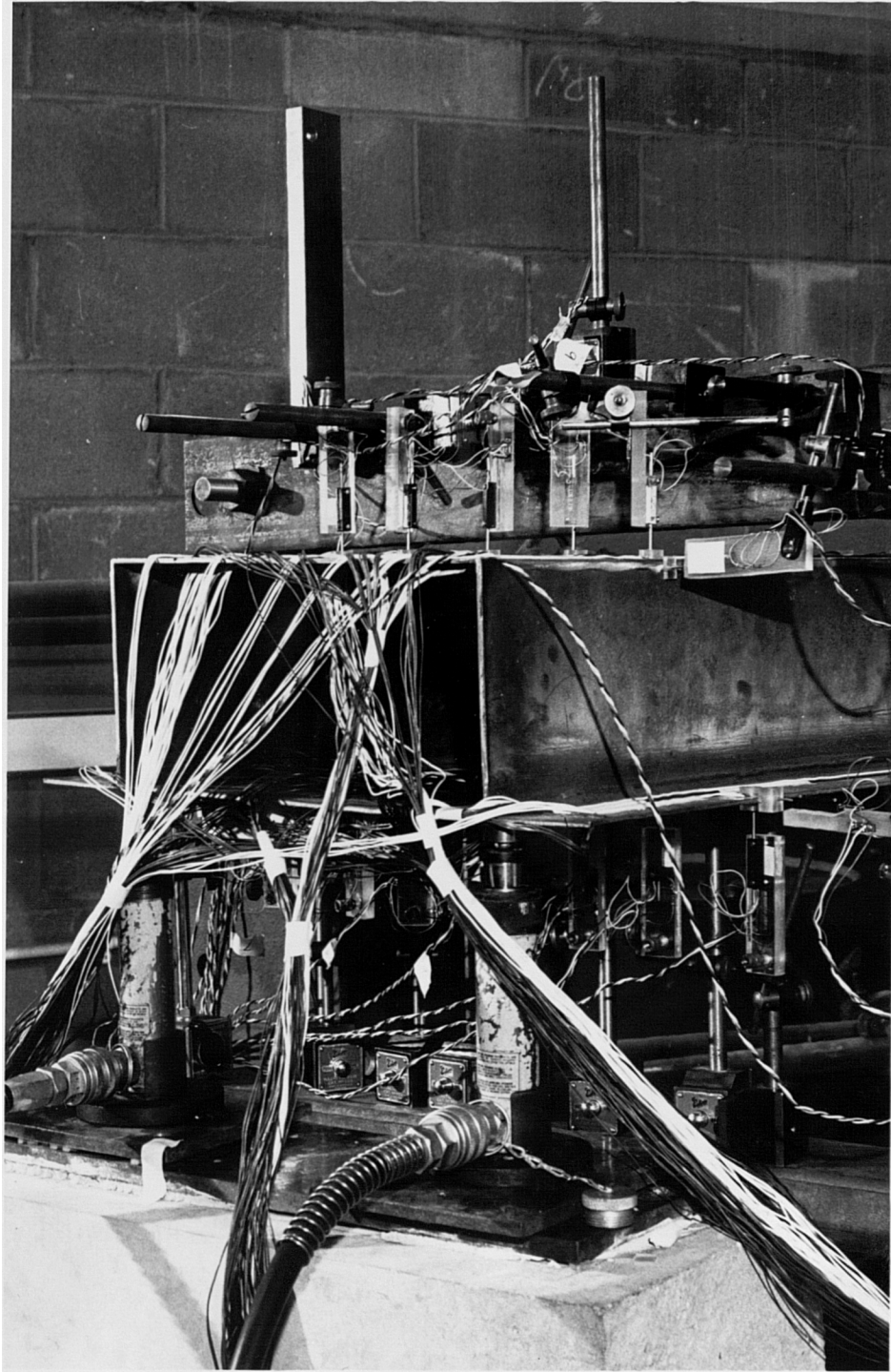


Figure 9 Layout of the transducers and loading system for the curved box beam model

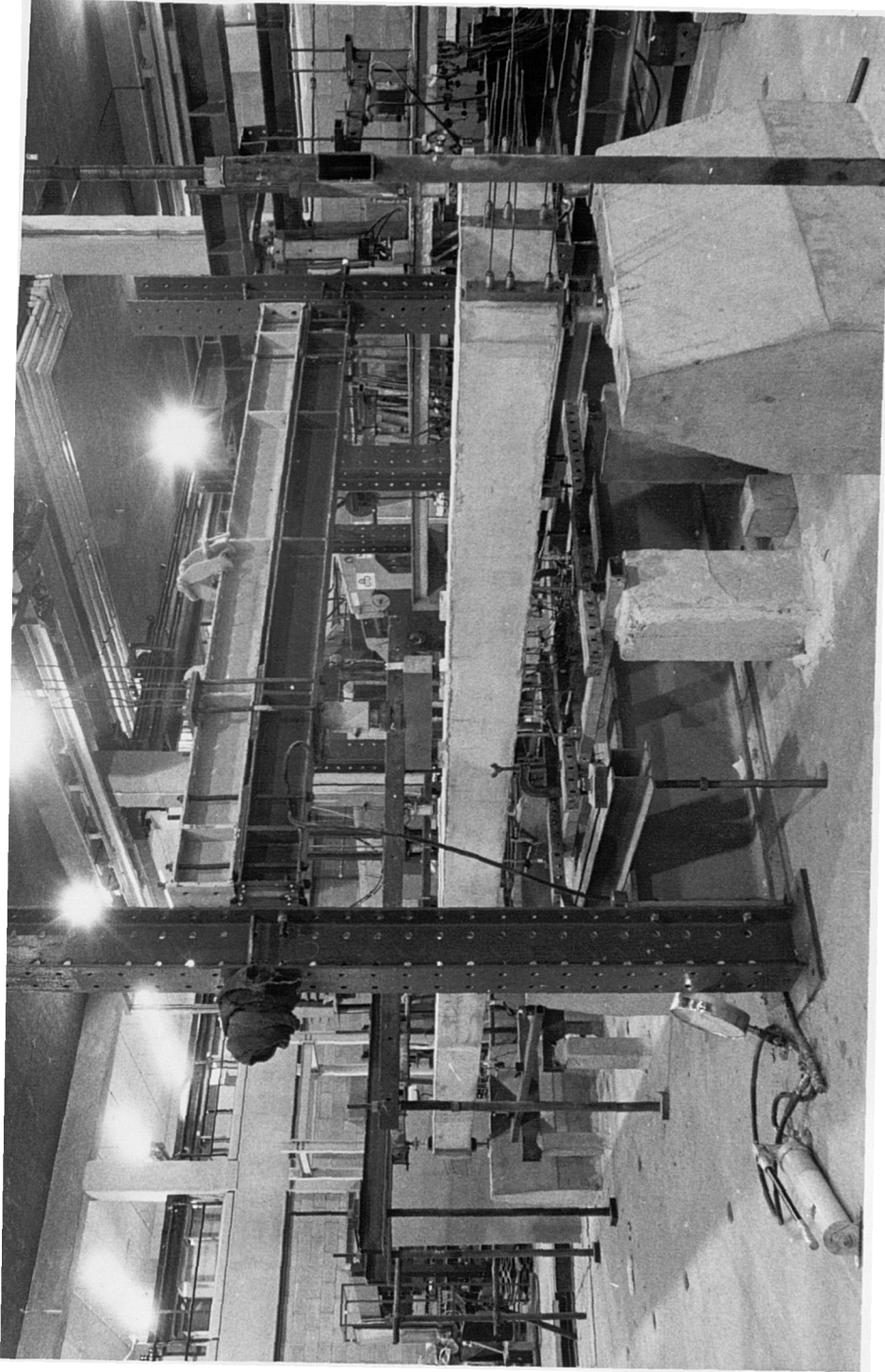


Figure 10 A general view of the two-span continuous box beam model



Figure 11 Failure of the two-span continuous box beam model

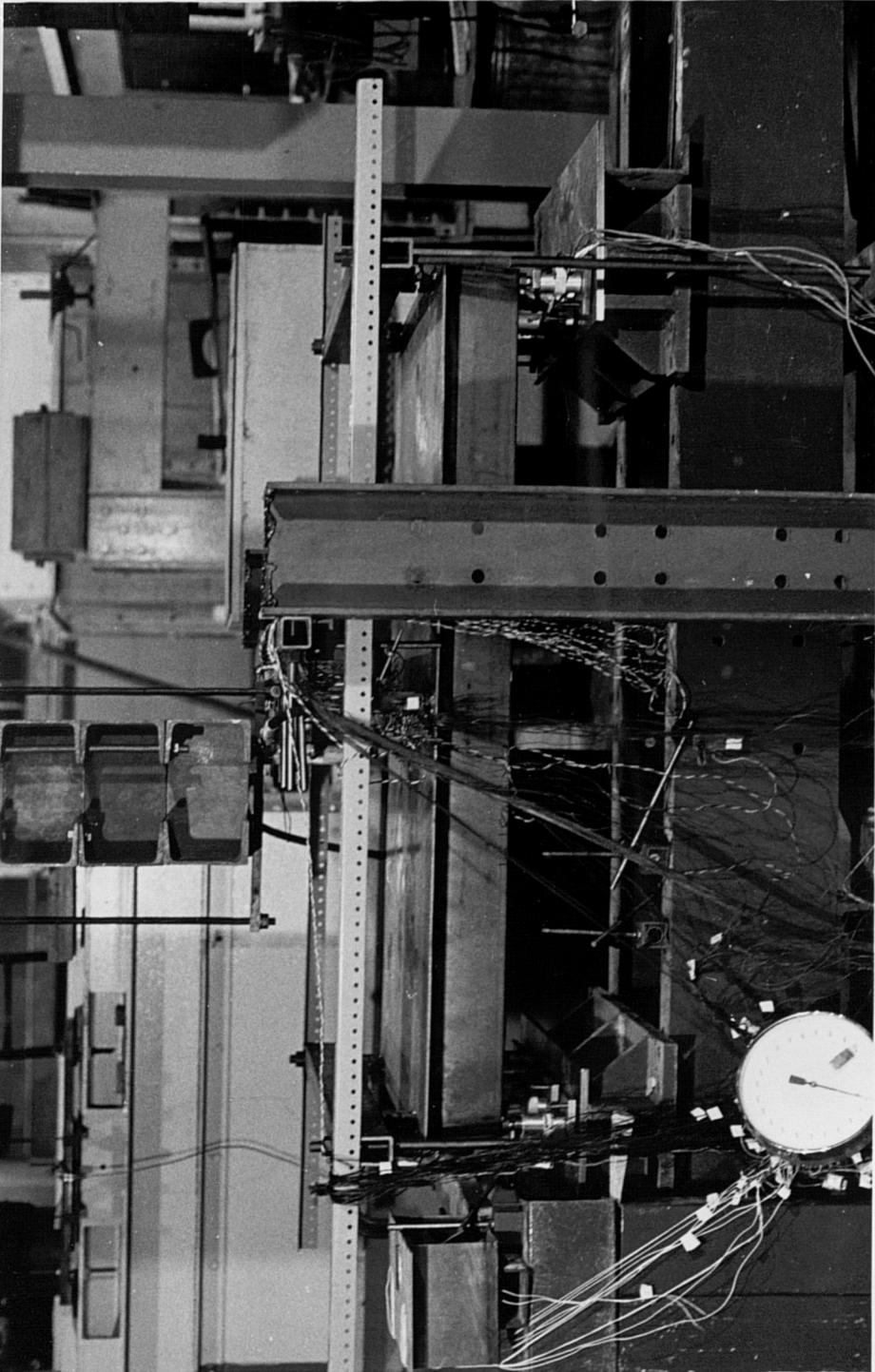


Figure 12 A general view of the twin-box beam model

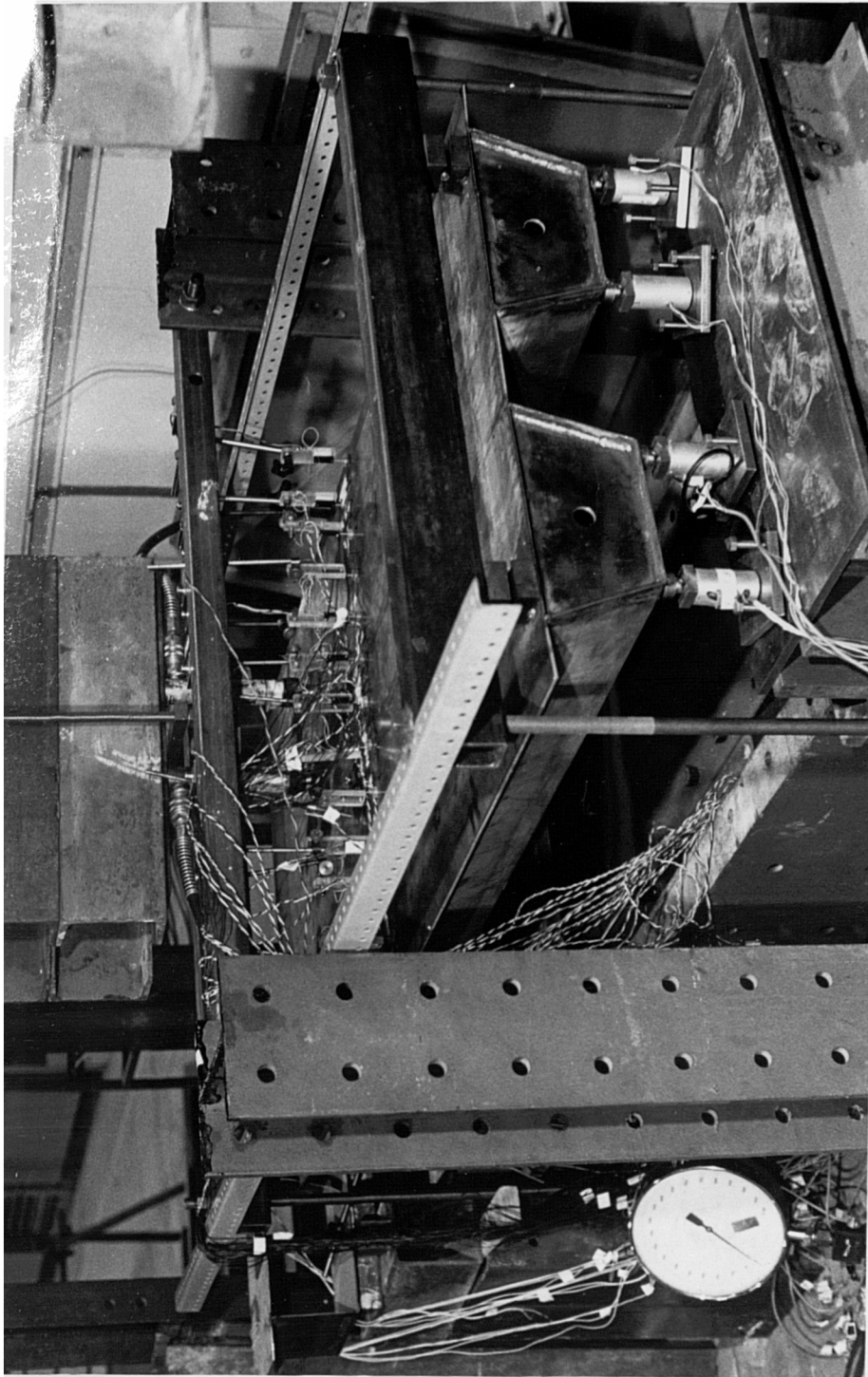
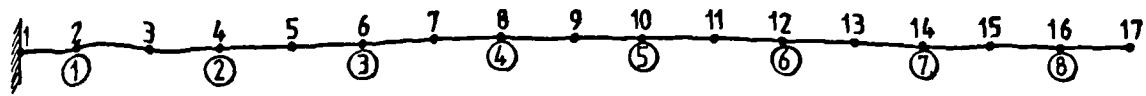


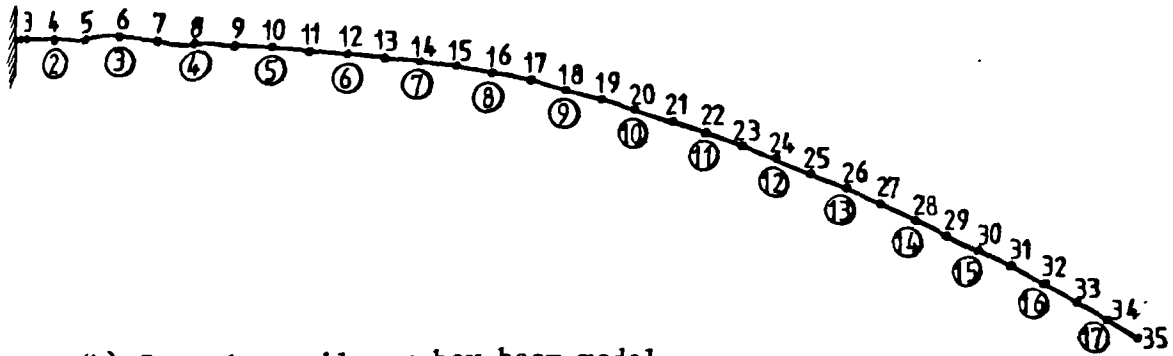
Figure 13 End view of twin-box beam model showing end reaction frame and support load cells



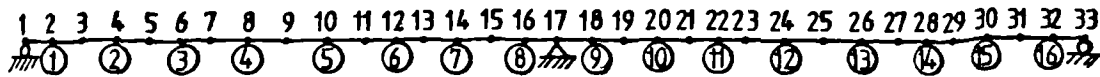
Figure 14 Layout of the transducers and loading system for the twin-box beam model



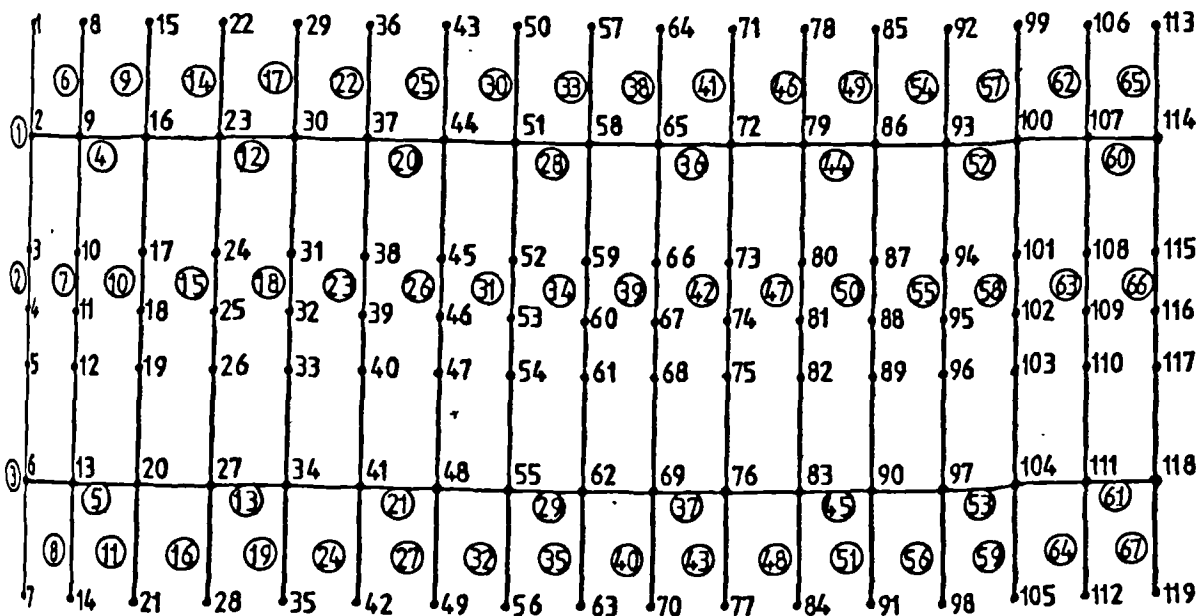
(a) Straight cantilever box beam model



(b) Curved cantilever box beam model



(c) Two-span continuous box beam model



(d) Simply-supported twin-box beam model

Fig. 8.12 Finite element mesh for the models using thin-walled box beam elements

Table 8.3 Sectional properties for the individual models ( 1 CM = 10 mm)

Structures	Cross- Sectional Area A (CM <sup>2</sup> )	Bending Moment of Inertia I <sub>xx</sub> (CM <sup>4</sup> )	Bending Moment of Inertia I <sub>yy</sub> (CM <sup>4</sup> )	Torsional Moment of Inertia J <sub>T</sub> (CM <sup>4</sup> )	Torsional Warping Moment of Inertia J <sub>I</sub> (CM <sup>6</sup> )	Distortional Second Moment of Area J <sub>D</sub> (CM <sup>2</sup> )	Distortional Moment of Inertia J <sub>II</sub> (CM <sup>6</sup> )
Straight Cantilever Box Beam Model	28.62	1252.45	3578.02	2862.96	13415.63	0.0014293	30185.16
Curved Cantilever Box Beam Model	36.21	1608.21	5714.92	3115.45	16334.92	0.0018398	50470.55
Two-span Continuous Box Beam Model	534.0	50657.13	272037.38	131396.74	6640311.66	1.1896537	5340779.30
Simply-supported Twin-box Beam Model	37,975	1446.52	5496.12	2529.56	3301.70	0.0015297	35655.60

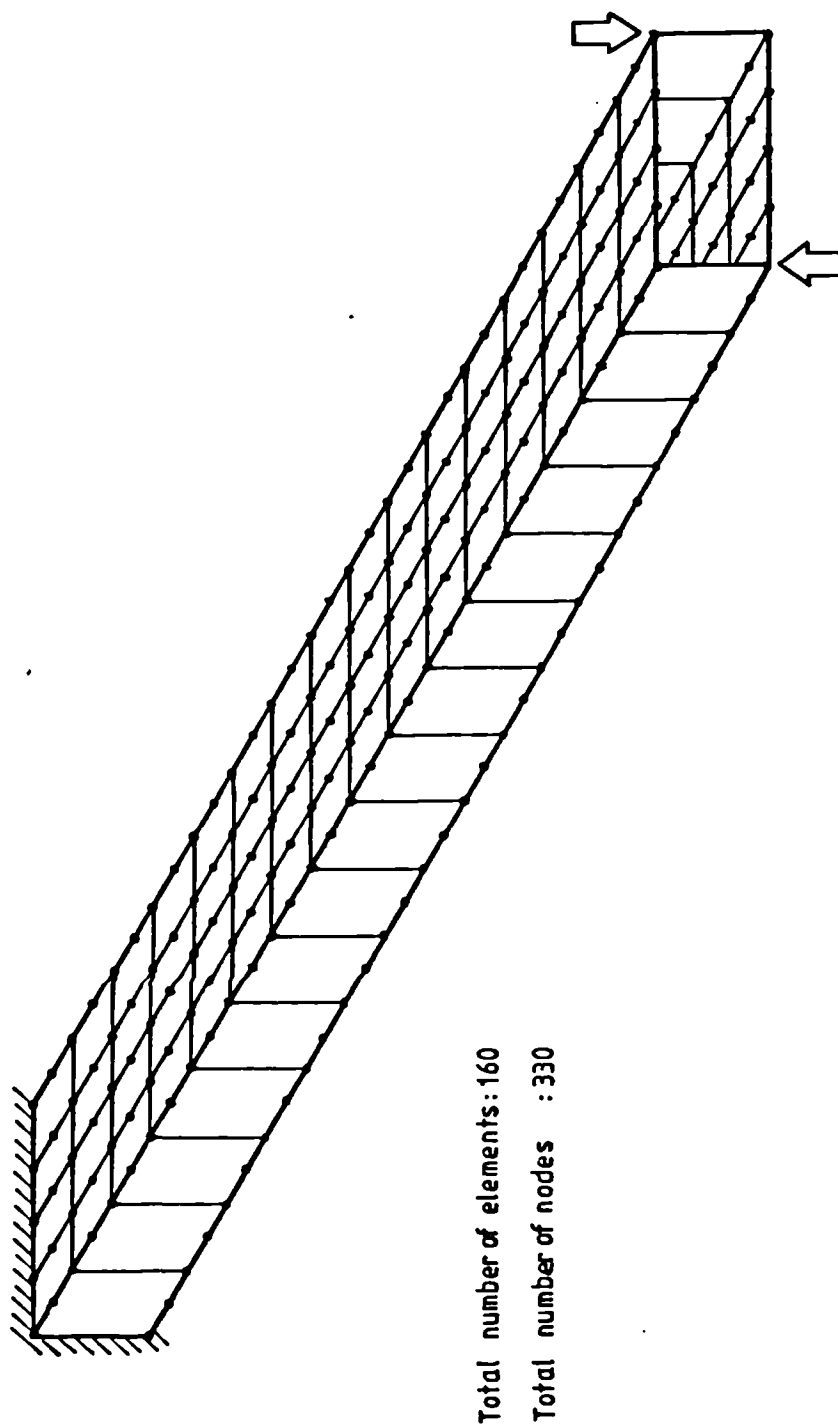


Fig. 8.13 Straight cantilever model finite element idealization using thin shell box elements (LUSAS)

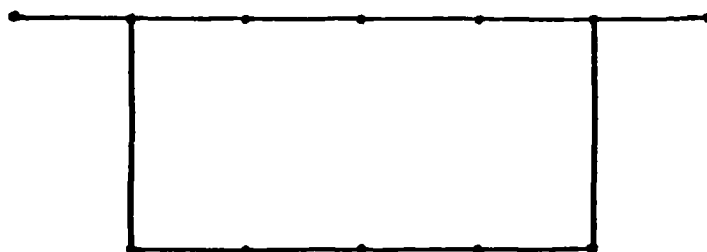
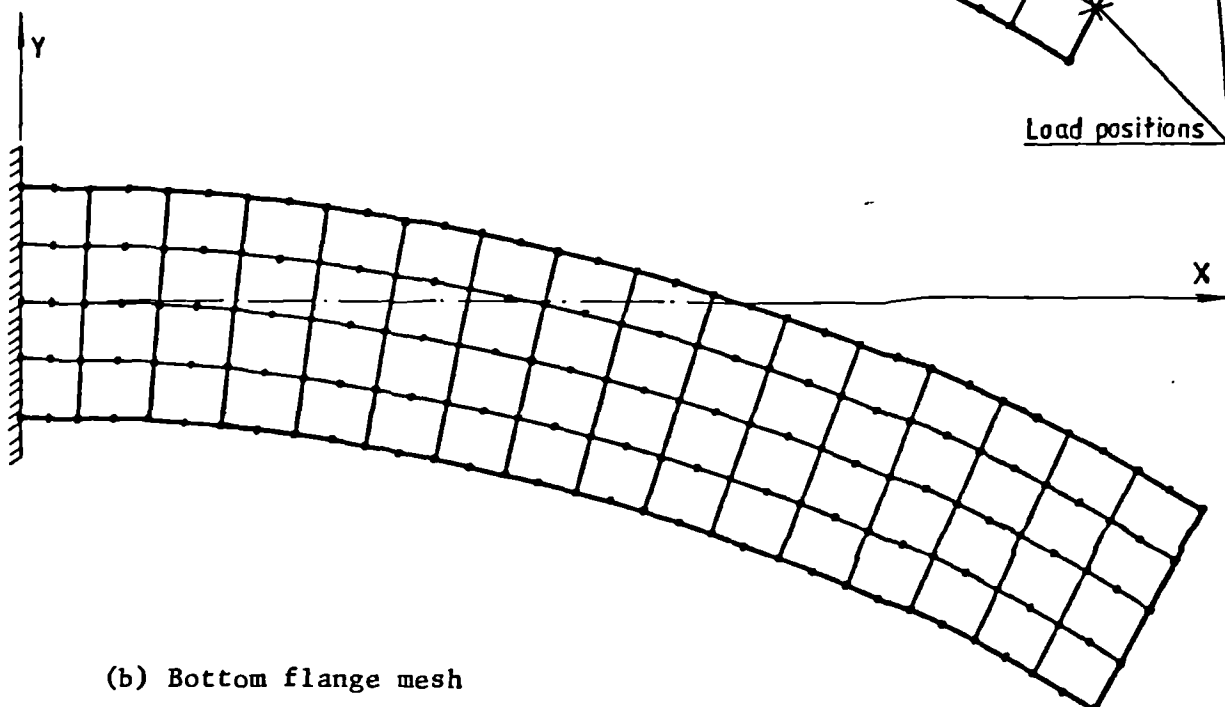
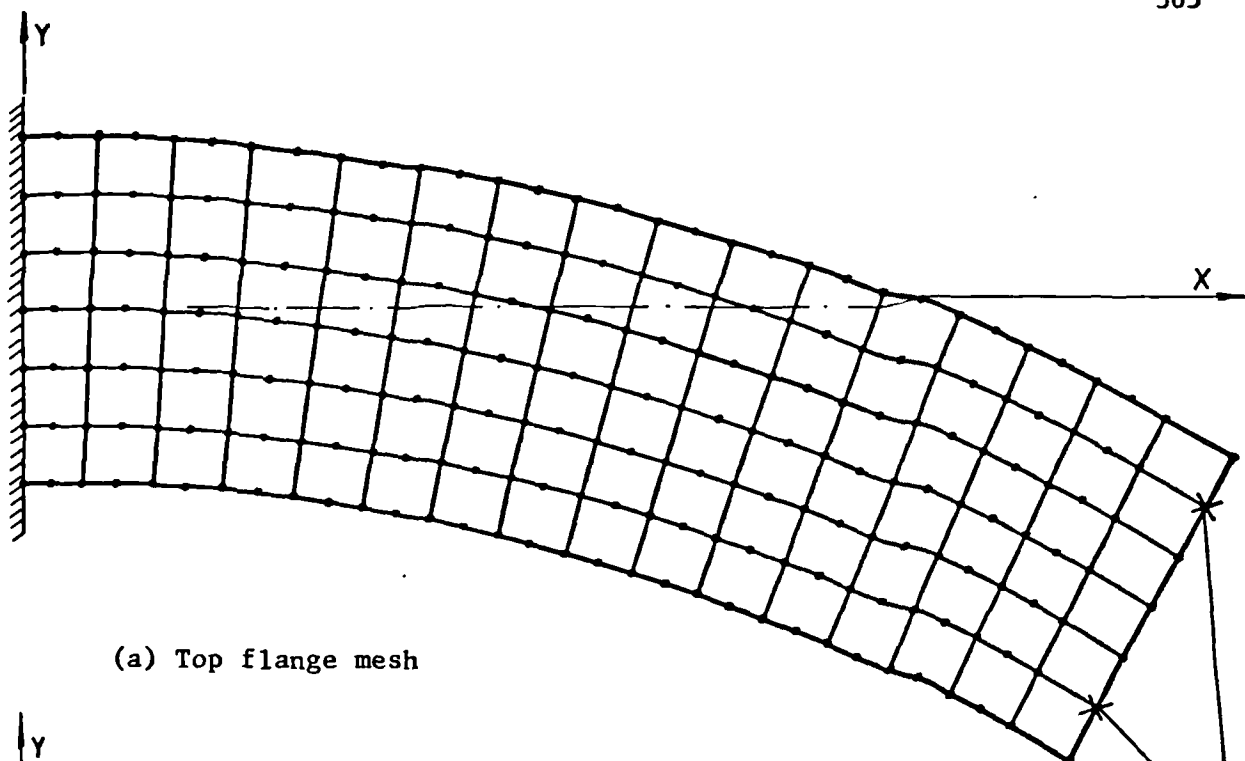
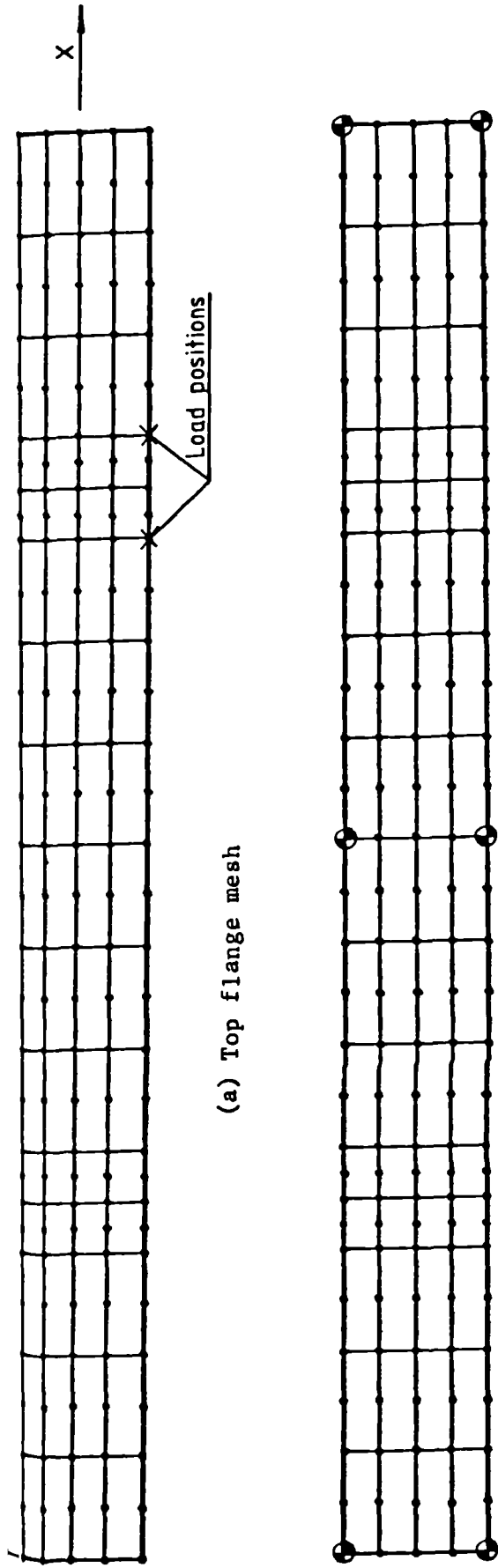


Fig. 8.14 Curved cantilever box beam model finite element idealization using thin shell box elements (LUSAS)



Total number of elements : 188  
Total number of nodes : 330

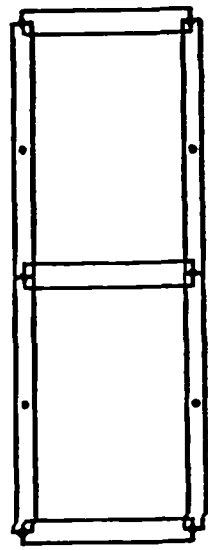
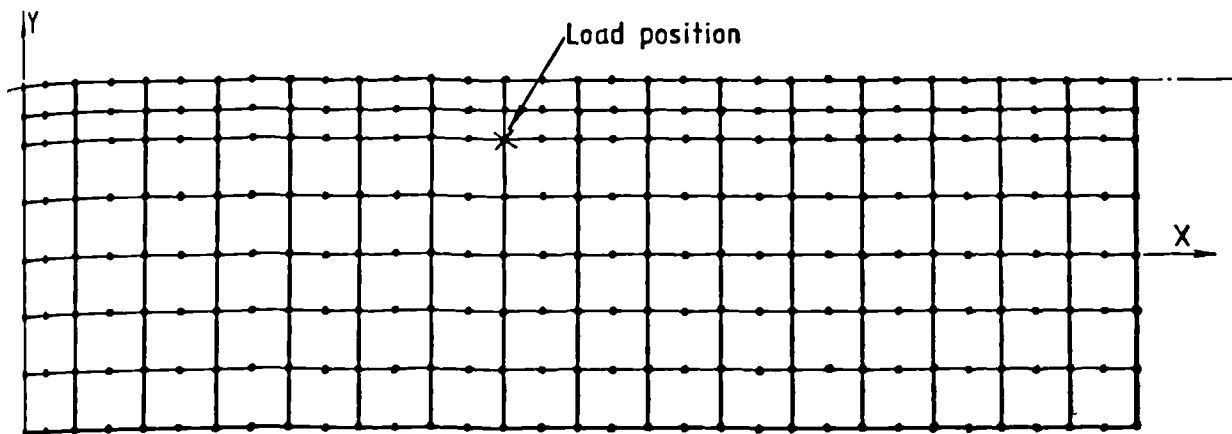
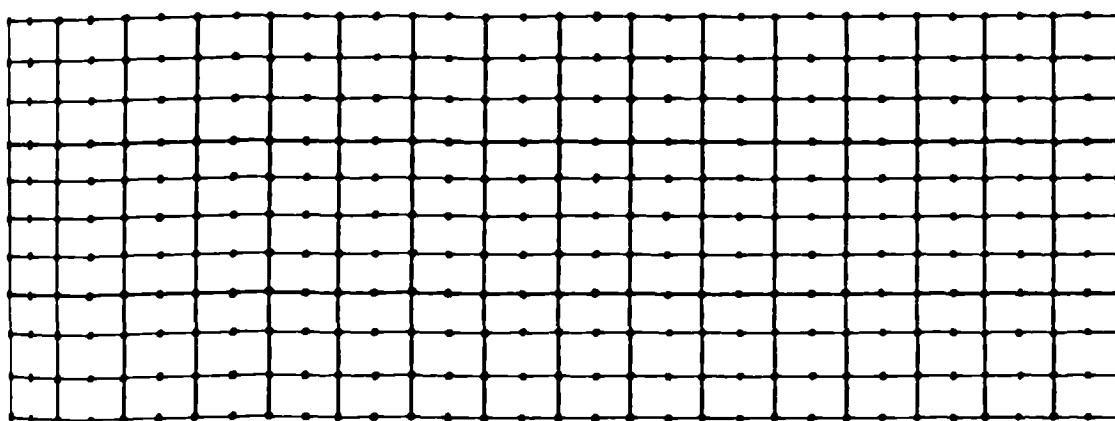


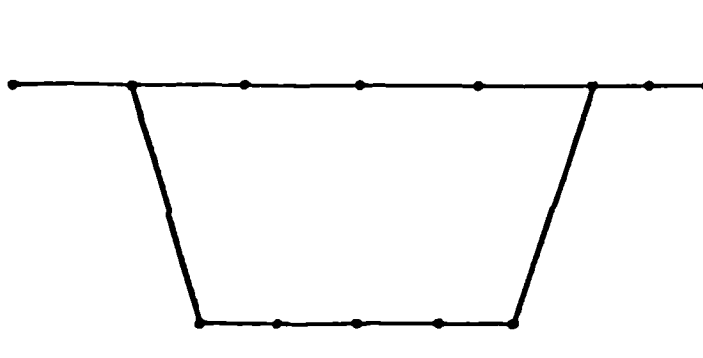
Fig. 8.15 Two span continuous box beam model finite element idealization using thin shell box elements (LUSAS)



(a) 1/2 top flange mesh



(b) Mesh of 1/2 bottom flange and webs



(c) Cross-section

Total number of elements : 296

Total number of nodes : 573

Fig. 8.16 Twin-box beam model finite element idealization using thin shell box elements (LUSAS)

Table 8.3 Calculation of the Rotations of the Flange and Web in the Straight Cantilever Beam Model

Cross section	Observed horizontal displacements				Rotation of vertical web $\phi_z$ (Radius)		Observed vertical displacements		Rotation of horizontal flange $\psi_z$ (Radius)
	$u_{t1}$ (mm)	$u_{t2}$ (mm)	$u_{b1}$ (mm)	$u_{b2}$ (mm)	Obs. from dial gauges	Obs. from Angel Dekkor	$v_{b1}$ (mm)	$v_{b2}$ (mm)	
1/4 span	0.1356	0.1328	0.090	0.0724	0.0015386	0.0016202	0.2496	0.3318	0.0020400
3/8 span	0.2666	0.2736	0.1966	0.2064	0.0033686	0.0034325	0.4940	0.6466	0.0040021
1/2 span	0.4244	0.4382	0.3806	0.3702	0.0057621	0.0058236	0.8806	1.0582	0.0068028
5/8 span	0.6552	0.6938	0.5456	0.5584	0.0087607	0.0089361	1.2940	1.5468	0.0099677
3/4 span	0.9180	0.9954	0.8648	0.7616	0.0126421	0.0125373	1.8248	2.1340	0.0138905
7/8 span	1.1322	1.3312	1.2402	1.1056	0.0171757	0.0172002	2.4440	2.8964	0.0187382

Table 8.4 Calculated and Observed Twisting and Distortional Angles

Cross section	Obs. rotation of vertical web $\phi_z$ (Radius)	Obs. rotation of horizontal flange $\psi_z$ (Radius)	Twisting angle $\theta_z$		Distortional angle $\gamma_d$		
			Obs. (Radius)	Calc. (Radius)	Obs. (Radius)	Calc. (Radius)	Difference, as a percentage
1/4 span	0.0016202	0.0020400	0.0002099	0.0001742	0.0036602	0.0030194	-17.5%
3/8 span	0.0034325	0.0040021	0.0002848	0.0002930	0.0074346	0.0067810	-8.8%
1/2 span	0.0058236	0.0068028	0.0004896	0.0004133	0.012626	0.012011	-4.9%
5/8 span	0.0089361	0.0099677	0.0005158	0.0005339	0.018904	0.018639	-1.4%
3/4 span	0.0125373	0.0138905	0.0006766	0.0006545	0.026532	0.026523	+0.4%
7/8 span	0.0172002	0.0187382	0.0007690	0.0007751	0.035938	0.035410	-1.5%

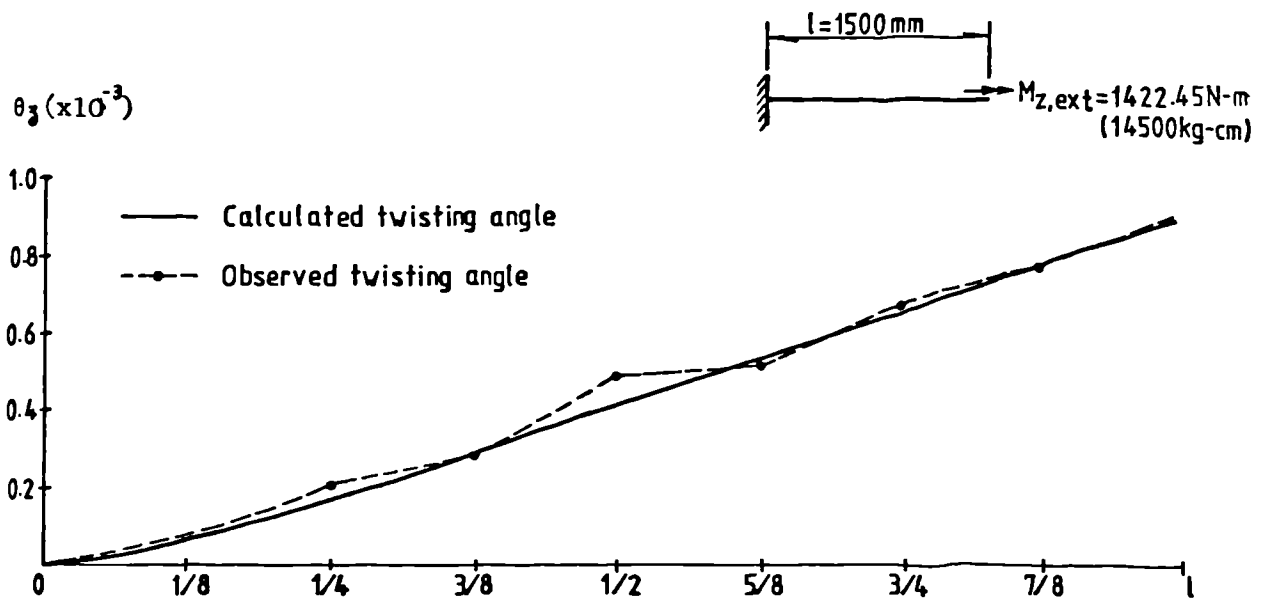


Fig. 8.17 Distribution of the twisting angle along beam in Model 1

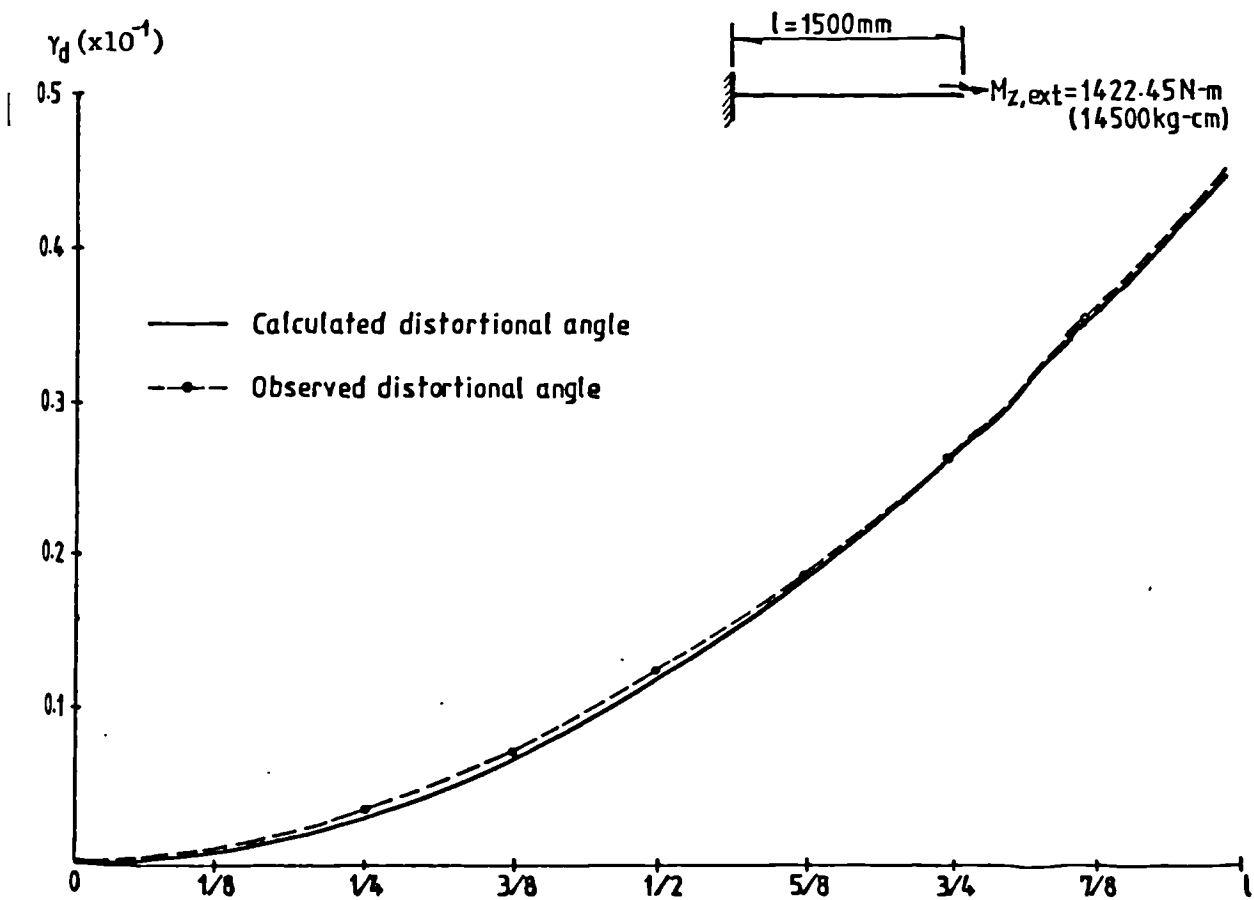


Fig. 8.18 Distribution of the distortional angle along beam in Model 1

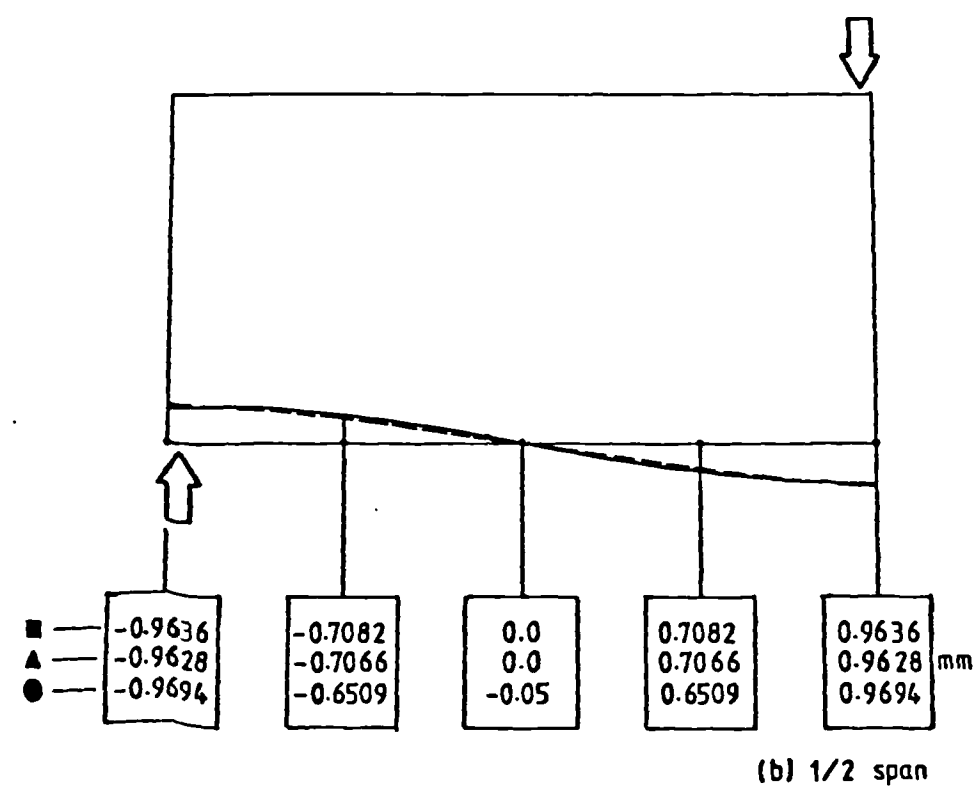
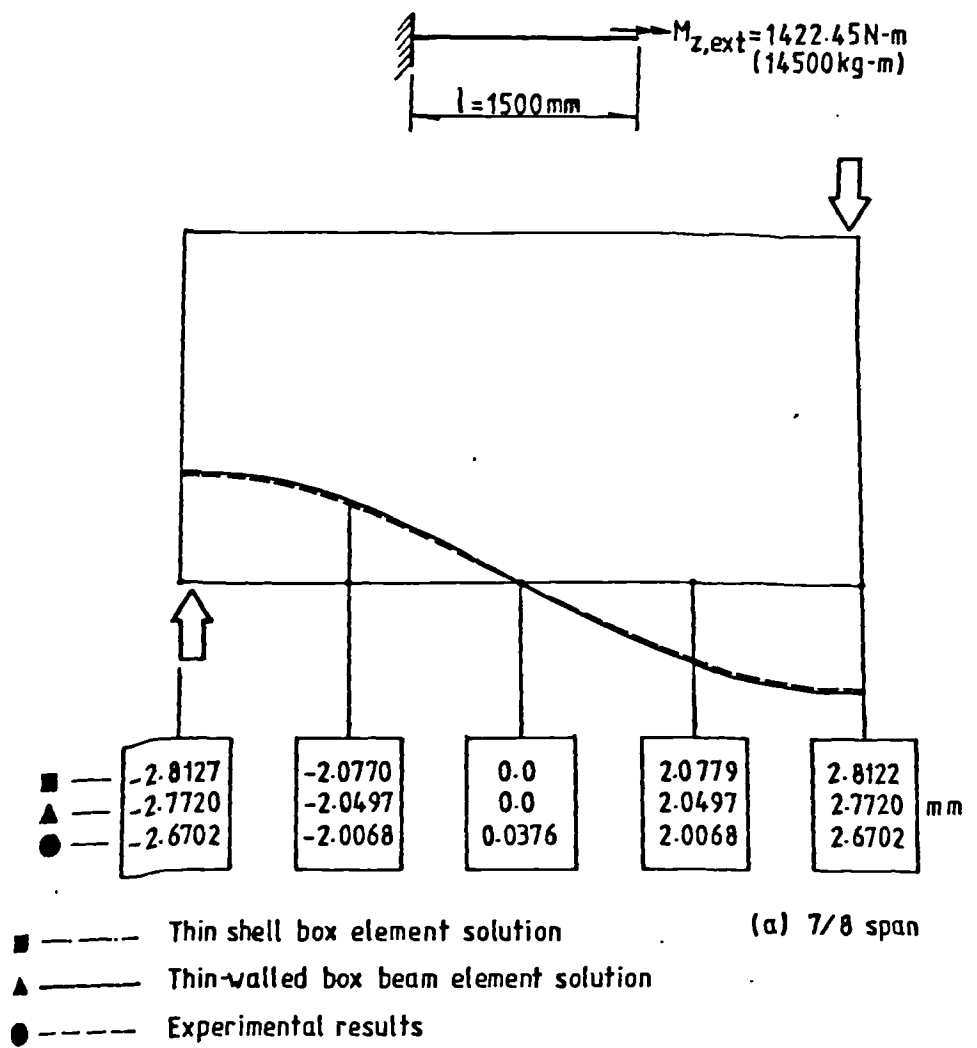
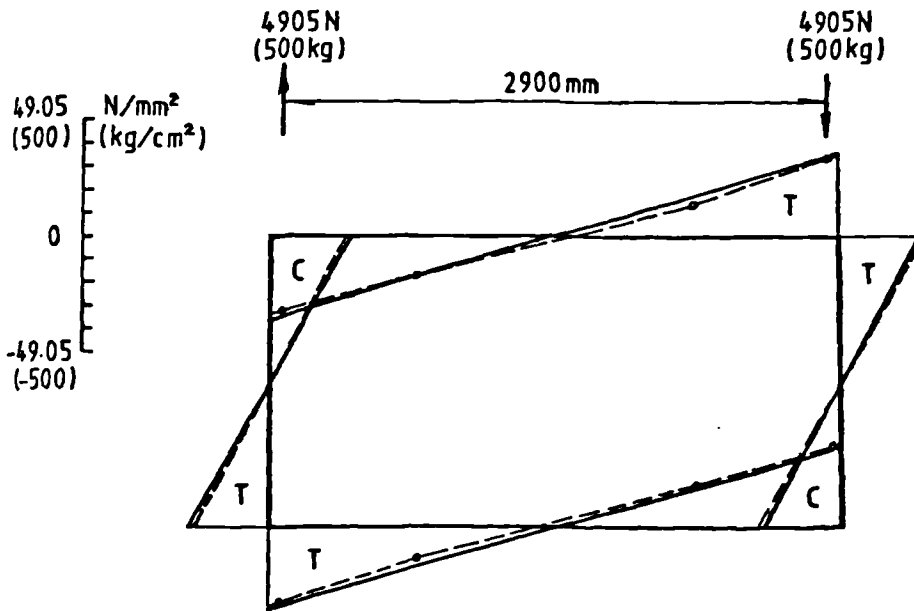
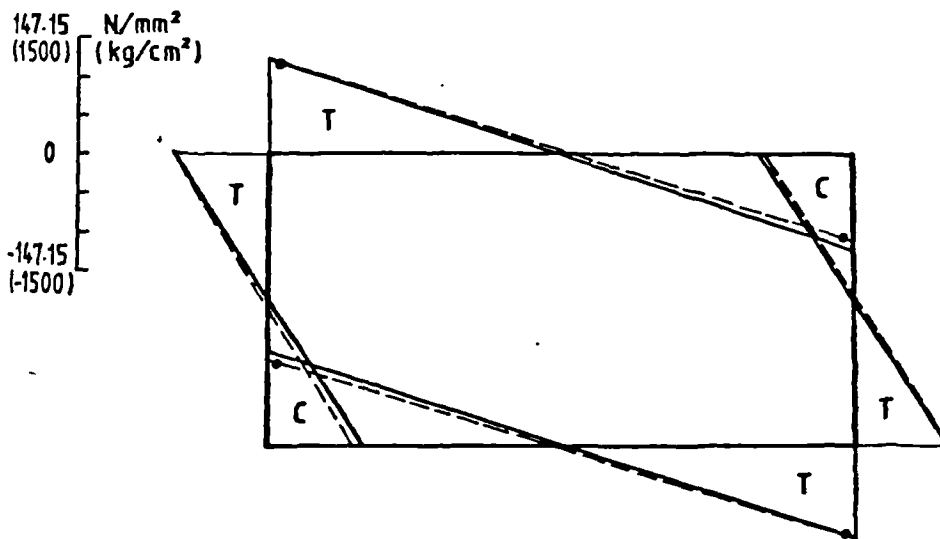


Fig. 8.19 Transverse distribution of vertical deflection in straight cantilever box beam model



(a) Membrane warping stresses ( $\sigma_I + \sigma_{II}$ )

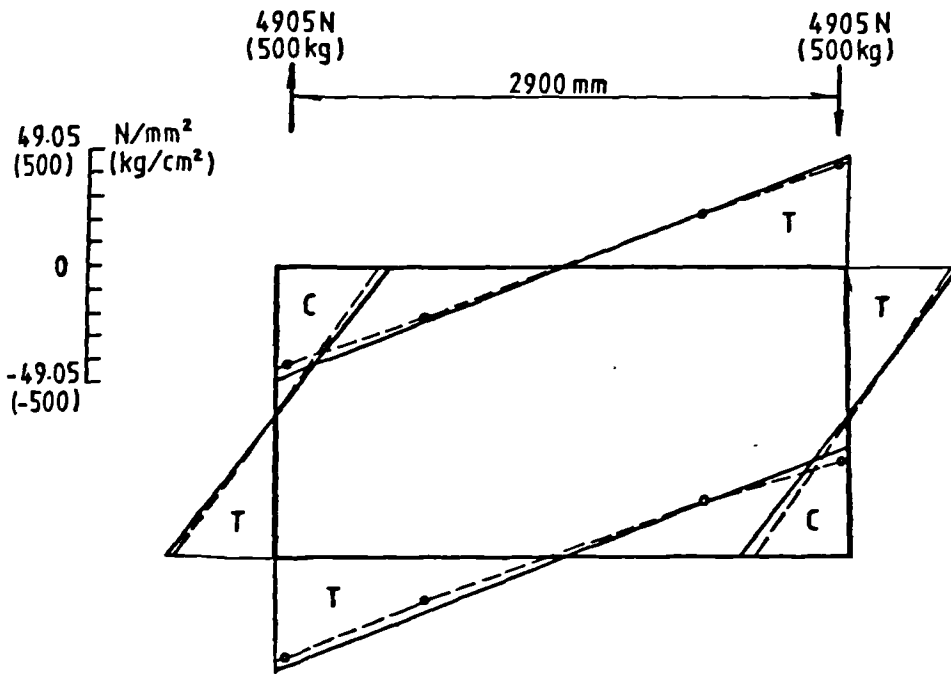


(b) Outer surface transverse bending stresses

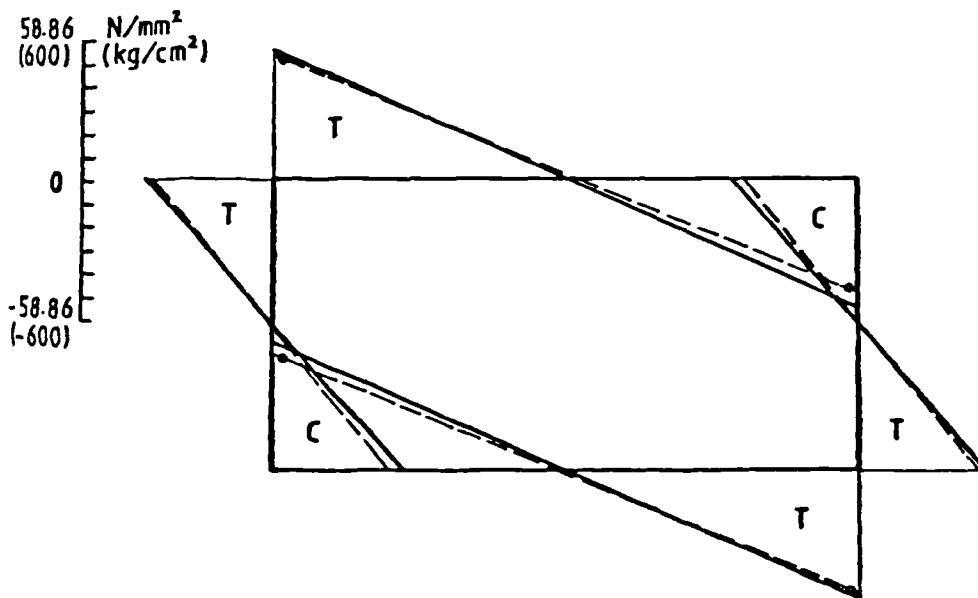
Key

- Calculated      T tensile stress
- Observed      C compressive stress

Fig. 8.20 Comparison of warping and transverse bending stresses at 3/4 span in straight cantilever box beam model



(a) Membrane warping stresses

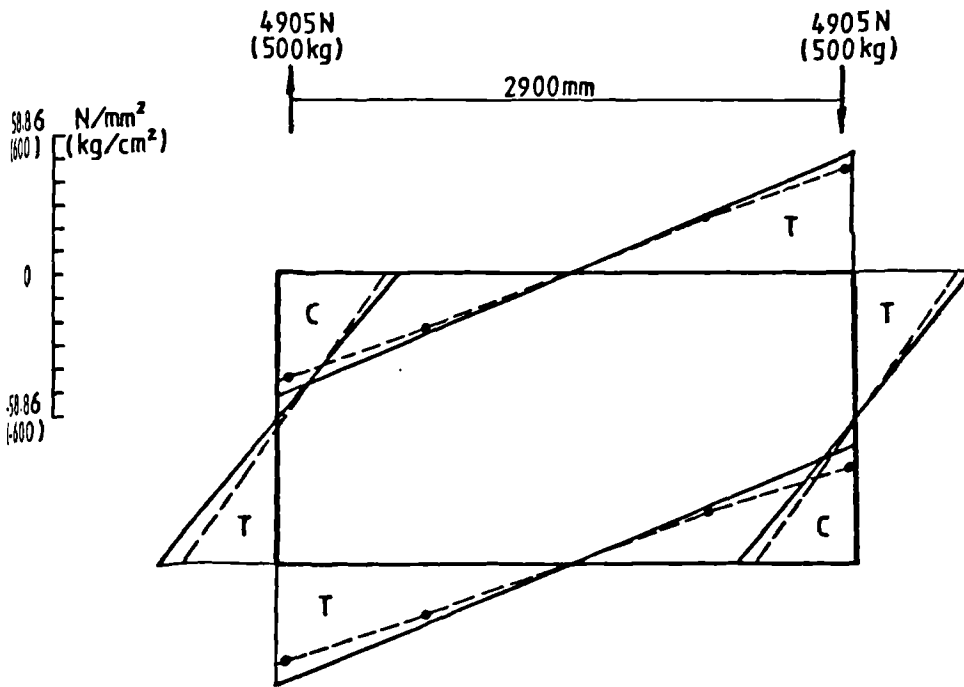


(b) Outer surface transverse bending stresses

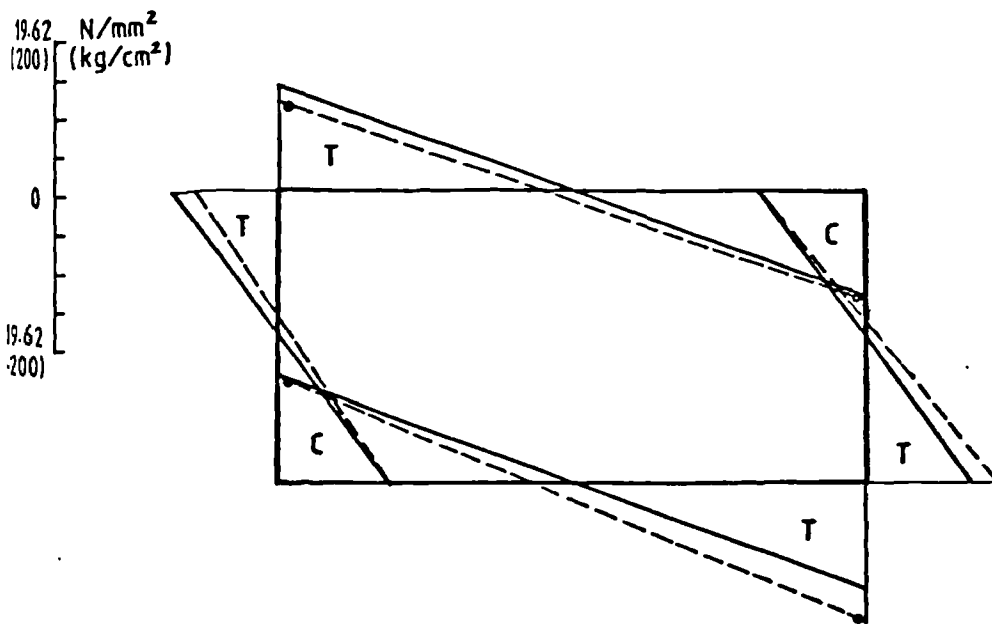
## Key

- |     |            |   |                    |
|-----|------------|---|--------------------|
| —   | Calculated | T | tensile stress     |
| -•- | Observed   | C | compressive stress |

Fig. 8.21 Comparison of warping and transverse bending stresses at midspan in straight cantilever box-beam model



(a) Membrane warping stresses



(b) Outer surface transverse bending stresses

Key

- Calculated    T tensile stress
- Observed    C compressive stress

Figure 8.22 Comparison of warping and transverse bending stresses at 1/4 span in straight cantilever box beam model

Table 8.3 Comparison of the observed and calculated stresses in top flange near the web ( $1 \text{ kg/cm}^2 = 0.0981 \text{ N/mm}^2$ )

Cross-section	Membrane Normal Stresses				Normal Stresses of Outer Surface				Transverse Bending Stresses of Outer Surface			
	Experimental Results ( $\text{kg/cm}^2$ )	Box Beam Element Solution ( $\text{kg/cm}^2$ )	Thin Shell Box Element Solution ( $\text{kg/cm}^2$ )	Experimental Results ( $\text{kg/cm}^2$ )	Box Beam Element Solution ( $\text{kg/cm}^2$ )	Thin Shell Box Element Solution ( $\text{kg/cm}^2$ )	Experimental Results ( $\text{kg/cm}^2$ )	Box Beam Element Solution ( $\text{kg/cm}^2$ )	Thin Shell Box Element Solution ( $\text{kg/cm}^2$ )	Experimental Results ( $\text{kg/cm}^2$ )	Box Beam Element Solution ( $\text{kg/cm}^2$ )	Thin Shell Box Element Solution ( $\text{kg/cm}^2$ )
Fixed End	-	570.5	521.3	-	570.5	543.8	-	0.0	132.9	-	0.0	132.9
1/8 span	427.6	529.1	506.6	381.9	519.8	494.6	381.9	-34.6	-27.3	-54.0	-34.6	-27.3
1/4 span	444.1	519.0	489.8	373.3	481.7	467.9	373.3	-138.1	-126.4	-142.4	-138.1	-126.4
3/8 span	462.2	508.3	484.1	349.8	424.5	415.8	349.8	-310.1	-296.3	-291.6	-310.1	-296.3
1/2 span	442.1	484.6	465.8	271.1	336.3	343.5	271.1	-549.3	-535.5	-514.2	-549.3	-535.5
5/8 span	406.0	436.6	424.2	159.4	206.4	206.3	159.4	-852.4	-841.6	-803.8	-852.4	-841.6
3/4 span	348.1	350.8	345.8	29.8	23.3	45.7	29.8	-1213.0	-1209.3	-1141.8	-1213.0	-1209.3
7/8 span	228.5	211.2	215.9	-179.4	-226.1	-228.5	-179.4	-1619.5	-1640.6	-1448.8	-1619.5	-1640.6
Tip End	-	0.0	75.3	-	-554.3	-513.9	-	-2053.1	-2049.0	-	-2053.1	-2049.0

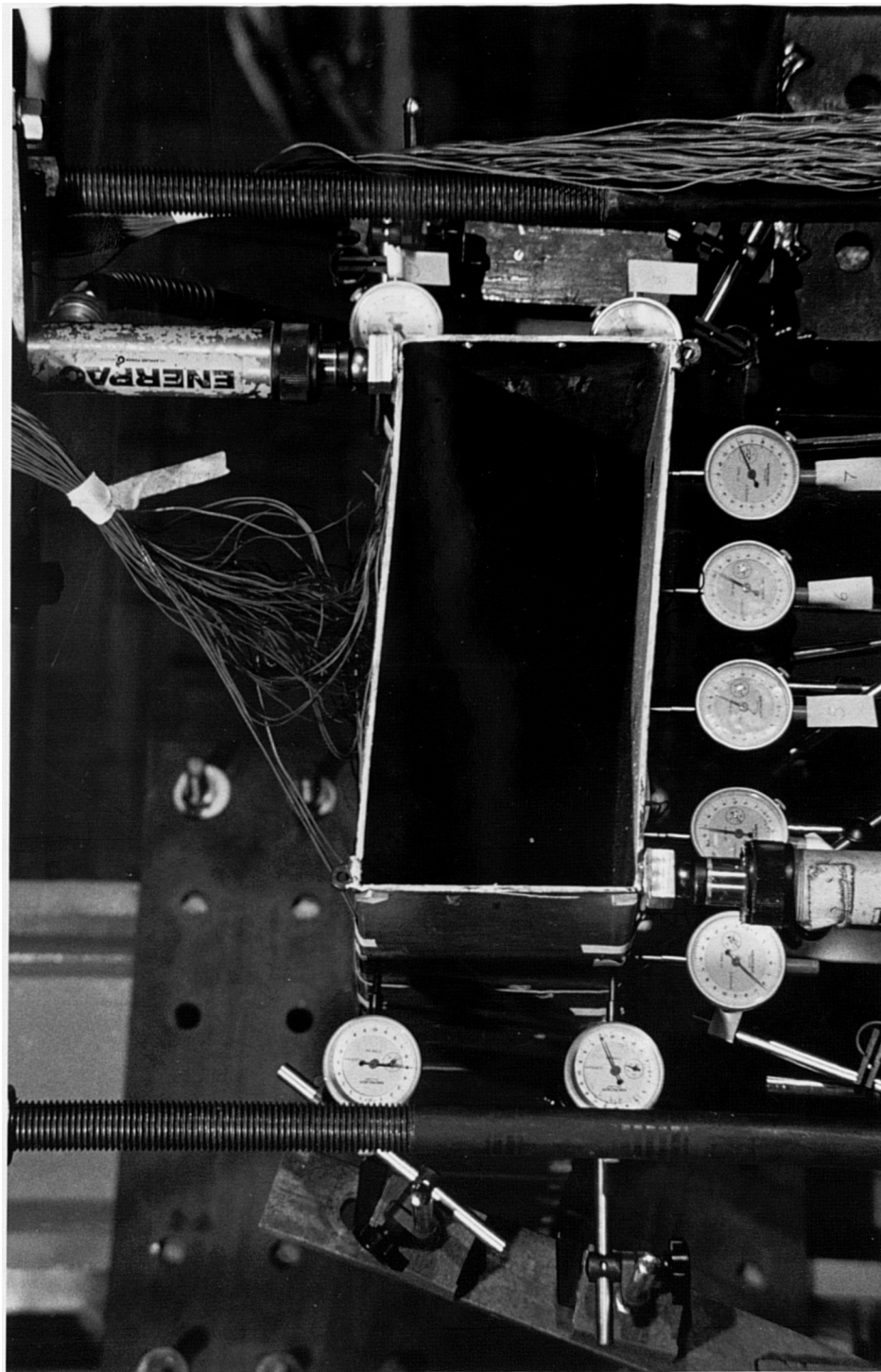


Figure 15 Deformational shape of the tip section after loading for the straight cantilever model

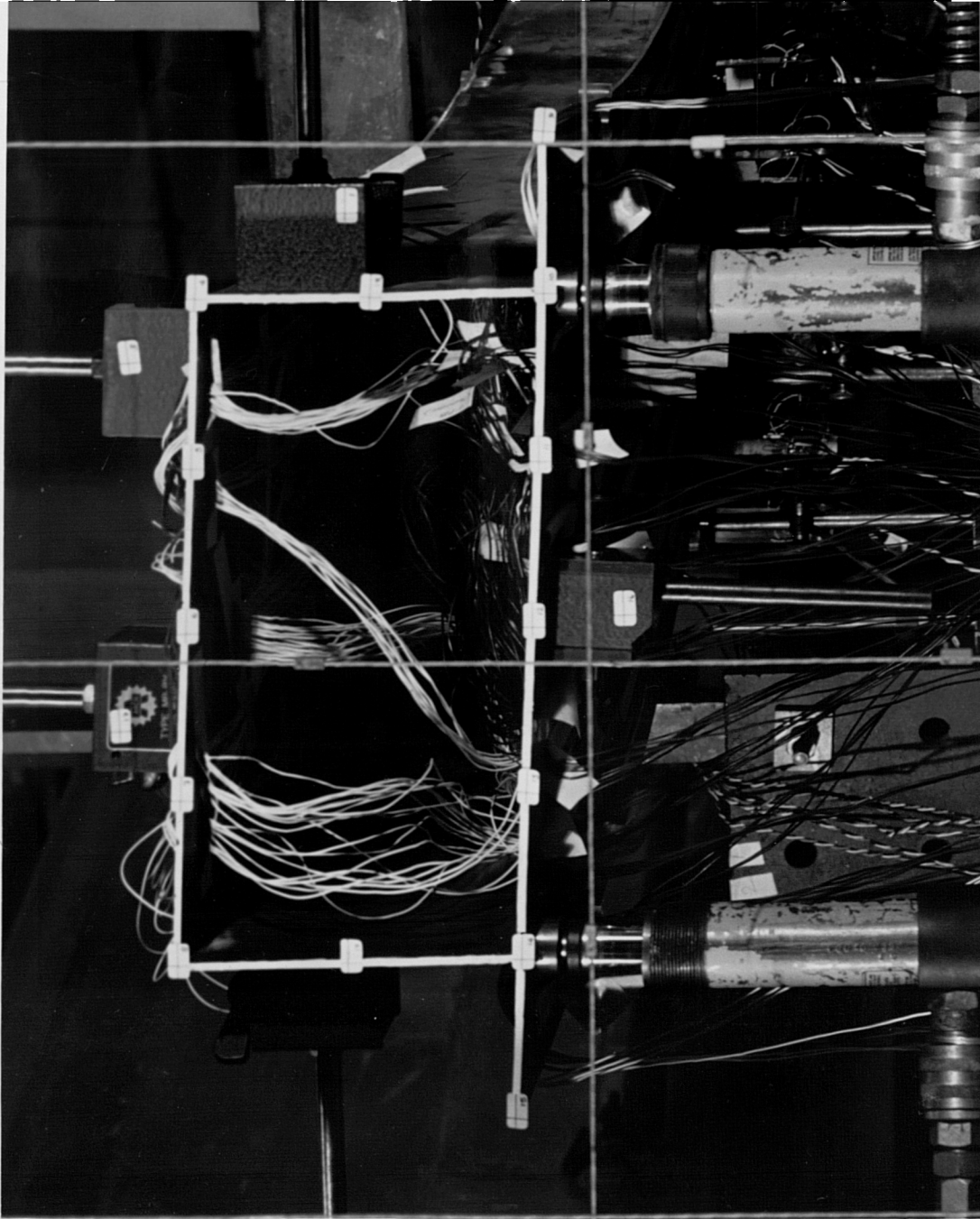


Figure 16 Deformational shape of the tip section due to two-point loading for curved cantilever model

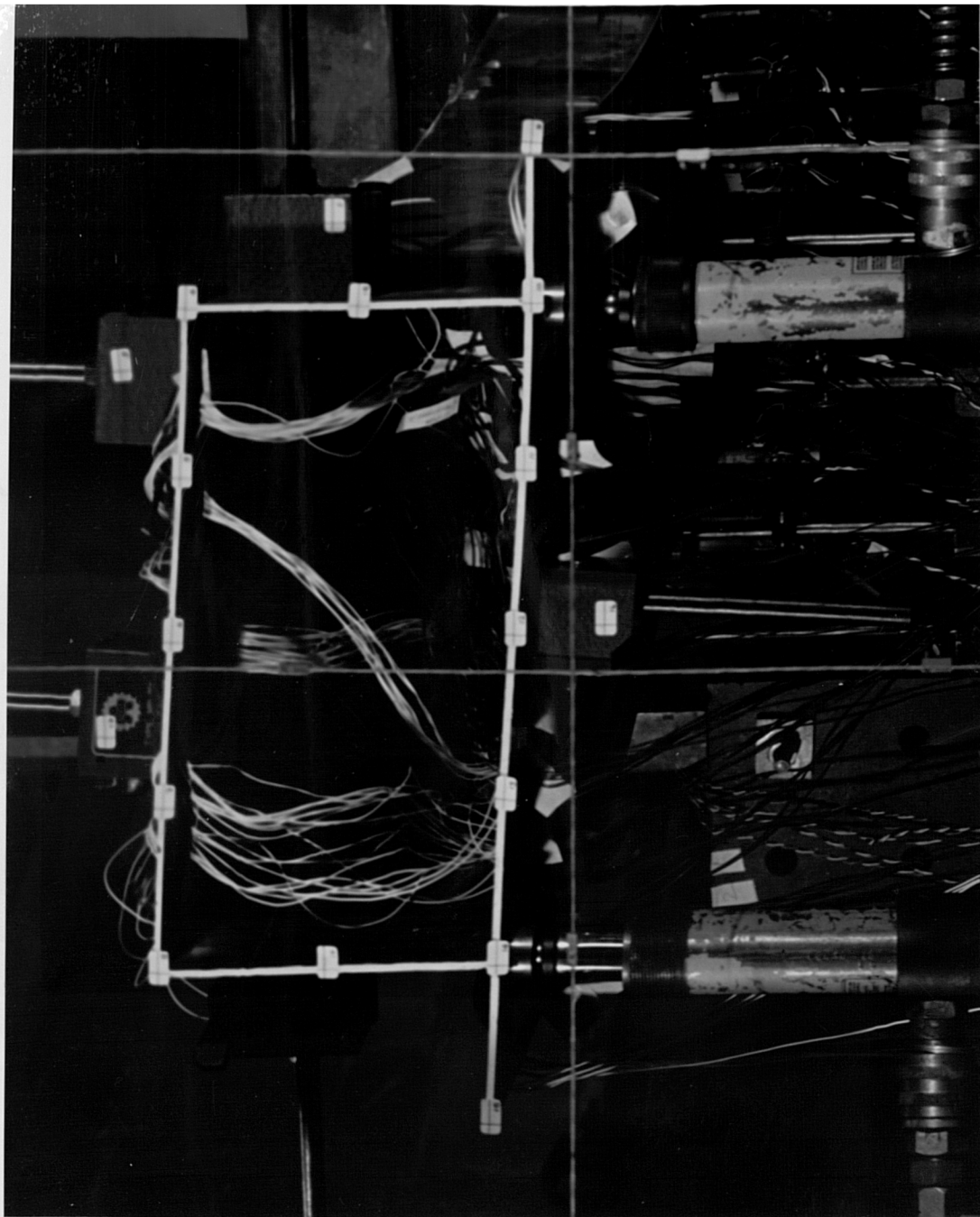
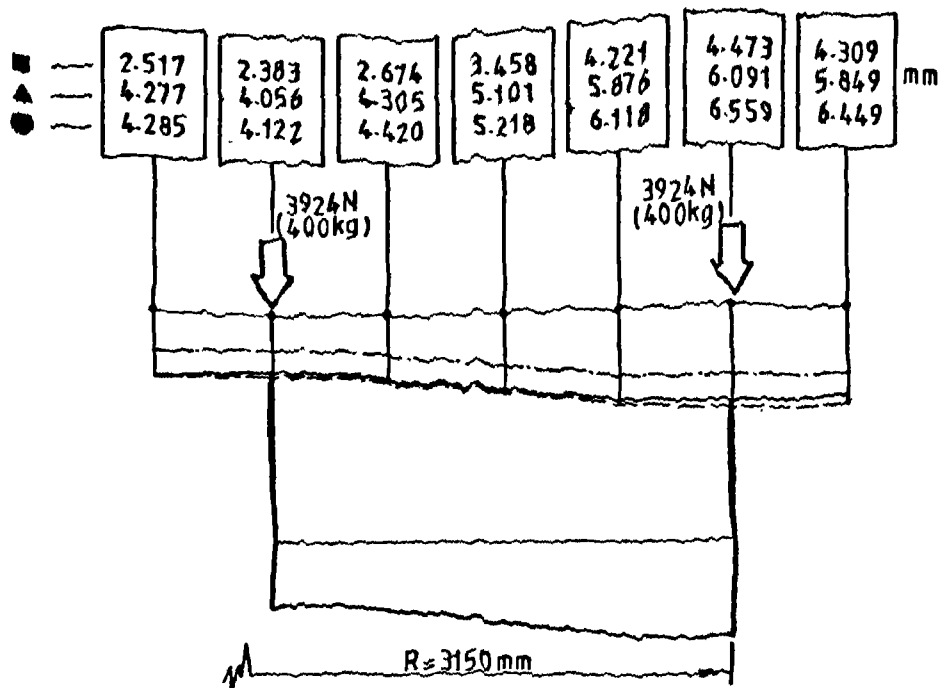
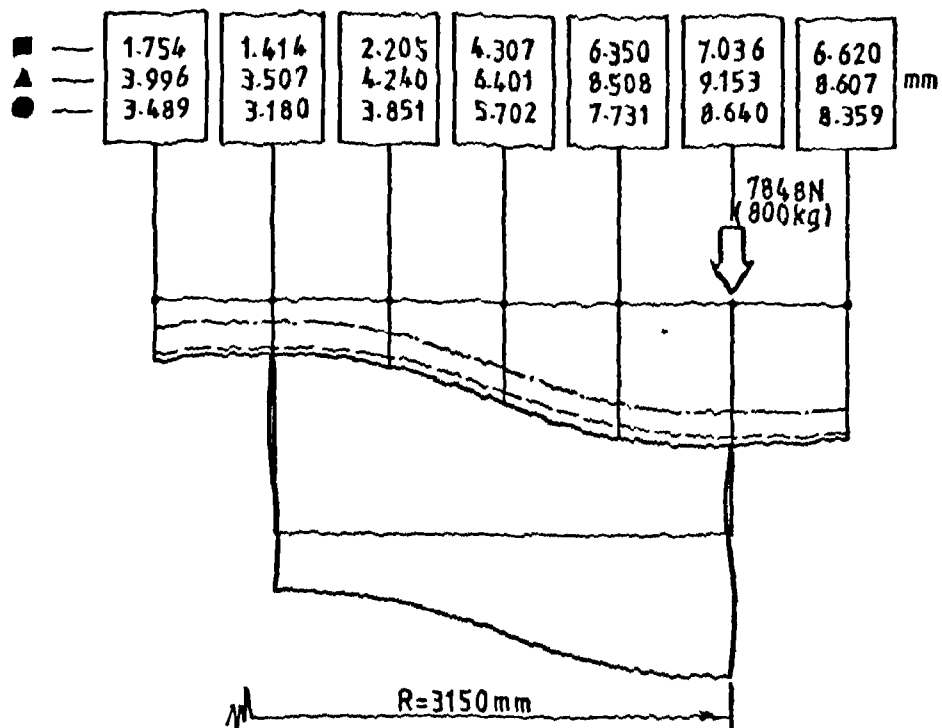


Figure 17 Deformational shape of the top section due to one-point loading for curved cantilever model



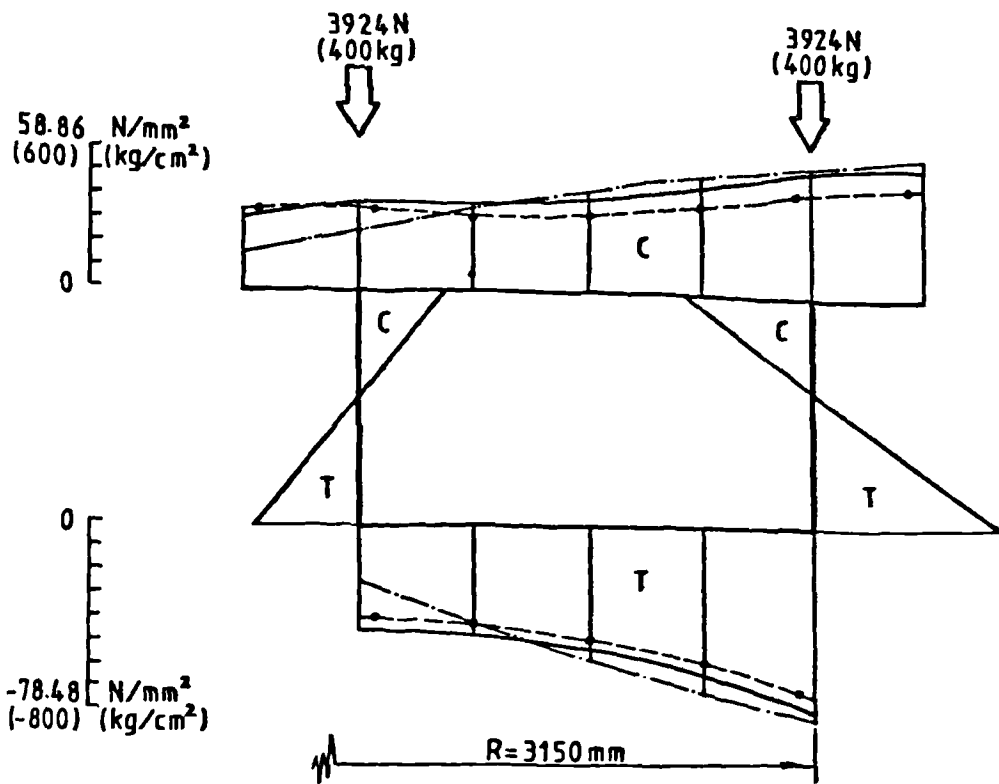
(a) Shape of deformed cross-section due to two point loads at the tip



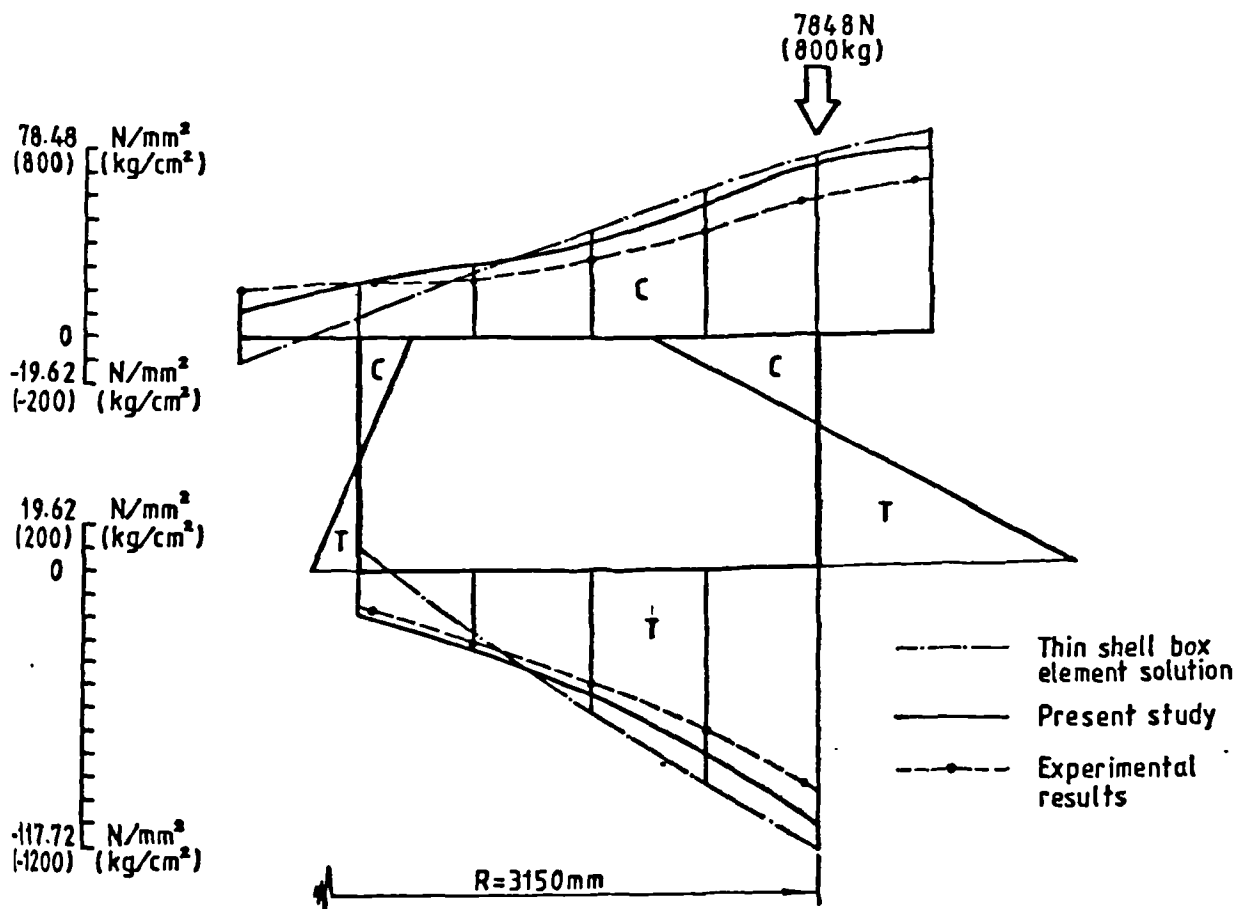
(b) Shape of deformed cross-section due to one point load at the tip

- ——— Thin shell box element solution
- ▲ ——— Box beam element solution
- ——— Experimental results

fig. 8.23 Transverse distributions of vertical deflection at 7/8 arc length section from fixed end

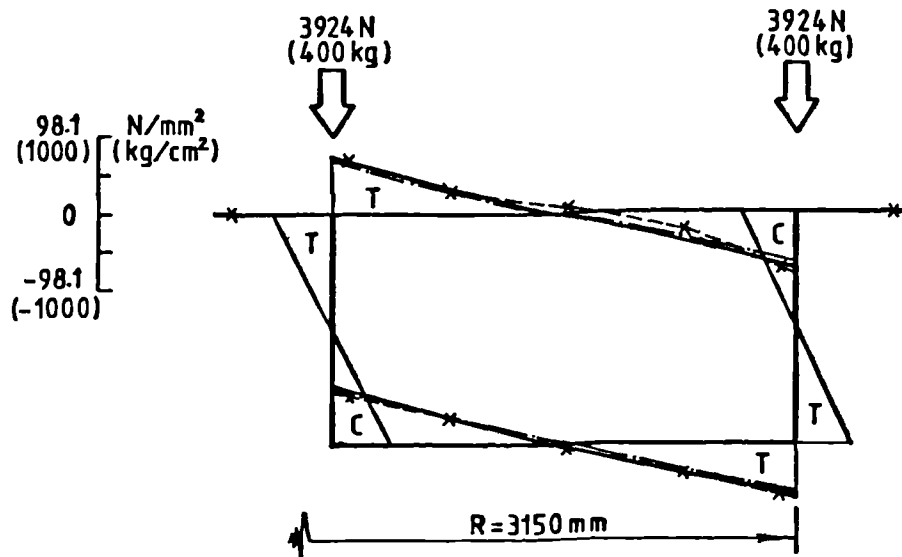


(a) Longitudinal membrane stresses due to two point loads at the tip

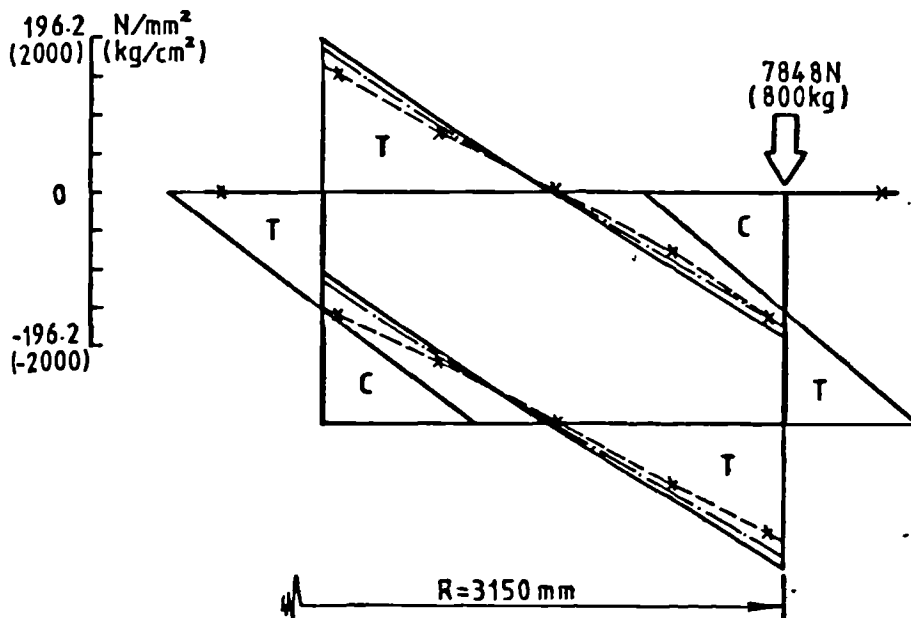


(b) Longitudinal membrane stresses due to one point load at the tip

Fig. 8.24 Transverse distribution of longitudinal membrane stresses at 1/8 arc length section from fixed end



(a) Transverse bending stresses at outer surface due to two point loads at the tip



(b) Transverse bending stresses at outer surface due to one point load at the tip

- Present study
- \*- Experimental results
- Thin shell element solution

Fig. 8.25 Transverse bending stresses at outer surface at  $7/8$  arc length section from fixed end

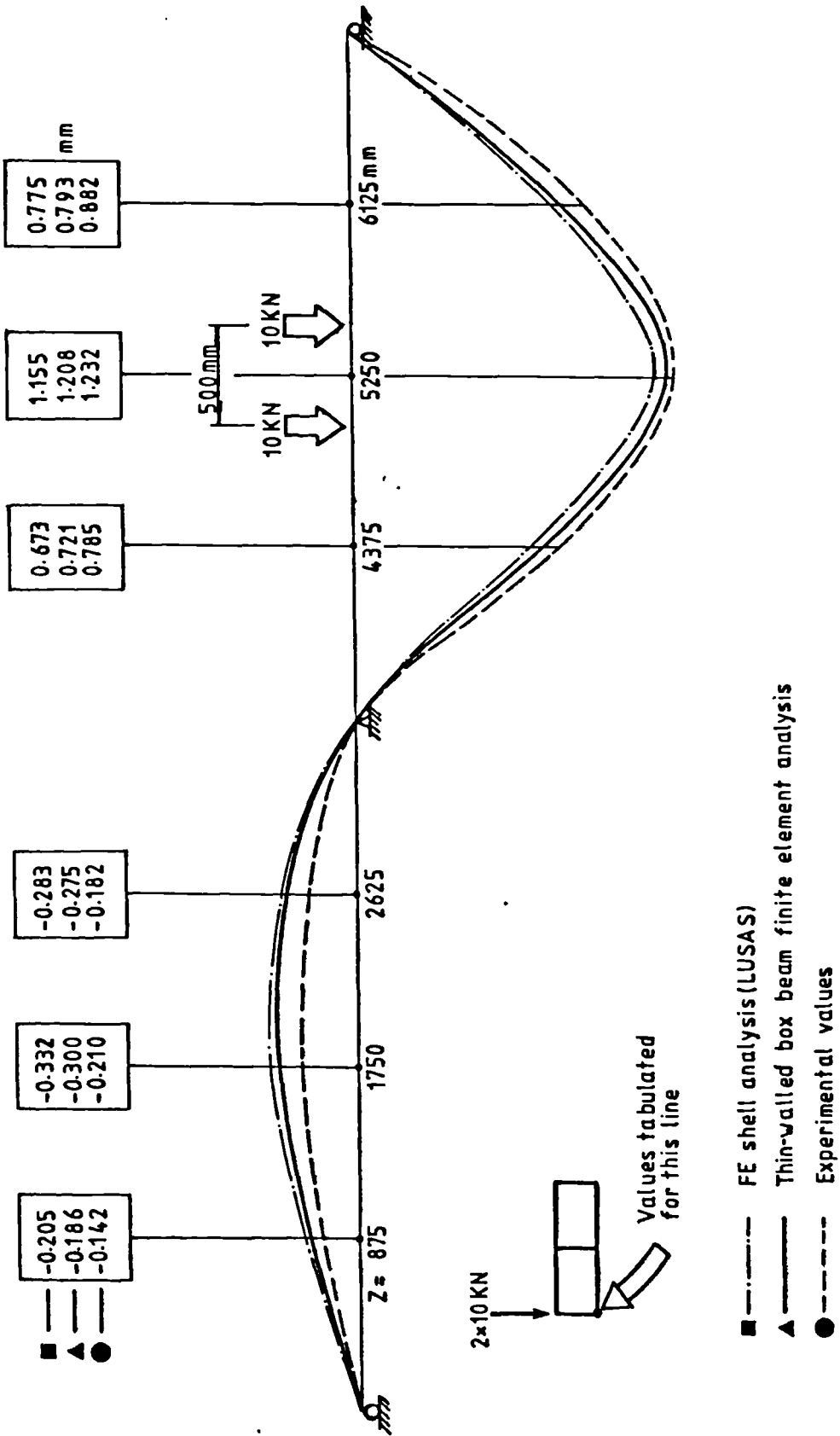


Fig. 8.26 Vertical deflection along longitudinal line at bottom of the girder

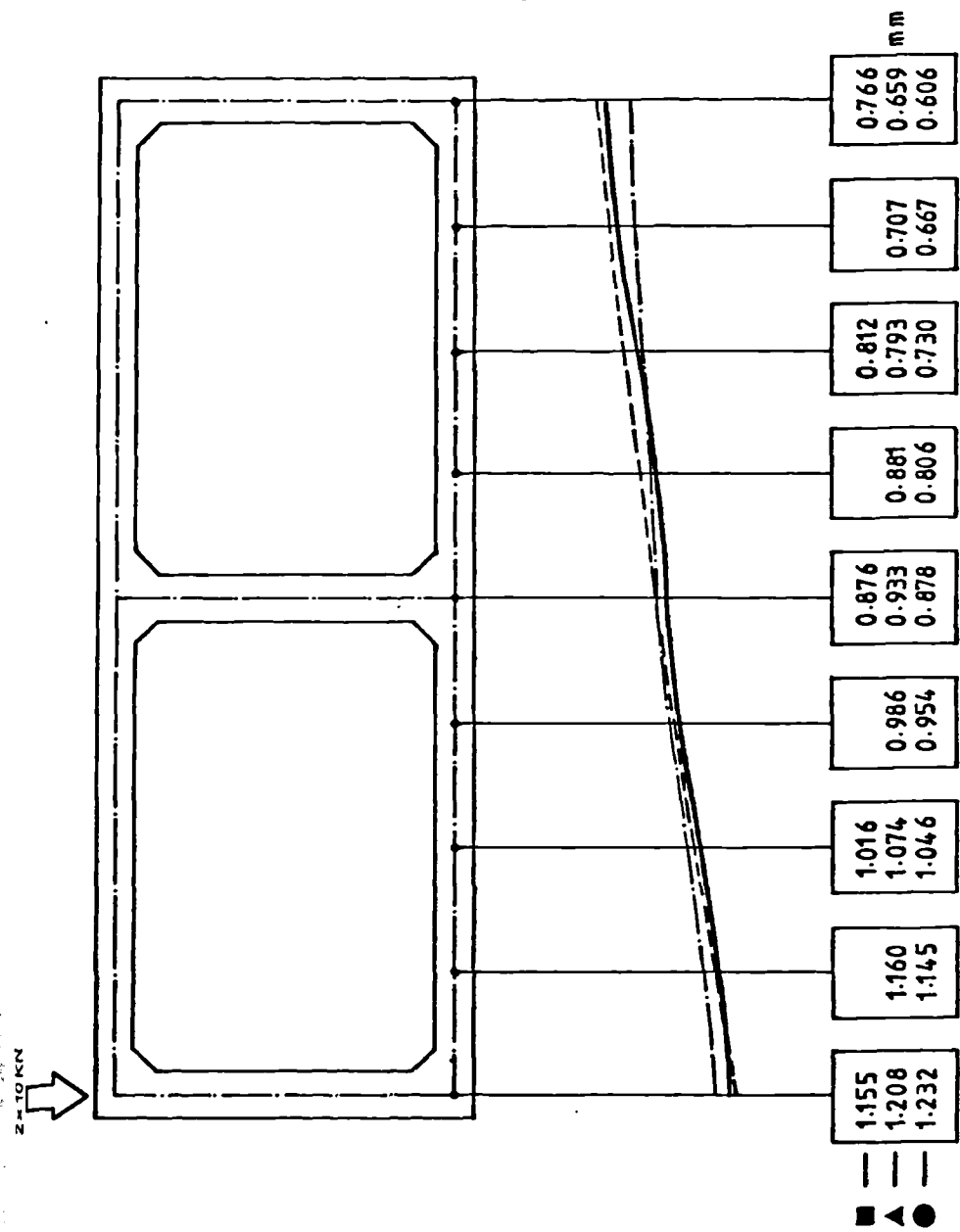


Fig. 8.27 Transverse distribution of vertical deflection at mid-span section of the loaded span

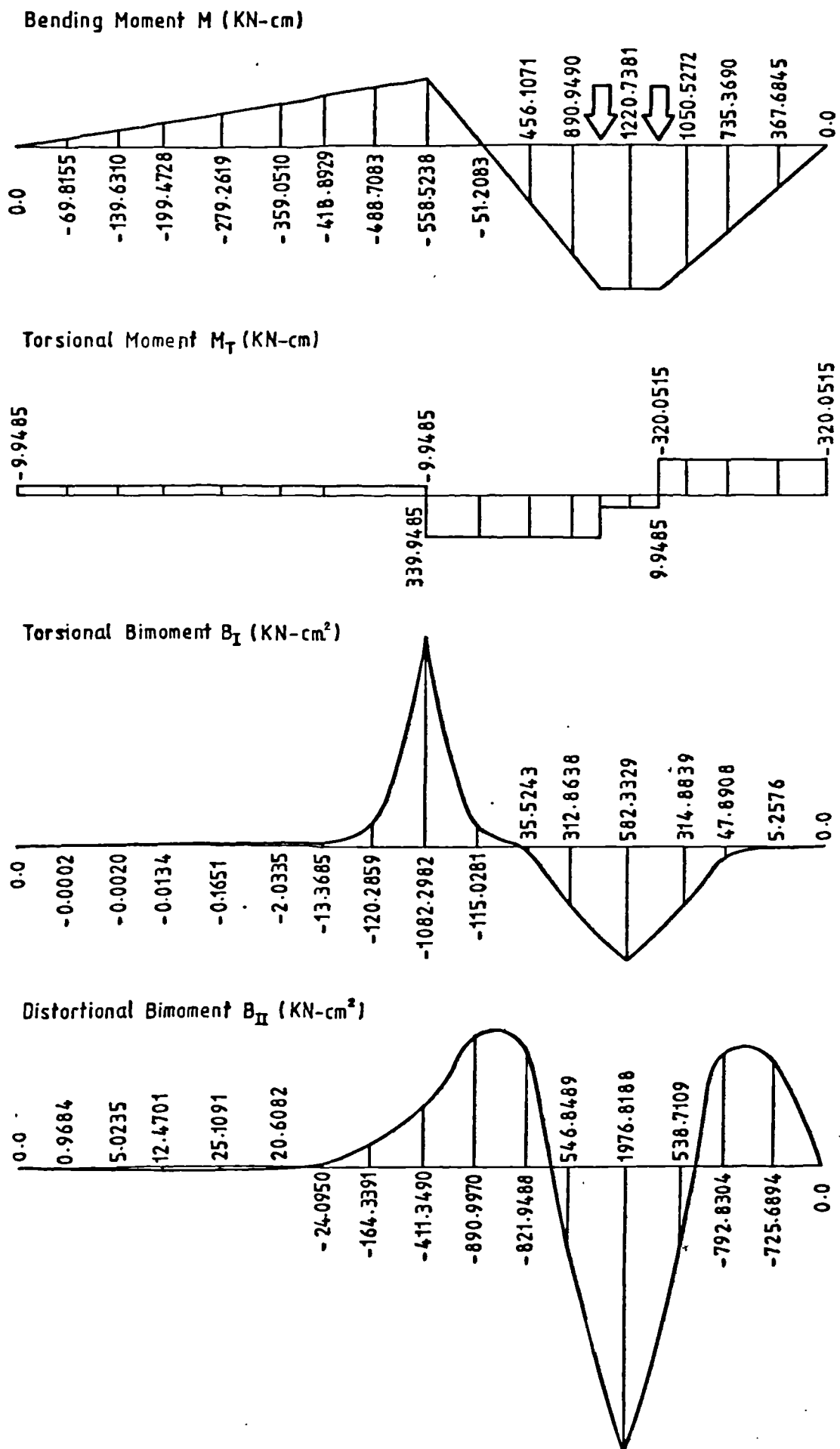


Fig. 8.28 Longitudinal distributions of internal forces along the girder (1 cm = 10 mm)

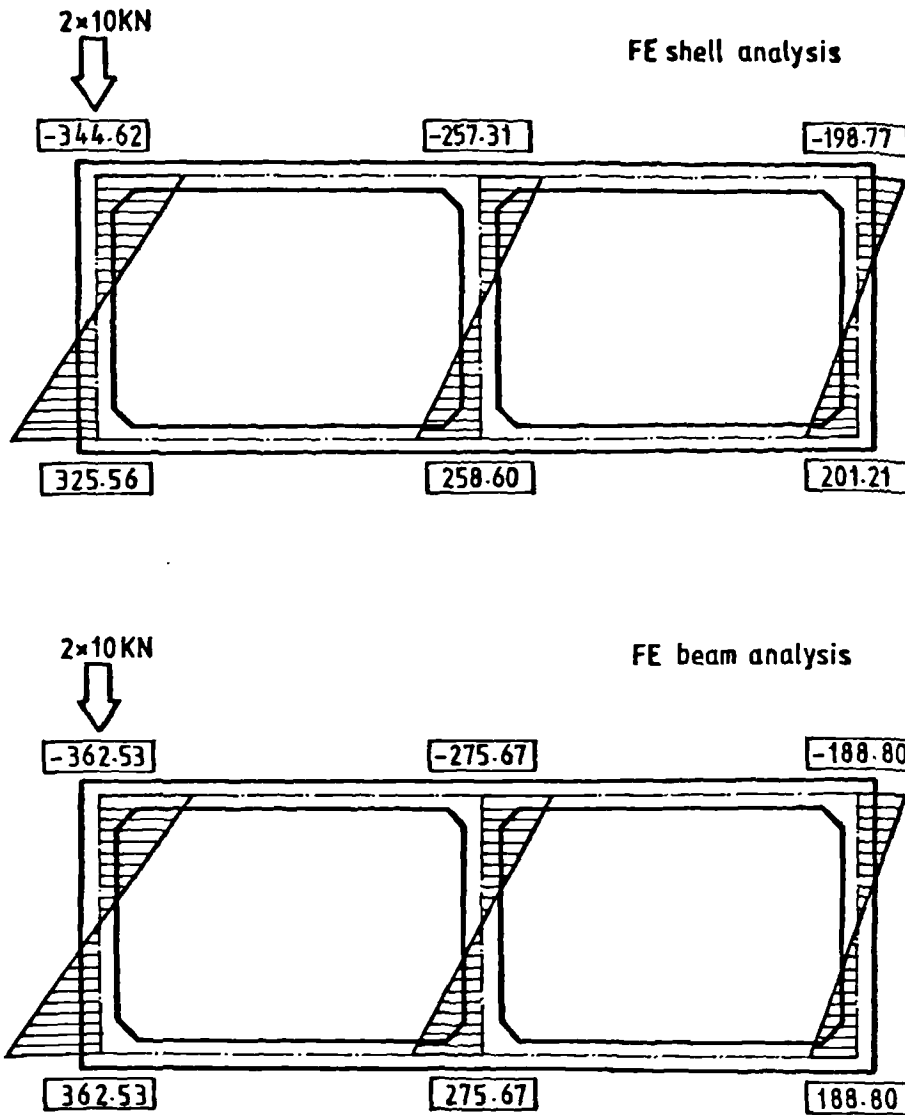


Fig. 8.29 Comparison of longitudinal stresses at midspan section ( $\text{N}/\text{cm}^2$ ,  $1 \text{ cm} = 10 \text{ mm}$ )

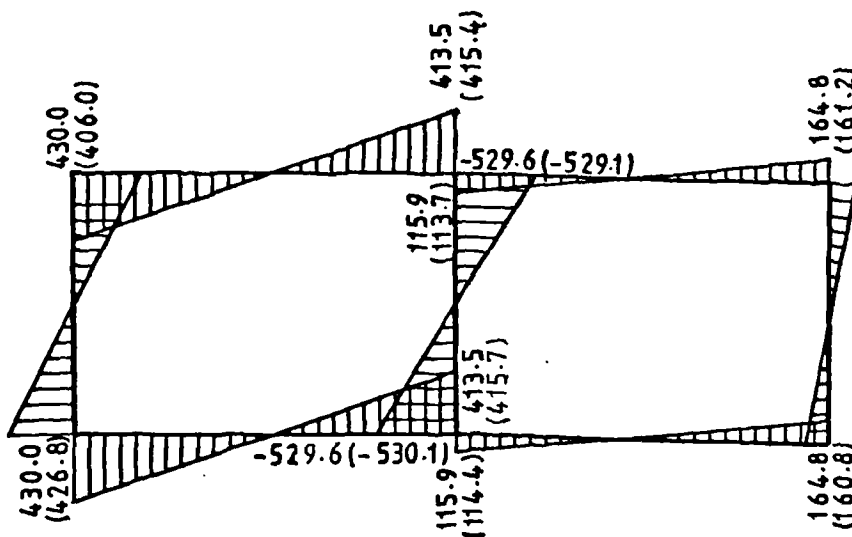


Fig. 8.30 Distribution of transverse bending moments at midspan section ( $\text{N-cm}/\text{cm}$ ,  $1 \text{ cm} = 10 \text{ mm}$ )

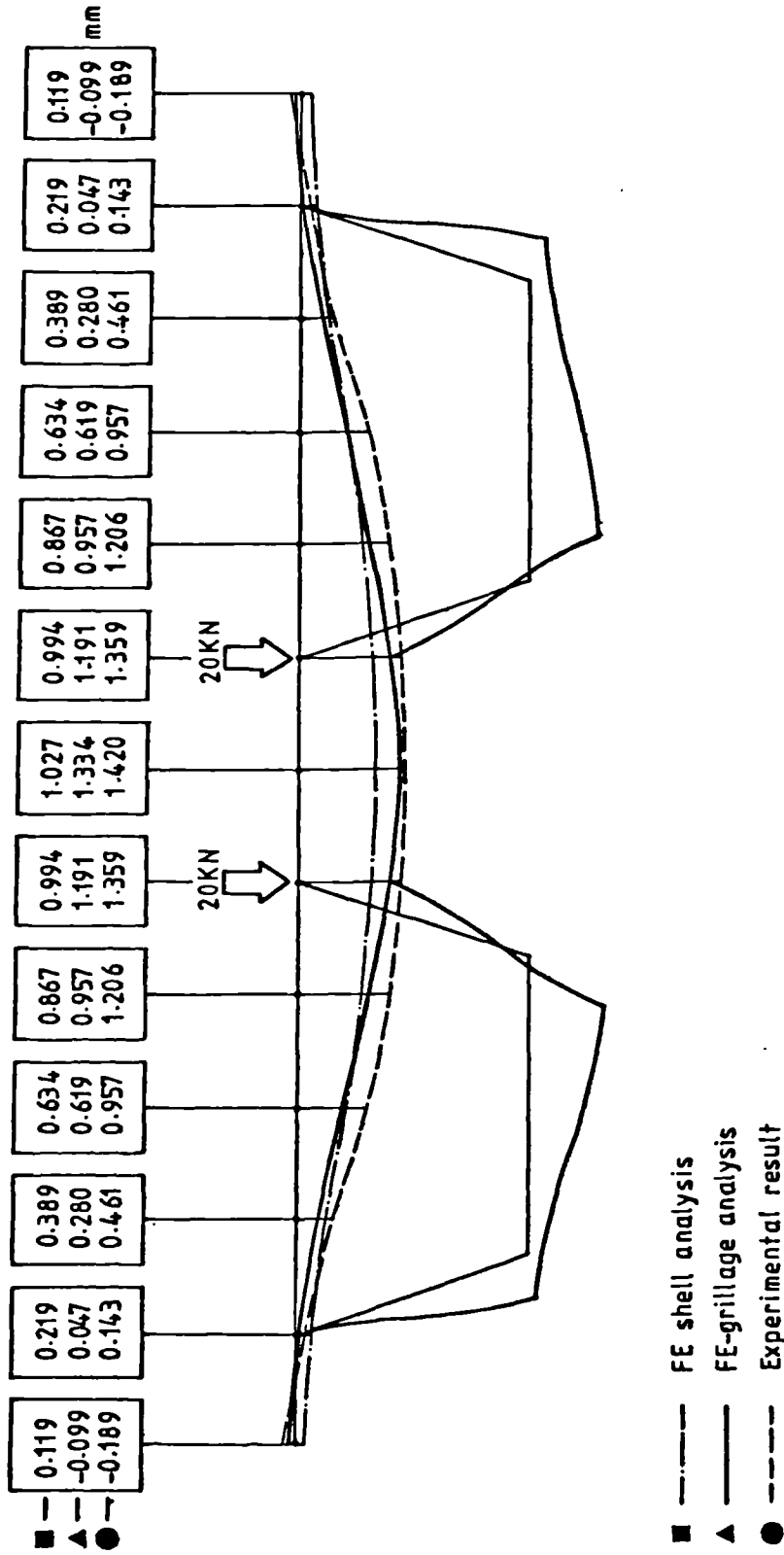


Fig. 8.31 Shape of deformed cross-section at midspan due to transverse symmetrical loading

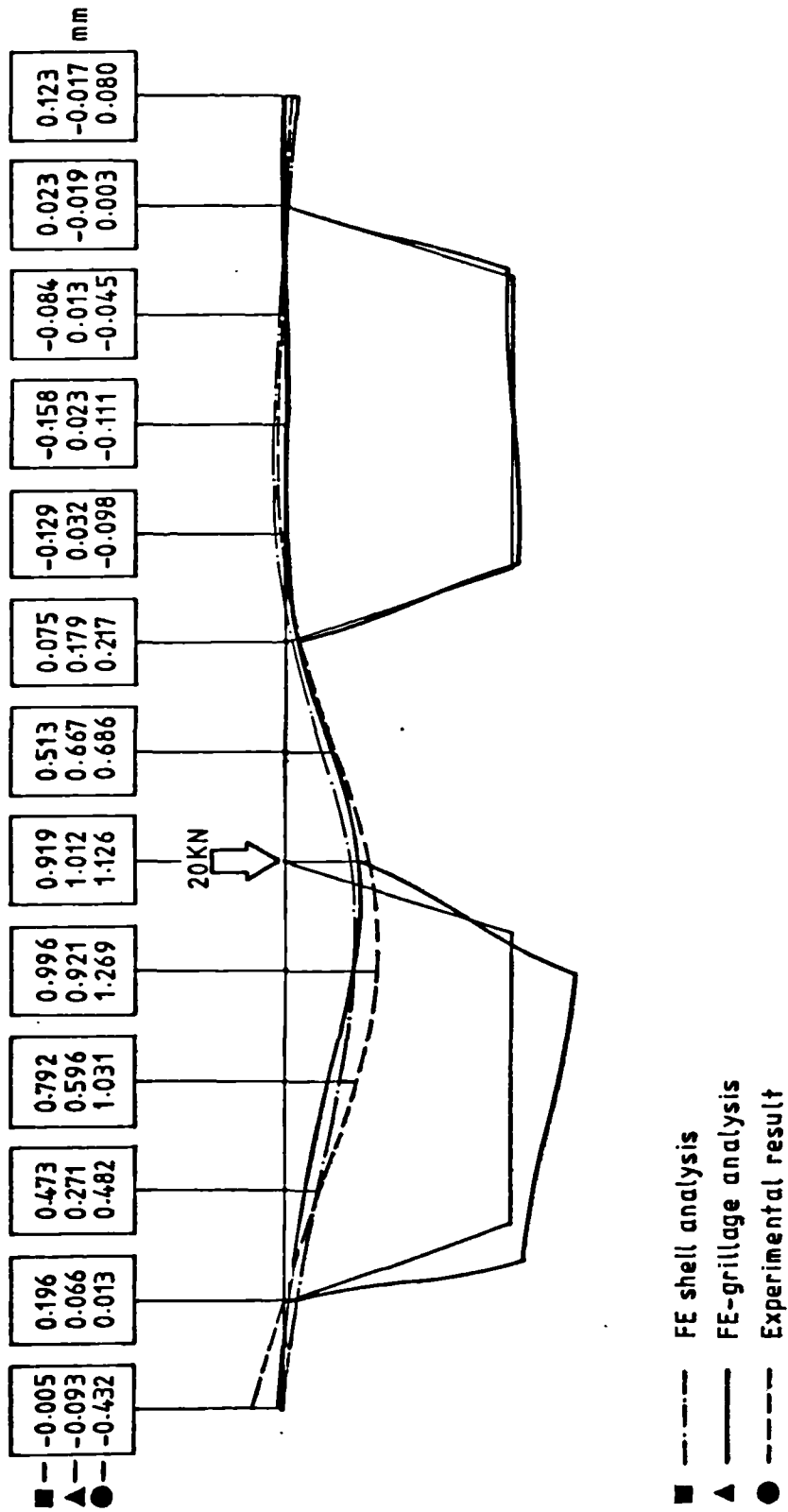


Fig. 8.82 Shape of deformed cross-section at midspan due to assymmetrical loading

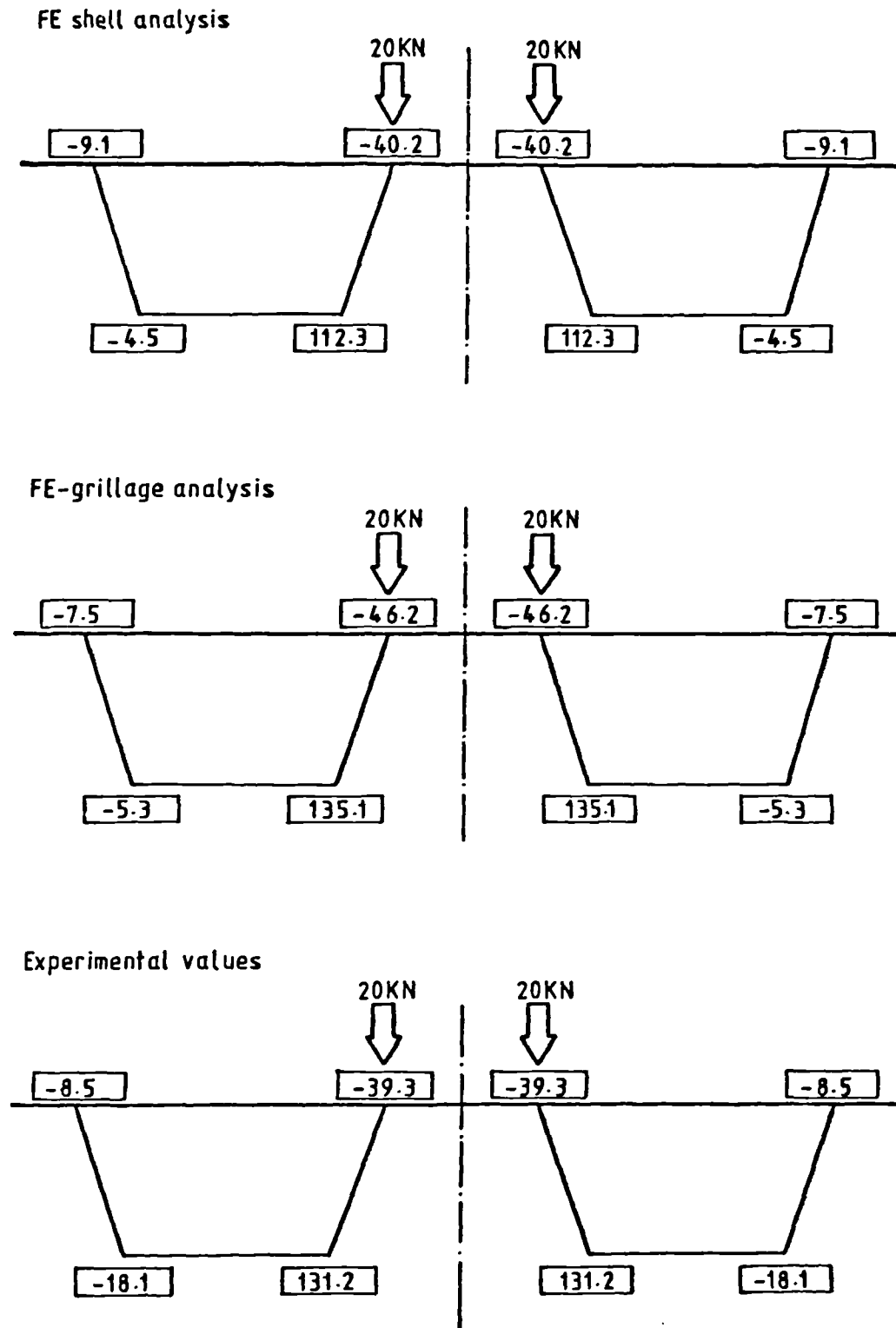


Fig. 8.33 Comparison of longitudinal stresses of outer surfaces at midspan for symmetrical point loads applied above inner webs (in  $\text{N/mm}^2$ )

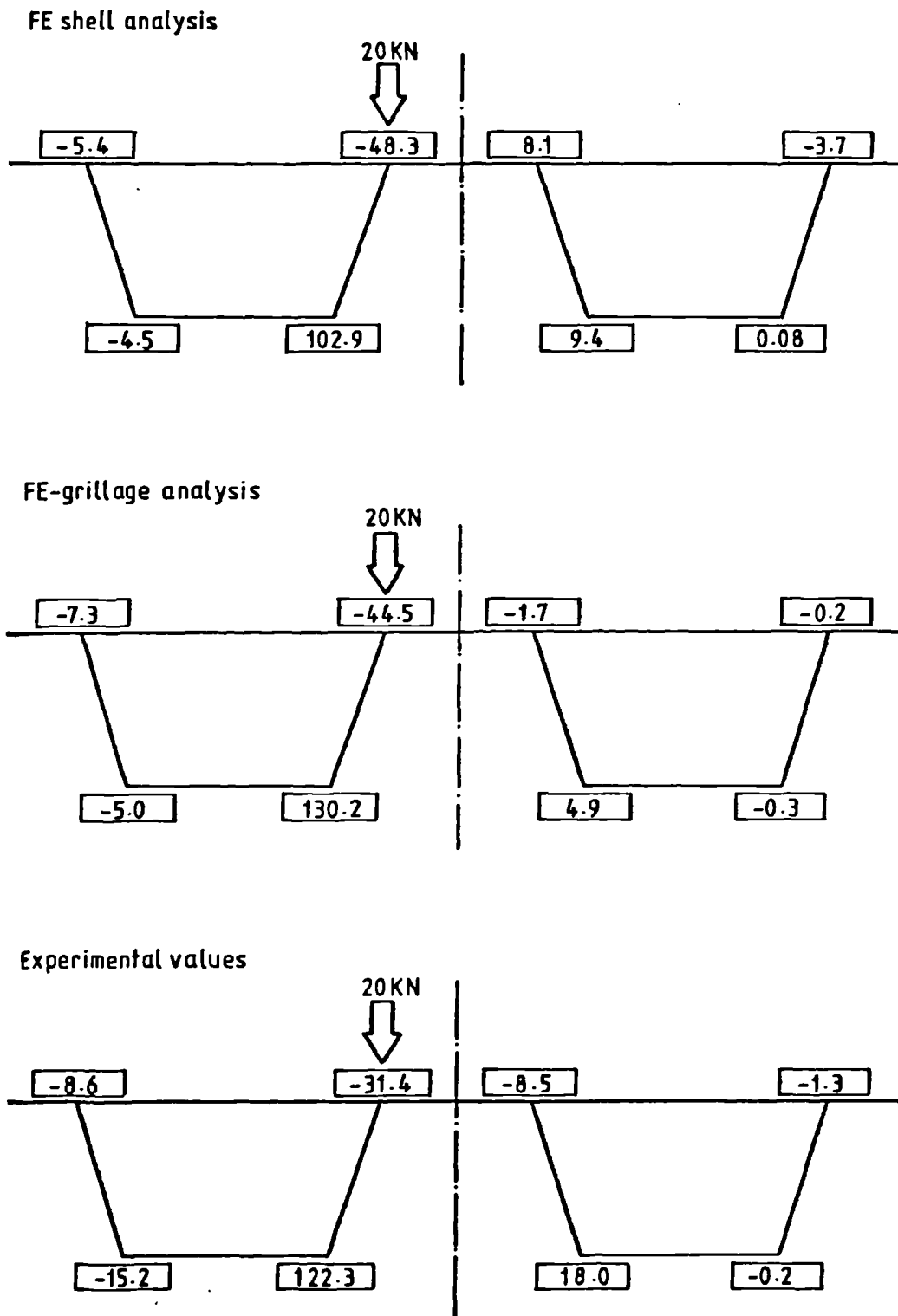


Fig. 8.34 Comparison of longitudinal stresses of outer surfaces at midspan in twin-box model for a concentrated load applied above an inner web (in  $\text{N/mm}^2$ )

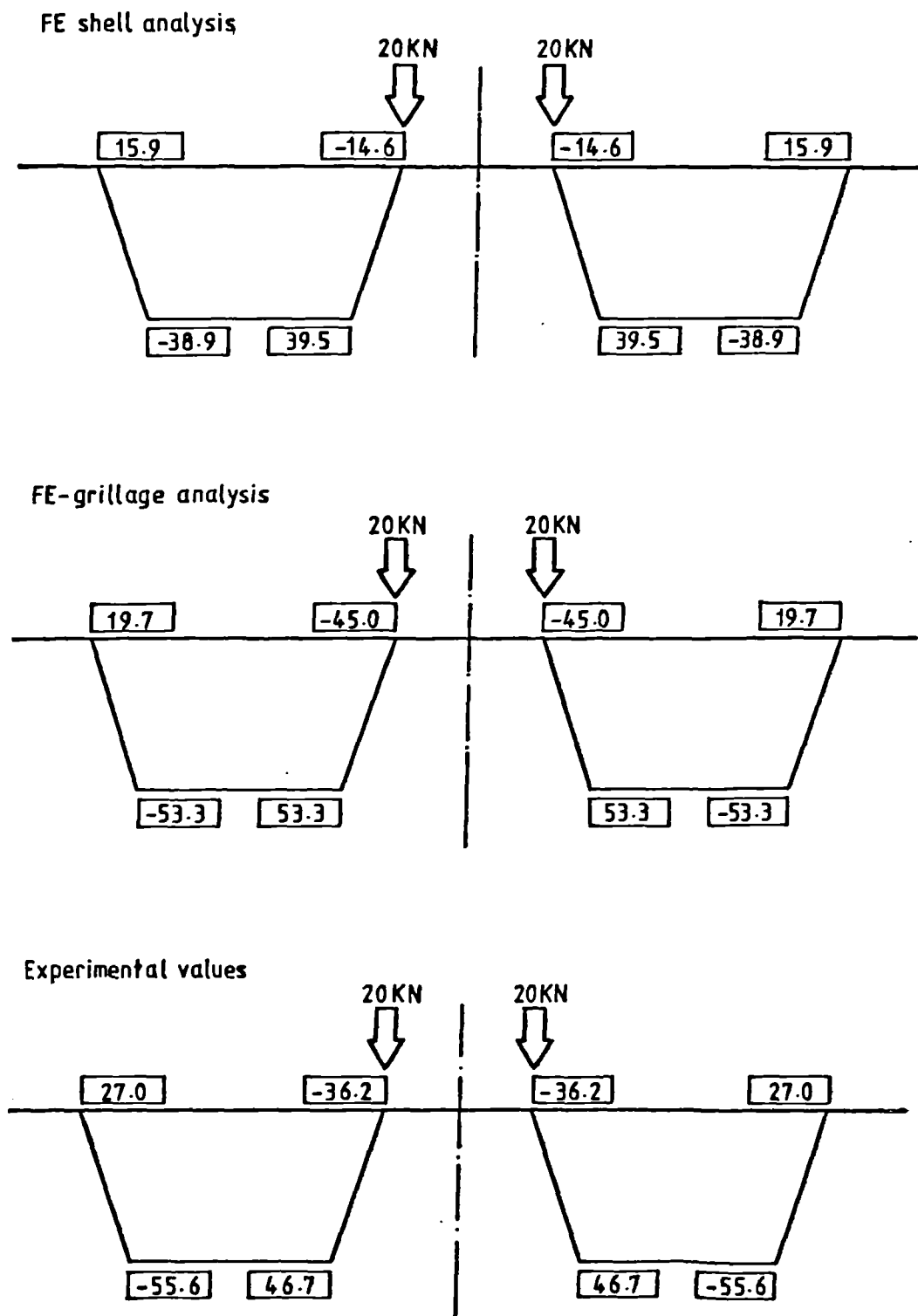
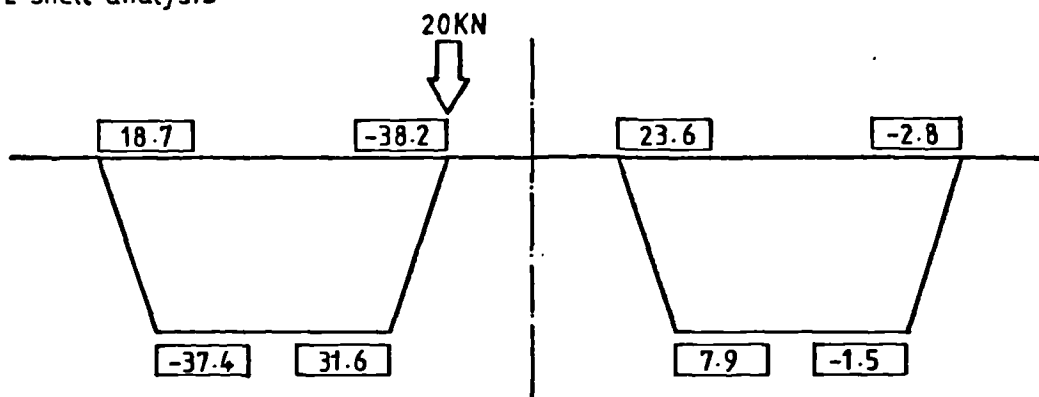
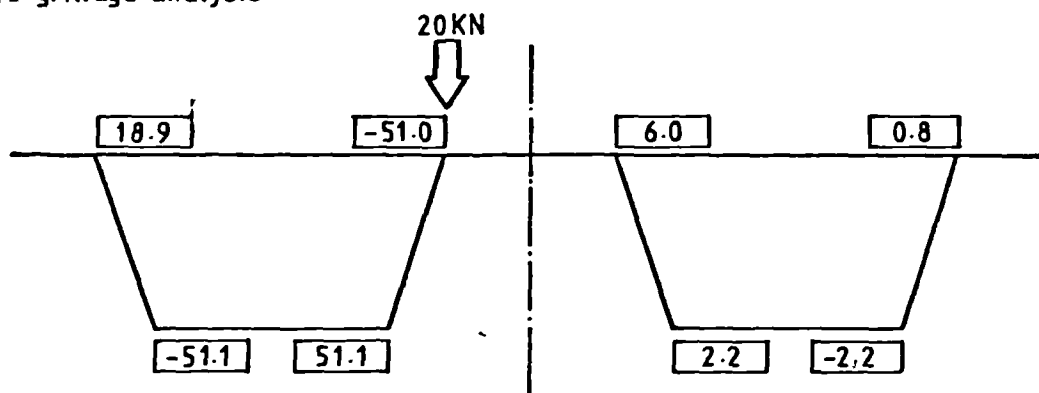


Fig. 8.35 Comparison of cross sectional distributions of  $\sigma$  at midspan in twin-box model for symmetrical concentrated loads applied above inner webs (in  $N/mm^2$ )

FE shell analysis



FE-grillage analysis



Experimental values

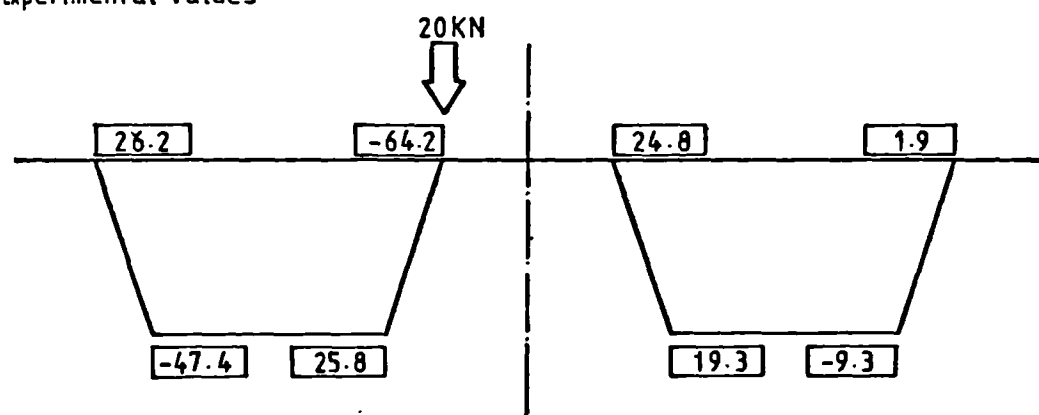


Fig. 8.36 Comparison of cross sectional distribution of  $\sigma$  at midspan in twin-box beam model for an asymmetrical load applied above an inner web (in  $\text{N/mm}^2$ ).

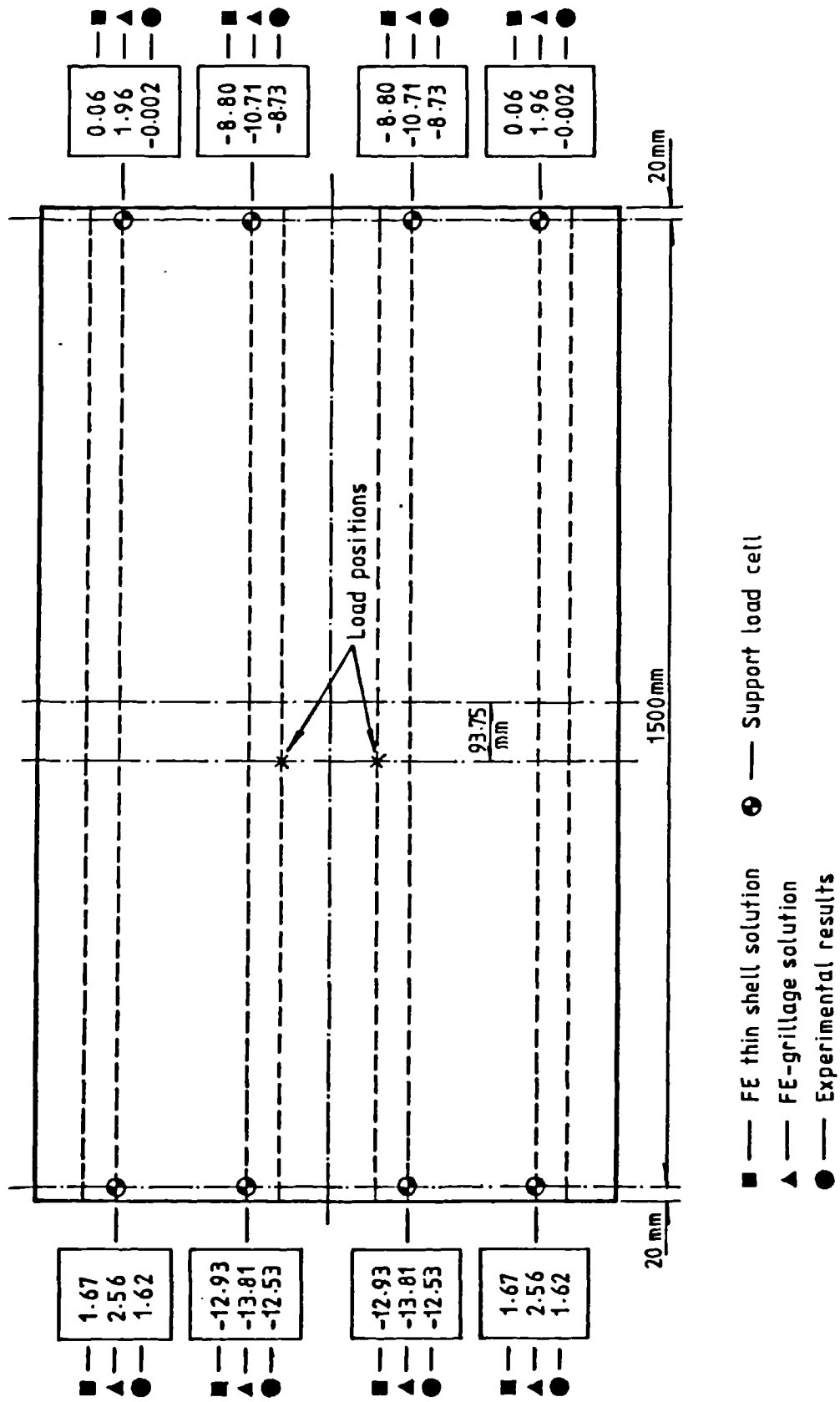


Fig. 8.37 Support reactions due to transverse symmetrical loads in twin-box model (in kN)

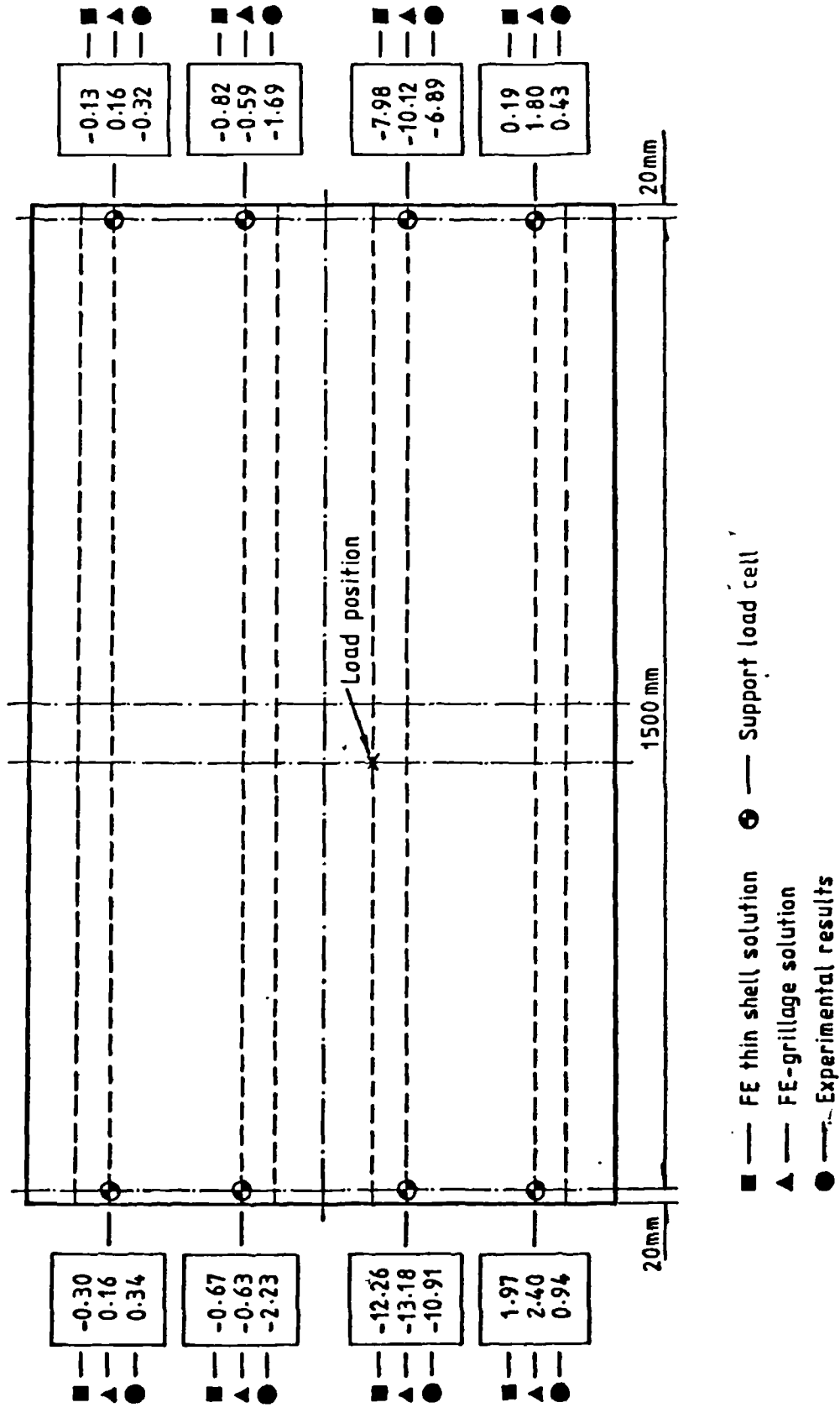


Fig. 8.38 Support reactions due to a concentrated load in twin-box beam model (in kN)

## CHAPTER 9

## CONCLUSIONS AND RECOMMENDATIONS FOR FUTURE WORK

Conclusions

A method of analysis which is based upon the finite element technique has been developed for the analysis of thin-walled box-spine beam bridges having complex geometry and boundary conditions. The important stages in the development of the analysis may be summarized as follows:

(i) Existing thin-walled beam theory has been extended for single-cell as well as multi-cell box beams. This extension considers the structural effects arising from longitudinal bending, warping torsion and cross-sectional distortion.

(ii) The development of a general one-dimensional finite element family, and in particular, the development of a thin-walled box beam element which includes the effects of warping and distortion, has been carried out.

(iii) A finite element-grillage approach is proposed for the analysis of multibox structures. Also, an inclined cable element and an iterative procedure for the nonlinear analysis of cable-stayed bridges have been developed.

The above theoretical work has been incorporated into a computer program called CUBAS. The main program, with a supplementary program called PFRAN, can be used for a wide range of bridge structures having various geometries, boundary and loading conditions.

Extensive experimental tests on elastic box beam models have been conducted by the author and numerical results for various types of box spine-beams have been calculated and compared with alternative theoretical results, in particular three-dimensional finite element analyses. An actual

cable-stayed bridge has been analysed and compared with a field loading test. On the basis of the investigations carried out, several conclusions may be drawn, and these may be summarized as follows:

1. The comparison between the author's finite element beam solutions, the finite element shell solutions calculated by the LUSAS program, and the box beam model experimental values shows good agreement. These results support the appropriateness and the accuracy of the beam elements. The general one-dimensional finite element can then be used successfully for the elastic analysis of a variety of general box-type bridge decks, such as spined box beams, multibox girders and articulated bridge decks.

2. The main advantage of the proposed method of analysis is that it may be used for bridge analysis in situations where a full three-dimensional analysis is unnecessary, such as during preliminary design procedures. The method possesses a simple solution procedure, economical storage and execution time requirements, ease of data preparation and of output interpretation.

It can be observed from the following comparisons that the time required to obtain a solution by the present method is substantially less than that required for a solution by the three-dimensional finite element method:

Structure	Total No. of Elements		No. of Degrees of Freedom		Proc. Time (Sec.)	
	(1)	(2)	(1)	(2)	(1)	(2)
Straight cantilever box model	8	160	153	1180	11.16	210.73
Curved cantilever box model	17	192	315	1416	68.22	232.70
Two-span continuous box beam model	16	188	297	1180	18.72	243.05
Twin-box beam model	67	296	1071	2078	182.52	454.36
Sawko and Cope's Simply supported box girder model (20,118,119)	8	84	153	620	10.08	113.35
A 2-cell box beam given by Richmond (104,106)	8	268	153	1752	16.56	375.54
Curved box girder bridge given by Meyer (87)	8	200	153	1416	19.44	333.76
A 2-span 3-cell box bridge given by Scordelis (126)	8	140	153	868	11.52	322.82
A composite twin-box girder given by Billington (11)	67	264	1071	1770	176.40	419.56

N.B., Column (1) is the general beam solution; Column (2) is the shell solution by LUSAS program.

It can also be emphasized that a major advantage over other existing methods is the versatility of the proposed method. The method is available for single-cell as well as multi-cell box spine-beams, and is applicable to the elastic analysis of concrete, steel and composite structures. The method can account for the effects of transverse stiffening, curvature in plan, variations in cross-sectional properties, and random positioning of supports.

3. Unlike the three-dimensional analysis,<sup>7</sup> the structure in the proposed method is subdivided only in the longitudinal direction. The proposed method thus lacks the accuracy of the finite element method using shell elements with membrane and/or plate bending properties. It is,

however, advantageous in cases of primary design where the overall response is of most significance and many repetitions of calculation are necessary for establishing an efficient design. Detailed investigation using the three-dimensional finite element method can, if required, then be applied to chosen sub-sections of the structure. This considerably simplifies the design procedure for thin-walled box spine-beam bridges.

4. The results obtained experimentally have illustrated the specific structural actions of thin-walled box beams which must be considered in design. The most important conclusions have been summarized in the section 8.4 of Chapter 8.

5. By including non-linear interaction effects, cable-stayed bridges can be represented adequately by the one-dimensional finite element family. The proposed method of analysis using this family is a convenient and practical design tool for this type of bridge. The results obtained by the method have been compared with previous results of a numerical example and the results obtained from an actual field loading test. These comparisons are favourable.

#### Recommendations for future research

(1) The present project has been concerned only with the static analysis of thin-walled box spine-beam bridges. However, some structures such as cable-stayed bridges are prone to the effects of elastic instability arising from beam-column action. Although classical formulations continue to be applicable to digital computer analyses of large-scale systems for such circumstances, an opportunity exists for improved efficiency, though at the expense of approximation by virtue of finite element concepts (8,14). In addition, consideration of problems associated with space frameworks suggests the need to cope with torsional instability as well as combined

torsional-flexural instability. Consequently, the extension of the general beam element to the analysis of torsional and torsional-flexural stability problems, thereby incorporating the warping bimoment and distortion contributions to stability effects of thin-walled assemblages, would be very valuable. It should be noted that a prismatic thin-walled beam element with a rigid open section has been studied by Barsoum and Gallagher (8), and Chai Hong Yoo (14), to deal with the problem of torsional-flexural buckling.

(2) Practical experience shows that vibration is often important for long span bridges such as cable-stayed bridges. Future research should also be directed at investigating the dynamic response of thin-walled box girder bridges. The natural vibrations of a box girder can have three characteristic forms, flexural vibrations, torsional vibrations and distortional vibrations. The general beam element gives the opportunity for the economic resolution of bending-torsional vibration problems (70,71).

(3) Large displacements and material nonlinearity for cable-stayed bridges are predicted in an approximate manner in the present approach. Although in bridge structures other than cable-stayed bridges non-linear effects are normally not significant, it is still preferable to further develop a more complex procedure capable of predicting geometrical and material non-linear effects more accurately.

(4) For predicting the shear lag effects associated with the longitudinal bending an empirical procedure has been used. It would seem possible to use the generalized coordinate method of Vlasov (146) to include the structural action of shear lag directly in the element formulation. Such an approach would also make the method more accurate for complex support conditions.

(5) Large finite element systems are often more useful in pure research work than in the practical work carried out in design offices. The CUBAS computer program has been developed successfully to predict the appropriateness of the theoretical concepts derived in this thesis. Thus the program can be a basis for further developments for the analysis and design of actual bridge structures.

## REFERENCES

1. Abdel-Samad, S.R., Wright, R.N., and Robinson, A.R., "Analysis of Box Girders with Diaphragms," *Journal of the Structural Division, ASCE*, Vol. 94, No. ST10, Proc. Paper 6153, Oct. 1968, pp.2231-2253.
2. Al-Rifaie, W.N., *Structural Behaviour of Curved Box Girder Bridges*, Ph.D. Thesis, Dept. of Civil and Structural Engineering, University College, Cardiff, Jan. 1975.
3. Al-Rifaie, W.N., and Evans, H.R., "An Approximate Method for the Analysis of Box Girder Bridges that are Curved in Plan," *Proceedings of the Int. Assoc. for Bridge & Struct. Engng.*, p.21/79.
4. Aneja, I., and Roll, F., "An Experimental and Analytical Investigation of a Horizontally Curved Box-Beam Highway Bridge Model," *American Concrete Institute Special Publication SP-26*, 1971, pp.379-410.
5. Argyris, J.H., *Recent Advances in Matrix Methods of Structural Analysis*, Pergamon Press, London, 1964, pp.115-145.
6. ASKA Reference Manual, University of Stuttgart, ISD-Report No. 73, 1971.
7. Baron, F., and Lien, Shen-Ying, "Analytical Studies of a Cable Stayed Girder Bridge," *Computers and Structures*, Vol.3, Pergamon Press, New York, Publication 33-11, 1973.
8. Barsoum, R.S., and Gallagher, R.H., "Finite Element Analysis of Torsional-Flexural Stability Problems," *Int. J. Numer. Meth. Engng.*, Vol.2, 1970, pp. 335-352.
9. Bažant, Z., and El Nimeiri, M., "Stiffness Method for Curved Box Girders at Initial Stress," *Journal of the Structural Division, ASCE*, Vol. 100, No. ST10, Proc. Paper 10877, Oct. 1974, pp. 2071-2089.
10. Bescoter, S.U., "A Theory of Torsion Bending for Multicell Beams," *Journal of Applied Mechanics*, Mar. 1954, pp. 25-34.

11. Billington, C.J., The Theoretical and Experimental Elastic Behaviour of Box Girder Bridges, Ph.D. Thesis, University of London, 1974.
12. Billington, C.J., and Dowling, P.J., Construction, Instrumentation and Testing of Four Linearly Elastic Models, Engineering Structures Laboratories, Imperial College of Science and Technology, London, 1972, CESLIC Report BB1.
13. British Standards, BS 5400, "Part 5 : Steel, Concrete and Composite Bridges," 1979.
14. Chai Hong Yoo, "Bimoment Contribution to Stability of Thin-Walled Assemblages," Computers and Structures, Vol. 11, No.5, 1980, pp. 465-471.
15. Chapman, J.C., Dowling, P.J., Lim, P.T.K., and Billington, C.J., "The Structural Behaviour of Steel and Concrete Box Girder Bridges", The Structural Engineer, Vol. 49, London, Mar. 1971, pp.111-120.
16. Cheung, Y.K., Finite Strip Method in Structural Analysis, Pergamon International Library, 1976.
17. Cheung, Y.K., and Yeo, M.F., A Practical Introduction to Finite Element Analysis, Pitman Publishing Ltd., 1979.
18. Committee of Inquiry into the Basis for Design and Method of Erection of Steel Box Girder Bridges, Interim Design and Workmanship Rules, Department of the Environment, London, 1973.
19. Conner, J.J., et al, "Nonlinear Analysis of Elastic Framed Structures," Journal of the Structural Division, ASCE, Vol. 94, No. ST6, Proc. Paper 6011, June 1968, pp. 1525-1548.
20. Cope, R.J., discussion of "The Western Avenue Extension - The Design of Section Five," by B. Richmond, The Structural Engineer, Vol. 49, No. 3, London, Mar. 1971.

21. Dabrowski, R., "Der Schubverformungseinfluss auf die Wölbkrafttorsion der Kastenträger mit Verformbaren Biegesteifem Profil (The Effect of Shear Deformation on the Warping Tension of Box Girders with Deformable Section and with Flexural Stiffness)", Der Bauingenieur, Nov. 1965, pp. 444-449.
22. Dabrowski, R., Curved Thin-Walled Girders, Cement and Concrete Association, London, 1972, Translation No. 144.
23. Dalton, D.C., and Richmond, B., "Twisting of Thin-Walled Box Girders of Trapezoidal Cross Section," Proceedings, Institution of Civil Engineers, Paper No. 7031, London, 1968, pp. 61-73.
24. Davies, J.D., Somerville, I.J., and Zienkiewicz, O.C., "Analysis of Various Types of Bridges by the Finite Element Method," Development in Bridge Design and Construction, Crosby Lockwood and Son, Ltd., London, 1971, pp.217-236.
25. Design Manual for Orthotropic Steel Plate Deck Bridges, American Institute of Steel Construction, New York, 1963.
26. Ernst, H.J., "Der E-Modul von Seilen unter Berücksichtigung des Durchhanges (The E-Modulus of Cables Considering the Deflection)," Der Bauingenieur, Vol. 40, No.2, Feb. 1965.
27. Ettouney, M.M., and Kirby, J.B., "Warping Restraint in Three-Dimensional Frames," Journal of the Structural Division, ASCE, Vol.107, No. ST8, Proc. Paper 16475, Aug. 1981, pp. 1643-1656.
28. Evans, H.R. and Al-Rifaie, W.N., "An Experimental and Theoretical Investigation of the Behaviour of Box Girders Curved in Plan", Proceedings, Institution of Civil Engineers, Part 2, Paper No. 7799, London, June 1968, pp. 323-352.
29. Evans, H.R., and Rockey, K.C., "A Folded Plate Approach to the Analysis of Box Girders," Developments in Bridge Design and Construction, Crosby Lockwood and Son Ltd., London, 1971, pp.246 - 263.

30. Evans, H.R., and Shanmugam, N.E., "An Approximate Grillage Approach to the Analysis of Cellular Structures," Proceedings, Institution of Civil Engineers, Part 2, Paper No. 8198, London, Mar. 1979, pp. 133-154.
31. Evans, H.R., and Taherian, A.R., "The Prediction of the Shear Lag Effect in Box Girders," Proceedings, Institution of Civil Engineers, Part 2, Paper No. 7978, London, Mar. 1977, pp. 69-92.
32. Evans, H.R., and Taherian, A.R., "A Design Aid for Shear Lag Calculations," Proceedings, Institution of Civil Engineers, Part 2, Paper No. 8330, London, June 1980, pp.403-424.
33. Fam, A., and Turkstra, C., "A Finite Element Scheme for Box Girder Bridges," Computers and Structures, Vol. 5, 1975, pp. 179-186.
34. Feige, A., "Stahlbrückenbau," Stahlbau, Handbuch für Studium und Praxis, Band 2, Stahlbau-Verlags-GMBH, Köln, 1964.
35. Flint, A.R., and Horne, M.R., "Conclusion of Research Program and Summary of Parametric Studies," Proc. International Conference on Steel Box Girder Bridges, Institution of Civil Engineers, London, 1973.
36. Goldberg, J.E., and Leve, H.L., "Theory of Prismatic Folded Plate Structures," Publications of Int. Assoc. for Bridge & Struct. Engng., Vol. 17, 1957, pp.59-86.
37. Goldstein, A., Lightfoot, E., and Sawko, F., "Analysis of a Three-Span Continuous Grillage Having Varying Section Properties," The Structural Engineer, London, Aug. 1961, pp. 245-254.
38. Goschy, B., "Der Kastenträger ohne Zwischenschotte, Berechnung auf Torsion," Bautechnik, No. 5, 1966, pp. 159-163.
39. Goschy, B., "Dynamics of Cable-Stayed Pipe Bridges," Acier-Stahl-Steel (English version), No. 6, June 1961, pp. 277-282.
40. Goschy, B., "The Torsion of Skew-Cable Suspension Bridges," Space Structures, Ed. Davies, R.M., Blackwell Scientific Publications, Oxford, 1967, pp. 213-220.

41. Hambly, E.C., and Pennells, E., "Grillage Analysis Applied to Cellular Bridge Decks," *The Structural Engineer*, Vol. 53, No. 7, London, 1975, pp. 367-375.
42. Heilig, R., *A Contribution to the Theory of Box Girders of Arbitrary Cross-Sectional Shape*, Cement and Concrete Association, London, Translation No. 145, 1971.
43. Heins, C.P., "Behaviour and Design of Curved Girder Bridges," *Developments in Bridge Design and Construction*, Crosby Lockwood and Son Ltd., London, 1971, pp. 287-303.
44. Hibbitt, H.D., Marcal, P.V., and Rice, J.R., "A Finite Element Formulation for Problems of Large Strain and Large Displacements," *Int. J. Numer. Meth. Engng.*, Vol. 6, 1970, pp. 1069-1086.
45. Hinton, E., and Owen, D.R.J., *Finite Element Programming*, Academic Press Inc. Ltd., London, 1977.
46. Homberg, H., *Fahrbahnplatten mit veränderlicher Dicke. (Highway deck slabs of variable thickness)* Vol. 2, Springer, 1968.
47. Homberg, H., and Ropers, W., *Fahrbahnplatten mit veränderlicher Dicke. (Highway deck slabs of variable thickness)* Vol.1, Springer-Verlag, 1965.
48. Hughes, T.J.R., Taylor, R.L., and Kanoknukulchai, W., "A Simple and Efficient Finite Element for Plate Bending," *Int. J. Numer. Meth. Engng.*, Vol. 2, 1977, pp. 1529-1543.
49. Irons, B.M., "The Semiloof Shell Element," *Finite Elements for Thin Shells and Curved Members*, Edited by Ashwell and Gallgher, Wiley, 1976.
50. Jirousek, J., Bouberguig, A., and Saygun, A., "A Marco-Element Analysis of Prestressed Curved Box-Girder Bridges," *Computers and Structures*, Vol. 10, No. 3, June 1979, pp. 467-482.
51. Jirousek, J., "A Family of Variable Section Curved Beam and Thick-Shell or Membrane-Stiffening Isoparametric Elements," *Int. J. Numer. Meth. Engng.*, Vol. 17, 1981, pp. 171-186.

52. Johnson, C.D., and Lee, T., "Long Nonprismatic Folded Plate Structures," Journal of the Structural Division, ASCE, Vol. 94, No. ST6, Proc. Paper 6001, June 1968, pp. 1457-1484.
53. Kazita, T., and Cheung, Y.K., "Finite Element Analysis of Cable Stayed Bridges", Publications 33-11, Int. Assoc. for Bridge & Struct. Engng., 1973.
54. Khan, A.J. and Tottenham, H., "The Method of Bimoment Distribution for the Analysis of Continuous Thin-Walled Structures Subject to Torsion," Proceedings, Institution of Civil Engineers, Part 2, Paper No. 8057, London, Dec. 1977, pp. 843-863.
55. Kollbrunner, C.F., and Basler, K., Torsion in Structures. An Engineering Approach, Translated from German, Springer, 1969.
56. Kollbrunner, C.F., and Basler, K., Sektorielle Grössen und Spannungen bei Offenen, dünnwandigen Querschnitten (Sectorial Quantities and Stresses in Open Thin-Walled Cross-Sections), Mitteilungen der Technischen Kommission, Heft 28, Schweizer Stahlbau-Vereinigung, Zurich, Jan. 1964.
57. Kollbrunner, C.F., and Hajden, N., Wölbkrafttorsion dünnwandiger Stäbe mit offenen Profil (Warping Torsion of Thin-Walled Beams of Open Section), Teil I, Mitteilungen der Technischen Kommission, Heft 29, Verlag Schweizer Stahlbau-Vereinigung, Zurich, Oct. 1964.
58. Kollbrunner, C.F., and Hajden, N., Wölbkrafttorsion dünnwandiger Stäbe mit offenen Profil (Warping Torsion of Thin-Walled Beams of Open Section), Teil II, Mitteilungen der Technischen Kommission, Heft 30, Verlag Schweizer Stahlbau-Vereinigung, Zurich, May 1965.
59. Kollbrunner, C.F., and Hajden, N., Wölbkrafttorsion dünnwandiger Stäbe mit geschlossenem Profil (Warping Torsion of Thin-Walled Beams of Closed Section), Mitteilungen der Technischen Kommission, Heft 32, Verlag Schweizer Stahlbau-Vereinigung, Zurich, 1966.
60. Krahula, J.L., "Analysis of Bent and Twisted Bars Using the Finite Element Method," AIAA Journal (American Institute of Aeronautics and Astronautics), Vol. 5, No. 6, June 1967, pp. 1194-1197.

61. Krajcinovic, D., "A Consistent Discrete Elements Technique for Thin-Walled Assemblages," *Int. J. of Solids and Structures*, 1969, pp. 639-662.
62. Křistek, V., "Tapered Box Girders of Deformable Cross-Section," *Journal of the Structural Division, ASCE*, Vol. 96, No. ST8, Proc. Paper 7489, Aug. 1970, pp. 1761-1793.
63. Křistek, V., "Box Girders of Deformable Cross-Section - Some Theory of Elasticity Solutions," *Proceedings, Institution of Civil Engineers*, Paper No. 7317, London, Oct. 1970, pp. 239-253.
64. Křistek, V., "Co-operation of Prestressed Concrete Box Girders with Deformable Cross Sections," *Stavebnicky, Časopis Bratislava*, 1970.
65. Lazar, Benjamin E., "Stiffness Analysis of Cable-Stayed Bridges," *Journal of the Structural Division, ASCE*, Vol. 98, No. ST7, Proc. Paper 9036, July 1972, pp. 1605-1612. Haribaran, M., discussion of "Stiffness Analysis of Cable-Stayed Bridges," by Benjamin E. Lazar, *Journal of the Structural Division, ASCE*, Vol. 99, No. ST7, Proc. Paper 9826, July 1973, pp. 1661-1663.
66. Lazar, Benjamin E., and Troitsky, M.S., "Load Balancing Analysis of Cable-Stayed Bridges," *Journal of the Structural Division, ASCE*, Vol. 98, No. ST8, Proc. Paper 9122, Aug. 1972, pp. 1725-1740.
67. Lee, D.J., "The Selection of Box Beam Arrangements in Bridge Design," *Developments in Bridge Design and Construction*, Crosby Lockwood and Son Ltd., 1971, pp. 400-426.
68. Leonhardt, F., and Zellner, W., "Cable-Stayed Bridges - Report on Latest Developments," Report submitted to the Canadian Structural Engineering Conference, 1970, CISC, Toronto, Ontario, Canada.
69. Leonhardt, F., and Zellner, W., "Cable-Stayed Bridges," *Surveys, Int. Assoc. for Bridge and Struct. Engng.*, S-13, 1980.
70. Lie, K.H., *The Torsion Theory of Truss Girders - Analysis of Torsion, Stability and Vibration of Truss Bridges (in Chinese)*, People's Communications Press, Beijing, China, 1975.

71. Lie, K.H., "Analysis of Stress, Stability and Vibration of Truss Bridges," (in English) Scientia Sinica, Vol. XXI, No. 6, 1978.
72. Lightfoot, E., and Sawko, F., "Structural Frame Analysis by Electronic Computer. Grid Frameworks Resolved by Generalized Slope Deflection," Engineering, Jan. 1959, pp. 18-20.
73. Lightfoot, E., and Sawko, F., "The Analysis of Grid Framework and Floor Systems by the Electronic Computer," The Structural Engineer, London, Mar. 1960, pp. 79-87.
74. Lim, P.T.K., Elastic Analysis of Bridge Structures by the Finite Element Method, Ph.D. Thesis, University of London, 1971.
75. Lim, P.T.K., Kilford, J.T., and Moffatt, K.R., "Finite Element Analysis of Curved Box Girder Bridges," Developments in Bridge Design and Construction, Crosby Lockwood and Son Ltd., 1971, pp. 264-286.
76. Livesley, R.K., "The Application of an Electronic Digital Computer to Some Problems of Structural Analysis," The Structural Engineer, Vol. 34, No. 1, London, 1964, pp. 1-12.
77. Loo, Y.C., and Cusens, A.R., "Developments of the Finite Strip Method in the Analysis of Bridge Decks," Developments in Bridge Design and Construction, Crosby Lockwood and Son Ltd., London, 1971, pp. 53-72.
78. Loo, Y.C. and Cusens, A.R., The Finite Strip Method in Bridge Engineering, Viewpoint Publications, 1978.
79. LUSAS - Finite Element Stress Analysis System, User's Manual, Finite Element Analysis Ltd., London, 1980.
80. Lyons, L.P.R., A General Finite Element System with Special Reference to the Analysis of Cellular Structures, Ph.D., Thesis, University of London, 1977.
81. MacLeod, I., "New Rectangular Finite Elements for Shear Wall Analysis," Journal of the Structural Division, ASCE, Vol. 95, No. ST3, Mar. 1969, pp. 399-409.

82. Maisel, B.I., Review of Literature Related to the Analysis and Design of Thin-Walled Beams, Technical Report TRA 440, Cement and Concrete Association, London, July 1970.
83. Maisel, B.I., and Roll, F., Methods of Analysis and Design of Concrete Boxbeams with Side Cantilevers, Technical Report 42.494, Cement and Concrete Association, London, Nov. 1974.
84. Maisel, B.I., "Analysis of Concrete Boxbeams Using Small Computer Capacity," Cement and Concrete Association Research Seminar, London, July 1981, pp. 9-12.
85. Mehrotra, B.L., Mufti, A.A., and Redwood, R.G., "Analysis of Three Dimensional Thin-Walled Structures, "Journal of the Structural Division, ASCE, Vol. 95, No. ST12, Dec. 1969, pp. 2863-2872; Vol. 96, No. ST9, Sep. 1970, pp. 1977-1978; Vol. 96, No. ST8, Aug. 1970, pp.1838-1846.
86. Merchant, W., and Brotton, D.M., "A Generalized Method of Analysis of Elastic Plane Frame," Int. Assoc. for Bridge and Struct. Engng., Symposium, Rio de Janeiro, Brazil, 1964.
87. Meyer, C., Analysis and Design of Curved Box Girder Bridges, University of California, Berkeley, Structural Engineering and Structural Mechanics, Report No. SESM 70-22, Dec. 1970.
88. Meyer, C., and Scordelis, A.C., Analysis of Curved Folded Plate Structures, University of California, Berkeley, Structural Engineering and Structural Mechanics, Report No. SESM 70-8, June 1970.
89. Meyer, M.L., "On a General Method of Compensation in Strain Gauge Work," Strain, Volume 4(1), 1968, pp.3-8.
90. Mikkola, M.J., and Paavola, J., "Finite Element Analysis of Box Girders," Journal of the Structural Division, ASCE, Vol. 106, No. ST6, Proc. Paper 15498, June 1980, pp.1343-1357.
91. Miller, M.A., Brotton, D.M., and Merchant, W., "A Computer Method for the Analysis of Nonlinear Elastic Plane Frame-work," International Symposium on Use of Computers in Structural Engineering, Dept. of Civil Engineering, University of Newcastle, England, 1966.

92. Mohammed, Abdel R.E., A Finite Element Study of a Thin Curved Beam Element, M.Sc. Thesis, The City University, London, Nov. 1978.
93. Moffatt, K.R., and Dowling, P.J., "Shear Lag in Steel Box Girder Bridges," The Structural Engineer, Vol. 53, London, Oct. 1975, pp. 439-448.
94. Moffatt, K.R., and Lim, P.T.K., "Some Finite Elements Having Particular Application to Box Girder Bridges," Proceeding of Int. Assoc. for Bridges & Struct. Engng., P1-/77.
95. Nour-Omid, S., A Finite Element Study Using the Semiloof Beam and Shell Elements, M.Sc. Thesis, The City University, London, Nov. 1977.
96. Podolny, W., Jr., Chmn., "Tentative Recommendations for Cable-Stayed Bridge Structures," by the Task Committee on Cable-Suspended Structures of the Committee on Special Structures, of the Committee on Metals, of the Structural Division, Journal of the Structural Division, ASCE, Vol. 103, No. ST5, Proc. Paper 12933, May 1977, pp. 929-939.
97. Podolny, W., Jr., Chmn., "Commentary on the Tentative Recommendations for Cable-Stayed Bridge Structures," by the Task Committee on Cable-Suspended Structures of the Committee on Special Structures, of the Committee on Metals, of the Structural Division, Journal of the Structural Division, ASCE, Vol. 103, No. ST5, Proc. Paper 12934, May 1977, pp. 441-959.
98. Podolny, W. Jr., and Scalzi, J.B., Construction and Design of Cable-Stayed Bridges, John Wiley & Sons, Inc., New York, 1976.
99. Powell, G.H., "Theory of Nonlinear Elastic Structures," Journal of Structural Division, ASCE, Vol. 95, No. ST12, Dec. 1969.
100. Przemieniecki, J.S., Theory of Matrix Structural Analysis, McGraw-Hill, New York, 1968.
101. Pucher, A., Einflussfelder Elastischer Platten (Influence Surfaces of Elastic Plates), Third Edition, Springer, 1964.

102. Renton, J.D., "Stability of Space Frames by Computer Analysis," *Journal of the Structural Division, ASCE*, Vol. 88, No. ST4, Proc. Paper No. 3237, Aug. 1962, pp. 81-103.
103. Richmond, B., "Twisting of Thin-Walled Box Girder," *Proceedings, Institution of Civil Engineers*, Paper No. 6868, London, April 1966, pp. 659-675.
104. Richmond, B., "Trapezoidal Boxes with Continuous Diaphragms," *Proceedings, Institution of Civil Engineers*, Paper No. 7189, London, Aug. 1968, pp. 641-650.
105. Richmond, B., "Matrix Difference Analysis of Box Girders," *Proceedings, Institution of Civil Engineers*, Paper No. 7174 abstract, London, Aug. 1969, pp. 651-655.
106. Richmond, B., "The Relationship of Box Beam Theories to Bridge Design," *Developments in Bridge Design and Construction*, Crosby Lockwood and Son Ltd., 1971, pp. 237-245.
107. Roark, R.J., *Formulas for Stress and Strain*, 4th edition, McGraw-Hill Book Company, New York, 1965.
108. Rockey, K.C., and Evans, H.R., "A Finite Element Solution for Folded Plate Structures," *Space Structures*, Blackwell Scientific Publications, 1967.
109. Rockey, K.C., and Evans, H.R., *A Report on the Nodal Section Method*, Report No. NS/C/9, University College, Cardiff, Nov. 1972.
110. Rockey, K.C., and Evans, H.R., "The Nodal Section Method for the Analysis of Box Girders," *Publications of the Int. Assoc. for Bridge & Struc. Engng.*, Vol. 35-1, 1975.
111. Roll, F., and Aneja, I., *Model Tests of Box-Beam Highway Bridges with Cantilevered Deck Slabs*, ASCE Transportation Engineering Conference, Philadelphia, Oct. 1966, Preprint 395.

112. Saafan, S.A., "Nonlinear Behaviour of Structural Plane Frame,"  
Journal of the Structural Division, ASCE, Vol. 89, No. ST4, Proc.  
Paper 3615, Aug. 1963, pp. 557-579.
113. Sawko, F., "Bridge Deck Analysis - Electronic Computers versus  
Distribution Methods," Civil Engineering and Public Works Review,  
April 1965, pp. 534-538.
114. Sawko, F., and Willcock, B.K., "Computer Analysis of Bridges Having  
Varying Section Properties," The Structural Engineer, No. 11, Vol. 45,  
London, Nov. 1967, PP. 395 - 400.
115. Sawko, F., "Computer Analysis of Grillages Curved in Plan,"  
Publications of the Int. Assoc. for Bridge & Struct. Engng., Vol. 27,  
1967.
116. Sawko, F., "Recent Developments in the Analysis of Steel Bridges  
Using Electronic Computers," Proceedings of the Conference on Steel  
Bridges, London, June, 1968. British Construction Steelwork Association,  
1969, pp. 39-48.
117. Sawko, F., and Cope, R.J., discussion of "Linear Analysis of Complete  
Structures by Computers," by K.I. Majid and M. Williamson, Proceedings,  
Institution of Civil Engineers, Vol. 40, London, June 1968, pp.205-209.
118. Sawko, F., and Cope, R.J., "Analysis of Multi-cell Bridges without  
Transverse Diaphragms - A Finite Element Approach," The Structural  
Engineer, London, Nov. 1969, pp. 455-460.
119. Sawko, F., and Cope, R.J., "Analysis of Spine Beam Bridges Using  
Finite Elements," Civil Engineering and Public Works Review, Feb. 1970,  
pp. 146-147.
120. Sawko, F., and Mills, J.H., "Design of Cantilever Slabs for Spine Beam  
Bridges," Developments in Bridge Design and Construction, Crosby  
Lockwood and Son Ltd., 1971, pp. 1 - 26.
121. Sawko, F., and Mosley, W.H., "Grillage Analysis of Composite Box  
Girder Bridge Decks," Civil Engineering and Public Works Review ,  
Oct. 1969, pp. 979-981.

122. Sawko, F., and Swaminadhan, D., "Analysis of Articulated Cellular Bridge Decks without Transverse Diaphragms - A New Method," Proceedings of Seminar Y, Summer Annual Meeting, University of Warwick, England, July 1974, pp. 110 - 139.
123. Sawko, F., and Willcock, B.K., "Computer Analysis of Bridges Having Varying Section Properties," The Structural Engineer, London, Nov. 1967, pp.395 - 400.
124. Scordelis, A.C., "Analysis of Simply Supported Box Girder Bridges," Structures and Materials Research Report, SESM 66-17, Division of Structural Engineering and Structural Mechanics, Department of Civil Engineering, University of California, Berkeley, Oct. 1966.
125. Scordelis, A.C., "Analysis of Continuous Box Girder Bridges," Structures and Materials Research Report, SESM 67-25, Division of Structural Engineering and Structural Mechanics, Department of Civil Engineering, University of California, Berkeley, Nov. 1967.
126. Scordelis, A.C., and Davis, R.E., "Stresses in Continuous Concrete Box Girder Bridges," ACI Publication, SP26-13, Concrete Bridge Design, 1969, pp. 284-319.
127. Scordelis, A.C., "Analytical Solutions for Box Girder Bridges," Developments in Bridge Design and Construction, Crosby Lockwood and Son Ltd., 1971, pp. 200-216.
128. Shanghai Design Institute on Municipal Engineering, Static Behaviour of Different Types of Cables in Prestressed Concrete Cable-Stayed Bridges, Research Report 76-16, Shanghai, China, April 1976.
129. Sisodiya, R.G., and Cheung, Y.K., "A Higher Order Inplane Parallelogram Element and Its Application to Skewed Curved Box-Girder Bridges," Developments in Bridge Design and Construction, Crosby Lockwood and Son Ltd., 1971, pp. 304-314.
130. Sisodiya, R.G., Cheung, Y.K., and Ghali, A., "New Finite Elements with Application to Box Girder Bridges," Proceedings, Institution of Civil Engineers, suppl. (XVII), 1972, pp. 207-225.

131. Smith, B.S., "The Single Plane Cable-Stayed Girder Bridge: A Method of Analysis Suitable for Computer Use," Proceedings, Institution of Civil Engineers, Paper No. 7040, London, 1968. "A Linear Method of Analysis for Double-Plane Cable-Stayed Girder Bridges," Proceedings, Institution of Civil Engineers, Paper No. 7011, London, 1968.
132. Spindel, J.E., A Study of Bridge Slabs Having no Transverse Flexural Stiffness, Ph.D. Thesis, University of London, 1961.
133. Stefanou, G.D., Dritos, S., and Bakas, G.J., "A Study of Deformations in Single-Cell Box-Beam Sections and Their Effects on Longitudinal Stresses and Transverse Moments," (Synopsis), The Structural Engineer, Vol. 58B, No. 4, London, Dec. 1980.
134. Steinle, A., Torsion und Profilverformung (Torsion and Cross-Sectional Distortion), Dissertation Universität (Technische Hochschule), Stuttgart, 1967.
135. Steinle, A., "Torsion und Profilverformung beim einzelligen Kastenträger (Torsion and Cross-Sectional Distortion of the Single-Cell Box Beam)," Beton-und Stahlbetonbau, Sep. 1970, pp. 215-222. Praktische Berechnung eines durch Verkehrslasten unsymmetrisch belasteten Kastenträgers am Beispiel der Henschbachtalbrücke. (Practical Calculation for a Box Beam Loaded Unsymmetrically by Traffic, Using the Example of the Henschbach Valley Bridge)," Beton-und Stahlbetonbau, Oct. 1970, pp. 249-254, June, 1972, pp. 143-144.
136. Swann, R.A., A Feature Survey of Concrete Box Spine-Beam Bridges, Cement and Concrete Association, London, Technical Report 42.469, June 1972.
137. Swaminadhan, D., Analysis of Articulated Cellular Bridge Decks, Ph.D. Thesis, University of Liverpool, England, Sep. 1973.
138. Taherian, A.R., and Evans, H.R., "The Bar Simulation Method for the Calculation of Shear Lag in Multi-Cell and Continuous Box Girders," Proceedings, Institution of Civil Engineers, Part 2, Paper No. 8065, London, Dec. 1977, pp. 881-897.

139. Tang, M.C., "Analysis of Cable-Stayed Girder Bridges," Journal of the Structural Division, ASCE, Vol. 97, No. ST5, Proc. Paper 8116, May 1971, pp. 1481-1496. Errata to "Analysis of Cable-Stayed Girder Bridges," Journal of the Structural Division, ASCE, Vol. 98, No. ST5, Proc. Paper 8861, May 1972, p. 1191. Lazar, Benjamin E., discussion of "Analysis of Cable-Stayed Girder Bridges," by Man Chung Tang, Journal of the Structural Division, ASCE, Vol. 97, No. ST10, Proc. Paper 8411, Oct. 1971, pp. 2631-2632. Johnatwoski, J.J., discussion of "Analysis of Cable-Stayed Girder Bridges," by Man Chung Tang, Journal of the Structural Division, ASCE, Vol. 98, No. ST3, Proc. Paper 8752, Mar. 1972, pp. 770-774.
140. Tang, M.C., "Design of Cable-Stayed Girder Bridges," Journal of the Structural Division, ASCE, Vol. 98, No. ST8, Proc. Paper 9151, Aug. 1972, pp. 1789-1802. Closure to "Design of Cable-Stayed Girder Bridges," Journal of the Structural Division, ASCE, Vol. 99, No. ST7, Proc. Paper 9826, July 1973, pp. 1666-1667.
141. Timoshenko, S.P., Strength of Materials (Part I Elementary Theory and Problems), Third Edition, D. Van Nostrand Company, Inc., 1955.
142. Timoshenko, S.P., and Goodier, J.N., Theory of Elasticity, Third Edition, McGraw-Hill Kogakusha, Ltd.
143. Troitsky, M.S., and Lazer, B., "Model Analysis and Design of Cable Stayed Bridges," Proceedings, Institution of Civil Engineers, Paper No. 7375, London, Mar. 1971, pp. 439-464.
144. Troitsky, M.S., Cable-Stayed Bridges, Theory and Design, Crosby Lockwood Staples, London, 1977.
145. Tung, D.H.H., and Kudder, R.J., "Analysis of Cables as Equivalent Two-Force Members," Engineering Journal, American Institute of Steel Construction, Jan. 1968, pp. 12-19.
146. Vlasov, V.Z., Thin-Walled Elastic Beams (2nd Edition), Israel Program for Scientific Translation Ltd., Jerusalem, 1961.

147. Wagner, H., Verdrehung und Knickung von offenen Profilen (Torsion and Bending of Open Sections), Festschrift, 25 Jahr Technische Hochschule Danzig, 1929, p.239, or Luftfahrt-forschung, Vol.11, 1934, pp.174-180.
148. West, R., Recommendations on the Use of Grillage Analysis for Slab and Pseudo-Slab Bridge Decks, Coment and Concrete Association, London, Publication 46.017, Aug. 1973.
149. Wood, R.D., and Zienkiewicz, O.C., "Geometrically Nonlinear Finite element Analysis of Beams, Frames, Arches and Axisymmetric Shells," Computers and Structures, Vol. 7, 1977, pp. 725-735.
150. Wright, R.N., Abdel-Samad, S.R., and Robinson, A.R., "BEF Analogy for Analysis of Box Girders," Journal of the Structural Division, ASCE, Vol. 94, No. ST6, Proc. Paper 6025, July 1968, pp. 1719-1743.
151. Wright, R.N., Design of Box Girders of Deformable Cross Section, Highway Research Record, No. 295, 1970.
152. Zbirohowski-Koscia, K., Thin-walled Beams, Crosby Lockwood and Son, Ltd., 1967.
153. Zienkiewicz, O.C., and Too, J.M., "Reduced Integration Technique in General Analysis of Plates and Shells," Int. J. Numer. Meth. Engng., Vol. 3, 1971, pp. 275-290.
154. Zienkiewicz, O.C., The Finite Element Method in Engineering Science, McGraw-Hill Publishing Co., 1971.
155. Zienkiewicz, O.C., The Finite Element Method (3rd edition), McGraw Hill Book Company Ltd., London, 1977.
156. Zyl, S.F.V., Analysis of Curved Segmentally Erected Prestressed Concrete Box Girder Bridges, Ph.D. Thesis, University of California, Berkeley, June 1978.

## APPENDIX I COMPUTER PROGRAM - CUBAS

I.1 General introduction

This appendix is written as a user's guide for the computer program, CUBAS, which is based on the finite element displacement method covered in Chapters 4, 6 and 7. The scope and a general procedure of the program are briefly described in section I.2. Section I.3 provides users instructions for preparing input data, associated with the description of the variable names concerned. The interpretation of error diagnostics and illustrative examples for data input are presented in sections I.4 and I.5 respectively.

The program, compiled on a Honeywell computer, has been written using the Fortran IV language and contains a range of spatial one-dimensional finite elements and solution procedures. It is particularly suitable for the analysis of a variety of types of bridge structure during the design stage. The program incorporates facilities mainly for linear static stress analysis, yet the prediction of nonlinear effects in cable-stayed bridges, arising from large displacements, bending moment-axial force interaction and the catenary action of the inclined cables, is also included. The support node conditions may be restrained, restrained with prescribed displacements, or free. The load types available are concentrated point loads, gravity loading, temperature and uniformly distributed loads.

The data input is completely free-format and thus suitable for input from a terminal. It is, however, very easy to modify to accept formatted data input, as shown in the instructions. Some automatic data generation facilities are available, which enable considerably economy in data input. The program contains a set of error diagnostics which advise the user of improbable or wrong input. The results output are clear and self-explanatory. It should be borne in mind that all the

stress resultants output are referred to the positive faces of cross-sections. Units of output will be the same as those used for input.

The method of solving the load-deflection equations in CUBAS is the frontal technique (45), which has earned the reputation of being easy and inexpensive to use. The maximum size of problem which can be solved is governed by the maximum frontwidth specified with the value of 140 in the present program code. The actual frontwidth in an individual analysis is controlled by the order in which the elements are introduced for solution. Since CUBAS always solves the structure equations according to ascending element numbers, the user should number the element across the narrow direction of the structure to minimise the frontwidth.

The size of structure that can be analysed is expandable depending on the size of core storage of the computer being used. Typically, up to 250 elements and 350 nodes could be used to one analysis in the present program code.

### I.2 Scope and general procedure

The computer program, CUBAS, is available for the analysis of the following ten types of structures, which are identified by representative numbers:

- NTYPE = 1 plane or space truss
- 2 plane or space framework assembled by members having solid cross-sections
- 3 thin-walled assemblage with members having open or closed rigid cross-sections
- 4 articulated open or cellular bridge deck
- 5 straight single-spined box beam with deformable cross-sections
- 6 straight multi-spined box beam with deformable cross-sections

- 7 single-spined box beam curved in plan with deformable cross-sections
- 8 multi-spined box beam curved in plan with deformable cross-sections
- 9 cable-stayed bridge with main girder having rigid cross-sections
- 10 cable-stayed bridge with single-spined box girder having deformable cross-sections

There are six essential types of elements available in the CUBAS program for modelling a bridge structure. Each type of element is given an identifying three-digit number. The first digit indicates the number of nodes in an element, and the second one shows the degrees of freedom at each node. The final digit is five for cable elements or elements which are specially used for modelling the connecting plates between neighbouring boxes in a finite element-grillage analysis. For all other elements the final digit is zero. The available elements in the program are listed below:

- NETYPE = 230 two-node truss element
- 235 inclined cable elements with two side nodes
- 260 two-node solid beam element
- 265 transverse solid beam element with two side nodes
- 360 three-node solid beam element
- 365 three-node transverse solid beam element
- 370 three-node thin-walled beam element with rigid cross-sections
- 390 three-node thin-walled box beam element with deformable cross-sections

It is permissible in CUBAS to mix different types of elements together in an analysis.

The input data comprises: options, specifying problem type and output required, element numbers, node numbers, node coordinates, geometric and material properties for each element, support nodes and the loading etc. Reference should be made to Chapter 1 and Chapter 4 with regard to coordinate systems and sign conventions.

On processing the input data the general program (CUBAS) calls the submatrices for generation of the stiffness matrix and nodal forces. The stiffness matrix and the nodal forces are then modified in accordance with the support conditions.

Repeating this for all elements the program assembles the overall structure stiffness and forms and solves the governing equations of the structure for the load case specified. The reactions are then calculated and the results of both displacements and reactions are written out.

With displacements now known the program calls the subroutine for calculation of stress resultants and the subroutine for writing the stress resultants. For nonlinear analysis of cable-stayed bridges the residual force vector is then calculated and the above computing process is repeated until convergence requirements are satisfied.

A simplified flow chart of these operations is given in Fig. A.1.

### 1.3 Data input to CUBAS

Although specified input format will be indicated in the following instructions, the data input is completely free-format in the present program.

+ Optional data. Card is omitted if not required

\* Minimum data necessary.

\*1. Problem Card (I5) — One card

notes	columns	variable	entry
(1)	1-5	NPROB	Total number of problems to be solved in one run.

## Notes/

(1) This rerun facility can be used for the erection analysis of bridge structures, which could be carried on through some stages with different structural forms. It can also be used effectively for the non-linear analysis of cable-stayed bridges considering the effects of initial stress state. The first problem can then be solved as the initial state of the cable-stayed bridge.

\*2. Title Card (A80) — One card

notes	columns	variable	entry
(1)	1-80	ITITLE	Title of the problem - limited to 80 alphanumeric characters

## Notes/

(1) Begin each new data case with a new title card.

\*3. Option card (10I5) — One card

notes	columns	variable	entry
(1)	1-5	IOPTION(1)	Output intermediate computing results
	6-10	IOPTION(2)	Output displacements in local coordinate system
	11-15	IOPTION(3)	Output local displacements in each iterative process for the analysis of multi-spined box beams

16-20	IOPTION(4)	Output local displacements and stress resultants in each iterative process for the non-linear analysis of cable-stayed bridges
21-25	IOPTION(5)	Evaluate and output initial stress matrix for the non-linear analysis of cable-stayed bridges
26-30	IOPTION(6)	Consider the effects of initial stress state in the non-linear analysis of cable-stayed bridges
31-35	IOPTION(7)	Input directly the initial displacement vector for the non-linear analysis of cable-stayed bridges. Normally this code should be taken as zero.
36-40	IOPTION(8)	Carry out the iterative process for considering the interaction between distortion and bending-torsion in the analysis of single-spined box beams curved in plan
41-45	IOPTION(9)	Input node coordinates to be references to a global cylindrical system (R,Y, $\theta$ )
46-50	IOPTION(10)	Input prescribed displacements at the support nodes

Notes 1

(1) EQ.0 no execution; EQ.1 optional execution.

\*4. Structure Type Card (I5) — One card

notes	columns	variable	entry
(1)	1-5	NTYPE	Identifying number (1-10) for the structure considered

## Notes/

(1) The representation of the number can be referred to the description in section I.2.

\*5. Control Card (16I5) — One card

notes	columns	variable	entry
(1)	1-5	NOLIN	Analysis type code: EQ.0; linear analysis EQ.1; non-linear analysis
(2)	6-10	LCASE	Total number of different loading cases to be analysed
(3)	11-15	NPOIN	Total number of nodal points in the model
(4)	16-20	NVFIX	Total number of restrained boundary nodes, where one or more degrees of freedom are all restrained with reference to the global axes
(5)	21-25	LVFIX	Total number of support nodes restrained relative to the local axes
(6)	26-30	NDOFN	Number of degrees of freedom per node
(7)	31-35	NTRUS	Total number of truss and/or cable elements
	36-40	NSOLB	Total number of solid beam elements
	41-45	NTHIN	Total number of thin-walled beam elements

	51-55	NTRAN	Total number of transverse solid beam elements
(8)	56-60	NMATS	Total number of differential material types
(9)	61-65	NSECS	Number of individual nodal sections having different sectional properties
(10)	66-70	NBOXS	Number of deformable box sections having different sectional properties
(11)	71-75	NDIAP	Number of intermediate solid diaphragms
(12)	76-80	MAXCARD	Maximum number of cards necessary to be input for each data case.

## Notes/

- (1) Non-linear analysis is only available for the cable-stayed bridges.
- (2) The total number of load cases to be solved for provided that the structural geometry remains unchanged. The element stiffness need not be recomputed for each additional loading case.
- (3) Nodes are labeled with integers ranging from "1" to the total number of nodes in the system, "NPOIN". The ordering of nodal numbering is irrelevant. The program exists with diagnostic message if NPOIN.LE.0 or NPOIN.GT.350.
- (4) This includes all nodes that are supported in the structure considered.
- (5) This includes only the nodes that are restrained corresponding to the specified local axes.
- (6) If different types of element are mixed together in the analysis, NDOFN should be input as the maximum one.
- (7) Elements are assigned integer labels ranging from "1" to the total number of elements, NELEM, which should be the sum of the elements in each group, i.e.,  

$$NELEM = NTRUS + NSOLB + NTHIN + NBSBE + NTRAN.$$

Illegal references are: NELEM.LE.0 or NELEM.GT.225.

- (8) Different materials are numbered with integers ranging from "1" to the total number of different materials, NMATS.
- (9) All the nodal sections are arranged into different groups, in which sectional properties are the same. They are assigned integer labels ranging from "1" to the total number of section groups, NSECS.
- (10) NBOXS should be always less than or equal to NSECS, and the individual deformable box sections should always be labeled following all the other rigid section groups.
- (11) Support diaphragms and bracings are not included.
- (12) MAXCARD is a program testing parameter which allows the user to test if the number of input cards is correct. The maximum cards can be calculated by the formula:

$$\begin{aligned} \text{MAXCARD} = & \text{NCARD1} + (\text{NELEM}-\text{NCARD2}) + (\text{NPOIN}-\text{NCARD3}) + (\text{NVFIX}-\text{NCARD4}) \\ & + (2\text{NSECS}+\text{NBOXS}-\text{NCARD5}) + (\text{NUELP}-\text{NCARD6}) + (\text{NPOIN}-\text{NCARD7}) \end{aligned}$$

where, NCARD1 is the actual number of input cards for one problem not including the first problem card,

NCARD2 is the actual number of element data cards for one problem,

NCARD3 is the actual number of node data cards for one problem,

NCARD4 is the actual number of prescribed displacement cards for one problem,

NCARD5 is the actual number of sectional property cards for one problem,

NCARD6 is the actual number of distributed load cards for one problem,

NCARD7 is the actual number of temperature cards for one problem.

Note that each two successive cards for the initial displacement data cards, the distributed load cards and the concentrated load cards are accounted as a single card in the above formula.

\*6. Load Control Cards (5I5) — One card for each loading case. Total of LCASE cards (see Card Set 5)

notes	columns	variable	entry
(1)	1-5	IULOD	Loading case number
	6-10	NGRAV(IULOD)	Gravity loading control parameter 0 no gravity loads to be considered 1 gravity loads to be considered
	11-15	NUPOL(IULOD)	Number of applied concentrated point loads, and zero (0) implies no applied concentrated loads to be input
	16-20	NUELP(IULOD)	Number of elements subjected to uniformly distributed loads, and zero (0) implies no distributed loads to be input
	21-25	NITHER(IULOD)	Thermal loading control parameter 0 no thermal loading to be considered 1 thermal loading to be considered

Notes/

(1) Loading cases are assigned integer labels ranging from "1" to the total number of loading cases, LCASE. The program terminates reading corresponding loading data when a zero number is encountered.

\*7. Element Data Cards (2I3,I4,2(I3,I2), 9I5,F15.0) — One card for each element. If there is no data generating process to be incorporated, total of NELEM cards (see Card Set 5)

notes	columns	variable	entry
(1)	1-3	NUMEL	The first element number of a series of elements to be generated
(2)	4-6	MUMEL	The last element number of a series of elements to be generated

(3)	7-10	KE1	Difference between element numbers of the series of elements to be generated
(4)	11-13	NETYP (NUMEL)	Element type number
(5)	14-15	NERLE (NUMEL)	Moment releasing option parameter 0 no member end moment releasing procedure to be incorporated 1 member end moment releasing procedure to be incorporated
	16-18	MATNO (NUMEL)	Material property number
(6) '	19-20	NUBOX (NUMEL)	Identifying number for individual box-spines
(7)	21-25	LNODS (NUMEL,1)	1st nodal connection number
	26-30	LNODS (NUMEL,2)	2nd nodal connection number
	31-35	LNODS (NUMEL,3)	mid-node number
	36-40	KE2	Difference between node numbers of the series of elements to be generated
(8)	41-45	NGEOM (NUMEL,1)	Sectional property number at the 1st node
	46-50	NGEOM (NUMEL,2)	Sectional property number at the 2nd node
	51-55	NGEOM (NUMEL,3)	Sectional property number at the mid-node
	56-60	KE3	Difference between sectional property numbers of the series of elements to be generated.
	61-65	NORIE (NUMEL)	Element orientation number 1 the principal planes yz of the element are parallel to the YZ plane 2 the principal planes xz of the element are parallel to the XZ plane 3 the principal planes yz of the element are parallel to the XY plane 4 the element orientates in the three-dimensional space arbitrarily

66-80      TENFO(NUMEL)      Initial axial force existing in the element

Notes/

- (1) The input order of the element data cards can be arbitrary, however, all the elements in the model must be specified.
- (2) NUMEL = MUMEL implies no data generation to be operated.
- (3) If a series of elements occurs in which each element number  $(NUMEL)_i$  is KE1 greater than the previous number  $(NUMEL)_{i-1}$  i.e.  $(NUMEL)_i = (NUMEL)_{i-1} + KE1$  only the element data card for the first element in the series need be given as input, provided the
  - (i) nodal connection number
  - (ii) sectional property number
 can be generated following the same sequence, and the
  - (iii) element type number
  - (iv) moment releasing code
  - (v) material property number
  - (vi) box-spine identifying number
  - (vii) element orientation code
  - (viii) initial axial force
 are the same for each element in the series.
- (4) Each group of elements must be specified by a three-digit identifying number, see section I,2.
- (5) The moment releasing information is specifically for the transverse grillage members in the analysis of articulated bridge decks.
- (6) Each box-spine between diaphragms should be given a unique identifying number starting from "1".
- (7) The nodal point numbers of the series are
 
$$LNODS(i,1) = LNODS(i-1,1) + KE2$$

$$LNODS(i,2) = LNODS(i-1,2) + KE2$$

$$LNODS(i,3) = LNODS(i-1,3) + KE2.$$

(8) The sectional property numbers of the series are

$$\text{NGEOM}(i,1) = \text{NGEOM}(i-1,1) + \text{KE3}$$

$$\text{NGEOM}(i,2) = \text{NGEOM}(i-1,2) + \text{KE3}$$

$$\text{NGEOM}(i,3) = \text{NGEOM}(i-1,3) + \text{KE3}$$

+8. Transverse Beam Element Cards (8I5, 4F10.0)— One card for each transverse solid beam element. Total of NTRAN cards (see Card Set 5), and omit this card set if NTRAN = 0.

notes	columns	variable	entry
(1)	1-5	IUTRA	Sequence number
(2)	6-10	NETRA(IUTRA)	Transverse solid beam element number
(3)	11-15	NODEL(IUTRA,1)	1st nodal connection number of the transverse beam element
	16-20	NODEL(IUTRA,2)	Box beam element number associated with the transverse beam element at its 1st side node
	21-25	NODEL(IUTRA,3)	Node identifying code of the box beam element associated with the transverse beam element at its 1st side node -1 1st side node 0 mid-node 1 2nd side node
	26-30	NODEL(IUTRA,4)	2nd nodal connection number of the transverse beam element
	31-35	NODEL(IUTRA,5)	Box beam element number associated with the transverse beam element at the 2nd side node
	36-40	NODEL(IUTRA,6)	Node identifying code of the box beam element associated with the transverse beam element at its 2nd side node.

(4)	41-50	XYTRA(IUTRA,1)	x-ordinate of the 1st side node of the transverse beam element
	51-60	XYTRA(IUTRA,2)	y-ordinate of the 1st side node of the transverse beam element
	61-70	XYTRA(IUTRA,3)	x-ordinate of the 2nd side node of the transverse beam element
	71-80	XYTRA(IUTRA,4)	y-ordinate of the 2nd side node of the transverse beam element

## Notes/

- (1) the Sequence number starts from "1" and ends to "NTRAN", however, the input order in the card set can be arbitrary.
- (2) The transverse solid beam elements include only those representing connecting plates between neighbouring boxes.
- (3) These informations indicate the connecting positions between the transverse solid beam element and the neighbouring boxes
- (4) The coordinates are all referred to the local coordinate system of the box sections where the additional distortional forces from the transverse beam element are incorporated, i.e., they are the local coordinates of the box top corner points.

\*9. Node Data Cards (2I5, 7F10.0)—One card for each node, if there is no generating procedure; or two sequence cards for a series of nodes

notes	columns	variable	entry
(1)	1-5	NUMPO	Node number
(2)	6-10	KN	Total number of intervals in the series, and zero implies no generation to be involved
(3)	11-20	COORD(NUMPO,1)	X(or R) -ordinate
	21-30	COORD(NUMPO,2)	Y -ordinate
	31-40	COORD(NUMPO,3)	Z(or $\theta$ ) -ordinate (degrees)

- |     |       |                |   |
|-----|-------|----------------|---|
| (4) | 41-50 | COORD(NUMPO,4) | X(or R) -ordinate of the reference node at the mid-point of the bottom flange of the box-section          |
|     | 51-60 | COORD(NUMPO,5) | Y -ordinate of the reference node at the mid-point of the bottom flange of the box-section                |
|     | 61-70 | COORD(NUMPO,6) | Z(or $\theta$ ) -ordinate of the reference node at the mid-point of the bottom flange of the box-section. |
| (5) | 71-80 | RADIU(NUMPO)   | Radius of the in plan curvature at the position of the node   |

## Notes/

(1) Node data cards need not be input in node-order sequence; eventually, however, all nodes in the integer set {1,NPOIN} must be defined.

(2) Node data for a series of nodes

{NUMPO, NUMPO+1xKN1,....,NUMPO+(KN-1)xKN1, MUMPO}

may be generated from information given on two (2) cards in sequence:

Card 1/NUMPO,KN,COORD(NUMPO,1),....,RADIU(NUMPO)/

Card 2/MUMPO,KN,COORD(MUMPO,1),....,RADIU(MUMPO)/

KN1 is the mesh generation parameter given by

$$KN1 = \frac{MUMPO - NUMPO}{KN}$$

The first generated node is NUMPO + 1 x KN1; the second generated node is NUMPO + 2 x KN1, etc. Generation continues until the node number MUMPO is established. Note that the node difference MUMPO-NUMPO must be evenly divisible by KN.

Intermediate node coordinates are found by linear interpolation between NUMPO and MUMPO at equal intervals.

- (3) A special cylindrical coordinate system is allowed for the global description of nodal point locations. If a "1" is entered in card column forty-five (45) of the option card (see Card Set 3), then the entries given in cc 11-70 are taken to be references to a global (R,Y, $\theta$ ) system rather than to the standard (X,Y,Z) system. The program converts cylindrical coordinate references to cartesian coordinates using the formulae:

$$X = -R\sin\theta$$

$$Y = Y$$

$$Z = R\cos\theta$$

Cylindrical coordinate input is merely a user convenience for locating nodes in the standard (X,Y,Z) system, and no other references to the cylindrical system are implied; i.e., boundary condition specifications, output displacement components, etc. are referred to the (X,Y,Z) system.

- (4) If the element orientation number equals 1-3, the coordinates of the reference node can be specified arbitrarily.
- (5) If the element axis is curved in space, the radius of curvature should be taken as the component to be reference to the local x-axis of the nodal section.

\*10. Restrained Node Cards (12I5)—One card for each restrained node.

Total of NVFIX cards (see Card Set 5)

notes	columns	variable	entry
(1)	1-5	NUFIX	Sequence number
	6-10	NOFIX(NUFIX,1)	Restrained node number
(2)	11-15	NOFIX(NUFIX,2)	Reference element number indicating restrained direction

(3)	16-20	IFPRE(NUFIX,1)	X(or x)-translation boundary condition code
	21-25	IFPRE(NUFIX,2)	Y(or y)-translation boundary condition code
	26-30	IFPRE(NUFIX,3)	Z(or z)-translation boundary condition code
	31-35	IFPRE(NUFIX,4)	X(or x)-rotation boundary condition code
	36-40	IFPRE(NUFIX,5)	Y(or y)-rotation boundary condition code
	41-45	IFPRE(NUFIX,6)	Z(or z)-rotation boundary condition code
	46-50	IFPRE(NUFIX,7)	Torsional warping condition (rate of twist) code
	51-55	IFPRE(NUFIX,8)	Distortion condition (distortional angle) code
	56-60	IFPRE(NUFIX,9)	Distortional warping condition (rate of distortion) code

## Notes/

- (1) The sequence number starts from "1" and ends to "NUFIX", however, the input order in the card set can be arbitrary.
- (2) If reference element number equals zero (0), this implies that the boundary condition specifications are taken to be references to the global (X,Y,Z) system. Whilst, the restrained conditions are taken to be references to the local (x,y,z) system specified by the reference element axis.
- (3) Boundary condition codes can only be assigned the following values (M = 1, 2, ..., 9):
  - IFPRE(NUFIX,M)=0; unspecified (free) displacement (or rotation) component
  - IFPRE(NUFIX,M)=1; deleted (fixed) displacement (or rotation) component, or prescribed displacement component.

The maximum number of equilibrium equations is always less than the largest degree of freedom per node times the total number of nodes in the model.

- +11. Prescribed Displacement Cards (I5, 6F10.0, 3F5.0)—One card is required for each restrained node having any prescribed displacement components.

notes	columns	variable	entry
(1)	1-5	MUFIX	Restrained node number
(2)	6-15	PRESU(MUFIX,1)	Specified displacement along the X-(or x-) axis
	16-25	PRESU(MUFIX,2)	Specified displacement along the Y-(or y-) axis
	26-35	PRESU(MUFIX,3)	Specified displacement along the Z-(or z-) axis
	36-95	PRESU(MUFIX,4)	Specified rotation about the X-(or x-) axis
	46-55	PRESU(MUFIX,5)	Specified rotation about the Y-(or y-) axis
	56-65	PRESU(MUFIX,6)	Specified rotation about the Z-(or z-) axis
	66-70	PRESU(MUFIX,7)	Specified rate of twist
	71-75	PRESU(MUFIX,8)	Specified distortional angle
	76-80	PRESU(MUFIX,9)	Specified rate of distortion

Notes/

- (1) Only the restrained nodes having any non-zero prescribed displacement components need be specified by the input cards.
- (2) For any unspecified displacement components zero values should be put in the corresponding columns.

\*12. Material Cards (I5, 5F15.0)—One card for each different material.

Total of NMATS cards (see Card Set 5)

notes	columns	variable	entry
(1)	1-5	NUMAT	Material identification number
	6-20	ELMAT(NUMAT,1)	Young's modulus of elasticity, E
	21-35	ELMAT(NUMAT,2)	Shear modulus of elasticity, G
	36-50	ELMAT(NUMAT,3)	Poisson's ratio, $\nu$
	51-65	ELMAT(NUMAT,4)	Weight density (used to calculate gravity loads), $\rho$
	66-80	ELMAT(NUMAT,5)	Coefficient of thermal expansion (used to calculate thermal loads) $\alpha$

Notes/

- (1) The material identification number starts from "1" and ends to "NMATS", however, the input order in the card set can be arbitrary.

\*13. Sectional Property Cards—Maximum three cards are required to be input in sequence for each unique set of sectional properties

Card 1 (I3, I2, 5F15.0):

notes	columns	variable	entry
(1)	1-3	NUSEC	Sectional property number
(2)	4-5	IDENT	Input specified number
			0 The following two cards can be omitted
			1 The following second card must be input
	6-20	GPROP(NUSEC,1)	Cross-sectional area, A
	21-35	GPROP(NUSEC,2)	Bending moment of inertia, $I_{xx}$
	36-50	GPROP(NUSEC,3)	Bending moment of inertia, $I_{yy}$
	51-65	GPROP(NUSEC,4)	Torsional moment of inertia, $J_T$
	66-80	GPROP(NUSEC,5)	Torsional warping moment of inertia, $J_T$

Card 2 (I5, 6F5.0, 2F15.0)

notes	columns	variable	entry
	1-5	NUSEC	Sectional property number
(3)	6-10	PARAM(NUSEC,1)	Shear-deformation factor, $F_{S,x}$
	10-15	PARAM(NUSEC,2)	Shear-deformation factor, $F_{S,y}$
	16-20	PARAM(NUSEC,3)	Torsional warping shear parameter, $\mu_t$
	21-25	PARAM(NUSEC,4)	Ratio of the width of the bottom flange to the top flange, $\alpha_d = b_b/b_t$
	26-30	PARAM(NUSEC,5)	Distortional distribution factor, $\zeta_d$
	31-35	PARAM(NUSEC,6)	Initial curvature multiplication factor, $\mu_d$
(4)	36-50	XYSHE(NUSEC,1)	local x-ordinate of the shear centre
	51-65	XYSHE(NUSEC,2)	local y-ordinate of the shear centre

Card 3 (I5, 2F15.0)

notes	columns	variable	entry
(5)	1-5	NUSEC	Sectional property number
	6-20	GPROP(NUSEC,6)	Distortional second moment of area, $J_d$
	21-35	GPROP(NUSEC,7)	Distortional warping moment of inertia, $J_{\Pi}$

## Notes/

- (1) One card is necessary for each different section, and total of NSECS cards (see Card Set 5)
- (2) Input specified number equals zero implies that the sectional properties specified by the following two cards are the same as those prescribed by the previous card set.
- \* (3) Shear-deformation factors are used for evaluating the effective shear areas; torsional warping shear parameter is for the consideration of the deformational influence due to the warping shear stresses; ratio  $\alpha_d$  is used for the calculation of distortional force; and  $\zeta_d$  and  $\mu_d$  are the effects to the

distortional force due to side cantilevers and initial in plan curvature respectively.

- (4) Shear forces and torsional moment are with reference to the shear centre of the section.
- (5) The third data card need be input only when  
 NUSEC.GE.(NSECS-NBOXS + 1).

+14. Diaphragm Data Cards (3I5, 4F15.0) — One card per diaphragm

Total of NDIAP cards, and if NDIAP = 0 in Card Set 5 omit this set.

notes	columns	variable	entry
(1)	1-5	NUDIA	Diaphragm number
	6-10	NODIP(NUDIA)	Node number where diaphragm is located
	11-15	MADIP(NUDIA)	Material type number
	16-30	DIAPH(NUDIA,1)	Top-width of the diaphragm
	31-45	DIAPH(NUDIA,2)	Bottom-width of the diaphragm
	46-60	DIAPH(NUDIA,3)	Height of the diaphragm
	61-75	DIAPH(NUDIA,4)	Thickness of the diaphragm

Notes/

- (1) The diaphragm number starts from "1" and ends to "NDIAP", however, the input order in the card set can be arbitrary.

+15. Initial Displacement Data Cards (I5, 7F15.0) — Two successive cards per node. Total of NPOIN independent cards, and if IOPTION(7) = 0 in Card Set 3 omit this set.

notes	columns	variable	entry
(1)	1-5	IPOIN	Node number
	6-20	ASDIS(1)	Displacement component along the X-axis
	21-35	ASDIS(2)	Displacement component along the Y-axis
	36-50	ASDIS(3)	Displacement component along the Z-axis
	51-65	ASDIS(4)	Rotation component about the X-axis

66-80	ASDIS(5)	Rotation component about the Y-axis
81-95	ASDIS(6)	Rotation component about the Z-axis
96-110	ASDIS(7)	Rate of the twisting angle

## Notes/

- (1) These data cards are necessary only when the option code, "IOPTION(7)" is taken as unit (1), see Card Set 3. The node numbers should be input in ascending order.

+16. Distributed Load Cards (2I3, I4, 2I5, 9F15.0) — Two successive cards for each elemental load. If there is no generating procedure to be involved, total of NUELP(ICASE) independent cards. Omit this card set if NUELP(ICASE) = 0.

notes	columns	variable	entry
(1)	1-3	IUELP	First sequence number
	4-6	JUELP	Last sequence number
(2)	7-10	KN	Number of intervals, zero(0) implies no data generation to be involved
	11-15	LOELE(IUELP)	First element number in the series
	16-20	LOELE(JUELP)	Last element number in the series
(3)	21-35	PLDIS(IUELP,1)	Distributed force component per unit length, $p_x$
	36-50	PLDIS(IUELP,2)	Distributed force component per unit length, $p_y$
	51-65	PLDIS(IUELP,3)	Distributed force component per unit length, $p_z$
	65-80	PLDIS(IUELP,4)	Distributed moment component per unit length, $m_{x,ext}$
	81-95	PLDIS(IUELP,5)	Distributed moment component per unit length, $m_{y,ext}$
	96-110	PLDIS(IUELP,6)	Distributed moment component per unit length, $m_{z,ext}$

111-125	PLDIS(IUELP,7)	Distributed torsional bimoment per unit length, $b_T$
126-140	PLDIS(IUELP,8)	Distributed distortional force per unit length, $m_d$
141-155	PLDIS(IUELP,9)	Distributed distortional bimoment per unit length, $b_{II}$

## Notes/

- (1) Elemental load sequence number starts from "1" and ends to "NUELP(ICASE)". Elemental load cards need not be input in element-order sequence; eventually, however, all loads in the set must be defined.
- (2) A series of elements having the same distributed loads may be generated from information given on the data card. The generation increments are given by

$$\text{INCRE1} = \frac{\text{JUELP} - \text{IUELP}}{\text{KN}},$$

and

$$\text{INCRE2} = \frac{\text{LOELE}(\text{JUELP}) - \text{LOELE}(\text{IUELP})}{\text{KN}}$$

Generation continues until the last sequence number JUELP and the last element LOELE(JUELP) in the series are established. Note that the sequence number difference and the element difference must be evenly divisible by KN.

- (3) The distributed components per unit length are all related to the local coordinate system of the cross-section, and are assumed to be constant along the element.

+17. Concentrated Load Cards (2I5, F10.0, 9F15.0)—Two successive cards for each concentrated load. Total of NUPOL(ICASE) independent cards. If NUPOL(ICASE) = 0 in Card Set 6 omit this set.

notes	columns	variable	entry
(1)	1-5	JUPOL	Sequence number

	6-10	NUPEL(JUPOL)	Element number subjected to the concentrated load
	11-20	PZETA(JUPOL)	Point of application of the concentrated load defined by the natural coordinate $\zeta$
	21-35	WIDTH(JUPOL)	Top-width of the box section
(2)	36-50	PCOMP(JUPOL,1)	Load component in X-direction
	51-65	PCOMP(JUPOL,2)	Load component in Y-direction
	65-80	PCOMP(JUPOL,3)	Load component in Z-direction
	81-95	PCOMP(JUPOL,4)	Moment component about X-axis
	96-110	PCOMP(JUPOL,5)	Moment component about Y-axis
	111-125	PCOMP(JUPOL,6)	Moment component about Z-axis
	126-140	XPCOR(JUPOL)	local x-ordinate of the point of application of the concentrated load
	141-155	YPCOR(JUPOL)	local y-ordinate of the point of application of the concentrated load

## Notes/

- (1) The sequence number starts from "1" and ends to "NUPOL(ICASE)", however, the input order in the card set can be arbitrary.
- (2) Any point load applied on an element is specified in terms of its global components. The point of application of the concentrated load is defined by the natural coordinate  $\zeta$  and the local coordinates  $x$  and  $y$ .

+18. Temperature Cards (3I5, F15.0)— One card for each node. Total of NPOIN cards, if there is no generating procedure to be involved. If NTHET(ICASE) = 0 in Card Set 6 omit this set.

notes	columns	variable	entry
(1)	1-5	IPOIN	First node number in the series
	6-10	JPOIN	Last node number in the series
	11-15	KN	Number of intervals in the series, zero(0)

implies no generation to be involved.

16-30      TEMPE(IPOIN)      Temperature at node

Notes/

- (1) A series of nodes having the same values of temperature may be generated by the increment:

$$\text{INCRE} = \frac{\text{JPOIN} - \text{IPOIN}}{\text{KN}}$$

Generation continues until the last node number in the series are established. Note that the node difference must be evenly distributed to KN.

I.4 Error diagnostics

Any errors which are detected are signalled by the printing of an error number and an associated number, which indicates how many times the particular error has been diagnosed. The interpretation of each error number is as indicated below.

Diagnosed by Subroutines CHECK1 and CHECK2

Error Label	Interpretation
1	The specified total number of problems, NPROB, in the analysis is less than or equal to zero.
2	The structure type number, NTYPE, is not specified as one of the integers between 1 to 10.
3	The analysis type code, NOLIN, is not specified as either 0 or 1.
4	The specified total number of loading cases, LCASE, is less than or equal to zero, or greater than the maximum possible loading cases (50) defined in the program.
5	The specified total number of nodes, NPOIN, in the structure is less than or equal to zero, or greater than the possible maximum nodes (350) coded in the program.

Error Label	Interpretation
6	The sum of nodes per element over all the elements in the structure is less than the specified node number, NPOIN.
7	The specified restrained nodes, NVFIX, have a number less than 1 or greater than the specified maximum value, NPOIN.
8	The number of support nodes restrained relative to the local axes, LVFIX, is greater than the specified maximum value, NVFIX.
9	The moment releasing option parameter, NERLE, equals 1, but the element type number, NETYP, is not chosen as 360.
10	The specified maximum number of degrees of freedom per node, NDOFN, in the structure is less than 3 or greater than 9.
11	A total of x elements whose numbers of nodes/element implied in the element type numbers, NETYP, are not equal to either 2 or 3.
12	The maximum number of degrees of freedom per node implied in the element type numbers, NETYP, is not equal to the specified value, NDOFN.
13	The specified total number of input cards, MAXCARD, is not compatible to the actual input cards.
14	The total number of elements, NELEM, is less than or equal to zero or greater than the possible maximum elements (225) specified in the program.
15	The specified total number of different materials, NMATS, is less than or equal to zero or greater than the possible maximum different materials (100) specified in the program.
16	The specified total number of different sections, NSECS, is less than or equal to zero or greater than the specified maximum value, NPOIN, or greater than the possible maximum different sections

(100) limited in the program.

- 17 The specified total number of intermediate diaphragms, NDIAP, is greater than the specified maximum value, NPOIN, or greater than the possible maximum value (150) coded in the program.
- 18 The number of different deformable box-sections, NBOXS, is greater than the specified total, NSECS.
- 19 The total number of truss and/or cable elements, identified by type number 230 or 235, is not equal to the specified value, NTRUS.
- 20 The total number of solid beam elements, identified by type number either 260 or 360, is not equal to the specified value, NSOLB.
- 21 The total number of transverse solid beam elements, identified as either 265 or 365, is not equal to the specified value, NTRAN.
- 22 The total number of thin-walled beam elements, identified by 370, is not equal to the specified value, NTHIN.
- 23 The total number of thin-walled box beam elements, identified by 390, is not equal to the specified value, NBSBE.
- 24 A total of  $x$  identical nodal coordinates have been detected, i.e.  $x$  nodes have coordinates which are identical to those of one or more of the remaining nodes.
- 25 A total of  $x$  material identifying numbers are less than or equal to zero or greater than the specified value, NMATS.
- 26 A total of  $x$  nodal section identifying numbers are less than or equal to zero or greater than the specified value, NSECS.
- 27 A total of  $x$  elements whose orientation numbers are specified as 1, but their principal planes  $yz$  are not parallel to the  $YZ$  plane.
- 28 A total of  $x$  elements whose orientation numbers are specified as 2, but their principal planes  $xz$  are not parallel to the  $XZ$  plane.

Error Label	Interpretation
29	A total of x elements whose orientation numbers are specified as 3, but their principal planes yz are not parallel to the XY plane.
30	A total of x nodal connection numbers are negative or equal to zero.
31	A total of x nodal connection numbers are greater than the specified maximum value, NPOIN.
32	A total of x repetitions of node numbers within individual elements have been detected.
33	A total of x nodes exists in the list of nodal points which do not appear anywhere in the list of element nodal connection numbers.
34	Non-zero coordinates have been specified for a total of x nodes which do not appear in the list of element nodal connection numbers.
35	A total of x node numbers which do not appear in the element nodal connections list have been specified as restrained nodal points.
36	The largest frontwidth encountered in the problem has exceeded the maximum value specified in solution subroutines of the program.
37	A total of x restrained nodal points have numbers less than or equal to zero or greater than the specified maximum value, NPOIN.
38	A total of x restrained nodal points at which all the fixity codes are less than or equal to zero have been detected.
39	A total of x repetitions in the list of restrained nodal points have been detected.
40	The total number of support nodes restrained with respect to the local axes does not equal the specified value, LVFIX.

## I.5 Data input examples

### I.5.1 A simply-supported single-box girder bridge curved in plan

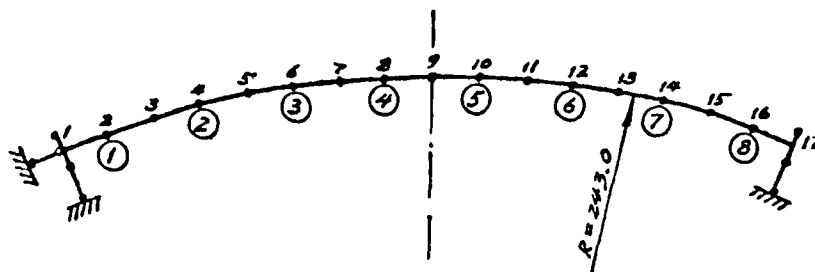
The example shown below has been described as a numerical example in Chapter 5. The curved girder is idealized using eight thin-walled box beam elements. The support conditions at node 1 are restrained in the tangent and radius directions and in the Y direction. The support conditions at node 17 are restrained only in the radius and Y directions. Both of the two restrained nodes are restrained against rotation about the tangent to the curved longitudinal axis. Also rotations about the vertical axes and distortions are restrained.

The curved girder is subjected to a single concentrated 1 kip (4.45 kN) load at midspan over the outer web. Data input:

```

10  1
20  ANALYSIS OF A SIMPLY-SUPPORTED BOX BEAM CURVED IN PLAN
30  0 1 1 0 0 0 0 1 1 0
40  7
50  0 1 17 2 2 9 0 0 0 8 0 1 5 5 0 51
60  1 0 1 0 0
70  1 2 1 390 0 1 1 1 3 2 2 1 1 1 0 2 0.0
80  3 4 1 390 0 1 1 5 7 6 2 1 3 2 2 2 0.0
90  5 6 1 390 0 1 1 9 11 10 2 5 3 4 -2 2 0.0
100 7 8 1 390 0 1 1 13 15 14 2 1 1 1 0 2 0.0
110 1 1 243.0 0.0 101.46 243.0 0.0 101.46 243.0
120 17 1 243.0 0.0 78.54 243.0 0.0 78.54 243.0
130 1 1 1 1 1 1 0 1 1 0 1 0
140 2 17 8 1 1 0 0 1 1 0 1 0
150 1 432000.0 187826.0869 0.15 0.150 0.00001
160 1 1 24.89924 89.04434 1433.99317 183.43894 781.07360
170 1 1.36 3.60 0.40919 0.71429 0.53430 0.48858 0.0 -0.35239
180 1 0.030270596 491.6527893
190 2 0 24.89924 85.13712 1433.99317 183.43894 781.07360
200 3 0 24.89924 85.13712 1433.99317 183.43894 781.07360
210 4 0 24.89924 85.13712 1433.99317 183.43894 781.07360
220 5 0 24.89924 85.13712 1433.99317 183.43894 781.07360
230 1 4 1.0 14.0 0.0 1.0 0.0 0.0 0.0 0.0 -7.0 -1.49696

```



I.5.2 Simply-supported twin-box beam model

This data input example has been described in detail in Chapter 8.

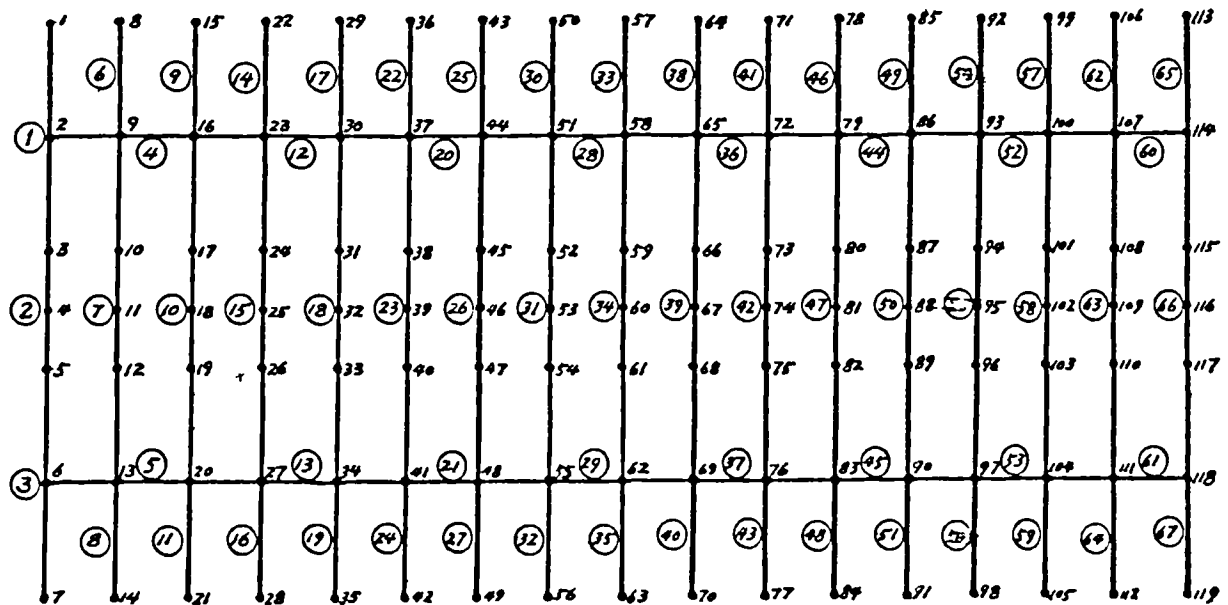
Data input:

```

10 1
20 ANALYSIS OF A TWIN-BOX BEAM WITH TRAPEZOIDAL SECTIONS
30 0 1 0 0 0 0 0 0 0 0
40 6
50 0 1 119 4 0 9 0 34 0 16 17 1 9 5 0 241
60 1 0 1 0 0
70 1 3 2 360 0 1 0 1 3 2 4 1 1 1 0 2 0.0
80 6 8 2 360 0 1 0 8 10 9 4 3 3 3 0 2 0.0
90 9 11 2 360 0 1 0 15 17 16 4 3 3 3 0 2 0.0
100 14 16 2 360 0 1 0 22 24 23 4 3 3 3 0 2 0.0
110 17 19 2 360 0 1 0 29 31 30 4 3 3 3 0 2 0.0
120 22 24 2 360 0 1 0 36 38 37 4 3 3 3 0 2 0.0
130 25 27 2 360 0 1 0 43 45 44 4 3 3 3 0 2 0.0
140 30 32 2 360 0 1 0 50 52 51 4 3 3 3 0 2 0.0
150 33 35 2 360 0 1 0 57 59 58 4 3 3 3 0 2 0.0
160 38 40 2 360 0 1 0 64 66 65 4 3 3 3 0 2 0.0
170 41 43 2 360 0 1 0 71 73 72 4 3 3 3 0 2 0.0
180 46 48 2 360 0 1 0 78 80 79 4 3 3 3 0 2 0.0
190 49 51 2 360 0 1 0 85 87 86 4 3 3 3 0 2 0.0
200 54 56 2 360 0 1 0 92 94 93 4 3 3 3 0 2 0.0
210 57 59 2 360 0 1 0 99 101 100 4 3 3 3 0 2 0.0
220 62 64 2 360 0 1 0 106 108 107 4 3 3 3 0 2 0.0
230 2 2 0 365 0 1 0 3 5 4 0 2 2 2 0 2 0.0
240 7 7 0 365 0 1 0 10 12 11 0 4 4 4 0 2 0.0
250 10 15 5 365 0 1 0 17 19 18 7 4 4 4 0 2 0.0
260 18 23 5 365 0 1 0 31 33 32 7 4 4 4 0 2 0.0
270 26 31 5 365 0 1 0 45 47 46 7 4 4 4 0 2 0.0
280 34 39 5 365 0 1 0 59 61 60 7 4 4 4 0 2 0.0
290 42 47 5 365 0 1 0 73 75 74 7 4 4 4 0 2 0.0
300 50 55 5 365 0 1 0 87 89 88 7 4 4 4 0 2 0.0
310 58 63 5 365 0 1 0 101 103 102 7 4 4 4 0 2 0.0
320 66 66 0 365 0 1 0 115 117 116 0 2 2 2 0 2 0.0
330 4 12 8 390 0 1 1 2 16 9 14 5 5 5 0 2 0.0
340 20 28 8 390 0 1 1 30 44 37 14 5 7 6 2 2 0.0
350 36 44 8 390 0 1 1 58 72 65 14 9 7 8 -2 2 0.0
360 52 60 8 390 0 1 1 86 100 93 14 5 5 5 0 2 0.0
370 5 13 8 390 0 1 2 6 20 13 14 5 5 5 0 2 0.0
380 21 29 8 390 0 1 2 34 48 41 14 5 7 6 2 2 0.0
390 37 45 8 390 0 1 2 62 76 69 14 9 7 8 -2 2 0.0
400 53 61 8 390 0 1 2 90 104 97 14 5 5 5 0 2 0.0
410 65 67 2 360 0 1 0 113 115 114 4 1 1 1 0 2 0.0
420 1 2 3 4 -1 5 5 -1 15.0 -4.367 -15.0 -4.367
430 2 7 10 4 0 12 5 0 15.0 -4.367 -15.0 -4.367
440 3 10 17 12 -1 19 13 -1 15.0 -4.367 -15.0 -4.367
450 4 15 24 12 0 26 13 0 15.0 -4.367 -15.0 -4.367
460 5 18 31 20 -1 33 21 -1 15.0 -4.367 -15.0 -4.367
470 6 23 38 20 0 40 21 0 15.0 -4.367 -15.0 -4.367
480 7 26 45 28 -1 47 29 -1 15.0 -4.367 -15.0 -4.367
490 8 31 52 28 0 54 29 0 15.0 -4.367 -15.0 -4.367
500 9 34 59 36 -1 61 37 -1 15.0 -4.367 -15.0 -4.367
510 10 39 66 36 0 68 37 0 15.0 -4.367 -15.0 -4.367
520 11 42 73 44 -1 75 45 -1 15.0 -4.367 -15.0 -4.367
530 12 47 80 44 0 82 45 0 15.0 -4.367 -15.0 -4.367

```

540	13	50	87	52	-1	89	53	-1	15.0	-4.367	-15.0	-4.367
550	14	55	94	52	0	96	53	0	15.0	-4.267	-15.0	-4.367
560	15	58	101	60	-1	103	61	-1	15.0	-4.367	-15.0	-4.367
570	16	63	108	60	0	110	61	0	15.0	-4.367	-15.0	-4.367
580	17	66	115	60	1	117	61	1	15.0	-4.367	-15.0	-4.367
590	1	7	-37.5	0.0	0.0	0.0	-37.5	0.0	0.0	0.0	0.0	0.0
600	113	7	-37.5	0.0	150.0	-37.5	0.0	150.0	0.0	150.0	0.0	0.0
610	2	7	-22.5	0.0	0.0	-22.5	0.0	0.0	0.0	0.0	0.0	0.0
620	114	7	-22.5	0.0	150.0	-22.5	0.0	150.0	0.0	150.0	0.0	0.0
630	3	7	-7.5	0.0	0.0	-7.5	0.0	0.0	0.0	0.0	0.0	0.0
640	115	7	-7.5	0.0	150.0	-7.5	0.0	150.0	0.0	150.0	0.0	0.0
650	4	7	0.0	0.0	0.0	0.0	0.0	0.0	0.0	0.0	0.0	0.0
660	116	7	0.0	0.0	150.0	0.0	0.0	150.0	0.0	150.0	0.0	0.0
670	5	7	7.5	0.0	0.0	7.5	0.0	0.0	0.0	0.0	0.0	0.0
680	117	7	7.5	0.0	150.0	7.5	0.0	150.0	0.0	150.0	0.0	0.0
690	6	7	22.5	0.0	0.0	22.5	0.0	0.0	0.0	0.0	0.0	0.0
700	118	7	22.5	0.0	150.0	22.5	0.0	150.0	0.0	150.0	0.0	0.0
710	7	7	37.5	0.0	0.0	37.5	0.0	0.0	0.0	0.0	0.0	0.0
720	119	7	37.5	0.0	150.0	37.5	0.0	150.0	0.0	150.0	0.0	0.0
730	1	2	0	1	1	0	1	1	0	1	0	0
740	2	6	0	1	1	1	0	1	1	0	1	0
750	3	114	0	1	1	0	0	1	1	0	1	0
760	4	118	0	1	1	0	0	1	1	0	1	0
770	1	200000	0.0	787401.5748	0.27	7.85	0.00001					
780	1	12.85000	603.02004	10573.4000	595.71665	0.0						
790	1	1.0	1.71132	1.0	1.0	1.0	0.0	0.0	0.0	0.0	0.0	0.0
800	2	2	3.34375	0.06966	6608.36458	0.0						
810	2	1.2	2400.0	1.0	1.0	1.0	0.0	0.0	0.0	0.0	0.0	0.0
820	3	3	7.5	648.21734	14822.5	833.76563	0.0					
830	3	1.0	605.70682	1.0	1.0	1.0	0.0	0.0	0.0	0.0	0.0	0.0
840	4	4	4.6875	0.09766	9264.06250	0.39063	0.0					
850	4	1.2	2400.0	1.0	1.0	1.0	0.0	0.0	0.0	0.0	0.0	0.0
860	5	5	37.97460	1425.04138	5496.12104	2529.55510	3301.70121					
870	5	1.33244	4.67852	0.10117	0.66667	0.86461	0.0	0.0	0.0	1.278		
880	5	0.00239	35655.59741									
890	6	0	37.97460	1350.73881	5496.12104	2529.55510	3301.70121					
900	7	0	37.97460	1350.73881	5496.12104	2529.55510	3301.70121					
910	8	0	37.97460	1350.73881	5496.12104	2529.55510	3301.70121					
920	9	0	37.97460	1350.73881	5496.12104	2529.55510	3301.70121					
930	1	29	0.0	30.0	0.0	2038.0	0.0	0.0	0.0	0.0	-15.0	0.0



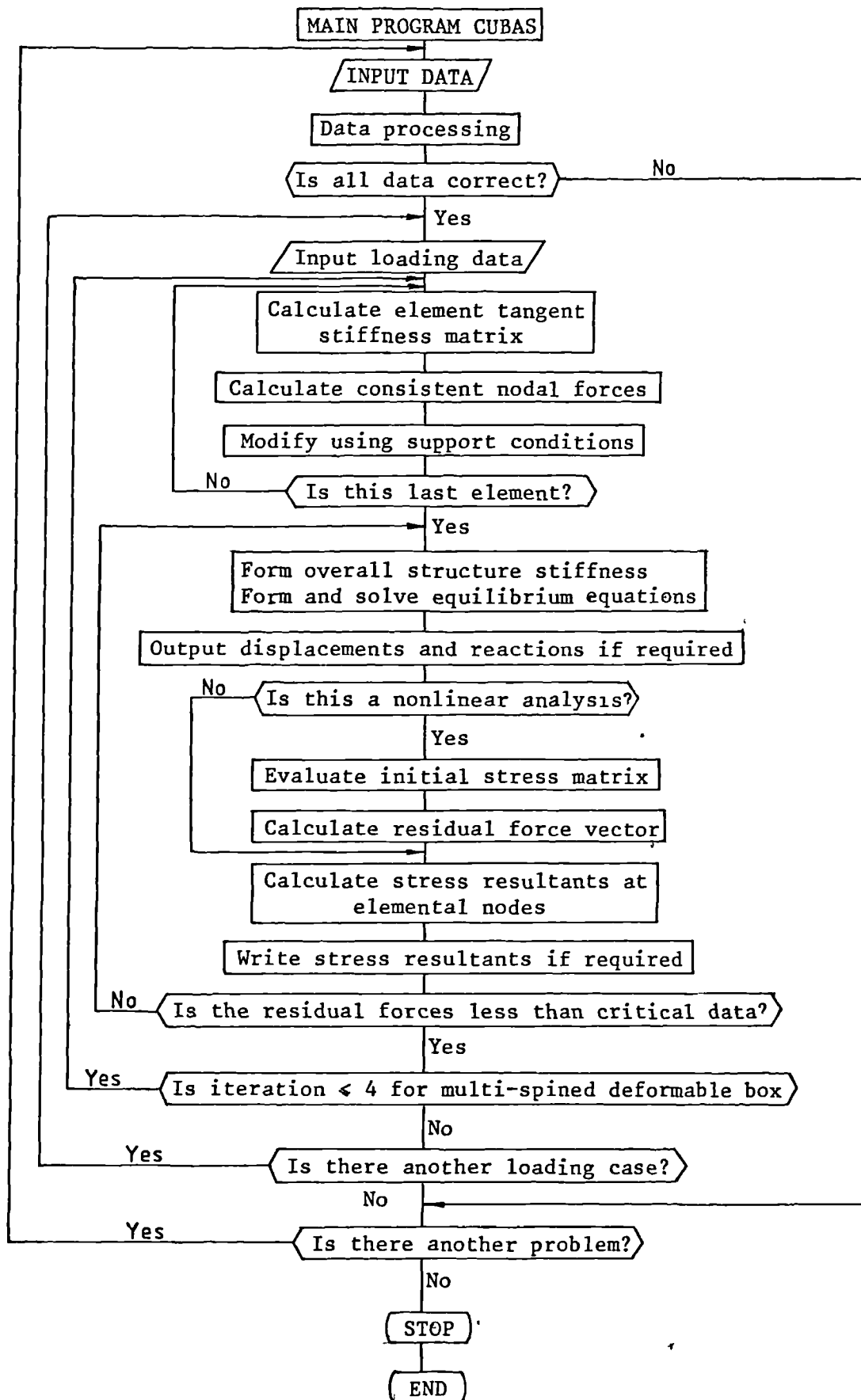


Fig. A.1 Flow diagram of the general computing procedure

## APPENDIX II DATA INPUT TO COMPUTER PROGRAM PFRAN

The plane frame analysis program PFRAN, is written as a supplement of the main analysis computer program, CUBAS, for calculating the distortional sectional properties and for obtaining the influence values of the Vierendeel frame of the box-section considered. The theoretical basis of the program is the plane frame stiffness method and related parts included in the thesis.

The necessary information required for resolving the problem is described by the following sequence of cards, and note that completely free-format is actually available for the present code of program:

1. Problem Card (I5) — One card

Columns	1-5	NRPROB	Total number of problems to be solved in one run
---------	-----	--------	---

2. Loading Case Card (I5) — Begin each new problem data with a new loading case card

Columns	1-5	LCASE	Total number of different loading cases to be solved
---------	-----	-------	---

3. Title Card (A80) — One card

Columns	1-80	ITITLE	Title of the loading case - limited to 80 alphanumeric characters
---------	------	--------	--

4. Control Card (9I5, 2F15.0) — One card

Columns	1-5	NTYPE	Thin-walled type number
		{ <370	Normal section to be analysed
		{ >370	Thin-walled section to be analysed
	6-10	NPOIN	Total number of nodes

11-15	NELEM	Total number of elements
16-20	NMATS	Total number of different materials
21-25	NSECS	Total number of different sections
26-30	M1	Node number of the top-left corner point of the box-section represented by the frame
31-35	M2	Node number of the top-right corner point of the box-section represented by the frame
36-40	M3	Node number of the bottom-left corner point of the box-section represented by the frame
41-45	M4	Node number of the bottom-right corner point of the box-section represented by the frame
46-60	Ec	Notional modulus of elasticity of the frame
61-75	GNUC	Notional Poisson's ratio of the frame.

5. Element Data Cards (5I5, F15.0)—One card for each element. Total  
of NELEM cards

columns	1-5	NUMEL	Element number
	6-10	NATNO(NUMEL)	Material property number
	11-15	NGEOM(NUMEL)	Sectional property number
	16-20	LNODS(NUMEL)	1st nodal connection number
	21-25	LNODS(NUMEL)	2nd nodal connection number
	26-40	WIDTH(NUMEL)	Width of the element

6. Node Data Cards (I5, 2F15.0)—One card for each node. Total of  
NPOIN cards

columns	1-5	NUMPO	Node number
	6-20	COORD(NUMPO,1)	x-ordinate
	21-35	COORD(NUMPO,2)	y-ordinate

7. Material Cards (I5, 2F15.0)—One card for each different material.

Total of NMATS cards

columns	1-5	NUMAT	Material identification number
	6-20	ELMAT(NUMAT,1)	Modulus of elasticity, E
	21-35	ELMAT(NUMAT,2)	Poisson's ratio, $\nu$

8. Sectional Property Cards (I5, 2F15.0)—One card for each different

section, Total of NSECS cards

columns	1-5	NUSEC	Sectional property number
	6-20	GPROP(NUSEC,1)	Cross-sectional area, A
	21-35	GPROP(NUSEC,2)	Bending moment of inertia, I

9. Boundary and Loading Control Cards (3I5)—Begin each new loading case

with a new control card

columns	1-5	NVIFX	Total number of restrained nodes
	6-10	NUPOL	Total number of nodes subjected to point loading
	11-15	IOPTION	Analytical type number
		0	Conventional frame analysis
		1	Evaluation of distortional second moment of area, $J_d$
		2	Evaluation of equivalent bending moment of inertia for the transverse grillage element across the box-section, $I_{xx}$
		3	Evaluation of equivalent shear area for the transverse grillage element across the box-section, $A_{sy}$
		4	Evaluation of distortional distribution factor, $\zeta_d$

10. Restrained Node Cards (5I5)—One card for each restrained node and total of NUFIX cards in each loading case

columns	1-5	NUFIX	Sequence number
	6-10	NOFIX(NUFIX)	Restrained node number
	11-15	IFPRE(NUFIX,1)	x-translation boundary condition
	16-20	IFPRE(NUFIX,2)	y-translation boundary condition code
	21-25	IFPRE(NUFIX,3)	z-rotation boundary condition code
		$\left\{ \begin{array}{l} 0 \\ 1 \end{array} \right.$	$\left\{ \begin{array}{l} \text{free displacement (or rotation) component} \\ \text{fixed displacement (or rotation) component} \end{array} \right.$

11. Concentrated Load Cards (2I5, 3F15.0)—One card for each nodal point load and total of NUPOL cards in each loading case

columns	1-5	JUPOL	Sequence number
	6-10	NPNOD(JUPOL)	Node number subjected to concentrated point load
	11-25	PCOMP(JUPOL,1)	Load component in x-direction
	26-40	PCOMP(JUPOL,2)	Load component in y-direction
	41-55	PCOMP(JUPOL,3)	Moment about the z-axis

Note that the x, y axes are regarded as the global axes located at the plane of the frame, and the z axis is normal to the frame plane. Note also that the sign convention of the output internal forces follows that adopted in the conventional displacement method. It states that tensile axial forces are defined as positive, and end moments and shear forces which tend to rotate the element clockwise are assumed to be positive (Fig.A.2)



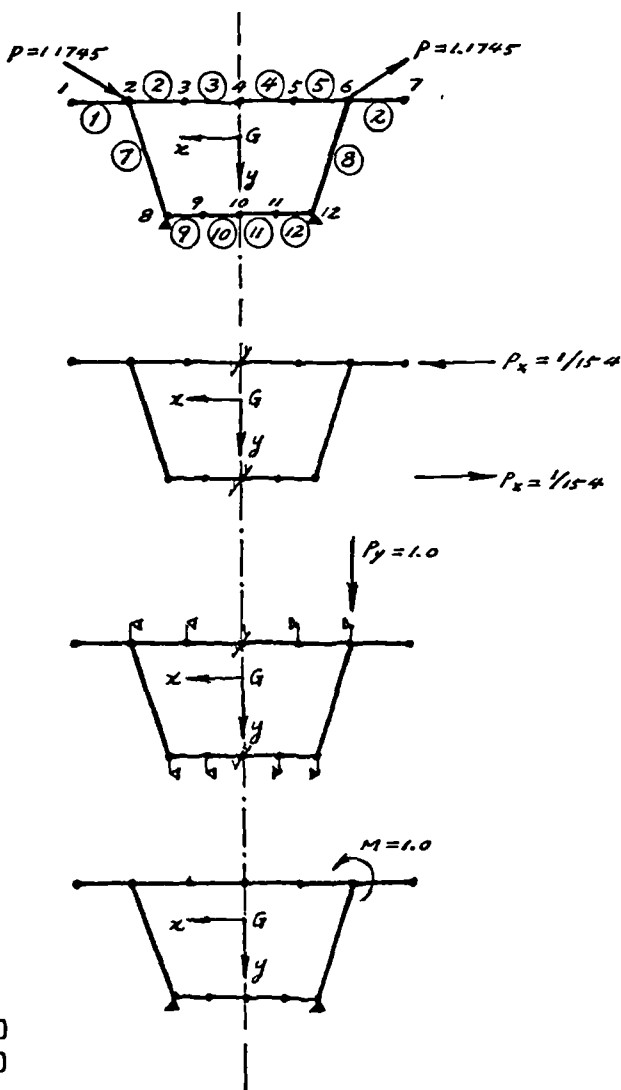
Fig. A.2 Positive internal forces

Data input example:

```

10 1
20 4
30 SECTIONAL PROPERTIES OF A TWIN-BOX MODEL FOR DISTORTION
40 390 12 12 1 2 2 6 8 12 2000000.0 0.270
50 1 1 1 1 2 1.0
60 2 1 1 2 3 1.0
70 3 1 1 3 4 1.0
80 4 1 1 4 5 1.0
90 5 1 1 5 6 1.0
100 6 1 1 6 7 1.0
110 7 1 2 2 8 1.0
120 8 1 2 6 12 1.0
130 9 1 2 8 9 1.0
140 10 1 2 9 10 1.0
150 11 1 2 10 11 1.0
160 12 1 2 11 12 1.0
170 1 22.5 -4.367
180 2 15.0 -4.367
190 3 7.5 -4.367
200 4 0.0 -4.367
210 5 -7.5 -4.367
220 6 -15.0 -4.367
230 7 -22.5 -4.367
240 8 10.0 11.033
250 9 5.0 11.033
260 10 0.0 11.033
270 11 -5.0 11.033
280 12 -10.0 11.033
290 1 2000000.0 0.270
300 1 0.5 0.010416667
310 2 0.3 0.00225
320 2 2 1
330 1 8 1 1 0
340 2 12 1 1 0
350 1 2 -1.0 0.616 0.0
360 2 6 -1.0 -0.616 0.0
370 2 2 2
380 1 4 1 1 1
390 2 10 1 1 1
400 1 6 0.064935064 0.0 0.0
410 2 12 -0.064935064 0.0 0.0
420 10 1 3
430 1 2 1 0 0
440 2 3 1 0 0
450 3 4 1 1 1
460 4 5 1 0 0
470 5 6 1 0 0
480 6 8 1 0 0
490 7 9 1 0 0
500 8 10 1 1 1
510 9 11 1 0 0
520 10 12 1 0 0
530 1 6 0.0 1.0 0.0
540 2 1 4
550 1 4 1 1 0
560 2 10 1 1 0
570 1 6 0.0 0.0 1.0

```



*APPENDIX III Sectional Property Formulae for a Trapezoidal Single-Cell  
Box-Section*

For the cross-section of a box beam shown in Fig. A.3, some of the sectional properties with references to the warping torsion and distortion are expressed as follows:

1. Shear centre

The position of the shear centre determined by the distance from the centre line of the top flange is

$$y_s = \frac{h}{I_{yy}} \frac{\left( \frac{h_c b_b}{t_h} - \frac{b_b t_t}{2t_b} - \frac{b_t^2}{2t_t} \right) \left[ (b_t + 2b_b) \frac{h_c t_h}{12} + \frac{b_b^2 t_b}{12} \right] + \frac{b_t}{8} (b_t + b_b) \left[ \frac{h_c t_t}{t_t} (b_t + b_b) - \frac{b_t^2}{6} + \frac{1}{2} b^2 + \frac{b_b^2 t_b}{3t_t} \right]}{\left( \frac{b_b}{2t_b} + \frac{b_t}{2t_t} + \frac{h_c}{t_h} \right)} \quad (A1)$$

where  $b = b_t + 2b_c$

For a rectangular cross-section, Eq. A1 can be simplified as

$$y_s = \frac{b_t^2 h}{I_{yy}} \left[ \frac{K_1 + K_2 + K_3 + K_4}{K_5} \right] \quad (A2)$$

where  $K_1 = \frac{1}{4} b_t t_b t_h \left( \frac{1}{3} b_t t_b + 3h \cdot t_h \right)$

$$K_2 = b_t h t_t \left( \frac{1}{6} t_b^2 - \frac{1}{4} t_h^2 \right) \quad (A3)$$

$$K_3 = \frac{1}{2} t_t t_b t_h \left( \frac{1}{6} b_t^2 + h^2 \right)$$

$$K_4 = b_c t_t t_b t_h (b_c + b_t)$$

$$K_5 = b_t t_h (t_t + t_b) + 2h t_t t_b$$

2. Torsional moment of inertia  $J_T$

$$J_T = \frac{1}{3} (b t_t^3 + 2h_c t_h^3 + b_b t_b^3) + \frac{(b_t + b_b)^2 h^2}{\frac{b_t}{t_t} + \frac{b_b}{t_b} + \frac{2h_c}{t_h}} \quad (A4)$$

3. Normalized torsional warping function  $\hat{\omega}_I$ 

$$\hat{\omega}_{I,1} = 0$$

$$\hat{\omega}_{I,2} = \frac{y_s}{2} b_t - \frac{1}{2} \frac{b_t}{t_t} \bar{q}_B$$

$$\hat{\omega}_{I,3} = \frac{y_s}{2} b - \frac{1}{2} \frac{b_t}{t_t} \bar{q}_B \quad (A5)$$

$$\hat{\omega}_{I,4} = \frac{y_s}{2} b_b + \frac{h}{2} b_t - \left( \frac{b_t}{2t_t} + \frac{h_c}{t_h} \right) \bar{q}_B$$

$$\hat{\omega}_{I,5} = 0$$

where

$$\bar{q}_B = \frac{(b_t + b_b)h}{\frac{b_t}{t_t} + \frac{b_b}{t_b} + \frac{2h_c}{t_h}} \quad (A6)$$

4. Normalized distortional warping function  $\omega_{II}$ 

$$\omega_{II,1} = 0$$

$$\omega_{II,2} = - \frac{hb_t^2 b_b}{2(b_t + b_b)(\beta b_t + b_b)}$$

$$\omega_{II,3} = - \frac{hb_t b_b b}{2(b_t + b_b)(\beta b_t + b_b)} \quad (A7)$$

$$\omega_{II,4} = \frac{\beta hb_t^2 b_b}{2(b_t + b_b)(\beta b_t + b_b)}$$

$$\omega_{II,5} = 0$$

where

$$\beta = \frac{\alpha_0^3 b_t^2 t_t + 2h_c t_h (b_t + \frac{b_b}{2})}{b_b^2 t_b + 2h_c t_h (b_b + \frac{b_t}{2})} \quad (A8)$$

and

$$\alpha_0 = b/b_t$$

### 5. Torsional and distortional warping moments of inertia $J_I, J_{II}$

By using Simpson's integration method we obtain the following formulae:

$$J_I = \frac{2}{3} t_t [b_c (\hat{\omega}_{I,2} \cdot \hat{\omega}_{I,3} + \hat{\omega}_{I,3}^2) + \frac{b}{2} \hat{\omega}_{I,2}^2] + \frac{2}{3} t_h h_c (\hat{\omega}_{I,2}^2 + \hat{\omega}_{I,4}^2 + \hat{\omega}_{I,2} \cdot \hat{\omega}_{I,4}) + \frac{1}{3} t_b b_b \hat{\omega}_{I,4}^2 \quad (A9)$$

and

$$J_{II} = \frac{1}{3} b t_t \omega_{II,3}^2 + \frac{2}{3} t_h h_c (\omega_{II,2}^2 + \omega_{II,4}^2 + \omega_{II,2} \cdot \omega_{II,4}) + \frac{1}{3} t_b b_b \omega_{II,4}^2 \quad (A10)$$

### 6. Distortional second moment of area $J_d$

$$J_d = \frac{24 I_h}{\eta_h} \quad (A11)$$

where

$$\eta = \frac{2}{h} \cdot \frac{b_t^3 b_b + 2h_c b_t^3 \frac{I_b}{I_h} + 2h_c b_b b_t^2 \frac{I_t}{I_h} + 3b_t^2 h_c^2 \frac{I_t I_b}{I_h}}{\frac{I_b}{I_h} b_t^3 + \frac{I_t}{I_h} b_b^3 + 2h_c (b_t^2 + b_t b_b + b_b^2) \frac{I_t I_b}{I_h^2}} \quad (A12)$$

in which  $I_t$ ,  $I_b$  and  $I_h$  are the plate bending moments of inertia per unit length of the top flange, bottom flange and webs respectively.

### 7. Central second moment of area $J_c$

$$J_c = y_s^2 t_t b + \frac{1}{2} \frac{t_h}{h_c} [b_t (h - y_s) + b_b y_s]^2 + (h - y_s)^2 t_b b_b \quad (A13)$$

### 8. Warping shear parameter $\mu_t$

$$\mu_t = 1 - \frac{J_g}{J_c} \quad (A14)$$

where

$$J_g = \frac{(b_t + b_b)^2 h^2}{\frac{b_t}{t_t} + \frac{b_b}{t_b} + \frac{2h_c}{t_h}} \quad (A15)$$

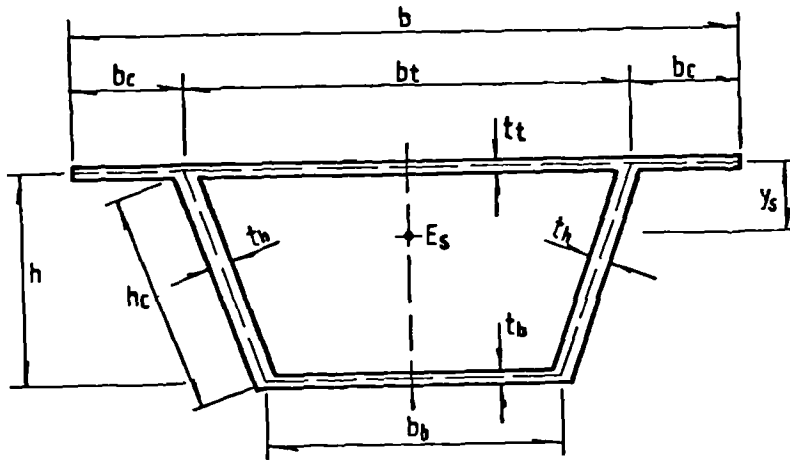


Fig. A.3 Trapezoidal single-cell box-section

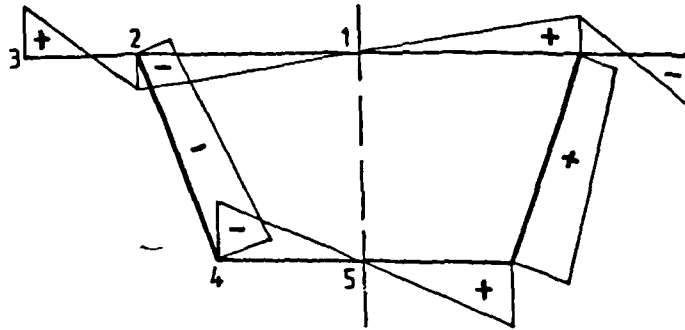


Fig. A.4 Normalized torsional warping function  $\hat{\omega}_I$

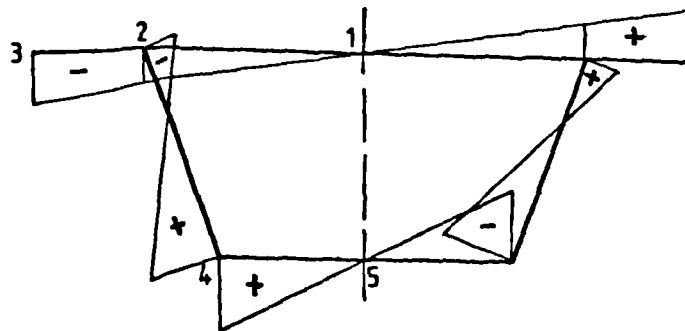


Fig. A.5 Normalized distortional warping function  $\omega_{II}$